

# REPORT DOCUMENTATION PAGE

Form Approved  
OMB No. 0704-0188

Public reporting burden for this collection of information is estimated to average 1 hour per response, including the time for reviewing instructions, searching existing data sources, gathering and maintaining the data needed, and completing and reviewing the collection of information. Send comments regarding this burden estimate or any other aspect of this collection of information, including suggestions for reducing this burden, to Washington Headquarters Services, Directorate for Information Operations and Reports, 1215 Jefferson Davis Highway, Suite 1204, Arlington, VA 22202-4302, and to the Office of Management and Budget, Paperwork Reduction Project (0704-0188), Washington, DC 20503.

1. AGENCY USE ONLY (Leave blank) 2. REPORT DATE 3. REPORT TYPE AND DATES COVERED  
FINAL REPORT 20 Feb 94 - 19 Feb 97

4. TITLE AND SUBTITLE  
HTS FILMS AND MULTILAYERS FOR ELECTRONICS

5. FUNDING NUMBERS

6. AUTHOR(S)  
Dr Talvacchio

61102F  
2305/GS

7. PERFORMING ORGANIZATION NAME(S) AND ADDRESS(ES)

Northrop Grumman Corporation  
Science and Technology Center  
1350 Beulah Road  
Pittsburgh, PA 15235-5098

AFOSR-TR-97

0304

8. FORMERLY WESTINGHOUSE ELECTRIC CORPORATION

9. SPONSORING/MONITORING AGENCY NAME(S) AND ADDRESS(ES)

AFOSR/NE  
110 Duncan Avenue Suite B115  
Bolling AFB DC 20332-8050

10. SPONSORING/MONITORING  
AGENCY REPORT NUMBER

PA9420-04-C-0021

11. SUPPLEMENTARY NOTES

19971002 083

12a. DISTRIBUTION/AVAILABILITY STATEMENT

12b. DISTRIBUTION CODE

APPROVED FOR PUBLIC RELEASE: DISTRIBUTION UNLIMITED

This program established a materials and fundamental device base for an integrated circuit fabrication process for HTS digital electronics based on edge SNS Josephson junctions. The process was qualified by demonstration of small-scale single flux quantum (SFQ) logic circuits fabricated for the first time in an extendible configuration which integrated junctions and HTS groundplanes. Junction materials properties were investigated which affect the reproducibility of critical currents and, ultimately, the scale of circuit integration. Materials properties included the cumulative roughness of multilayer film structures, oxygen mobility in junction electrodes, second-phase precipitates, and crystalline orientation of junction edges. Processing steps investigated in detail included film deposition techniques, parameters, and composition; ion milling angles, gas compositions, and edge profiles; film edge morphology, cleaning, and film coverage; groundplanes over and under junctions; groundplane oxidation and magnetic penetration depths; and use of epitaxial buffer layers, protective cap layers, and low-loss insulations. Technology developed under this program was transferred to an Air Force WL/ML program where the junctions were optimized with critical current spreads reduced from 1-sigma values of 30% early in the program to 12% by the program's conclusion. Progress is also reported on tasks which address problems fundamental to the understanding of the superconducting state in HTS films, the application of HTS films in passive microwave circuits, and the development of new superconducting devices.

17. SECURITY CLASSIFICATION  
OF REPORT

UNCLASSIFIED

18. SECURITY CLASSIFICATION  
OF THIS PAGE

UNCLASSIFIED

19. SECURITY CLASSIFICATION  
OF ABSTRACT

UNCLASSIFIED

20. LIMITATION OF ABSTRACT

NSN 7540-01-280-5500

Standard Form 298 (Rev. 2-89)  
Prescribed by ANSI Std. Z39-18

# **HTS FILMS AND MULTILAYERS FOR ELECTRONICS**

**John Talvacchio  
Cryoelectronics**

**Final Report for the Period  
February 20, 1994 to February 19, 1997**

AFOSR Contract No. F49620-94-C-0021  
Research Sponsored by the  
Air Force Office of Scientific Research  
Air Force Systems Command  
United States Air Force

April 10, 1997

Approved for public release, distribution unlimited

**Northrop Grumman STC  
1350 Beulah Road  
Pittsburgh, Pennsylvania 15235-5080**

## **1. FINAL REPORT: HTS FILMS AND MULTILAYERS FOR ELECTRONICS**

February 20, 1994 to February 19, 1997

AFOSR Contract No. F49620-94-C-0021

John Talvacchio

## 2. ABSTRACT

This program established a materials and fundamental device base for an integrated circuit fabrication process for HTS digital electronics based on edge SNS Josephson junctions. The process was qualified by demonstration of small-scale single flux quantum (SFQ) logic circuits fabricated for the first time in an extendible configuration which integrated junctions and HTS groundplanes. Junction materials properties were investigated which affect the reproducibility of critical currents and, ultimately, the scale of circuit integration. Materials properties included the cumulative roughness of multilayer film structures, oxygen mobility in junction electrodes, second-phase precipitates, and crystalline orientation of junction edges. Processing steps investigated in detail included film deposition techniques, parameters, and composition; ion milling angles, gas compositions, and edge profiles; film edge morphology, cleaning, and film coverage; groundplanes over and under junctions; groundplane oxidation and magnetic penetration depths; and use of epitaxial buffer layers, protective cap layers, and low-loss insulators. Technology developed under this program was transferred to an Air Force WL/ML program where the junctions were optimized with critical current spreads reduced from 1-sigma values of 30% early in the program to 12% by the program's conclusion. Progress is also reported on tasks which address problems fundamental to the understanding of the superconducting state in HTS films, the application of HTS films in passive microwave circuits, and the development of new superconducting devices.

### **3. OBJECTIVES**

The overall objective of this program was to develop a materials and fundamental device base for high-transition-temperature superconducting (HTS) electronics capable of operation at temperatures  $>50K$ . The fundamental physics and materials science of superconductors were investigated to enhance their properties for application in passive devices based on transmission line structures, active devices based on Josephson junctions, and novel active device structures based on the unique properties of superconductors.

The specific objectives of the Northrop Grumman-AFOSR program are described in the following program tasks:

1. Search for thin-film superconductors with enhanced  $T_c$ s and other superconducting properties.
2. Determine the fundamental lower limit of HTS rf surface resistance.
3. Investigate epitaxial multilayers, including Josephson junctions, incorporating deposited insulators and normal conductors with HTS films.
4. Develop materials and processing for alternative HTS devices.

## 4. ACCOMPLISHMENTS

### 4.1 PREAMBLE

The research reported here was performed under a three-year Northrop Grumman-AFOSR program which began February 20, 1994. This section presents an overview of the significant accomplishments. More detailed descriptions are available in the published scientific papers that were generated by this program. These papers are listed by title in Section 5, reproduced in the appendices, and are referenced in the following sections.

### 4.2 ENHANCED SUPERCONDUCTING FILM PROPERTIES

The work on this task focused on tailoring superconducting film properties to optimize the performance of critical HTS electronic devices.

#### **Growth of Ca, Co, and Pr-Doped YBCO Films for SNS Junction Normal Layers**

The ideal normal-conducting coupling material for SNS junctions fabricated with YBCO electrodes would have a similar structure, normal-state conductivity, chemical stability, dependence on oxygen content, and thermal expansion match to YBCO. We joined with several other laboratories in recent years in exploring the use of  $\text{PrBa}_2\text{Cu}_3\text{O}_7$  for these reasons. However, relatively light cation doping of YBCO provides a better match than complete substitution of Pr for Y. Following this approach, we investigated Pr-doped, Ca-doped, and Co-doped YBCO films for normal-conducting barriers. Films of all three materials were optimized for sharp superconducting transitions, narrow spread in crystal lattice constant, and minimum normal-state resistivity by adjusting the growth parameters of temperature, rate, and oxygen partial pressure. The film technology was

transferred to an Air Force Wright Laboratory program where SNS edge junctions were fabricated.<sup>26</sup>

Doping levels for the Ca, Co, and Pr-doped YBCO systems were set to reduce  $T_c$  to 55-60K. At these relatively low doping levels, the normal-state resistivity is comparable to that of YBCO while junctions could operate in the range of 65-77K. The lowest resistivity,  $\rho(77K) = 80 \mu\Omega\text{-cm}$ , which implies the longest coherence length, was obtained for  $Y_{0.7}Ca_{0.3}Ba_2Cu_3O_{7.5}$ . The highest resistivity,  $\sim 400 \mu\Omega\text{-cm}$ , was found for  $YBa_2Cu_{2.79}Co_{0.21}O_{7.5}$ . Junctions made with 0 Å, 100 Å, 250 Å, 400 Å, and 550 Å thick doped YBCO barriers had critical current densities and  $I_cR_n$  products that were shown to scale exponentially with barrier thickness as expected for proximity-effect coupling.<sup>27</sup> Junction resistance was highest for Co-doped barriers, followed by Pr-doped and Ca-doped barriers in agreement with their relative normal-state resistivity values.<sup>26</sup>

In our most recent experiments, doped YBCO N-layers and SNS edge junctions grown by pulsed laser deposition (PLD) were compared with results obtained with sputtered films. Although films of the PLD N-layers could be grown with sharper superconducting transitions indicative of a more homogeneous dopant distribution, the junction results were surprisingly similar.<sup>32</sup>

### **Properties of High-Oxygen-Stability YBCO Films for Junction Electrodes**

Doped YBCO films were investigated for junction electrodes as well as for junction barriers. The objective is to determine whether the high oxygen mobility in YBCO is related to large spreads in critical currents from junction to junction. We worked with a group at the University of Texas to show that Y-Ca-Ba-La-Cu-O (YCBLO) has excellent corrosion resistance.<sup>18,21</sup> In 1995, we grew epitaxial thin films of this compound and measured oxygen diffusion rates by two techniques for comparison with undoped YBCO. Both in-furnace resistivity measurements to monitor time-dependent changes in oxygen concentration at 400-600°C and room temperature electromigration measurements showed lower oxygen mobility in

YCBLCO than in YBCO. In 1996, we fabricated SNS junctions with YCBLCO electrodes and published our results.<sup>24,26</sup> Nearly ideal RSJ-type I-V characteristics were obtained and high  $I_c R_n$  products of 500  $\mu$ V at 65K were measured. YCBLCO base electrodes were not as smooth as standard YBCO and film roughness was thought to be a more important factor in determining junction reproducibility than oxygen stability.

Even for standard YBCO SNS edge junctions, the smoothness of junction electrodes correlated more strongly with junction reproducibility than does any other film property. We routinely used an atomic force microscope (AFM) for both qualitative and quantitative analysis of film roughness. The best YBCO surfaces had an rms roughness of 10  $\text{\AA}$  on 2000  $\text{\AA}$  thick films - better than any numbers found in the literature. An understanding of the surface dynamics which lead to these smoothest films would have an immediate and substantial technological impact if it led to routine growth of such smooth films.

### **Yttria Nanoparticles in YBCO Films**

We have observed by x-ray diffraction measurements that many of the smoothest YBCO films have a small volume fraction of yttria,  $\text{Y}_2\text{O}_3$ , on the order of 1%, even though they were grown with stoichiometric YBCO sputtering targets. The x-ray measurements show that the particles tend to be small, on the order of 40-50  $\text{\AA}$  in diameter, and epitaxially oriented with the YBCO matrix in which they grow. We worked with NRL to study YBCO films that were intentionally produced with excess yttria to confirm the crystalline orientation by TEM.<sup>23</sup> However, when we grew films from  $\text{Y}_{1+x}\text{Ba}_2\text{Cu}_3\text{O}_{7.8}$  with  $x=0.10$  and 0.25, a-axis-oriented YBCO grains tended to nucleate and roughen the surface. Ultimately, the best approach was to start from a stoichiometric target and to use deposition parameters that resulted in an effective  $x \sim 0.01$ . At this small volume fraction of yttria, it is possible to obtain smooth films with high  $J_c (>>10^6 \text{ A/cm}^2 \text{ at 77K})$  and low  $R_s(77\text{K}, 10 \text{ GHz}) < 0.5 \text{ m}\Omega$ .

It is worthwhile to consider a possible role for yttria in the anomalously high junction resistances we have measured in our SNS edge junctions. The high resistance is desirable for circuit applications, particularly since such junctions were just as reproducible as low-resistance junctions, but the origin of the excess resistance is not understood. We have collaborated with researchers from Argonne National Laboratory to examine with TEM whether yttria tends to concentrate at the S-N interfaces, although none were observed in the few samples measured in this way.<sup>26</sup> This model of yttria nanoparticles at the S-N interfaces is still one of several that we consider as the key to understanding junction resistances

### **Overdoping of Oxygen in YBCO Films**

We perceived that there was resistance in the technical community to the idea that  $\text{YBa}_2\text{Cu}_3\text{O}_{7,\delta}$  films could easily be overdoped with oxygen so we followed up on some initial observations and published data on the effects of oxygen content in the range of  $\delta = 0$  to 0.1. Our data and discussion of the effects on  $T_c$ , rf surface resistance,  $R_s$ , and normal-state resistivity were published in *IEEE Trans. on Applied Superconductivity*.<sup>8</sup> It is now clear from data in the literature on YBCO single crystals that there is no significant difference in the effects of overdoping on bulk samples vs. thin films - only the means for characterizing samples in these configurations are different.

### **BKBO Films and Tunnel Junctions**

This study began under previous AFOSR programs at Northrop Grumman and at Carnegie Mellon University. The investigation was completed during the first year of the current program. Results on film growth, tunneling studies, and all-BKBO junction formation were published. An article reviewing all aspects of this material that differentiate it from other high- $T_c$  superconductors was published in the *Journal of Superconductivity*.<sup>11</sup>

### 4.3 RF SURFACE RESISTANCE

The research done under this task was directed toward gaining an understanding of the critical factors which determine the rf surface resistance,  $R_s$ , in YBCO and relatedly in other oxide superconductors. From research performed on an earlier AFOSR/Northrop Grumman program, we found that neither an optimum  $T_c > 90K$ , or  $J_c$  was a sufficient indicator that a YBCO film would have a low rf surface resistance,  $R_s(77K, 10 \text{ GHz}) \leq 0.5 \text{ m}\Omega$ . We did find microstructural features that characterized low- $R_s$  films.<sup>31</sup> During this program, we examined the factors that affect reproducibility of both  $R_s$  and film microstructure, and the ultimate lower limit of  $R_s$  at temperatures of practical interest.

#### Optimized Anneal for Low rf Surface Resistance

Bormann and Hammond observed several years ago that the highest  $T_c$  and  $J_c$  YBCO films produced by any vapor deposition technique formed near the decomposition line in the oxygen partial phase diagram. Our measurements of  $R_s$  indicate that the same conditions of oxygen partial pressure and film growth temperature minimize  $R_s$ . For YBCO film growth on substrates large enough for technological interest,  $\geq 2$  inches in diameter, oxygen partial pressure can be controlled to within 0.5% but wafer temperature during growth is not only more difficult to measure, but is subject to significantly larger changes due to varying extents of coverage by previously patterned film layers and changes in emissivity from accumulation of a deposit.

Based on this assumption that inadequate temperature control during film growth is the most important factor in reproducibility of  $R_s$ , we initiated a series of experiments in which the  $R_s$  of YBCO films grown on large wafers was measured non-destructively immediately after growth and then after an anneal at the decomposition line in the phase diagram in a tube furnace where temperature and oxygen pressure could both be well-controlled. It was discovered that the  $R_s$  of single-phase YBCO films were always improved by the anneal if (1) the as-deposited film did not already have a low  $R_s(77K, 10 \text{ GHz}) < 0.5 \text{ m}\Omega$  and (2) the film was truly

single phase without the presence of copper oxide precipitates which are often observable on the surface of YBCO films with desirable superconducting properties. This well-controlled annealing step has been implemented in the Northrop Grumman microwave component programs.<sup>16</sup>

### **RF Power-Dependence of Surface Resistance**

One of the Northrop Grumman HTS microwave programs is a DARPA-funded TRP performed in collaboration with STI. In addition to films with low rf surface resistance, the three applications which are being addressed in the TRP program require films with a highly linear rf response to provide high dynamic range. Whereas the TRP program is being used to quantify and measure the required *device* linearity in terms of third-order intermodulation and intercept (TOI), the AFOSR/Northrop Grumman program is being used to measure the rf power dependence of unpatterned YBCO *films*.

Preliminary results under the AFOSR / Northrop Grumman program indicated that copper-oxide precipitates which are often present in YBCO films contribute to intermodulation products even at low power (<1 dBm). High power amplifiers which will permit measurements to be made up to 20 W have been purchased by Northrop Grumman for high-power measurements in 1997. High-power measurements (to 10 dBm) made at STI showed that YBCO films deposited by sputtering at Northrop Grumman have good high-power properties in comparison with other films but the STI measurements are not quantifiable in terms of third-order intermodulation products. When the high-power TOI measurements are in operation at Northrop Grumman, we plan to exchange samples and data with Air Force Rome Labs.

### **In-Plane Isotropy of rf Surface Resistance**

The d-wave pairing model for superconductivity in YBCO predicts anisotropy in reciprocal space in the a-b plane. We discussed with several theorists the

possibility that there could be anisotropy in real space detectable by measurement of  $R_s$  as a function of the direction of rf currents. Although this possibility is counter to conventional views of electronic structure of solids, we were encouraged to proceed with a measurement.

Neither our standard technique for measurement of  $R_s$ , a dielectric/HTS resonator, nor the microwave devices we have produced under other programs was suitable for this measurement since rf currents could not be oriented in specific directions. However, use of the lowest order mode in a parallel-plate resonator with epitaxial films on rectangular substrates permitted the direction of rf current flow to be unambiguously oriented with respect to the crystalline structure of the substrate and film. We measured  $R_s$  as a function of temperature on  $1/4 \times 1/2$  inch samples cut from a YBCO-coated 2-inch diameter single-crystal wafer with sample edges aligned with either [100] or [110] directions. Although there was some variation in  $R_s$  from one 2-inch wafer to another, no difference was observed for samples cut along different directions from any particular wafer.<sup>16</sup> A practical implication of this result is that microwave device structures do not need to be patterned in alignment with specific YBCO crystalline directions.

#### 4.4 EPITAXIAL FILMS AND LAYERED STRUCTURES

Multilayer film structures are required for any application of HTS materials in digital electronics and for many analog devices. The minimum multilayer structure for high-speed Josephson digital circuits is a configuration with junctions and SQUID loops over a ground plane to keep SQUID inductances low. In 1995, we became the first laboratory to demonstrate 77K junctions, SQUIDs, and SFQ circuits fabricated on integrated ground planes.<sup>13</sup> During the remainder of the program, we extended that capability from a step-edge grain-boundary junction technology to edge SNS junctions which show more promise for large-scale integration.<sup>15,28</sup>

### **Integrated Circuit Process for Edge SNS Junctions**

We developed an HTS digital integrated circuit fabrication process based on edge SNS junctions which used six epitaxial film layers and six mask levels.<sup>4,26</sup> The process was successfully applied to fabrication of small-scale circuits ( $\leq 10$  junctions). Circuit design and test were performed under another US Government program. The circuits included basic building blocks for analog to digital converters and signal processing such as an R/S flip-flop, toggle flip-flop, quantizer, and 1-bit A/D converter (the quantizer and T-flip-flop together).<sup>25</sup> Average voltage measurements indicated that the toggle flip-flop operated at 15 GHz.

The most important considerations in developing our HTS integrated circuit process were the reproducibility of YBCO-based SNS junctions, the low inductance provided by an integrated YBCO ground plane, and electrical isolation by  $\text{SrTiO}_3$  or  $\text{Sr}_2\text{AlTaO}_6$  ground-plane and junction insulator layers. Some of the critical processing parameters identified by electrical measurements, TEM, SEM, and AFM were control of second-phase precipitates in YBCO, oxygen diffusion, Ar ion-milling parameters, and preparation of surfaces for subsequent high-temperature depositions.<sup>26</sup>

### **Edge SNS Junction Reproducibility**

Northrop Grumman, Conductus, and TRW collaborated on HTS integrated circuit development. Technology developed under this program was transferred to the joint effort. We agreed with Government representatives from the Air Force, Navy, DARPA, and other non-DoD agencies to meet a milestone schedule for junction reproducibility that called for improvements in the one-sigma spread of junction critical currents from the value of 30% achievable in early 1995. We reached the milestone of  $1\sigma = 20\%$  by the end of 1995,<sup>19,27</sup> and  $1\sigma = 15\%$  by the end of 1996. Individual 20-junction test chips have shown spreads as low as 10%, the level where circuits dense enough for technological interest could be fabricated successfully.

The edge SNS junctions we produced were configured in low-inductance SQUIDs. To achieve the low inductances required for SFQ circuits, on the order of 5 pH, SQUIDs were generally grown on top of an HTS ground plane. The period of voltage modulation due to injection of current from a control line was measured as a function of temperature. Microstrip inductances obtained from these measurements gave us the inductance per square of conductor, the parameter needed to design SQUIDs for SFQ. They also allowed us to infer the magnetic penetration depth of YBCO films. Total SQUID inductance measured from  $I_c$  modulation was used to evaluate novel low-inductance configurations.<sup>15,28</sup>

In some cases, we found that junction reproducibility was better for junctions grown directly on a substrate when compared with those grown on an HTS ground plane and epitaxial ground-plane insulator. So, we fabricated some sets of junctions with ground planes on top.<sup>22</sup> These successful experiments will leave circuit designers with an additional degree of freedom.

Some of the junction fabrication parameters that we investigated were mentioned in Section 4.2 for cases where we used film growth conditions to modify the properties of junction electrodes and N-layers. We also examined the crystalline orientation dependence of SNS junction critical currents and effects of annealing in oxygen.<sup>26</sup> We found that critical currents of SNS junctions grown on <110> edges and those grown on the same chip but on <100> edges usually had a bimodal distribution based on edge orientation. Although the spreads were comparable, we have emphasized <100> edges in subsequent work. Since either orientation has the possibility of coupling a-axis domains in one YBCO electrode to either a or b-axis domains on the other electrode on a random basis, this work is additional motivation to use tetragonal YCBLO films for junction electrodes. Based on our investigation with the Materials Directorate at Wright Laboratory of the microstructure of YBCO film grown on vicinal-cut single-crystal LaAlO<sub>3</sub> substrates,<sup>7</sup> we recommend that the effects of these modified microstructures on junction reproducibility be investigated.

## 4.5 MATERIALS AND PROCESSING FOR ALTERNATIVE HTS DEVICES

The effort under this task focused on process development and processing requirements for alternative HTS Josephson junction configurations and active HTS device alternatives to Josephson junctions. One set of processing requirements is the formation of both structural and electrical interfaces between HTS films and semiconductors, normal conductors, ferroelectrics, ferrites, etc., that couple HTS circuits with the rest of an electronic system.

### Novel Configurations for Flux-Flow Devices

HTS devices based on flux flow phenomena are potentially important for application in the electrical interface between SFQ circuits and semiconductor electronics. Although such devices can be based on either Abrikosov or Josephson vortex flow, the former type is attractive for its simplicity and based upon some data that have appeared among mixed results in the literature. We attempted to make our own, independent, assessment based on our unique device layouts and strength in depositing and patterning smooth and very thin YBCO films.<sup>9</sup>

With our final, optimized design,<sup>29</sup> we patterned Abrikosov vortex flow devices with direct-injection-current control lines. Junction I-V curves changed with injected control current, but were insensitive to magnetic field. A significant part of the experiment was successive thinning and measurement of individual devices. With this technique, we were able to change the effective penetration depth from smaller-than to larger-than the characteristic size of the structure but still observed insensitivity to magnetic field. Results were published in *IEEE Trans. on Applied Superconductivity*.<sup>29</sup>

### Alternative HTS Josephson Junction Configurations

In agreement with the other significant industrial laboratories that are developing HTS junctions for digital circuits, we have focused on edge SNS junctions as the most promising configuration for large-scale HTS digital circuits. One of the alternative configurations that merits attention is a nanoscale-bridge of

oxygen-depleted YBCO created by writing with a 120 keV electron beam in a transmission electron microscope. One of the requirements for circuit to be fabricated is that the starting YBCO film must be sufficiently free of defects that no junction will be written where a defect exists. We grew low-defect-density 500 Å thick YBCO films which were not obtainable elsewhere and sent them to SUNY Stony Brook for use in circuit demonstrations with e-beam written junctions. We also sent low-oxygen-mobility YCBLCO composition films to address problems with long-term stability.

With Argonne National Laboratory, we fabricated bicrystal junctions and found that the grain boundary in YBCO that exhibits Josephson behavior meanders across the straight boundary that was present in the bi-crystal substrate. The meander introduces randomness into the junction width.<sup>14</sup>

Northrop Grumman continues to invest in new facilities for HTS electronics. In 1994, a state-of-the-art atomic force microscope (AFM) was installed which has become a standard tool in the development of multilayer structures. A pulsed laser deposition (PLD) system was installed early in 1996 which permitted us to make direct comparisons between sputtered and laser-ablated films in devices. Although sputtered HTS films developed under this program have been the smoothest and can more readily be grown on large-area substrates than PLD films, laser ablation provides shorter turnaround times for new materials experiments. The PLD system also became a critical tool in the program we are performing for the Materials Directorate at Wright Laboratory.

## 5. PUBLICATIONS

1. M. G. Forrester, A. Davidson, J. Talvacchio, and J. R. Gavaler, "Inductance Measurements in Multilevel High-T<sub>c</sub> Step-Edge Grain Boundary SQUIDs," *Appl. Phys. Lett.* 65(14), 1835 (1994).
2. R. Sobolewski, W. Xiong, W. Kula, and J. R. Gavaler, "Laser Patterning of YBCO Thin-Film Devices and Circuits," *Appl. Phys. Lett.* 64(5), 643 (1994).
3. A. Davidson, J. Talvacchio, M. G. Forrester, and J. R. Gavaler, "High-T<sub>c</sub> Materials Expand Superconductive Circuit Applications," *Microwaves & RF* 33(4), 140 (1994).
4. J. Talvacchio, M. G. Forrester, and J. R. Gavaler, "Properties of Passive Structures for Multilayer HTS Digital Circuits," *IEEE Trans. Appl. Superconductivity* 5(2), 3139 (1995).
5. W. Kula, W. Xiong, R. Sobolewski, and J. Talvacchio, "Laser Patterning of YBCO Thin Films Protected by In-Situ Grown SrTiO<sub>3</sub> Cap Layer," *IEEE Trans. Appl. Superconductivity* 5(2), 1177 (1995).
6. M. G. Forrester, J. X. Przybysz, J. Talvacchio, J.-H. Kang, A. Davidson, and J. R. Gavaler, "A Single Flux Quantum Shift Register Operating at 65K," *IEEE Trans. Appl. Superconductivity* 5(2), 3401 (1995).
7. R. R. Biggers, M. G. Norton, I. Maartense, T. L. Peterson, E. K. Moser, D. Dempsey, M. A. Capano, J. Talvacchio, J. L. Brown, and J. D. Wolf, "Microstructure and Properties of YBCO Thin Films Grown on Vicinal LaAlO<sub>3</sub> Substrates," *IEEE Trans. Appl. Superconductivity* 5(2), 1241 (1995).
8. J. R. Gavaler, J. Talvacchio, and R. W. Weinert, "Effect of Oxygen Over-Doping on T<sub>c</sub> and R<sub>s</sub> of YBCO Films," *IEEE Trans. Appl. Superconductivity* 5(2), 1173 (1995).
9. A. Davidson and N. F. Pedersen, "Discrete Models of Abrikosov Vortex Flow Transistors," *IEEE Trans. Appl. Superconductivity* 5(2), 3373 (1995).
10. D. J. Miller, T. A. Roberts, J. H. Kang, J. Talvacchio, D. B. Buchholz, and R. P. H. Chang, "Meandering Grain Boundaries in YBCO Bi-Crystal Thin Films," *Appl. Phys. Lett.* 66(19), 2561 (1995).

11. B. A. Baumert, "Barium Potassium Bismuth Oxide: A Review," *J. of Superconductivity* 8(1), 175 (1995).
12. D. G. Steel, D. H. Kim, K. E. Gray, S. E. Pfanstiel, P. G. Landis, J. E. Sharping, J. H. Kang, and J. Talvacchio, "Electrical Noise Signatures of Possible Vortex Transitions in Epitaxial YBCO Thin Films," *Phys. C* 248, 55 (1995).
13. D. L. Miller, M. G. Forrester, J. X. Przybysz, B. D. Hunt, and J. Talvacchio, "Single-Flux-Quantum Circuits based on YBCO Step-Edge-Grain-Boundary Junctions," *Proc. Intl. Superconductivity Electronics Conf. (ISEC '95)*, 40 (1995).
14. D. G. Steel, J. D. Hettinger, F. Yuan, D. J. Miller, K. E. Gray, J.-H. Kang, and J. Talvacchio, "Electrical Transport Properties of (001) Tilt Bicrystal Grain Boundaries in YBCO," *Appl. Phys. Lett.* 68(1), 120 (1995).
15. B. D. Hunt, M. G. Forrester, J. Talvacchio, J. D. McCambridge, and R. M. Young, "High- $T_c$  SNS Edge Junctions and SQUIDs with Integrated Groundplanes," *Appl. Phys. Lett.* 68(26), 3805 (1996).
16. S. H. Talisa, M. A. Janocko, D. L. Meier, J. Talvacchio, C. Moskowitz, D. C. Buck, R. S. Nye, S. J. Pieseski, and G. R. Wagner, "High-Temperature Superconducting Space-Qualified Multiplexers and Delay Lines," *IEEE Trans. Microwave Theory and Techniques* 44(7), 1229 (1996).
17. X. F. Zhang, D. J. Miller, and J. Talvacchio, "Control of Meandering Grain Boundary Configurations in  $\text{YBa}_2\text{Cu}_3\text{O}_y$  Bicrystal Thin Films Produced Based on Deposition Rate," *J. Mater. Res.* 11(10), 2440 (1996).
18. J. T. McDevitt, J. P. Zhou, C. E. Jones, and J. Talvacchio, "Crystal Engineering of Chemically Stabilized, Cation-Substituted YBCO Structures," *Proc. 10th Anniversary HTS Workshop on Physics, Materials, and Applications* (1996).
19. M. G. Forrester, B. D. Hunt, J. Talvacchio, J. D. McCambridge, R. M. Young, D. L. Miller, and J. X. Przybysz, "HTS Multilayer Process Development for Digital Circuits," in *Proc. 4<sup>th</sup> NATO Workshop on Physics and Materials Science in High Temperature Superconductivity* (1996).
20. H. Darhmaoui, J. Jung, J. Talvacchio, M. A.-K. Mohamed, and L. Friedrich, "Temperature Dependence of the Magnetic Flux Penetration into Disk-Shaped YBCO Thin Films," *Phys. Rev. B* 53, 12330 (1996).
21. J. T. McDevitt, J. P. Zhou, C. E. Jones, R-K. Lo, J. E. Rithchie, J. Zhao, C. A. Mirkin, F. Xu, K. Chen, and J. Talvacchio, "Molecular and Crystal Engineering of High- $T_c$  Superconductor Thin Films Structures and Devices," *Proc. ISTE International Workshop on Superconductor Applications*, Iwate, Japan, 26 (1996).
22. B. D. Hunt, M. G. Forrester, J. Talvacchio, J. D. McCambridge, and R. M. Young, "High- $T_c$  SNS Edge Junctions for Digital Circuit Applications," in *Proc. 9<sup>th</sup> International Symposium on Superconductivity - ISS'96* (1996).

23. P. R. Broussard, M. A. Wall, and J. Talvacchio, "Structural Characterization of YBCO/Y<sub>2</sub>O<sub>3</sub> Composites," accepted for publication in *J. Mater. Res.* (1997).
24. J.-P. Zhou, R.-K. Lo, S. M. Savoy, M. Arendt, J. Armstrong, D.-Y. Yang, J. Talvacchio, and J. T. McDevitt, "Environmental Degradation Properties of Y<sub>ba</sub><sub>2</sub>Cu<sub>3</sub>O<sub>7-δ</sub> and Y<sub>0.6</sub>Ca<sub>0.4</sub>Ba<sub>1.6</sub>La<sub>0.4</sub>Cu<sub>3</sub>O<sub>7-δ</sub> Thin Film Structures," *Physica C* 273, 223 (1997).
25. J. D. McCambridge, M. G. Forrester, D. L. Miller, J. X. Przybysz, B. D. Hunt, J. Talvacchio, and R. M. Young, "Multilayer HTS Counting A/D Converter," accepted for *IEEE Trans. Appl. Superconductivity* 7(2), (June, 1997).
26. J. Talvacchio, M. G. Forrester, B. D. Hunt, J. D. McCambridge, R. M. Young, X. F. Zhang, and D. J. Miller, "Materials Basis for a Six-Level Epitaxial HTS Digital Circuit Process," accepted for publication in *IEEE Trans. Appl. Superconductivity* 7(2), (June, 1997).
27. B. D. Hunt, M. G. Forrester, J. Talvacchio, J. D. McCambridge, and R. M. Young, "High-T<sub>c</sub> SNS Edge Junctions with Integrated YBCO Groundplanes," accepted for publication in *IEEE Trans. Appl. Superconductivity* 7(2), (June, 1997).
28. M. G. Forrester, B. D. Hunt, J. D. McCambridge, D. L. Miller, J. X. Przybysz, J. Talvacchio, and R. M. Young, "Multilayer Edge-SNS SQUIDs for Digital Circuits," accepted for publication in *IEEE Trans. Appl. Superconductivity* 7(2), (June, 1997).
29. A. Davidson and N. F. Pedersen, "A New Three-Terminal Vortex Flow Device," accepted for *IEEE Trans. Appl. Superconductivity* 7(2), (June, 1997).
30. J. D. Hettinger, K. E. Gray, D. J. Miller, D. H. Kim, D. G. Steel, B. R. Washburn, J. Sharping, C. Moreau, M. Eddy, J. E. Tkaczyk, J. DeLuca, J. H. Kang, and J. Talvacchio, "Identification of Grain Boundary Effects in Current-Voltage Curves of Polycrystalline High-T<sub>c</sub> Superconductors," *Physica C* 273, 275 (1997).
31. J. P. Zhou, R.-K. Lo, J. T. McDevitt, J. Talvacchio, M. G. Forrester, B. D. Hunt, Q. X. Jia, and D. Reagor, "Crystal Engineering of Chemically Stabilized, Cation-Substituted YBCO Structures," accepted for publication in *J. Mater. Res.* 12(11), (1997).
32. B. D. Hunt, M. G. Forrester, J. Talvacchio, J. D. McCambridge, and R. M. Young, "High-Resistance SNS Edge Junctions," *Proc. Intl. Superconductivity Electronics Conf. (ISEC)*, (1997).
33. M. G. Forrester, B. D. Hunt, J. Talvacchio, and R. M. Young, "High-Resistance HTS Junctions for Digital Circuits," in *Proc. ISTEC-MRS International Workshop on Superconductivity* (1997).

## **6. PERSONNEL**

**J. Talvacchio, Principal Investigator**

**A. Davidson**

**M. G. Forrester**

**B. D. Hunt**

**J. D. McCambridge**

**S. H. Talisa**

**R. W. Weinert**

**R. M. Young**

## 7. COUPLING ACTIVITIES

Speaker's name is underlined.

1. B. D. Hunt, M. G. Forrester, J. Talvacchio, J. D. McCambridge, and R. M. Young, "Status of HTS Digital Integrated Circuit Fabrication at Northrop Grumman," TRW/Conductus/Northrop Grumman Collaboration on HTS Digital Integrated Circuit Fabrication, technical meetings and presentations to Government representatives: Sunnyvale, May 1995; Los Angeles, August, 1995; Pittsburgh, October 1995; Los Angeles, January 1996; Sunnyvale, April 1996; Washington, August 1996, Los Angeles, November 1996; Sunnyvale, February 1997.
2. J. Talvacchio, D. L. Meier, S. H. Talisa, R. W. Weinert, J. R. Gavaler, and R. L. Grassel, "Surface Studies of YBCO Films during Processing of Microwave Circuits," March Meeting of the American Physical Society, Pittsburgh, March 1994.
3. J. Talvacchio, M. G. Forrester, A. Davidson, J. R. Gavaler, and J. X. Przybysz, "Integration of Step-Edge Junctions in an HTS Flash A/D Converter," Invited presentation to the Materials Research Society Spring Meeting, San Francisco, April 1994.
4. J. Talvacchio, "Epitaxial Oxide Film Requirements for HTS Electronics," Invited presentation to the 2nd International Workshop on MOCVD of High-Temperature Superconductors, San Francisco, April 1994.
5. J. Talvacchio, "Applications of High-T<sub>c</sub> Superconductors in Signal Processing," Ohio State University Nanostructure Materials and Devices Seminar, Columbus, May 1994.
6. M. G. Forrester, J. Talvacchio, A. Davidson, and J. R. Gavaler, "HTS Junction Development at Westinghouse," Invited presentation to the ARPA HTS Josephson Junction Workshop, Washington, August 1994.
7. A. Davidson, M. G. Forrester, J. Talvacchio, J. R. Gavaler, and S. H. Talisa, "Progress in HTS Electronics," Invited presentation to the Nonlinear Superconducting Devices and High T<sub>c</sub> Materials Conference, Capri, Italy, October 1994.

8. W. Kula, W. Xiong, R. Sobolewski, and J. Talvacchio, "Laser Patterning of YBCO Thin Films Protected by In-Situ Grown SrTiO<sub>3</sub> Cap Layer," Applied Superconductivity Conference, Boston, October 1994.
9. J. Talvacchio, M. G. Forrester, and J. R. Gavaler, "Properties of Passive Structures for Multilayer HTS Digital Circuits," Applied Superconductivity Conference, Boston, October 1994.
10. J. R. Gavaler, J. Talvacchio, and R. W. Weinert, "Effect of Oxygen on Properties of YBa<sub>2</sub>Cu<sub>3</sub>O<sub>x</sub>," Applied Superconductivity Conference, Boston, October 1994.
11. R. R. Biggers, M. G. Norton, I. Maartense, T. L. Peterson, E. K. Moser, D. Dempsey, M. A. Capano, J. Talvacchio, J. L. Brown, and J. D. Wolf, "Microstructure and Properties of YBCO Thin Films Grown on Vicinal LaAlO<sub>3</sub> Substrates," Applied Superconductivity Conference, Boston, October 1994.
12. M. G. Forrester, A. Davidson, J. Talvacchio, and J. R. Gavaler, "Multilayer HTS SQUIDs for Digital Circuit Applications," Applied Superconductivity Conference, Boston, October 1994.
13. D. L. Meier, M. G. Forrester, R. L. Grassel, S. H. Talisa, and J. Talvacchio, "Fabrication of YBCO Filters and Delay Lines," Applied Superconductivity Conference, Boston, October 1994.
14. F. Yuan, D. G. Steel, J. D. Hettinger, D. J. Miller, K. E. Gray, J. Talvacchio, and J.-H. Kang, "Microstructure/Transport Relationships of (001) Tilt Grain Boundaries in YBCO," Materials Research Society Fall Meeting, Boston, November 1994.
15. M. G. Forrester, "Digital Applications of High Temperature Superconductivity," Invited presentation to the March Meeting of the American Physical Society, San Jose, March 1995.
16. J. Feller, C. Hucho, M. McKenna, M. Levy, B. K. Sarma, and J. R. Gavaler, "Surface Acoustic Wave Investigation of Mixed-State Phases in Thin Films of YBCO," March Meeting of the American Physical Society, San Jose, March 1995.
17. D. G. Steel, D. H. Kim, J. D. Hettinger, K. E. Gray, S. E. Pfanstiel, G. B. Thompson, P. G. Landis, J. E. Sharping, J.-H. Kang, and J. Talvacchio, "Electrical Noise Signatures of Vortex Dynamics in High T<sub>c</sub> Superconductors," March Meeting of the American Physical Society, San Jose, March 1995.
18. R. R. Biggers, I. Maartense, E. K. Moser, T. L. Peterson, D. Dempsey, J. L. Brown, M. Grant Norton, and J. Talvacchio, "The Effects of Substrate Misorientation on the Microstructure and Properties of YBCO Thin Films," Materials Research Society Spring Meeting, San Francisco, April 1995.

19. J. Talvacchio, M. G. Forrester, and J. R. Gavaler, "In-Situ High-Temperature Measurements of Oxygen Diffusion through Epitaxial Oxide Films," Materials Research Society Spring Meeting, San Francisco, April 1995.
20. J. P. Zhou, S. M. Savoy, J. T. McDevitt, and J. Talvacchio, "Investigation of Corrosion-Resistant High-T<sub>c</sub> Phases in the YBa<sub>2</sub>Cu<sub>3</sub>O<sub>x</sub> System," Materials Research Society Spring Meeting, San Francisco, April 1995.
21. J. Talvacchio, "Requirements for Thin Films Used in High-Speed Analog and Digital HTS Circuits," Invited presentation to the International Cryogenic Materials Conference, Columbus, July 1995.
22. D. J. Miller, D. G. Steel, F. Yuan, J. D. Hettinger, K. E. Gray, J. Talvacchio, and J.-H. Kang, "Structure and Transport Properties of (001) Tilt Grain Boundaries in YBCO: Structural Variations and Effective Coupling Area," ISTE/MRS International Workshop on Superconductivity, Hawaii, June 1995.
23. D. L. Miller, M. G. Forrester, J. X. Przybysz, B. D. Hunt, and J. Talvacchio, "Single-Flux-Quantum Circuits based on YBCO Step-Edge-Grain-Boundary Junctions," Intl. Superconductivity Electronics Conf. (ISEC '95), Nagoya, September 1995.
24. B. D. Hunt, M. G. Forrester, J. Talvacchio, and J. D. McCambridge, "High-T<sub>c</sub> SNS Edge Junctions for SFQ Digital Circuit Applications," Workshop on Superconductive Electronics, Farmington, Pennsylvania, October, 1995.
25. M. G. Forrester, D. L. Miller, J. Talvacchio, J. X. Przybysz, and B. D. Hunt, "Single Flux Quantum Circuits Based on YBCO Step-Edge Grain Boundary Junctions," Workshop on Superconductive Electronics, Farmington, Pennsylvania, October, 1995.
26. B. D. Hunt, M. G. Forrester, J. D. McCambridge, and J. Talvacchio, "Epitaxial High-T<sub>c</sub> SNS Edge Junctions using Sputtered Ca, Co, and Pr-Doped-YBCO Normal Metal Layers," Materials Research Society Fall Meeting, Boston, November 1995.
27. X. F. Zhang, D. J. Miller, and J. Talvacchio, "Microstructures of Artificially-Induced Grain Boundaries in YBa<sub>2</sub>Cu<sub>3</sub>O<sub>x</sub> Thin Films Grown on SrTiO<sub>3</sub> Bicrystal Substrates at Different Deposition Rates," Materials Research Society Fall Meeting, Boston, November 1995.
28. J. Talvacchio and M. G. Forrester, "Defects in Epitaxial YBCO/Insulator/YBCO Trilayer Capacitor Structures," Materials Research Society Fall Meeting, Boston, November 1995.
29. B. D. Hunt, M. G. Forrester, J. D. McCambridge, J. Talvacchio, and R. M. Young, "High-T<sub>c</sub> SNS Edge Junctions and SQUIDs with YBCO Ground Planes," March Meeting of the American Physical Society, St. Louis, March 1996.

30. J. T. McDevitt, J. P. Zhou, C. E. Jones, and J. Talvacchio, "Crystal Engineering of Chemically Stabilized, Cation-Substituted YBCO Structures," 10th Anniversary HTS Workshop on Physics, Materials, and Applications, Houston, March 1996.
31. J. Talvacchio, M. G. Forrester, B. D. Hunt, J. D. McCambridge, R. M. Young, and D. L. Miller, "HTS Films and Multilayers for Electronics," AFOSR Mtg. of contractors in Quantum Electronics, Pittsburgh, March 1996.
32. M. G. Forrester, B. D. Hunt, J. D. McCambridge, J. Talvacchio, D. L. Miller, J. X. Przybysz, and R. M. Young, "Inductance Measurements in Multilayer Edge- and Step-Edge SQUIDs," Materials Research Society Spring Meeting, San Francisco, April 1996.
33. B. D. Hunt, M. G. Forrester, J. D. McCambridge, J. Talvacchio, and R. M. Young, "High-T<sub>c</sub> SNS Edge Junctions Integrated with Epitaxial YBCO Ground Planes," Materials Research Society Spring Meeting, San Francisco, April 1996.
34. J.-P. Zhou, J. T. McDevitt, and J. Talvacchio, "Superconducting and Corrosion Properties of the R<sub>1-x</sub>Ca<sub>x</sub>Ba<sub>2-y</sub>La<sub>y</sub>Cu<sub>3</sub>O<sub>7</sub> System," Invited presentation to the Materials Research Society Spring Meeting, San Francisco, April 1996.
35. J. Talvacchio, M. G. Forrester, B. D. Hunt, J. D. McCambridge, and R. M. Young, "HTS Digital Integrated Circuit Fabrication," Invited presentation to the Materials Research Society Spring Meeting, San Francisco, April 1996.
36. J. Talvacchio, M. G. Forrester, B. D. Hunt, and R. M. Young, "HTS Film Deposition at Northrop Grumman," Invited presentation to the DARPA Workshop on HTS Thin Film Manufacturing, Washington DC, June 1996.
37. J. Talvacchio and S. H. Talisa, "HTS Channelized and Switched Filterbanks," Invited presentation to the ISTEC International Workshop on Superconductor Applications, Iwate, Japan, June 1996.
38. J. T. McDevitt, J. P. Zhou, C. E. Jones, R-K. Lo, J. E. Rithchie, J. Zhao, C. A. Mirkin, F. Xu, K. Chen, and J. Talvacchio, "Molecular and Crystal Engineering of High-T<sub>c</sub> Superconductor Thin Films Structures and Devices," ISTEC International Workshop on Superconductor Applications, Iwate, Japan, June 1996.
39. M. G. Forrester, B. D. Hunt, J. Talvacchio, J. D. McCambridge, R. M. Young, D. L. Miller, and J. X. Przybysz, "HTS Multilayer Process Development for Digital Circuits," Invited presentation to the 4<sup>th</sup> NATO Workshop on Physics and Materials Science in High Temperature Superconductivity, Slovakia, July 1996.
40. J. Talvacchio, "High Frequency Superconducting Devices," Invited presentation to the Midwest Superconductivity Consortium Summer School on Thin Films, South Bend, August 1996.

41. B. D. Hunt, M. G. Forrester, J. Talvacchio, J. D. McCambridge, and R. M. Young, "Transport in High-T<sub>c</sub> SNS Edge Junctions," Workshop on Fundamental Processes of Electron Transport in High-T<sub>c</sub> Junctions, Argonne, August 1996.
42. J. Talvacchio, M. G. Forrester, B. D. Hunt, J. D. McCambridge, R. M. Young, X. F. Zhang, and D. J. Miller, "Six-Level Epitaxial Film Process for HTS Digital Circuits," Invited presentation to the Applied Superconductivity Conference, Pittsburgh, August 1996.
43. B. D. Hunt, M. G. Forrester, J. Talvacchio, J. D. McCambridge, and R. M. Young, "High-T<sub>c</sub> SNS Edge Junctions with Integrated YBCO Groundplanes," Applied Superconductivity Conference, Pittsburgh, August 1996.
44. J. D. McCambridge, M. G. Forrester, D. L. Miller, J. X. Przybysz, B. D. Hunt, J. Talvacchio, and R. M. Young, "Multilayer HTS Counting A/D Converter," Applied Superconductivity Conference, Pittsburgh, August 1996.
45. M. G. Forrester, B. D. Hunt, J. D. McCambridge, D. L. Miller, J. X. Przybysz, J. Talvacchio, and R. M. Young, "Multilayer SQUIDs and SFQ Circuits Fabricated with HTS Step-Edge and Edge-SNS Junctions," Applied Superconductivity Conference, Pittsburgh, August 1996.
46. A. Davidson and N. F. Pedersen, "A New Three-Terminal Vortex Flow Device," Applied Superconductivity Conference, Pittsburgh, August 1996.
47. B. D. Hunt, M. G. Forrester, J. Talvacchio, J. D. McCambridge, and R. M. Young, "High-T<sub>c</sub> SNS Edge Junctions for Digital Circuit Applications," in Proc. 9<sup>th</sup> International Symposium on Superconductivity - ISS'96, Sapporo, October 1996.
48. B. D. Hunt, "High-T<sub>c</sub> SNS Edge Junctions for Digital Applications," Invited presentation to the American Physical Society March Meeting, Kansas, City, March 1997.
49. J. Talvacchio, "Northrop Grumman Experience and Capabilities for FAME," DARPA FAME Workshop, Washington, scheduled for May 1997.
50. M. G. Forrester, B. D. Hunt, J. Talvacchio, and R. M. Young, "High-Resistance HTS Junctions for Digital Circuits," Invited presentation to the ISTEC-MRS International Workshop on Superconductivity, Hawaii, scheduled for June 1997.
51. B. D. Hunt, M. G. Forrester, J. Talvacchio, and R. M. Young, "High-Resistance SNS Edge Junctions," Intl. Superconductivity Electronics Conf. (ISEC'97), Berlin, scheduled for June 1997.

## **8. PATENTS**

None.

# Inductance measurements in multilevel high $T_c$ step-edge grain boundary SQUIDS

## APPENDIX 1

M. G. Forrester, A. Davidson, J. Talvacchio, J. R. Gavaler, and J. X. Przybysz  
Westinghouse Science and Technology Center, Pittsburgh, Pennsylvania 15235

(Received 23 May 1994; accepted for publication 25 July 1994)

Multilevel high  $T_c$  SQUIDS, suitable for digital circuit applications, have been fabricated and tested. The devices employ a  $\text{YBa}_2\text{Cu}_3\text{O}_{7-\delta}$  (YBCO) ground plane, an epitaxial  $\text{SrTiO}_3$  insulator, and a YBCO microstrip layer. Junctions are formed by the step-edge grain boundary process, with a ground plane contact for the "low" side of each junction, using only isotropic sputtering and milling techniques. Control current is directly injected in a microstrip segment of the SQUID loop, allowing us to measure the microstrip inductance, and thus to infer the magnetic penetration depth of the YBCO. The SQUIDS are operational above 77 K, at which temperature we infer a penetration depth of 350 nm. The temperature dependence of the penetration depth is found to be in reasonable agreement with the Gorter-Casimir form close to  $T_c$ . © 1994 American Institute of Physics.

The development of a high-temperature superconducting (HTS) digital circuit process requires the development of reproducible Josephson junctions, and the integration of these junctions into an epitaxial, multilayer process. Such layers would include superconductors, epitaxial insulators, and probably epitaxial resistors. Of particular importance is the use of a superconducting ground plane, to keep circuit inductances values both low and well defined.

Low inductances are essential for single flux quantum circuits, so that a single quantized voltage pulse,  $\Phi_0 = h/2e = 1000 \text{ pH } \mu\text{A}$ , can generate sufficient current in a load inductor. Even simple structures, like Josephson digital transmission lines for logic gate interconnections, will need inductors as small as 5 pH between junctions.

Single flux quantum circuits can obtain logic clock speeds above 10 GHz with junction  $I_c R_n = 100 \mu\text{V}$ . In contrast, circuits built without ground planes will have large interconnection inductances, requiring voltage-state logic gates, and are unlikely to operate at GHz clock rates.

Here, we report the first demonstration of multilayer high-temperature superconducting SQUIDS, suitable for digital circuit applications in the 65- to 77-K temperature range. Further, our process employs isotropic film deposition and etching techniques, with no favored direction for the junctions, and thus is potentially extendible to complex circuits.

A previous report by Missert *et al.* described the fabrication of step-edge superconductor-normal-superconductor (SNS) junctions over a ground plane, using directional deposition of the YBCO to ensure a discontinuity in the YBCO over a step in a deposited insulator, with a noble metal deposited as the normal barrier.<sup>1</sup> These devices operated as SQUIDS only up to 20 K, preventing the measurement of inductance as a function of temperature up to the more useful 65- to 77-K temperature range.

We have fabricated step-edge grain boundary junctions over a YBCO ground plane, using a process which is designed from the outset to allow junctions to be fabricated in four directions, for flexibility in circuit layout. Since the fabricated devices operate to above 77 K, we have measured the inductance of a microstrip portion of the SQUID loop as a

function of temperature, and have inferred the temperature-dependent magnetic penetration depth for our YBCO films.

Our fabrication process uses off-axis rf magnetron sputtering for both YBCO and  $\text{SrTiO}_3$  films, with YBCO sputtered in oxygen, argon, and water,<sup>2</sup> and  $\text{SrTiO}_3$  in oxygen and argon. Typical deposition temperatures were in the 670–700 °C range for both materials. Substrates rotated during deposition to ensure uniformity and edge coverage. Patterning of each layer was by argon ion milling with a 20-cm diam rf ion source, with beam energies of 150 and 300 eV for the YBCO and  $\text{SrTiO}_3$ , respectively. Samples were clamped to a water-cooled, rotating sample table during milling. The choice of a higher voltage for the  $\text{SrTiO}_3$  is dictated by the need for a well-collimated beam for etching of sharp steps in this layer, while the slightly more divergent beam obtained at 150 eV is more suitable for milling tapered edges in the YBCO layers. An end-point detector based on secondary ion mass spectroscopy was used to determine when to terminate each etch step.

A YBCO (001) ground plane, typically 200 nm thick, was deposited first on a single-crystal substrate of  $\text{NdGaO}_3(110)$  or  $\text{LaAlO}_3(001)$  (cubic crystal approximation), and its pattern defined with photoresist, with a process designed to give tapered photoresist sidewalls. The film was etched by ion milling at a shallow angle, which, in combination with the tapered resist, ensured that the edges of the YBCO should be tapered to ensure good contact with the second YBCO layer and good coverage by the  $\text{SrTiO}_3$ . After ion milling the photoresist was stripped using a combination of rf oxygen plasma, and soaking in acetone. We have found from XPS observation that this process leaves the surface of the YBCO relatively free of both hydrocarbons and carbonates.

After deposition of a 200-nm  $\text{SrTiO}_3$  layer, another photoresist process, this one designed to produce a steep resist profile, was used to define its pattern. Ion milling at close to normal incidence was then used to etch the  $\text{SrTiO}_3$  film, producing sidewalls with angles thought to be between 0° and 20° from vertical, based on the observation of test samples, viewed in cross section in a scanning electron microscope (SEM). After the resist clean-up a second 200-nm

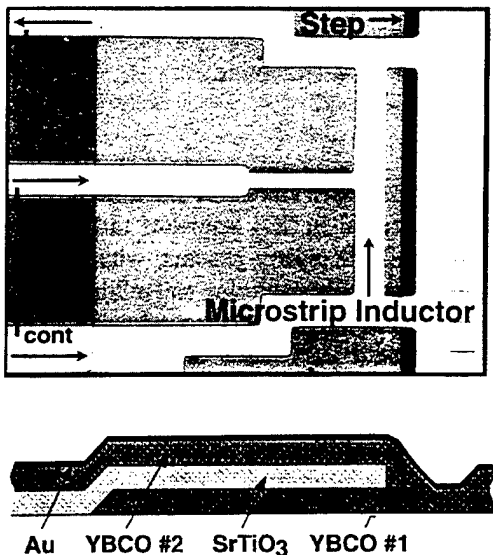


FIG. 1. Micrograph of a fabricated multilayer HTS SQUID, and schematic cross-sectional view. The microstrip inductor is 10  $\mu\text{m}$  wide.

layer of YBCO was deposited, followed by approximately 30 nm of Au, *in situ*. This bilayer was then patterned by photolithography and ion milling, with no particular precautions taken in defining the profile of the etched material for this last layer. The Au was left in place both to provide low resistance contacts and to protect the grain boundary junctions from processing damage, which we have observed in “uncovered” junctions.

It is worth noting that we have not found it necessary to use a deposited milling mask, such as Nb<sup>3,4</sup> or diamondlike carbon,<sup>5</sup> to produce sharp steps in our deposited SrTiO<sub>3</sub>, a significant process simplification. This is also in contrast to our own work in making junctions on a step etched into a single-crystal NdGaO<sub>3</sub> substrate, where a metal mask was required to obtain sharp steps. This is an example of the often significant differences in the etching properties of the various materials being employed in HTS process development.

Figure 1 shows a photograph and a schematic cross-sectional view of a fabricated SQUID. The SQUIDS incorporate microstrip inductors,  $L_\mu$ , of 10- $\mu\text{m}$  width and various lengths, into which a control current,  $I_{\text{cont}}$  can be directly injected to provide a flux,  $\Phi = L_\mu I_{\text{cont}}$ . The junctions, of width 6 or 10  $\mu\text{m}$ , contact the ground plane in a region that contains a grid of holes, seen on the right in Fig. 1, which allow both *c*-axis and *a*-*b*-axis contact between the two YBCO layers.

In exploring the processing parameters involved in fabricating these devices we have produced ten chips, with six SQUIDS on each. The quality of the devices, as measured by, for example, amplitude of voltage modulation, varied with the detailed process parameters, which are still being optimized, but the overall yield of modulating SQUIDs was about 70%. Failures of many of the remaining 30% can be traced to observable defects in the fabrication process.

The current-voltage characteristic of a typical SQUID at 70 K is shown in Fig. 2(a), with and without 10-GHz radia-

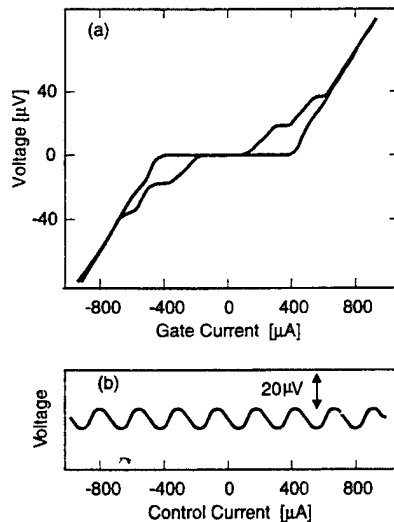


FIG. 2. Current-voltage characteristic, with and without 10-GHz radiation, (a), and voltage vs control current, (b), for a SQUID with a 50- $\mu\text{m}$ -long microstrip inductor. Both are at 70 K.

tion, and exhibits behavior generally consistent with the resistively shunted junction model, with the expected downward curvature. Most devices show evidence for weak constant-voltage steps in the *I*-*V* characteristic in the absence of microwaves, which we have not seen in junctions fabricated directly on NdGaO<sub>3</sub> and LaAlO<sub>3</sub> substrates, without a ground plane. This may be due to *L*-*C* resonances associated with the high dielectric constant of the SrTiO<sub>3</sub>.

Figure 2(b) shows SQUID voltage versus control current, at 70 K. The period of this modulation is determined by the inductance of the microstrip portion of the loop,  $L_\mu$  including any parasitic inductance associated with the center tap and the ends, through

$$\Delta I_{\text{cont}} = \frac{\Phi_0}{L_\mu}, \quad (1)$$

where  $\Phi_0$  is the superconducting flux quantum. By measuring this period, directly from oscilloscope traces, as a function of temperature we determine the inductance as a function of temperature. This is shown in Fig. 3(a) for a 50- $\mu\text{m}$ -long, 10- $\mu\text{m}$ -wide microstrip inductor.

To infer an effective penetration depth,  $\lambda$ , for our YBCO films we assume that the two films are identical, and use the following expression for the inductance per square of a superconducting strip over an infinite ground plane:<sup>6</sup>

$$L = \frac{\mu_0 d \kappa}{w} \left[ 1 + \frac{2\lambda}{d} \coth\left(\frac{b}{\lambda}\right) \right], \quad (2)$$

where,  $d$  is the insulator thickness,  $w$  the microstrip width,  $b$  the superconductor thickness, and  $\kappa$  is a factor that determines the field strength at the center of the finite width microstrip. Here,  $\lambda$  is for transport current and magnetic field (neglecting small fringing fields) parallel to the *a*-*b* plane, and thus is  $\lambda_{ab}$  of Ref. 7. The value of  $\kappa$  for our microstrip can be determined to be approximately 0.93 from Fig. 3.09d of Ref. 6, using our experimental values of  $d = 200$  nm and  $w = 10$   $\mu\text{m}$ . Combining this with the experimental value,  $b = 220$  nm, and measured values of  $L_\mu$  for the 50- $\mu\text{m}$ -long

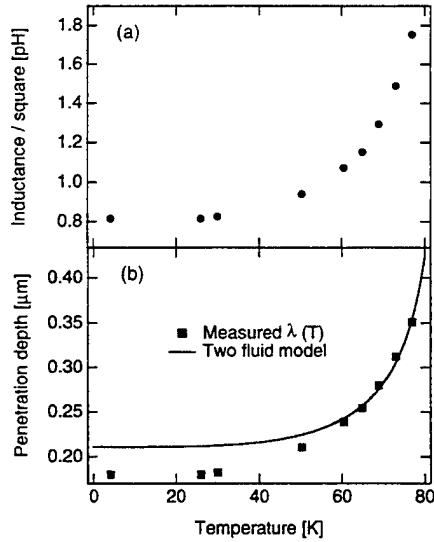


FIG. 3. (a) Measured inductance per square, in picohenries for a SQUID with a 50- $\mu\text{m}$ -long microstrip inductor. (b) Penetration depth of our YBCO films, inferred from the measured inductance. The solid line is a fit to the data above 60 K using the Gorter-Casimir form for the temperature dependence of the penetration depth:  $\lambda(T)=\lambda_0[1-(T/T_c)^4]^{1/2}$ .

microstrip of Fig. 3(a), we solve Eq. (2) to determine  $\lambda$ . The result is shown in Fig. 3(b) as a function of temperature. The magnitude of the inferred penetration depth is in good agreement with measurements by other techniques.<sup>7</sup> The solid line in Fig. 3(b) is a fit to the Gorter-Casimir form for the temperature dependence of the penetration depth:  $\lambda(T)=\lambda_0[1-(T/T_c)^4]^{1/2}$ , for the data above 60 using the measured zero-resistance transition temperature of 86 K.

In summary, we have fabricated HTS step-edge grain boundary SQUIDs incorporating a HTS ground plane, using a process which allows junctions to face in all four directions. These SQUIDs have critical currents of a magnitude useful for digital circuit operation in the 65- to 77-K temperature range, and exhibit good Josephson behavior. Measurements of the inductance of the microstrip portion of the SQUID loop have allowed us to infer a penetration depth for our YBCO films, whose magnitude and temperature dependence are consistent with other measurements, and with the requirements of low-inductance interconnects in digital circuits. Further work is required to determine the reproducibility of the process, especially that of junction critical current, and to replace the  $\text{SrTiO}_3$  with a lower loss insulator.

The authors wish to acknowledge the assistance of G. J. Faychak and J. H. Uphoff in sample fabrication. This work was supported in part by the Air Force Office of Scientific Research, Contract No. F49620-94-C-0021.

<sup>1</sup> N. Misset, T. E. Harvey, R. H. Ono, and C. D. Reintsema, *Appl. Phys. Lett.* **63**, 1690 (1993).

<sup>2</sup> J. R. Gavalier, J. Talvacchio, T. T. Braggins, M. G. Forrester, and J. Gregg, *J. Appl. Phys.* **70**, 4383 (1991).

<sup>3</sup> K. Herrmann, Y. Zhang, H. M. Muck, J. Schubert, W. Zander, and A. I. Braginski, *Supercond. Sci. Technol.* **4**, 583 (1991).

<sup>4</sup> J. Luine, J. Bulman, J. Burch, K. Daly, A. Lee, C. Pettiette-Hall, S. Schwarzbeck, and D. Miller, *Appl. Phys. Lett.* **61**, 1128 (1992).

<sup>5</sup> J. Z. Sun, W. J. Gallagher, A. C. Callegari, V. Foglietti, and R. H. Koch, *Appl. Phys. Lett.* **63**, 1561 (1993).

<sup>6</sup> T. Van Duzer and C. W. Turner, *Principles of Superconductive Devices and Circuits* (Elsevier, New York, 1981), p. 114.

<sup>7</sup> L. Krusin-Elbaum, R. L. Greene, F. Holtzberg, A. P. Malozemoff, and Y. Yeshurun, *Phys. Rev. Lett.* **62**, 217 (1989).

# Laser patterning of Y-Ba-Cu-O thin-film devices and circuits

## APPENDIX 2

Roman Sobolewski, W. Xiong, and W. Kula<sup>a)</sup>

Department of Electrical Engineering and Laboratory for Laser Energetics, University of Rochester, Rochester, New York 14627

J. R. Gavalier

Westinghouse Science and Technology Center, Pittsburgh, Pennsylvania 15235

(Received 2 July 1993; accepted for publication 15 November 1993)

We report our studies on electrical properties of Y-Ba-Cu-O test devices and circuits fabricated using a laser-writing patterning technique. The patterning procedure is noninvasive, does not require a patterning mask, and does not contaminate nor damage the surface of patterned films. Our laser-written, oxygen-rich lines (typically 4–100  $\mu\text{m}$  wide) possess excellent superconducting properties with zero resistivity at 89.5 K and critical current densities of above 2 MA/cm<sup>2</sup> at 77 K. On the other hand, oxygen-poor regions are semiconducting and exhibit thermally activated transport, well described by a three-dimensional, variable-length hopping process. Their resistance below 100 K is above 10 M $\Omega$ /square. A number of test structures patterned by laser writing, such as a microbridge, coplanar transmission line, open-ended microwave resonator, photoconductive switch, and Y-Ba-Cu-O field-effect transistor, have been presented.

Planar patterning of  $\text{YBa}_2\text{Cu}_3\text{O}_{7-x}$  (YBCO) thin films is one of the key technological issues that must be resolved before successful fabrication of even moderately complex, high- $T_c$  superconducting circuits will be possible.<sup>1</sup> YBCO is a multielement material with highly anisotropic crystalline structure that makes the etching process difficult and often results in patterns with fuzzy edges and a degraded (e.g., oxygen deficient) chemical composition. In addition, the YBCO surface is extremely sensitive to contamination by chemicals used in standard patterning procedures.

Recently, a new laser method for patterning YBCO circuits has been developed.<sup>2–6</sup> The technique is based on the observation that YBCO electrical and optical properties are very sensitive to the material's oxygen content. Oxygen can be diffused in or out of the YBCO film by heating the sample in either the presence or the absence of an oxygen atmosphere. The heating can be done locally with a focused laser beam. Thus, an intentionally oxygen-depleted (insulating at low temperatures) YBCO film can be patterned by embedding in it oxygen-rich (superconducting) lines or vice versa. The writing is fully reversible, and the patterns can be either erased by furnace annealing or rewritten by subsequent laser writing. Most importantly, the technique is noninvasive, does not require a patterning mask, and results in completely planar structures, free of surface contamination or edge degradation.

The aim of this article is to demonstrate that the laser-writing method is a reliable and practical technique, perfectly suited for patterning even complicated YBCO thin-film devices and circuits. We examine several laser-written test devices and show that they exhibit very good superconducting properties and can survive, without degradation, longterm storage in air at room temperature. Some of them also combine in a new and unique way the superconducting and dielectric properties of the oxygen-rich and oxygen-poor

YBCO phases. These latter structures are, in our opinion, prime candidates for the proposed high- $T_c$  superconducting optoelectronics.<sup>7</sup>

Our laser-patterning apparatus consisted of an Ar-ion continuous-wave laser ( $\lambda=0.514 \mu\text{m}$ ), shutter, focusing microscope, and computer-controlled X-Y translational stage with a gas chamber and sample holder. The sample ambient atmosphere was either pure nitrogen or oxygen. Contrary to our previous arrangement,<sup>6</sup> the substrate of the YBCO film was not in a direct heat contact with the metallic substrate holder, but it was suspended on a thin thermal insulator. This change allowed us to reproducibly write two-dimensional patterns not only on YBCO-on-LaAlO<sub>3</sub> films but also on films deposited on MgO and SrTiO<sub>3</sub>. Typical line dimensions of our patterns varied from <5 to 100  $\mu\text{m}$ . Laser-power intensity applied to the film was kept between 0.2 and 5 mW/ $\mu\text{m}^2$ , and a translational stage speed was in the range of 0.5–5  $\mu\text{m/s}$  for writing oxygen-rich lines and  $\sim 50 \mu\text{m/s}$  for (written in N<sub>2</sub>) oxygen-poor structures.

The test structures were laser patterned on about 80- to 300-nm-thick epitaxial YBCO films grown on LaAlO<sub>3</sub> and SrTiO<sub>3</sub> substrates using a single-target rf sputtering technique.<sup>8</sup> The best as-deposited films exhibited about 0.5-K-wide (10%–90%) superconducting transition  $\Delta T_c$  with the zero resistivity  $T_{c0}$  at 89.5 K, and the critical current density  $J_c$  of above 2 MA/cm<sup>2</sup> at 77 K. The films have been intentionally deoxygenated by radiative heating for 60 min in 15 mT of argon at 680 °C to become nonsuperconducting. Indeed, after the argon annealing, the film resistance vs temperature  $R(T)$  curve was a rapidly increasing function of the temperature decrease with no signs of the superconducting transition. The film sheet resistance below 100 K was above 10 M $\Omega$ /square, which corresponded to the upper limit of our resistance-measurement apparatus.

Optical transmission micrographs of a superconducting microbridge, oxygen-poor YBCO gap, coplanar microwave structure, and YBCO electric-field device—the four laser-written test structures presented in this letter—are shown in

<sup>a)</sup>Also at the Institute of Physics, Polish Academy of Sciences, PL-02668 Warszawa, Poland.

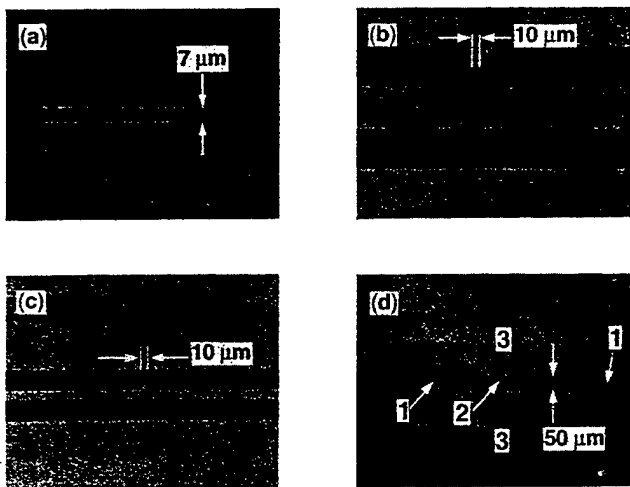


FIG. 1. Optical transmission micrographs of oxygen-rich (dark) test structures, laser written in oxygen-depleted (light-gray) YBCO films. (a) 7- $\mu$ m-wide and 160- $\mu$ m-long superconducting microbridge; (b) 10- $\mu$ m-wide oxygen-poor YBCO gap incorporated into a superconducting transmission line; (c) left end of an open-ended coplanar microwave resonator; and (d) field-effect test structure prepared in a single YBCO film.

Figs. 1(a)–1(d), respectively. All patterns exhibit very sharp (less than 1  $\mu$ m wide) superconducting-semiconducting interfaces with linear current-voltage characteristics.<sup>9</sup> The devices presented in Figs. 1(a)–1(c) were patterned by writing oxygen-rich (superconducting) lines in fully oxygen-depleted YBCO films. A reverse procedure, based on overwriting oxygen-rich lines in  $N_2$  atmosphere, was implemented for patterning the two, 10- $\mu$ m-wide coupling slits in the coplanar resonator [one slit is shown in Fig. 1(c)]. In the case of a field-effect transistor structure [Fig. 1(d)], we started the fabrication process with a partially deoxygenated film ( $T_c$  between 10 and 60 K, depending on the design) and patterned in  $O_2$  atmosphere fully oxygenated drain and source electrodes (the two dark regions). Next, we changed the sample's ambient atmosphere from  $O_2$  to  $N_2$  and produced oxygen-depleted areas (the light-gray regions) above and below the electrodes, completely insulating the transistor structure from the rest of the film. As a result, we obtained at the center of the device a 1-mm-long and 60- $\mu$ m-wide, partially deoxygenated transistor's channel.

Figure 2 shows the  $R(T)$  and  $J_c(T)$  curves measured for the 7- $\mu$ m-wide microbridge presented in Fig. 1(a). We note a sharp superconducting transition of our laser-patterned line. A somewhat unconventional shape of the normal-state  $R(T)$  curve is due to the fact that at high temperatures a test current also flows through the oxygen-poor YBCO, which is parallel to the microbridge [see Fig. 1(a)]. At low temperatures (below 150 K),  $R(T)$  decreases linearly, since in this temperature range, the resistivity of the oxygen-poor material is extremely high. The low temperature extrapolation of the  $R(T)$  curve crosses the resistance axis at the axis origin. The  $J_c(T)$  dependence is almost linear, and  $J_c$  increases at the rate of about 0.2 MA/cm<sup>2</sup>/K, reaching above 2 MA/cm<sup>2</sup> at 77 K.

Figure 3 shows in detail the resistive transition presented in Fig. 2 (sample A, open squares), together with the transi-

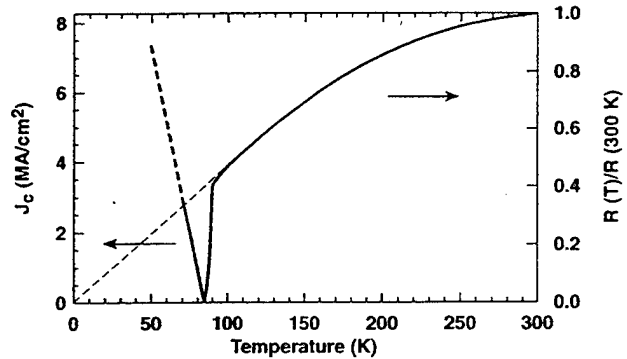


FIG. 2. Resistance and critical current density dependence on temperature for the microbridge shown in Fig. 1(a).

tion from the original, as-deposited film (sample A, closed squares) and the traces (sample A, closed and open circles) measured on the same sample, but two and eight months after the original patterning. We see that instead of expected degradation in the sample's superconducting properties, the laser-written structures actually exhibit slightly *enhanced*  $T_{c0}$ 's and improved  $R(100 K)/R(300 K)$  ratios. We associate these effects with a slow process of longterm oxygen ordering, which should lead to the film's "self-improvement." The room-temperature storage in air also did not degrade physical appearance of our samples nor their superconducting-semiconducting interfaces. Figure 3 also presents the two superconducting transitions (sample B, open and closed squares) for a laser-written microbridge patterned in a magnetron-sputtered YBCO-on-SrTiO<sub>3</sub> film. Comparing the sets of curves for the A and B samples, we note that in both cases the laser-patterned lines and the original films exhibit the same  $\Delta T_c$  and  $T_{c0}$ . Thus, a depressed  $T_c$ , observed in the B sample, should not be associated with oxygen deficiency or improper patterning but is, apparently, due to the film's nonoptimal Y:Ba:Cu cation ratio, or large concentration of defects.

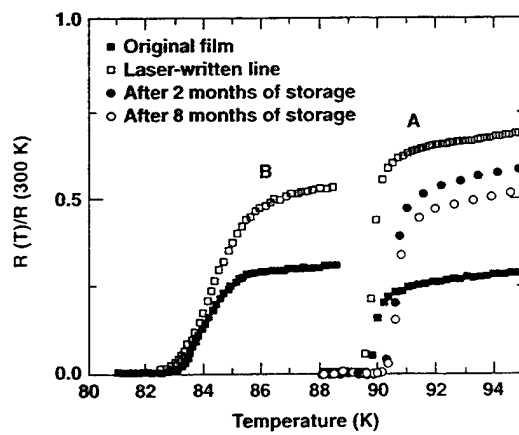


FIG. 3. Comparison between the superconducting transitions of laser-written, oxygen-rich lines and the original, as-deposited superconducting films. "A" denotes the 280-nm-thick, YBCO-on-LaAlO<sub>3</sub> film, while "B" corresponds to the 80-nm-thick film deposited on SrTiO<sub>3</sub>.

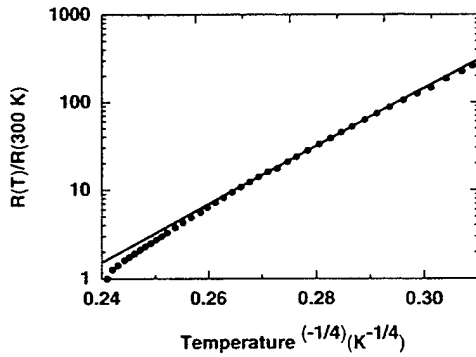


FIG. 4. Logarithmic  $R(T)/R(300 \text{ K})$  dependence vs the fourth root of the inverse temperature for the oxygen-poor YBCO gap shown in Fig. 1(b).

Resistive measurements of the oxygen-poor YBCO were performed on the sample shown in Fig. 1(b). We observed a thermally activated transport, which is characteristic for disordered semiconductors. This latter fact is illustrated in Fig. 4, where the  $\ln[R(T)/R(300 \text{ K})]$  dependence is plotted as a function of the fourth root of the inverse temperature. We note that most of our experimental data points follow a straight line, demonstrating that the low-temperature transport in oxygen-poor YBCO is controlled by three-dimensional, variable-length hopping. We also note that the complete structure presented in Fig. 1(b)—a gap incorporated in a transmission line—is very similar to that of a GaAs photoconductive switch (so-called “Auston switch”), routinely used in generating ultrafast electrical transients.<sup>10</sup> Indeed, we fabricated the above structure with the intention to study the dynamics of the optical electron-hole pair generation in semiconducting YBCO.

Figure 1(c) shows one end of a coplanar microwave resonator. The entire resonator is 7.5 mm long and is incorporated into an oxygen-rich coplanar transmission line. A resonator structure identical to that shown in Fig. 1(c) but with the line separation of 285  $\mu\text{m}$  has been tested and has shown very good microwave properties. Its quality factor measured at 24 K was about 5000 at 6.5 GHz. We also studied a 50  $\Omega$  coplanar transmission line, laser written in the same process as the resonator. The measurements were performed in the frequency range of 1–15 GHz, and we observed more than 60 dB improvement in the line-transmitted power  $S_{21}$ , as the temperature was lowered from 300 K to that below  $T_c$ . At all temperatures below  $T_c$ , the  $S_{21}$  was practically constant and near 0 dB, indicating low microwave losses of the oxygen-poor YBCO.

A top view of a YBCO field-effect transistor with a partially deoxygenated channel is presented in Fig. 1(d). The homogeneous regions with three different levels of gray, visible in this figure, correspond to (1) highly oxygenated ( $T_c \approx 90 \text{ K}$ ) drain and source electrodes, (2) partially deoxygenated ( $T_c \approx 25 \text{ K}$ ) channel, and (3) oxygen-poor (insulating) transistor borders. The structure was patterned in a 100-nm-thick YBCO-on-SrTiO<sub>3</sub> film, with the film substrate serving as the device’s gate dielectric. Figure 5 presents the drain voltage vs the channel current characteristics for an as-fabricated device, operated in a common-source mode at

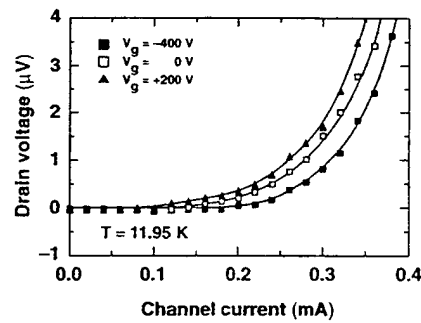


FIG. 5. Drain voltage vs channel current characteristics of the sample of Fig. 1(d), registered at 11.95 K for three different values of  $V_g$ .

12 K. We note that the positive gate voltage,  $V_g$ , caused suppression of  $J_c$ , while the negative  $V_g$  enhanced  $J_c$ . We observed up to 43%  $J_c$  enhancement in our best sample, and even higher  $J_c$  increase is expected, since we applied to the gate, electric fields which were about an order of magnitude lower than those typically applied by the other groups. We need to stress, however, that the  $J_c$  changes observed by us were partially irreversible and samples measured more than one week after their fabrication did not exhibit any measurable field effect. The above observation, as well as the magnitude and the sign of the  $J_c$  modulation, leads us to believe that the field effect in oxygen-depleted YBCO is of a chemical nature and is related to the electric-field-induced modification of the oxygen order in YBCO, exactly as it has been predicted by Chandrasekar *et al.*<sup>11</sup> Detailed studies on the physics of the charging effect in oxygen-deficient YBCO thin films will be presented elsewhere.<sup>12</sup>

The authors would like to thank Professor Donald P. Butler for providing us with the microwave data. This work was supported by the Air Force Office for Scientific Research Grants F49620-92-J-0075 (Rochester) and F49620-91-C-0034 (Westinghouse). W.X. also acknowledges support from the Frank Horton Graduate Fellowship Program.

<sup>1</sup> See, e.g., A. I. Braginski, in *Superconducting Devices and Their Applications*, edited by H. Koch and H. Lübbig, Springer Proceedings in Physics (Springer, Berlin, 1992), Vol. 64, pp. 3–18.

<sup>2</sup> M. Rothschild, J. H. C. Sedlacek, J. G. Black, and D. J. Ehrlich, *Appl. Phys. Lett.* **52**, 404 (1988).

<sup>3</sup> R. R. Krchnavek, S.-W. Chan, C. T. Rogers, F. De Rosa, M. K. Kelly, P. F. Miceli, and S. J. Allen, *J. Appl. Phys.* **65**, 1802 (1989).

<sup>4</sup> R. C. Dye, R. E. Muenchhausen, N. S. Nogar, A. Mukherjee, and S. R. J. Brueck, *Appl. Phys. Lett.* **57**, 1149 (1990).

<sup>5</sup> Y. Q. Shen, T. Freloft, and P. Vase, *Appl. Phys. Lett.* **59**, 1365 (1991).

<sup>6</sup> R. Sobolewski, W. Xiong, and W. Kula, *IEEE Trans. Appl. Supercond.* **3**, 2986 (1993).

<sup>7</sup> R. Sobolewski, *AIP Conf. Proc.* **251**, 659 (1992).

<sup>8</sup> J. R. Gavaler, J. Talvacchio, T. T. Braggins, M. G. Forrester, and J. Greggi, *J. Appl. Phys.* **70**, 4383 (1991).

<sup>9</sup> R. Sobolewski, W. Xiong, W. Kula, and B. McIntyre, *Physica B* (to be published).

<sup>10</sup> D. H. Auston, *Appl. Phys. Lett.* **26**, 101 (1975).

<sup>11</sup> N. Chandrasekhar, Oriol T. Valls, and A. M. Goldman, *Phys. Rev. Lett.* **71**, 1079 (1993).

<sup>12</sup> W. Kula and R. Sobolewski (unpublished).

# HIGH-T<sub>c</sub> MATERIALS EXPAND SUPERCONDUCTIVE CIRCUIT APPLICATIONS

*Progress in film-deposition techniques is permitting new applications for high-temperature superconductivity.*

ELCTRONICS based on high-temperature superconductivity (HTS) is viable in some important niches, notably passive microwave circuits. Improvements in thin-film materials and deposition methods are extending the use of HTS electronics to such applications as active devices, high-speed digital circuitry, and multi-chip modules (MCMs) supporting both CMOS and superconductive chips.

The rapid-single-flux-quantum<sup>1</sup> Josephson-junction family of digital circuits was invented before the discovery of HTS, while the flux-flow transistor (FFT)<sup>2</sup> was developed using classic helium-temperature superconductive materials. Superconductive microwave devices<sup>3</sup> are also not new, and complementary-metal-oxide-semiconductor (CMOS) devices were developed for reasons having nothing to do with competition from superconductive devices.

A. DAVIDSON, J. TALVACCHIO, M.G. FORRESTER, and J.R. GAVALER, Westinghouse Electric Corp., Science and Technology Center, 1310 Beulah Rd., Pittsburgh, PA 15235; (412) 256-1000.



All of these independent advances are now being combined as a result of the discovery and unique material properties of HTS oxides, as well as the steady improvement of HTS thin films and structures.

Applications in radar and communications using passive devices<sup>4</sup> are most imminent because of the structures' simplicity and large performance improvement over the normal-state equivalent. Signal-processing and data-switching circuits are also under development, but will require a much better understanding of materials to be equally advantageous.

## FILM DEPOSITION

Despite a lot of early work using co-evaporation,<sup>5</sup> there are currently two preferred methods of film deposition: sputtering<sup>6</sup> and laser ablation.<sup>7</sup> These two deposition techniques work in similar ways, as they

both involve transport of material from a stoichiometric target to a heated substrate.

In laser ablation, this transport is accomplished by focusing a nanosecond-scale laser pulse of sufficient energy onto a target. The pulse heats the target immediately under the surface, vaporizing it and causing an explosive discharge of material perpendicular to the target surface. Some of the ejected material is energetic enough to be in the form of a plasma, while some is apparently in the form of particles and droplets. A heated substrate a few centimeters away collects the material to build up a film. Laser-ablated films are typically of high quality, with excellent stoichiometry and good superconductive parameters. Work is being done to improve surface roughness and allow for larger (>5 cm) wafers. The deposition rate for small wafers, however, is fairly rapid, typically a

1. This 4-GHz HTS filter developed at Westinghouse has a wafer length of approximately 5 cm. Such a filter can outperform normal components with dimensions of 30 cm or more.

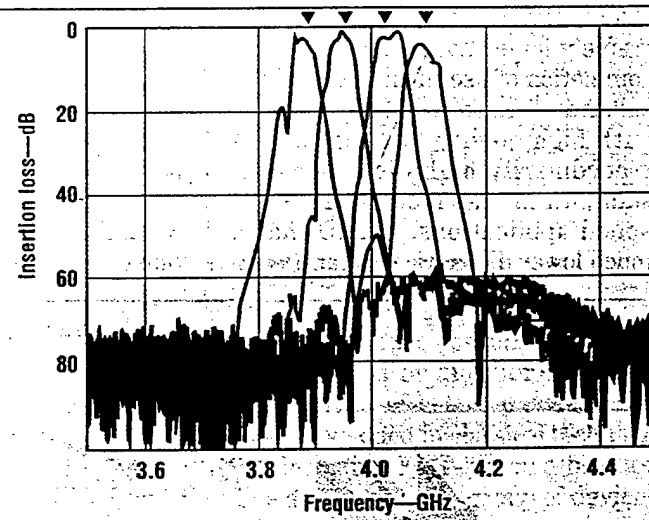
## HTS APPLICATIONS

few angstroms per second.

The sputtering method is in many ways complementary to laser ablation. It is slow (often in the range of 0.1 angstroms per second) but easily accommodates large wafers, with 5-cm diameters being common (10-cm capability is under development). The most common kind of sputtering employs RF magnetron systems and uses an off-axis geometry. In the off-axis arrangement, the substrates are orthogonal to the target and usually placed off to the side to avoid direct bombardment by negative ions. These are ionized oxygen atoms which can be released by either the sputter gas or the target itself, and which are energetically emitted from the target.

Under conditions which minimize resputtering from hot surfaces in the vicinity of the substrate, sputtered YBCO films were the first to be grown without the presence of CuO precipitates. Smooth films resulting

■  
2. Measured insertion loss is shown for a prototype four-filter bank. The four triangles at the top mark the intended center frequencies. ■



from the elimination of CuO particles have also been produced via laser ablation by employing an off-axis configuration.<sup>8</sup> This off-axis structure, however, reduces the high-deposition-rate advantage of laser ablation compared to sputtering.

The ultimate importance of uni-

form deposition on large wafers should be emphasized. For this reason, other deposition techniques, such as metal-organic chemical vapor deposition (MOCVD),<sup>9</sup> may prove to be the most effective. For now, however, ablation and sputtering produce the best films.

**HTS APPLICATIONS**

The choice of substrate is extremely important to the successful completion of useful circuits.  $\text{SrTiO}_3$  substrate<sup>10</sup> can be used to grow films with high quality but with an extraordinarily-high dielectric constant, which rules it out for any high-speed applications.  $\text{LaAlO}_3$  has a much lower dielectric constant<sup>11</sup> (ap-

proximately 24) and has been used successfully for single-layer applications, such as microstrip or coplanar microwave filters and delay lines.

It has not worked as well in multilayer circuits, however, because of the motion of twin boundaries<sup>12</sup> when the wafer is heated for application of new HTS layers. The moving

twin boundaries can shift the bottom film layers by several microns over the width of even a 1-cm chip, making alignment of subsequent layers impossible. At the moment,  $\text{NdGaO}_3$  appears to be the substrate of choice for multilayer circuits.<sup>13</sup> It provides a low dielectric constant (similar to  $\text{LaAlO}_3$ ) without the shifting-twin problem.

Consideration of multilayer structures also determines the choice of HTS film material. The materials with the highest transition temperature ( $T_c$ ) are TBCCO and  $\text{HgBCO}$ ,<sup>14</sup> but their lack of stability prevents the production of multiple levels. YBCO has exhibited the best combination of  $T_c$  and superconduc-

**The use of HTS films in passive microwave devices promises excellent insertion-loss performance as well as compact size.**

tive properties, with enough stability that subsequent layers can be formed without degradation of prior layers.

In addition to superconducting films, epitaxial insulating films are required in multilayer superconducting circuits for isolation of ground planes, crossovers, lumped-element capacitors and inductors, and flux transformers. Epitaxial growth is not essential for obtaining the desired insulator properties, but it is needed to support growth of subsequent high-quality superconducting film layers.

The obvious candidate materials for epitaxial insulators are the ones that work well as substrates. Other oxide and fluoride compounds which,

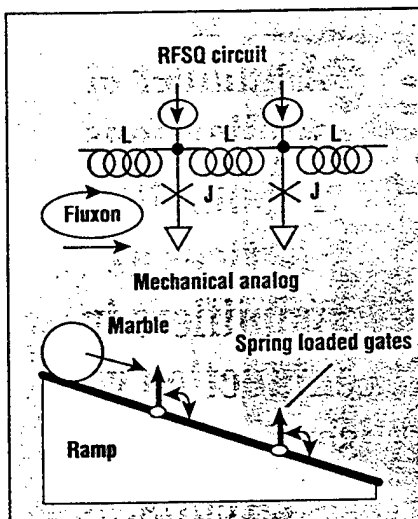
## HTS APPLICATIONS

for example, cannot be grown as large single crystals but provide a good lattice match to YBCO, have been tested.

It is possible to find substrate materials that are compatible with both HTS films and ordinary semiconductor devices so that hybrid circuits for use in liquid nitrogen can be produced monolithically.<sup>15</sup> For example, a layer of silicon can be grown epitaxially on sapphire and formed into semiconductor circuits. This technology has a long history and is known as silicon-on-sapphire (SOS). After the transistors are formed, areas for the HTS devices can be stripped down to the substrate, and with the appropriate buffer films, good YBCO layers can be grown. The 750°C temperature will not hurt the transistors, particularly if the HTS deposition is quick (as in laser ablation).

## HTS APPLICATIONS

Commercial and military use of HTS films for microwave passive components (such as filters or delay lines) can be expected in the near future, with HTS-based ground planes and interconnection wires on MCMs available further along in time. Passive microwave devices using HTS films are particularly attractive because they combine very-low insertion loss with small size and low weight. Even including the necessary refrigeration, these devices save space and weight while providing a performance advantage,<sup>16</sup> par-

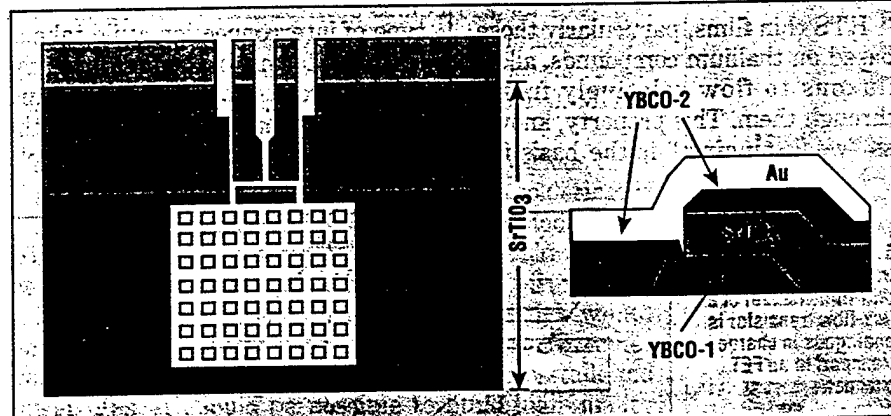


4. In an RFSQ circuit, the Josephson circuit treats the fluxon as a conserved particle which is forced through the circuit by bias currents. This is analogous to a marble forced down a ramp by gravity. The Josephson junctions act like spring-loaded gates which interact with the marble on the ramp.

ticularly in remote-sensing and communications applications.

An example is a prototype X-band filter developed at Westinghouse (Fig. 1). A plot illustrates the insertion-loss performance of a switchable bank composed of four of these X-band filters (Fig. 2).<sup>17</sup>

In the longer term, HTS film structures can be expected to play a key role in the interconnection of semiconductor chips.<sup>18</sup> CMOS silicon devices work better at 77 K than at room temperature, as they exhibit a lower operating voltage, less dissipation, and faster switching. By putting low-temperature silicon chips



3. A top view is shown for a device fabricated with an HTS step-edge Josephson junction (left). A cross-sectional diagram shows two layers of YBCO, an insulating step, and a gold layer which provides the Josephson coupling (right).

on an HTS board, this speed advantage can be enhanced by the nearly-lossless characteristics of HTS microstrip transmission lines. The advantage could be increased even further if hybrid CMOS HTS circuits are developed to drive these transmission lines.

## ACTIVE DEVICES

The classical superconductive active device is the Josephson junction (in one form or another). Several other types of active devices have been developed in classical technology, including FET-like and bipolar-like devices<sup>19</sup> and a group of devices which control the movement of magnetic flux (known as flux-flow devices). With present HTS technology, two device types have achieved some success: the Josephson junction and the flux-flow device.

Interestingly, the performance characteristics of the two device types relative to classical superconductive technology are reversed. In many ways, flux-flow devices take advantage of the natural properties of HTS material, whereas Josephson junctions must fight against them.

It is very difficult to make the exact analog of a classical Josephson junction out of HTS materials. The trouble stems from a combination of extreme anisotropy due to the layered nature of HTS and very-short coherence lengths (roughly 3 to 30 angstroms). This means that superconductivity, and hence the Josephson effects, are suppressed at almost all interfaces of these materials. Usable junctions, however, have been developed with some interesting techniques.

For electronics, the most successful methods so far involve "edge junctions,"<sup>20</sup> in which some property or configuration is altered when a film goes up over an edge of an underlying film, usually an insulator. In some cases, a thin normal metal at the edge provides the coupling between films, while in others, a deposited oxide is used. For example, in a typical step-edge geometry, gold couples to HTS films across a small (100-nm) gap (Fig. 3). The edge geometry produces the distinctive fea-

## HTS APPLICATIONS

tures of a classical non-hysteretic Josephson junction. Where parasitic capacitance has been large, hysteresis has been observed, but never with a true gap structure. Therefore, these junctions are not suited for many of the classical superconductive circuit families that require hysteresis or a sharp gap.

There is one class of digital circuits which requires just what HTS-edge Josephson junctions seem to deliver, and that is the rapid-single-flux-quantum (RSFQ)<sup>21</sup> type of circuit. RSFQ circuits do not use voltage or current levels to represent ones and zeroes, as all transistors and most superconductive circuits do. Instead, bits are represented by the presence or absence of quantized fluxoids in different parts of the circuits.

Quantization of the magnetic flux ( $\Phi$ ) is an integral part of superconductive circuits, where the magnetic flux enclosed by a superconductive path is forced to take on a value corresponding to an integral multiple of  $\Phi_0 = 2.07 \times 10^{-15}$  Webers. By controlling inductance and critical-current values, it is relatively simple to control the motion of single-flux quanta (or fluxons) in superconductive circuits using Josephson junctions.

The transmission of fluxons in a simple RSFQ circuit is analogous to a marble forced down a ramp with spring-loaded gates (Fig. 4). The marble corresponds to the fluxon while the spring-loaded gates are roughly analogous to Josephson junctions. The bias current exerts a force on the fluxon (via the Lorentz force), just as gravity applies a force to the marble. It is possible to achieve any logic function by using some fluxons to control the motion of other fluxons through their interaction with the Josephson junctions. In this approach, it is necessary to use some Josephson junctions to allow surplus fluxons to escape from the circuit, as spring-loaded gates would be used in the mechanical analog as trap doors to dispose of excess marbles.

The focus of research on edge junctions is to find ways to minimize the spread in critical-current values. At

■ **A number of applications use flux-flow devices as amplifiers in conjunction with semiconductor circuits.** ■

present, it is common for junctions on the same chip to have a critical-current spread of 50 percent or more, though some chips have been produced with spreads of only about 20 percent. This amount of variation is adequate for only the smallest digital circuits with, at most, a few dozen junctions. To allow development of RSFQ circuits with thousands of junctions, critical-current spreads of no more than 1 or 2 percent will have to be developed. At the moment, a certain type of nanobridge junction<sup>22</sup> is much better than the edge geometry for minimizing current spread, but these junctions have critical currents that are too low for reliable operation at liquid-nitrogen temperature and are not amenable to higher currents.

**FLUX-FLOW TRANSISTORS**

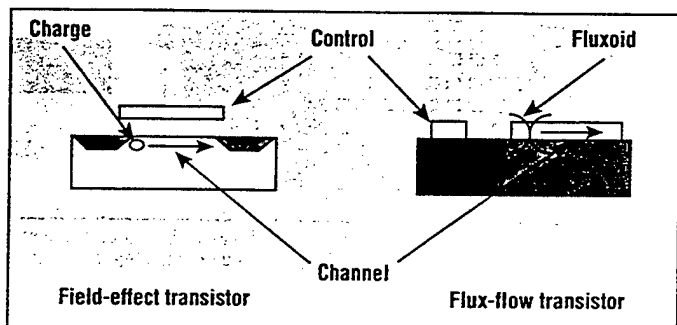
HTS thin films, particularly those based on thallium compounds, allow fluxons to flow relatively freely through them. This property, known as "weak pinning," is the basis for

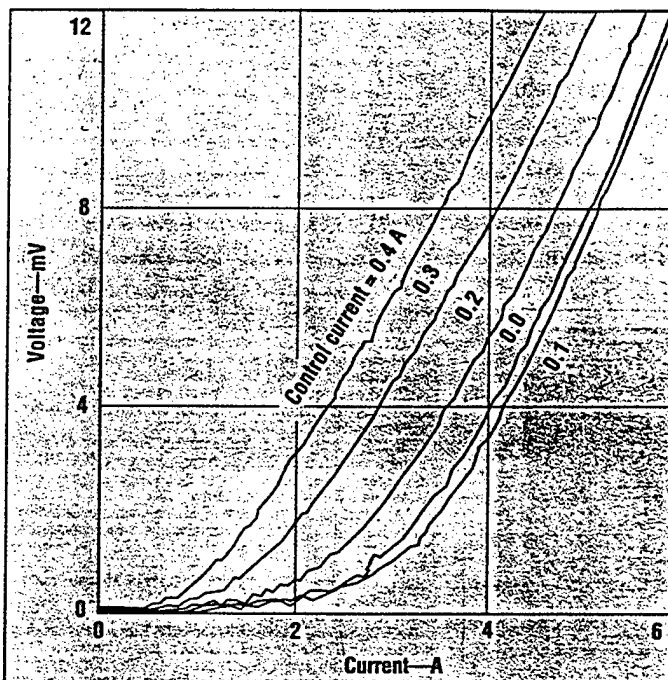
the FFT, a true three-terminal superconductive device.<sup>23</sup> The control of flux motion in an FFT is comparable to charge motion in an FET (Fig. 5). An I-V curve was obtained for a large-scale FFT (a few millimeters on a side) made from a piece of bulk ceramic YBCO with a coil wound around it (Fig. 6). For a load of a few milliohms, it is apparent that the device provides both current gain and voltage gain. Smaller devices fabricated with thin films have produced similar gain or transimpedance with much smaller currents and higher voltages.

Martens has demonstrated a wide variety of circuits employing these devices, including microwave amplifiers and oscillators, as well as digital logic and memory. From a circuit viewpoint, the main problem with these devices is that they are fairly leaky. That is, their high-resistance state is still a fairly-low resistance, generally a few ohms. Some advantages are that they can be made from a single HTS-film deposition and that they have been reported to have very-high effective  $I_c R_n$  products (sometimes over 10 mV). These devices are consequently useful for applications involving semiconductor interfacing.

There are opportunities to use flux-flow superconductive devices as amplifiers in significant military and civilian applications. These applications utilize the interconnection of fast but very-low-voltage Josephson-junction devices with semiconductors such as CMOS circuits. This type of interconnection could take at least two forms. In the first form, the CMOS circuits at room temperature are the ultimate destination of the Josephson circuit outputs. A Joseph-

5. Magnetic flux transport in the HTS thin-film channel of a flux-flow transistor is analogous to charge transport in an FET channel.



**HTS APPLICATIONS**

6. A current-voltage (I-V) characteristic plot was obtained for an HTS bulk FFT device. Veteran engineers will note the similarity to vacuum-triode characteristics.

son signal processor in a cryogenic environment, for instance, is of no value unless there is a way of reading the cryogenic output bytes into conventional computing equipment. The other form of interconnection would be between Josephson circuits and CMOS circuits, all at low temperature. There is at least one proposal,<sup>24</sup> for example, to use Josephson devices as output drivers for FET memory cells. In the processor (where the memory bytes are received), another superconductive circuit would be used to pick up the low-level signal and deliver it to another semiconductor.

**MULTICHP MODULES**

A natural application for HTS thin films is MCM technology. Here the idea is to eliminate one level of chip packaging. In present desktop computers, for example, chips are mounted in epoxy packages with multiple pins sticking out. These pins are plugged into sockets or soldered directly to printed-circuit boards (PCBs). MCMs can serve to eliminate the epoxy package.

Bare chips are mounted to the board by various techniques, including wire bonding and flip-chip soldering. If the PCB were constructed of HTS thin films and the appropriate dielectrics, several advantages could be realized. Because resistance is eliminated, the wiring channels could employ a much finer pitch, which would simplify board construction. Power and ground planes would be more ideal, helping to eliminate crosstalk and power dips. It should be possible to build high-quality transmission-line structures with either stripline or coplanar geometries. If terminations can be used, these lines could be charged up by one-way transmission of the signal, so HTS MCMs could also be significantly faster

## HTS APPLICATIONS

than normal metal boards which rely on multiple reflections to transfer data.

The challenge is to find ways to grow high-quality HTS films in multiple layers with compatible insulators, making use of materials which have an acceptable thermal-expansion match to the chips and connec-

tors. Also needed are stable and reliable interface materials for all the connections, as well as some means of modification and repair. ••

## Acknowledgments

The authors express their gratitude for data and helpful consultation to Salvador Talisa, John X. Przybysz, Mike Janocko, Don Miller, Dan Meier, Joon-Hee Kang, Hodge Worsham, and George Wagner. This work was supported in part by ONR/ARPA Contract No. N00014-91-C-0112, AFOSR Contract No. F49620-91-C-0034, and NRL Contract No. N00014-92-C-2043.

## References

1. K.K. Likharev, O.A. Mukhanov, and V.K. Semenov, "Resistive Single-Flux Quantum Logic for Josephson Junction Technology," *SQUID '85 Conference Proceedings*, Berlin, Germany, 1985, pp. 1103-1108.
2. D.P. McGinnis, J.E. Nordman, and J.B. Beyer, "Optimization of Circuit Parameters for the Vortex Flow Transistor," *IEEE Transactions on Magnetics*, Vol. 23, 1987, p. 699.
3. R.A. Davidheiser, "Superconducting Microstrip Filters," *American Institute of Physics Conference Proceedings*, New York, NY, 1978, pp. 219-222.
4. M. Nisenoff, J.C. Ritter, G. Price, and S.A. Wolf, "The High-Temperature Superconductivity Space Experiment," *IEEE Transactions on Applied Superconductivity*, Vol. 3, 1993, p. 285.
5. P.M. Phillips *et al.*, "Comparison of  $\text{Ba}_2\text{YCu}_3\text{O}_{7-x}$  Films on  $\text{NdGaO}_3$  and  $\text{LaAlO}_3$ ," *IEEE Transactions on Magnetics*, Vol. 27, No. 2, 1991, p. 1006.
6. J.R. Gavalier *et al.*, "Critical Parameters in the Single-Target Sputtering of  $\text{YBa}_2\text{Cu}_3\text{O}_7$ ," *Journal of Applied Physics*, Vol. 70, No. 8, 1991, p. 4383.
7. T. Venkatesan *et al.*, "Laser Processing of High-T<sub>c</sub> Superconducting Thin Films," *IEEE Journal of Quantum Electronics*, Vol. 25, No. 11, 1989, p. 2388.
8. R.J. Kennedy, "A New Geometry for Laser Ablation for the Production of Smooth, Single-Layer YBCO/PBCO Multilayer Films," *Advances in Cryogenic Engineering (Materials)*, Vol. 38, 1992, p. 1005.
9. A. Eribil *et al.*, "Review of Metal-Organic Chemical Vapor Deposition of High-Temperature Superconducting Thin Films," *Processing of Films for HTS Electronics*, 1990, p. 104.
10. P. Chaudhari *et al.*, "Critical Current Measurements in Epitaxial Films of  $\text{YBa}_2\text{Cu}_3\text{O}_{7-x}$ ," *Physics Review Letters*, Vol. 58, 1987, p. 2684.
11. R.W. Simon, "Substrates for HTS Films," *Processing of Films for HTS Electronics*, 1990, p. 2.
12. G.-D. Yao *et al.*, "Synchrotron X-Ray Topography Studies of Twin Structures in Lanthanum Aluminate Single Crystals," *Journal of Materials Research*, Vol. 7, 1992, p. 1847.
13. M. Sassa, S. Miyazawa, and M. Mukaida, "Thermal Expansion Coefficients of High-T<sub>c</sub> Superconductor Substrate  $\text{NdGaO}_3$  Single Crystal," *Journal of Applied Physics*, Vol. 68, No. 7, 1990, p. 3643.
14. A. Schilling *et al.*, "Superconductivity above 130 K in the Hg-Ba-Cu-O System," *Nature*, Vol. 30, 1993, p. 56.
15. M.J. Burns *et al.*, "Demonstration of YBCO and Complementary Metal-Oxide-Semiconductor Device Fabrication on the Same Sapphire Substrate," *Applied Physics Letters*, Vol. 63, 1993, p. 1252.
16. R.R. Bonetti, M. Nisenoff, and D.L. Johnson, invited presentations at the "High-T<sub>c</sub> Superconductivity in Microwave Systems: A Technology Assessment" Workshop, International Microwave Symposium, Atlanta, GA, June 1993.
17. Data provided prior to publication by S. Talisa and M. Janocko, Westinghouse Science and Technology Center, Pittsburgh, PA.
18. M.J. Burns *et al.*, "Multichip Module Using Multilayer  $\text{YBa}_2\text{Cu}_3\text{O}_7$  Interconnects," *Applied Physics Letters*, Vol. 62, 1993, p. 1435.
19. D.J. Frank and A. Davidson, "Prospects for High-T<sub>c</sub> Superconductor/Semiconductor Transistor-Like Devices," 5th International Workshop on Future Electron Devices, Miyagi, Japan, June 1988.
20. R.P. Robertazzi *et al.*, " $\text{Y}_1\text{Ba}_2\text{Cu}_3\text{O}_7/\text{MgO}$  /  $\text{Y}_1\text{Ba}_2\text{Cu}_3\text{O}_7$ ," *Applied Physics Letters*, Vol. 61, 1992, p. 711.
21. K.K. Likharev and V.K. Semenov, "RSFQ Logic Memory Family," *IEEE Transactions on Applied Superconductivity*, Vol. 1, 1991, p. 3.
22. J.R. Wenot *et al.*, "YBCO Nanobridges Fabricated by Direct-Write Electron-Beam Lithography," *Applied Physics Letters*, Vol. 61, 1992, p. 1597.
23. J.S. Martens *et al.*, "Flux Flow Microelectronics," *IEEE Transactions on Applied Superconductivity*, Vol. 3, 1993, p. 2295.
24. H. Kroger and U. Ghoshal, "Can Superconductive Digital Systems Compete with Semiconductor Systems?" *IEEE Transactions on Applied Superconductivity*, Vol. 3, 1993, p. 2307.

## For further reading

A.T. Findikoglu *et al.*, "Sr<sub>2</sub>AlTaO<sub>6</sub> Films for Multilayer High-Temperature Superconducting Device Applications," *Applied Physics Letters*, Vol. 61, 1993, p. 1718.

# Properties of Passive Structures for Multilayer HTS Digital Circuits

J. Talvacchio, M. G. Forrester, and J. R. Gavaler  
Westinghouse STC, Pittsburgh, PA, USA

**Abstract** — The passive structures required for HTS digital circuits that must be formed at high temperature (650–750°C) were evaluated by fabricating crossovers, vias, YBCO/YBCO contacts, and multiple coverage of steps with trilayer structures of YBCO / epitaxial insulator / YBCO. Two insulator materials were used, high- $\epsilon$  SrTiO<sub>3</sub> and relatively low- $\epsilon$  Sr<sub>2</sub>AlTaO<sub>6</sub> (SAT). The deposition conditions for both insulators had to be optimized to simultaneously obtain smooth surfaces, sufficiently high oxygen diffusion rates to re-oxidize underlying YBCO, and resistivities in planar capacitor structures of  $> 10^9 \Omega\text{-cm}$  at 77K. The particular process used to clean film surfaces after photolithography and Ar ion milling was also critical in obtaining smooth surfaces for a subsequently deposited film layer. For the non-planar capacitor structures formed at crossovers, the effective resistivity of insulators decreased as a function of linewidth, particularly for lines less than 10  $\mu\text{m}$  wide. However, even for narrow lines patterned in the top YBCO layer, critical current densities,  $J_c$ (77K), exceeded  $10^6 \text{ A/cm}^2$ .

## I. INTRODUCTION

The primary requirements for a high-temperature superconductor (HTS) digital circuit process are reproducible Josephson junctions and the integration of these junctions into an epitaxial, multilayer process that includes a superconducting ground plane. The status of the latter requirement is described in two recent papers on the fabrication of SQUIDs operable to 20K and 77K, respectively, which were isolated from an integrated HTS ground plane by an epitaxial insulating oxide film [1], [2]. The requirements for insulating film layers in digital circuits are more demanding than for integrated SQUID magnetometers since the large area of overlap between YBCO devices and a ground plane makes electrical properties more sensitive to the presence of pinholes in the insulator or outgrowths in the underlying HTS layer.

This paper presents some results on the passive structures required in HTS digital circuits studied in realistic circuit configurations but ones for which their properties can be easily separated from those of active devices. References [3] and [4] report work performed with a similar objective and report similar success in achieving high-resistance isolation between HTS film layers using one of the insulators reported here, SrTiO<sub>3</sub>. Their results will be discussed in places where a direct comparison can be made with this work.

Manuscript received October 18, 1994

This work was supported in part by AFOSR Contract No. F49620-94-C-0021 and ONR/ARPA Contract No. N00014-91-C-0112.

## II. EXPERIMENTAL PROCEDURE

Off-axis rf magnetron sputtering was used to deposit YBCO and epitaxial insulating oxide films. The sputter-gas composition was typically 100 mtorr Ar, 50 mtorr O<sub>2</sub>, and 20 mtorr H<sub>2</sub>O [5]. The deposition temperature was an important parameter in this work and was varied between 650 and 750°C. Both LaAlO<sub>3</sub> and NdGaO<sub>3</sub> substrates were used. For substrates silver-pasted to a nickel block during deposition, good agreement was obtained between a thermocouple mounted in a cavity in the block and measurements with an optical pyrometer capable of correcting for a measured emissivity. It is the block temperature that is reported here. In some cases, substrates were heated solely by radiation and their temperature during growth is estimated from a calibration of film properties. All samples were rotated during film deposition to aid in step coverage and maintain a process that is isotropic in the plane of the films. Other details of our deposition process have been published [5], [6].

Patterning of all film layers was by argon ion milling with photoresist milling masks, a beam energy of 150 eV, and a milling angle of 50° from the normal of the rotating film. An endpoint detector based on secondary ion mass spectroscopy (SIMS) was used to control etch depth.

Preliminary results led us to focus on two epitaxial insulating materials, SrTiO<sub>3</sub> and Sr<sub>2</sub>AlTaO<sub>6</sub>. SrTiO<sub>3</sub> is an obvious candidate material since it is an excellent substrate for YBCO and has been widely used as a thin-film insulator in YBCO-based structures since the work by Kingston et al. [7]. We began our work with SAT films after learning of their potential for HTS substrates [8]. Epitaxial SAT films have also been grown by laser ablation [9] and MOCVD [10].

Electrical measurements were made on four types of samples: (1) unpatterned YBCO/insulator bilayers on which 0.8 mm Ti/Au contacts were evaporated through a mechanical mask, (2) YBCO/insulator/YBCO trilayers where the top two layers were patterned by ion milling into large-area mesas, (3) YBCO/insulator bilayers which had the insulator removed at the four corners of 1 cm × 1 cm chips by ion milling to make contact to the base layer, and (4) YBCO/insulator/YBCO trilayers in which each film layer was patterned before depositing the next layer.

One of the mask sets for patterning test chips of type (4) for crossovers and vias is shown in Fig. 1a. Cross-sectional views of the structures around the edge of the chip are shown. The standard measurement for each of these structures is a four-point resistance and critical current density as a function of temperature. The 16 smaller structures in the middle of the

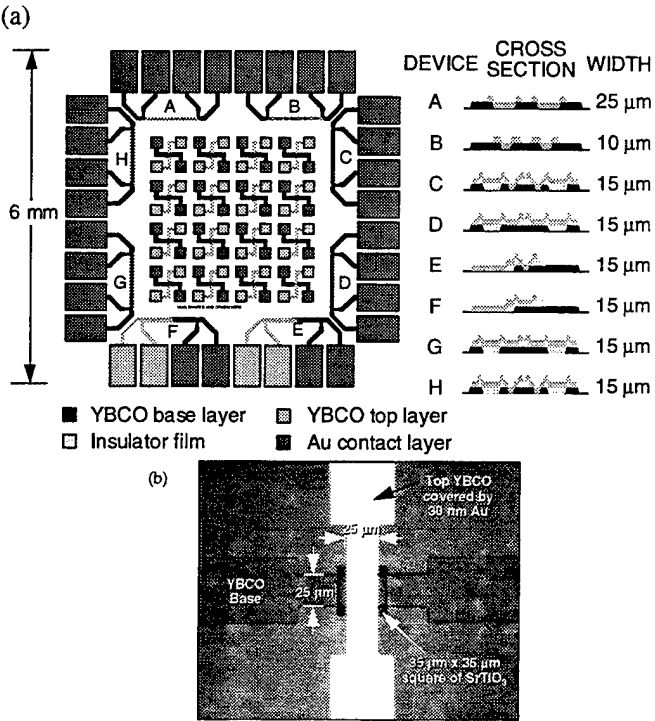


Fig. 1. (a) Mask drawing for YBCO/epitaxial insulator/YBCO structures to study crossovers, vias, step coverage, and crossovers and (b) optical micrograph of one of the 16 completed crossovers from the center of the chip.

chip are for measurement of the electrical isolation of crossovers. An optical micrograph of a completed crossover structure is shown in Fig. 1b.

A procedure was developed for cleaning each film layer after patterning and prior to depositing the subsequent film. It was developed empirically in an effort to eliminate surface roughness of epitaxial insulators deposited on relatively smooth YBCO. The roughness was particularly evident for insulators deposited at less than 700°C. X-ray photoelectron spectroscopy (XPS) measurements as shown in Fig. 2 were made with a spectrometer located in the same vacuum system where YBCO films were grown. They show the effect of our procedure — ashing the ion-milled photoresist in an oxygen plasma followed by an acetone rinse and second ash — on the presence of hydrocarbon and carbonates on the film surface. This procedure restores the film surface to a composition similar to that obtained by exposure of a fresh surface to air. Heating in the sputter gas removes the rest of the carbon compounds from the surface.

### III. RESULTS AND DISCUSSION

Fig. 3 summarizes the dielectric losses at 77K for four insulator film materials that were investigated and compares their dc resistivity at 77K with an estimation of requirements for a number of HTS applications. Loss tangents are based on bulk values for the materials and dc resistivities show the range of experimental results on planar capacitor structures

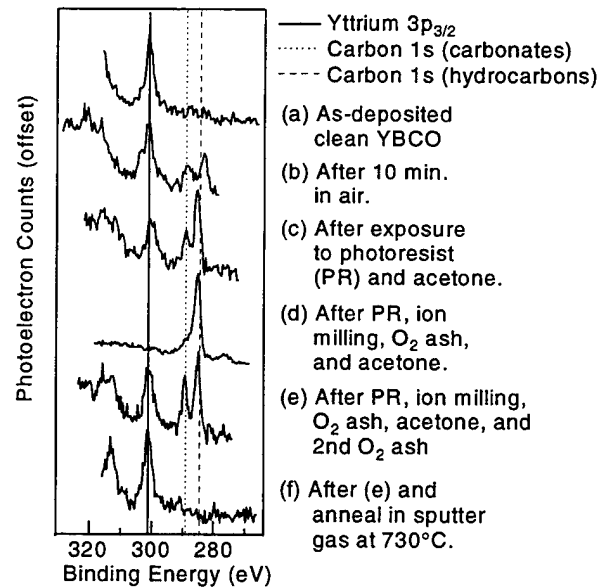


Fig. 2. XPS measurements showing the removal of carbon compounds from the surface of YBCO with the cleaning sequence described in step (e).

described previously as sample types (1) and (2). The YBCO layers were approximately 200 nm thick and no difference was observed for insulators in the measured thickness range of 100 to 300 nm. The samples used for the data in Fig. 3 had surfaces which were free of Cu-O and z-axis-oriented outgrowths. Two YBCO/SrTiO<sub>3</sub> bilayer chips with rough YBCO surfaces were measured and all 10 measurements on each chip showed higher SrTiO<sub>3</sub> conductivity at 77K by 4 to 9 orders of magnitude.

Fig. 3 shows that both SAT and SrTiO<sub>3</sub> provide high-resistance isolation between superconducting film layers. Data from [3] and [4] on SrTiO<sub>3</sub> are in good agreement with this result. In contrast, LaAlO<sub>3</sub> and MgO insulating films

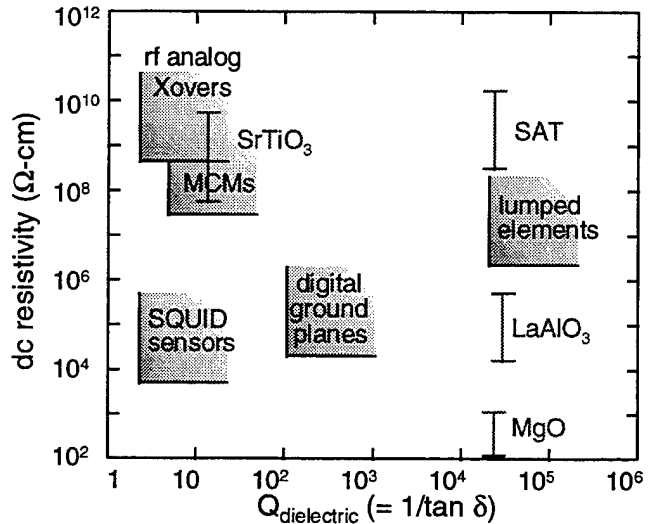


Fig. 3. Summary of dielectric losses in epitaxial insulator film materials in comparison with estimates of application requirements. The error bars show the range of resistivity data obtained from planar capacitor structures. The shaded areas are estimates of the minimum values required for various applications. Tan δ values are for bulk materials.

supported larger leakage currents. The results for  $\text{LaAlO}_3$  are comparable to those in [11] and [12] for  $\text{NdAlO}_3$  and  $\text{PrGaO}_3$ .

The most important conclusion from Fig. 3 is that  $\text{Sr}_2\text{AlTaO}_6$  (SAT) films appear to satisfy dielectric loss requirements for all of the applications considered. Another consideration for applications is the real part,  $\epsilon$ , of the dielectric constant. Bulk  $\text{SrTiO}_3$  has a large and highly temperature-dependent value for  $\epsilon$  that will limit the speed of HTS digital circuits. In contrast, the dielectric constant reported for SAT films of  $\epsilon \approx 23\text{-}30$  in [9] indicates that it is an excellent choice for high-speed digital circuits.

We found that the data in Fig. 3 were independent of insulator deposition temperature in the range of 650 to 750°C. However, the YBCO base layers under  $\text{SrTiO}_3$  films deposited at  $> 680^\circ\text{C}$  and SAT films deposited at  $> 700^\circ\text{C}$  were oxygen-deficient. In some cases, long anneals in an oxygen atmosphere at 400 to 450°C restored superconductivity in the base layers but, in other cases, no superconductivity was measured in the base layer and x-ray diffraction showed that it had a tetragonal crystal structure even after a 72 hr anneal. Confirmation that the YBCO base was simply oxygen deficient was made by etching off the insulator and subsequently restoring a  $T_c$  of  $\sim 90\text{K}$  with a 30 min anneal in oxygen at 450°C.

To obtain direct evidence of the diffusion rates of oxygen through insulator films, the resistance of samples of type (3), YBCO/insulator bilayers, was monitored during annealing at temperatures as high as 600°C. The base YBCO film was used as an oxygen sensor. Fig. 4 shows typical curves of YBCO resistivity versus time as the oxygen gas pressure in the furnace was decreased from 1 atm to 1 torr and then, at a later time, changed back to 1 atm for a bare YBCO film, a YBCO film covered by  $\text{SrTiO}_3$  grown at 670°C and a YBCO film covered by a SAT film grown at 690°C. The diffusion rate was slowed significantly by the presence of an epitaxial insulating overlayer. Overlays grown at higher temperatures lowered diffusion rates by at least 2 orders of magnitude.

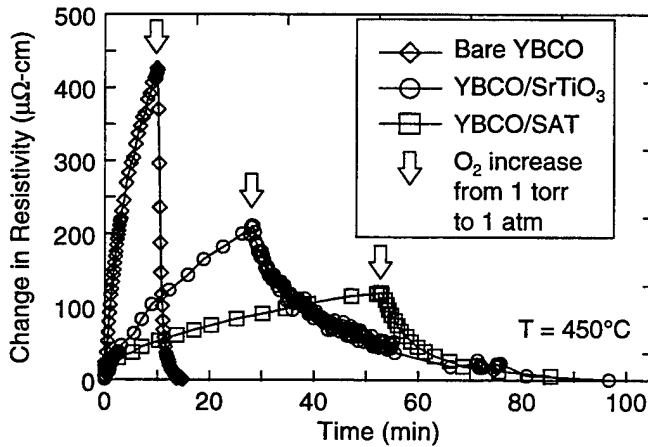


Fig. 4. Change in resistivity with time for YBCO films held at 450°C when oxygen pressure was first reduced to 1 torr from 1 atm (at Time = 0 min) and then increased back to 1 atm. Overlays of  $\text{SrTiO}_3$  or SAT reduced the diffusion rate.

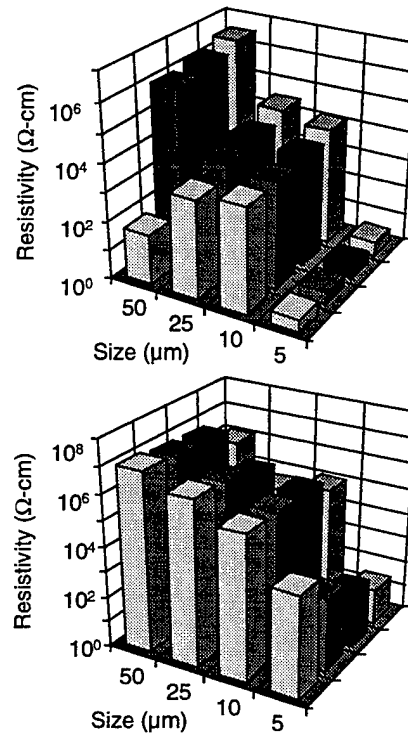


Fig. 5. Resistivity of YBCO/ $\text{SrTiO}_3$ /YBCO crossovers in the configuration shown in Fig. 1. Results are shown from two chips with four rows of crossovers of four different widths to indicate both on-chip and chip-to-chip reproducibility.

X-ray diffraction did not help to identify the defects in insulator films that permitted oxygen diffusion. Typical rocking curve widths were  $\Delta\omega = 0.4$  to  $0.6^\circ$  for base YBCO layers,  $\Delta\omega = 0.4$  to  $0.65^\circ$  for  $\text{SrTiO}_3$  grown on YBCO,  $\Delta\omega = 0.55$  to  $0.8^\circ$  for SAT grown on YBCO, and  $\Delta\omega \leq 0.5^\circ$  for the top YBCO layer. The variation in  $\Delta\omega$  for SAT and  $\text{SrTiO}_3$  did not correlate with either its deposition temperature, or the time required to oxidize the underlying YBCO. It should not be surprising that the defects are unrelated to  $\Delta\omega$ . In one case, we grew  $\text{SrTiO}_3$  on a rough YBCO film at a temperature  $>> 680^\circ\text{C}$ . Despite the good crystallinity that is expected to result from growth at high temperature, the YBCO underlayer oxidized rapidly due to defects introduced by its roughness.

Data for crossover structures where the insulator must cover a step in samples of type (4) is shown in Figs. 5a and 5b. Resistivity is plotted as a function of position on the chip for two YBCO/ $\text{SrTiO}_3$ /YBCO chips of the type shown in Fig. 1. The conclusions reached from examination of such data are: 1) There is an unexplained trend to lower resistivity in smaller crossovers. The trend is stronger than the linear scaling with the length of the step that has to be covered. 2) A large variability was measured in resistivity for a set of chips processed together. The higher values were in agreement with the lower end of the range measured for planar trilayers. 3) The target value of  $\rho > 10^4 \Omega\text{-cm}$  is attainable for all but the smallest crossovers. However, since crossovers of lines  $> 5 \mu\text{m}$  wide are needed, the low resistivity of these structures must be improved.

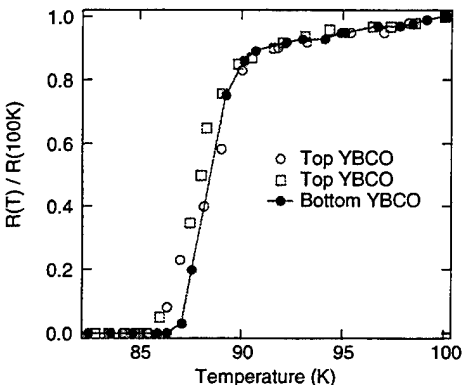


Fig. 6. Resistive superconducting transitions are shown for two bridges patterned in the top YBCO film of a trilayer and one bridge in the bottom film. The measurements show that multiple exposures to photoresist, solvents, ion milling, and air followed by anneals does not significantly degrade YBCO films when effective surface cleaning procedures are used.

A comparison of resistive superconducting transitions is made in Fig. 6 for two bridges patterned in a top YBCO layer on YBCO/SrTiO<sub>3</sub> and in the bottom YBCO layer. All three superconducting transitions were lower than an unprocessed companion film by 2-3K. However, the agreement between the three curves shows that neither coverage of steps by the top layer or growth on a patterned epitaxial insulating film significantly degraded the transition.

Fig. 7 shows the result of a critical current measurement,  $J_c(T)$ , made for a top-layer YBCO bridge. The benchmark for high-quality YBCO,  $J_c(77K) > 10^6$  A/cm<sup>2</sup>, is exceeded despite the fact that the film covered steps in the insulator and base YBCO layers. An early attempt to obtain this result is reported in [4] where  $J_c(77K) \approx 10^5$  A/cm<sup>2</sup>.

#### IV. CONCLUSIONS

Planar structures consisting of YBCO superconducting films and heteroepitaxial insulating oxide films were studied to determine growth conditions in which smooth layers could be obtained that provided electrical isolation with resistivities  $> 10^9$  Ω·cm<sup>2</sup> yet permitted oxygen to diffuse through to underlying YBCO. For SrTiO<sub>3</sub> and SAT insulators, these conditions are satisfied for growth at temperatures  $< 680^\circ\text{C}$

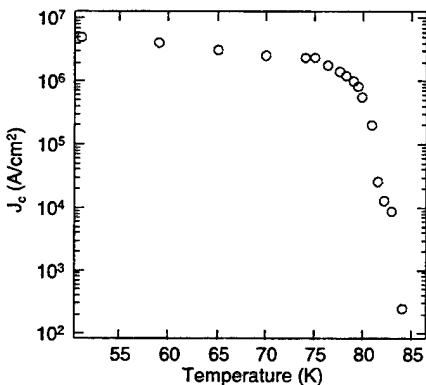


Fig. 7. Critical current density versus temperature for a bridge patterned in a top YBCO film that covers steps in the insulator and the base YBCO layer.

and  $< 700^\circ\text{C}$ , respectively.

Surfaces of YBCO films were examined for roughness and contamination by carbon compounds to establish a suitable cleaning procedure for multiple lithography and deposition steps. Using this procedure, a surface can be obtained which is as clean as that of a freshly deposited film.

Trilayers of YBCO/insulator/YBCO were formed by three successive deposition and patterning steps into the passive structures required for HTS digital circuits. Although the critical temperature and critical current density of superconductor layers are relatively unaffected by the processing sequence, electrical isolation of crossovers with linewidths  $< 10$  μm is less than what is required for HTS integrated digital circuits.

#### ACKNOWLEDGMENT

We thank G. J. Faychak for valuable assistance in patterning films and J. H. Uphoff for assisting in film deposition.

#### REFERENCES

- [1] N. Misset, T. E. Harvey, R. H. Ono, and C. D. Reintsema, "High-T<sub>c</sub> multilayer step-edge Josephson junctions and SQUIDS," *Appl. Phys. Lett.*, vol. 63, pp. 1690-1692, September 1993.
- [2] M. G. Forrester, A. Davidson, J. Talvacchio, J. R. Gavaler, and J. X. Przybysz, "Inductance measurements in multilevel high-T<sub>c</sub> step-edge grain boundary SQUIDS," *Appl. Phys. Lett.*, vol. 65, pp. 1835-1837, October 1994.
- [3] J. J. Kingston, F. C. Wellstood, D. Quan, and J. Clarke, "Photolithographically patterned thin-film multilayer devices of YBa<sub>2</sub>Cu<sub>3</sub>O<sub>x</sub>," *IEEE Trans. Magn.*, vol. 27, pp. 974-977, March 1991.
- [4] J. A. Beall, M. W. Cromar, T. E. Harvey, M. E. Johansson, R. H. Ono, C. D. Reintsema, D. A. Rudman, S. E. Asher, A. J. Nelson, and A. B. Swartzlander, "YBa<sub>2</sub>Cu<sub>3</sub>O<sub>x</sub>/insulator multi-layers for crossover fabrication," *IEEE Trans. Magn.*, vol. 27, pp. 1596-1599, March 1991.
- [5] J. R. Gavaler, J. Talvacchio, T. T. Braggins, M. G. Forrester, and J. Greggi, "Critical parameters in the single-target sputtering of YBa<sub>2</sub>Cu<sub>3</sub>O<sub>x</sub>," *J. Appl. Phys.*, vol. 70, pp. 4383-4390, October 1991.
- [6] J. Talvacchio, M. G. Forrester, J. R. Gavaler, and T. T. Braggins, "YBCO and LSCO films Grown by off-axis sputtering," in *Science and Technology of Thin Film Superconductors II*, R. McConnell and S. A. Wolf, Eds., Plenum, New York, 1990, pp. 57-66.
- [7] J. J. Kingston, F. C. Wellstood, P. Lerch, A. H. Miklich, and J. Clarke, "Multilayer YBa<sub>2</sub>Cu<sub>3</sub>O<sub>x</sub>-SrTiO<sub>3</sub>-YBa<sub>2</sub>Cu<sub>3</sub>O<sub>x</sub> films for insulating crossovers," *Appl. Phys. Lett.*, vol. 56, pp. 189-191, July 1990.
- [8] L. E. Cross and R. Roy, "Low-loss substrates for high-T<sub>c</sub> superconductor thin films for microwave applications," *3rd Annual DARPA HTS Workshop*, Seattle, 1991, pp. 107-135.
- [9] A. T. Firdikoglu, C. Doughty, S. Bhattacharya, Q. Li, X. X. Xi, T. Venkatesan, R. E. Fahey, A. J. Strauss, and J. M. Phillips, "Sr<sub>2</sub>AlTaO<sub>6</sub>/YBa<sub>2</sub>Cu<sub>3</sub>O<sub>x</sub> heterostructures for superconducting device applications," *IEEE Trans. Appl. Supercond.*, vol. 3, pp. 1425-1428, March 1993.
- [10] B. Han, D. A. Neumayer, B. R. Goodreau, T. J. Marks, H. Zhang, and V. P. Dravid, "In-situ growth of epitaxial SAT films using MOCVD," *Chem. Mater.*, vol. 6, pp. 18-25, 1994.
- [11] W. Rauch, H. Behner, G. Gieres, B. Sipos, R. J. Seeböck, O. Eibl, R. Kerner, G. Sölkner, and E. Gornik, "Sputtering of YBCO/NdAlO<sub>3</sub>/YBCO trilayers," *Appl. Phys. Lett.*, vol. 60, pp. 3304-3306, June 1992.
- [12] P. A. Nilsson, G. Bronsson, E. Olsson, Z. G. Ivanov, and T. Claeson, "Crossovers and vias in YBCO/PrGaO<sub>3</sub>/YBCO trilayers," *IEEE Trans. Appl. Supercond.*, vol. 3, pp. 2958-2961, March 1993.

# Laser Patterning of $\text{YBa}_2\text{Cu}_3\text{O}_x$ Thin Films Protected by *in-situ* Grown $\text{SrTiO}_3$ Cap Layer

Witold Kula,\* Wei Xiong, and Roman Sobolewski

Department of Electrical Engineering and Laboratory for Laser Energetics, University of Rochester, Rochester, NY 14627

John Talvacchio

Westinghouse Science and Technology Center, Pittsburgh, PA 15235

**Abstract**—We report our studies on laser processing techniques suitable for patterning of  $\text{YBa}_2\text{Cu}_3\text{O}_{7-x}$  (YBCO) thin films, as well as YBCO/SrTiO<sub>3</sub> bilayers, consisting of *in-situ* grown YBCO films with 100-nm-thick single-crystalline SrTiO<sub>3</sub> cap layers. The patterning is achieved through both laser inhibition, in which an intense, focused laser beam locally melts YBCO transferring it into an insulating glass-like material, and laser writing, based on a laser-controlled diffusion of oxygen in or out of the YBCO film. We have found that oxygen easily migrates through the SrTiO<sub>3</sub> layer, allowing to reversibly convert the underlying YBCO film between the superconducting and semiconducting (virtually insulating at low temperatures) phases. Using laser inhibition and writing, we were able to form in a single YBCO/SrTiO<sub>3</sub> sample well-defined regions of various electrical properties, showing that laser processing can be successfully used in patterning and/or electrical trimming of multilayered YBCO circuits. Aging studies, performed on an almost 2-years-old laser-written YBCO film, showed a very good, both structural and electrical stability of our laser-processed structures.

## I. INTRODUCTION

Despite the tremendous progress over the past few years, patterning of  $\text{YBa}_2\text{Cu}_3\text{O}_{7-x}$  (YBCO) thin films and/or multilayers into more complex high-temperature superconducting (HTS) devices and circuits is still in many aspects a challenging technological issue [1]. Standard patterning procedures, applied to a multielement, highly anisotropic and chemically reactive YBCO often result in structures with fuzzy edges and/or a degraded (e.g., oxygen-deficient) chemical composition, lowering the performance of fabricated devices. Recently, a laser-writing patterning technique has been developed for processing of YBCO thin films [2]. The technique, based on local, laser-induced changes of the YBCO oxygen content, offers an interesting alternative to the standard HTS patterning methods, since it allows to overcome some of the above mentioned obstacles. Using laser writing, one can obtain completely planar structures, containing well-defined (on a micrometer scale), uniform superconducting and semiconducting/insulating YBCO regions that are free of surface contamination or edge degradation.

Manuscript received October 17, 1994.

This work was supported in part by the Air Force Office for Scientific Research under Grants F49620-94-1-0094 (Rochester) and F49620-91-C-034 (Westinghouse). W. X. acknowledges support from the Frank Horton Graduate Fellowship Program.

\*Also at the Institute of Physics, Polish Academy of Sciences, PL-02668 Warszawa, Poland.

In this article, we report our studies on a comprehensive laser processing technique for patterning of YBCO thin films and multilayers. In particular, we discuss the laser-inhibition method, in which selected YBCO areas are irreversibly converted into a glass-like, electrically-insulating material, as well as our latest progress in the reversible, oxygen-diffusion-based laser patterning of YBCO. We demonstrate that both the laser-inhibition and laser-writing techniques can be successfully applied to pattern bilayer structures containing YBCO films with *in-situ* deposited insulating SrTiO<sub>3</sub> (STO) coating. We show that in this latter case, electrical properties of the underlying YBCO film can be precisely controlled by a laser-induced, non-invasive diffusion of oxygen atoms through the STO top layer. Several test structures, including superconducting microbridges and field-effect devices, have been prepared from YBCO films and YBCO/STO bilayers with the laser-processing technique and tested. Our results show that the selective, laser-driven diffusion of oxygen through the STO cap layer can be successfully implemented as a practical method of patterning and/or electrical trimming of multilayered YBCO circuits.

## II. LASER PROCESSING OF YBCO

### A. Experimental Techniques

Both the laser-inhibition and laser-writing processing of YBCO thin films and YBCO/STO bilayers were performed using our laser-patterning system described in detail elsewhere [3]. Briefly, the system consists of an Ar-ion ( $\lambda = 514$  nm) CW laser, shutter, focusing microscope, and computer-controlled two-dimensional translational stage (of the minimum step size of 1  $\mu\text{m}$ ) with a gas chamber and sample holder. The laser beam is focused to a 5-100  $\mu\text{m}$  diameter and used to selectively heat up parts of the sample to activate the oxygen diffusion process. The laser spot size corresponds to the range of line widths of our typical, laser-created patterns (wider patterns can be fabricated using multiple scans). The patterns themselves are written by a programmed motion of X and Y translational stages.

For the laser-inhibition patterning, our YBCO sample is placed in a nitrogen atmosphere and laser-heated to the local temperature well above the YBCO melting/decomposition point. The process results in an irreversible conversion of the illuminated YBCO region into a glass-like, highly electrically insulating material. The typical laser power density, applied during the writing process is of the order of 30 mW/ $\mu\text{m}^2$  and the speed of the translational stage is 50  $\mu\text{m}/\text{s}$ . In order to avoid the effect of accumulative heating of the entire YBCO

sample during the inhibition process, the incident laser beam is mechanically chopped at the frequency of  $\sim 400$  Hz, with the duty cycle of 1/6. Implementation of the chopper significantly decreases the total light power delivered to the film, limiting the laser-induced increase in the sample average temperature to only few Celsius.

For the laser-writing patterning, the sample's ambient atmosphere is either pure nitrogen or oxygen, depending on the desired direction of the diffusion of oxygen out of (semiconducting patterns) or into (superconducting patterns) the YBCO film. The laser power density is much lower than in the case of laser inhibition and kept between 0.2 and 5 mW/ $\mu\text{m}^2$ .<sup>2</sup> The speed of translational stages typically ranges from 1 to 5  $\mu\text{m/s}$  for writing oxygen-rich patterns and from 10 to 50  $\mu\text{m/s}$  for oxygen-poor lines. The same process parameters are used for patterning of both plain YBCO films and bilayer YBCO/STO structures.

Our test structures were prepared on 80- to 300-nm-thick epitaxial YBCO films and 150-nm-YBCO/100-nm-STO epitaxial bilayers. The YBCO films were grown on  $\text{LaAlO}_3$  and  $\text{SrTiO}_3$  substrates using a single-target rf sputtering technique [4]. The films exhibited typically a 0.5-K-wide (10%-90%) superconducting transition with the zero resistivity temperature  $T_{\text{c0}}$  of about 89 K. The film critical current density  $J_{\text{c}}$  exceeded 3 MA/cm<sup>2</sup> at 77 K. The YBCO/STO bilayers were fabricated *in-situ* on  $\text{LaAlO}_3$  substrates using rf sputtering technique with interchangeable sputtering guns. After the deposition, the STO layer was photolithographically patterned and plasma etched to expose parts of the YBCO film for the purpose of making electrical contacts. YBCO films and YBCO/STO bilayers, designated for writing oxygen-rich (superconducting) patterns, were intentionally deoxygenated prior to the laser processing by furnace annealing at 700 °C for 1-2 hours in an argon atmosphere.

### B. Laser Inhibition

Fig. 1 presents transmission optical micrographs of the patterns fabricated using the laser-inhibition technique on a (a) superconducting YBCO film and (b) YBCO/STO bilayer. Picture in Fig. 1(a) shows a fragment of a 6-contact structure for Hall-effect measurements, with a 50- $\mu\text{m}$ -wide superconducting YBCO bridge (in the central part) and contact-pad patterns on both sides, while Fig. 1(b) presents a part of a 50- $\mu\text{m}$ -wide channel of a YBCO/STO superconducting field-effect transistor (SuFET). On both photographs, the bright (i.e., optically transparent) lines represent the laser-inhibited YBCO regions. The width of the inhibited lines is about 8  $\mu\text{m}$ . The interface between the inhibited and superconducting YBCO regions is relatively sharp (estimated to be  $<2$   $\mu\text{m}$ ). We also note that the inhibition process does not damage (e.g., by depleting the oxygen content) the adjacent superconducting regions. The latter damage would be indicated in Fig. 1 by a change in the gray level (light absorption) of the YBCO located very close to inhibited lines. The laser-inhibited regions exhibit excellent electrical insulating properties with the room-temperature sheet resistance in excess of 1 G $\Omega$ /square. The above features indicate that the laser-inhibition technique is a

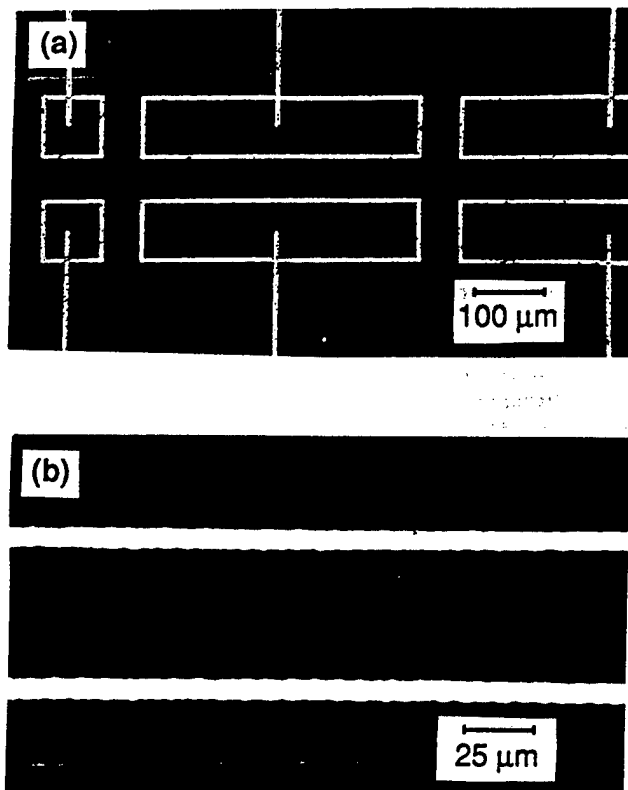


Fig. 1. Optical transmission micrographs of YBCO laser-inhibited patterns: (a) a fragment of a 6-contact-pad structure for Hall-effect and magnetoconductivity measurements with a 50- $\mu\text{m}$ -wide central channel; (b) a part of a 50- $\mu\text{m}$ -wide superconducting channel of a SuFET patterned on 150-nm-YBCO/100-nm-STO bilayer.

fast, mask-free method for patterning of moderately complex YBCO devices and circuits, and it gives results comparable to conventional pulse-laser ablation techniques. We want to stress that our laser-inhibited structures for the Hall-effect and magnetoconductivity measurements exhibited the geometrical and electrical characteristics significantly better than those of the analogous structures prepared using a conventional photolithography and wet chemical etching [5]. Besides YBCO, laser inhibition was also successfully implemented for patterning of Bi-Sr-Ca-Cu-O films and should be applicable for other HTS materials.

### C. Laser Writing

Laser-induced heating of YBCO films up to 400-500 °C in an oxygen or oxygen-free ambient atmosphere leads to fully reversible local changes of the sample's oxygen content and, thus, allows one to precisely adjust the electrical properties of the patterned regions from semiconducting/insulating (oxygen-poor YBCO) to 90-K superconducting (oxygen-rich YBCO). We demonstrated [2] that superconducting properties of the laser-written patterns were essentially the same as those of the original YBCO films, with the  $T_{\text{c0}}$  up to 90 K and  $J_{\text{c}}$  of 3 MA/cm<sup>2</sup> at 77 K. We also showed that the width of the YBCO semiconducting/superconducting

interface in the patterned structures, as analyzed by transmission optical as well as scanning electron microscopy, was less than 1  $\mu\text{m}$ , which was absolutely satisfactory for fabricated by us devices, such as coplanar strip microwave transmission lines and resonators [6], or laser-written charging effect structures [7].

An additional evidence for the sharp, well-defined phase transition from the oxygen-poor to the oxygen-rich YBCO in laser-written patterns is provided by a direct, Raman-spectroscopy measurement of the oxygen-concentration change across the YBCO film containing several semiconducting/superconducting interfaces. Fig. 2 shows the oxygen-concentration profile calculated from the Raman measurements of a sample containing approximately 70- $\mu\text{m}$ -wide oxygen-poor (labeled  $\text{YBa}_2\text{Cu}_3\text{O}_{6.3}$  in Fig. 2) and oxygen-rich ( $\text{YBa}_2\text{Cu}_3\text{O}_{6.9}$ ) lines laser-written on a partially oxygen-depleted ( $\text{YBa}_2\text{Cu}_3\text{O}_{6.5}$ ) YBCO film. The spatial resolution of the Raman microscope was 2  $\mu\text{m}$ . We can clearly see that the transitions between the various YBCO regions are very distinct and in the each case the interface width is limited by the 2- $\mu\text{m}$  instrument resolution.

The long-term stability of our patterns was tested by an electrical characterization and visual inspection of a laser-written superconducting microbridge. The resistivity versus temperature ( $R$  vs.  $T$ ) measurements of the bridge were performed right after the sample fabrication, as well as two, eight, and twenty months later (see Fig. 3). Between the measurements the sample was stored at room temperature without any special precautions regarding ambient atmosphere, humidity, etc. Comparing the curves plotted in Fig. 3, we see that  $T_{\text{c}0} = 89\text{--}90\text{ K}$  of the bridge remained practically unchanged, meaning that the bridge's electrical properties did not degrade over the tested 20-month period. Also the physical appearance of our sample, as analyzed by transmission optical microscopy did not change after the 20 months of the air storage. In particular, we did not observe any smearing or degradation of the YBCO semiconducting/superconducting interface over that period.

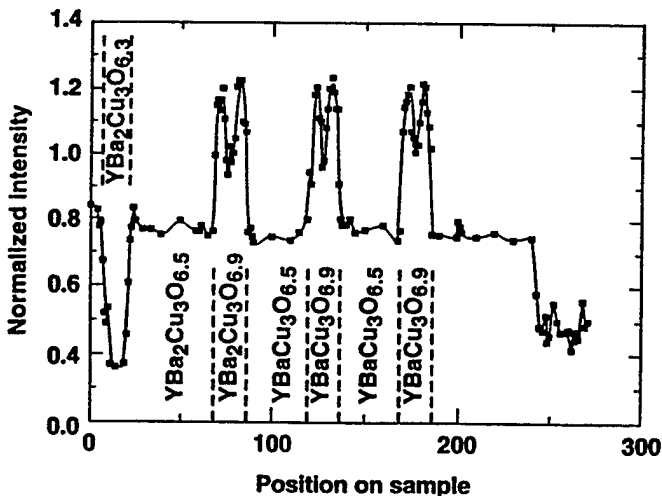


Fig. 2. Oxygen profile calculated from the Raman spectra measured across a laser-written YBCO structure with three different oxygen contents.

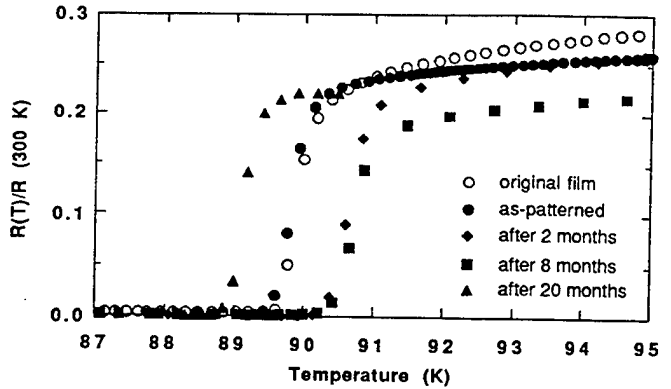


Fig. 3. Comparison between the superconducting transitions of a laser-written, oxygen-rich line measured right after the patterning process (closed circles), as well as two (closed diamonds), eight (closed squares), and 20 (closed triangles) months later.

An important advantage of the laser-writing processing of YBCO is its applicability for noninvasive patterning of not only simple YBCO films, but also bilayers, containing a YBCO film covered by the *in-situ* deposited STO protection layer. In this latter case, focused laser light heats up the underlying YBCO and activates the diffusion of oxygen in and out of YBCO *through* the STO top layer. We found that oxygen easily migrated through the 100-nm-thick STO layer, allowing us to reversibly convert the underlying YBCO between the superconducting and semiconducting/insulating phases and create patterns containing various YBCO regions, in a way similar to that described before for the single YBCO films. Two examples of laser-written structures fabricated from YBCO/STO bilayers are presented in Fig. 4. Fig. 4(a) shows two superconducting lines (dark regions, each approx. 35- $\mu\text{m}$ -wide), patterned on a oxygen-depleted YBCO/STO bilayer. For the testing purposes, the lines were subsequently cut by a perpendicular, oxygen-poor YBCO line, laser-written in nitrogen. As we see, all laser-patterned YBCO regions are homogeneous and display sharp YBCO semiconducting/superconducting interfaces, similarly as in the case of our laser-patterned plain YBCO films.

It is worth to note that in a YBCO/STO bilayer, an STO film deposited on top of YBCO may serve not only as a protection layer, but can also be used as an important element in some HTS devices. A good example is the SuFET structure, shown in Fig. 4(b). In our SuFET, the top STO layer is used as a gate dielectric. The dark region represents a superconducting source electrode, connected to a partially oxygen-depleted YBCO channel [not shown in Fig. 4(b)]. The light/dark-gray interface across the picture is the edge of the STO gate dielectric, so that the left part of the photograph is a STO-free YBCO film (to be covered by silver contact pads), while the right part shows the YBCO pattern prepared through the STO layer. A distinct advantage of using laser writing for fabrication of SuFET devices is the possibility of an *in-situ* deposition of the YBCO/STO bilayer (i.e., assuring the best possible YBCO/STO interface), and a subsequent non-invasive patterning of the device structure.

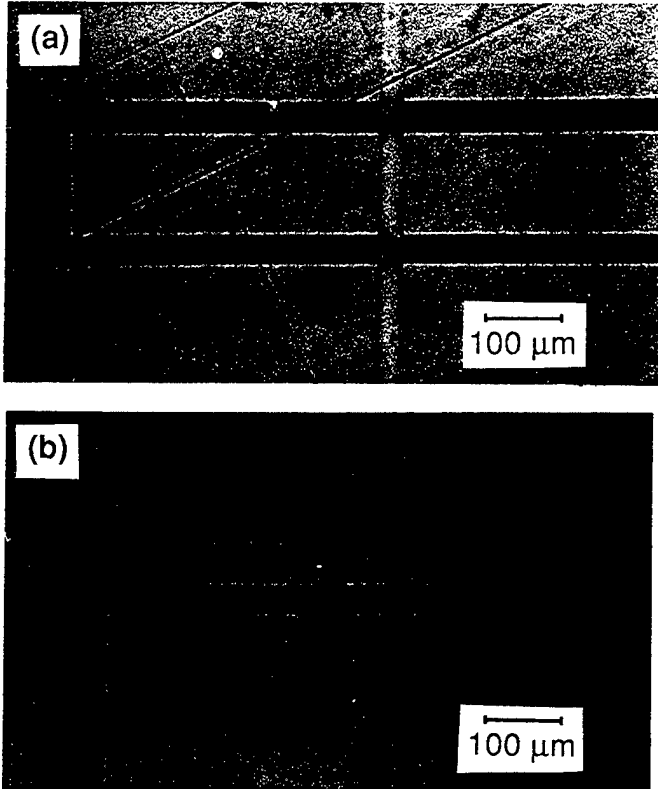


Fig. 4. Laser-written patterns fabricated on YBCO/STO bilayers: (a) two 35- $\mu$ m-wide superconducting lines (dark regions) cut by a perpendicular oxygen-poor line; (b) a part of a SuFET structure (see text for details).

Fig. 5 demonstrates superconducting properties of a 35- $\mu$ m-wide and 4-mm-long oxygen-rich pattern laser-written on the furnace-deoxygenated YBCO/STO bilayer. For the comparison, we also show in Fig. 5 an  $R$  vs.  $T$  curve for the original, superconducting YBCO/STO bilayer (measured before the sample deoxygenation and processing). We see that the superconducting transition of the laser-patterned line is sharper than that of the original bilayer. However, both curves exhibit  $T_{c0}$  of 84 K, indicating that our laser patterning recovered superconducting properties of the original sample. This latter finding was further supported by  $J_c$  measurements performed on our laser-written line. The microbridge  $J_c$  was estimated to be 1.7 MA/cm<sup>2</sup> at 77 K (see Fig. 5), which was close to the value measured for the original YBCO/STO bilayer.

### III. CONCLUSIONS

We have shown that laser inhibition and laser writing are effective methods of patterning YBCO devices and circuits. Both techniques are very suitable for processing of STO/YBCO bilayers. We demonstrated that local laser heating of the STO/YBCO structure promotes a fast diffusion of oxygen through the STO film, allowing to vary electrical properties of the underlying YBCO film from fully superconducting to semiconducting (almost insulating at low temperatures). Thus, laser processing enables to pattern a

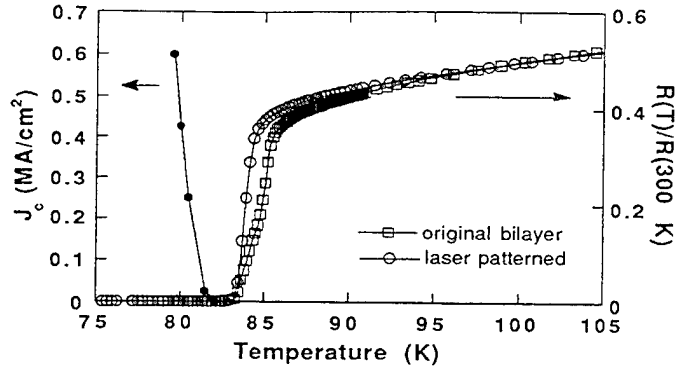


Fig. 5. Resistance and critical current density dependencies on temperature for a laser-written superconducting line (circles), patterned on the deoxygenated YBCO film with the in-situ grown STO cap layer. Superconducting transition for the same YBCO/STO bilayer (squares), measured before sample's deoxygenation, is shown for comparison.

YBCO film (protected by the STO film) without any exposure to ambient conditions. This latter property is especially important for fabricating structures requiring the highest quality STO/YBCO interfaces (e.g., field-effect devices). The patterned STO/YBCO structures exhibit superconducting properties ( $T_{c0} = 84$  K and  $J_c = 1.7$  MA/cm<sup>2</sup> at 77 K) as good as the original bilayers. Finally, aging studies performed on plain YBCO films, showed that laser patterning results in highly stable structures which, over the period of almost 2 years, exhibit practically no deterioration.

### ACKNOWLEDGMENT

The authors would like to thank Val Loh for his initial contribution to the above project. The Raman measurements were performed by D. Dukes and A. D. Caplin from the Centre for High Temperature Superconductivity at the Imperial College, London, UK.

### REFERENCES

- [1] See, e.g., A. I. Braginski, in *Superconducting Devices and Their Applications*, edited by H. Koch and H. Lübbig, Springer Proceedings in Physics, vol. 64, Springer-Verlag, Berlin, 1992, pp. 3-18.
- [2] R. Sobolewski, W. Xiong, W. Kula, and J. R. Gavaler, "Laser patterning of Y-Ba-Cu-O thin-film devices and circuits," *Appl. Phys. Lett.*, vol. 64, no. 5, pp. 643-645, Jan. 1994, and references therein.
- [3] R. Sobolewski, W. Xiong, and W. Kula, "Patterning of thin-film high- $T_c$  circuits by the laser-writing method," *IEEE Trans. Appl. Supercond.*, vol. 3, no. 1, pp. 2986-2989, March 1993.
- [4] J. R. Gavaler, J. Talvacchio, T. T. Braggs, M. G. Forrester, and J. Gregg, "Critical parameters in the single-target sputtering of  $\text{YBa}_2\text{Cu}_3\text{O}_7$ ," *J. Appl. Phys.*, vol. 70, pp. 4383-4391, Oct. 1991.
- [5] W. Gob, private communication.
- [6] W. N. Maung, D. P. Butler, W. Xiong, W. Kula, and R. Sobolewski, "Propagation characteristics of monolithic YBaCuO coplanar transmission lines fabricated by laser writing patterning technique," *IEEE Microwave and Guided Wave Lett.*, vol. 4, no. 5, pp. 132-134, May 1994.
- [7] W. Kula and R. Sobolewski, "Charging effect in partially oxygen-depleted superconducting Y-Ba-Cu-O thin films," *Phys. Rev. B*, vol. 49, no. 9, pp. 6428-6431, March 1994.

## A Single Flux Quantum Shift Register Operating at 65 K

Martin G. Forrester, John X. Przybysz, John Talvacchio, Joonhee Kang,\* Arthur Davidson, and John R. Gavaler  
Westinghouse Science and Technology Center, 1310 Beulah Rd., Pittsburgh, PA 15235-5098 USA

**Abstract** – We report the fabrication and quasi-static testing of a two-stage, high-temperature superconducting, Single Flux Quantum shift register. The five-junction circuit was fabricated using a single YBCO film, with step-edge grain boundary junctions. Storage of flux, and its motion in response to LOAD and SHIFT signals, was demonstrated at 65 K.

### I. INTRODUCTION

Superconducting digital circuits based on Single Flux Quantum (SFQ) logic are expected to enable clock frequencies in the tens of GHz, while dissipating only microwatts per gate. SFQ logic is particularly well suited to moderate size circuits which perform various specialized digital signal processing functions, in applications such as infrared focal plane image processing, encrypted communications, and radar. Demonstrations of SFQ logic in low-temperature superconducting (LTS) technology, operating at 4.2 K, have included a flip flop counting at a rate of 500 GHz [1], a 60 GHz shift register, using about 1  $\mu$ W per stage [2], and a 12-bit A/D converter with a total estimated power of less than 100  $\mu$ W [3].

As HTS Josephson junctions become more reproducible the high speed of SFQ circuits will become attainable in the more easily utilized 65–77 K temperature range, albeit with somewhat higher power dissipation than in LTS circuits. This allows for the possibility of HTS digital circuits being used in a wide variety of applications where the weight and power of a 4.2 K cryocooler are unacceptable.

The development of such HTS digital circuits will require reproducible Josephson junctions, with critical current spreads of a few percent, and a multilayer circuit process incorporating a superconducting ground plane, and probably additional superconducting layers, with associated epitaxial insulators. While these developments are ongoing, it is essential to (1) gain experience with the design of HTS digital circuits; (2) prove the principles of SFQ operation at high temperatures, and (3) gain experience with the testing of such circuits. To these ends we have chosen to fabricate an extremely simple SFQ shift register, using a design which does not *require* a ground plane, and utilizing a junction type which is relatively easily fabricated. It is important to note, however, that such a simple circuit and fabrication process is incapable of demonstrating the high-speed potential of SFQ, but rather serves as a proof of principle of the basic SFQ operations of flux storage and controlled flux motion. They may also allow some estimation of bit error rates associated with thermal phase slippage in the HTS junctions.

### II. CIRCUIT DESIGN AND FABRICATION

The shift register is one of the few digital circuits that is

Manuscript received October 17, 1994.

\*Present address: Dept. of Physics, University of Inchon, 177 Dohwadong, Nam-ku, Inchon, 402-769, Korea.

This work was supported in part by AFOSR Contract No. F49620-94-C-0021.

simple enough in function and concept to be designed for fabrication in a single layer of YBCO. It passes data from one storage loop to next, bucket brigade style, with a fan-in of 1 and a fan out of 1. In principle, a chain of storage loops can be extended to very long shift registers with hundreds or thousands of junctions. Hence, it is an attractive vehicle for the demonstration of SFQ circuits in HTS.

The layout of an SFQ circuit without a ground plane presented new challenges. It was difficult to predict where lines of magnetic flux would go. Additionally, without a second layer of Meissner-effect metal, it was hard to couple flux from the data storage loop into the READ SQUID. Figure 1 shows the fabricated circuit and the design values for the components.

The devices were fabricated on 1-cm square, single-crystal NdGaO<sub>3</sub> substrates using a process similar to that reported by others [4]–[6]. Briefly, a Nb film approximately 400 nm thick was sputtered onto the substrate, and patterned by reactive ion etching with CF<sub>4</sub> and O<sub>2</sub>. This then served as the mask for definition of the approximately 200 nm step, by ion milling with a 500 eV Ar ion beam, at normal incidence. The Nb mask was then removed, again by RIE. A 200 nm film of YBCO was then deposited, using off-axis RF magnetron sputtering in a mixture of argon, oxygen, and water vapor [7]. A thin layer of gold, typically 30 nm, was then sputtered over the YBCO, *in-situ*.

The YBCO/Au bilayer was patterned by ion milling at 150 eV. The Au was left on in order to provide low resistance contacts, and to protect the step-edge grain boundary junc-

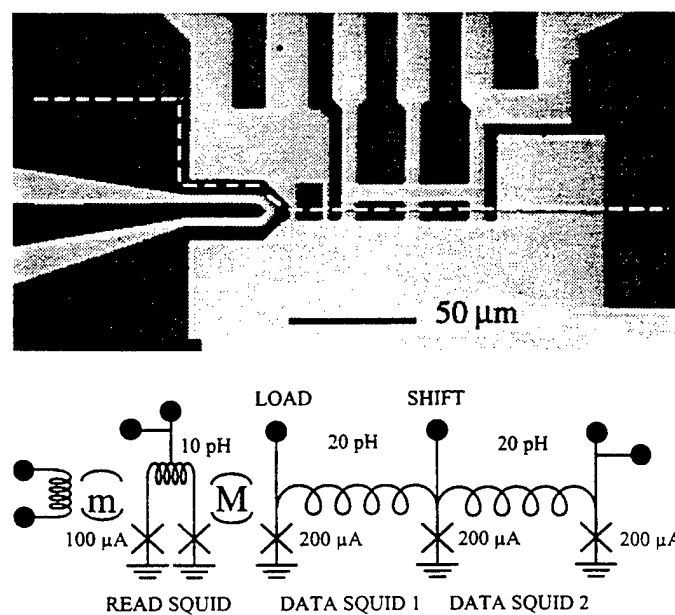


Fig. 1. Photograph of the fabricated circuit, and schematic, for the two-stage shift register, with nominal design values of critical current and inductance. The dashed line in the photograph indicates the location of the step at which the junctions are formed.

### III. JUNCTION & SQUID RESULTS

In order to qualify the chips for circuit testing, a number of test junctions and SQUIDs were first tested in liquid nitrogen, with a single mu-metal shield to reduce ambient field to about 10 milligauss. Figure 2 shows current-voltage characteristics for a 10- $\mu\text{m}$  single junction, with 10 GHz radiation applied at various power levels. The characteristics are consistent with the Resistively Shunted Junction (RSJ) model, with RF steps oscillating qualitatively as expected. Rounding of the IV curve at the critical current is well fit by a thermal noise rounding model, although typically with an effective noise temperature higher than the bath temperature. This discrepancy is thought to be due to external noise.

### IV. CIRCUIT TESTING

After the qualification of the junction and SQUID test devices, the substrates were wire bonded in a ceramic, 68-pin leadless chip carrier and mounted in a 100-lead, LakeShore MTD-150, open-cycle helium cryostat. No magnetic shielding was used for these measurements. Bias currents were supplied by a set of 15-bit D/A converters (HP3235/34524), operating in voltage mode with  $1\text{ k}\Omega$  series resistors. Voltage lines were routed, as signal/ground pairs, through an HP3488A multiplexer, and to a Keithley 181 Nanovoltmeter. All instruments were controlled, and data recorded, by a personal computer.

Since these measurement instruments all produce a significant amount of digital noise, which will artificially depress junction critical currents and "round" the IV curves, all lines were filtered with R-C filters with cutoff frequencies of a few Hertz. The detailed arrangement of these filters evolved during the course of the measurements reported here, in an attempt to minimize external noise.

Figure 3 shows the IV curve of the shift-register READ SQUID as a function of temperature, exhibiting RSJ-like behavior over a wide range of critical current values. The nominal design value of  $200\text{ }\mu\text{A}$  for this SQUID was obtained at a temperature of approximately 75 K. However, it was initially found that circuit operation was more stable at 65 K, where critical currents were approximately three times their design values, hence the following data were taken at 65 K. The stability of the circuit at 75 K was subsequently improved dramatically as the degree of filtering in the bias and voltage lines was improved, suggesting that the instability was due to

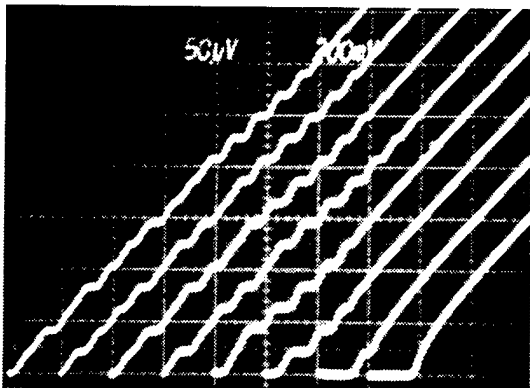


Fig. 2. Current-voltage characteristics of a 10- $\mu\text{m}$  wide step-edge grain boundary junction at 77 K, showing behavior consistent with the RSJ model. The rightmost curve has no microwave power applied, while the others have various power levels of 10 GHz radiation applied. The horizontal scale is 200  $\mu\text{A}/\text{div}$ , and the vertical 50  $\mu\text{V}/\text{div}$ .

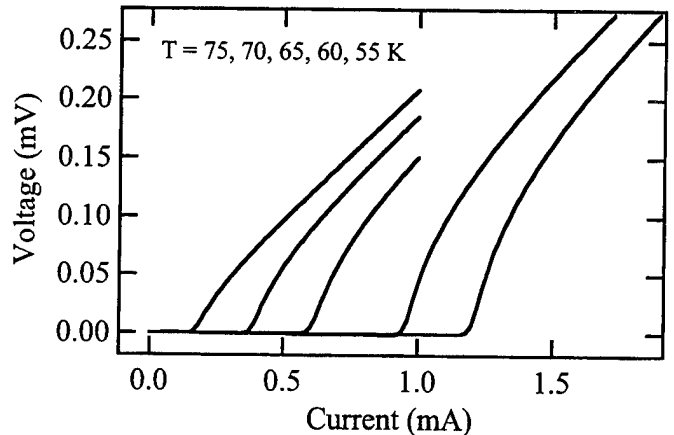


Fig. 3. Current-voltage characteristics of the shift register READ SQUID as a function of temperature. Although the junctions achieved their design values of critical current at about 75 K the circuit was operated at 65 K to improve stability against external noise.

external noise, and not intrinsic to the junctions or circuit.

To verify the inductance value for the DATA SQUIDs, the periodic voltage response was measured using direct injection of current into a DATA inductor, as shown in Fig. 4, with the three DATA junctions biased into the voltage state by applying  $500\text{ }\mu\text{A}$  to each junction. As shown in Fig. 4, the measured period of  $200\text{ }\mu\text{A}$  corresponded to the design value of  $20\text{ pH}$  for the full inductor. The overall envelope of the modulation is thought to be due to two factors: the modulation of individual junction critical currents by the field from the bias currents, and the effect of the third parallel DATA junction, through which some current redistributes.

The response of the READ SQUID to the data state of the shift register was demonstrated by overdriving the data LOAD line to  $1500\text{ }\mu\text{A}$ , to fill the shift register with flux. The READ SQUID voltage was then measured as a function of

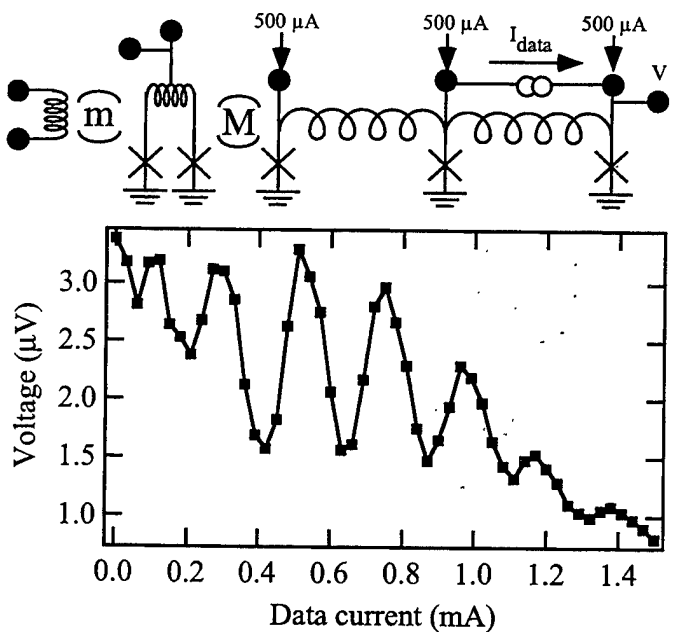


Fig. 4. The data inductor value was determined by measuring the periodic dependence of data line voltage on the inductor current. The data line voltage modulated with a period of about  $200\text{ }\mu\text{A}$ , which corresponds to an inductance of  $10\text{ pH}$  for half of the data inductor.

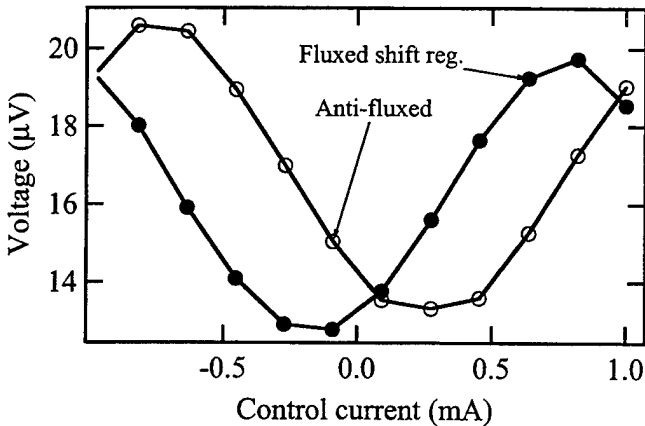


Fig. 5. Filling the first stage of the shift register with maximum circulating current or counter-circulating current shifted the response of the READ SQUID.

the flux bias current through the control line (extreme left in Fig. 1). Then the shift register was filled with anti-flux (currents circulating in the opposite direction) by driving 1500  $\mu$ A into the SHIFT line. As shown in Fig. 5, the SQUID voltage versus flux characteristic shifted in response to these flux and anti-flux states.

The temperature of the sample was found to oscillate with a period of order tens of minutes, so that the absolute value of the voltage developed by the READ SQUID drifted up and down over time. However, as illustrated in Fig. 6, which shows two measurements taken about 40 minutes apart, the positions of the maxima and minima remained stable.

To minimize the effects of these slow changes in the READ SQUID critical current, the voltage was measured at both the rising and falling parts of the modulation curve (+0.5 and -0.5 mA in Fig. 6). The difference between these voltages was then recorded and plotted as the data signal.

Since the measurements were taken at a temperature where the critical current values were larger than the design values, the DATA SQUIDs were able to store several flux quanta, instead of one or two. It was therefore necessary to determine the data signal corresponding to a single quantum of magnetic flux, by using an analog of Millikan's oil drop experiment. The shift register was filled with counter-circulating current (anti-flux). Then progressively larger impulses were

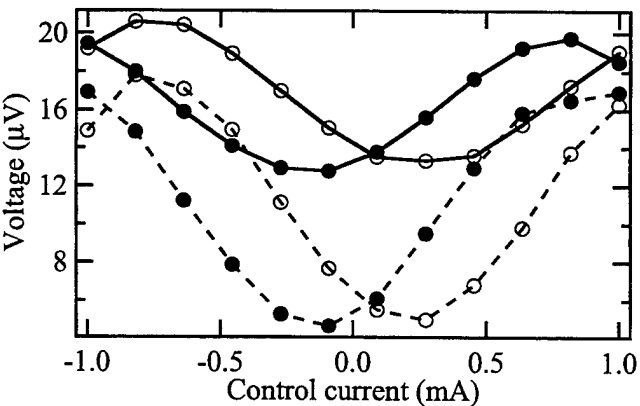


Fig. 6. The positions of the READ SQUID flux modulation maxima and minima were stable, however the magnitude of the voltage drifted over time. Dotted line data was taken 40 minutes after the solid line data. As in Fig. 5, filled and unfilled circles correspond to maximally fluxed and anti-fluxed states, respectively, of the data SQUIDS.

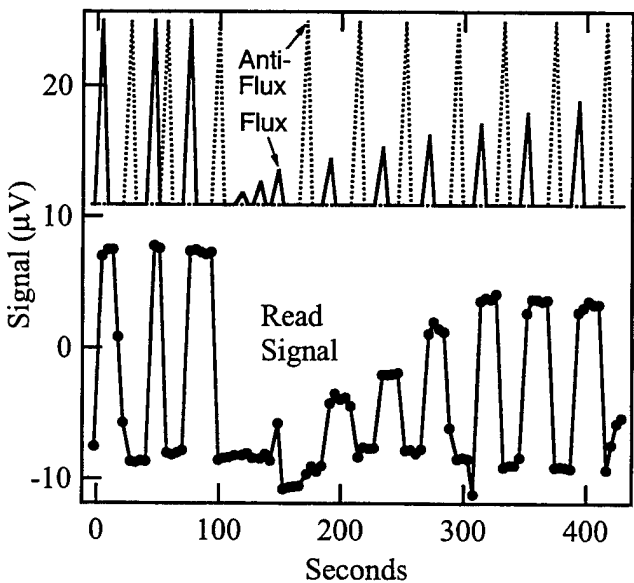


Fig. 7. Pulsing the load line with gradually increasing current, in 100  $\mu$ A increments, allowed the enumeration of the flux states of the data SQUIDS, which are capable of storing several flux quanta at 65 K.

applied to drive more circulating current (flux) into the shift register. The shift register was designed to have data currents of approximately 100  $\mu$ A per flux quantum, so the fluxing current was incremented in 100  $\mu$ A steps. The data signal settled into quantized states as shown in Fig. 7. The smallest step, corresponding to a change of one flux quantum, was about 2.6  $\mu$ V.

The planar structure of the shift register was necessary to enable the circuit to be constructed using a single layer of HTS. But a consequence was that the READ SQUID could only sense the state of the first stage of the shift register. At 65 K, the junction critical currents were high enough to support multiple flux states in any stage of the shift register. Hence it was decided to operate the shift register so that only the first stage could hold data. A dc bias on the second stage ensured that any flux shifted into it would exit the shift register.

Figure 8 shows single flux quantum shifting at 65 K. The low level of the signal voltage required slow operation, since the settling time of the nanovoltmeter was 2 seconds. The intrinsic speed of the circuit is much faster, capable of shifting at GHz rates, but GHz tests reveal only the average voltage. By running slowly, it was possible to display the response of the shift register to individual commands. Note that an error is observed at about 130 seconds, where the flux quantum is shifted in the absence of a shift command. The occurrence of such errors was found to be extremely sensitive to the degree to which external noise from the instruments was filtered out. Further improvements in this area are necessary in our apparatus.

## V. DISCUSSION & CONCLUSIONS

This is the first report of an HTS shift register which describes the design, layout, fabrication technique, and measurement methodology in detail. The shift register was operated as an SFQ circuit, and shifted single flux quanta into and out of the first storage loop in response to LOAD and SHIFT commands.

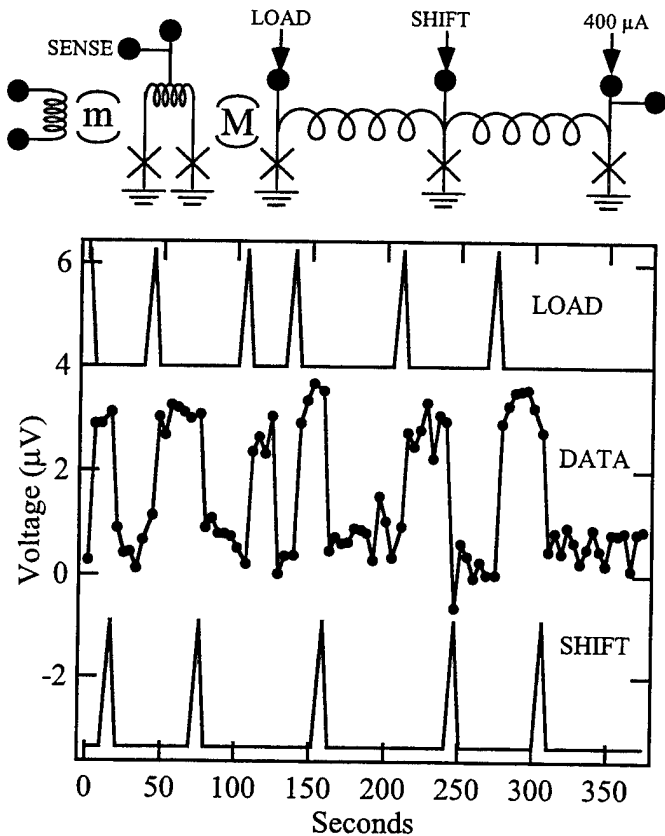


Fig. 8. Data was loaded as single flux quanta into the first stage of the shift register, then shifted out. The HTS shift register loaded and shifted SFQ data on command at 65K. Note an error occurred at approximately 130 sec.

The measurement in Fig. 4 showed that the data loop inductance of the fabricated circuit was determined almost entirely by the magnetic field, with little kinetic inductance effect. This is due to the coplanar layout of the loop. The magnetic penetration depth in YBCO is small compared to the  $8 \mu\text{m} \times 30 \mu\text{m}$  loop dimensions. In contrast, a SQUID fabricated in a multilayer structure with 200-nm thick films exhibited significant amounts of kinetic inductance [8].

The periodicity of the measurement in Fig. 4 showed that only half of the storage inductance was being measured. This is because the data junctions were not truly grounded, merely connected on one side to the largest piece of superconductor. When data flux was stored in the loop, the Meissner current was confined to the inner edges of the loop. But the measurement of Fig. 4 permitted  $I_{\text{data}}$  to flow along both the inner and outer edges of the data inductor strip. Consequently, the Meissner current that flowed on the "ground" side of the loop was only half of  $I_{\text{data}}$ . In contrast, for a multilayer structure, all of the test current flows on the inner surface of the SQUID loop and an equal and opposite current flows in the ground plane layer. The net result of these effects is that the technique of Fig. 4 measured only half of the storage loop inductance because the probe current only flowed half way around the loop.

Besides electrical noise from some external source, there is another possible explanation for the shift error seen in Fig. 8 at 130 sec. The circuit was operated at a temperature where the data junctions had critical currents of  $500 \mu\text{A}$ , instead of the design value of  $200 \mu\text{A}$ . Since the junctions were  $8 \mu\text{m} \times 0.2 \mu\text{m}$ , they were longer than four Josephson penetration depths at that temperature. It is possible that the shift error was caused by motion of flux into or out of a long junction.

The single layer fabrication process utilized here puts severe constraints on the performance of the circuit. In particular, the coupling efficiency between the READ SQUID and first DATA SQUID is estimated to be only about 4%. This, combined with the low resistance of the junctions, means that the voltage signal associated with a single flux quantum in a DATA SQUID is extremely small, necessitating the use of low-bandwidth measurements. The coupling efficiency would be dramatically improved with a multilayer process, either by overlaying the READ and DATA SQUIDs or, more simply, by a coplanar transformer scheme where inductors in the two SQUIDs are laid side-by-side over a hole in the ground plane. We have recently demonstrated such a multilayer process, fabricating HTS step-edge grain boundary SQUIDs over a ground plane [8]. In order to increase junction resistances we are exploring the use of an insulating passivation layer.

In summary, we have demonstrated storage of single flux quanta, and their motion in response to applied signals, in an HTS circuit at 65 K, thus verifying the most basic operations of SFQ logic in a temperature range which will enable much broader application of the architecture.

#### ACKNOWLEDGMENT

The authors would like to thank G. J. Faychak and J. U. Uphoff for assistance with sample fabrication.

#### REFERENCES

- [1] A. Oliva, M. Bhushan, P. Bunyk, V. Semenov, J. E. Lukens, and K. Likharev, "Ultra fast SFQ pulse frequency divider", unpublished.
- [2] O. Mukhanov, "Rapid single flux quantum (RSFQ) shift register family," *IEEE Transactions on Applied Superconductivity*, **3** (1), 2578, 1993.
- [3] D. L. Miller, J. X. Przybysz, J. H. Kang, C. A. Hamilton, and D. M. Burnell, "Josephson counting analog-to-digital converter," *IEEE Transactions on Magnetics*, **27**, 2761, 1991.
- [4] K. Herrmann, Y. Zhang, H. -M. Mück, J. Schubert, W. Zander, and A. I. Braginski, "Characterisation of YBCO step-edge Josephson junctions," *Supercond. Sci. Technol.* **4**, 583 (1991).
- [5] J. Luine, J. Bulman, J. Burch, K. Daly, A. Lee, C. Pettiette-Hall, S. Schwarzbek, and D. Miller, "Characteristics of high performance YBCO step-edge junctions," *Appl. Phys. Lett.* **61** (9), 1128 (1992).
- [6] J. Z. Sun, W. J. Gallagher, A. C. Callegari, V. Foglietti, and R. H. Koch, *Appl. Phys. Lett.* **63**, 1561 (1993).
- [7] J. R. Gavaler, J. Talvacchio, T. T. Braggins, M. G. Forrester, and J. Gregg, "Critical parameters in the single-target sputtering of  $\text{YBa}_2\text{Cu}_3\text{O}_7$ ," *J. Appl. Phys.* **70** (8), 4383 (1991).
- [8] M. G. Forrester, A. Davidson, J. Talvacchio, J. R. Gavaler, and J. X. Przybysz, "Inductance measurements in multilevel high  $T_c$  step-edge grain boundary SQUIDs," *Appl. Phys. Lett.* **65** (14), 1835 (1994).

## Microstructure and Properties of $\text{YBa}_2\text{Cu}_3\text{O}_7$ Thin Films Grown on Vicinal $\text{LaAlO}_3$ Substrates

Rand R. Biggers

US Air Force Wright Laboratory, WL/MLPO, Wright-Patterson AFB, OH 45433

M. Grant Norton

Department of Mechanical and Materials Engineering, Washington State University, Pullman WA 99164

I. Maartense, T.L. Peterson, E.K. Moser, D. Dempsey, and M.A. Capano,  
US Air Force Wright Laboratory, WL/MLPO, Wright-Patterson AFB, OH 45433

J. Talvacchio

Westinghouse Electric Corporation, Pittsburgh, PA 15235

Jeff L. Brown

US Air Force Wright Laboratory, WL/ELOT, Wright-Patterson AFB, OH 45433

J.D. Wolf

University of Dayton, Dayton, OH 45469

**Abstract**—Thin films of  $\text{YBa}_2\text{Cu}_3\text{O}_7$  have been grown on vicinal  $\text{LaAlO}_3$  substrates by pulsed-laser deposition. In most cases, the substrate surface, nominally (001), has been rotated  $\sim 6^\circ$  about an axis parallel to the  $\langle 110 \rangle$  direction. Films grown on these surfaces were found to have substantially improved properties compared to those obtained for films deposited on (001)-oriented substrates under equivalent conditions at our facility. The surface morphology of the films exhibited an elongated granular structure which differed markedly from the more equiaxed grain structure found in films grown on (001)-oriented substrates. Furthermore, this particular elongated morphology and improvement in properties seems to occur only for films deposited at higher laser energies ( $\sim 30\text{J/cm}^2$ ).

### I. INTRODUCTION

In pulsed laser deposition (PLD), as with other growth techniques for high temperature superconductors (HTS), there is a number of factors that directly influence the properties of the films. The substrate surface is one of the most important and can be varied to provide increased control of film nucleation and growth during the deposition process. This additional control could improve large area depositions and provide film microstructures with more desirable intrinsic characteristics.

For  $\text{YBa}_2\text{Cu}_3\text{O}_7$  (YBCO) thin films, the (001)-oriented perovskites are the substrates of choice. Since most of these materials, such as  $\text{LaAlO}_3$ , have a lattice mismatch with respect to YBCO of greater than 1%, the nominal film growth mechanism is through 2-dimensional island nucleation from adatom supersaturation, followed by island coalescence [1].

The c-axis of the film and the substrate are generally aligned and the fastest growth directions are the inplane a and b-axes. If the surface has been miscut away from a low-index plane then a series of step or ledges are often produced as shown in Fig. 1a, 1b, and 1c.

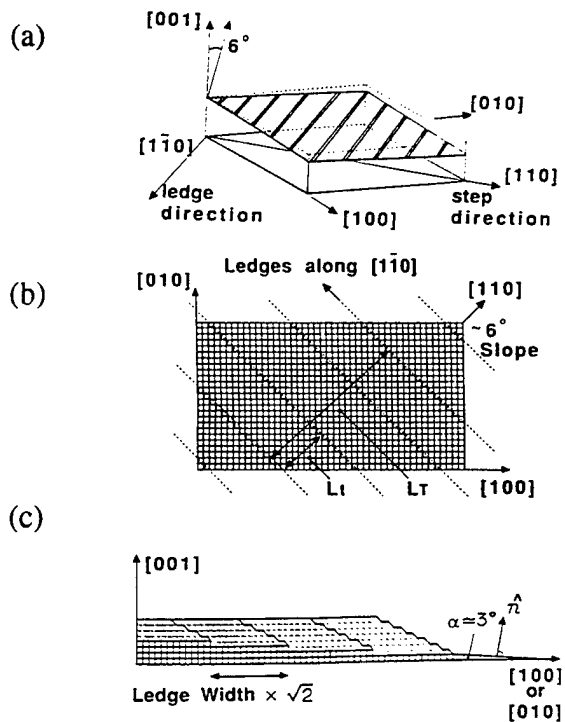


Fig. 1. (a) Schematic view of (001)-oriented surface rotated  $\sim 6^\circ$  about the  $\langle 110 \rangle$  axis, after T. Satoh et. al. [2], (b) An atomic-scaled top view of the series of ledges after A. Lamagna et. al. [3], and (c) An atomic-scaled side view of the  $\sim 6^\circ$  miscut steps and ledges after A. Lamagna et. al. [3].

These ledges may provide aligned and enhanced nucleation sites. The evolution of the film microstructure from these initial preferred nucleation sites to the final macrostructure is strongly affected by the relative magnitude of ledge width ( $L_t$ ) to that of the adatoms diffusion length ( $L_d$ ) [1,4,5] as shown in Fig. 2.

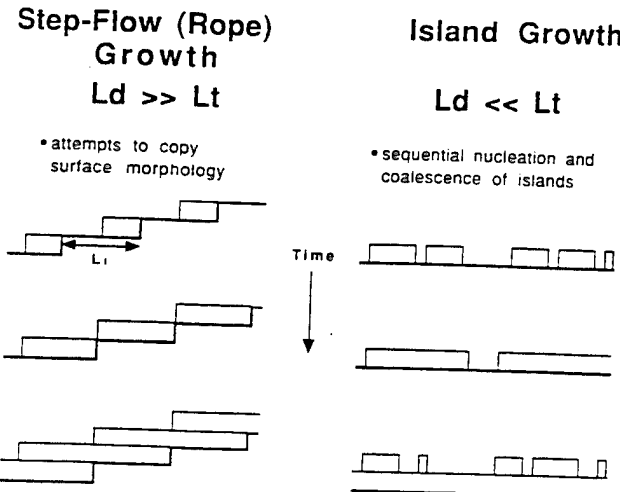


Fig. 2. Schematic showing the two basic growth mechanisms and the transition between them, after S.J. Pennycook et. al. [4].

In general, if  $L_d \gg L_t$  then step-flow growth is dominant and the final structures range from overlapping platelets to aligned and elongated rope-like grains. If  $L_d \ll L_t$  then island growth remains dominant. The crossover from step-flow to island growth should occur when  $L_d \sim L_t$ .  $L_d$  is probably a strong function of adatom kinetic energy which is controlled, in part, by laser fluence and substrate temperature whereas  $L_t$  is a strong function of the substrate surface. Reduced numbers of outgrowths, aligned or elongated grain structures, and suppression of the spiral growth defects are some of the intrinsic properties [1,4,5,6] of YBCO films grown on vicinally-cut substrates.

In this paper we present a comparison of YBCO thin films deposited, under equivalent conditions, onto vicinal and oriented "(001)-oriented"  $\text{LaAlO}_3$  substrates. Surface morphology, crystallographic structure, critical current density ( $J_c$ ), and transition temperature ( $T_c$ ) of the films were determined. In addition, several films grown by PLD and sputtering on equivalent vicinal and on-axis substrates at other institutions have been examined to determine the effect of different deposition processes.

## II. EXPERIMENTAL

The PLD process used in our laboratory have been reported in detail elsewhere [6,7]. The YBCO films were formed by focusing either a Lumonics Hyper EX-400 (L-400) or a Lambda Physik LPX 305i (L-305) excimer laser operating on  $\text{KrF}$  ( $\lambda = 248 \text{ nm}$ ) onto a stoichiometric YBCO pellet. For film deposition, an average pulse energy of 200 or 400 mJ gave laser fluences of  $\sim 20$  or  $\sim 40 \text{ J/cm}^2$  respectively, or equivalent power densities of  $\sim 2 \times 10^9 \text{ W/cm}^2$

with a beam footprint of  $\sim 1 \text{ mm}^2$  and pulse durations of 13 or 25 ns respectively at a pulse repetition rate of 20 Hz.

The vendor prepared the vicinal substrates by miscutting nominally (001)-oriented  $\text{LaAlO}_3$  substrates  $\sim 6^\circ$  or  $\sim 10.5^\circ$  about an axis parallel to  $\langle 110 \rangle$  direction. The substrates were polished to a mirror finish after cutting. All orientations were confirmed by Laue back-reflection.

In each film growth experiment,  $\text{LaAlO}_3$  substrates ( $5 \times 5 \times 0.5 \text{ mm}$  and/or  $10 \times 10 \times 0.5 \text{ mm}$ ) were mounted close to each other on a 1 inch stainless steel plate using silver paint. The distance between the YBCO target and the central substrate was  $\sim 6.8 \text{ cm}$ ; the angle between the plane of the target surface and the stainless steel plate was either  $0^\circ$  (L-400) or  $\sim 26^\circ$  (L-305) depending on the heater-holder utilized. The substrates were heated by a tungsten filament lamp located below the stainless steel plate. The temperature of the substrate holder was monitored by a sheathed thermocouple in contact with the stainless steel plate. The substrate/film temperature was measured by means of a two-color infra-red pyrometer which could be focused onto the surface of any of the substrates. The substrate temperature during deposition was either  $\sim 810^\circ \text{ C}$  (L-400) or  $\sim 770^\circ \text{ C}$  (L-305); the variation in the temperature across holder #1 (L-400) was as high as  $50^\circ \text{ C}$  while that of holder #2 (L-400 and L-305) was  $\sim 5^\circ \text{ C}$ . Film deposition was performed in a flowing oxygen ambient (from 100 to 160 mTorr). Following film deposition, the heater was turned off, the chamber was filled with oxygen, and the samples allowed to cool to room temperature (about 30 minutes) at a pressure of  $\sim 490 \text{ Torr}$  of oxygen.

It should be noted that all the substrate positions on the stainless steel plate were not equivalent, for either laser; there was a large thermal gradient intrinsic to holder #1 used only with the L-400 laser whereas there was an asymmetry in the footprint energy of the L-305. The L-305 plume provided growth regions with fluences of  $\sim 40$ ,  $\sim 30$ , and  $\sim 25 \text{ J/cm}^2$ . The estimated average deposition rates for the lasers are as follows:  $3.8 \text{ nm/sec}$  for the L-400 and  $1.7$ ,  $1.2$ , and  $1.0 \text{ nm/sec}$  at the three fluence levels of the L-305.

Several films were grown by PLD and sputtering on our vicinal and oriented substrates at other institutions. The PLD processes were similar to ours except that the laser fluences were  $\sim 3 \text{ J/cm}^2$ .

The surface morphology of the films was determined using a Digital Instruments Nanoscope II scanning probe microscope (AFM and STM).  $J_{cs}$  and  $T_{cs}$  were obtained from AC susceptibility and DC transport measurements.

## III. RESULTS

Seventeen films, all grown on  $\text{LaAlO}_3$  substrates miscut by the same  $\sim 6^\circ$  except for one cut at  $10.5^\circ$ , were examined in this study. A number of the critical deposition and film parameters for both vicinal and oriented films are listed in Table 1. The measured  $T_{cs}$  ranged from  $\sim 40 \text{ K}$  to greater than  $90 \text{ K}$  while the  $J_{cs}$  varied from  $\sim 6 \times 10^6 \text{ A/cm}^2$  to essentially zero (no superconducting connectivity or) at  $77 \text{ K}$ . All films grown on vicinal substrates exhibited a characteristic elongated granular structure (so called rope-like

[8] in some areas. The best films all exhibited a surface morphology consisting of elongated and aligned ropes similar to those in Fig. 3a and 3b.

TABLE 1  
Critical Deposition and Film Parameters

Film #	Sub.	Dep. -Tech.	Tc/Jc(77K)	Laser/Fac.	a <sub>1</sub>	Rope Width	Step-Flow
		V(#°) or O /J/cm <sup>2</sup> )	(K)/(10 <sup>6</sup> A/cm <sup>2</sup> )		(μm <sup>2</sup> )	Height (nm)	(%)
115	V(6°)	PLD/30	88.6/-2	L-400/WL	<0.01	~500x60	100
116	V(6°)	PLD/30	90.0/-5.0	L-400/WL	-1	N/A	0
117	O	PLD/30	90.3/-2.0	L-400/WL	<0.01	~400x60	100
118	V(6°)	PLD/30	90.0/-5.0	L-400/WL	<0.01	~400x60	100
109	V(6°)	PLD/30	88.4/-3.7	L-400/WL	<0.5	~400x60	100
110	V(6°)	PLD/30	89.0/-3.6	L-400/WL	<<0.01	~500x40	100
115R	V(6°)	PLD/30	84.4/-2.9	L-305/WL	-0.5	~400x40	100
462	V(6°)	PLD/40	88.8/-3.0	L-305/WL	-0.5	~500x20	100
416	O	PLD/40	75/-0.1	L-305/WL	-0.5	N/A	0
463	V(6°)	PLD/30	89.0/-2.0	L-305/WL	-1.7	~400x20	100
417	O	PLD/30	87.4/-4.0	L-305/WL	-2.2	N/A	0
464	V(6°)	PLD/25	88.2/-1.5	L-305/WL	>1.7	~160x15	100
418	O	PLD/40	86.8/-2.0	L-305/WL	-2.0	N/A	0
480	V(6°)	PLD/40-25	88.4/-1.5	L-305/WL	-1.0	~400x30	100
493	V(6°)	PLD/40	62.0/-0.1	L-305/WL	-0.2	100	
494	V(6°)	PLD/30	75.5/-0.1	L-305/WL	<1.0	100	
495	V(6°)	PLD/25	84.0/-0.1	L-305/WL	>1.5	100	
L7	V(6°)	Sputtering	89.0/-2.0	Westinghouse	V	~400x15	100
L5	O	Sputtering	88.0/-1.0	Westinghouse	<0.1	N/A	0
McM-6	V(6°)	PLD/2.5	90.4/-0	McMaster	<0.1	~250x20	-5
McM-0	O	PLD/2.5	92.1/-2.0	McMaster	-0.4	N/A	0
STI-6	V(6°)	PLD/3.0	86.4/-<<0.1	STI	<0.03	~160x15	-5
STI-10	V(10.5°)	PLD/3.0	89.5/-1.0	STI	<0.03	100	
STI-0	O	PLD/3.0	89.8/-1.0	STI	<<0.01	N/A	0

— = ~50 nm film

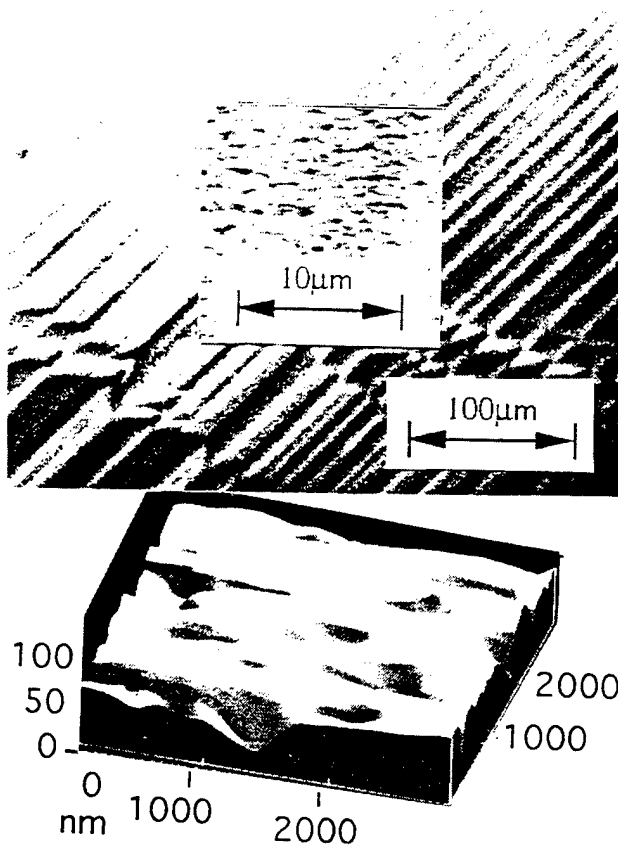


Fig. 3. (a) An overlay of the ledge-aligned ropes on the twin pattern in this area of the substrate. (b) A 3d image of the ropes.

The ropes in Fig. 3 are ~ 400 nm x 60 nm and all aligned along the direction of the substrate ledges as shown in Fig. 1b. They are also at 45° to the (001) and (101) twin planes intersection with the substrate surface. The c-axis of the film is aligned with the c-axis of the substrate whereas the surface is rotated ~ 6° about the [110] direction. The ropes seem to consist of over-lapping platelets one unit cell thick with about 12 to 20 nm of exposed terrace at each level (see Fig. 4a and 4b).

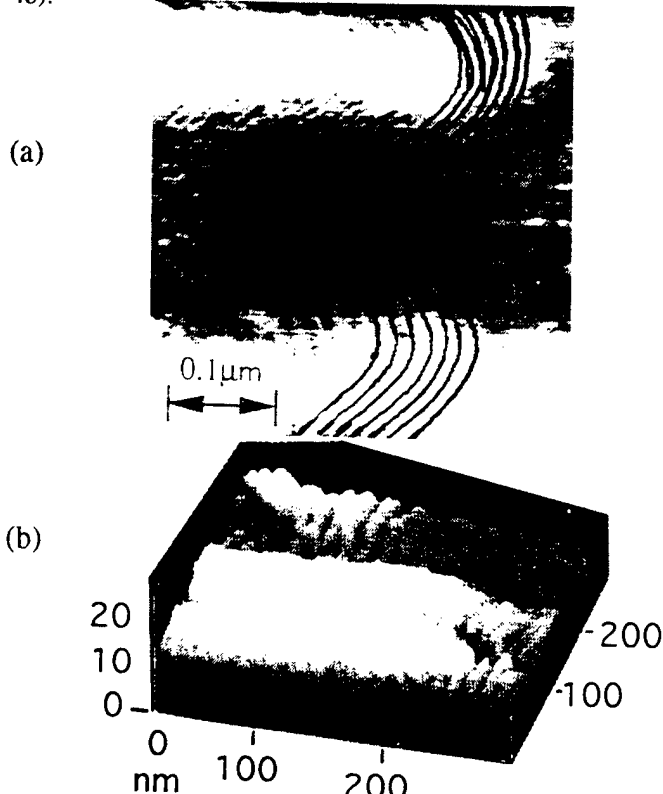


Fig. 4. AFM images (400 x 400 x 20 nm) of rope-like structures. (a) Top view, note ~ 20 nm wide terraces and directionality along crests and troughs. (b) STM image of same film.

The image shown in Fig. 4a suggests there is a 3° inclination in the platelets going from the lowest to the highest levels. When examined under the highest magnifications, the terraces at the ridge of the ropes displayed an almost right angle change in direction for all vicinal substrates (see highlighted region in Fig. 4a). In addition the apex of this angle always points in the same direction for all ropes in all measured areas on the same film.

Some of the best films produced on the vicinal substrates ( $T_{CS}$  of 89 K and  $J_{CS}$  estimated at  $4 \times 10^6$  A/cm<sup>2</sup> at 77 K) were grown under conditions that produced the poorest films ( $T_{CS}$  from 40 to 75 K and  $J_{CS} \leq 10^5$  A/cm<sup>2</sup>) on the oriented substrates. Rocking-curve widths of 0.39° indicate very good film crystallinity. Among the films produced on the vicinal substrates, the width and height of ropes was largest (500 nm x 80 nm) and the  $T_{CS}$  and  $J_{CS}$  the highest for films grown from the 40 J/cm<sup>2</sup> region of the plume while those grown at lower energies (30 to ~ 3 J/cm<sup>2</sup>) were the smallest (~ 200 x

15 nm, see Fig. 5a, 5b, and 5c). Similar variations in rope size in arc edged regions were seen in L-400 films on vicinal substrates. Regions with the highest and widest rope-like structures also had significantly better  $T_{Cs}$  and  $J_{Cs}$ .

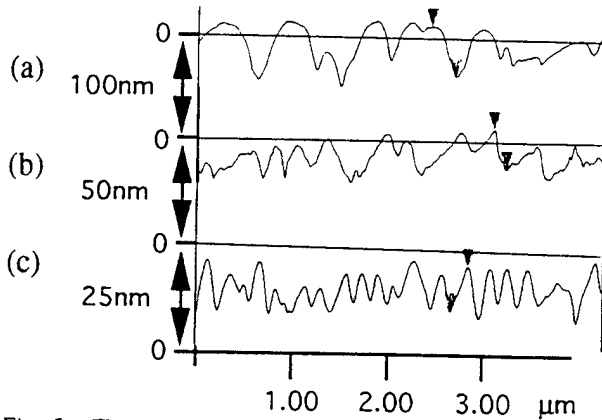


Fig. 5 AFM profiles taken perpendicular to the ledges/ropes for vicinal films grown in the part of the plume with the (a) highest energy ( $40 \text{ J/cm}^2$ ), (b) mid-range ( $30 \text{ J/cm}^2$ ), and (c) lowest energies (25 to  $\sim 3 \text{ J/cm}^2$ ).

The critical current density  $J_C$  was found to be anisotropic with respect to the ledge (rope alignment) direction. The  $J_C$  along the ropes ranged from 40 to 78% of the  $J_C$  measured perpendicular to the ropes. The microwave surface resistance,  $R_s$ , was  $28 \text{ m}\Omega$  at 71 GHz and 77 K for the only film measured to date.

$A$ -axis outgrowths ( $a_{\perp}$ ) are an often unwanted occurrence in  $c$ -axis ( $c_{\perp}$ ) oriented YBCO films. In general, there were less  $a_{\perp}$  outgrowths on films grown on vicinal substrates than on those grown under identical conditions on oriented substrates (compare Figs. 6a and 6b).

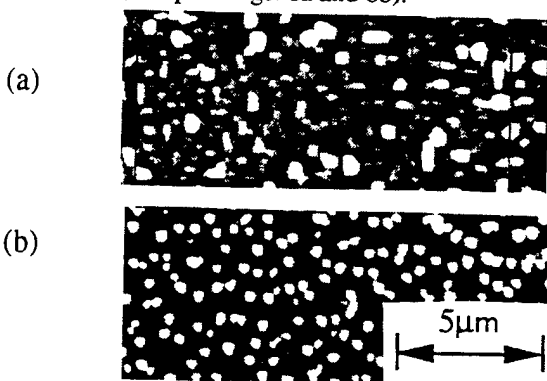


Fig. 6(a) AFM image ( $15 \times 15 \times 0.2 \mu\text{m}$ ), top view of ( $-25 \text{ J/cm}^2$ ) film on oriented substrate with  $> 2/\mu\text{m}^2$  of  $a_{\perp}$ . (b) Similar image of ( $-25 \text{ J/cm}^2$ ) film on vicinal substrate  $\sim 1.7/\mu\text{m}^2$  of  $a_{\perp}$ .

The films grown on our vicinal substrates at other facilities were strikingly different than those grown in our laboratory. The  $T_{Cs}$  ranged from  $\sim 88$  K to more than 90 K while the estimated  $J_{Cs}$  ranged from  $\sim 10^6 \text{ A/cm}^2$  to essentially zero at 77 K. The surface morphologies of the two very low energy ( $2 - 3 \text{ J/cm}^2$ ) laser-deposited vicinal substrate-films exhibited island-like surfaces with the rope-

like structures only in small ( $2 \times 2 \mu\text{m}$ ), generally isolated areas, with size similar to those in Fig. 6c. Curiously, on one film the ropes were most densely grouped along the twin-substrate interfaces yet all aligned in a common direction. The sputtered film on vicinal substrate had a rope-like structure that was less regular but of a size scale midway between the high and midrange energy films in Figs 7a and b. The  $T_C$  was  $\sim 88$  K and the  $J_C$  was estimated to be  $> 10^6 \text{ A/cm}^2$  at 77 K. The sputtered film on the oriented substrate displayed a surface morphology suggestive of spiral growth.

#### IV. DISCUSSION

All films grown on the vicinal substrates show, at some scale, a rope-like structure; this is consistent with the step-flow growth nucleated at the steps/ledges in the substrate. The competition between step-flow and island growth is strongly influenced by the mobility,  $L_d$ , of the adatoms and the width of the ledges,  $L_t$ . According to [4]  $L_d$  is controlled by temperature, deposition rate and  $O_2$  partial pressure. Given that all the ledges were of similar dimensions and that the films were grown at similar temperatures and oxygen pressures (unless otherwise noted), the largest growth differences are in deposition/kinetic energies and deposition rates. The deposition rate is increased with increasing laser fluence and pulse frequency, both of which are significantly higher for our films. The kinetic energy of the arriving adatoms will also increase (increasing  $L_d$ ) with laser fluence given other parameters remain constant. Our deposition parameters using the L-305 at fluences less than  $40 \text{ J/cm}^2$  clearly favor island growth with numerous  $a_{\perp}$  outgrowths on the oriented substrates. This would suggest a high effective supersaturation [9]. In addition, the highest fluence ( $40 \text{ J/cm}^2$ ) plume region produced a thick and rather jumbled films on oriented substrates, suggesting unstable island growth. This implies very high levels of supersaturation [9]. However, the growth exhibited at the same fluence on vicinal substrates is similar to that of Fig. 3 and implies that  $L_d \gg L_t$ .

All the microstructures of films on the vicinal substrates indicated step-flow growth over some surface areas. Films grown at  $\sim 30 \text{ J/cm}^2$ , whether possessing good or poor material properties, exhibited a rope-like morphology on a  $15 \times 15 \mu\text{m}$  scale over essentially the whole film. The sputtered film showed the rope-like features but only at a higher magnification ( $4 \times 4 \mu\text{m}$ ), whereas films grown by PLD at  $\sim 2$  to  $3 \text{ J/cm}^2$  showed a minimal amount of rope-like structures and only in very small regions. These films displayed mostly island growth with a few rope-like structures occurring between some islands and along the intersections of the twin planes and the substrate surface.

All the individual deposition processes used here have been designed to grow the best possible films on (001)-oriented substrates, which in general promote island growth. Witness films on oriented substrates display island growth and have good to excellent  $J_{Cs}$  and  $T_{Cs}$ . Through island growth on oriented substrates, the L-305 simultaneously produced the following films in the different fluence regions

of the plume: the best films at  $\sim 30 \text{ J/cm}^2$ , good films at  $\sim 25 \text{ J/cm}^2$ , and the worst and substantially thickest films at  $\sim 40 \text{ J/cm}^2$ . This resulted in two entirely different film morphologies side by side films on a common substrate. Such films display a sharp boundary region where the microstructure shifts from a normal island to a seemingly unstable island structure. This switch in microstructure suggests there is an energy threshold in the beam (between 30 and  $40 \text{ J/cm}^2$ ) above which stable island growth is disrupted. However, a film grown on a vicinal substrate in this same fluence range has a significantly different microstructure and improved overall properties. The  $\sim 40 \text{ J/cm}^2$  film is then the best and the thickest, with a slight decrease in  $J_c$ ,  $T_c$ , and rope height and width with decreasing laser fluence. This is consistent with decreasing kinetic energies and deposition rates being less favorable to step-flow growth. However, this does not differentiate between an increased deposition rate due to either increased beam energy or higher pulse frequency.

In addition, the fluence gradient in the laser beam significantly varies the number and size of  $a\perp$  outgrowths [7] among L-305 films grown on both vicinal and oriented substrates. On oriented  $\text{LaAlO}_3$  substrates the density of outgrowths ranges from essentially none in the  $\sim 40 \text{ J/cm}^2$  area of the plume to  $>2/\mu\text{m}^2$  in the  $\sim 25 \text{ J/cm}^2$  portion. The vicinal substrates reduce these numbers by about one third as can be seen in Fig. 7a and 7b. The ledges provide enhanced nucleation sites for  $c\perp$  growth thereby reducing the overall number of possible  $a\perp$  nucleation sites. The number of  $a\perp$  outgrowths is found to be the same after 15 seconds of growth as at 250 seconds [7]. Only the average size increases with deposition time, from  $125 \times 250 \text{ nm}$  to  $\sim 400 \times 400 \text{ nm}$ .

With a  $6^\circ$  rotation about a  $\langle 110 \rangle$  direction, the distance between ledges on the  $\text{LaAlO}_3$  is calculated to be  $\sim 3.6 \text{ nm}$  along the diagonals of the unit cells. For one unit cell of YBCO the distance becomes  $\sim 12 \text{ nm}$  at which unit cell platelets can overlap. Assuming that the substrate formed ledges as depicted in Fig. 1, the closest the rope structures could be is  $\sim 11.8 \text{ nm}$  apart. However, they are at least 10 times this distance apart, indicating significant merging of these structures. The ropes have been determined to run along the ledges with the crest-to-crest distances ranging from  $\sim 500$  to  $\sim 150 \text{ nm}$ . The anisotropy in the  $J_c$  relative to ledge direction suggests that there is increased connectivity perpendicular to the ledges. The ledges thus may provide a two dimensional grid pattern on which the ledge controlled growths, the rope-like structures, can merge in a well connected manner thereby providing better overall connectivity and current density ( $J_c$ ).

## V. CONCLUSIONS

On vicinal substrates our deposition conditions resulted in YBCO films with higher  $T_c$ s,  $J_c$ s, and less  $a\perp$  outgrowths, especially in the  $40 \text{ mJ/cm}^2$  region of the plume, when compared to island growth films on (001)-oriented substrates. The films grown on vicinal substrates all exhibited a strongly

ledge-direction aligned rope-like structure consistent with step-flow growth. The laser plume deposited energy is strongly coupled to the  $L_d$  (adatom mobility) probably through the kinetic energy and ionization of the adatoms. On these vicinal substrates an increase of a factor of 10 in laser fluence switches the basic growth mechanism from island to step-flow and the  $J_c$  from essentially zero to state-of-the-art,  $5 \times 10^6 \text{ A/cm}^2$  at 77 K. The control of film microstructure provided by vicinal substrate cuts may provide an effective tool to improve many of the material properties of HTS films such as noise levels, flux flow, or power handling capabilities.

## ACKNOWLEDGMENT

R. R. B. thanks Dr. R. Hughes (McMaster Univ.) and Dr. M. Eddy (Superconductor Technologies), for their sample films and helpful discussions and also Dr. T. Murray (Univ. of Dayton), Dr. D. Dorsey, Mr. D. Buchanan, Mr. S. Murray, and Mr. B. Lovett for their support. The work at Westinghouse was completed under AFOSR Contract F49620-94-C-0021.

## REFERENCES

- [1] M. G. Norton, B. H. Moeckly, C. B. Carter, and R. A. Burhman, "Growth Mechanism of  $\text{YBa}_2\text{Cu}_3\text{O}_{7-\delta}$  Thin Films on Vicinal  $\text{MgO}$ ," *Cryst. Growth*, vol. 114, pp. 258, 1991
- [2] T. Satoh, J. Fujita, T. Yoshitake, and H. Igarashi, "Microstructure of  $\text{Bi}_2(\text{Sr,Ca})_3\text{Cu}_2\text{O}_x$  thin films on vicinal  $\text{SrTiO}_3$  substrates," *Physica C* vol. 191, pp. 359-362, 1992
- [3] A. Lamagna, S. Nicoletti, M. S. Balmaseda, A. Migliori, R. Fabbri, and L. Correra, "In-plane texture and transport properties of YBCO films grown on  $\text{MgO}$  cut off-axis," vol. , pp. 117-122, 1992
- [4] S. J. Pennycook, M. F. Chisholm, D. E. Jesson, R. Feenstra, S. Zhu, X. Y. Zheng, and D. J. Lowndes, "Growth and relaxation mechanisms of  $\text{YBa}_2\text{Cu}_3\text{O}_{7-x}$  films," *Physica C*, vol. 202, pp. 1-11, 1992
- [5] S. A. Kukushkin and A. V. Osipov, "Microscopic theory of epitaxial film growth on vicinal surfaces," *Thin Solid Films*, vol. 227, pp. 119-127, 1993
- [6] M. G. Norton, R. R. Biggers, I. Maartense, E. K. Moser, and J. L. Brown, "Surface Outgrowths on Laser-Deposited  $\text{YBa}_2\text{Cu}_3\text{O}_7$  Thin Films," *Physica C* (1994 in press)
- [7] M. G. Norton, R. R. Biggers, I. Maartense, E. K. Moser, and J. L. Brown, "Examination of Particles and Outgrowths on the Surface of Epitaxial  $\text{YBa}_2\text{Cu}_3\text{O}_7$  Thin Films," *Mater. Res. Soc. Proc.* vol. 341, pp. 183 1994
- [8] D. H. Lowndes, X. Y. Zheng, S. Zhu, J. D. Budai, and R. J. Warmack, "Suppression of the spiral-growth mechanism in epitaxial  $\text{YBa}_2\text{Cu}_3\text{O}_{7-\delta}$  films grown on miscut substrates," *Appl. Phys. Lett.* vol. 61, (7), pp. 852-854, 17 Aug 1992
- [9] H. J. Scheel, "Problems in Epitaxial Growth of High-Tc Superconductors," *Adv. in Supercond. VI* (Springer, Tokyo 1994)

Manuscript received October 18, 1994.

## Effect of Oxygen Over-Doping on $T_c$ and $R_s$ of YBCO Films

J. R. Gavaler, J. Talvacchio, and R. W. Weinert  
Westinghouse STC, Pittsburgh, PA, USA

**Abstract**—Data on bulk  $\text{YBa}_2\text{Cu}_3\text{O}_{7-x}$  (YBCO) have shown that optimum critical temperatures are obtained in material that has less than the maximum (stoichiometric) oxygen content,  $x=0$ . We have prepared films of YBCO that were over-doped with oxygen and have measured their properties. In some of these films,  $T_c$ 's were degraded to as low as 85K and  $R_s$ 's to  $>10 \text{ m}\Omega$  (at 77K and 10 GHz). Re-annealing at 450°C at experimentally optimized oxygen pressures raised  $T_c$ 's significantly in all cases but had only a marginal effect on  $R_s$  values. Large improvements in  $R_s$  were obtained in the films which initially had very high surface resistances only by annealing them at higher temperatures. Growth and annealing conditions are described by which YBCO films with  $T_c$ 's of  $>90\text{K}$  and  $R_s$ 's of  $\leq 0.5 \text{ m}\Omega$  (at 77K and 10 GHz) were prepared.

### I. INTRODUCTION

Following the discovery of  $\text{YBa}_2\text{C}_3\text{O}_{7-x}$  (YBCO) it was commonly assumed that optimum superconductivity in this compound was obtained when it was completely oxidized, i.e., when  $x=0$ . In the past few years, however, several papers have challenged this assumption [1]–[4]. They have presented data on bulk samples which indicate that when  $x=0$  the YBCO is actually over-doped and that the best superconducting properties are obtained at a slightly lower oxygen composition. We have also observed the phenomenon of oxygen over-doping in films of YBCO. In this paper we report on the effect of over-doping in these films on critical temperature,  $T_c$ , and on rf surface resistance,  $R_s$ .

### II. EXPERIMENTAL PROCEDURE

We have previously reported in detail the procedures that we employ for depositing YBCO films [5], [6]. The films discussed in this paper were sputtered from a two inch diameter stoichiometric YBCO target mounted in the 90° off-axis configuration, using 90 watts of rf power. Single crystal  $\text{LaAlO}_3$  substrates were positioned on a quartz holder as described in [6]. Targets were purchased from two different commercial suppliers. The sputtering gas was a mixture of 100 mTorr argon, 65 mTorr Argon and 10 mTorr of water vapor. The deposition temperatures were either 620 or 700°C.

Critical temperatures were measured resistively, using the standard Van der Pauw technique and also inductively by noting the change of inductance for a copper coil driven at

100 kHz which was positioned against the film. The resistive  $T_c$  is defined as the temperature at which the resistance goes to zero and the inductive  $T_c$  as the temperature at the midpoint of the change in inductance. RF surface resistances of the films were determined using the parallel plate resonator method developed by Taber [7]. Structural analyses were done by x-ray diffraction and by scanning electron microscopy (SEM). Chemical analyses were done by secondary ion mass spectroscopy (SIMS).

Following deposition, the films were in situ annealed at 450°C for twenty minutes at a pressure of oxygen ranging from one to 760 Torr. To change the oxygen content of a film, it was first heated in vacuum ( $\sim 10^{-6} \text{ Torr}$ ) to 550°C then oxygen was introduced at the desired pressure. The film was held at 450°C for twenty minutes before cooling to room temperature. Because the YBCO film samples are so small accurate analyses of oxygen compositions to the precision required was not possible. Oxygen compositions, therefore, were inferred from the resistivities of the films.

### III. RESULTS AND DISCUSSION

#### A. Critical Temperature

The first clear-cut evidence of oxygen over-doping in YBCO films was obtained in a group of films that were deposited at a relatively low temperature of  $\sim 620^\circ\text{C}$  and then in-situ annealed in 100 Torr of oxygen. The transition curve for one of these films is shown in Fig. 1a. As can be noted, the critical temperature is only 85K. The growth of YBCO films with less than optimum  $T_c$ 's is, of course, not unusual. However, in contrast to most films with depressed  $T_c$ 's, these films had unusually low room temperature resistivities of  $\sim 150 \mu\Omega\text{cm}$  and high resistivity ratios,  $R_{300\text{K}}/R_{100\text{K}}$  of almost four. This unusually high carrier (hole) concentration suggested that the films were over-doped with oxygen.

To investigate this possibility, oxygen was first removed from the films by heating in vacuum and then they were re-annealed at different oxygen pressures ranging from 1 to 760 Torr. In Fig. 1 the transition curves of one of these films is shown, as grown (a), and after being re-annealed in 20 Torr of oxygen (b). The observed rise in  $T_c$  to over 90K and the corresponding increase in normal state resistivities are strong confirmation that, as grown, the film indeed had an excess hole concentration from being over-doped with oxygen. An estimate of the change in oxygen content obtained by re-annealing at a lower pressure, based on the bulk data of Claus et al. [4], is that it went from approximately 6.97 to 6.92.

Manuscript received October 17, 1994

This work was supported in part by AFOSR Contract No. F49620-94-C-0021 and ONR/ARPA Contract No. N00014-91-C-0112.

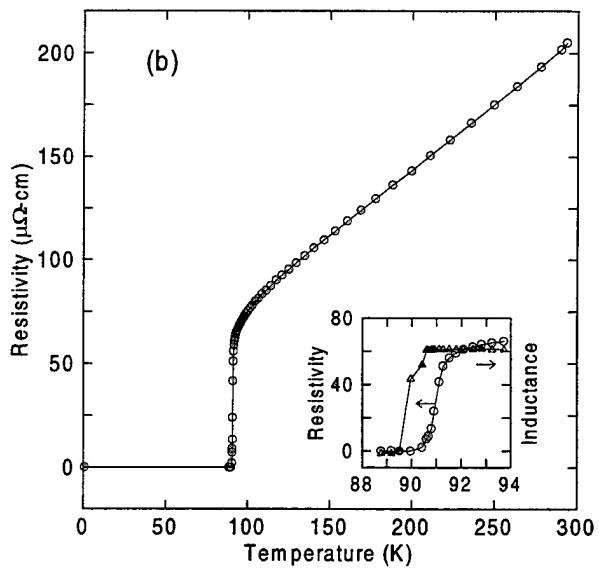
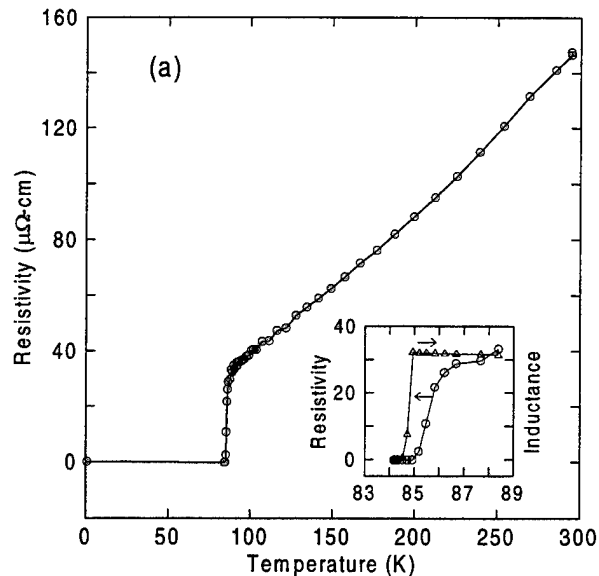


Fig. 1. Transition curves for a YBCO film grown at 620°C then in situ annealed in 100 Torr oxygen (a) and for the same film re-annealed in 25 Torr oxygen after first removing oxygen (b).

The film of Fig. 1 was re-annealed several more times in a series of different oxygen pressures. The data from these experiments are shown in Fig. 2, where resistive  $T_c$ 's are plotted versus oxygen pressures. Here one can see a maximum in  $T_c$  in the vicinity of 25 Torr. The other notable feature of these data is that at high oxygen pressures the critical temperatures are higher than that of the as-grown film. For example, at 100 Torr the critical temperature is 89K, four degrees higher than what it was when it was originally in situ annealed at that pressure. Even when annealed in one atmosphere of oxygen the  $T_c$  is 88K. One can conclude from these data that some other factor(s), in addition to oxygen content, were influencing the hole concentration, and relatedly, the  $T_c$  of the film.

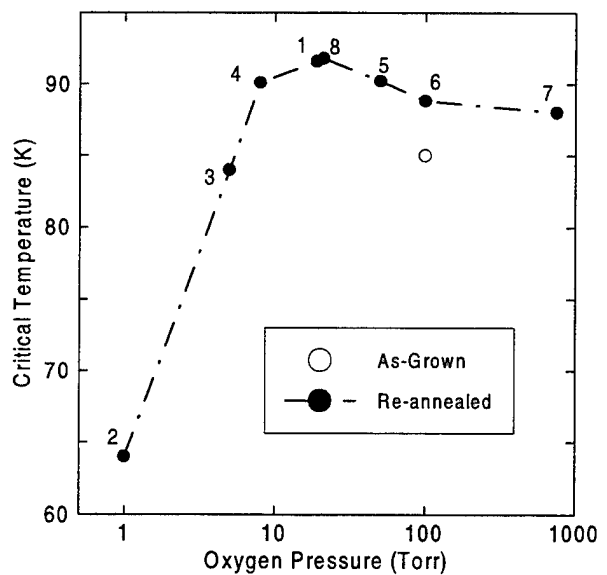


Fig. 2. Critical temperature vs. oxygen annealing temperature for a YBCO film. The film was initially annealed in situ (open circle) and then re-annealed eight times (solid circles) each time after first having oxygen removed. The numbers refer to the order in which the film was re-annealed.

Other data supporting this conclusion were obtained from the study of a large series of films which were grown at a higher temperature (700°C). These films were sputtered from several different targets supplied by two different vendors. All of the films were in situ annealed in one atmosphere of oxygen. The common result among these films was that, as before, they exhibited depressed  $T_c$ 's of 85 to 87K after being annealed at this high oxygen pressure. In most cases, but not all, removing oxygen and then re-annealing at lower pressures again raised both the critical temperatures and the normal state resistivities. However, differing from the previous results, the room temperature resistivities were higher and the  $R_{300K}/R_{100K}$  ratios lower compared to the films grown at lower temperature. Data on one of the films grown at 700°C are shown in Fig. 3, as grown (a), and after re-annealing (b). Another important result from this series of experiments was the discovery that the oxygen pressure needed to optimize the hole concentration was not always the same for each film. In fact, among this group of films, several were found which already exhibited  $T_c$ 's of  $\geq 90$ K after the initial in situ anneal in one atmosphere of oxygen. Also, in a few instances films were obtained which even after being annealed in one atmosphere of oxygen apparently still had a deficiency of holes. Initially, the  $T_c$ 's of these films were also  $\sim 87$ K. However, annealing them at successively lower oxygen pressures produced only a gradual degradation in critical temperature.

Factors, in addition to oxygen content, which can influence hole concentration are structural disorder and foreign impurities, both of which are common in sputtered films. The concept that impurities would be incorporated into the present films is not surprising. The pressed and sintered targets used in the sputtering process are themselves a prime source of

contamination. An analysis of a nominally 99.96% pure YBCO target showed the presence of no less than sixteen impurity elements including Sr, Na, K, Ca, Cl, Si, S, Mg, and Al, among others. It would not be difficult to create a scenario by which various combination of these elements could produce YBCO films which had either an excess, a deficiency, or a near-optimum concentration of holes.

Because of the impurity problem it is apparent that the reproducible preparation of  $\geq 90$ K YBCO films can not be done routinely by simply establishing a single set of annealing conditions. When the impurity environment is changed, as for example, when a new target is installed, optimum annealing conditions must be re-established. Of course, if it were

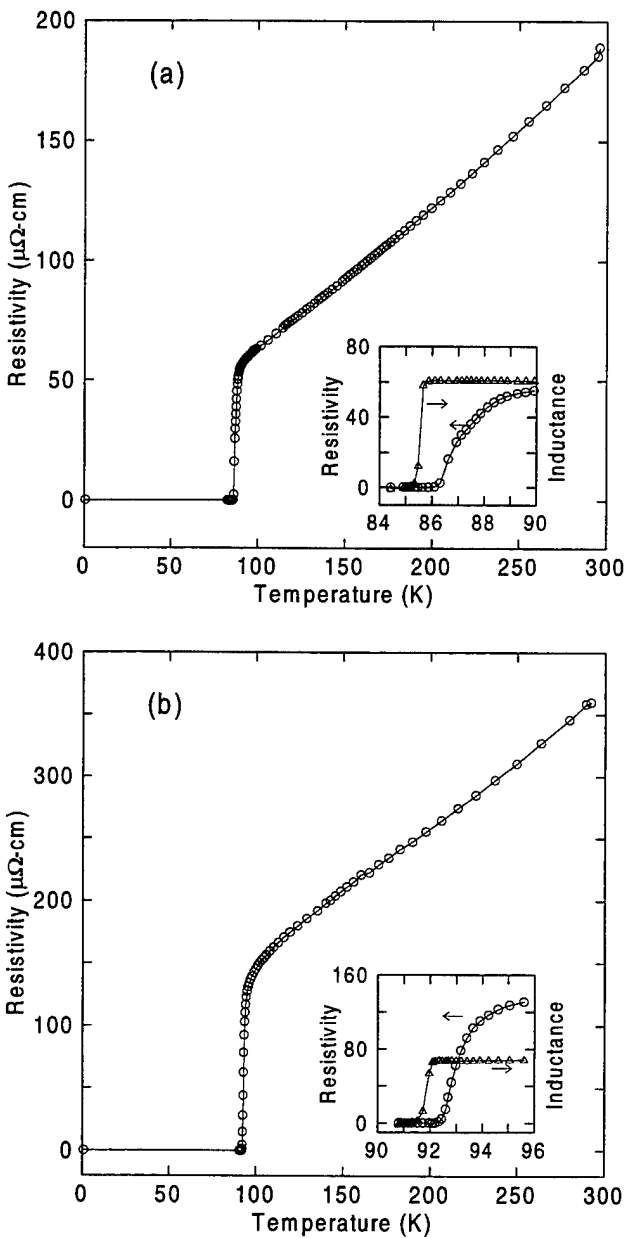


Fig. 3. Transition curves for a YBCO film grown at 700°C then in situ annealed in 760 Torr oxygen (a) and for the same film re-annealed in 25 Torr oxygen after first removing oxygen (b).

deemed to be sufficiently important, one could minimize this problem by using more expensive higher-purity targets and by taking all the time-consuming precautions required to maintain an ultra-high purity deposition system.

### B. RF Surface Resistance

To determine the effect of over-doping on rf surface resistance in YBCO we obtained data on several oxygen over-doped samples which had been deposited and annealed under conditions similar to those used for the films of Fig. 1 and Fig. 3. As described, the major difference in the preparation of these two sets of films was the relatively low growth temperature (LGT) of  $\sim 620$  °C in one case, and the more typical higher growth temperature (HGT) of  $\sim 700$  °C in the other. Standard x-ray diffraction analyses of the as-prepared films showed them all to be single-phase c-axis. Their thicknesses were all in the vicinity of 300 nm. They had similarly smooth surfaces with no Cu-O outgrowths (boulders). Their lattice parameters were  $\sim 1.1680$  (LGT) and  $\sim 1.1700$  nm (HGT) and the resistive and inductive  $T_c$ 's were similar to those shown in Figs. 1a and 3a. Despite having all of these similarities, they were found to have dramatically different  $R_s$  values. At 77K and 10 GHz, the surface resistances of the HGT films were all below 1 mΩ, while those of the LGT films ranged between 10 and 80 mΩ.

Both sets of films were re-annealed to optimize hole concentration thereby raising  $T_c$ 's to  $> 90$ K. In spite of this improvement in critical temperature of up to 6K in some cases, the remeasurement of these films at 77K produced  $R_s$  values that were essentially unchanged. These results indicate that overdoping has no significant negative effect on  $R_s$  at 77K and that the much higher values observed in the LGT films were solely due to their low growth temperatures. To reinforce this conclusion, some LGT films were heated to 700°C in one atmosphere of oxygen and again remeasured. This time the surface resistance dropped sharply down to a few mΩ. One of

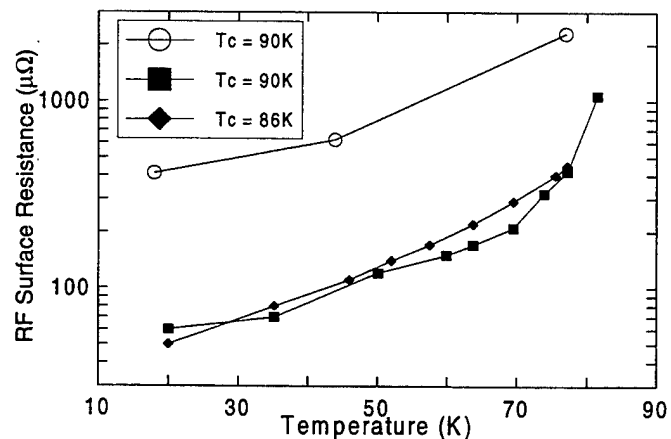


Fig. 4. RF surface resistance vs. temperature at 10 GHz for YBCO films with optimized (open circles and solid squares) and non-optimized (solid triangles) hole concentrations.

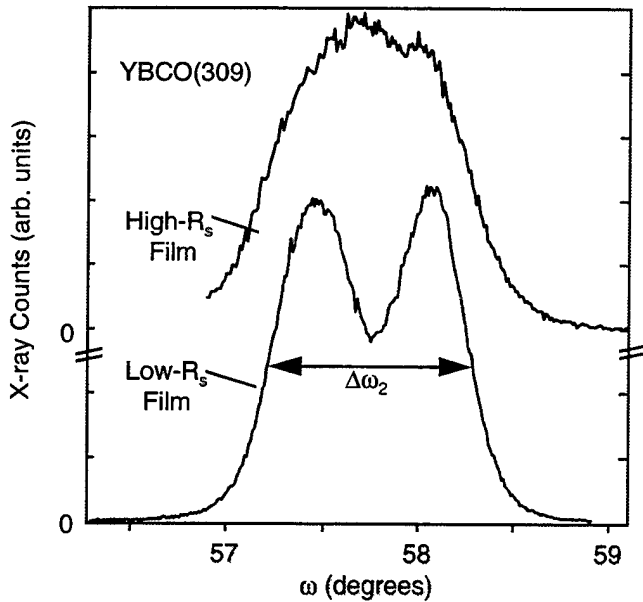


Fig. 5. X-ray rocking curve data illustrating an observed correlation between low  $R_s$  values and a-b twinning in YBCO films.

these LGT films is shown in Fig. 4. Its critical temperature is 90K. The other two curves in this figure are from data on a HGT film with an optimized hole concentration ( $T_c \sim 90K$ ) and from another HGT film with a non-optimized concentration ( $T_c \sim 86K$ ). As can be seen from this figure, if over-doping exerts any influence at all on  $R_s$  values at temperatures of 77K and less, it is only marginal.

Although it could not be proven from the  $T_c$  or the x-ray data, we believe that the very high  $R_s$  of the LGT films was due an incomplete reaction of the YBCO at the relatively low growth temperature of 620°C. However, even after further treatment in oxygen at much higher temperatures of up to 900°C,  $R_s$  was not lowered below 2 mΩ in any of these films. A more detailed x-ray analysis indicated an interesting structural difference between LGT and HGT films which could not be changed even by such very high temperature oxygen annealing and which may account for the different surface properties. Fig. 5 shows rocking curve data on a LGT and a HGT film. The (309) peaks of the two films are shown. As can be noted there is a clear splitting into two peaks, due to a-b

twinning for the lower  $R_s$  film but there is a single peak with the same overall width for the higher- $R_s$  film.

#### IV. CONCLUSION

We have obtained data which clearly demonstrate the phenomenon of oxygen over-doping in YBCO films. Films were sputtered which had depressed  $T_c$ 's, due to an excess of oxygen, down to 85K. With respect to rf surface properties, over-doping was found to have, essentially, no effect on  $R_s$  values at temperatures of 77K and lower. The prime parameter affecting surface resistance was found to be growth temperature. At the low growth temperature ~620°C, structural defects were incorporated into films which degraded surface resistance and which could not be removed even by re-annealing at temperatures up to 900°C.

#### ACKNOWLEDGMENT

We thank J. H. Uphoff and J. E. Williams for their valuable contributions in film preparation, S. H. Talisa for developing our surface resistance measurement technique, and G. B. Draper in surface resistance measurement.

#### REFERENCES

- [1] J.L. Tallon and N.E. Flower, "Stoichiometric  $\text{YBa}_2\text{Cu}_3\text{O}_7$  is Overdoped," *Physica C* 204, 237-246 (1993).
- [2] H. Claus, S. Yang, H.K. Viswanathan, G.W. Crabtree, J.W. Downey, and B.W. Veal, "Comparison of Au-Free versus Au-Doped  $\text{YBa}_2\text{Cu}_3\text{O}_{7-\delta}$  Crystals," *Physica C* 213, 185-189 (1993).
- [3] E. Janod, A. Junod, T. Graf, K.-Q. Wang, G. Triscone, and J. Muller, "Split Superconducting Transitions in the Specific Heat and Magnetic Susceptibility of  $\text{YBa}_2\text{Cu}_3\text{O}_x$  versus Oxygen Content," *Physica C* 216 129-139 (1993).
- [4] H. Claus, U. Gebhard, G. Linker, K. Rohberg, S. Riedling, J. Franz, T. Ishida, A. Erb, G. Muller-Vogt, and H. Wuhl, "Phase Separation  $\text{YBa}_2\text{Cu}_3\text{O}_{7-\delta}$  Single Crystals near  $\delta=0$ ," *Physica C* 200, 271-276 (1992).
- [5] J.R. Gavaler, J. Talvacchio, T.T. Braggins, M.G. Forrester, and J. Gregg, "Critical Parameters in the Single-Target Sputtering of  $\text{YBa}_2\text{Cu}_3\text{O}_7$ ," *J. Appl. Phys.* 70(8), 4383 (1991).
- [6] T.T. Braggins, J.R. Gavaler, and J. Talvacchio, "In-Situ Deposition of  $\text{YBa}_2\text{Cu}_3\text{O}_7$  Films on Both Sides of Two-Inch-Diameter Wafers by Off-Axis Sputtering," *Microwave Journal* 35(8), 106 (1992).
- [7] R.C. Taber, "A Parallel Plate Resonator Technique for Microwave Loss Measurements on Superconductors," *Rev. Sci. Instrum.* 61(8), 2200 (1990).

## Discrete Models of Abrikosov Vortex Flow Transistors

Arthur Davidson and N.F. Pedersen\*

Westinghouse Electric Corporation, Science and Technology Center, Pittsburgh, PA 15235

**Abstract**—Electronic devices based on flux flow phenomena in oxide superconductors have been under development, and are potentially important for applications, particularly in the interface between RSFQ circuits and silicon based room temperature electronics. Models for these flux flow transistors (FFT's) usually have been based on discrete Josephson elements, ignoring the physics of fluxoid nucleation. We have explored a numerical simulation of flux flow, also using discrete Josephson elements, but at the level of the Abrikosov vortex, so that nucleation at the film edge becomes part of the model. Our results imply that the inhomogeneous coupling of the magnetic control is important for a saturated transfer function, rather than a periodic one, and that there is no advantage in putting flux flow strips in parallel, separated by open gaps. Furthermore, gain may be increased by arranging the bias to separately optimize nucleation and transfer to the load.

### I. INTRODUCTION

Flux flow devices are unique in superconductivity, in that they are the only devices that have operated as three terminal amplifiers with gain, isolation, saturation, and non-latching behavior [1]. As such, there are multiple possibilities for these devices. They could function as the active device in logic and memory circuits. They could serve as an interface device, amplifying very small signals from Josephson RSFQ circuits, and sending them on to semiconductor discriminators and laser diodes. Moreover, flux flow is a mode of operation which is easier in HTS technology than in LTS. The higher temperature of operation and the natural granularity of the films, together with their very short coherence lengths makes flux pinning less strong than in all but the most granular of LTS superconducting materials and films.

Manuscript received October 17, 1994.

\*Permanent Address, Dept. of Physics, The Technical University of Denmark, DK2800, Lyngby, Denmark

This work was supported in part by Air Force Office of Scientific Research Contract No. F49620-94-C-0021

The basic operating concepts of an Abrikosov vortex flux flow device is shown in Fig. 1, below. For this figure data were taken from a bulk (1 mm) size device shaped by filing a ceramic sample, and measured with pressed indium voltage and current contacts. The control magnetic field was supplied from a few turns of fine copper wire wrapped around the device. Although this device had current and power gain, the impedance was 3 orders of magnitude too low for any useful application. Clearly, the impedance problem would be solved by going to a thin film device.

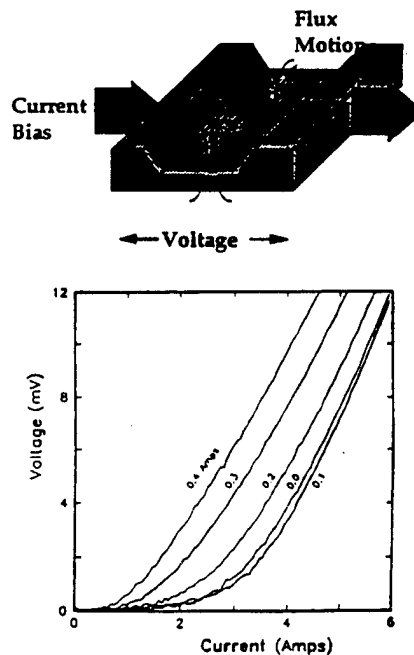


Fig. 1. Top: geometrical configuration of a millimeter size bulk ceramic YBCO flux flow device. Bottom: experimental output curves from this ceramic device. Note that both current and power gain are implicitly available.

The original idea of flux flow amplifiers goes back to the work of Likharev [2], Van Zeghbroeck [3], and of McGinnis et al [4]. Nordman's group has been leading in this area, having explored flux flow in LTS long Josephson junctions, using them for low noise wide band amplifiers, and also having studied fluxoid motion in HTS films [1]. This and other work [5] has established these devices as high speed amplifiers with many desirable properties. The work reported in this paper mixes the long junction concept [6] of flux flow with that of flux flow in a uniform thin film [7] (no junction). The goal is to understand flux flow in thin films.

But we have chosen to model the motion of vortices in a uniform thin film as the motion of fluxons in a network of thin film inductors and Josephson junctions. We will show that we can indeed model flux flow with such a network, and in an analogy with tetrode vacuum tubes we will show that the addition of a fourth electrode can improve the performance of the device.

## II. ANALYSIS OF STRIP

Consider a narrow strip of film parallel to the direction of current flow in a flux flow thin film. This strip will have an inductance, and a critical current, above which a voltage will appear, caused by fluxoid nucleation and movement across the strip. Our lumped element model of this situation is an ideal inductance in series with a Josephson element. The inductance will be governed by kinetic effects if it is sufficiently thin, and will be given by

$$L = \frac{\mu_0 \lambda_L^2 \ell}{wd} \quad (1)$$

where  $\lambda_L$  is the London penetration depth,  $\ell$  is the strip length, and  $w$  and  $d$  are its width and thickness. Note that the  $LI_0$  product of such a strip is thus independent of the width and thickness of the strip, depending only on the critical current density and  $\lambda_L$ .

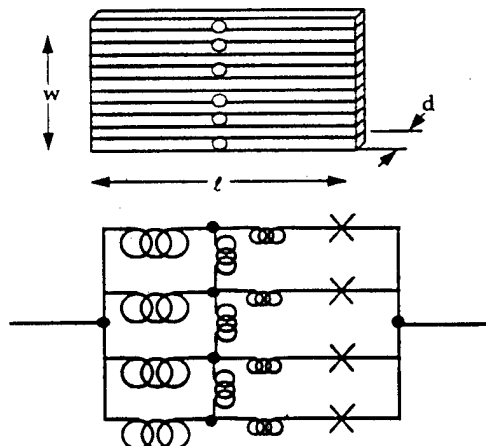


Fig. 2. Lumped element model of flux flow strip. The figure at the top shows how the strip is divided, and the circles represent the induced flux.

Now we model the full width of the flux flow strip by placing a number of these narrow strip elements together, as in Fig. 2, and we have added some transverse inductance, which is clearly needed to model the circulating current of a vortex in the film. In Fig. 2 there is still some inductance in series with the junctions, on the ground side of the transverse inductors. These represent the kinetic inductance part of the inductance associated with a single vortex. The transverse inductors themselves represent the mutual inductance of the

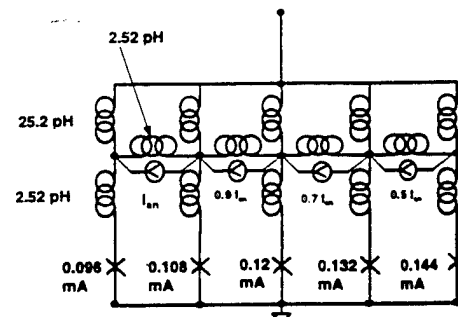


Fig. 3. The complete circuit with parameter values. The current sources model coupling to an outside current carrying electrode.

vortex to external sources. If we assume 5 elemental strips,  $w = 2 \mu\text{m}$ ,  $\ell = 10 \mu\text{m}$ ,  $d = 0.05 \mu\text{m}$ , and  $\lambda_L = 0.2 \mu\text{m}$ , then Eq. 1 yields about 25 pH for a strip element. Eq. 1 can also be used to estimate the inductance of a vortex: for  $\ell = 2\pi\lambda_L$ , and  $w = \lambda_L$ , we obtain about 6 pH of self inductance associated with a vortex. For historical reasons our simulations used a value of about 5 pH per vortex, divided into two 2.52 pH inductors. A third 2.52 pH inductor completes the vortex loop, representing mutual inductance to an outside field. The complete circuit model for a flux flow film is thus shown in Fig. 3.

The model is complete if we assume a critical current density of  $3 \text{ mA}/\mu\text{m}^2$  ( $3 \times 10^5 \text{ A}/\text{cm}^2$ ). This yields a critical current for the individual elements of 0.12 mA, or about 0.6 mA for a 1  $\mu\text{m}$  wide strip. The  $LI_0$  product for one strip is then  $25 \times 0.12 = 0.14 \phi_0$ . The  $LI_0$  product of a typical loop is  $(3 \times 2.5 \times 0.12) = 0.43 \phi_0$ . The simulation, using the schematic of Fig. 3, incorporated a systematic shift in critical current from right to left

Notice that the four current sources represent the coupling of the vortices to an applied field, and that the coupling varies, declining from the left hand edge, as if a current carrying electrode were. This models the physical situation where an electrode carrying current is about 2 microns away from the left edge of the thin film. If the four current sources were of uniform amplitude, the response of the model would be periodic, like a SQUID. The non-uniform coupling is what is responsible for the saturated response of the system. Simulations were run to confirm both of these facts: Uniform coupling produces a periodic response, and non uniform coupling produces a saturated response. The saturated response is much more desirable in most applications

## III. SIMULATION RESULTS

Fig. 4 illustrates the results of simulating the circuit of Fig. 3. At the left is a schematic representation of the device being modeled, including the control electrode. The simulations were run using the PSCAN package. The

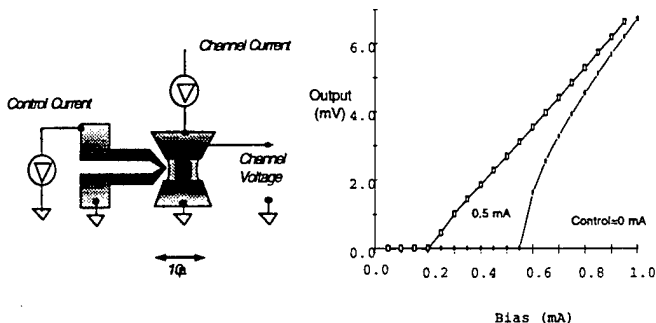


Fig. 4. On the left, a symbolic representation of flux flow device. The circuit in Fig. 3 models the flux dynamics in the path of the channel current. On the right is the IV curve from a PSCAN simulation of the circuit in Fig. 3.

dynamical state of the junctions could be watched as a function of time, and the averaged IV results are shown in Fig. 4, using the parameters of Fig. 3, except that 5 strips and 5 junctions were used, instead of the four shown in Fig. 3. The family of curves as the control current (external field) increased saturated. There was very little change above the 0.2 mA, as seen in the output characteristic in Fig. 5.

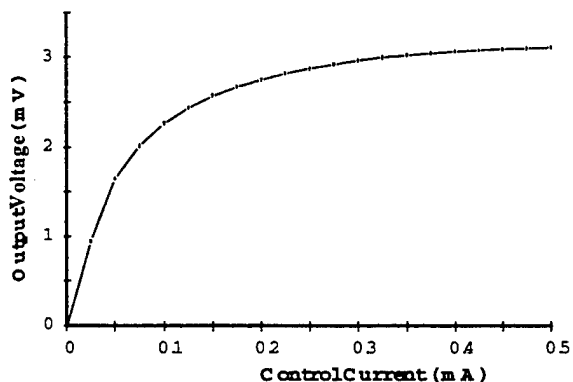


Fig. 5. Output characteristic for the simulation in Fig. 4, biased close to the top of the critical current. Under these conditions the transresistance could be as high as 30  $\Omega$ .

A similar simulation was tried, modeling the effect of doubling the width of the strip ( $w$  in Fig. 2). This was done by extending the model of Fig. 3 to the right with 5 more identical units, except that the control current couplings continue to decline as the inverse of the distance from the control line. Under these conditions, the simulated IV curve was identical to that in Fig. 4, except that the current axis was doubled: current gain was proportional to the width of the device.

#### A. Variation 1: Loops

Since the reports of Martens [1] [6], it has been thought the gain of a flux flow device could be raised by incorporating multiple flux flow bridges separated by gaps, or loops. The idea evidently is that the loops would couple through mutual inductance to the control line, and so increase the sensitivity of the device. We tested this idea in

our model by adding loops with more junctions onto the right hand end of the basic model in Fig. 3. We found that by adding junctions with inductors this way, the critical current of the device would rise in proportion to the number of junctions, but the modulation, or current gain would not scale. In some cases, where we did not couple the extra loops back to the control, the modulation did not scale up at all. In other cases, where we added coupling again in proportion to one over the distance from the control, the gain rose only a small fraction of the scaling factor.

#### B. Variation 2: Tetrode

Much more interesting was the idea of splitting the bias current to the strip, so that an independent current source would supply most of the current flowing along the edge where vortices must nucleate. Thus the current flowing there would vary less as the load current swings up and down, and so keep conditions for nucleation closer to optimum. Ideally, it would be desirable to have the vortex nucleation rate controlled only by the external control current, and not be affected whatsoever by the load current. In the simulations this was accomplished in the following way. We used the circuit of Fig. 3, with 10 junctions instead of 5. We stated already that this circuit had gain that scaled with the number of junctions. But now we tied the two left most junctions to one current source, and the 6 right most junctions to another current source, with two junctions in the middle left without their own bias. This geometry is equivalent to a film in which a slit had been cut in the current lead, down to the flux flow region, splitting the bias in two.

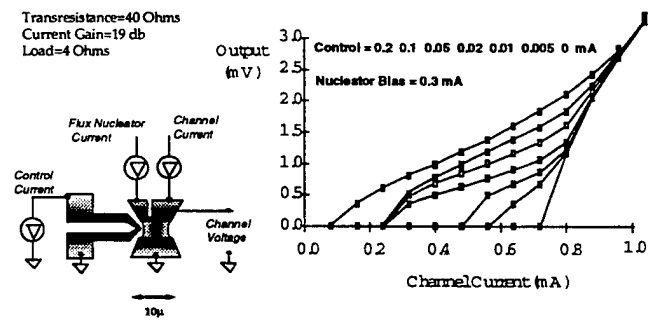


Fig. 6. Sketch and simulated IV curve of tetrode flux flow device. Gain and the operating region have both been increased

The results are shown in Fig. 6. The sketch on the left illustrates how the electrode might be cut to make a tetrode. The current scale would be about double the current of Fig. 4, since in effect this circuit is double the width, except that the nucleator current is biased close to critical, so in fact the load critical current, which is what is plotted, is quite similar to that in Fig. 4. But now the current gain has scaled more than the width, and the IV curves are flatter than before, showing that the nucleation rate is less influenced by the load current. This is very significant for the use of these

devices as amplifiers and as isolation stages in digital designs.

### III. DISCUSSION

We have observed classic flux flow in the macroscopic ceramic sample, characterized by the smoothly curving characteristics in Fig. 1. Since our lumped element model takes into account neither temperature nor a distribution of pinning strength, it is not surprising that they show a more abrupt critical current for zero applied field. However, the devices simulated in Fig. 4 and 6 do show characteristic flux flow IV curves in a finite magnetic field. In fact, flux pulses could be observed directly in the PSCAN simulations, confirming that the observed properties of these devices is indeed connected with vortex motion.

Our work has not supported some of the results reported earlier by Martens. He had observed a significant increase in gain, for example, when putting gaps between operating flux flow strips. Our simulations do not support that conclusion. We see improvement that scales with the width of the film when no extra inductors are placed so as to model holes or gaps between the flux flow strips. We argue that the success in [1] and [7] is difficult to understand, in view of the barriers to nucleating flux at the edge of a single strip. It seems unlikely that requiring nucleation at multiple strips in sequence could enhance the transport of vortices. The rational for the multiple strip configuration has been that the loops could couple to the control current, and so enhance the gain. On the other hand a flat film with no holes or gaps would have a larger demagnetizing factor, thus amplifying the magnitude of the field at the edge of the device, and enhancing nucleation. This is the rationale for the scaling behavior we observed when we scaled up the width of the flux flow strips and observed that the current gain scaled directly as the width.

Finally, we have shown that by adding another electrode, placed so as to provide a constant current bias to

the vortex nucleation region of the device, the nucleation rate can be at least partially isolated from the load current. This produces a device with more gain and operating margins, which could make an important difference in applications.

### REFERENCES

- [1] J.S. Martens, V.M. Hietala, T.A. Plut, D.S. Ginley, G.A. Vawter, C.P. Tigges, M.P. Siegal, Julia M. Phillips, and S.Y. Hu, "Flux Flow Microelectronics," *IEEE Trans. on Appl. Supercond.*, 3, 2295 (1993).
- [2] K.K. Likharev, V.K. Semenov, O.V. Snigirev, and B.N. Todorov, "Josephson Junction with Lateral Injection as a Vortex Transistor," *IEEE Trans. on Mag.* MAG-15, 420, (1979).
- [3] B.J. Van Zeghbroeck, "Superconducting Current Injection Transistor," *Appl. Phys. Lett.*, 42, 736 (1983).
- [4] D.P. McGinnis, J.E. Nordman, and J.B. Beyer, "Optimization of Circuit Parameters for the Vortex Flow Transistor," *IEEE Trans. Mag.* MAG-23, 699 (1987).
- [5] Y.M. Zhang, D. Winkler, P.A. Nilsson, and T. Claeson, "Flux Flow Transistors Based on Long  $YBa_2Cu_3O_{7-\delta}$  Bicrystal Grain Boundary Junctions," *Appl. Phys. Lett.* 64, 1153 (1994), and  
L. Alff, B. Meyer, S. Schuster, O. Frolich, R. Gerdemann, A. Beck, and R. Gross, "Magnetic Field Effect Three Terminal Device Based on  $YBa_2Cu_3O_{7-\delta}$  Grain Boundary Junctions," *J. Appl. Phys.* 75, 1843 (1994).
- [6] G. Filatrella and N.F. Pedersen, "Flux flow in High-Tc Josephson Junctions," *Appl. Phys. Lett* 63, 1420 (1993)
- [7] J.S. Martens, D.S. Ginley, J.B. Beyer, J.E. Nordman, and G.K.G. Hohenwarter, "A Model and Equivalent Circuit for a superconducting flux Flow Transistor," *IEEE Trans. Appl. Supercond.*, 1, 95 (1991).

## Meandering grain boundaries in $\text{YBa}_2\text{Cu}_3\text{O}_y$ bi-crystal thin films

D. J. Miller and T. A. Roberts

Materials Science Division and Science and Technology Center for Superconductivity, Argonne National Laboratory, Argonne, Illinois 60439

J. H. Kang and J. Talvacchio

Westinghouse Science and Technology Center, Pittsburgh, Pennsylvania 15235

D. B. Buchholz and R. P. H. Chang

Northwestern University and Science and Technology Center for Superconductivity, Evanston, Illinois 60208

(Received 11 October 1994; accepted for publication 23 February 1995)

Artificially induced [001] tilt grain boundaries in epitaxial  $\text{YBa}_2\text{Cu}_3\text{O}_y$  (YBCO) thin films were prepared by deposition onto  $\text{SrTiO}_3$  bi-crystal substrates and subsequently examined by transmission electron microscopy and atomic force microscopy (AFM). It was found that the YBCO grain boundary deviated from the path defined by the underlying substrate boundary, with the "meandering" YBCO boundary only generally following the path defined by the boundary in the underlying substrate. The AFM studies suggest this "meandering" behavior is related to the nucleation and growth mechanisms of the film, and based on this, we were able to vary the magnitude of the meandering by changing the growth conditions. The implications of this meandering behavior are significant, suggesting potential variations in electrical behavior from point to point along these boundaries. This effect is likely to be exacerbated by reduced junction linewidths and may lead to inconsistent behavior in devices which utilize this type of boundary. © 1995 American Institute of Physics.

The weak link behavior of high angle grain boundaries has been documented for  $\text{YBa}_2\text{Cu}_3\text{O}_y$  (YBCO), Bi-based, and Tl-based superconductors.<sup>1–5</sup> In most cases, these results have been based on measurements across artificially induced grain boundaries formed by thin film growth on bi-crystal substrates. While the electrical behavior of such boundaries has been widely studied, the microstructure of these boundaries has not been as well characterized. In fact, although a variety of studies have suggested several possible mechanisms for weak link grain boundary behavior, most of the work related to the structure of grain boundaries in these materials appears to have been carried out on polycrystalline samples.<sup>6–11</sup> In order to avoid potential ambiguity, it may be more insightful to characterize a well-defined grain boundary which has been documented to exhibit weak link behavior. Thus, studies of the structure of artificially induced grain boundaries are essential.

Many microstructural studies of artificially induced grain boundaries have concentrated on understanding the microscopic mechanisms for weak link behavior and consequently utilized transmission electron microscopy (TEM) and, in particular, high-resolution electron microscopy. Among the early studies of grain boundary behavior, for example, high-resolution images were used to show that the artificially induced grain boundaries were clean and free of second phases.<sup>1</sup> However, the authors also noted that the grain boundaries were not always straight, suggesting that some deviations from the underlying boundary were observed. More recently, Alarco *et al.*<sup>12</sup> reported that 45°[001] tilt grain boundaries in YBCO deposited onto yttria-stabilized zirconia (YSZ) bi-crystal exhibited "wavy" grain boundaries. In that work, the wavy nature of the grain boundary in the film was clearly shown by TEM images. However, both the (100) and (110) orientations are frequently observed in polycrystalline

films on YSZ (or  $\text{ZrO}_2$ ).<sup>7,13,14</sup> Thus, in this special case, any portion of the film which grows over the substrate boundary finds itself in another orientation which is favorable for epitaxial growth. Similarly, both (100) and (110) orientations are prevalent in polycrystalline YBCO films on  $\text{MgO}$ , and 45° tilt boundaries in those films have been shown to meander as well.<sup>10</sup> In this letter, we report on the structure of a similar type of boundary produced on a different substrate material with a very different misorientation angle to show that such "meandering" is a general phenomenon and to confirm the correlation between island-like growth of the films and the magnitude of the grain boundary deviations. Furthermore, based on this correlation, we have been able to vary the magnitude of the "meandering" boundary by changing the growth conditions.

The YBCO films were deposited by *in situ* growth onto  $\text{SrTiO}_3$  bi-crystal substrates using two different techniques. Some samples were prepared by off-axis magnetron sputtering from a stoichiometric target at a growth rate of about 4 Å/min. Another sample was prepared using pulsed organometallic beam epitaxy (POMBE). This sample was grown at a slower growth rate of ≈1.6 Å/min. The misorientation angle defined by the substrate was 24° for all of the samples discussed in this letter. Samples were prepared for plane-view TEM examination by conventional techniques.

The typical structure of the boundary as imaged at lower magnification in the TEM is shown in Fig. 1. For this image the sample was oriented to maximize the contrast difference between the two portions of the film while minimizing interfering contrast from the underlying substrate. In this image, one of the film orientations (film A) appears darker while the other orientation, rotated by 24° with respect to the first part, appears lighter (film B). The grain boundary in the substrate is visible in the middle of the micrograph as a straight line.

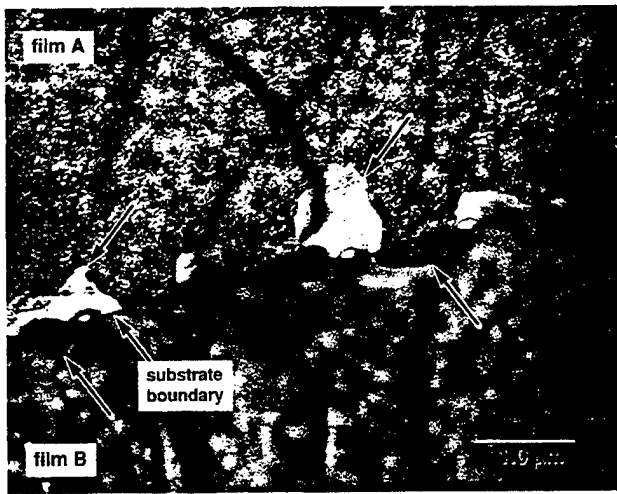


FIG. 1. Bright-field TEM image of the structure of the grain boundary in a film prepared by sputtering. The grain boundary in the substrate is visible as a straight line, as indicated, while some of the meandering segments of the YBCO boundary are marked by arrows.

In contrast, the boundary in the YBCO film is not straight, but "meanders," as the two orientations of the YBCO film grow over the substrate boundary in places. Selected area electron diffraction patterns confirmed that the portion of the film which overgrew the substrate boundary is in the same orientation as the other half of the film, as suggested by the image contrast.

Images collected along the length of the boundary indicate that both parts of the film grow into each other and that the degree of the meandering is about equal on both sides of the underlying substrate boundary. The magnitude of the deviation varies along the boundary, reaching 250 nm in places. This appears to be the same type of "wavnness" reported by Alarco *et al.*<sup>12</sup> except that the magnitude of the deviations is much larger in the boundary shown here. A more important difference is that both the substrate material and the angle of rotation between the two halves of the underlying substrate are very different in the two cases. As noted above, in the case of YBCO on YSZ, both (100) and (110) orientations are low energy, epitaxial configurations. Thus, in the special case of a 45° rotation, any portion of the film which grows over the substrate boundary finds itself in another orientation which is favorable for epitaxial growth. In the case of the films discussed here, the rotation angle was 24°, and thus any part of the film which overgrows the substrate boundary finds itself in an orientation which has very poor matching with the substrate and little tendency for epitaxial growth. Thus, the observation of meandering in these films suggests that this meandering is a general phenomenon.

The most likely explanation for the presence of meandering boundaries is the island-like growth mechanism of these YBCO films, as suggested by Alarco *et al.* In this situation, islands nucleate at various points on the substrate, and continued deposition results in lateral growth of the islands. Studies of the growth of YBCO on MgO have shown island nucleation,<sup>15</sup> and studies of YBCO films on MgO and SrTiO<sub>3</sub> have indicated an island-like growth mechanism.<sup>16,17</sup> In order to confirm this, atomic force microscopy (AFM)

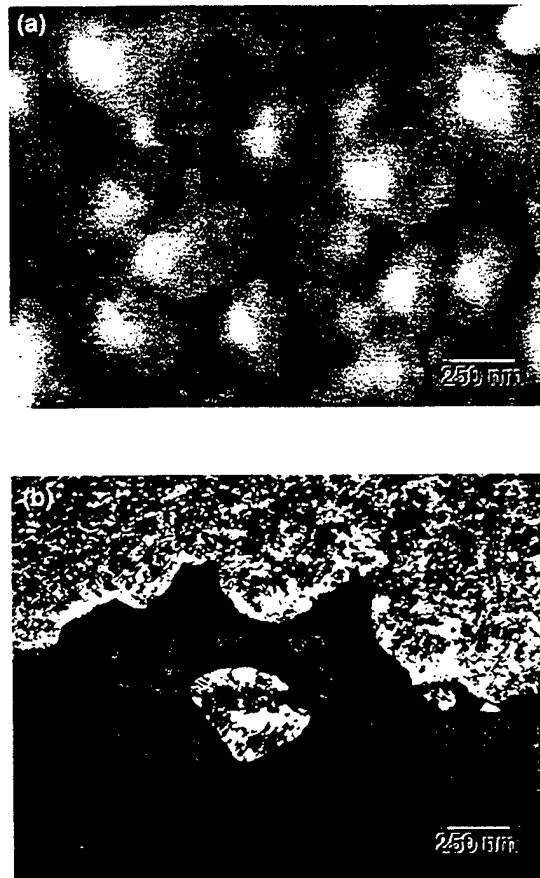


FIG. 2. (a) AFM image of the surface topography of the YBCO film and (b) TEM image of the boundary. Both images are reproduced to the same scale.

studies were performed on one of our films to identify the topographical features which are indicative of island size in these films.<sup>17</sup> Figure 2(a) shows an AFM image from a randomly selected area in the film while Fig. 2(b) shows a TEM image of another portion of the film, printed to the same scale as the AFM image. The magnitude of the islands imaged by the AFM is the same as the magnitude of the meandering observed in the boundary. Furthermore, the island-like topography was continuous across the boundary and the boundary itself could not be imaged directly by AFM except by the presence of a few second phase particles at the surface. Both of these observations support the conclusion that island growth is responsible for meandering boundaries. The growth of a meandering boundary in spite of such poor matching to the substrate implies that the energy due to nucleation of a grain boundary is greater than the difference in energy between a coherent and an incoherent interface between the film and the substrate (for this particular misorientation).

Meandering grain boundaries have also been observed in Au films deposited onto NaCl substrates for which the growth mechanism was found to be island coalescence.<sup>18</sup> In those films, the grain boundaries were pinned by holes in the film. During subsequent annealing, coalescence of the holes allowed the grain boundary to relax towards a more planar configuration. This confirms that there is an energy "penalty" associated with the growth of a meandering boundary in that the energy of an incoherent film/substrate interface is

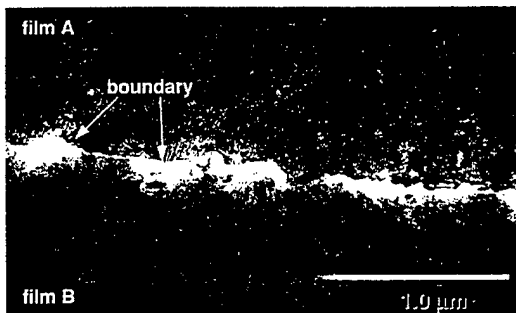


FIG. 3. Bright-field TEM image of the structure of the boundary of a film prepared by POMBE.

greater than that of a coherent interface. In this situation, it is likely that the magnitude of the grain boundary deviations can be altered by changing the growth conditions such that the growing islands have more time to assume the lowest energy configuration. The small energy difference between a coherent and an incoherent interface will provide a driving force for migration from islands which overgrow the substrate boundary to islands which are epitaxially oriented. In order to confirm this, a YBCO film was deposited by POMBE. In this case, the lower growth rate allowed more time for additional surface diffusion. The structure of the boundary produced in this film is shown in Fig. 3. The boundary is again seen to meander, but the average magnitude of the deviation is significantly less than that seen in the sputtered films. Thus the magnitude of the meandering can be controlled by controlling the growth conditions of the film.

The implications of this type of meandering on current transport across the boundary are not known, but it is clear that if the specific grain boundary plane plays a role in current transport, this type of meandering could lead to significant local differences in transport properties along the boundary. As a result of the meandering, the grain boundary plane varies from point to point along the boundary. Figure 4 shows a higher magnification image of the grain boundary in the film grown by POMBE. In this image, the apparent width of the boundary varies due to the varying degree of overlap between the two parts of the film as a result of a twist component to the boundary. It is interesting to note that the symmetric facets which conform to the underlying substrate exhibit only tilt character while the "meandering" asymmetric segments show varying degrees of twist character. While the specific role these facets play is not yet clear, recently Meilikov<sup>19</sup> used a dislocation model to suggest that asymmetric facets are more strongly coupled than symmetric facets.

In summary, meandering grain boundaries have been observed in YBCO films grown on  $\text{SrTiO}_3$  bi-crystal substrates. The nature of the substrate and crystallography suggest that this a general phenomenon, and AFM studies indicate a correlation between island-like growth and the magnitude of the meandering in these films. The meandering results in a change of the grain boundary plane, and facets with some twist component were observed in asymmetric, "meandering" segments of the boundary. Changing the growth condi-



FIG. 4. A higher magnification image of the YBCO grain boundary in a film prepared by POMBE imaged with the beam direction a few degrees from [001] for both halves of the film.

tions allowed the magnitude of the meandering to be reduced. The implications of this meandering behavior are significant, suggesting potential variations in electrical behavior from point to point along these boundaries.

Valuable contributions of Jennifer Helfrich (NU), Ken Gray (ANL), and Boris Vuchic (ANL) are gratefully acknowledged. This work was partially supported by the NSF Office of Science and Technology Centers (No. DMR 91-20000; T.A.R., D.B.B.) and the U.S. DOE, Basic Energy Sciences—Materials Sciences, Energy Efficiency and Renewable Energy—Advanced Utility Concepts—Superconducting Technology Program (No. W-31-109-ENG-38; D.J.M.).

- <sup>1</sup>D. Dimos, P. Chaudhari, J. Mannhart, and F. K. LeGoues, Phys. Rev. Lett. **61**, 219 (1988).
- <sup>2</sup>D. Dimos, P. Chaudhari, and J. Mannhart, Phys. Rev. B **41**, 4038 (1990).
- <sup>3</sup>Z. G. Ivanov, P. A. Nilsson, D. Winkler, J. A. Alarco, T. Claeson, E. A. Stepanov, and A. Ya. Tzalenchuk, Appl. Phys. Lett. **59**, 3030 (1991).
- <sup>4</sup>M. Kawasaki, E. Sarnelli, P. Chaudhari, A. Gupta, A. Kussmaul, J. Lacey, and W. Lee, Appl. Phys. Lett. **62**, 417 (1993).
- <sup>5</sup>A. H. Cardona, H. Suzuki, T. Tamashita, K. H. Young, and L. C. Bourne, Appl. Phys. Lett. **62**, 411 (1993).
- <sup>6</sup>N. D. Browning, M. F. Chisholm, S. J. Pennycook, D. P. Norton, and D. H. Lowndes, Physica C **212**, 185 (1993).
- <sup>7</sup>L. A. Tietz and C. B. Carter, Physica C **182**, 241 (1991).
- <sup>8</sup>Y. Zhu, H. Zhang, H. Wang, and M. Suenaga, J. Mater. Res. **6**, 2507 (1991).
- <sup>9</sup>J. Y. Laval and W. Swiatnicki, Physica C **221**, 11 (1994).
- <sup>10</sup>S. McKernan, M. G. Norton, and C. B. Carter, J. Mater. Res. **7**, 1052 (1992).
- <sup>11</sup>D. M. Hwang, T. S. Ravi, R. Ramesh, S. W. Cahn, C. Y. Chen, L. Nazar, X. D. Wu, A. Inam, and T. Venkatesan, Appl. Phys. Lett. **57**, 1690 (1990).
- <sup>12</sup>J. A. Alarco, E. Olsson, Z. G. Ivanov, P. A. Nilsson, D. Winkler, E. A. Stepanov, and A. Ya. Tzalenchuk, Ultramicroscopy **51**, 239 (1993).
- <sup>13</sup>J. P. Zheng, S. Y. Dong, and H. S. Kwok, Appl. Phys. Lett. **58**, 540 (1991).
- <sup>14</sup>Q. Li, O. Meyer, X. X. Xi, J. Geerk, and G. Linker, Appl. Phys. Lett. **55**, 1792 (1989).
- <sup>15</sup>M. G. Norton, L. A. Tietz, S. R. Summerfelt, and C. B. Carter, Appl. Phys. Lett. **55**, 2348 (1989).
- <sup>16</sup>C. C. Chang, X. D. Wu, R. Ramesh, X. X. Xi, T. S. Ravi, T. Venkatesan, D. M. Hwang, R. E. Muenchhausen, S. Folty, and N. S. Nogar, Appl. Phys. Lett. **57**, 1814 (1990).
- <sup>17</sup>M. Hawley, I. D. Raistrick, J. G. Beery, and R. J. Houlton, Science **251**, 1589 (1991).
- <sup>18</sup>R. Scholz and C. L. Bauer, Scr. Metall. **18**, 411 (1984).
- <sup>19</sup>E. Z. Meilikov, Physica C **226**, 69 (1994).

# Barium Potassium Bismuth Oxide: A Review

B. A. Baumert<sup>1</sup>

Received 22 May 1994

$\text{Ba}_{1-x}\text{K}_x\text{BiO}_3$  (BKBO) has a  $T_c$  (onset) of 34 K. It is the highest-temperature oxide superconductor which is cubic, with a coherence length of 30–60 Å. The basic properties of this compound are reviewed.

**KEY WORDS:** BKBO; oxide; superconductor; cubic.

## 1. INTRODUCTION

BKBO is the highest-temperature oxide superconductor which is cubic for  $0.375 < x < 0.5$  [1]. Its  $T_c$  allows Josephson junctions made from it to be operated with reliable, closed-cycle helium refrigeration; this type of cooling conserves liquid helium. In addition, BKBO has a relatively long coherence length compared to those of the higher- $T_c$  superconductors. For these reasons, it is an interesting material for study.

During the 1960s and 1970s, in the search for new superconducting compounds with higher transition temperatures, studies of oxide compounds became very important. The  $\text{BaBi}_{1-x}\text{Pb}_x\text{O}_3$  system, with a  $T_c$  of ~13 K, is the most notable of the early discoveries. Studies of this compound by Arthur Sleight and coworkers showed that superconductivity existed in the Pb-rich composition range  $0.05 \leq x \leq 0.3$  in  $\text{BaPb}_{1-x}\text{Bi}_x\text{O}_3$  (BPBO) [2]. The maximum  $T_c$  was obtained near  $x = 0.25$ . A metal-semiconductor transition was observed near  $x = 0.35$ .

Electronic-structure calculations [3] explain the semiconducting behavior of  $\text{BaBiO}_3$  and how Pb doping increases conductivity. Further calculations [4] indicated that this semiconductor-like gap could be suppressed as well by doping substitutionally on the Ba rather than Bi sites. Studies were done with a combination of K and Pb doping [5] but only resulted in

$T_c$ 's of ~12 K. Some very important observations were made as a result of the experiments, however. The authors pointed out the following, for example, for BPBO and other superconductors with alkaline or alkaline earth constituents:

- (1) Superconductivity occurs only over a limited range of  $x$  (as in  $\text{BaPb}_{1-x}\text{Bi}_x\text{O}_3$ ), between a conducting and semiconducting phase.
- (2)  $T_c$  increases rapidly as  $x$  approaches the semiconducting phase boundary and disappears abruptly beyond the phase boundary.
- (3) All of the compounds have atoms occupying octahedral sites with six oxygen nearest neighbors.

These observations established principles which were considered in further exploration of possible superconducting compounds and indeed were found to be true for BKBO as well.

Emphasis was then placed on substituting alkali metals for Ba. Superconductivity was subsequently observed with transitions of ~15 K for  $\text{Ba}_{0.9}\text{Rb}_{0.1}\text{BiO}_3$  and ~20 K for  $\text{Ba}_{0.9}\text{K}_{0.1}\text{BiO}_3$  [6]. Yet higher  $T_c$ 's in these compounds were predicted [7] and observed in 1988 in BKBO [8].

## 2. DISCUSSION OF BKBO PROPERTIES

### 2.1. Structure

BKBO has the perovskite structure, upon which the higher- $T_c$  oxides are based. Common among BKBO and the other high-temperature superconductors is an extreme sensitivity of the materials to

<sup>1</sup>Department of Materials Science and Engineering, Carnegie Mellon University, Pittsburgh, Pennsylvania 15213; currently at Motorola Semiconductor Products Sector, 2200 West Broadway Road, Mail Drop M350, Mesa, Arizona 85202.

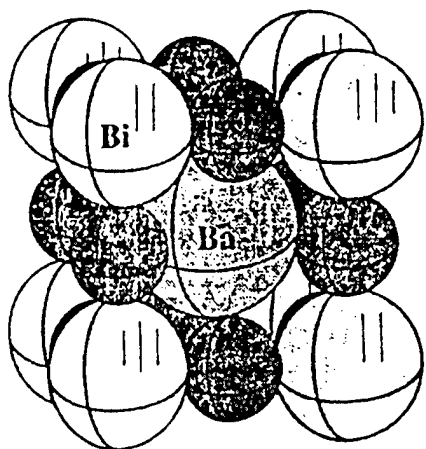


Fig. 1. Structure of  $\text{Ba}_{0.6}\text{K}_{0.4}\text{BiO}_3$ . This compound has the perovskite structure and is cubic for  $0.375 < x < 0.5$ , with a space group of  $Pm\bar{3}m$ .

oxygen stoichiometry [9,10]. The superconducting phase, however, is cubic, thus making BKBO similar to the isotropic lower- $T_c$  superconductors such as the Nb compounds. Its parent structure is  $\text{BaBiO}_3$ , and the superconductor contains potassium which occupies the barium sites in the structure shown in Fig. 1. Superconductivity occurs only in the cubic perovskite phase (with a space group of  $Pm\bar{3}m$ ) which exists for  $0.37 < x < 0.5$  in  $\text{Ba}_{1-x}\text{K}_x\text{BiO}_3$  [1]. A structural "phase" diagram of crystal structures present as a function of temperature and  $K$  content is shown in Fig. 2. Each phase is a derivative structure, so the transitions represent higher-order ones. The diagram shows that too little potassium results in an orthorhombic  $Ib\bar{m}m$  phase, whereas too much causes a second phase,  $\text{KBiO}_2$ , to precipitate [11,12]. Figure 3 shows how the monoclinic  $\text{BaBiO}_3$ , with tilted  $\text{BiO}_6$  octahedra becomes cubic for  $\text{Ba}_{0.6}\text{K}_{0.4}\text{BiO}_3$  [13].

This compound has not been widely studied and there is little information available on its basic properties. There was no JCPDS card and it was therefore

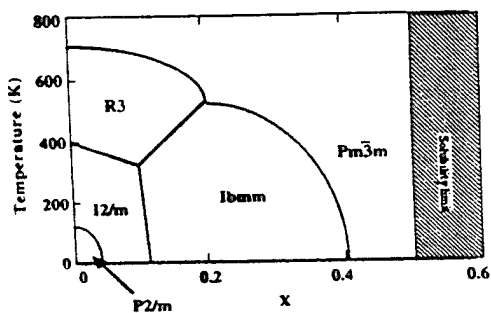


Fig. 2. Structural phase diagram of BKBO as a function potassium content  $x$ .

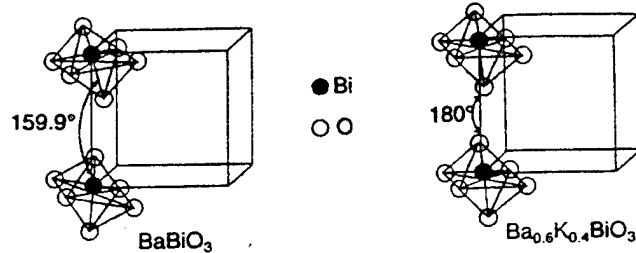


Fig. 3. Schematic showing  $\text{BiO}_6$  octahedra tilting in the monoclinic  $\text{BaBiO}_3$  and alignment in the cubic  $\text{Ba}_{0.6}\text{K}_{0.4}\text{BiO}_3$ .

necessary to generate the structure factor calculations. The relative intensities of peaks in a powder pattern for BKBO are listed in Table I, using a lattice parameter of  $4.283 \text{ \AA}$  for  $\text{Ba}_{0.6}\text{K}_{0.4}\text{BiO}_3$  at 295 K [1]. This pseudocubic lattice parameter scales linearly with potassium content [1], as shown in Fig. 4. From this diagram, one can see that in the range of  $x = 0.37$  to  $x = 0.5$ , the lattice parameter varies from  $4.289 \text{ \AA}$  to  $4.270 \text{ \AA}$ , respectively. It is helpful to use the lattice parameter determined from x-ray diffraction data to predict the potassium content as an indication of whether a BKBO thin film may be superconducting. This prediction is not necessarily straightforward, however, because lattice parameter changes with oxygen content as well [14,15]. If one considers the stoichiometry  $\text{Ba}_{1-x}\text{K}_x\text{BiO}_{3-\delta}$ , it has been found [14] that the lattice parameter of  $\text{Ba}_{0.6}\text{K}_{0.4}\text{BiO}_{3-\delta}$  changed by  $0.0276 \text{ \AA}$ , a  $0.64\%$  expansion, upon changing  $\delta$  from  $0.121$  to  $0.464$ , which is an  $11.9\%$  reduction in oxygen content. The change in lattice parameter may not seem significant, but the difference between the lattice parameters at limiting stoichiometries of the  $Pm\bar{3}m$  phase, which are  $4.270$  and  $4.289 \text{ \AA}$ , is only

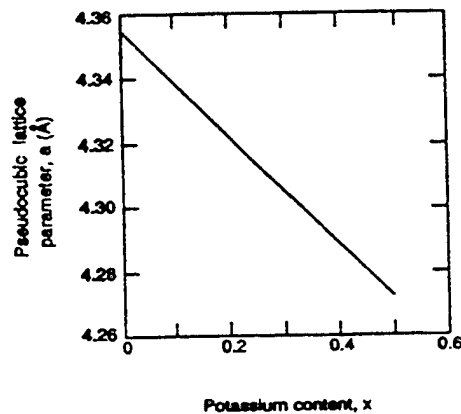


Fig. 4. Pseudocubic lattice parameter of BKBO as a function of potassium content, following the form  $a = 4.3548 - 0.1743x$ .

**Table I.** Positions of Reflections and Intensities Calculated for BKBO<sup>a</sup>

<i>hkl</i>	<i>h<sup>2</sup> + k<sup>2</sup> + l<sup>2</sup></i>	2θ	<i>d</i>	( <i>I</i> / <i>I</i> <sub>0</sub> ) × 100
100	1	20.74	4.283	10
110	2	29.50	3.028	100
111	3	36.33	2.473	0.9
200	4	42.20	2.141	14
201	5	47.47	1.915	5
211	6	52.33	1.748	21
220	8	61.22	1.514	9
300	9	65.37	1.428	2.6
221	9	65.37	1.428	2.6
310	10	69.40	1.354	9
311	11	73.32	1.291	6
222	12	77.16	1.236	3

<sup>a</sup>Note that  $h^2 + k^2 + l^2$  is the same for 300 and 221, so these reflections are both at 65.37° 2θ. For this reason, the intensities for 300 and 221 were added together, then the relative intensity was calculated from the sum.

0.44%. This means that a slight deficiency in oxygen content could cause films to be nonsuperconducting. This stresses the importance of a post-anneal in O<sub>2</sub>. It is felt that it is better to add the excess oxygen later rather than during deposition, so that enough potassium is incorporated. This is in order to maintain charge balance; if the average Bi charge is not to exceed +4, the K can only enter the compound if there are oxygen vacancies present [16].

It is important in film growth that films and substrates have similar lattice parameters and also structures. It has been found [17] that BKBO grows well consistently on SrTiO<sub>3</sub>, despite the 9% mismatch in lattice parameters between these materials. By contrast, BKBO films grew poorly on MgO despite an only 1.7% mismatch. This is probably due to the fact that BKBO and SrTiO<sub>3</sub> both have the perovskite

structure (*Pm*3*m*), while MgO has the NaCl structure (*Fm*3*m*). Table II is a summary of lattice parameters of BKBO and typical substrate materials.

## 2.2. Pairing Mechanism

Tunneling measurements by tunneling spectroscopy [24], in SIN junctions [25-28], and SIS point-contact junctions [29,30] have demonstrated a superconducting energy gap with a low density of electronic states below the gap energy. The observation of the gap has led to the calculation of  $2\Delta/kT_c$ , which has yielded values of 3.7-4.0 [24,25,27,31-33]. These values are indicative of moderate-to-strong coupling. It is believed by many that the pairing reflects electron-phonon coupling, which has been substantiated by the results of a number of different measurements. Electron-phonon coupling is indicated by the relatively high values of the exponent  $\alpha$  obtained in measurements of the oxygen isotope effect [34-37]. Tunneling spectroscopy results [31] link optical phonons to superconducting electrons, as does Raman spectroscopy [38], and the softening of oxygen phonon modes associated with the doping of BaBiO<sub>3</sub> by potassium (and the consequent change in charge) [39] also points to this conclusion. Similarly, the gap measured by infrared reflectivity [40] is consistent with moderate coupling in BCS theory, and the oxygen atom vibrations observed by x-ray diffraction techniques indicate strong electron-phonon coupling [13-41]. The change seen in the isotropic thermal parameter at the superconducting transition [42] as well as specific heat measurements [43-45] show this, as does the observation of a structural transformation at the same composition as an electronic one to a

**Table II.** Properties of Typical Substrate Materials Compared to Those of BKBO

Substrate	Crystal system or space group [18]	Pseudocubic lattice [18] parameter (Å)	Percent lattice mismatch to BKBO	Coefficient of thermal expansion ( $\times 10^{-6}/\text{K}$ )	Dielectric Constant at RT [23]
LaAlO <sub>3</sub>	<i>R3m</i> → cubic (at 400°C)	$d_{100}(c) = d_{012}(h) = 3.792$	11.5	31.8 [19]	16.23
MgO	<i>Fm</i> 3 <i>m</i>	4.212	1.7	10.5 [20]	8-10
NdGaO <sub>3</sub>	Orthorhomb.	$d_{110}(0) = d_{100}(c) = 3.855$	10	9.96 [21]	24
Al <sub>2</sub> O <sub>3</sub>	Hexagonal	$a = b = 4.758$ $c = 12.991$	11.1	5.4 [20]	8.5-11.5
SrTiO <sub>3</sub>	<i>Pm</i> 3 <i>m</i>	3.905	8.8	11 [20]	200-300
BKBO	<i>Pm</i> 3 <i>m</i>	4.283 [1]		10 [22]	

superconducting phase [1]. Calculated electron-phonon coupling strengths are in agreement with experimental observations [46-50].

### 2.3. Electronic Structure

It is surprising that BKBO has such a high  $T_c$  compared to other BCS-like superconductors because of its low density of states at the Fermi energy [51]. According to BCS theory, the transition temperature is exponentially proportional to the number of states at the Fermi level. The band structure of BKBO is shown in Fig. 5. It can be seen from this band diagram that the Fermi level cuts through the uppermost band of a ten-band Bi(6s)-O(2p) complex. The uppermost band is parabolic and therefore free-electron-like; such symmetry around the  $\Gamma$ , or center, point of the Brillouin zone indicates an *s*-like character. The flat, low-lying bands correspond to Ba 5p states, while the unoccupied bands at the top are those of Ba 5d and Bi 6p states [7].

A more simplified version of the diagram for  $\text{Bi}_2\text{O}_3$  is shown in Fig. 6. In this diagram, it can be seen that the O 2p band can be considered the valence band and the Bi 6p band, the conduction band,

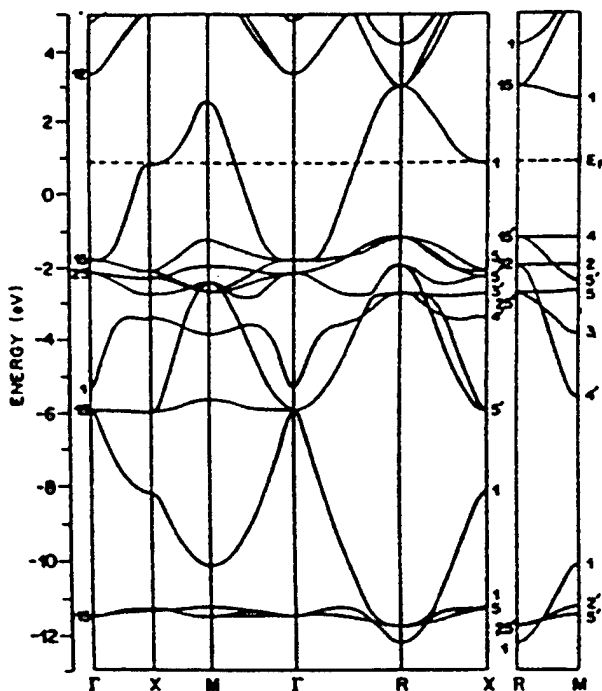


Fig. 5. Energy-band diagram for BKBO as a function of direction in the Brillouin zone. From L. F. Mattheiss and D. R. Hamann, PR1 60, reprinted with permission.

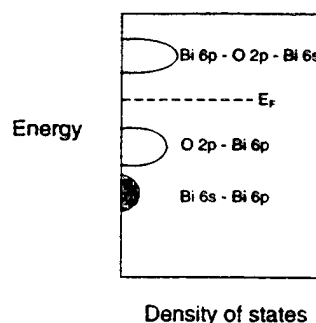


Fig. 6. Density of states for  $\text{Bi}_2\text{O}_3$ .

although it should be noted that these bands all contain hybrid orbitals. The positions in energy of these bands with respect to each other is dependent on the Bi-O distance. As this distance decreases, the metal levels increase in energy relative to the oxygen levels. Thus, when electrons are removed, as in  $\text{KBiO}_3$ , the Bi-O distance decreases and the Bi 6s band lies just above the O 2p band and the Fermi level. In  $\text{BaBiO}_3$ , however, only half of the Bi 6s band is above the Fermi level [52]. This is due to the disproportionation in  $\text{BaBiO}_3$ . A simple charge balance will show that the effective charge of Bi must be +4. The electronic configuration of this element, however, is  $\text{Xe}4f^{14}5d^{10}6s^26p^3$ . A valence of +4 for Bi would lead to a very undesirable  $6s^1$  state. It is therefore energetically favorable for charge neutrality to be maintained by Bi assuming the charges of +3 and +5, so this compound can actually be written  $\text{Ba}\{0.5\text{Bi}^{+3}0.5\text{Bi}^{+5}\}\text{O}_3$ . The band structure for this compound has the Bi 6s band at the Fermi level, and this band has split due to the two different Bi-O distances. The  $\text{Bi}^{+3}$ -O distance in  $\text{BaBiO}_3$  is  $2.31 \text{ \AA}$ , while the  $\text{Bi}^{+5}$ -O distance is  $2.12 \text{ \AA}$  [53]. The  $\text{Bi}^{+3}$  half of the Bi 6s band is below the Fermi level, whereas the  $\text{Bi}^{+5}$  half is above.  $\text{BaBiO}_3$  therefore exhibits a gap; conduction will occur if the reaction  $\text{Bi}^{+3} + \text{Bi}^{+5} \rightarrow \text{Bi}^{+4}$  takes place [52]. Doping is necessary for the effective charge to change. When potassium is added, the compound is depleted of electrons because  $\text{K}^{+1}$  ions occupy  $\text{Ba}^{+2}$  sites. At the composition  $\text{Ba}_{0.6}\text{K}_{0.4}\text{BiO}_3$ , for example, the effective charge on Bi is 4.4, so with increasing K concentration, the Bi valence approaches +5. This closes the energy band gap and increases conduction.

The oxidation of  $\text{Bi}^{+3}$  to  $\text{Bi}^{+5}$  upon addition of K has been demonstrated experimentally [54]. This result would lead one to believe that the electrons freed as a result of this oxidation would then be available for conduction. Hall Effect measurements have

determination BKBO to indeed be *n*-type [36,55-58], which indicates that electrons rather than holes are responsible for conduction.

#### 2.4. Transition Temperature

The highest onset transition temperature obtained for bulk BKBO is 34 K [59]. This allows devices made with BKBO, which would be operated at  $\sim 15$  K, to be cooled by convenient closed-cycle helium refrigeration, in which He gas is recondensed rather than requiring an endless supply of expensive liquid helium.

It has been found [58,60,61] that  $T_c$  increases with increasing pressure up to 15. kbar, but this trend only occurs up to a point, and then there is a downward slope as the  $T_c$  of the material at zero pressure increases [62].

The highest- $T_c$  thin films thus far have been deposited by off-axis rf magnetron sputtering with zero-resistance transition temperatures of 29.2 K [63]. Laser ablation has been used in growing 28 K  $T_c$  films [27] and 27.5 K  $T_c$  films [64]. The maximum  $T_c$  will be obtained at a potassium composition of  $x=0.37$  [1] and  $T_c$  then decreases with increasing  $x$ , as shown in Fig. 7. The transition temperature is affected by oxygen content as well [65].

#### 2.5. Resistivity

The resistivity of a polycrystalline BKBO sample fabricated by the powder-in-a-tube method with an onset  $T_c$  of 32 K was  $\sim 16,000 \mu\Omega\cdot\text{cm}$  just above the transition [66]. This sample had a very broad (10 K) transition, however, and may therefore have been rather inhomogeneous. Another melt-processed,

highly dense sample had a normal-state resistivity of  $12,000 \mu\Omega\cdot\text{cm}$  [67]. Yet another sample was estimated, from thermal-conductivity data and the application of the Wiedemann-Franz law, to be  $120 \mu\Omega\cdot\text{cm}$  [44]. The Wiedemann-Franz law states that for metals, the ratio of the thermal conductivity to electrical conductivity is directly proportional to the temperature [68], i.e.,  $K/\sigma = \pi^2/3(k/e)^2T$ .

Metallic behavior is not always observed in BKBO superconducting thin films. There is often a rise in resistivity with decreasing temperature in the normal state, indicating semiconductor-like behavior. It is felt by some [44,55] that each BKBO sample is a mixture of both of these, which is modeled by a metal and semiconductor in series. The rise in resistivity with lowering of temperature seen in BKBO films is indicative of variable-range hopping conduction [44,69-72] and follows a  $T^{-1.4}$  dependence.

It has been demonstrated [73] that in the  $\text{La}_{2-x}\text{Sr}_x\text{CuO}_2$  system, conductivity increases with increasing Sr doping up to  $x=0.34$ . The transition temperature, however, initially rises but then from Sr concentrations of  $x=0.15$  to 0.25,  $T_c$  decreases until superconductivity disappears. An analogous situation would be expected in BKBO. Conductivity increases with increasing K concentration [6], but  $T_c$  decreases as well [1], implying that a film with a higher  $T_c$  would have a higher resistivity. There have been no reports of a systematic study of this. The highest critical current densities reported for BKBO films are  $>3 \times 10^6 \text{ A/cm}^2$  at 4 K [74].

#### 2.6. Magnetic Properties

BKBO is obviously unlike the cuprates because it does not have two-dimensional Cu-O planes (or chains) which are believed to play a significant role in superconductivity of higher- $T_c$  compounds. In addition, there are no local moments on any of the ions involved (BKBO is diamagnetic in the normal state as well as in the superconducting state) [75].

A value of  $H_{c1}=419 \pm 24$  Oe has been obtained for the lower critical field of BKBO [76], while values ranging from  $96 \pm 2$  kOe at 0 K [76] to 300 kOe at 2 K [77] have been obtained for the upper critical field,  $H_{c2}$ .

BKBO has a hexagonal flux lattice symmetry [78] and a penetration depth,  $\lambda_0$ , of  $3300$ – $3400 \text{ \AA}$  [32,79]. The value of the penetration depth will increase with increasing temperature for  $T < T_c/2$  [33] according to

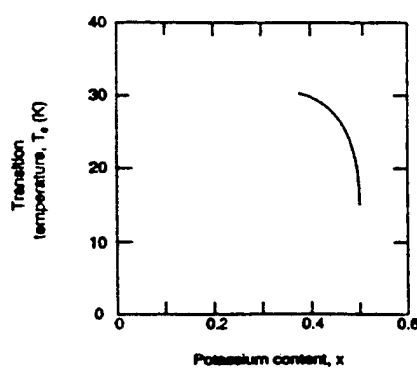


Fig. 7. Transition temperature of BKBO as a function of potassium content  $x$ .

the following relation:

$$\frac{\lambda(T)}{\lambda(0)} = 1 + \sqrt{\frac{\pi\Delta(0)}{2kT}} \exp\left(\frac{-\Delta(0)}{kT}\right) \quad (1)$$

where  $\lambda$  = penetration depth, and  $\Delta$  = gap size. At higher temperatures, the relation will be of the form [80]:

$$\lambda(T) = \frac{\lambda_0}{\sqrt{1 - (T/T_c)^4}} \quad (2)$$

The advantage of cubic superconductors is that they are isotropic with respect to the coherence length. This length tends to be longer than those of the anisotropic higher- $T_c$  superconductors. BKBO has a coherence length of 30-60 Å [45,74,76,77,81-86]. This value needs to be carefully considered when fabricating tunnel junctions. High-quality superconductor/insulator interfaces are necessary so that the superconductor coherence length is not exceeded by the defect region length and so that the superconducting electron pair wavefunction does not decay before the barrier is reached, or the probability of pair tunneling will be too small and the critical current will be diminished.

### 3. CONCLUSION

The most exasperating challenges in working with this material are the difficulty in reproducibly depositing high-quality films due to target degradation and the volatility of the potassium as well as the instability of the films themselves. This is particularly true of poor-quality films, which change color and become highly resistive over time. High-quality superconducting films retain the blue shine seen in reflection and their  $T_c$ 's. All films, however, react with the atmosphere to form an insulating layer on the surface. Observation of BKBO films with XPS have shown the introduction of a carbon peak in the spectrum after exposure of the film surface to air, indicating that the native insulating layer formed on the BKBO was mostly one of carbonates [87]. No chlorine, which was found in the surface layer of  $\text{Ba}_{1-x}\text{Rb}_x\text{BiO}_3$  films [88], was present.

Despite the difficulty in working with this material, a great deal of significant progress has already been made. BKBO junctions have been fabricated with YBCO base electrodes and a natural [89] or artificial [90] insulating barrier. BKBO SIS trilayer junctions have been produced using  $\text{BaBi}_2\text{O}_y$  [91],  $\text{KNbO}_3$  [92],  $\text{SrTiO}_3$  [17], and  $\text{MgO}$  [93] barriers.

Bicrystal junctions which introduce a grain boundary between the electrodes have been studied [94], and an  $\text{Au}/\text{BKBO}/\text{SrTiO}_3(\text{Nb})$  superconducting-base transistor has been fabricated [95]. Most of these junctions, however, are highly resistive with little or no supercurrent and exhibit leakage. The challenge with all of these materials is to fabricate junctions reproducibly.

### ACKNOWLEDGMENTS

The author is grateful to M.E. McHenry and J. Talvacchio for their advice. This work was supported by the Air Force Office of Scientific Research under contract number F49620-92-J-0415.

### REFERENCES

1. S. Pei *et al.*, *Phys. Rev. B* **41**, 4126-4141 (1990).
2. A. W. Sleight, J. L. Gillson, and P. E. Bierstedt, *Solid State Commun.* **17**, 27-28 (1975).
3. L. F. Mattheiss and D. R. Hamann, *Phys. Rev. B* **28**, 4227-4241 (1983).
4. W. Weber, *Jpn. J. Appl. Phys.* **26**, Suppl. 3, 981 (1987).
5. C. W. Chu, S. Huang, and A. W. Sleight, *Solid State Commun.* **18**, 977-979 (1976).
6. L. F. Mattheiss, E. M. Gyorgy, and D. W. Johnson, Jr., *Phys. Rev. B* **37**, 3745-3746 (1988).
7. L. F. Mattheiss and D. R. Hamann, *Phys. Rev. Lett.* **60**, 2681-2684 (1988).
8. R. J. Cava *et al.*, *Nature (London)* **332**, 814-816 (1988).
9. D. Tseng and E. Ruckenstein, *J. Mater. Res.* **5**, 742-745 (1990).
10. D. G. Hinks *et al.*, *Physica C* **156**, 477-480 (1988).
11. S. Pei *et al.*, *J. Solid State Chem.* **95**, 29-38 (1991).
12. M. T. Weller *et al.*, *Physica C* **156**, 265-268 (1988).
13. L. F. Schneemeyer *et al.*, *Nature (London)* **335**, 421-423 (1988).
14. K. Ueki *et al.*, in *Advances in Superconductivity II*, T. Ishiguro and K. Kagimura, eds. (Springer, Tokyo, 1990), pp. 489-492.
15. Y. Idemoto, Y. Iwata, and K. Fueki, *Physica C* **201**, 43-49 (1992).
16. D. G. Hinks *et al.*, *Nature (London)* **333**, 836-838 (1988).
17. B. A. Baumert, J. Talvacchio, and M. G. Forrester, *Appl. Phys. Lett.* **62**, 2137-2139 (1993).
18. JCPDS Card File Data
19. R. W. Simon *et al.*, in *Science and Technology of Thin-Film Superconductors*, R. McConnell and S. A. Wolf, eds. (Plenum Press, New York, 1989), p. 339.
20. *Thermophysical Properties of Matter* (Purdue Research Foundation, New York, 1977).
21. M. Sasaura, S. Miyazawa, and M. Mukaida, *J. Appl. Phys.* **68**, 3643-3644 (1990).
22. R. M. Fleming *et al.*, *Phys. Rev. B* **38**, 7026-7028 (1988).
23. J. Talvacchio and G. R. Wagner, in *Superconductivity Applications for Infrared and Microwave Devices*, K. B. Bhasin and V. O. Heinen, eds., Vol. 1292 (SPIE, Bellingham, Washington, 1990), p. 2.
24. Q. Huang *et al.*, *Nature (London)* **347**, 369-372 (1990).
25. H. Sato, H. Takagi, and S. Uchida, *Physica C* **169**, 391-395 (1990).
26. H. Suzuki *et al.*, International Symposium on Superconductivity, Japan, 1991.
27. B. M. Moon *et al.*, *Appl. Phys. Lett.* **59**, 1905-1907 (1991).
28. C. J. Hou *et al.*, *Appl. Phys. Lett.* **60**, 1262-1264 (1992).

29. A. N. Pargellis *et al.*, *Appl. Phys. Lett.* **58**, 95-96 (1991).

30. F. Sharifi *et al.*, *Phys. Rev. B* **44**, 12521-12524 (1991).

31. J. F. Zasadzinski *et al.*, *Physica C* **158**, 519-524 (1989).

32. Y. Liu, J. F. Whitaker, and C. E. Platt, submitted to the Ultrafast Electronics and Optoelectronics Conference, San Francisco, California January 25-27, 1993.

33. M. S. Pambianchi *et al.*, *Appl. Phys. Lett.* **64**, 244-246 (1994).

34. D. G. Hinks *et al.*, in *High-Temperature Superconductors: Relationships between Properties, Structure, and Solid-State Chemistry*, J. R. Jorgensen, K. Kitazawa, J. M. Tarascon, M. S. Thompson, and J. B. Torrance, eds. (Materials Research Society, Pittsburgh, 1989), pp. 357-367.

35. D. G. Hinks *et al.*, *Nature (London)* **335**, 419-421 (1988).

36. S. Kondoh, *et al.*, *Physica C* **157**, 469-477 (1989).

37. C. K. Loong *et al.*, *Phys. Rev. Lett.* **66**, 3217-3220 (1991).

38. K. F. McCarty *et al.*, *Phys. Rev. B* **40**, 2662-2665 (1989).

39. C. K. Loong *et al.*, *Phys. Rev. Lett.* **62**, 2628-2631 (1989).

40. Z. Schlesinger *et al.*, *Phys. Rev. B* **40**, 6862-6866 (1989).

41. J. P. Wignacourt *et al.*, *Appl. Phys. Lett.* **53**, 1753-1755 (1988).

42. Y. Ono, K. Yamauchi, and N. Yamada, *Jpn. J. Appl. Phys.* **30**, L182-L184 (1991).

43. K. C. Ott *et al.*, in *High-Temperature Superconductors: Relationships between Properties, Structure, and Solid-State Chemistry*, J. R. Jorgensen, K. Kitazawa, J. M. Tarascon, M. S. Thompson, and J. B. Torrance, eds. (Materials Research Society, Pittsburgh, 1989), pp. 369-376.

44. S. D. Peacor *et al.*, *Phys. Rev. B* **42**, 2684-2687 (1990).

45. J. E. Graebner, L. F. Schneemeyer, and J. K. Thomas, *Phys. Rev. B* **39**, 9682-9684 (1989).

46. M. Shirai, N. Suzuki, and K. Motizuki, *J. Phys. Condens. Matter* **2**, 3553-3566 (1990).

47. A. I. Liechtenstein *et al.*, *Phys. Rev. B* **44**, 5388-5391 (1991).

48. M. J. Rice and Y. R. Wang, *Physica C* **157**, 192-197 (1989).

49. N. Hamada, *et al.*, *Phys. Rev. B* **40**, 4442-4452 (1989).

50. H. C. Gupta, *Physica C* **158**, 153-154 (1989).

51. R. J. Cava and B. Batlogg, *MRS Bull.* **XIV**, 49-52 (1989).

52. A. W. Sleight, in *High-Temperature Superconductivity*, D. P. Tunstall and W. Barford, eds. (The Scottish Universities Summer School in Physics, Philadelphia, 1991), pp. 97-143.

53. D. E. Cox and A. W. Sleight, *Acta Crystallogr.* **B35**, 1-10 (1979).

54. R. C. Taylor, M. M. Plechaty, and D. B. Beach, *Mut. Res. Bull.* **26**, 1185-1192 (1991).

55. E. S. Hellman and E. H. Hartford, Jr., *Phys. Rev. B* **47**, 11,346-11,353 (1993).

56. H. Sato *et al.*, *Nature (London)* **338**, 241-243 (1989).

57. M. Affronte, J. Marcus, and C. Escribe-Filippini, *Solid State Commun.* **85**, 501-506 (1993).

58. H. Takahashi *et al.*, *Physica C* **210**, 485 (1993).

59. N. L. Jones *et al.*, *J. Solid State Chem.* **78**, 319-321 (1989).

60. H. Uwe *et al.*, *Physica C* **162-164**, 743-744 (1989).

61. J. E. Schirber, B. Morosin, and D. S. Ginley, *Physica C* **157**, 237-239 (1989).

62. M. L. Norton, in *Chemistry of Superconductor Materials*, T. A. Vanderah, ed. (Noyes Publications, Park Ridge, New Jersey, 1992), pp. 347-379.

63. R. Hu *et al.*, *IEEE Trans. Appl. Supercond.* **3**, 1556-1558 (1993).

64. R. C. Laco, J. P. Wendt, and P. M. Adams, *IEEE Trans. Appl. Supercond.* **3**, 1563-1566 (1993).

65. Y. Idemoto, Y. Iwata, and K. Fueki, *Physica C* **222**, 257-266 (1994).

66. S. Jin *et al.*, *Appl. Phys. Lett.* **53**, 1116-1118 (1988).

67. D. G. Hinks *et al.*, *Appl. Phys. Lett.* **54**, 1585-1587 (1989).

68. C. Kittel, *Introduction to Solid State Physics* (Wiley, New York, 1986).

69. N. F. Mott, *Conduction in Non-Crystalline Materials* (Clarendon Press, Oxford, 1987).

70. B. Dabrowski *et al.*, *Physica C* **156**, 24-26 (1988).

71. D. Tseng and E. Ruckenstein, *Materials Lett.* **8**, 69-71 (1989).

72. E. S. Hellman *et al.*, *Phys. Rev. B* **44**, 9719-9722 (1991).

73. J. B. Torrance *et al.*, *Physica C* **162-164**, 291-295 (1989).

74. R. A. Schweinfurth *et al.*, *Appl. Phys. Lett.* **61**, 480-482 (1992).

75. B. Batlogg, in *Mechanisms of High-Temperature Superconductivity*, H. Kamimura and A. Oshiyama, eds. (Springer-Verlag, Berlin, 1989), pp. 324-331.

76. G. T. Seidler *et al.*, *Physica C* **195**, 373-378 (1992).

77. C. Escribe-Filippini *et al.*, *Physica C* **210**, 133-137 (1993).

78. D. McK. Paul *et al.*, *Physica C* **185-189**, 1837-1838 (1991).

79. E. J. Ansaldi *et al.*, *Physica C* **185-189**, 1889-1890 (1991).

80. T. Van Duzer and C. W. Turner, *Principles of Superconductive Devices and Circuits*, (Elsevier North-Holland, Inc., New York, 1981).

81. B. Batlogg *et al.*, *Phys. Rev. Lett.* **61**, 1670-1673 (1988).

82. U. Welp *et al.*, *Physica C* **156**, 27-34 (1988).

83. W. K. Kwok *et al.*, *Phys. Rev. B* **40**, 9400-9403 (1989).

84. Y. Nagata, N. Suzuki, and T. Uchida, *Physica C* **195**, 195-198 (1992).

85. N. Savvides *et al.*, *Physica C* **171**, 181-186 (1990).

86. H. C. Yang *et al.*, *Phys. Rev. B* **42**, 2551-2553 (1990).

87. B. A. Baumert and J. Talvacchio, *IEEE Trans. Appl. Supercond.* **3**, 1567-1570 (1993).

88. M. A. Sobolewski *et al.*, *J. Vac. Sci. Technol. A* **9**, 2716-2720 (1991).

89. Y. Enomoto and K. Moriwaki, *Jpn. J. Appl. Phys.* **29**, L1455-L1457 (1990).

90. R. L. Fink *et al.*, *Appl. Phys. Lett.* **61**, 595-597 (1992).

91. E. S. Hellman *et al.*, *Physica C* **201**, 166-170 (1992).

92. R. L. Fink *et al.*, *IEEE Trans. Appl. Supercond.* **3**, 2199-2221 (1993).

93. J. Amano *et al.*, *J. Appl. Phys.* **74**, 4620-4626 (1993).

94. A. Kussmaul *et al.*, *Appl. Phys. Lett.* **63**, 2824-2826 (1993).

95. H. Suzuki *et al.*, *IEEE Trans. Appl. Supercond.* **3**, 2906-2909 (1993).

## Electrical-noise signatures of possible vortex transitions in epitaxial $\text{YBa}_2\text{Cu}_3\text{O}_7$ thin films

D.G. Steel <sup>a,\*</sup>, D.H. Kim <sup>a,1</sup>, K.E. Gray <sup>a</sup>, S.E. Pfanstiel <sup>a</sup>, J.H. Kang <sup>b</sup>,  
J. Talvacchio <sup>b</sup>

<sup>a</sup> *Science and Technology Center for Superconductivity and Materials Science Division, Argonne National Laboratory,  
Argonne, IL 60439, USA*

<sup>b</sup> *Westinghouse Science and Technology Center, Pittsburgh, PA 15235, USA*

Received 7 April 1995

### Abstract

Measurements of the electrical noise have been used to probe the vortex dynamics in epitaxial  $\text{YBa}_2\text{Cu}_3\text{O}_7$  thin films at magnetic fields up to 8 T, and they display two sharp features as a function of temperature. A sharp onset of noise occurring at  $T_{\text{on}} < T_{\text{c2}}(H)$  is a new feature. A separate noise peak shows striking correlation to hysteresis previously observed in single crystals and is interpreted as melting. The temperature of both features did not change over two decades in the applied current, indicating that they may be signatures of thermodynamic transitions within the vortex state.

The field of vortex dynamics in high-temperature superconductors (HTS's) has been of major interest since the discovery of these materials. Many experimental studies have been performed using a wide range of techniques to probe the behavior of the flux lines, including possible phase transitions. Voltage fluctuations (noise) in HTS near the superconducting transition temperature ( $T_c$ ) have been studied by several groups in single crystals and thin films. Almost all of these previous measurements of the noise were performed in applied magnetic fields less than about 100 Oe. For such fields, typically a single vortex limit is appropriate and the noise has been

found to display a  $1/f$  spectrum, sometimes with one or two peaks near  $T_c$ . In these studies, the structural properties of the samples are often found to be important factors [1]. Proposed explanations have included motion of flux vortices [2–8], as well as resistance fluctuations (possibly at grain boundaries) [9–10] and critical-current fluctuations [11].

In this paper, we describe noise power spectral density,  $S_v$ , measurements to probe the flux dynamics at high fields in high-quality, *c*-axis oriented, epitaxial  $\text{YBa}_2\text{Cu}_3\text{O}_7$  films, as a function of temperature, magnetic field applied parallel to the *c*-axis, and bias current in the *a*–*b* plane. The field range, 0.1–8 T, is significantly higher than in almost all previous studies. The data display a background Johnson noise which dominates above  $T_c$ , plus significant excess noise peaks which occur below  $T_c$  as a function of temperature and of current for different

\* Corresponding author.

<sup>1</sup> Permanent address: Department of Physics, Yeungnam University, Kyungsan 712-749, Korea.

fields. The enhanced noise emerges from a sharp onset from the background level on cooling. Analysis of our results strongly suggests that the noise originates from flux motion, which can provide a simple qualitative understanding [12]. At sufficiently low temperatures, most vortices are pinned and flux-motion noise will be small. It will also be small at higher temperatures when most of the vortices are thermally depinned, so they tend to move at a more uniform flow velocity. Between these two limiting temperatures, flux lines will be erratically pinned and unpinned during their motion, and measurements of the noise may explore details of these processes.

Films of  $\text{YBa}_2\text{Cu}_3\text{O}_7$  were grown in-situ by sputtering from a stoichiometric target onto  $\text{SrTiO}_3$  substrates. The films were  $\sim 150$  nm thick and shown by transmission electron microscopy (TEM) to be epitaxial and  $c$ -axis oriented. They exhibited a mid-point resistive transition at  $\approx 89.6$  K. Conventional photolithography and ion milling were used to form a 10  $\mu\text{m}$  wide line. Noise spectra were measured by a DC four-probe method and with greater sensitivity using an AC Wheatstone bridge technique [13]. In the DC technique, a current was fed into two sample leads through a large ballast resistor. The voltage across two separate leads was connected to a room-temperature transformer and a preamplifier, the output of which was connected to a spectrum analyzer to measure the noise. In the AC technique, the sample was in one arm of a balanced Wheatstone bridge and the “null” voltage across the bridge went directly to a lock-in amplifier. The lock-in output was connected to a spectrum analyzer to measure the fluctuations within the bridge circuit. The background noise in zero field in the fully superconducting state was  $\approx 2 \times 10^{-19} \text{ V}^2/\text{Hz}$  over the frequency range of 1–200 Hz.

Fig. 1 shows the noise spectral density  $S_v(T)$  taken at an applied field of 1 T at 11 Hz and 70 Hz, respectively, using the AC technique with an rms sample current of 10  $\mu\text{A}$ . The figure also shows a measurement at 51 Hz made on the same sample using the DC technique with a current of 10.5  $\mu\text{A}$ . Except for a small temperature shift, the data are almost indistinguishable within experimental scatter, and show a sharp onset from the high-temperature background level at a temperature  $T_{\text{on}}$  and a sharp peak at a temperature  $T_p$ . The measured two-terminal

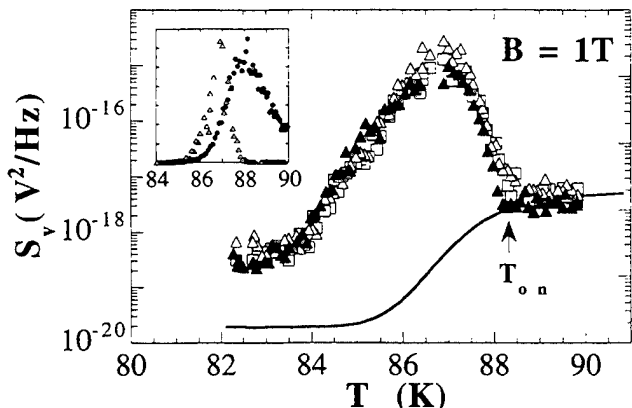


Fig. 1. Temperature dependence of  $S_v$  at a field of 1 T and a current of 10  $\mu\text{A}$ . The open triangles and squares show the noise at 11 and 70 Hz, respectively, using the AC technique, and the solid triangles show the noise at 51 Hz using the DC technique. The Johnson noise calculated from the measured two-terminal sample resistance is shown by the solid line. The inset shows the peak in  $S_v$  (open triangles) and  $\partial R / \partial T$  (circles) on a linear plot (scaled for comparison).

resistance at the same small current density of  $\sim 700 \text{ A cm}^{-2}$  used for measurements of  $S_v$ , was used to calculate the expected Johnson noise, which is shown in Fig. 1 as the solid line. The *two-terminal* resistance is the appropriate quantity to use for calculating the current-independent, i.e. Johnson, noise. The non-zero value of the resistance at low temperatures is due to the contacts, while the four-terminal resistance becomes vanishingly small. This closely resembles the  $S_v(T)$  data above  $T_c$ , although there is usually a small enhancement over Johnson noise, assumed due to the leads and contacts. At low temperatures,  $S_v(T)$  does not fall to the Johnson noise level, indicating that there are other contributions, e.g. non-perfect electrical contacts.

We first discuss and dismiss sources of excess noise in superconductors other than flux motion. Thermal fluctuations produce fluctuations in resistance  $R$  proportional to  $\partial R / \partial T$  and hence give voltage fluctuations with a current flowing [14]. We have measured  $R(T)$  at each magnetic field value and find that the peak in  $S_v(T)$  occurs at a lower temperature than the peak in  $\partial R / \partial T$  (see inset of Fig. 1) and that the separation of these peaks increases with field (from  $\sim 0.4$  K at 0.1 T to  $\sim 3$  K at 4 T). Thus we conclude that thermal fluctuations are not the source of the noise peaks for a finite field. We have also measured the resistance as a function of magnetic

field  $R(B)$  and find a similar separation between the peak in the noise and the peak in  $\partial R/\partial B$ , which rules out magnetic-field fluctuations as the primary noise source. Published noise measurements of  $\text{YBa}_2\text{Cu}_3\text{O}_7$  bicrystal grain-boundary junctions showed a sharp noise peak at low bias currents, which was fit to a model of critical current fluctuations [10]. Unlike those studies, we observe a linear  $I-V$ , from which we conclude that our noise peaks are not due to critical-current fluctuations across possible weak links in the films.

Fig. 2 shows  $S_v(T)$  at 71 Hz using the AC technique. The data display a sharp onset and a peak as a function of temperature for all fields. The value of  $S_v(T)$  at the peaks decreases with field, while the peak width in temperature increases. Despite the striking behavior of the noise, note that no evidence has been observed of any features in the resistance at either  $T_{\text{on}}$  or  $T_p$ . The peaks occur at temperatures where the four-terminal resistance is reduced to 4–10% of the normal-state value.

The frequency dependence of  $S_v$  is shown in Fig. 3 at a field of 4 T. The three temperatures for which data are shown correspond to well below the peak in the noise, at the peak, and well above  $T_c$ . A similar behavior was observed at magnetic fields of 0.1 T, 1 T, and 2 T. Above  $\sim 5$  Hz,  $S_v(f)$  exhibits a flat overall response at all temperatures, except for the sharp peaks due to extraneous pickup. All the measurements presented in this paper were made at

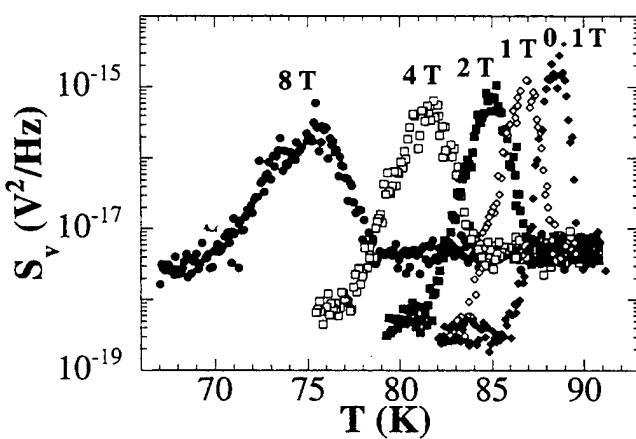


Fig. 2. Temperature dependence of  $S_v$ , measured using the AC technique with a current of 10  $\mu\text{A}$ . Data are shown for fields of 0.1, 1, 2, 4 and 8 T. Note the background value of  $S_v(T)$  at low temperatures increases with field, such that by a field of 8 T, it is almost at the level of the noise above  $T_c$ .

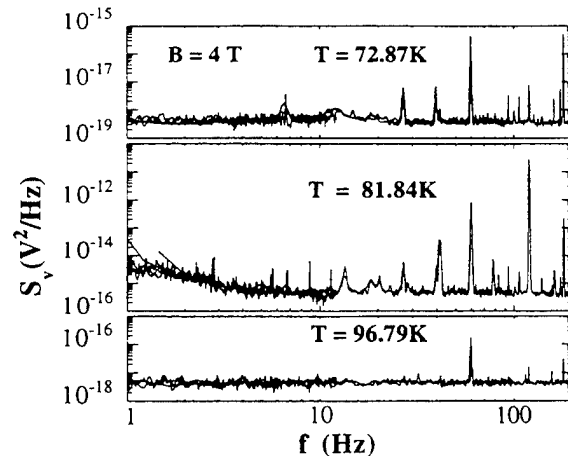


Fig. 3. Frequency dependence of  $S_v$  at a field of 4 T and three different temperatures: 72.87 K (well below the peak in  $S_v$ ), 81.84 K (at the peak), and 96.79 K (well above  $T_c$ ).

frequencies in this flat response region. At the temperature of the noise peak, a significant  $f^{-\alpha}$  response is seen ( $\alpha \sim 2$ ) below  $\sim 5$  Hz. This low-frequency behavior may not be an intrinsic effect and could be related to the less-than-perfect electrical contacts. Discussion of this will be deferred to a further paper [15]. We interpret the flat behavior as follows. In the normal state, it is due mainly to Johnson noise, and the magnitude agrees quite well with that expected from the measured sample resistance. Noise in the fully superconducting state shows an enhancement over Johnson noise, which is likely due to the contacts and electrical leads [16]. By contrast, the temperature-dependent noise in the flux-creep state is due to the hopping motion of vortices. Simple models of such noise calculate the power spectrum considering voltage pulses of height  $\Delta V$  and average rate  $\nu_p$  (rate of depinning). The details of the frequency spectrum [17] depend on the length of the pulses  $\tau_0$ , and not on the average time between pulses,  $1/\nu_p$ . Shot noise results from constant  $\tau_0$  while a Lorentzian spectrum corresponds to a Poisson distribution of  $\tau_0$ . In both cases, there is a flat frequency spectrum with a roll-off at higher frequencies, which is determined by the average pulse length  $\tau_0$ . We observe only a flat response, consistent with the low-frequency end of these spectra. The *upper limit* for the roll-off is the transit time  $\tau_1$  to cross the sample at the free flux-flow velocity ( $\tau_1 = wB/E$ , where  $w$  is the sample width,  $B$  is the magnetic field and  $E$  is the electric field). For the

parameters used in this paper, we estimate the minimum possible roll-off frequency to be 3 kHz, getting larger as  $T_c$  is approached. We have not observed the roll-off directly due to the minimum time constant of the lock-in amplifier in the AC technique and the frequency response of the transformer in the DC technique.

Fig. 4 shows the dependence of  $S_v$  on the current  $I$  at a field of 1 T measured close to the peak temperature. Although the lowest current density data are rounding off to a background level, for the region above this, it appears that  $S_v \propto I^2$ , which is expected for a linear response. At still higher current densities, the noise displays a peak at around  $I \sim 10^{-4}$  A above which  $S_v$  falls for increasing current densities. We also studied the variation of the temperatures of the onset and the peak with current density, and within experimental accuracy found them to be independent over the two orders of magnitude examined, shown in the inset of Fig. 4.

Fig. 5 shows the temperatures of the onset of the excess noise  $T_{on}$  (triangles) and the noise peaks  $T_p$  (circles) for different fields. The data for the onset temperature are well fit by a straight line, shown as the thin dashed line, which extrapolates to a zero-field temperature of 89.8 K. This is  $\approx 0.2$  K above the midpoint of the zero-field resistive transition, which may be a less representative value for  $T_c$ , given the width of the transition. The figure also shows the mean field upper critical field line  $B_{c2}(T)$ , plotted

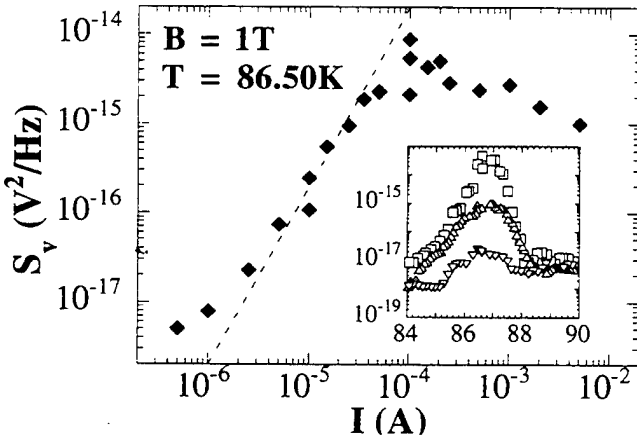


Fig. 4. Current dependence of  $S_v$  at a field of 1 T and a temperature of 86.50 K (close to the peak.) The data have not been corrected for the background level at the lowest current densities. The dashed line shows a slope of 2. The inset shows  $S_v$  as a function of temperature at 1 T using currents of 1, 10, and 100  $\mu$ A.

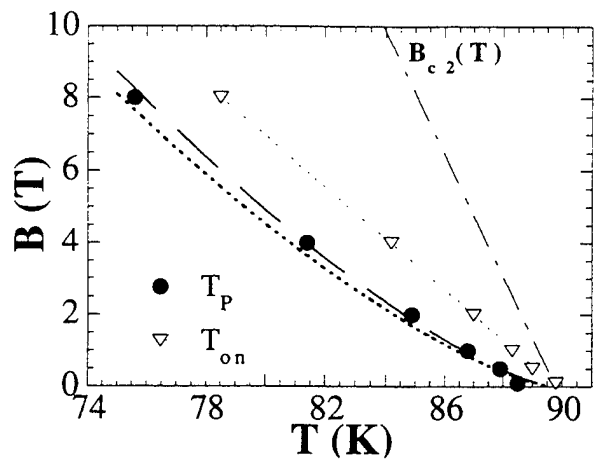


Fig. 5. "Phase" diagram for the vortex state, showing the peak temperatures  $T_p$  (circles) and onset temperatures  $T_{on}$  (Triangles) at different fields. The mean-field upper critical field line  $B_{c2}(T)$  is plotted using a field slope of 1.7 T/K [18]. The vortex-melting lines according to Kwok et al. [19] (dotted line) and Safar et al. [20] (dashed line) are also shown.

from magnetization measurements [18] with a slope of 1.7 T/K.

The sharp onset in the noise at  $T_{on}$  is a feature which might have been expected at  $B_{c2}(T)$ . But as Fig. 5 demonstrates, the onset occurs well below  $B_{c2}(T)$ , so it is a new feature, thus far only visible in noise data. One possibility is that the onset signals a change in the vortex dimensionality. A very similar field dependence was found in the zero-current-density extrapolation of transport measurements on  $\text{YBa}_2\text{Cu}_3\text{O}_7$  single crystals using a modified DC flux transformer geometry [15]: these experiments have a natural interpretation in terms of a thermally induced change in vortex dimensionality. Significantly however, their data [15] showed a strong shift to lower temperatures as the current density was increased. Our  $T_{on}$  data are relatively unaffected by the current density, which was, however, well above their 'zero-current' limit. Such differences still need to be understood and they may be a clue to determining the complex dynamics of the vortex system in this temperature region.

The peak, which is sharp when displayed on a linear scale, as shown in the inset of Fig. 1, may be connected with previous work on electrical-transport measurements of the resistance of untwinned  $\text{YBa}_2\text{Cu}_3\text{O}_7$  single crystals, which have also shown sharp features, such as kinks [19] and hysteresis [20]. These have been interpreted as due to a vortex-melt-

ing transition. Within this interpretation, Kwok et al. [19] quote a melting-line relationship  $H_m(T) = 103(1 - T/T_c)^{1.41}$  for their data and  $H_m(T) = 107(1 - T/T_c)^{1.39}$  for the data of Safar et al. [20]. These are shown in Fig. 5 as the dotted and dashed lines, respectively. There is remarkable agreement between the melting lines and  $T_p$  from our noise measurements, which motivates a consideration of our work within theories of possible phase transitions in the vortex state.

The sharpness of the onset and the peak (suggesting a discontinuity in the slope) indicates a significant change in the vortex dynamics above and below these features. The measured independence of  $T_{on}$  and  $T_p$  on current is one of the requirements for the features to be associated with thermodynamic vortex phase transitions. A true thermodynamic determination requires that the system not be perturbed from equilibrium; however, for a sufficiently small bias current (such that changing its magnitude does not affect the measurement), the thermodynamic limit may still apply. Although the onset and peak may thus be associated with vortex transitions, we should state that there is no unambiguous signature of this in our measurements.

It is important to note that the earlier transport measurements, referred to above, were made on high-quality, untwinned single crystals. Much importance has been attached to the relatively small amount of pinning in such samples, since that transition has been looked for and has not been seen in samples with strong pinning. For our films, however, the pinning is substantial. Our results therefore have important consequences for the observation of vortex transitions in less-clean samples. Although the exact nature of any transition may be different in samples with higher disorder, our results suggest there may still be an underlying connection. Although our measurements provide no information about the order of a possible transition, no sign of hysteresis in a magnetic field has been observed, which is consistent with theoretical predictions in the high pinning regime [21]. We note also the similarity of the power-law temperature dependence of the vortex-melting transition (with an exponent of 1.39–1.41) and the vortex-glass transition (exponent 1.33) [22], although our data are fit much better by the higher exponent. In addition, the linear field dependence of

$T_{on}$  may be important with respect to the power-law dependence of  $H_m$ .

In summary, measurements of the electrical noise in fields up to 8 T have provided new information about the vortex state and dynamics in HTS's. Two sharp features in this noise have been observed as a function of temperature: an onset of enhanced noise from the high-temperature background and a peak. Measurements have been made as a function of temperature, current and magnetic field, and provide evidence of strong changes in the vortex dynamics. There is a striking correlation with previous transport measurements interpreted as a phase transition within the vortex state. The temperature of the features did not change over two decades in current, indicating that they may be direct signatures of thermodynamic transitions in the vortex state in thin films of  $\text{YBa}_2\text{Cu}_3\text{O}_7$ , which is highly significant given the strong pinning. Further work is required to describe theoretically the noise characteristics of predicted vortex states, as well as to make true thermodynamic measurements of the postulated transitions.

## Acknowledgements

We thank J.D. Hettinger and V.M. Vinokur for valuable discussions and E. Dirnbach, D. Howell, C.M. Klapperich, P.G. Landis, R.S. Nye, and J.E. Sharpen for technical assistance. This work is partially supported by the National Science Foundation Office of Science and Technology Centers under contract DMR 91-20000 (DGS, DHK), the U.S. Department of Energy, Division of Basic Energy Sciences–Materials Sciences under contract #W-31-109-ENG-38 (KEG), the AFOSR under contract F49620-94-C-0021 (JHK, JT) and the Argonne Division of Educational Programs (SEP).

## References

- [1] Y. Song, A. Misra, P.P. Crooker and J.R. Gaines, Phys. Rev. Lett. 66 (1991) 825; R.D. Black, L.G. Turner, A. Mogro-Campero, T.C. McGee and A.L. Robinson, Appl. Phys. Lett. 55 (1989) 2233.
- [2] E.R. Nowak, N.E. Israeloff and A.M. Goldman, Phys. Rev. B 49 (1994) 10047.
- [3] K.H. Han, M.K. Joo, S-H.S. Salk, H.J. Shim and S-I. Lee, Phys. Rev. B 46 (1992) 11835.

- [4] M.S. Dilorio, K-Y. Yang, J. Zhang, S. Yoshizumi and M. Maung, IEEE Trans. Magn. 27 (1991) 2573.
- [5] Y. Song, A. Misra, P.P. Crooker and J.R. Gaines, Phys. Rev. B 45 (1992) 7574.
- [6] W.N. Kang, D.H. Kim, J.H. Park, S.S. Yom, S.S. Choi and K.E. Gray, Physica C 233 (1994) 402.
- [7] M.J. Ferrari, M. Johnson, F.C. Wellstood, J. Clarke, D. Mitzi, P.A. Rosenthal, C.B. Eom, T.H. Geballe, A. Kapitulnik and M.R. Beasley, Phys. Rev. Lett. 64 (1990) 72.
- [8] L. Wang, Y. Zhu, H.L. Zhao and S. Feng, Phys. Rev. Lett. 64 (1990) 3094; Phys. Rev. Lett. 66 (1991) 1800.
- [9] J.H. Lee, S.C. Lee and Z.G. Khim, Phys. Rev. B 40 (1989) 6806.
- [10] M. Kawasaki, P. Chaudhari and A. Gupta, Phys. Rev. Lett. 68 (1992) 1065.
- [11] A.H. Miklich, J. Clarke, M.S. Colclough and K. Char, Appl. Phys. Lett. 60 (1992) 1899.
- [12] For a review of flux flow noise, see J.R. Clem, Phys. Reports 75 (1981) 1.
- [13] J.H. Scofield, Rev. Sci. Instrum. 58 (1987) 985.
- [14] R.F. Voss and J. Clarke, Phys. Rev. B 13 (1976) 556.
- [15] F. de la Cruz, D. Lopez and G. Nieva, Phil. Mag. B 70 (1994) 773.
- [16] We note that enhanced noise is systematically observed in high fields. For example, see K.C. Woo, K.E. Gray, R.T. Kampwirth, J.H. Kang, S.J. Stein, R. East and D.M. McKay, Phys. Rev. Lett. 63 (1989) 1877.
- [17] R.P. Huebener, Magnetic Flux Structures in Superconductors (Springer Berlin, 1979).
- [18] U. Welp, S. Fleshler, W.K. Kwok, J. Downey, G.W. Crabtree, H. Claus, A. Erb and G. Müller-Vogt, Phys. Rev. B 47 (1993) 12369;
- U. Welp, W.K. Kwok, G.W. Crabtree, K.G. Vandervoort and J.Z. Liu, Phys. Rev. Lett. 62 (1989) 1908.
- [19] W.K. Kwok, S. Fleshler, U. Welp, V.M. Vinokur, J. Downey, G.W. Crabtree and M.M. Miller, Phys. Rev. Lett. 69 (1992) 3370.
- [20] H. Safar, P.L. Gammel, D.A. Huse, D.J. Bishop, J.P. Rice and D.M. Ginsberg, Phys. Rev. Lett. 69 (1992) 824.
- [21] V.M. Vinokur, private communication.
- [22] P.L. Gammel, L.F. Schneemeyer and D.J. Bishop, Phys. Rev. Lett. 66 (1991) 953.
- For the vortex glass phase, see M.P.A. Fisher, Phys. Rev. Lett. 62 (1989) 1415;
- R.H. Koch, V. Foglietti, W.J. Gallagher, G. Koren, A. Gupta and M.P.A. Fisher, Phys. Rev. Lett. 63 (1989) 1511.

## Single-Flux-Quantum Circuits Based on YBCO Step-Edge-Grain-Boundary Junctions

Donald L. Miller, Martin G. Forrester\*, John X. Przybysz, Brian D. Hunt, and John Talvacchio\*  
Westinghouse Science and Technology Center  
1310 Beulah Rd., Pittsburgh, PA 15235 USA

**Abstract** - A consistent motivation for the investigation of high temperature superconductor (HTS) Josephson junctions has been the desire for high-speed, low-power digital circuits. The fabrication of meaningful single-flux-quantum (SFQ) circuits in HTS technology requires a multilayer process for control of circuit inductances. Previous investigators have reported simple SFQ circuits in a single  $\text{Y}_1\text{Ba}_2\text{Cu}_3\text{O}_x$  (YBCO) layer process or two junction SQUIDs in a two YBCO layer process. Based on these previous results, we have designed and fabricated simple SFQ circuits using a two YBCO layer process with step-edge-grain-boundary junctions.

### I. Introduction

Superconductive digital circuits have been shown to operate at multi-GHz clock rates with orders of magnitude lower power consumption than semiconductor circuits of similar complexity. The extension of this technology to encompass the use of high temperature superconductivity (HTS), coupled with the availability of compact, low-cost cryocoolers, will have an immediate impact on advanced communication, signal processing, and defense electronics systems.

Single-Flux-Quantum (SFQ) logic has advantages over other types of superconducting logic in terms of speed and power [1]. Moreover, SFQ logic uses non-latching Josephson junctions, and thus is compatible with HTS junctions demonstrated to date. This has been demonstrated through SFQ circuits fabricated using a single level  $\text{Y}_1\text{Ba}_2\text{Cu}_3\text{O}_x$  (YBCO) process[2]. This paper describes the design and fabrication of simple SFQ circuits in a multilevel YBCO technology. The choice of technology was based on the ability to fabricate both Josephson junctions and multilayer HTS films. For practical digital circuits, junctions with critical currents ( $I_c$ ) ranging from 100  $\mu\text{A}$  to 500  $\mu\text{A}$ , and products of  $I_c$  and normal state resistance ( $R_n$ ) of more than 300  $\mu\text{V}$  are desired.

Approaches to YBCO junction fabrication have met with varying degrees of success. Bi-crystal junctions which

require fused substrates have yielded good junction properties, but at high cost and with severe limitations on circuit layouts. Junctions with deposited barriers, such as edge junctions, are difficult to integrate into multilayer structures since they require additional epitaxial film depositions. Step-edge-grain-boundary (SEGB) junctions, which are formed by discontinuities in crystal orientation as the HTS film covers a step in the substrate, have the disadvantage of rather large spreads in  $I_c$ , but are more easily integrated with multilayers. For circuits with few junctions, variations from designed critical currents can be compensated by adjusting the dc bias current to each junction.

### II. Fabrication

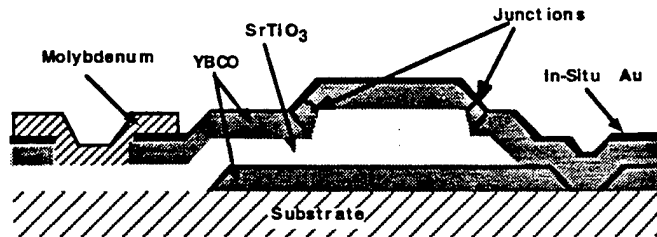


Fig. 1 Cross section of the process used to fabricate single-flux-quantum circuits with step-edge-grain-boundary junctions.

We have fabricated circuits using a five mask level process as illustrated in Fig. 1. This process, which uses two levels of YBCO deposition, is based upon that used by Forrester et al. to fabricate dc SQUIDs [3].

The first deposition of YBCO (2000 Å) formed the ground plane. This layer was removed from the region outside the active circuits by ion milling to reduce the possibility of shorting from bias leads to ground and to provide reliable end-point detection for the milling operation.

Following patterning of the ground level YBCO, a 3000-4000 Å layer of  $\text{SrTiO}_3$  was deposited as a dielectric. This level was patterned twice using two different masks and two different sets of ion-milling conditions. The first etch,

\* Supported in part by AFOSR contract No. F49620-94-C-0021

(1500-2000 Å) was used to define steps for the formation of junctions. This process step was designed to produce a sharp step, with rotation of the substrate during milling allowing junctions of arbitrary orientation. In practice, only orthogonal junctions were used. The second milling step penetrated the dielectric and was designed to produce a much shallower ramp ( $\leq 30^\circ$ ). This shallow ramp was intended to permit a transition from the microstrip level to the ground plane level without introducing an unwanted junction. By using a two-step dielectric etch we were able to combine floating and grounded junctions, a requirement for SFQ decision circuits, while fabricating all junctions with the same process steps. This, in turn, reduced run-to-run process variations which contribute to non-uniform junction critical currents.

The second level of YBCO formed the inductors and junctions of the SFQ circuits. Junction contacts to ground were made through ground plane vias to provide a- and b-axis contact. Following the active layer YBCO deposition a thin layer of gold was deposited in-situ both to act as a passivation layer and to provide a good contact for wire bonding.

The final process step was deposition of a molybdenum film for 1 ohm per square resistors.

### III. Circuit Layout

Circuit layouts were generated for the following circuits: set-reset flip-flop, T-flip-flop (TFF) with digital readout, T-flip-flop with voltage mode readout, SFQ quantizer, one-bit SFQ analog-to-digital converter, and sigma-delta modulator. These circuits are well known [1], [4], [5] and will not be described in detail here. A T-flip-flop will be used as an example to illustrate layout concepts.

Figure 2 shows the circuit diagram and the corresponding mask layout for a SFQ TFF with a magnetically coupled readout SQUID. Junctions in the TFF have designed critical currents of 233  $\mu$ A for the upper junctions and 333  $\mu$ A for the lower junctions. Critical currents are scaled by the width of the junction. Individual dc bias leads to each junction were included to allow compensation for variations in junction critical currents. Additional leads were provided for average voltage mode testing.

While, in principle, the process allows junctions in arbitrary orientation, only x and y orientations were used in the present work. The fact that two junctions are formed at each step has been ignored in the circuit layout, under the assumption that one of the junctions will dominate, with the second junction having minor phase variations. This is not inconsistent with the observed behavior of dc SQUIDs fabricated by a similar process [3].

Junction contacts to ground are formed through the edges of ground plane vias, as shown in Fig. 2, to allow a- and b-axis current flow. As noted in the previous section, the

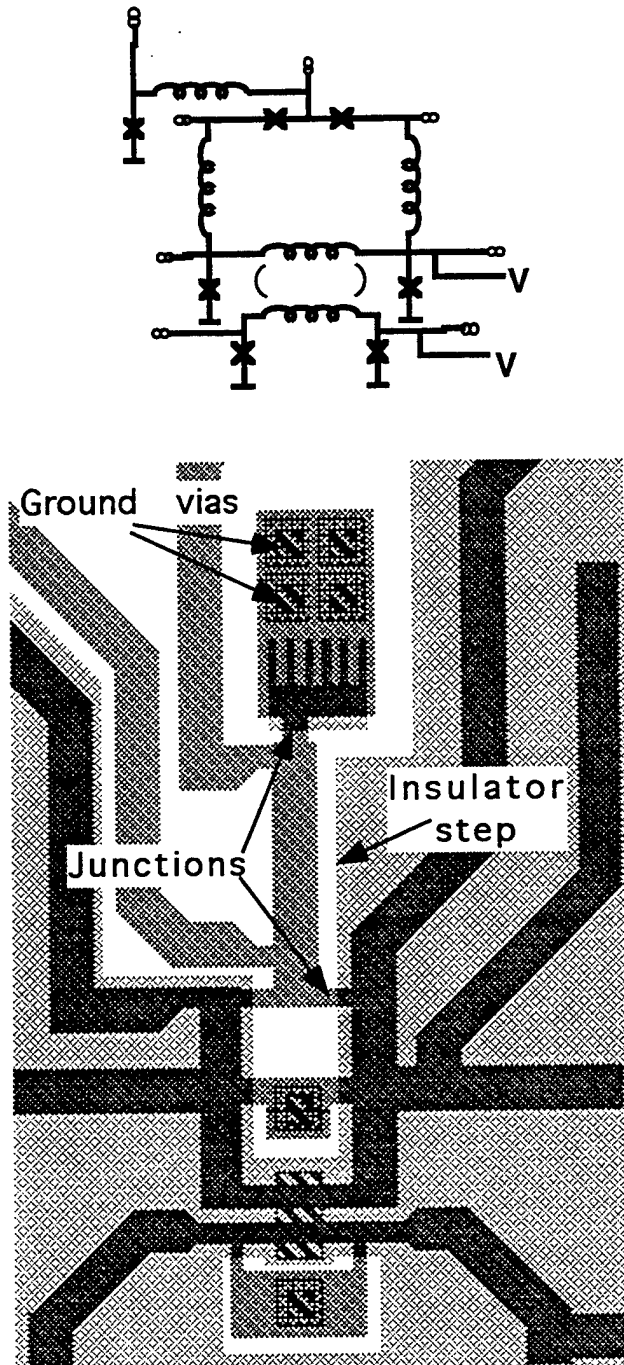


Fig. 2 Circuit diagram and mask layout of a T-flip-flop.

shallow ramp of the insulator vias was not expected to result in junctions.

The use of SEGB junctions in our process requires an even number of junctions between each pair of ground contacts. Where circuit designs differed from this process requirement, an additional, interdigitated, junction was introduced as shown at the top of Fig. 2.

Circuit inductances were scaled from the SQUID measurements of Forrester et al [3], taking into account differences in the dielectric layer thickness.

Included in the circuit of Fig. 2 is a readout SQUID magnetically coupled to the storage inductor of the TFF. Coupling is achieved through a common ground plane hole following Chang [6].

#### IV. Conclusions

We have identified a process for the fabrication of HTS digital circuits using step-edge-grain-boundary junctions. The process incorporates multilayer YBCO films for inductance control, arbitrary location of Josephson junctions, and resistors. With the addition of an additional superconducting wiring level, the process is extendible to complex circuits, limited only by process yields. Simple SFQ circuits using this process have been designed and fabricated. Measurements of these circuits are in progress.

#### References

1. K. Likharev and V. Semenov, IEEE Trans. Appl. Supercond., 1, 3 (1991).
2. M. G. Forrester, J. X. Przybysz, J. Talvacchio, J. Kang, A. Davidson, and J. R. Gavaler, IEEE Trans. Appl. Supercond., 5, 3401(1995).
3. M.G. Forrester, A. Davidson, J. Talvacchio, J. R. Gavaler, and J. X. Przybysz, Appl. Phys. Lett. 65, 1835 (1994).
4. J. X. Przybysz, D. L. Miller, E. H. Naviasky, and J. H. Kang, IEEE Trans. Appl. Supercond., 3, 2732(1993).
5. J. P. Hurrell, D. C. Pridmore-Brown, and A. H. Silver, IEEE Trans. Electron Dev., ED-27, 1887 (1980).
6. W. H. Chang, J. Appl. Phys., 52, 1417(1981).

# Electrical transport properties of [001] tilt bicrystal grain boundaries in $\text{YBa}_2\text{Cu}_3\text{O}_7$

## APPENDIX 14

D. G. Steel,<sup>a)</sup> J. D. Hettinger, F. Yuan, D. J. Miller, and K. E. Gray

Science and Technology Center for Superconductivity and Materials Science Division, Argonne National Laboratory, Argonne, Illinois 60439

J. H. Kang and J. Talvacchio

Westinghouse Science and Technology Center, Pittsburgh, Pennsylvania 15235

(Received 15 June 1995; accepted for publication 19 October 1995)

The zero-field electrical transport properties of  $24^\circ$  [001] tilt bicrystal grain boundaries in  $\text{YBa}_2\text{Cu}_3\text{O}_7$  were found to be in excellent agreement with the Ambegaokar–Halperin model over an extended range of currents and voltages. This model gives a firm basis for characterizing and comparing boundaries, and provides two independent measures of the critical current, which were proportional to  $(1 - T/T_c)^2$  close to the transition temperature  $T_c$ . © 1996 American Institute of Physics. [S0003-6951(96)01401-8]

Since the discovery of high temperature superconductors (HTS), grain boundaries have been the focus of a substantial amount of research. They can be responsible for much of the dissipation in a polycrystalline material, so it is important to understand their properties for applications of bulk materials as high current carrying conductors. In addition, certain thin film device applications of HTS are based on the weak-link properties of grain boundaries and these require a high degree of reproducibility. Consistent with other reports, Miller *et al.*<sup>1</sup> have shown that artificially induced grain boundaries are not always straight, but instead meander along the path of the underlying substrate boundary.<sup>2,3</sup> Inhomogeneities along the boundary dictate that measurements should be made in a small and well-defined area across the interface.<sup>4,5</sup> An insightful study of the electrical transport properties of grain boundaries clearly has to connect them to the microstructure, but also requires a reliable and quantitative description of the transport properties to give a basis for comparing boundary characteristics.

In this letter, we present results for the zero-field electrical transport in microbridges across  $24^\circ$  [001] tilt bicrystal grain boundaries in  $\text{YBa}_2\text{Cu}_3\text{O}_7$ . Many studies have been published on the transport properties of grain boundaries,<sup>4–8</sup> particularly the behavior in a magnetic field. We show that important information may also be obtained from zero-field measurements, and specifically report on the advantages of taking voltage–current characteristics over an extended range to demonstrate excellent agreement with the Ambegaokar–Halperin (A–H) model for Josephson-coupled superconductors. This provides an important quantitative technique for studying such junctions; for example, defining a critical current independent of any electric field criterion, and for comparing different boundaries.

Films of  $\text{YBa}_2\text{Cu}_3\text{O}_7$  were grown *in situ* using off-axis rf magnetron sputtering onto  $\text{SrTiO}_3$  substrates composed of two crystals rotated from each other by  $24^\circ$ . This gives epitaxial films on each side with a grain boundary due to the

interface.<sup>7,8</sup> The films were  $\sim 1500$  Å thick and shown by transmission electron microscopy to be epitaxial and *c*-axis oriented. Films were patterned using standard projection lithography and a chemical etch to define microbridges of width  $36\ \mu\text{m}$  for four-terminal electrical transport measurements. Measurements were made across both intergrain and intragrain sections. Although the purpose of this study was to examine grain boundary properties, the intragrain sections are important to indicate the quality of the film.

The lower inset of Fig. 1 shows the junction resistance (logarithmic scale) as a function of temperature for three different intergrain sections and one intragrain section, measured with a current of  $36\ \mu\text{A}$ . The intragrain measurement shows a sharp decrease in the resistance to the measurement noise level at  $T_c \sim 91$  K. This indicates the high quality of the film and shows that it was not degraded by lithographic processing and etching. The three intergrain sections also show a decrease at  $T \sim 91$  K, corresponding to the film becoming

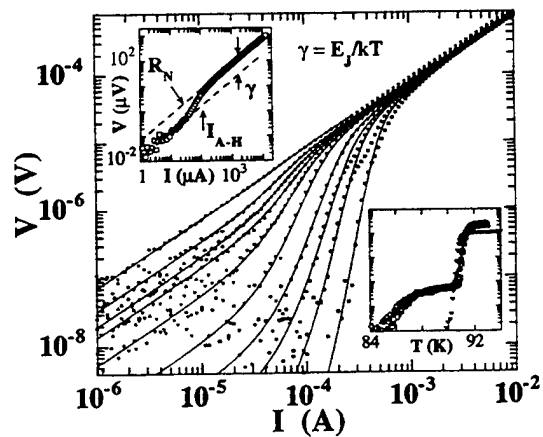


FIG. 1. Grain boundary voltage–current characteristics at different temperatures in the range 81–88 K. Lines show fits to the Ambegaokar–Halperin model. The upper inset shows data at 86 K, indicating the three fit parameters:  $I_{\text{A}-\text{H}}$ ,  $\gamma$ , and  $R_N$ . The lower inset shows resistance (logarithmic scale) vs temperature for three intergrain microbridges and one intragrain microbridge.

<sup>a)</sup>Electronic mail: david\_steele@qmgate.anl.gov

superconducting on both sides of the grain boundary, but have a finite resistance plateau down to lower temperatures. This low resistance of  $\sim 8 \times 10^{-2} \Omega$  corresponds to the "normal-state" resistance of the grain boundary itself and agrees very well between the three sections. This implies the uniformity of transport measurements over three separate 36  $\mu\text{m}$  wide regions of the grain boundary. The rolloff of the grain boundary resistance at low temperatures was found to depend on current and this motivated a detailed examination of the nonlinear response.

The symbols of Fig. 1 show extended voltage-current characteristics in zero magnetic field for an intergrain section measured at a series of temperatures between 81 and 88 K. At the highest temperature, the data show linear (ohmic) behavior over the full current range, with the boundary normal-state resistance of  $\sim 8 \times 10^{-2} \Omega$ . At lower temperatures, there is linear behavior in the low-current and high-current limits, with a crossover between these. (The small dip at low temperatures just below the normal-state resistance is not understood, but was observed in measurements of other intergrain sections.)

To describe the  $I$ - $V$  curves, we have fit them using the A-H model for Josephson coupled superconductors,<sup>9</sup> and the results of these fits are shown by the lines in Fig. 1. The data are clearly very well fit by the A-H model over the extended range of currents and voltages, and this provides a basis for quantitative description of the grain boundary behavior. In order to cover the extended range of currents, we use the expansion of the A-H functional given by Falco *et al.*<sup>10</sup> These fits contain three parameters as shown in the upper inset of Fig. 1 for data at 86 K:  $R_N$  is the grain boundary normal-state resistance,  $\gamma$  is the ratio of the Josephson coupling energy  $E_J$  to the thermal energy  $k_B T$  and  $I_{A-H}$  is the unfluctuated total critical current. The best fits are obtained with  $R_N$  as a parameter, consistent with the temperature dependence observed in the range 88–90 K. At higher currents, a constant value of  $R_N$  may be found, as expected from general concepts of tunneling. The value of  $\gamma$  characterizes the difference in resistance of the linear regions at low and high currents. An important consequence of these fits is that  $I_{A-H}$  gives a value for the critical current that is *independent* of any criterion for the electric field. This is in sharp contrast to the usual treatments of critical currents, which require the definition of some arbitrary criterion for the dissipation level and can be swamped by thermal fluctuations. The upper inset also establishes the value of an extended range of measurement in demonstrating the crossover between linear behavior in the low-current and high-current limits.

We next consider the temperature dependence of the critical current  $I_c$ , which can provide information about the nature of the junction coupling mechanism; in particular, whether a model based on tunneling is appropriate. We use the data from Fig. 1 to obtain two measures of the critical current, and these are shown in Fig. 2. The left axis displays  $I_{A-H}$  obtained directly from the fits as described above. The right axis shows the coupling current based on thermal activation  $eE_J/\hbar$  that was calculated from the fit values of  $\gamma$ . The two sets of values of critical current show similar tem-

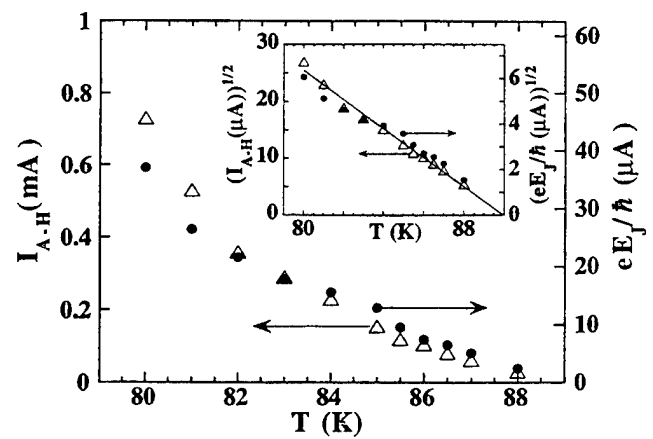


FIG. 2. Critical current  $I_c$  vs temperature for both  $I_{A-H}$  extracted directly from the Ambegaokar-Halperin fits and  $eE_J/\hbar$  from the Josephson coupling energy  $E_J$ , based on thermal activation. Inset shows the quadratic behavior  $I_c \sim (1-t)^2$ , where  $t = T/T_c$  and  $T_c \sim 89.9$  K.

perature dependence, although the values  $I_{A-H}$  obtained *directly* from the fits are a factor of  $\sim 16$  larger than  $eE_J/\hbar$  and this will be discussed later.

The inset of Fig. 2 shows  $I_{A-H}$  and  $eE_J/\hbar$  plotted as  $I_c^{1/2}$  vs temperature, to demonstrate quadratic dependence  $I_c \sim (1-t)^2$ ,  $t = T/T_c$ , with the slope giving a value of  $T_c \sim 89.9$  K.<sup>11</sup> This dependence has been seen before<sup>8</sup> for a measured critical current but not for  $eE_J/\hbar$ . It differs from the behavior predicted by the Ambegaokar-Baratoff (A-B) expression<sup>12</sup> for superconductor-insulator-superconductor (SIS) junctions, for which  $I_c \sim (1-t)$  and the values of  $I_{A-H}$  and  $eE_J/\hbar$  are significantly smaller in magnitude than predicted by the A-B expression. (We also find a significant departure from the A-B formula at low temperatures, where the  $I_c R_N$  product is measured to be  $\sim 1$  mV at 4 K, compared to a gap voltage of  $\sim 20$  mV from tunneling studies.<sup>13</sup>)

We now discuss these findings as regards a possible understanding. The excellent fits to the A-H model appear to confirm the nature of the Josephson coupling across the interface, and an SIS tunneling description is appropriate. Other studies, such as electromagnetic resonances along a bicrystal grain boundary<sup>14</sup> have also shown SIS behavior. However, the quadratic temperature dependence of the critical current that we observe does not agree with the usual, linear result for Josephson tunneling and requires explanation. This quadratic dependence is consistent with a superconductor-normal metal-superconductor (SNS) interface, although the normal resistance of our grain boundary junction appears too large for a reasonable thickness of normal metal in such a junction. In contrast, our observed temperature dependence may be explained within an SIS picture, modified by including proximity effects on normal layers adjacent to each side of the barrier. This gives a structure that is effectively SNINS and that shows both high resistance and quadratic temperature dependence of the critical current.<sup>15,16</sup>

We now return to the difference in the values of  $I_{A-H}$  and  $eE_J/\hbar$ . To explain this difference as due to rf pickup at the junction would require the noise temperature  $T_n$  to be  $\sim 16$

times larger than the bath temperature, such that  $T_n \sim 1400$  K. All our experiments were performed in an electromagnetically screened room, with rf interference filters<sup>17</sup> on the incoming power lines and room temperature pi filters on the cryostat leads. Previous studies of low- $T_c$  superconductors in our laboratory have shown little difference between the sample and bath temperatures for measurements in an unshielded environment using only resistors to filter the sample leads; thus, we believe it very unlikely that the data can be explained by a sufficiently increased noise temperature.

It has been suggested by several authors that grain boundaries are in fact composed of smaller junctions in parallel along the interface.<sup>18-21</sup> Calculation of the Josephson penetration length  $\lambda_J$ , which is given by  $\lambda_J = (\phi_0/2\pi\mu_0 J_c d)^{1/2}$ , where  $d$  is approximately twice the London penetration depth  $\lambda_L$ , confirms self-consistently that our junctions are *macroscopically* within the large junction limit.<sup>8</sup> This  $\lambda_J$  is consistent with recent experiments that *directly* image the Josephson vortices in tricrystal grain boundaries.<sup>22</sup> However, since the Josephson currents reflected in  $I_{A-H}$  flow only within  $\sim \lambda_J$  of the edges in large junctions, the value of  $eE_J/\hbar$  depends on the junction area, i.e., whether the effective energy barrier to thermal activation involves the entire junction or just the edge regions. Thus,  $I_{A-H}$ , which only probes the edges, may be considered as a lower limit on  $eE_J/\hbar$ , which is inconsistent with the experimental observations.<sup>23</sup> This inconsistency suggests that the effective Josephson coupled area that contributes to  $eE_J/\hbar$  is less than the geometrical area and that the grain boundary may be comprised of a number of smaller junctions effectively in parallel. Since the overall behavior is so well fit by the A-H model, the size of each junction is expected to be less than  $\lambda_J$ . Both scanning and transmission electron microscopy studies have shown clear evidence of impurity phases along the boundary, which occur on a length scale of a few  $\mu\text{m}$ .<sup>1</sup> This seems reasonable since impurities and precipitates frequently tend to segregate at and along grain boundaries. The impurities may provide a microstructural understanding of the apparent small junction behavior of the electrical transport. Additional work is required to establish a definite correlation.

Another possible picture considers the microbridge as a long Josephson junction, within which dissipation occurs by the motion of Josephson vortices along the boundary. This motion is mediated by small defects along the boundary that act as pinning centers. We have made preliminary fits to a modified flux creep model, and although this also gives linear behavior in the low-current and high-current limits, it gives a poorer fit compared to the A-H model for the intermediate region. In addition, the pinning energy  $E_p$ , extracted from the fits has a linear dependence on reduced temperature  $E_p \sim (1 - T)$  and not the expected quadratic behavior based on condensation energy.

In summary, the zero-field electrical transport properties of 24° [001] tilt bicrystal grain boundaries in  $\text{YBa}_2\text{Cu}_3\text{O}_7$  have been fit by the Ambegaokar-Halperin model over several decades in current, including the linear regimes at low and high currents. Analysis of these detailed fits provides a

sound quantitative basis for characterizing junctions and describing their quality. For example, the critical current may be obtained from the model without using a criterion for the electric field. In addition, the temperature dependence of the critical current is different from conventional Josephson tunneling, but that dependence and the high junction resistance may be consistently understood within an SNINS model.

The authors thank R. A. Buhrman, A. M. Goldman, D. H. Kim, and V. M. Vinokur for useful comments, and S. E. Pfanstiel, C. M. Klapperich, and G. B. Thompson for technical assistance. This work is partially supported by the National Science Foundation Office of Science and Technology Centers under Contract No. DMR 91-20000 (D.G.S., F.Y.), the U.S. Department of Energy, Basic Energy Sciences-Materials Sciences, and Energy Efficiency and Renewable Energy, as part of a program to develop electric power technology, under Contract No. W-31-109-ENG-38 (J.D.H., D.J.M., K.E.G.), and the AFOSR under Contract No. F49620-94-C-0021 (J.H.K., J.T.).

- 1 D. J. Miller, T. A. Roberts, J. H. Kang, J. Talvacchio, D. B. Buchholz, and R. P. H. Chang, *Appl. Phys. Lett.* **66**, 2561 (1995).
- 2 J. A. Alarco, E. Olsson, Z. G. Ivanov, P. A. Nilsson, D. Winkler, E. A. Stepanov, and A. Ya. Tzalenchuk, *Ultramicroscopy* **51**, 239 (1993).
- 3 C. Træholt, J. G. Wen, H. W. Zandbergen, Y. Shen, and J. W. M. Hilgenkamp, *Physica C* **230**, 425 (1994).
- 4 C. Sarma, G. Schindler, D. G. Haase, C. C. Koch, A. M. Saleh, and A. I. Kingon, *Appl. Phys. Lett.* **64**, 109 (1994).
- 5 P. Chaudhari, J. Mannhart, D. Dimos, C. C. Tsuei, J. Chi, M. M. Oprysko, and M. Scheuermann, *Phys. Rev. Lett.* **60**, 1653 (1988).
- 6 R. Gross, P. Chaudhari, D. Dimos, A. Gupta, and G. Koren, *Phys. Rev. Lett.* **64**, 228 (1990).
- 7 D. Dimos and P. Chaudhari, *Phys. Rev. B* **41**, 4038 (1990).
- 8 R. Gross, in *Interfaces in High- $T_c$  Superconducting Systems*, edited by S. L. Shindé and D. A. Rudman (Springer, New York, 1994).
- 9 V. Ambegaokar and B. I. Halperin, *Phys. Rev. Lett.* **22**, 1364 (1969).
- 10 C. M. Falco, W. H. Parker, S. E. Trullinger, and P. K. Hansma, *Phys. Rev. B* **10**, 1865 (1974).
- 11 This value for the transition temperature is low compared to the intragrain sections, for which  $T_c \sim 91$  K. This suggests a reduced  $T_c$  close to the grain boundary.
- 12 V. Ambegaokar and A. Baratoff, *Phys. Rev. Lett.* **10**, 486 (1963); *Phys. Rev. Lett.* **11**, 104 (1963).
- 13 M. Gurvitch, J. M. Valles Jr., A. M. Cuolfo, R. C. Dynes, J. P. Gorno, L. F. Schneemeyer, and J. V. Waszczak, *Phys. Rev. Lett.* **63**, 1008 (1989).
- 14 D. Winkler, Y. M. Zhang, P. A. Nilsson, E. A. Stepanov, and T. A. Claeson, *Phys. Rev. Lett.* **72**, 1260 (1994).
- 15 R. Gross, P. Chaudhari, M. Kawasaki, and A. Gupta, *IEEE Trans. Magn.* **27**, 3227 (1991).
- 16 A. A. Golubov and M. Yu. Kupriyanov, *Phys. Lett. A* **154**, 181 (1991).
- 17 Axel Electronics Inc., Model 9B301.
- 18 B. H. Moeckly, D. K. Lathrop, and R. A. Buhrman, *Phys. Rev. B* **47**, 400 (1993).
- 19 E. Sarnelli, P. Chaudhari, and J. Lacey, *Appl. Phys. Lett.* **62**, 777 (1993).
- 20 M. B. Field, A. Pashitski, A. Polyanskii, D. C. Larbalestier, A. S. Parikh, and K. Salama (unpublished).
- 21 E. A. Early, R. L. Steiner, A. F. Clark, and K. Char, *Phys. Rev. B* **50**, 9409 (1994).
- 22 J. R. Kirtley, C. C. Tsuei, M. Rupp, J. Z. Sun, L. S. Yu-Jahnes, A. Gupta, M. B. Ketchen, K. A. Moler, and M. Bhushan (unpublished).
- 23 Another possible explanation might be if the junctions are underdamped, such that a dissipation parameter replaces the value of  $R_N$  in fitting  $E_J$ ; see, for example, J. D. Hettinger, K. E. Gray, B. W. Veal, A. P. Paulikas, P. Kostic, B. R. Washburn, W. C. Tonjes, and A. C. Flewelling, *Phys. Rev. Lett.* **74**, 4726 (1995). However, underdamped junctions should not give such excellent fits to the A-H model and any reasonable estimate of the Stewart-McCumber parameter places these junctions in the overdamped regime.

# High- $T_c$ superconductor/normal-metal/superconductor edge junctions and SQUIDs with integrated groundplanes

## APPENDIX 15

B. D. Hunt,<sup>a)</sup> M. G. Forrester, J. Talvacchio, J. D. McCambridge, and R. M. Young  
Northrop Grumman Science and Technology Center, Pittsburgh, Pennsylvania 15235

(Received 14 March 1996; accepted for publication 12 April 1996)

Epitaxial, high- $T_c$  superconductor/normal-metal/superconductor (SNS) edge-geometry weak links and superconducting quantum interference devices (SQUIDs) have been fabricated with integrated  $\text{YBa}_2\text{Cu}_3\text{O}_7$  (YBCO) groundplanes and  $\text{SrTiO}_3$  insulators, using a process which incorporates six epitaxial layers. The SNS edge junctions were produced using off-axis sputtered films and Co-doped-YBCO normal metal interlayers. These devices show excellent performance with typical critical current-resistance ( $I_c R_n$ ) products of 500–800  $\mu\text{V}$  for 100–150  $\text{\AA}$  thick normal metal layers at 65 K, and 1- $\sigma$  critical current density ( $J_c$ ) spreads as small as 12%. SNS SQUIDs incorporating groundplanes exhibit voltage modulation of up to 130  $\mu\text{V}$  at 65 K and 40  $\mu\text{V}$  at 77 K. SQUID inductance measurements indicate microstrip inductance values of 1 pH per square at 65 K.

© 1996 American Institute of Physics. [S0003-6951(96)00925-4]

Single flux quantum (SFQ) digital circuits based on high-temperature superconductors (HTS) have the potential to perform logic operations at 10 GHz clock rates while dissipating only a microwatt per gate. In order to fully realize this potential, it is necessary to develop a circuit process which integrates reproducible Josephson junctions into epitaxial multilayers. In particular, a superconducting groundplane is required to keep circuit inductances low enough that a single quantized voltage pulse can generate sufficient current in a load inductor.

We have previously reported the incorporation of YBCO-based step-edge grain boundary junctions with a HTS groundplane, demonstrating multilayer SQUIDs with microstrip inductances as low as 1 pH per square at 65 K.<sup>1</sup> The practicality of such junctions for large-scale circuits was, however, limited by their  $I_c R_n$  values (typically 50–100  $\mu\text{V}$  at 65 K) and poor critical current uniformity (typically no better than 30%, 1- $\sigma$ , on chip).

Here we report the demonstration of superior SNS edge junctions, integrated with a groundplane, in a process incorporating six epitaxial layers. These junctions exhibit  $I_c R_n$  values of 500–800  $\mu\text{V}$  at 65 K, and critical current uniformities as low as 12% (1- $\sigma$ ), making them more promising candidates for a manufacturable HTS digital circuit process. Along with results reported by Conductus,<sup>2</sup> these are the first SNS edge junctions with separate but integrated HTS groundplanes,<sup>3</sup> which operate above 50 K.<sup>4</sup>

The YBCO, Co-doped YBCO, and  $\text{SrTiO}_3$  (STO) films used in this work were deposited by off-axis rf magnetron sputtering following processes detailed elsewhere.<sup>5</sup> An essential condition for circuit-compatible YBCO growth is the production of smooth, outgrowth-free films, which helps ensure good electrical isolation between successive YBCO layers. In practice it is found that smooth YBCO film growth by off-axis sputtering is sensitive to deposition system cleanliness, as well as surface cleanliness of the underlying epilayer. In our process, each epitaxial growth step over a patterned underlayer was preceded by *ex situ* oxygen plasma

and 150 eV Ar/O<sub>2</sub> ion mill cleaning steps. We also optimized insulator growth temperatures to enable proper oxidation of the buried groundplane, while maintaining an adequate epitaxial template for growth of high quality overayers.<sup>6</sup> Acceptable STO growth temperatures were in the range of 670–690 °C, compared to typical YBCO deposition temperatures of 720–730 °C. The normal metal layers were  $\text{YBa}_{2.79}\text{Co}_{0.21}\text{O}_{7-\delta}$  (7% Co-doped YBCO), optimized for smoothness and maximum Co incorporation (minimum  $T_c$ ). Typical  $T_c$  values for Co-YBCO layers were 51–58 K.

Our multilayer device structure, shown in cross section in Fig. 1, is based on SNS edge-geometry weak links fabricated over a YBCO groundplane. We chose the buried groundplane geometry to minimize the processing steps needed to complete the SNS device after the counterelectrode deposition, although there is no *a priori* reason to rule out the use of groundplanes on top. The choice of YBCO SNS edge junctions was driven by the known advantages of this technology,<sup>7,8</sup> and by the promising device results that have been achieved using SNS edge junctions with Co-doped-YBCO normal metal layers.<sup>9,10</sup>

The process used to pattern each layer except the counterelectrode was designed to produce an edge taper of 20°–30° from the horizontal, independent of edge orientation. This was achieved by using Hoechst 1518 resist, reflowed

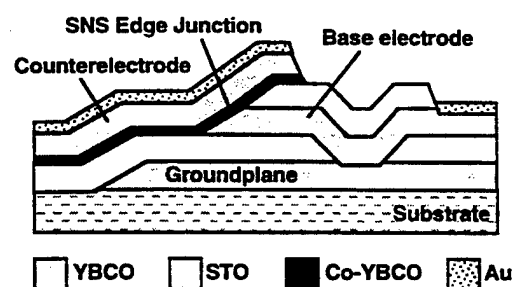


FIG. 1. Schematic cross section of an YBCO/Co-YBCO/YBCO SNS edge junction integrated with an epitaxial YBCO groundplane. The multilayer structure includes six epitaxial layers and contact vias to the groundplane and base electrode.

<sup>a)</sup>Electronic mail: bdhunt@cis.pgh.wec.com

after patterning for 5 min at 130 °C, and then Ar ion milling the rotating substrate at 150 eV and 50° from normal. Each patterning step was followed by the cleaning process described above. The fabrication began with the deposition of a *c*-axis-oriented 2250 Å YBCO groundplane on a (110) NdGaO<sub>3</sub> substrate, followed by growth of a STO passivation layer. The groundplane was patterned, a 2400 Å STO layer was deposited, and via holes to the groundplane were defined. Next, an 1100–3500 Å YBCO base electrode and 1500 Å STO capping layer were grown and patterned. After an *in situ* Ar ion mill clean we deposited 100–250 Å of epitaxial Co-doped YBCO, followed by growth of the YBCO counterelectrode, an *in situ* anneal, and finally *in situ* sputtering of a gold contact layer near room temperature. Via holes were patterned down to the base electrode, and gold was sputtered and lifted off in the vias to provide base electrode contacts. Finally, the YBCO counterelectrodes were defined with a straight-wall resist process and Ar ion milling.

Our standard test pattern consisted of 20 junctions arrayed on four sides of a square base electrode with nominal widths of 2, 4, and 6  $\mu\text{m}$ , and  $75 \times 75 \mu\text{m}^2$  groundplane patches under half the junctions. The layout had four or nine subchips on each 1-cm<sup>2</sup> chip, and the subchip to be tested was wire bonded into a 44 pin carrier. Subchip designs included junction test structures, SQUIDs, and SFQ circuits. Automated chip testing was done in a temperature controlled, magnetically shielded cryostat with three orthogonal pairs of magnetic field coils.

The  $I$ – $V$  characteristics on a typical chip for the four 4- $\mu\text{m}$ -wide SNS junctions over groundplane patches are shown in Fig. 2. The data were taken at 65 K on devices with 150 Å Co-doped-YBCO normal metal interlayers. The average device parameters for these junctions are:  $J_c = 1.27 \times 10^5 \text{ A/cm}^2$  with a 1- $\sigma$  spread of 20%;  $I_c R_n = 587 \mu\text{V}$  with a 1- $\sigma$  spread of 15%; and  $R_n A = 4.8 \times 10^{-9} \Omega \text{ cm}^2$  with a 1- $\sigma$  spread of 24%. A key point to note is that these junction parameters are essentially identical to those for junctions without groundplanes: fabricating the edge junctions above the patterned groundplane and groundplane insulator did not degrade the device quality. Isolation between the junction film layers and the groundplane was checked on test structures located adjacent to the actual junctions. Room-temperature measurements verified typical isolation resistivities greater than  $10^6 \Omega \text{ cm}$ . Studies of via test structures and circuits located on the junction chips demonstrated base-electrode-to-groundplane vias with critical currents greater than 9 mA, the current limit of the test setup.

Another important issue is that these SNS weak links have large  $I_c R_n$  and  $R_n A$  products relative to most reported SNS device results. For Co-doped YBCO thicknesses of 100–150 Å, the  $I_c R_n$  products are typically in the range of 500–800  $\mu\text{V}$  at 65 K, and 150–250  $\mu\text{V}$  at 77 K, values which are more than adequate for production of SFQ circuits. The  $R_n A$  products are  $\sim 5$ –10 times larger than expected from the Co-doped YBCO resistivity and layer thicknesses. We believe the relatively high junction resistances are due to inhomogeneous S–N interface resistances. Non-uniform conduction through a SNS device can reduce the active area and increase  $R_n$  without reducing  $I_c R_n$ , if highly conducting regions are separated by nonconducting

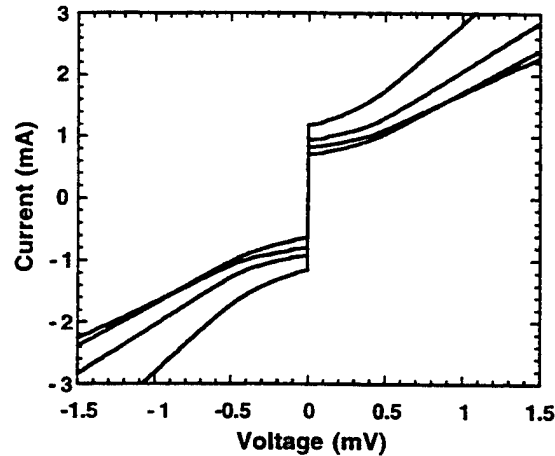


FIG. 2. Current–voltage characteristics at 65 K for the four 4- $\mu\text{m}$ -wide SNS junctions with integrated groundplanes on a typical test chip. The Co-doped YBCO thickness is 150 Å and the average  $I_c R_n$  product is 587  $\mu\text{V}$ .

areas.<sup>11,12</sup> We find, in fact, that the  $R_n A$  products vary as a function of the base electrode edge formation process, suggesting that the base electrode–normal metal interface contributes directly to the high observed resistances. Inhomogeneous conduction through this interface could result from nonuniform edge damage or a patchy insulator layer caused by sputtering the insulator overlayer down onto the base electrode edge. Although the origin of the large  $R_n A$  products is not fully understood, we have demonstrated reproducible control of device resistances, and the high resistances we obtain are important for many applications.

The 1- $\sigma$  critical current variations we observed ranged from 12% to over 40% on the eleven 1-cm<sup>2</sup> chips (16 subchips) we have tested with groundplanes. In most cases, the 1- $\sigma$  spreads for the devices over groundplanes were comparable to companion junctions without groundplanes. Larger  $I_c$  spreads were generally associated with rougher base electrode or counterelectrode films. As progress is made in optimizing film growth for smooth surface morphology we expect to routinely achieve the 10%–15%  $I_c$  spreads required for small-scale SFQ circuits (<1000 junctions).

Shielding of the groundplanes was qualitatively verified by magnetic-field  $I_c$  modulation studies. Figure 3 is a plot of  $I_c$  versus magnet current for a field perpendicular to the substrate at 77 K for junctions with and without a groundplane patch. Both curves show  $I_c$  modulation approximately consistent with the expected  $\sin(x)/x$  behavior, indicating good large-scale uniformity of the normal metal layers. However, the junction over the groundplane exhibits a modulation period approximately four times that of the other junction, demonstrating the magnetic shielding effect of the superconducting film. Complete shielding is not observed due to the large demagnetization factor associated with a field applied normal to the groundplane film.

In order to quantitatively characterize the effectiveness of the ground plane, we fabricated direct-injection SQUIDs, similar to those previously fabricated using step-edge grain boundary junctions.<sup>1</sup> The applied control current,  $I_\Phi$ , flowing through a microstrip portion of the SQUID inductor, is given by  $(I_1 - I_2)/2$ , where  $I_1$  and  $I_2$  are the current injected

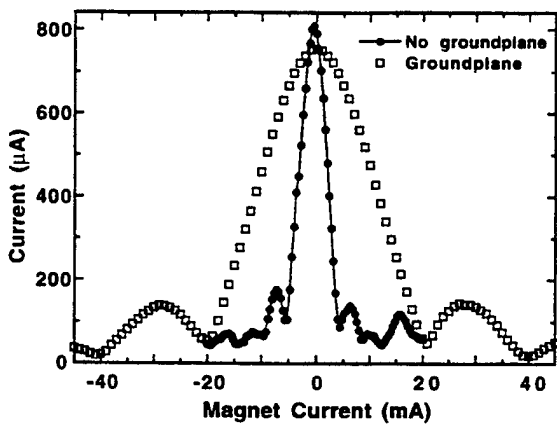


FIG. 3. Plot of critical current vs magnet current for fields normal to the substrate for 4-μm-wide junctions with and without groundplanes at 77 K.

in the left and right ends, respectively, of the inductor. Figure 4(a) shows the SQUID voltage as a function of  $I_\Phi$ , for various fixed values of the total bias current  $I_1 + I_2$ . The period,  $\Delta I_\Phi$ , of these modulation curves is related to the inductance of that portion of the SQUID loop,  $L_\mu$ , by

$$\Delta I_\Phi = \frac{\Phi_0}{L_\mu}, \quad (1)$$

where  $\Phi_0$  is the superconducting flux quantum. By measuring this period as a function of temperature we determined  $L_\mu(T)$ . This is shown, normalized to the inductor length, in Fig. 4(b) for five SQUIDs with varying lengths of microstrip inductor. The inductance per square values obtained are in good agreement with those reported in Ref. 1. Using the expression for the inductance of a strip over an infinite

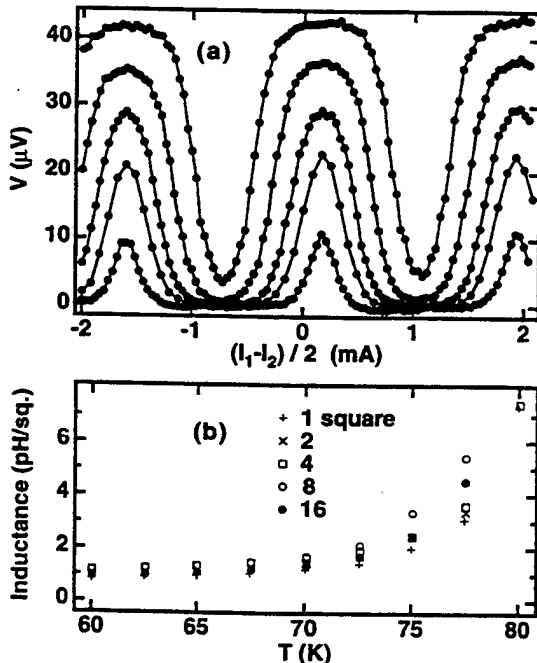


FIG. 4. (a) 77 K voltage modulation as a function of control current for a direct-injection SNS edge junction SQUID with integrated groundplane. The bias currents are 480, 490, 500, 510, and 520 μA. (b) Measured inductance per square for five SQUIDs as a function of temperature.

groundplane, as in Ref. 1, we infer an effective penetration depth, for current and field both in the  $a$ - $b$  plane, of  $\lambda_{a-b} \approx 0.2 \mu\text{m}$  at 65 K, consistent with our previous measurements.

While the period of the voltage modulation is related to the inductance of the microstrip inductor into which the control current is injected, the *depth* of modulation is related to the *total* inductance of the SQUID. Using standard SQUID models,<sup>13</sup> including the effects of thermal fluctuations,<sup>14</sup> we estimate an upper limit (assuming negligible asymmetry in the junction critical currents) on the total inductance of the smallest SQUID of Fig. 4(b) to be about 12 pH at 65 K. The inductance is thus dominated by the 3 μm wide junction legs of the SQUID, and their contacts to ground. Minimizing this unwanted inductance, especially for our relatively high  $J_c$  devices, will require careful layout and junction alignment.

In summary, we have demonstrated high quality SNS edge junctions and SQUIDs integrated with superconducting groundplanes using a circuit-compatible omnidirectional edge formation process. The junctions exhibit  $I_c R_n$  products of 500–800 μV at 65 K with 1- $\sigma$   $I_c$  spreads down to 12%. Effectiveness of the groundplanes was verified by single junction  $I_c$ -modulation studies and by direct injection SQUID measurements. The SQUIDs show voltage modulation of up to 130 μV at 65 K and 40 μV at 77 K, and analysis of the SQUID data gives microstrip inductances of  $\approx 1 \text{ pH}/\square$  at 65 K. These devices are suitable for fabrication of small-scale HTS SFQ circuits and our results in that area will be reported elsewhere.

We would like to acknowledge the assistance of J. Brown, G. Faychak, G. Madia, D. Matuza, R. Nye, S. Pieseski, and J. Uphoff. We also acknowledge useful discussions with A. Kleinsasser, K. Char, H. Mallison, and S. Berkowitz. This work was supported in part by the Air Force Office of Scientific Research, Contract F49620-94-C-0021.

- 1 M. G. Forrester, A. Davidson, J. Talvacchio, J. R. Gavaler, and J. X. Przybysz, *Appl. Phys. Lett.* **65**, 1835 (1994).
- 2 W. H. Mallison, S. Berkowitz, A. Hirahara, M. Neal, and K. Char, *Appl. Phys. Lett.* **68**, 3808 (1996).
- 3 In *IEEE Trans. Appl. Supercond.* **3**, 2621 (1993); E. Reuvekamp, P. Booi, M. Verhoeven, G. Gerritsma, and H. Rogalla use a SNS junction base electrode film as a groundplane.
- 4 S. Miura, W. Hattori, T. Satoh, M. Hidaka, S. Tahara, and J. Tsai, *5th International Superconductive Electronics Conference (ISEC'95) Extended Abstracts*, p. 240 (1995).
- 5 J. R. Gavaler, J. Talvacchio, T. T. Braggins, M. G. Forrester, and J. Gregg, *J. Appl. Phys.* **70**, 4383 (1991).
- 6 J. Talvacchio, M. G. Forrester, and J. R. Gavaler, *IEEE Trans. Appl. Supercond.* **5**, 3139 (1995).
- 7 J. Gao, W. A. M. Aarnink, G. J. Gerritsma, and H. Rogalla, *Physica C* **171**, 126 (1990).
- 8 B. D. Hunt, M. C. Foote, and L. J. Bajuk, *Appl. Phys. Lett.* **59**, 982 (1991).
- 9 K. Char, L. Antognazza, and T. H. Geballe, *Appl. Phys. Lett.* **65**, 904 (1994).
- 10 B. D. Hunt, M. C. Foote, W. T. Pike, J. B. Barner, and R. P. Vasquez, *Physica C* **230**, 141 (1994).
- 11 B. D. Hunt and J. B. Barner, *NASA Tech. Briefs* **20**, 33 (1996).
- 12 K. A. Delin and A. W. Kleinsasser, *Supercond. Sci. Technol.* **9**, 227 (1996).
- 13 C. D. Tesche and J. Clarke, *J. Low Temp. Phys.* **29**, 301 (1977).
- 14 K. Enpuku, Y. Shimomura, and T. Kisu, *J. Appl. Phys.* **73**, 7929 (1993).

# High Temperature Superconducting Space-Qualified Multiplexers and Delay Lines

Salvador H. Talisa, *Senior Member, IEEE*, Michael A. Janocko, D. L. Meier, John Talvacchio, C. Moskowitz, D. C. Buck, R. S. Nye, S. J. Pieseski, and George R. Wagner

(Invited Paper)

**Abstract**—A high temperature superconducting (HTS) four-channel multiplexer and a delay line were fabricated, space qualified and tested as part of the U. S. Navy's High Temperature Superconductivity Space Experiment II (HTSSE-II). The multiplexer had an architecture that included two branch-line hybrids and two identical parallel-coupled line filters per channel. Its operation was centered at 4 GHz, with 50-MHz-wide channels. It was fully integrated, with microstrip interconnections between channels and thin-film load terminations in the out-of-phase port of the output hybrid. The delay line was made up of two cascaded modules for a total delay of 45 ns between 2 and 6 GHz. Both devices were made using 5-cm-diameter  $\text{LaAlO}_3$  wafers coated with epitaxial thin film  $\text{YBa}_2\text{Cu}_3\text{O}_7$ , on both sides in the case of the delay line. Both devices operated at 77 K.

## I. INTRODUCTION

MICROWAVE multiplexers and delay lines are of interest in communications as well as radar and electronic warfare (EW) systems. Some of these applications have insertion loss requirements that make the use of high temperature superconductors (HTS) an attractive alternative to much bulkier conventional technology, specially in space-borne systems, where weight and volume are very expensive.

The high temperature superconductivity space experiment II (HTSSE-II) will provide an excellent vehicle for testing the technology with a view to applications not only in space systems but others as well, which would benefit from the rigorous testing and manufacturing schedule imposed by the program.

In this paper we discuss our participation in HTSSE-II with two HTS microwave components: A four-channel bandpass multiplexer and a 45 ns delay line. The design characteristics of both devices are given in Table I.  $\text{YBa}_2\text{Cu}_3\text{O}_7$  (YBCO) thin films deposited epitaxially by off-axis sputtering on single-crystal  $\text{LaAlO}_3$  (LAO) substrates were used to fabricate the devices, intended for operation at 77 K.

Only a handful of groups have published work on HTS bandpass multiplexers. Fathy *et al.* discussed the multiplexing

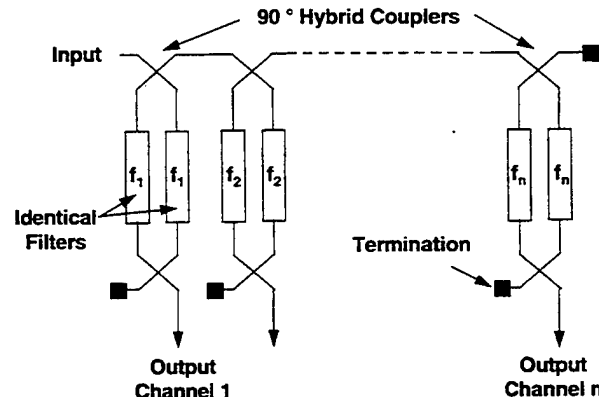


Fig. 1. HTS multiplexer architecture.

of HTS bandpass filters using ferrite circulators at cryogenic temperatures, but only included preliminary results in their paper [1]. The group lead by Mansour [2]–[5] have reported work on several types of multiplexers, including hardware delivered to the HTSSE-II program [5]. A comparison of conventional and HTS multiplexers is also given in [5].

Work on superconducting delay lines, on the other hand, started at Lincoln Laboratory well before the advent of high temperature superconductivity [6], and concentrated mostly on linearly dispersive delay lines for analog signal processing. Work on HTS nondispersive delay lines has taken place since [7]–[12], including two recent instantaneous frequency measurement subsystems based on banks of delay lines [9], [12]. A comparison between conventional and HTS nondispersive delay lines is given in [14].

Earlier accounts of the work to be presented here were given in [13] and [14]. In the present paper we elaborate on aspects related to the specific devices delivered to HTSSE-II and how we arrived at their final versions, including design, fabrication and test data not provided before.

## II. MULTIPLEXERS

### A. Design

The design goals for the four-channel multiplexer are listed in Table I. The multiplexing architecture chosen is shown in Fig. 1. It can accommodate as many channels as the bandwidth of the 90° hybrid coupler covers. Multiplexer architectures

Manuscript received November 27, 1995; revised March 6, 1996. This work was supported in part by the Naval Research Laboratory, Contract N00014-92-C-2043, and the Advanced Research Projects Agency through the Office of Naval Research, Contract N00014-91-C-0112.

The authors are with Northrop Grumman Corporation, Electronic Sensors and Systems Division, Science and Technology Center, Pittsburgh, PA USA. Publisher Item Identifier S 0018-9480(96)04796-5.

TABLE I  
MULTIPLEXER AND DELAY LINE DESIGN CHARACTERISTICS

Multiplexer	
Architecture (each channel):	Two 90° hybrids and two filters
Configuration:	Microstrip
Filter type:	Chebychev
Filter order:	4
Maximum passband ripple:	0.1 dB
Ripple bandwidth:	50 MHz
Topology:	Parallel $\lambda/4$ coupled sections
Guard band:	16 MHz
90° Hybrid type:	Branch-line
Channel #	Center Frequency (MHz)
1	3901
2	3967
3	4033
4	4099
Delay Line	
Configuration	Stripline
Frequency Range	2 GHz - 6 GHz
Delay	> 40 ns
Insertion Loss	< 1 dB

based on one filter per channel are generally limited to a maximum of ten or twelve channels. The effect of multiplexing on the filter responses and the need to introduce guard bands between channels was discussed in [13]. A 16 MHz guard band was introduced in order to mitigate this effect.

The hybrid coupler used in this project was of the branch-line type. It is a 10% bandwidth coupler which sufficed to cover the four-channel bandwidth. More sophisticated coupler designs can be used for wider bandwidth coverage.

A four-pole quarter-wavelength parallel-coupled section microstrip topology with 500- $\mu$ m-thick LAO was chosen for the channel filters. The filter structure and design parameters are shown schematically in Fig. 2. Because of the requirement to work at 4 GHz, which makes the filters relatively large, it was necessary to establish the practical constraint of having each filterbank channel fit on a 5-cm-diameter wafer. Other filter topologies or even thinner LAO substrate wafers could have been used to minimize the filter area. However, we adopted a conservative approach and chose the configuration in Fig. 2 based on previous experience [15], [16].

From calculated estimates of the insertion loss for the required 50 MHz bandwidth (1.25%) filter (see Fig. 3 in [13]),

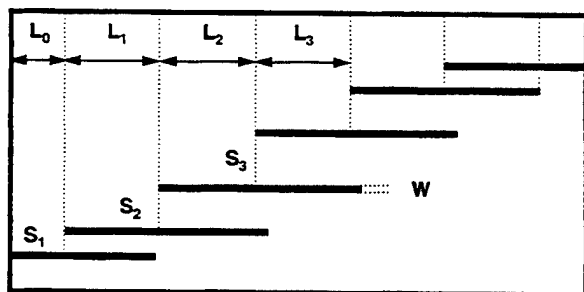


Fig. 2. HTS multiplexer filter topology.

it was decided that superconducting ground planes were not as critical as when working at higher frequencies. Hence, plated gold ground planes were used, with an insertion loss expected to be around 0.8 to 1 dB for YBCO films with  $R_s$  between 0.5 and 1.5 m $\Omega$  (at 10 GHz and 77 K).

A first, prototype version of the multiplexer was made prior to the final flight unit, to test our design and packaging concepts. The final version comprised a revision of the design and the overall fabrication and packaging approaches. The

TABLE II  
MULTIPLEXER VERSION DIFFERENCES

	Preliminary	Final
<b>Channel Interconnect</b>	External	Internal (microstrip)
<b>Terminations</b>	External (coaxial)	Thin film (integrated)
<b>Electrical Design</b>	Circuit model software	Circuit model and EM field solver softwares
<b>Package</b>	All niobium	Niobium and aluminum
<b>Device</b>	Prototype	Qualification and Flight Units

TABLE III  
LOOK-UP TABLE HTS FILTER DESIGN APPROACH

Step 1	Start with conventional approach design using circuit-model-based software
Step 2	Generate parallel coupled microstrip line Look-Up Table using EM field solver
Step 3	Interpolate table to obtain required coupling gap
Step 4	Analyze resulting filter using EM field solver
Step 5	Compute length correction for each section based on center frequency offset
Step 6	Iterate process. Go back to Step 4

TABLE IV  
COMPARISON BETWEEN CONVENTIONAL AND LOOK-UP TABLE APPROACHES  
 $W = 0.176$  mm  $L_1 \cong L_2 \cong L_3 \cong 4.788$  mm

Parameter	Required Coupling (dB)	Touchstone™ (mm)	Look-Up Table (mm)
$S_1$	-17.6	0.572	0.530
$S_2$	-35.8	2.367	1.931
$S_3$	-37.8	2.772	2.161

final filter design technique was developed based on iterations between conventional software tools, which use empirical models of microwave circuit elements, and an electromagnetic field solver. The differences between the preliminary and the final devices are listed in Table II.

The design for the preliminary version followed a conventional approach [15], [16]. The software Touchstone™ was used. As will be seen below, however, this yielded unsatisfactory results and a more sophisticated approach was developed, using the EM analysis software Sonnet™. This approach was based on the generation of a look-up table for the coupling parameters of edge-coupled lines [17]. The steps followed are summarized in Table III.

The conventional and the look-up table approaches resulted in substantially different filter dimensions as can be appreciated from Table IV, with reference to Fig. 2.

The reason for the discrepancy and for the inadequacy of the conventional design tools is that the range of validity of the empirical circuit models these tools are based on is rather

limited. Thus, the LAO substrate relative dielectric constant of 23.4 is higher than the values most of these models can support. In addition, the coupling values required for narrow band HTS microstrip filters of the type discussed here are smaller than these models can support. Hence the increasing discrepancy between conventional and the more involved look-up table approaches as the required coupling decreases.

Thin film load terminations were used for the out-of-phase port of the output hybrid coupler in every channel of the final version of the multiplexer (see Fig. 1). These terminations followed a simple design based on a resistive thin film and a shunt capacitance to ground to resonate out the inductance in the resistor section [13].

#### B. Mask Layout and Wafer Fabrication

The mask layout for each channel of the preliminary version multiplexer included only the channel. As the fabrication process and its monitoring were better understood by the time

TABLE V  
PROCESS SEQUENCE FOR FINAL VERSION OF HTS MULTIPLEXER  
SUBSTRATE IS 5-CM-DIA., 500- $\mu$ m-THICK LaAlO<sub>3</sub>, WITH YBCO ON ONE SIDE

Mask	Description	Material	Thickness	Process
1	Contact to YBCO	Au	2000 $\text{\AA}$	Lift-off
	Contact anneal	Au on YBCO	N/A	550°C
None	Ground plane base	Cr/Au	200/2000 $\text{\AA}$	Sputter
	Ground plane thick metal	Au	2 $\mu$ m	Electroplate
2	Filter	YBCO	4000 $\text{\AA}$	Ion mill
3	Resistor	Mo/Ti	1140/100 $\text{\AA}$	Lift-off
4	Capacitor and contact pads	Cr/Au	200/2000 $\text{\AA}$	Lift-off

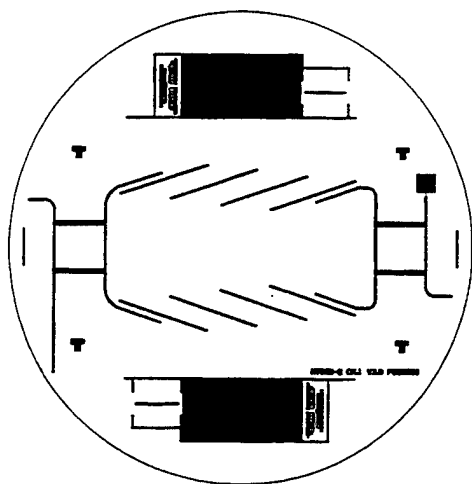


Fig. 3. Mask layout for channel 1 of the final HTS multiplexer. Mask includes microstrip transition chips for channel interconnection and post-processing test patterns.

the final version was designed, the corresponding mask layout, shown in Fig. 3, included several test patterns which allowed assessing and monitoring the YBCO quality during and after processing. The final version also had internal channel-to-channel interconnections and so the mask layout included microstrip line sections used for the connection.

The fabrication techniques used for the final device were more elaborate than for the preliminary one because of the integrated load terminations. However, the processing of wafers for the final version was more stable and reliable, as better techniques were developed for each of the fabrication steps needed.

The processing sequence used to fabricate the channels of the final version of the multiplexer comprised five major steps, requiring four mask levels, in addition to the step in which the filter chip is sown from the wafer. The sequence is summarized in Table V. The fabrication steps followed for the preliminary version were a subset of those shown in Table V, since only YBCO patterning and annealed contact

TABLE VI  
YBCO CHARACTERISTICS MEASURED AFTER PROCESSING

Wafer #	$R_s$ (m $\Omega$ ) <sup>*</sup> (10 GHz, 77 K)	YBCO Sheet Resistance (300 K) ( $\Omega/\text{sq}$ )	$J_c$ (A/cm $^2$ )	$T_c$ (K)
1	0.72	7.5	$10^6$	87
2	1.4	8.1	$2.2 \times 10^6$	90.3
3	2.97	15.7	$2.7 \times 10^5$	82
4	N/A	8.5	$1.2 \times 10^6$	86.4

<sup>\*</sup>Surface resistance measured with parallel plate resonator.

definition were required. Therefore only the fabrication of the final version will be discussed in detail here.

The starting wafer was LAO, 5 cm in diameter and 500  $\mu$ m thick, coated on one side with YBCO. Generally, the surface resistance of the YBCO film was measured at 77 K before processing was initiated to ensure that the starting film was of high quality. Au contacts were defined using lift-off (image-reversal lithography) of sputtered Au in the first mask level. The Au was then annealed into the YBCO at 55°C in a flowing-oxygen ambient. The ground plane was formed on the uncoated side of the substrate by sputtering Cr/Au (Cr promotes adherence between Au and LAO) and then plating an Au layer to adequate thickness (2  $\mu$ m). The second mask level was required for patterning the YBCO film into the filter structure by argon ion milling. The 50- $\Omega$  resistors were defined by lift-off in the third mask level. The resistor material was Mo, with a Ti capping layer to protect the Mo from oxidation under ambient conditions. The capacitance structure, which acted as an RF short from the load resistor to the ground plane, was created in the final mask level. Contact pads for test patterns on the wafer were also formed in this step.

The test patterns on the wafer allowed post-processing measurements of  $T_c$ ,  $J_c$ , and RF surface resistance of YBCO, Mo/Ti sheet resistance, and Au/YBCO contact resistance. In particular, the RF surface resistance was measured using a parallel-plate resonator technique [18]. Table VI shows the results of the post-processing measurements of the YBCO characteristics on four sample wafers. Table VII shows all

TABLE VII  
ADDITIONAL WAFER CHARACTERISTICS MEASURED AFTER PROCESSING  
(SEE TABLE VI FOR POST-PROCESSING YBCO CHARACTERISTICS)

Wafer #	Au/YBCO Contact Resistance <sup>(2)</sup> (77 K)( $\Omega$ /sq)	Mo/Ti Sheet Resistance (300 K)( $\Omega$ /sq)	Mo/Ti Sheet Resistance <sup>(1)</sup> (77 K)( $\Omega$ /sq)	Mo/Ti Sheet Resistance Ratio
1	$10^{-6}$	2.31	1.4	1.65
2	$1.5 \times 10^{-7}$	2.69	1.85	1.45
3	$7 \times 10^{-5}$	2.51	1.6	1.57
4	$1.2 \times 10^{-4}$	3.02	2.12	1.43

Notes:  
1. Mo/Ti sheet resistance target value was 1  $\Omega$ /sq. Variance not critical to filter performance.  
2. Au/YBCO contact resistance correlates with substrate cleaning technique prior to Au sputtering:  
Wafer 1 and 2 were ion milled; Wafers 3 and 4 cleaned by back-sputtering.

other characteristics measured. Notice that there is good correlation between the measured superconducting properties of the YBCO film ( $R_s$ ,  $T_c$ , and  $J_c$ ) and the YBCO sheet resistance at room temperature. From these results a simple process monitoring technique was developed, using a four-point-probe measurement at room temperature as a valid check for the film quality at every step of the fabrication.

### C. Packaging and Assembly

A major element of the packaging of the multiplexer and the delay lines was the need to house microwave circuitry fabricated on large area substrates. A significant milestone in this effort was the adoption of niobium as the thermal-expansion-matched carrier material for the LAO substrates. The LAO substrates were attached to the niobium carriers using thin indium sheets. Other important elements in the development of the packaging approach used were the adaptation of the gold plating technique used for stainless steel to niobium parts and the use of Wiltron K-connectors. Hermetic sealing was considered at first but was later dropped as a requirement when it became evident that good quality YBCO films do not degrade upon long exposure to even humid atmosphere.

Niobium was used for all package components in the preliminary version of the multiplexer. However, this resulted in a very heavy package which, nevertheless, demonstrated the viability of the entire concept under development. The niobium carrier-LAO substrate assembly was then attached to a niobium frame carrying the connectors by means of soldering with indium strips placed along ledges on the frame. All pieces were gold plated. The four-channel multiplexer consisted of four packages housing individual channels connected externally using semirigid coaxial cable. The entire assembly was then mounted on a copper plate for mechanical support and to facilitate cooling. The weight of the prototype device was 1.5 kg.

A significant improvement was added to the packaging of the flight device, however, by using aluminum as the major framework material for the package. Niobium carriers were still used to mount the patterned LAO substrates; however, the carrier-substrate assemblies were then mounted in an aluminum frame with the connectors by means of special springs attached to the frame. The springs accommodated the difference in thermal contraction between the niobium

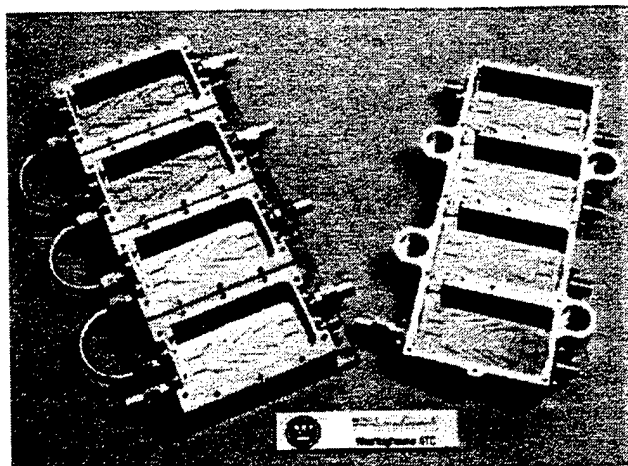


Fig. 4. Photograph of the prototype and final multiplexers.

carriers and the aluminum frames. The use of springs also resulted in relaxed internal dimensional tolerances and made mounting and demounting the carrier-substrate assemblies much easier. Top and bottom package lids were also made in aluminum. Further lightening of the package was achieved by removing material from the underside of the carriers, leaving a ribbed pattern to maintain mechanical strength. The result was a significantly (64%) lighter package than the all-niobium prototype, and a much more versatile and reliable packaging technique.

The prototype multiplexer channels were made each with four external connections that allowed thorough testing before assembly into a multiplexer. Fig. 4 is a photograph where both the prototype and the final multiplexers are shown side by side for comparison. The external coaxial 50- $\Omega$  terminations and interconnections between channels and the mounting plate can also be seen. The package of the final unit delivered includes mounting holes required by the space system integrator. Short microstrip sections on individual substrate pieces, described in the previous section, were used as interconnections between channels in the final device. The mounting technique for these interconnect pieces was optimized in a separate dual-channel package. Fig. 5 is a close-up photograph of the interconnect, made up of a separate microstrip line section mounted between two channel sections. Gap-welded gold ribbon was used for these interconnections as well as for the contact between the coaxial connector center pin and the YBCO microstrip lines.

### D. Experimental Results and Discussion

Fig. 6 shows a composite response for all four channels of the prototype multiplexer measured between 3.5 and 4.5 GHz at 77 K. The markers indicate the design goals for the center frequencies. The response of this prototype device was clean enough to show the viability of our overall approach. The deep notch on the lower skirt of the fourth channel is due to interaction with the previous channel; notice that the notch occurs in the center of the previous channel.

The measured responses for the channels in the final flight device were given in [13]. Fig. 7, the composite for all four

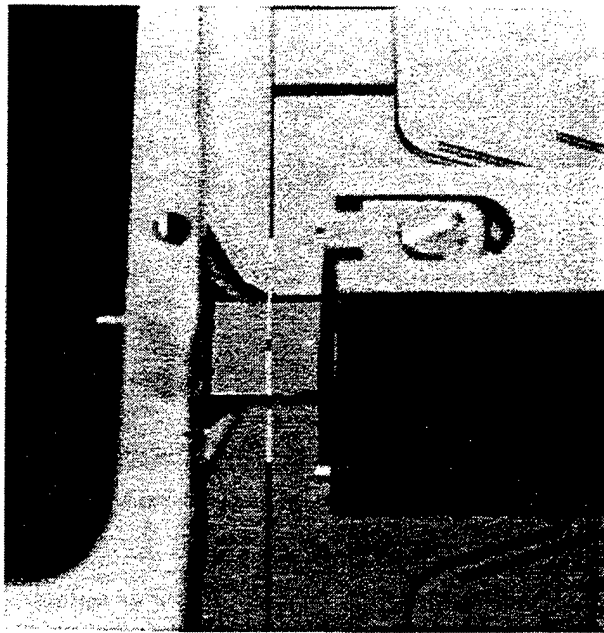


Fig. 5. Close-up photograph of the microstrip channel interconnection in the flight HTS multiplexer.

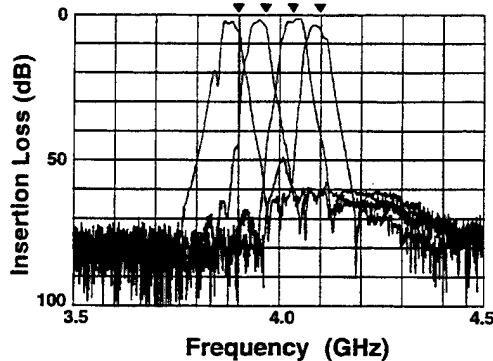


Fig. 6. Composite response of all four channels of the prototype multiplexer. The markers indicate the design center frequencies.

channels measured between 3.5 and 4.5 GHz at 77 K, is reproduced here for completeness. The notches on the lower skirts of channels 2-4 are due to the multiplexing effects discussed in [13]. The passbands are much cleaner and uniform than for the prototype device, and their shapes are much closer to the designed Chebychev response.

Fig. 8 shows the same composite response as in Fig. 7 but on an expanded vertical scale (2 dB/div). The markers are placed on the design goal center frequencies (see Table I). The insertion losses measured for all the channels is relatively high, around 2 dB, which is about 1 dB higher than expected from calculations of mid-band filter loss at 4 GHz using a gold ground plane (see Fig. 3 in [13]). Return loss data did not clearly shed light on the cause for the excess loss, because the input and output ports of the multiplexer are always looking into a  $50\Omega$  characteristic impedance, within the bandwidth covered by the multiplexer (see Fig. 1).

The reason for this excess loss was traced to an effective detuning, relative to each other, of the filters in a given

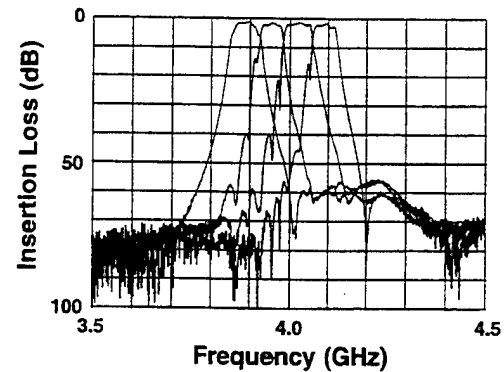


Fig. 7. Composite response of all four channels of the flight multiplexer.

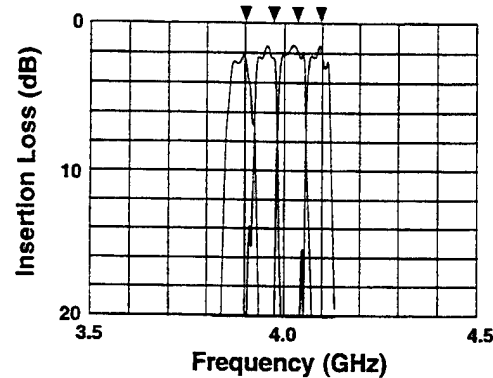


Fig. 8. Composite response of all four channels of the flight multiplexer, shown on an expanded 2 dB/div scale. The markers indicate the design center frequencies.

channel. Computer simulations using the ideal, lossless model of the channels, showed that center frequency offsets of 10 to 15 MHz are sufficient to produce an interference distortion in the passband. The resulting cancellation of energy yields a response that has a finite insertion loss which increases with the center frequency offset. This is shown in the series of plots in Fig. 9, made for different center frequency offsets between both filters in a channel. We conducted a systematic experimental and analytical search on the possible causes for this difference in center frequency between two filters in a channel. Table VIII shows the results of an analysis on the sensitivity of filter center frequency with respect to geometrical parameters and dielectric constant, assuming that only one at a time deviates from design. From Table VIII, a variation of  $25\ \mu\text{m}$  in substrate thickness causes a 5 MHz shift in center frequency, which is 10% of the design bandwidth (Table I). LAO substrate thickness was surveyed in our stock of both patterned and as yet unused wafers. It was found that the thickness was uniform to within  $3\ \mu\text{m}$  but that it was not uncommon to find substrates that were as much as  $25\ \mu\text{m}$  above or below the nominal  $500\ \mu\text{m}$  thickness. Although this is of serious concern in the future production of filters with accurate center frequencies, the substrate thickness nonuniformity was found to be too small to cause the shift in center frequency between the two filters on a channel.

The planar geometrical parameters, that is, the width and length of the resonators in a filter were found to require

TABLE VIII  
SENSITIVITY ANALYSIS OF A MICROSTRIP HTS FILTER CENTER FREQUENCY VARIATIONS. THE FILTER IS ASSUMED TO BE MADE UP OF RESONATORS WITH THE FOLLOWING CHARACTERISTICS:  $f_o = 4$  GHz ( $L = 1.001$  cm),  $\epsilon_r = 23.4$  (77 K),  $h = 508$   $\mu$ m,  $w = 176$   $\mu$ m,  $t = 0.4$   $\mu$ m

$\Delta\epsilon_r$	$\Delta h$	$\Delta w$	$\Delta L$	$\Delta f_o$
+0.1%	0	0	0	+2 MHz
0	+25 $\mu$ m	0	0	+5 MHz
0	0	+10 $\mu$ m	0	-5 MHz
0	0	0	+10 $\mu$ m	-4 MHz

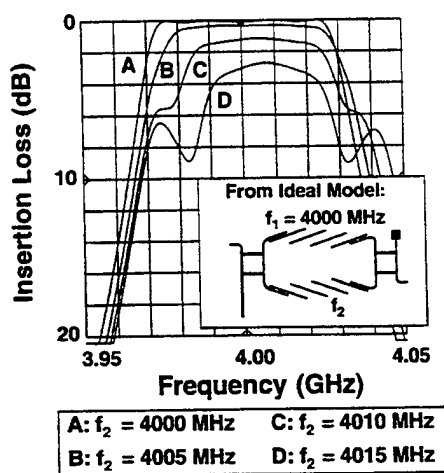


Fig. 9. Analysis from ideal channel model showing the effect of center frequency offsets between the two filters in a channel.

deviations from design that were too large to arise from tolerances in the standard photolithographic patterning process used to fabricate the filters.

As for the dielectric constant, Table VIII gives an idea of the effect of a change in  $\epsilon_r$  from substrate to substrate. Because the single crystal LAO substrates show a twinning effect that might give rise to local nonuniformities in dielectric constant, this effect was considered further as a possible reason for filter-pair detuning in a channel. Fig. 10 summarizes the analysis conducted. A worst-case scenario was assumed in which deviations from nominal  $\epsilon_r$  of 0, 1, and 2% were considered to occur in the weakest (and most sensitive) coupled section of the filter. It can be concluded from these plots that a significant alteration in the channel passband occurs for  $\Delta\epsilon_r$  between 1 and 2%. These are rather large values. Independent measurements of the relative dielectric constant nonuniformity in LAO substrates give values between 0.5 and 1% [19]. Nevertheless, this effect cannot be ruled out as yet and further research is needed in this area. It must be added that localized defects in the HTS films could cause the same effects as a local variation in dielectric constant.

Our experimental observations with a number of samples fabricated for this work support a different reason for the

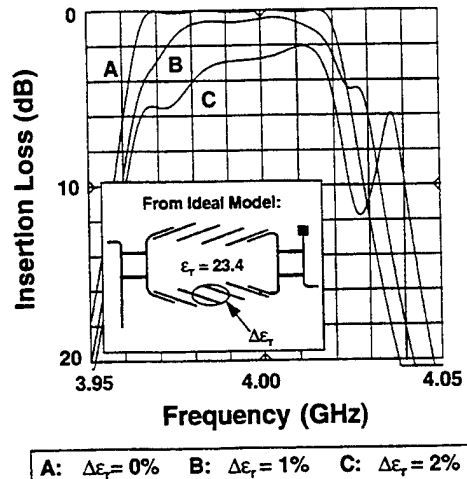
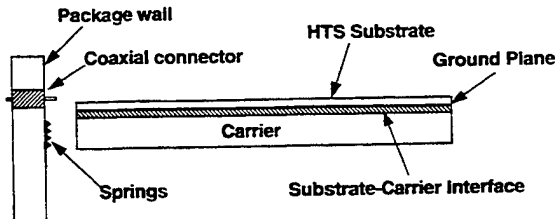


Fig. 10. Analysis from ideal channel model showing the effect of local changes in the substrate dielectric constant. This is a worst case where the change occurs in the weakest (most sensitive) coupled section.



Ground Return Path:

Ground Plane  $\Rightarrow$  Carrier  $\Rightarrow$  Springs  $\Rightarrow$  Coaxial Connector Outer Shield

Fig. 11. Schematic representation of the ground-current path. This diagram applies to both the HTS multiplexer and the delay line.

passband shapes and loss observed. We believe that the cause lies in the contact between the substrate ground plane and the package. Ground currents flow back to the coaxial connectors via the connection formed at the interface between the ground plane on the substrate and the carrier and then through the springs on the package frame. This is depicted schematically in Fig. 11. Our conclusion, from measurements after mounting and remounting several substrates patterned with multiplexer channels, is that the technique used to attach the substrates to the carriers in our packages, at the time this work was performed, needed further improvement to realize the full potential of High Temperature superconductivity. Spurious reactances caused by faulty ground contacts resulted in the somewhat degraded filter responses obtained.

### III. DELAY LINES

#### A. Design

The design goals for the delay line are given in Table I. The final flight delay line unit delivered to the Navy was evolved from three delay line versions. All three designs were based on the same doubly-wound stripline spiral defined on a 5-

TABLE IX  
PROCESS SEQUENCE FOR FINAL VERSION OF HTS DELAY LINE  
SUBSTRATES ARE 5-cm-DIA., 250- $\mu$ m-THICK LaAlO<sub>3</sub>, WITH YBCO ON ONE SIDE

Mask	Description	Material	Thickness	Process
<b>Bottom Wafer</b>				
None	Ground plane contact	Au	2000 Å	Sputter
	Contact anneal	Au on YBCO	N/A	550°C
1B	Contact to YBCO spiral	Au	2000 Å	Lift-off
	Contact anneal	Au on YBCO	N/A	550°C
2B	Delay line spiral	YBCO	4000 Å	Ion mill
<b>Top Wafer</b>				
None	Ground plane contact	Au	2000 Å	Sputter
	Contact anneal	Au on YBCO	N/A	550°C
2T	Delay line spiral (image)	YBCO	4000 Å	Ion mill
3T/B	Ground plane openings	Au/YBCO	2000/4000 Å	Ion mill

cm-diameter, 250- $\mu$ m-thick LAO wafer [14]. A discussion of why the stripline configuration was chosen over microstrip or coplanar waveguide is given in [14].

In all three versions, a  $-50$  dB backward coupling between windings was used, corresponding to a spacing of 900  $\mu$ m. The total delay on a 5-cm diameter wafer pair (stripline) was 22 ns, corresponding to a total delay line length of approximately 150 cm. The total required delay of greater than 40 ns was obtained by cascading two 22 ns delay line modules. Films on both surfaces of each LAO substrate were required in order to obtain the lowest insertion loss possible.

An initial version of the delay line was designed in which a  $50\Omega$  line was defined on only one of the substrate surfaces that come in contact to form the stripline structure. Because of the high dielectric constant of LAO, a  $50\Omega$  line is only 22  $\mu$ m wide on 250- $\mu$ m-thick substrates. This design was rejected early on because of practical difficulties in patterning such a long, narrow line without breaks due to film or fabrication defects.

A second version was then designed in which the line was widened to 150  $\mu$ m ( $27\Omega$ ) using 5-cm-long tapered impedance transformers at the input and output [20]. This solved the problem of low fabrication yield by making the line much less sensitive to small defects. Devices made with this design showed unacceptably high amplitude and phase ripple, however. The cause was traced to the effect of small air gaps between the contacting substrates making up the stripline structure. This effect was discussed in [14]. In order to avoid the deleterious effect of air gaps, mirror-image versions of the wider spirals described above were defined on both mating surfaces [20], [21]. Periodic contact between these two spirals then sufficed for good electrical characteristics. A short section of coplanar waveguide was inserted between the stripline and the coaxial connectors at the ends in order

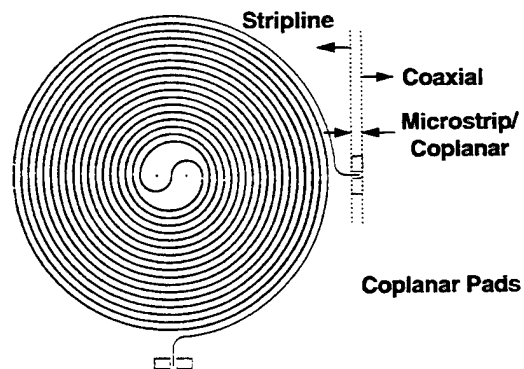


Fig. 12. Spiral stripline pattern for the bottom substrate of the HTS delay line.

to facilitate the in-phase excitation of currents in both the upper and lower stripline ground planes and thus obtain good broad-band input/output matching [14].

#### B. Mask Layout and Fabrication

Fig. 12 shows the mask layout for the bottom wafer of a 22-ns delay line module [14]. Notice the coplanar transition and the taper from 22  $\mu$ m ( $50\Omega$ ) to 150  $\mu$ m ( $27\Omega$ ). The top wafer pattern is similar, but the spiral pattern begins after the impedance transformer in order to make alignment with the bottom wafer pattern less critical.

Processing of two wafers with YBCO on both sides was required, as summarized in Table IX. The bottom wafer had input and output contacts to its YBCO spiral, while the top wafer had no gold contacts. Both wafers had an annealed gold contact layer on the YBCO ground plane side. Processing was similar to that for the multiplexer discussed above.

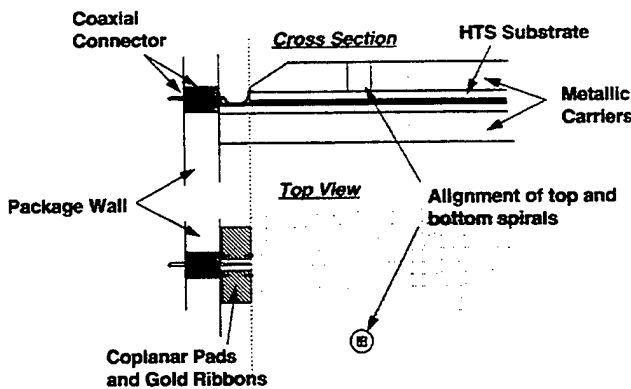


Fig. 13. Schematic diagram of the delay line coplanar transition and the alignment technique. For further details on the package refer to [14].

In order to align the mirror-image spiral patterns on top and bottom wafers during assembly, rectangular openings were milled into the ground plane of the top wafer opposite to alignment marks patterned on the spiral side. Since the LAO substrate is transparent, alignment marks on the fronts of the bottom and top wafers (i.e., the contacting surfaces) were visible through these rectangular openings on the ground plane, and matching openings in the top carrier, during delay line assembly. This is shown schematically in Fig. 13. Alignment of mirror-image spiral patterns will be discussed further in the next section.

The RF surface resistance at 77 K was measured for both sides of both wafers before fabrication began. The side with the lowest surface resistance was chosen as the spiral side.

#### C. Packaging and Assembly

Most of the packaging considerations applying to the filters also applied to the delay lines. But in contrast to the single-substrate microstrip filters, the stripline delay line required two contacting substrates for each device, half the thickness of those used for the multiplexer. An initial all-niobium package version was used for the early versions of the delay line design. However this package was upgraded to one similar to the final version of the multiplexer, using niobium only for the substrate carriers and aluminum for the frames with the connectors and for the lids. The carrier-substrate assemblies were also held on the aluminum frames by means of the same type of serrated springs attached to the frames.

Many of the packaging details used in the delay line were presented in [14]. A key feature of the package was the ability to accommodate and allow the alignment of the mirror-image spirals. The package incorporated a spiral spring contact around the periphery of the two substrates to make ground contact between the top and bottom carriers. The carriers were designed to allow slight differential lateral or rotational motion between upper and lower substrate-carrier assemblies, so that the contacting spirals could be brought into precise alignment. This was accomplished through the use of a fixture which produced the desired relative motion while fiducial marks on both substrates were brought into registration, as shown schematically in Fig. 13. The alignment was then held by

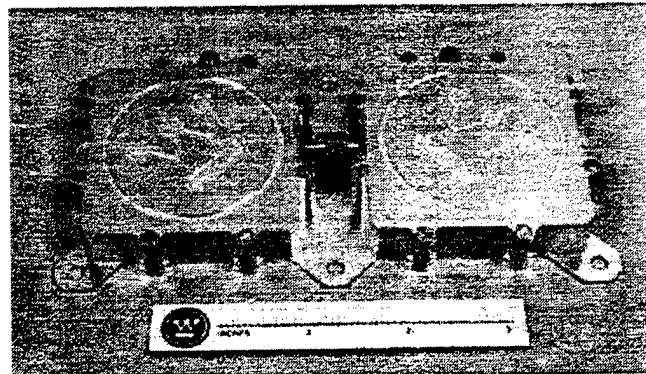


Fig. 14. Flight delay line package delivered to the Navy.

casting molten bismuth-alloy solder into the interstitial space between alignment pins fastened to the bottom carrier and oversized alignment holes in the top carrier (see Fig. 4 of [14]). Pressure was applied by means of nuts and belleville washers on these pins.

The completed assembly was then inserted into the aluminum frame through which Wiltron K-connector glass-bead coaxial feed-throughs led the input and output from the delay line. As with the multiplexer, gap-welded gold ribbon was used to connect the coaxial center pin with the center strip line as well as the coplanar ground pads with the package structure. Fig. 13 shows schematically the transition from coaxial to stripline.

The final flight delay line delivered to the Navy consisted of two of the delay line packages described above, connected in series using male and female K-connectors and mounted on an aluminum plate with appropriate mounting holes. A photograph of the assembly is included in Fig. 14.

#### D. Experimental Results and Discussion

The measured performance of the flight HTS delay line at 77 K between 2 and 6 GHz is given in Fig. 15(a) and (b). There is a notch in the passband at about 5.8 GHz that was traced to a faulty ground plane contact between one of the substrates and its carrier. Similar notches were observed in later delay line samples that were corrected with reseating of the substrates on their carriers by heating up the assemblies.

Nevertheless, the amplitude ripple of this delay line was held to 1 dB or less as shown in Fig. 15(a). The ripple is mostly due to triple-transit between input and output connections. In order to make further improvements in the delay line performance, these transitions must be optimized. As with the multiplexer, ground current returns are of primary importance here as well. This involves both good quality, reliable, and repeatable ground contacting techniques and equalization of top and bottom ground plane current phases in the stripline portion of the delay line. Fig. 15(b) shows a measurement of delay, giving an average of 45 ns.

One of the modules used in the final delivery was tested up to 20 GHz [14], giving excellent performance and establishing the viability of building long delay lines (200 ns or more) using modules similar to these, for wide band applications.

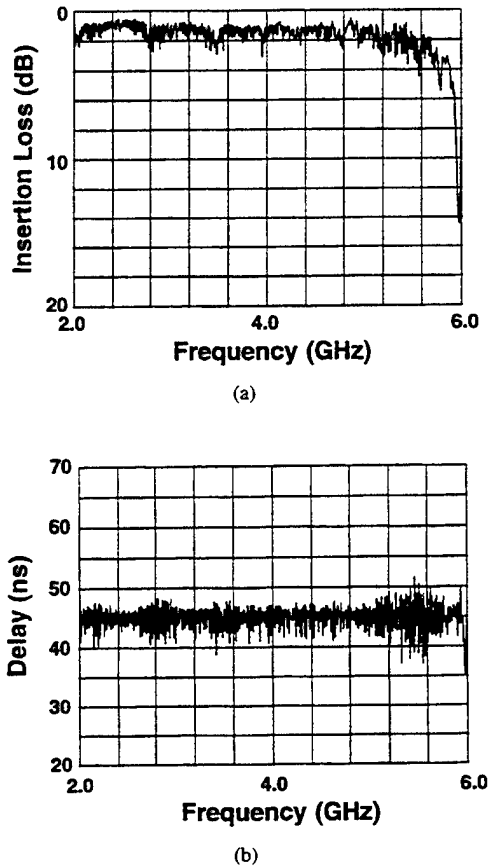


Fig. 15. Response of the flight HTS delay line between 2 GHz and 6 GHz at 10 dB/div scale (a) 2 dB/div scale. (b) Delay versus frequency.

#### IV. CONCLUSION

We have completed successfully the design, fabrication and space qualification of a high temperature superconducting four-channel multiplexer at 4 GHz and a 45 ns, 2-to-6-GHz delay line, both operating at 77 K. The space qualification of these devices was performed at the U.S. Naval Research Laboratory. This represents a milestone on the road toward practical, systems-qualified HTS microwave components. Many technological problems were solved in this effort and while many others remain, these two devices demonstrate the capability for design, fabrication and testing of high-performance, large-area HTS devices.

The ground plane contact between the substrate and the package was identified as a critical issue for obtaining desired loss and passband shape characteristics and will be the subject of future investigations for optimization.

#### ACKNOWLEDGMENT

The authors would like to thank Dr. R. S. Withers, Conductus, Inc., for bringing to their attention the deleterious effects of forward coupling caused by air gaps in stripline delay lines.

#### REFERENCES

[1] A. Fathy, D. Kalokitis, V. Pendrick, E. Belohoubek, A. Pique, and M. Mathur, "Superconducting narrow band pass filters for advanced

multiplexers," in *IEEE MTT-S Int. Microwave Symp. Dig.*, 1993, pp. 1277-1280.

[2] R. R. Mansour, F. Rammo, and V. Dokas, "Design of hybrid-coupled multiplexers and diplexers using asymmetrical superconducting filters," in *IEEE MTT-S Int. Microwave Symp. Dig.*, 1993, pp. 1281-1284.

[3] R. R. Mansour, "Design of superconductive multiplexers using single-mode and dual-mode filters," *IEEE Trans. Microwave Theory Tech.*, vol. 42, pp. 1411-1418, July 1994.

[4] R. R. Mansour, V. Dokas, G. Thomson, W. C. Tang, and C. M. Kudsia, "A C-band superconductive input multiplexer for communication satellites," *IEEE Trans. Microwave Theory Tech.*, vol. 42, no. 12, pp. 2472-2479, Dec. 1994.

[5] R. R. Mansour, S. Ye, V. Dokas, B. Jolley, W. C. Tang, and C. M. Kudsia, "Design considerations of superconductive input multiplexers for satellite applications," *IEEE Trans. Microwave Theory Tech.*, P.E.: X-REF THIS ISSUE.

[6] R. S. Withers and R. W. Ralston, "Superconductive analog signal processing devices," *Proc. IEEE*, vol. 77, no. 8, pp. 1247-1263, Aug. 1989.

[7] Z.-Y. Shen, P. S. W. Pang, W. L. Holstein, C. Wilker, S. Dunn, D. W. Face, and D. B. Laubacher, "High Tc superconducting coplanar delay line with long delay and insertion loss," in *IEEE MTT-S Int. Microwave Symp. Dig.*, vol. 8, 1993, pp. 1235-123.

[8] G. C. Liang, R. S. Withers, B. F. Cole, S. M. Garrison, M. E. Johansson, W. S. Ruby, and W. G. Lyons, "High temperature superconducting delay lines and filters on sapphire and thinned LaAlO<sub>3</sub> substrates," *IEEE Trans. Appl. Superconduct.*, vol. 3, pp. 3037-3042, Sept. 1993.

[9] G. C. Liang, C.-F. Shih, R. S. Withers, B. F. Cole, M. E. Johansson, and L. P. Suppan, "Superconductive digital instantaneous frequency measurement subsystem," *IEEE Trans. Microwave Theory Tech.*, vol. 41, no. 12, pp. 2368-2375, Dec. 1993.

[10] N. Fenzi, D. Aidnik, D. Skoglund, and S. Rohlffing, "Development of high temperature superconducting 100 nanosecond delay line," *SPIE Proc. on High-Tc Microwave Superconduct. Applicat.*, vol. 2156, pp. 143-151.

[11] V. M. Hietala, J. S. Martens, T. A. Plut, C. P. Tigges, T. E. Zipperian, D. S. Ginley, and J. K. Truman, "High temperature superconducting slow-wave coplanar transmission lines with normal-metal crossbars," *IEEE Trans. Microwave Theory Tech.*, vol. 42, no. 6, pp. 972-975, Jun. 1994.

[12] M. Biehl, A. Vogt, R. Herwig, M. Neuhaus, E. Crocoll, R. Lochschmid, T. Scherer, W. Jutzi, H. Kratz, P. Berberich, and H. Kinder, "A 4-bit instantaneous frequency meter at 10 GHz with coplanar YBCO delay lines," *IEEE Trans. Appl. Superconduct.*, vol. 5, no. 2, pp. 2279-2282, Jun. 1995.

[13] S. H. Talisa, M. A. Janocko, D. L. Meier, C. Moskowitz, R. L. Grassel, J. Talvacchio, P. LePage, G. Hira, D. C. Buck, S. J. Pieseski, J. C. Brown, and G. R. Wagner, "High temperature superconducting four-channel filterbanks," *IEEE Trans. Appl. Superconduct.*, vol. 5, no. 2, pp. 2079-2082, June 1995.

[14] S. H. Talisa, M. A. Janocko, D. L. Meier, C. Moskowitz, R. L. Grassel, J. Talvacchio, P. LePage, D. C. Buck, R. S. Nye, S. J. Pieseski, and G. R. Wagner, "High temperature superconducting wide band delay lines," *IEEE Trans. Appl. Superconduct.*, vol. 5, no. 2, pp. 2291-2294, June 1995.

[15] S. H. Talisa, M. A. Janocko, C. Moskowitz, J. Talvacchio, J. F. Billing, R. Brown, D. C. Buck, C. K. Jones, B. R. McAvoy, G. R. Wagner, "Low- and high temperature superconducting microwave filters," *IEEE Trans. Microwave Theory Tech.*, vol. 39, no. 9, pp. 1448-1454, Sept. 1991.

[16] S. H. Talisa, M. A. Janocko, C. K. Jones, B. R. McAvoy, J. Talvacchio, G. R. Wagner, C. Moskowitz, D. C. Buck, J. Billing, R. Brown, "Microwave superconducting filters," *IEEE Trans. Magn.*, vol. 27, no. 2, pp. 2544-2547, Mar. 1991.

[17] J. W. Bandler, R. M. Biernacki, S. H. Chen, P. A. Grobelny, C. Moskowitz, and S. H. Talisa, "Electromagnetic design of high temperature superconducting microwave filters," in *IEEE Int. Microwave Symp. Dig.*, May 1994, pp. 993-996.

[18] R. C. Taber, "A parallel plate resonator technique for microwave loss measurements on superconductors," *Rev. Sci. Instrum.*, vol. 61, no. 8, pp. 2200-2206, Aug. 1990.

[19] M. L. Farich, S. H. Talisa, C. D. Cubbage, F. A. Miranda, and R. Forse, "Measurement of LaAlO<sub>3</sub> dielectric parameter variations," *1996 Appl. Superconduct. Conf.*, submitted.

[20] Dr. R. S. Withers, Conductus, Inc., private communication.

[21] G. L. Matthaei, and G. L. Hey-Shipton, "High temperature superconducting 8.45-GHz bandpass filter for the Deep Space Network," *IEEE MTT-S Int. Microwave Symp. Dig.*, pp. 1273-1276, 1993.



**Salvador H. Talisa** (S'74-M'82-SM'93) obtained the degree of Telecommunications Engineer from the Polytechnic University of Catalonia, Barcelona, Spain in 1976, and the M.Sc. and Ph.D. degrees in electrical engineering from Brown University, Providence, RI, in 1978 and 1982, respectively.

Dr. Talisa joined the Westinghouse Science and Technology Center in 1982, now a department of the Northrop Grumman Electronic Sensors and Systems Division. He worked on microwave and optical applications of magnetic materials. Since 1989 he has been involved in the development of microwave applications of high temperature superconductors and has responsibility for all the programs in this area at the Science and Technology Center.

His early work dealt with the theoretical analysis of ferrite-loaded planar structures for use at microwave frequencies. He later performed feasibility studies for nonreciprocal devices based on surface magnetoplasmons in GaAs-dielectric interfaces for operation at submillimeter wavelengths.

Dr. Talisa is a member of the IEEE Transactions on Microwave Theory and Techniques Editorial Board and of the IEEE Microwave Theory and Techniques Society Committee for Superconducting Microwave Applications (MTT-18). He co-organized the Workshop on Computer-Aided Design of Superconducting Microwave Components and the Workshop on System Applications of high temperature Superconductors and Cryogenic Electronics at the IEEE MTT-S International Microwave Symposia in 1994 and 1995, respectively.



**John Talvacchio** received the B.S. degree in physics from Case Western Reserve University, Cleveland, OH, in 1997 and the Ph.D. degree in applied physics from Stanford University, Stanford, CA, in 1982. His dissertation was a study of the current-carrying limits of superconductors.

Since 1982, he has been with Northrop Grumman Corporation, formerly Westinghouse Science & Technology Center, Pittsburgh, PA, working mainly in the area of materials for superconducting electronics. His publications concern thin-film growth and characterization, electronic device development, surface and interface science, and the fundamental physics of superconductors.

Dr. Talvacchio is a member of the American Physical Society and the Materials Research Society.

**C. Moskowitz**, photograph and biography not available at the time of publication.

**D. C. Buck**, photograph and biography not available at the time of publication.

**R. S. Nye**, photograph and biography not available at the time of publication.

**S. J. Pieseski**, photograph and biography not available at the time of publication.



**Michael A. Janocko** received the B.S. degree in 1964 from Carnegie Institute of Technology and the M.S. degree in 1969 from Carnegie-Mellon University, both in physics.

He has been with Westinghouse Electric (now Northrop Grumman) since 1958 and is presently Fellow Scientist at the Science & Technology Center in Pittsburgh. He has worked in the field of superconductivity since 1968, on both large-scale and small-scale applications. His current area of interest is the fabrication, packaging, and cryocooling of high temperature superconductor thin-film microwave devices.

**D. L. Meier**, photograph and biography not available at the time of publication.

**George R. Wagner** received the B.S. degree in engineering physics from the University of Illinois in 1960 and the M.S. and Ph.D. degrees in physics from Carnegie-Mellon University in 1962 and 1965.

He retired from the Westinghouse Science & Technology Center in December 1994 where he had been since 1960. At the time of his retirement he was Manager of the Superconductor Materials and Electronics Section. He has been active in several areas of research involving the magnetic and optical properties of solids and, since 1975, superconductivity. He is currently a consultant for Northrop Grumman Corporation.

Dr. Wagner has published more than 40 scientific papers. He is a member of Tau Beta Pi and the American Physical Society and serves as a board member of the International Cryogenic Materials Conference.

## Control of meandering grain boundary configurations in $\text{YBa}_2\text{Cu}_3\text{O}_y$ bicrystal thin films based on deposition rate

X. F. Zhang and D. J. Miller

Materials Science Division and Science and Technology Center for Superconductivity, Argonne National Laboratory, Argonne, Illinois 60439

J. Talvacchio

Westinghouse Science and Technology Center, Pittsburgh, Pennsylvania 15235

(Received 8 November 1995; accepted 4 June 1996)

Changing the film deposition rate is shown to be one way to influence the meandering configurations of grain boundaries (GB's) formed in  $\text{YBa}_2\text{Cu}_3\text{O}_y$  (YBCO) bicrystal thin films. The magnitude and wavelength of the meander in YBCO films deposited at two different rates have been characterized by transmission electron microscopy (TEM) and statistically quantified. It has been found that the meander becomes more uniform and considerably less rough in films deposited at lower rates compared to that observed in films deposited at higher rates. A mechanism for the formation of the meandering GB is proposed based on heterogeneous nucleation and three-dimensional (3D) island growth together with overgrowth of the YBCO films across the substrate grain boundary. The different island sizes and tendency for overgrowth induced by changing the film deposition rate are believed to play important roles in controlling the meandering GB configuration. The possible effects of meandering configurations on transport properties are discussed.

### I. INTRODUCTION

It is well known that the weak link behavior of grain boundaries in high transition temperature ( $T_c$ ) superconductors contributes to a lower critical current density ( $J_c$ ) in polycrystalline samples compared with the  $J_c$  carried within individual grains. In order to characterize the transport properties and microstructures of individual grain boundaries (GB's), Dimos *et al.* prepared artificial  $\text{YBa}_2\text{Cu}_3\text{O}_y$  (YBCO) GB's by depositing epitaxial YBCO films on [001] tilt  $\text{SrTiO}_3$  bicrystal substrates.<sup>1</sup> A consistent reduction in  $J_c$  versus increased bicrystal misorientation angle was observed and attributed to dislocation arrays and other microstructural features associated with GB regions.<sup>1</sup> Later studies on YBCO bicrystals by Babcock *et al.* suggested the possibility of a hole depletion zone along the YBCO GB when the misorientation angle was large (28° and 31°), and the weak link effect measured for these grain boundaries was attributed to this hole depletion.<sup>2</sup> The factors affecting  $J_c$  across GB's in polycrystalline YBCO materials were analyzed from the microstructural point of view by Zhu *et al.*<sup>3</sup> Clean grain boundaries free of impurity phases, full oxygenation and good connections between  $\text{CuO}_2$  planes across the GB were identified as critical factors.<sup>3</sup> All of these results suggest a close relationship between transport properties and boundary microstructures in YBCO GB's.

In order to establish the link between the structure of the boundary and the transport properties across

the boundary, electromagnetic measurements and detailed microstructural studies of carefully prepared grain boundaries are required. Frequently, artificially induced grain boundaries prepared by thin film deposition onto bicrystal substrates are used for such studies because of the belief that the structure of the boundary can be controlled by the underlying substrate boundary. Recently, however, TEM investigations demonstrated a meandering configuration for grain boundaries formed in such YBCO bicrystal thin films.<sup>4-7</sup> This phenomenon has been observed in YBCO thin films grown on [001] tilt  $\text{SrTiO}_3$  bicrystal substrates with a variety of misorientation angles (10°, 24°, 36.8°, 45°, 53.2°, and 67°), and has also been observed in YBCO thin films grown on [001] tilt  $\text{Y-ZrO}_2$  bicrystal substrates.<sup>8</sup> The reported deviation of the meandering GB away from the underlying substrate GB varies from a few tens to hundreds of nanometers. The meandering YBCO GB's were shown to consist of symmetrical or asymmetrical segmental facets which may be a few tens to hundreds of nanometers in length. The formation of the meandering YBCO GB's was concluded to be a consequence of initial 3D island nucleation of the YBCO films.<sup>6,7</sup> Islands that nucleate in the vicinity of the substrate GB have some probability of growing across the underlying substrate GB, even though the orientation relationship between the growing island and the substrate must change on the opposite side.<sup>7</sup> Continued deposition leads to a lateral growth of these islands, and when

islands nucleated on one side of the substrate boundary coalesce with those nucleated on the other side of the substrate, the film boundary is formed. The degree of meander is related to the degree in which islands grow over the substrate boundary, and this is, in part, related to the relative difference between the grain boundary and the interfacial energies.<sup>7</sup>

Noting that the magnitude of the meander is related to the island size and overgrowth ability which can be influenced by growth conditions, we supposed that the meandering configuration may be controlled by changing the film deposition rate. Qualitatively, a reduction in the magnitude of meander was observed for a film deposited onto a 24° [001] tilt  $\text{SrTiO}_3$  bicrystal at a lowered deposition rate.<sup>7</sup> However, that work was based on films prepared using two different deposition techniques. In this paper, we present further TEM studies of grain boundaries in YBCO bicrystal films prepared at different deposition rates, in this case using the same deposition technique (sputtering). In addition, we present a statistical characterization of the meander in grain boundaries in these YBCO bicrystal thin films deposited on 36.8° [001] tilt  $\text{SrTiO}_3$  bicrystal substrates. The degree of meander, represented by the amplitude and wavelength of the deviations, was found to be significantly affected by deposition rate.

## II. EXPERIMENTAL

YBCO thin films were deposited on commercially available 36.8° (nominal) [001] tilt  $\text{SrTiO}_3$  substrates by off-axis magnetron sputtering at two different deposition rates. The off-axis sputtering configuration and deposition parameters used to deposit the YBCO films studied here are described elsewhere.<sup>9</sup> Briefly, rf magnetron sputter deposition was performed with a 2-inch diameter stoichiometric YBCO target, a sputter gas composed of 100 mTorr Ar, 50 mTorr  $\text{O}_2$ , and 10 mTorr  $\text{H}_2\text{O}$ , and a growth temperature of 720–730 °C. The axis of the target was oriented 90° from the normal to the substrate. The distance from the center of the target to the substrate was approximately 7 cm. Film growth rates were varied by a factor of 2.5 by changing rf power to the target from 50 to 80 W. The two deposition rates used were  $\approx 4 \text{ \AA/min}$ , referred to here as the higher rate, and  $\approx 1.6 \text{ \AA/min}$ , referred to as the lower rate. Deposition times were adjusted to yield film thicknesses of about 1500 Å. Immediately after growth, films were cooled in 20 Torr of oxygen.

Plane-view TEM samples were prepared by conventional techniques involving grinding, dimpling, and ion milling at liquid nitrogen temperature to final perforation from substrate side. Samples prepared in this manner generally yielded a viewable area of the YBCO GB without any of the underlying substrate remaining.

However, in some samples, both the film GB and the underlying substrate GB were visible in places. TEM characterizations were carried out in both a Philips CM30 and a JEOL 4000EX transmission electron microscope, operated at 200 kV and 400 kV, respectively.

## III. TEM RESULTS

A typical view of the meandering configuration of a GB in a film grown at the lower (1.6 Å/min) rate is shown in Fig. 1. For this image, the sample was intentionally tilted from the [001] direction of the  $\text{SrTiO}_3$  or YBCO by less than 10° to enhance the contrast between grains on the opposite sides of the GB's. Bicrystal GB configurations are more visible under these conditions and all other bright-field images presented in this paper were collected under similar imaging conditions. In Fig. 1, both the  $\text{SrTiO}_3$  substrate GB, indicated by a black arrow, and the YBCO film GB, indicated by a white arrow, are visible. The GB in the film is seen to meander, and the deviation from the underlying substrate GB can be over 100 nm. Note that fluctuations ( $< 30 \text{ nm}$ ) can be observed in the substrate boundary as well. However, the deviations are rare to see in the  $\text{SrTiO}_3$  bicrystals and generally much smaller than what is shown in Fig. 1 so that the substrate boundary may be regarded as straight relative to the GB's observed in the films. Similar small deviations in the  $\text{SrTiO}_3$  bicrystals have also been reported by Seo *et al.*<sup>6</sup>

Figure 2 shows a comparison of the typical meandering GB configurations in YBCO thin films deposited at (a) the higher rate (4 Å/min) and (b) the lower rate (1.6 Å/min). In these images, the straight boundary imaged in the underlying substrate is marked in places with a line. A significant difference between the boundaries in

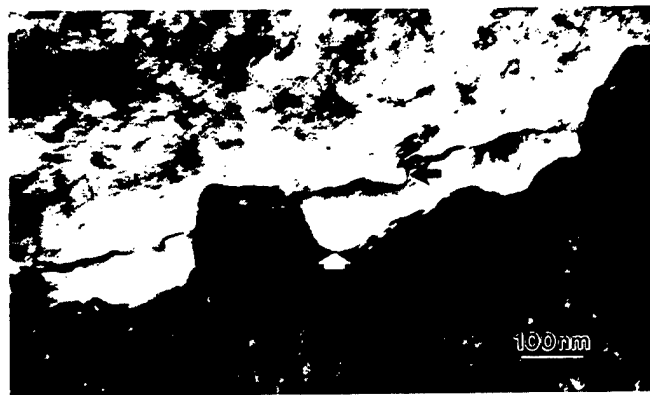


FIG. 1. A bright-field TEM image of a YBCO GB (indicated by a white arrow) and underlying  $\text{SrTiO}_3$  bicrystal GB (indicated by a black arrow). The film was deposited at the lower deposition rate (1.6 Å/min). Both GB's exhibit some meander. The sample is tilted away from the [001] direction of the YBCO film by a few degrees in order to enhance the contrast difference between the film on either side of the GB.

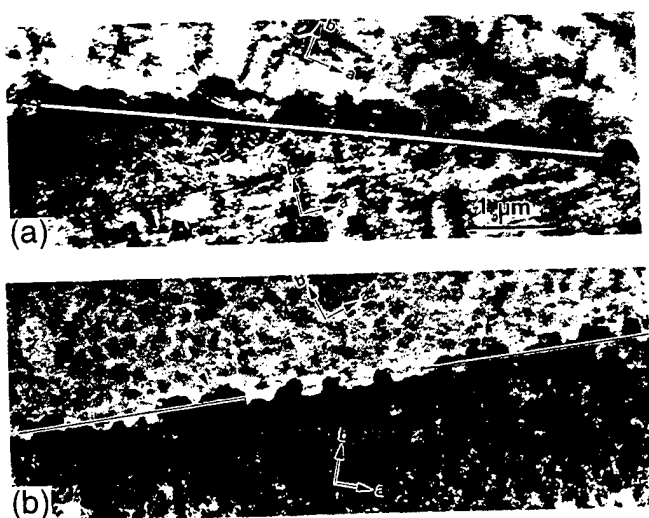


FIG. 2. Low magnification bright-field TEM images obtained from (a) the higher deposition rate film and (b) the lower deposition rate film. The substrate GB's are marked with lines, and the YBCO meandering GB's are indicated by arrowheads. Note the displacement of the boundary from the substrate boundary in the film in (a).

the two films in Fig. 2 is that the GB in Fig. 2(b) is symmetrically oriented along the boundary in the underlying substrate, whereas the GB in Fig. 2(a) is laterally displaced by  $\approx 500$  nm from the substrate boundary. The meandering configuration in Fig. 2(b) is consistent with that reported by other groups,<sup>4-7</sup> and its formation can be explained by the 3D island nucleation and growth model of YBCO films.<sup>6,7</sup> However, the same model cannot fully apply in the case in which the boundary is laterally displaced from the underlying substrate. While the specific mechanism for such a lateral displacement is not clear, we speculate that the specific bicrystal misorientation, especially small deviations from a perfect (001) surface plane, as well as surface morphology may play a role. Actually, our preliminary x-ray diffraction on these samples showed that the (00l) lattice planes of the  $\text{SrTiO}_3$  are not perfectly parallel to the substrate surface plane in both halves of the bicrystals. Instead, the [001] deviates from the surface normal of the  $\text{SrTiO}_3$  substrate by about  $0.5^\circ$  and  $0.9^\circ$  for the  $\text{SrTiO}_3$  bicrystal substrates used for the higher rate and the lower rate film depositions, respectively. Further studies of this aspect are currently in progress.

Selected-area electron diffraction (SAED) was used to establish the epitaxial relationship between the films and the substrate and to confirm the bicrystal geometry. Based on SAED patterns, the *c*-axes of the films are parallel to the [001] direction of the SrTiO<sub>3</sub>, within an experimental error of less than 1°. In addition, SAED patterns were used to measure the rotation angle about [001]. This angle was found to be 36.8° for the film deposited at the lower rate, while it was measured to be 36.0° for the film deposited at the higher rate.

In order to quantitatively characterize the meandering configuration of GB's for the low and high deposition rates used here, various TEM micrographs from both types of film were scanned with a digitizer to obtain numerical data of the position of the boundary as a function of distance. From this data, one can calculate the least square fit (LSF) line for each GB so that the meander amplitude at any given point can be defined as the height of the meander peak with respect to the LSF line. The LSF line rather than substrate GB line is used as the point of reference since the GB may be laterally displaced from the underlying substrate. The results of some of these measurements are shown in Fig. 3. Figures 3(a) and 3(b) correspond to the typical meandering GB segments shown in Figs. 2(a) and 2(b), respectively. In our analysis, we also included measurements from other portions of the grain boundaries which are not shown here. Over a length greater than  $10 \mu\text{m}$ , a rather uniform amplitude distribution can be seen in Fig. 3(b) (the lower

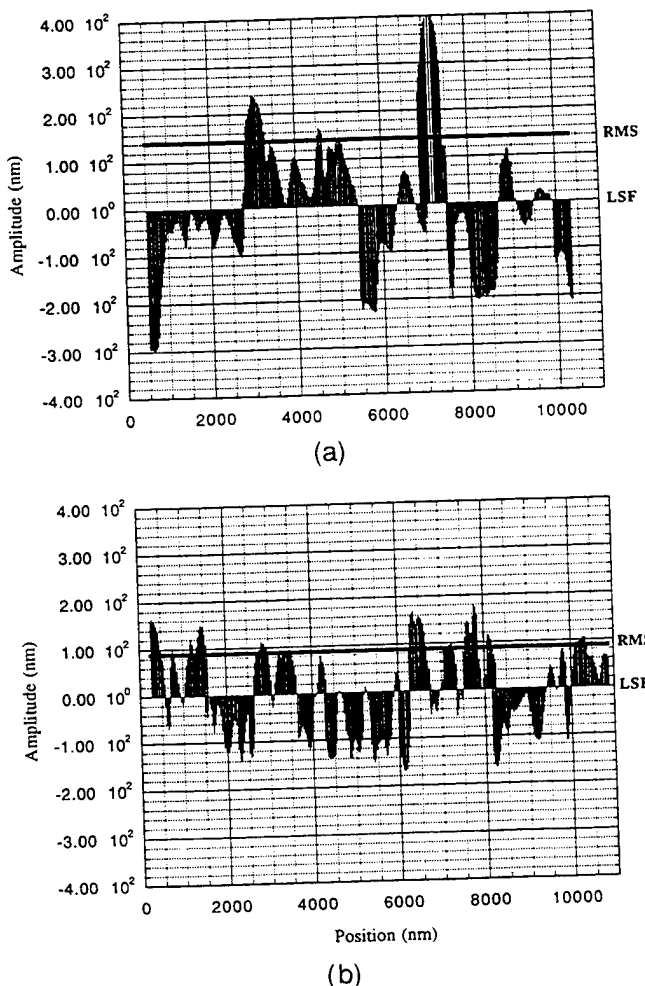


FIG. 3. Amplitude versus position plots of the typical YBCO meandering GB's shown in Fig. 2. Plots (a) and (b) correspond to Fig. 2(a) and 2(b), respectively. The least square fit lines and the root mean square lines are marked by LSF and RMS, respectively.

deposition rate film) with the maximum amplitude of about 180 nm. In contrast, the amplitude of the film deposited at the higher rate [Fig. 3(a)] varies widely, with a maximum of  $\approx 400$  nm. The average meander amplitude was determined by averaging the maxima (over 50 points) for each film. The average amplitude was found to be 124 nm for the higher deposition rate film and 98 nm for the lower rate film. It should be noted that the meander amplitude defined above may not be identical to the deviation of the film GB from the substrate GB because the GB may be displaced, as noted in Fig. 2(a).

Similarly to the meander amplitude, the meander wavelength also varies consistently with growth rate. Because of irregularities in the meander period, a half wavelength was defined as the distance between points where the boundary intersects the LSF line. Based on the statistical results of measurements over more than 10  $\mu\text{m}$ , the average half wavelength was found to be 400 nm for the film deposited at the higher rate and only 325 nm for the film grown at the lower rate, consistent with the results for the average amplitude described above. Likewise, the maximum half wavelength was found to be 830 nm for the higher rate film and 660 nm of the lower rate film. It is interesting to note that the meander peaks that have the maximum amplitude do not coincide with those of the maximum wavelength. The absence of correlation between wavelength and amplitude means that the meander cannot be described as a regular wave. As a consequence, we characterize the roughness or degree of meander by the "meander width", which we define as the root mean square (RMS) deviation of the boundary from the LSF line. The meander widths calculated from Figs. 3(a) and 3(b) are about 140 nm and 90 nm, respectively, indicating a considerable decrease ( $\sim 35\%$ ) of meander roughness in the lower deposition rate films. The observed roughness reduction for the 36.8° YBCO bicrystal film GB's produced by the lower deposition rate is in agreement with the observations by Miller *et al.* for the 24° YBCO bicrystal films.<sup>7</sup>

Figure 4 shows a part of a meandering YBCO GB composed of facets as indexed. The longest segment is a  $(310)_1/(310)_2$  facet which is the symmetrical  $\Sigma 5$  GB defined by the 36.8° misorientation angle.<sup>10</sup> Other symmetrical and asymmetrical facets contribute to the GB line meandering. Similar GB facets have also been reported by other groups.<sup>4</sup> It should be noted that the GB's do not always appear sharp. Instead, an apparent projected width of a couple of nanometers along the facet normal can be seen for some GB segments in Fig. 4. This projected width is a result of the inclination of the GB planes with respect to the viewing direction. Thus, in these images collected with the electron beam parallel to the [001] direction, this projected width

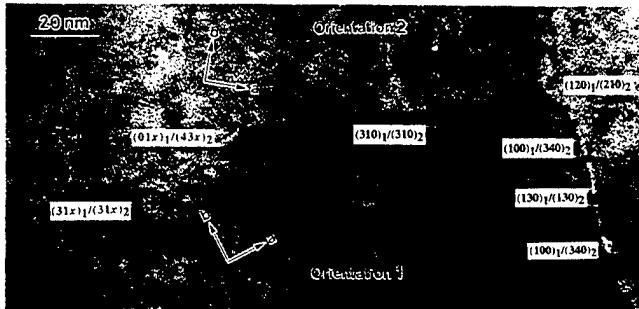


FIG. 4. Lattice-fringe image showing a portion of the YBCO meandering GB from a film deposited at the lower rate. Facet segments are marked by dots, and indices refer to orientation 1/orientation 2 as denoted. Grain boundary lines are not always sharp, and a projected width due to the inclination of the GB planes is distinguishable especially for the  $(01x)_1/(43x)_2$  facet.

indicates the GB containing some twist components in spite of the nominal pure [001] tilt geometry of the substrate. The index should be more accurately written as  $(hkx)$  for twist planes, and these  $(hkx)$  GB facet planes cannot be described as the pure tilt grain boundaries anymore. Such GB planes are apparent for the asymmetrical  $(01x)_1/(43x)_2$  facet segment in Fig. 4. Close inspection reveals that the projected width varies randomly from facet plane to facet plane.

A GB with a large projected width (about 10 nm) is shown in Fig. 5 where the projected boundary line is parallel to the  $(130)_1/(130)_2$  lattice planes. The coincident site lattice (CSL) plane corresponding to this  $\Sigma 5$  GB can be distinguished in the overlapping GB area (e.g., in framed region). Although the ideal rotation angle for the  $\Sigma 5$  boundary is 36.8°,<sup>10</sup> the actual rotation measured for this grain boundary using selected-area electron diffraction was found to be 36.0°. However, small deviations from perfect CSL misorientation angle may be accommodated by the introduction of additional dislocations along the boundary.<sup>11</sup> The irregular change of the projected width for this  $\Sigma 5$  GB can be seen in Fig. 6. It is important to note that the coincident site lattice (in this case) is fixed by the bicrystal misorientation independent of the specific GB plane, as is evident by Fig. 6. The observed film overlap in GB areas implies an irregular profile of the GB plane through the film thickness. A growth model is established to account for this phenomenon (see Sec. IV).

Although the emphasis of this work is on the structure of the grain boundaries, it should be noted that other microstructural features are also present in these films. The two predominant types of features observed were *a*-oriented grains and second phase impurity particles. Figure 7 shows a lattice-fringe image taken with incident electron beam parallel to the [001] in the YBCO film. The *a*- and *b*-axes for both halves of the YBCO film are indicated. The meandering YBCO GB is comprised of

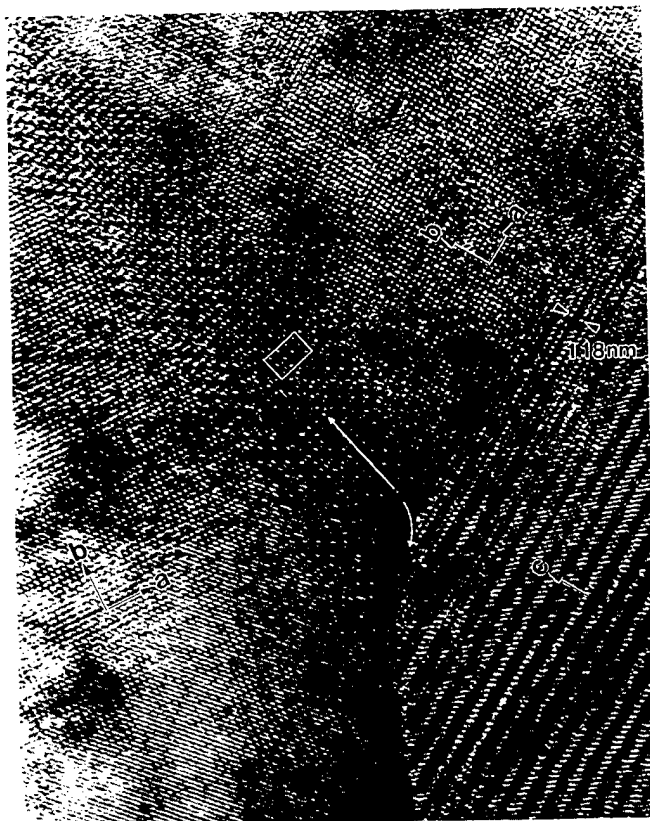


FIG. 5. Experimental image showing the CSL image (e.g., in framed region) in an overlapping area between two films. A straight white arrow indicates the  $[130]_1/[130]_2$  symmetrical line. A curved arrow indicates the change of the GB line due to the presence of an  $a$ -oriented grain ( $c$ -axis in the image plane).

straight facets several tens of nanometers long which are marked by black dots. Two  $a$ -oriented grains embedding within the  $c$ -oriented film are also evident. The  $c$ -axis of both  $a$ -oriented grains is parallel to the  $a$ - or  $b$ -axis of the remainder of the film which can also be verified by SAED. The typical shape for  $a$ -oriented grains is more or less rectangular with the long axis a few  $0.1 \mu\text{m}$  in length. In general,  $a$ -oriented grains can be found throughout the films deposited at both higher and lower rates. An example of an  $a$ -axis grain that locates on the YBCO GB is shown in Fig. 7; these regions, however, were excluded from our measurements described above in which the statistical variation of meandering was established.

Optical microscopy revealed the presence of small particles that were distributed along the GB in the low deposition rate samples. There are two typical particle sizes, i.e., about 500 nm and 200 nm in diameter, respectively. These particles were not observed in the YBCO films deposited by the higher rate, indicating that the formation of these particles is closely related to the film deposition conditions. We speculate that they are precipitates during the film growth. TEM images

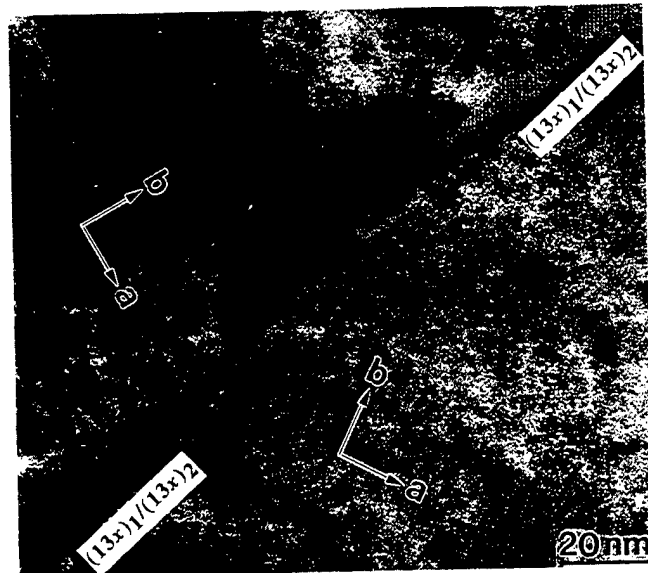


FIG. 6. Lattice-fringe image showing the irregular change of the projected GB width in the local area. Symmetrical GB facets are marked.

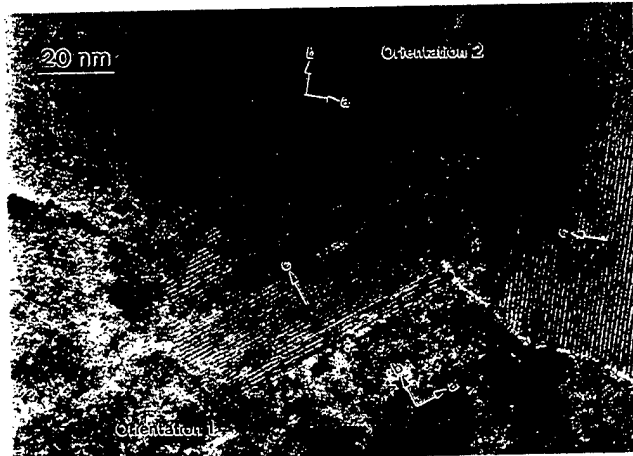


FIG. 7. Lattice-fringe image showing a part of YBCO meandering GB composed of nanometer scaled facet segments (marked by dots) and  $a$ -oriented grains embedding in the matrix film denoted with orientation 1 and orientation 2, respectively. The orientation relationships between the  $a$ -oriented grains and the matrix films are indicated.

[Fig. 8(a)] show a generally irregular shape and dark contrast for larger particles. These particles are typically between 400 and 600 nm in diameter, which is two to three times larger than the maximum meander amplitude found in this sample; therefore, it is hard to determine whether they nucleated on the substrate grain boundary or on the film grain boundary. The small particles are not located along the substrate boundary, but instead are observed along the GB in the film [Fig. 8(b)]. The distance between these particles along the YBCO GB varies from 0.1 to a few microns. In addition to these precipitates, voids with a diameter of about 200 nm have been found along the substrate GB in this sample. These

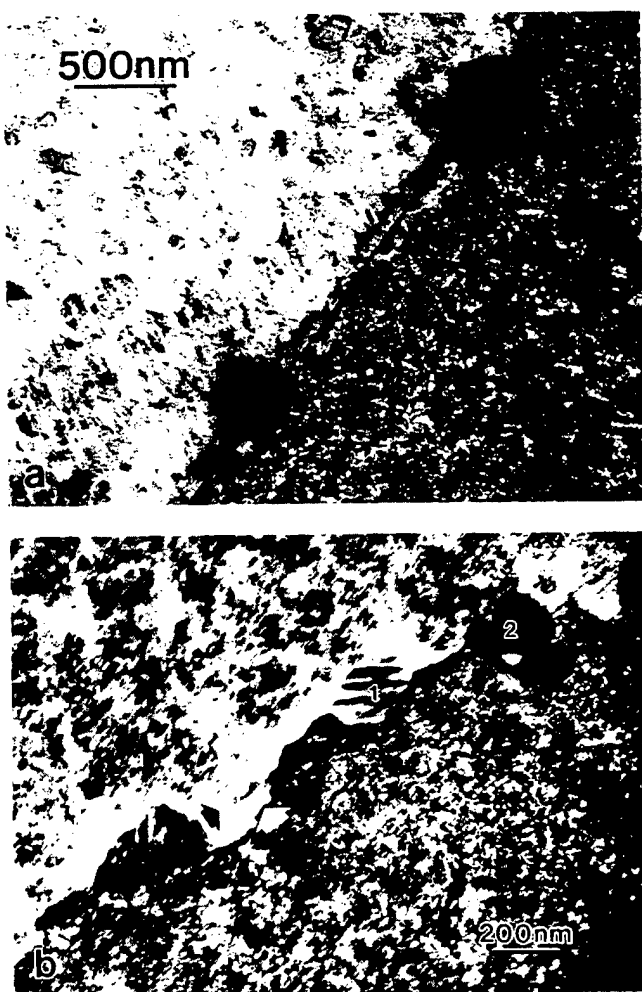


FIG. 8. Particles distributed along the film produced by the lower deposition rate. Two typical sizes of about 500 nm and 200 nm are shown in (a) and (b), respectively. (Note the change in scale.) The particles numbered by 1 and 2 in (b) are bounded by the meandering shape of the YBCO GB indicated by a white arrow. A black arrow in (b) indicates the substrate GB.

are similar to those that have been reported by others in similar films.<sup>4-6</sup>

#### IV. DISCUSSION

Experimentally, we have found that the degree of meander is different between these films prepared at two different growth rates; the amplitude and wavelength of the meander are significantly lower in the film deposited at the lower rate compared to that in the film deposited at the higher rate. In addition, we have also observed that the GB in the film may be laterally displaced from the GB in the substrate. As we have mentioned, the lateral displacement may be associated with the *c*-axis misorientation between two halves of the substrate bicrystal rather than the deposition rate. Besides, rotation angle for the film bicrystals may also affect the lateral displacement. Compared with the 36.0° rotation

angle measured for the higher deposition rate film, the 36.8° rotation of the YBCO bicrystal thin film deposited at the lower rate is much closer to the exact  $\Sigma 5$  GB rotation relationship (36.87°). Thus the interfacial energy could be lower, resulting in a reduced overgrown area as shown in Fig. 2(b). In this paper we will focus mainly on the mechanism for the formation of meandering GB's and the consequent influence of deposition conditions on grain boundary structure. In addition, the influence of the meandering configuration and other microstructural features on current transport properties will be discussed.

#### A. Formation of meandering GB's

##### 1. 3D/3D growth of the films

The nature of growth of YBCO films on  $\text{SrTiO}_3$  single crystal substrates has been studied in detail by several investigators. For example, Zhu *et al.*<sup>13</sup> studied growth of YBCO films on single crystal substrates in which the surface normal varied slightly (<1°) from the crystallographic  $\langle 001 \rangle$  direction in the substrate. They classified two types of  $\text{SrTiO}_3$  substrates: those in which the surface normal is exactly parallel to a  $\text{SrTiO}_3 \langle 001 \rangle$ , referred to as "flat" substrates, and those with a surface normal which deviates slightly from  $\langle 001 \rangle$ , referred to as "tilt" substrates. In their studies, it was found that growth proceeds by 3D island growth for flat substrates while initial growth proceeds by a 2D layer-by-layer mechanism in the case of tilt substrates. For the 3D growth of the YBCO films on "flat"  $\langle 001 \rangle$   $\text{SrTiO}_3$  substrates, Norton *et al.*<sup>14</sup> proposed a terraced-island-growth model for the films with the *c*-axis perpendicular to the (001) surface plane of the  $\text{SrTiO}_3$ . In this model, unit cell-by-unit cell nucleation and growth of the YBCO films on the (001) surface of the  $\text{SrTiO}_3$  substrate generate a terraced 3D island. Stacked terraces are formed due to a pronounced lateral growth rate of the YBCO films along the (*a*-*b*) plane compared to the *c*-axis direction.

The bicrystal substrates used in our experiments are all nominally prepared with the surface normal parallel to a  $\text{SrTiO}_3 \langle 001 \rangle$ . However, small deviations from this perfect orientation are possible. Using the same nomenclature as described above to define our  $\text{SrTiO}_3$  bicrystals, they may be described as flat/flat for those substrates in which both halves are perfectly oriented with the surface normal parallel to the  $\text{SrTiO}_3 \langle 001 \rangle$ , while flat/tilt describes substrates in which one half deviates slightly (<1°). On the surface of a flat/flat bicrystal substrate, heterogeneous nucleation and 3D island growth (Volmer-Weber growth) takes place on both sides of the substrate boundary. We denote this situation as 3D/3D growth. Complete films are formed when islands coalesce. Those islands that nucleate in the vicinity of the substrate GB may grow over the underlying substrate boundary before coalescence, although

the tendency for such overgrowth may be limited due to an unfavorable lattice match between the growing island and the “wrong” half of the substrate. Meandering film boundaries are thus generated as a consequence of the island overgrowth (Fig. 9). Presumably, islands on either side of the substrate GB have the same probability for overgrowth across the substrate GB for the case of isotropic nucleation and growth in the substrate surface plane. YBCO meandering GB’s are thus symmetrically oriented along the substrate GB, as in Fig. 2(b).

It should be noted, however, that on the flat/tilt bicrystal substrates the growth mechanism may be different. On this type of substrate, 3D island nucleation and growth may take place only on the flat part while 2D layer-by-layer growth is likely to occur on the tilt part during the early stage of the growth.<sup>13</sup> Such 3D/2D growth could be one of the mechanisms leading to a displacement of the film GB from the substrate GB. A tilt/tilt geometry for the substrate bicrystal may lead to a more complicated situation, depending on the specific misorientation.

## 2. Film overlap and multiple meander

We shall now explain the film overlap observed experimentally (Figs. 4–6). During the terraced-island growth of the YBCO film, the layers formed initially

may first coalesce to form the meandering GB (see layer 1 in Fig. 10). Continued deposition leads to epitaxial growth of subsequent terraces (layers 2, 3, and 4 in Fig. 10) on top of the previous layers. However, the growth front or overgrowth of each new terrace may not coincide exactly with those formed in the layers below. The height of each terrace has been determined to be only one or a few unit cells along the *c*-axis direction.<sup>13,14</sup> Therefore, the spacing between mutually shifted GB’s in adjacent terrace layers is not likely to be large along the (*a*-*b*) plane. A vertical or inclined GB line which is composed of atomic scale steps may be expected in a lateral cross section of the GB as shown in Fig. 10. This is consistent with cross-section observations of Traeholt *et al.*<sup>4</sup> In addition, the shape of the growth front in each layer may not be exactly the same, yielding different inclinations of GB planes in successive cross-section planes along the meandering GB. A twist meandering GB plane is then formed as shown in Fig. 10 for plate I and can be used to account for the change of the projected width of the GB facets along the facet-normal observed along the meandering GB’s (Fig. 4–Fig. 6). Unusual overgrowth (layer 5 in Fig. 10) could happen occasionally due to the local change of the growth environment, and a new twist meandering GB as in plate II is thus formed which has a distinguishable distance from the one in plate I. Multiple meander is resulted which can be equally described as a meander along the *c*-direction through the film thickness. The existence of such multiple meander has been confirmed experimentally, as shown in Fig. 11(a), in which three meandering GB lines are marked by dots in different sizes. This overlap is further confirmed by noting that

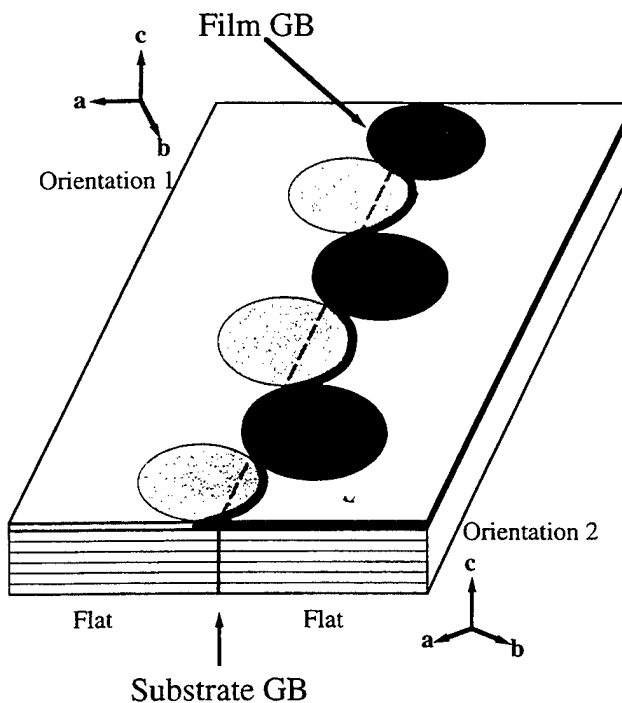


FIG. 9. Schematic drawing illustrating a growth on the [001] tilt  $\text{SrTiO}_3$  bicrystal substrates. 3D/3D island nucleation and growth on this flat/flat substrate are depicted (only around GB area). A meandering GB is generated when islands of orientation 1 coalesce with islands of orientation 2. The overgrowth of islands across the substrate GB occurs for both orientations.

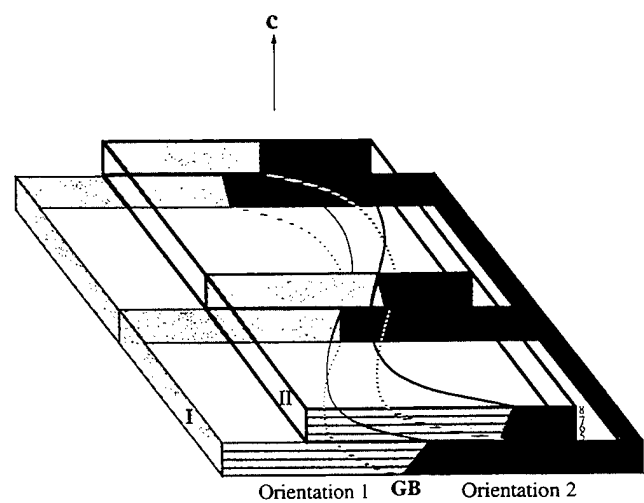


FIG. 10. Schematic drawing illustrating how twist component of the GB planes formed. Layers numbered from 1 to 8 represent terraces formed during the 3D island growth of the films. The meandering GB plane formed in plate II may be displaced from the one in plate I as shown (see text) resulting in observable multiple meandering GB’s.

either twin orientation can be seen in the overlapped area depending on the diffraction conditions. SAED patterns from this area do not show any indication that these features are caused by small in-plane rotations. Slight tilting ( $1^\circ$ ) of the sample in the electron microscope enhances the image contrast for one of these meandering GB's while the others become almost invisible [Fig. 11(b)]. This behavior is likely a result of subtle  $c$ -axis misorientations between plates, e.g., I and II in Fig. 10. Thus, individual meandering GB planes can be differentiated in diffraction-contrast images by tilting the sample in the transmission electron microscope. The fact that the multiple meandering GB's have been found mainly in the higher deposition rate films is consistent with a more rapid coalescence of individual

islands in these films compared with that in the lower deposition rate films as discussed more fully below.

### B. Effect of film deposition rate on the meandering configuration

As concluded from Fig. 3, the degree of meander in YBCO bicrystal GB's is considerably reduced by decreasing the film deposition rate. In particular, a large difference in the maximum amplitude and the wavelength have been found between meandering GB's in the higher rate films and in the lower rate films. Two factors are thought to be important for controlling the degree of meander: the nucleation density and overgrowth ability. As discussed below, both of these factors are related to the deposition rate. During deposition, incident atoms are loosely attracted to the substrate surface initially. These adatoms migrate along the surface until they form a nucleus or attach to a growing embryo. However, a critical number of atoms is required to create a nucleus, independent of deposition rate. Thus, during a given period of time, more atoms arrive for a higher deposition rate and it is possible to generate more nuclei per unit area during the initial stages of growth. As a result of the higher nucleation density and consequent smaller spacing between islands, interconnection may occur, leading to a random distribution of larger but more irregularly shaped islands (Fig. 12) as has been verified for YBCO



FIG. 11. Experimental evidence for the multiple GB planes. (a) Three meandering GB lines are marked by dots in three sizes. The substrate GB line is marked with a solid line. (b) The image contrast of the innermost meandering line in (a) is reinforced when tilting the sample by about  $1^\circ$  around the substrate GB line while the image contrast for other meandering GB's is weakened. The asterisk marks about the same point on the sample in both (a) and (b). Note the change in twin orientations for the overlapped region corresponding to the second and third terraces.

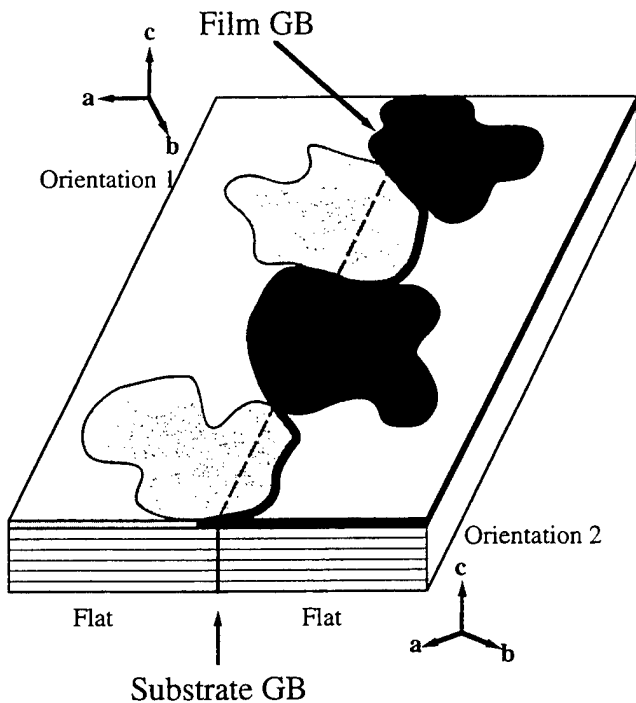


FIG. 12. A schematic illustration of a meandering GB formed by coalescence of irregularly shaped islands.

films grown on  $\text{MgO}$ .<sup>15</sup> In the case of a lower deposition rate, fewer nuclei can be generated during a given period of time. Thus, islands may be more widely spaced and interconnection less likely. This mechanism would lead to more uniform island sizes and a more regular meander pattern. However, a lower deposition rate also implies that an atom which has attached to a nucleus does not attain the full nearest neighbor coordination and lowest energy state for a longer time. Although thin film deposition is a nonequilibrium process, a lower deposition rate mitigates kinetic limitations and allows the system to approach a thermodynamically more stable configuration. Thus, there is an increased probability that an atom may detach from the nucleus. This factor can especially affect the overgrowth ability since an atom which attaches to an overgrown part of an island may detach and migrate to a different island which is epitaxially oriented. In addition to reducing the degree of meander, a lower deposition rate is also helpful in reducing the number of the  $a$ -oriented grains.<sup>16</sup>

### C. Influence of GB structures on transport properties

Previous studies have shown that transport properties across similar bicrystal thin film grain boundaries cannot be modeled completely assuming a homogeneous, linear junction. For example, previous measurements on  $24^\circ$  bicrystal films have suggested that the boundary may be divided into smaller segments, each of which dissipates independently from the others.<sup>17,18</sup> Although there are other possible explanations for the transport behavior, the present studies of the microstructure of such bicrystal films have shown several microstructural features which may serve to divide a boundary.

The meandering GB configuration itself is expected to have influence on GB transport properties. As a consequence of meander, the grain boundary contained within any particular microbridge may be comprised of a number of nanometer scale GB facets with different orientations where local changes of transport properties could be induced. The measured transport properties may represent the average behavior of these various segments. However, it is likely that some segments are very weakly coupled, so that even under small currents or fields, they are essentially uncoupled. Since these bicrystal films are only a few hundred nanometers thick, it is likely that these uncoupled regions extend through the thickness of the film and thus divide the boundary.

The idea that various facets may exhibit different transport behavior is likely to be related to the dislocation density contained within the facet. For example, Dimos *et al.* attributed their measured transport behavior across similar bicrystal films to the increased dislocation density as a function of increasing rotation angle.<sup>1</sup>

In our work, the nominal  $36.8^\circ$  bicrystal angle was selected to yield a  $\Sigma 5$  GB. It has been speculated that such “low-sigma” boundaries may exhibit particularly good transport behavior because of the relatively higher degree of coincidence between the two parts of the bicrystal. However, it is important to recognize that a wide range of grain boundary facet planes are possible for any particular coincident site lattice, which is determined only by the bicrystal misorientation. Some coincident or near-coincident planes may intersect many coincident lattice sites, while others only very few, resulting in differences in structure along such planes although certain sets of planes will always be parallel due to the CSL. The mismatch along the facet planes with various indices is influenced by the frequency of intersection of the facet plane with coincident lattice sites. For example, illustrated using the (100) and the (010) planes, an incommensurate lattice mismatch could occur as depicted schematically in Fig. 13, in which facets with indices typically presented in the experimental images (e.g., Fig. 4) are selected and randomly combined. For convenience, a good lattice match is assumed for the  $(130)_1/(130)_2$  facet at the top part of the drawing. Rather good lattice match is maintained

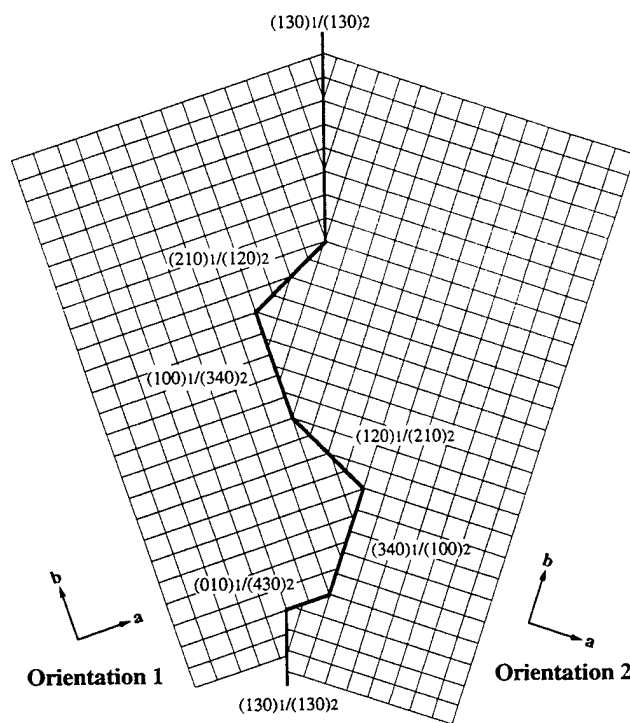


FIG. 13. A simplified model showing how the lattice match between orientation 1 and orientation 2 changes on different GB facets along the meandering GB line. Facets with typical indices found in experimental images are selected. A good lattice match is assumed on the  $(130)_1/(130)_2$  facet on the top part of the drawing. Misfit dislocations should be induced (not present in the drawing) when the lattice mismatch occurs in facet segments.

through the following  $(210)_1/(120)_2$  facet, but a severe lattice mismatch develops on the next  $(100)_1/(340)_2$  facet so that misfit dislocations (not drawn) should be induced. The changing lattice mismatch in different facets induces a changing misfit dislocation density along the GB, and therefore possibly a difference in  $J_c$  across various facets. In addition to the dislocation density, the character of the dislocations changes from edge- to screw-type as the boundary assumes more twist character, and the differences in the stress field generated by these dislocations may also play a role. In any case, the dislocation density depends strongly on which GB facet is under consideration and what neighboring facets it has. The meandering GB may thus be divided into segments with very different current transport properties. Other features such as  $a$ -oriented grains (Fig. 7) and secondary phases (Fig. 8) along GB's, could also contribute to the local change of transport properties.

It is important to note two other possible consequences of meander. Firstly, the effective grain boundary area becomes larger due to the meander. Increasing the effective area of the boundary may increase the current that may be carried in competition with the decrease expected by dividing the junction. In addition, the abrupt changes in the GB plane may serve as pinning sites for vortices which penetrate the junction. Clearly the potential effects of these factors complicate the analysis of transport behavior.

## V. CONCLUDING REMARKS

In conclusion, we have investigated by TEM the grain boundaries formed in YBCO bicrystal films deposited onto  $36.8^\circ$  [001]  $\text{SrTiO}_3$  bicrystal substrates at two different rates. The grain boundaries were found to meander, with submicrometer facets. The meandering configuration is believed to be produced by coalescence of YBCO islands which nucleate on opposite sides of the substrate GB. The mechanism for the formation of the meandering GB's is discussed in detail. Based on these studies, it was found that the deposition rate may be used to control the meandering configuration. According to quantitative analysis of the degree of meander, a lower rate deposition decreases the roughness of the meandering GB considerably, and therefore may be a useful way to control the degree of meander. The presence of meandering grain boundaries may play an important role in transport properties. In addition to  $a$ -oriented grains and second phase precipitates identified along the boundaries, the meandering configuration introduces twist-component facets and a variable disloca-

tion density along the boundary. These facets may have profoundly different transport properties and, together with  $a$ -oriented grains and second phase precipitates, may serve to divide the boundary into independently dissipating segments.

## ACKNOWLEDGMENTS

This work was partially supported by the National Science Foundation Office of Science and Technology Centers under Contract DMR 91-20000 and the U.S. Department of Energy, Basic Energy Sciences—Materials Sciences, Conservation and Renewable Energy—Advanced Utility Concepts—Superconducting Technology Program, under Contract No. W-31-109-ENG-38.

## REFERENCES

1. D. Dimos, P. Chaudhari, J. Mannhart, and F. K. LeGoues, *Phys. Rev. Lett.* **61**, 219 (1988).
2. S. E. Babcock, X. Y. Cai, D. C. Larbalestier, D. H. Shin, N. Zhang, H. Zhang, D. L. Kaiser, and Y. Gao, *Physica C* **227**, 183 (1994).
3. Y. Zhu, Z. L. Wang, and M. Suenaga, *Philos. Mag. A* **67**, 11 (1993).
4. C. Traeholt, J. G. Wen, H. W. Zandbergen, Y. Shen, and J. W. M. Hilgenkamp, *Physica C* **230**, 425 (1994).
5. B. Kabius, J. W. Seo, T. Amrein, U. Dahmen, A. Scholen, M. Siegel, K. Urban, and L. Schultz, *Physica C* **231**, 123 (1994).
6. J. W. Seo, B. Kabius, D. Dahmen, A. Scholen, and K. Urban, *Physica C* **245**, 25 (1995).
7. D. J. Miller, T. A. Roberts, J. H. Kang, J. Talvacchio, D. B. Buchholz, and R. P. H. Chang, *Appl. Phys. Lett.* **66**, 2561 (1995).
8. J. A. Alarco, E. Olsson, Z. G. Ivanov, D. Winkler, E. A. Stepanov, O. I. Lebedev, A. L. Vasiliev, A. Ya. Tzalenchuk, and N. A. Kiselev, *Physica C* **247**, 263 (1995).
9. J. Talvacchio, M. G. Forrester, J. R. Gavaler, and T. T. Braggins, in *Science and Technology of Thin Film Superconductors II*, edited by R. McConnell and S. A. Wolf (Plenum, New York, 1990), pp. 57–66.
10. A. Singh, N. Chandrasekhar, and A. H. King, *Acta Crystallogr. B* **46**, 117 (1990).
11. D. G. Brandon, *Acta Metall.* **14**, 1479 (1966).
12. V. Selvamanickam and K. Salama, *Appl. Phys. Lett.* **57**, 1575 (1990).
13. X. Zhu, G. C. Xiong, R. Liu, Y. J. Li, G. J. Lian, J. Li, and Z. Z. Gan, *Physica C* **216**, 153 (1993).
14. D. P. Norton, D. H. Lowndes, X. Y. Zheng, S. Zhu, and R. J. Warmack, *Phys. Rev. B* **44**, 9760 (1991).
15. M. G. Norton, L. A. Tietz, S. R. Summerfelt, and C. B. Carte, *Appl. Phys. Lett.* **55**, 2348 (1989).
16. T. Burmann, J. Geerk, O. Meyer, R. Schneider, and G. Linker, *Solid State Commun.* **90**, 599 (1994).
17. D. J. Miller, D. G. Steel, F. Yuan, J. D. Hettinger, K. E. Gray, J. Talvacchio, and J. H. Kang, *Proceeding of 1995 International Workshop on Superconductivity, Hawaii*.
18. D. G. Steel, J. D. Hettinger, F. Yuan, D. J. Miller, K. E. Gray, J. H. Kang, and J. Talvacchio, *Appl. Phys. Lett.* **68**, 120 (1996).

## CRYSTAL ENGINEERING OF CHEMICALLY STABILIZED, CATION SUBSTITUTED $\text{YBa}_2\text{Cu}_3\text{O}_{7-\delta}$ STRUCTURES

J. T. McDEVITT\*, J.P. ZHOU, C. E. JONES and J. TALVACCHIO<sup>‡</sup>

*Department of Chemistry and Biochemistry, University of Texas at Austin, Austin, TX 78712*  
<sup>‡</sup>*Northrop Grumman STC, Pittsburgh, PA 15235*

### ABSTRACT

To produce stable forms of  $\text{YBa}_2\text{Cu}_3\text{O}_{7-\delta}$  superconductors, a series of cation substituted reactions have been completed. It is found that the corrosion resistance increases with increasing substitution level in systems of  $\text{Y}_{1-y}\text{Ca}_y\text{Ba}_{2-y}\text{La}_y\text{Cu}_3\text{O}_{7-\delta}$ . Interestingly, the composition of  $\text{Y}_{0.6}\text{Ca}_{0.4}\text{Ba}_{1.6}\text{La}_{0.4}\text{Cu}_3\text{O}_{7-\delta}$  ( $T_c = 80$  K) is found to be at least 100 times more stable than the parent compound,  $\text{YBa}_2\text{Cu}_3\text{O}_{7-\delta}$ . Similar stable cuprate systems with transition temperatures above 85K have been prepared suggesting that the surface reactivity, processability and superconducting properties can be tailored with the use of the appropriate cation composition.

Recently, researchers worldwide have made considerable progress in the fabrication of high- $T_c$  superconductor products such as tapes, wires and thin film devices. Unfortunately, only in a few cases have efforts been successful to date to commercialize high- $T_c$  products. Much of the slow progress in this area can be traced to the poor materials properties, high chemical reactivity and poor oxygen stability exhibited by these systems. To improve the chemical stability, we have doubly doped  $\text{YBa}_2\text{Cu}_3\text{O}_{7-\delta}$ , forming  $\text{Y}_{1-x}\text{Ca}_x\text{Ba}_{2-y}\text{La}_y\text{Cu}_3\text{O}_{7-\delta}$ . These substitutions disrupt the integrity of the  $\text{CuO}_{1-\delta}$  chains while keeping the total oxidation state of the  $\text{Cu}(2)\text{-O}(2)/\text{O}(3)$  arrays nearly constant. In this study, the degradation behavior of  $\text{YBa}_2\text{Cu}_3\text{O}_{7-\delta}$  (YBCO) and substituted compound,  $\text{Y}_{0.6}\text{Ca}_{0.4}\text{Ba}_{1.6}\text{La}_{0.4}\text{Cu}_3\text{O}_{7-\delta}$  (TX-YBCO), in water vapor environments are established for bulk and thin film structures.

A dramatic demonstration of the increased stability afforded with the cation substitution is shown in Figure 1. Here bulk samples of YBCO and TX-YBCO following their exposure to aerated water at room temperature is provided. For YBCO, two days water exposure causes the formation of a significant amount of  $\text{BaCO}_3$  crystals which decorate the entire surface of the ceramic sample. This behavior is reminiscent of a sample that has decomposed to a large extent. On the other hand, the TX-YBCO sample treated for 30 days in a similar manner shows no visible signs of corrosion. A greater than 100 fold increase in stability is thus noted for the modified superconductor compound.

Thin films of YBCO and TX-YBCO have also been evaluated to explore their processability and durability. Lifetime measurements of the various samples were performed using our previous described resistivity measurement.<sup>1,2</sup> Accordingly, film samples were placed in a water vapor chamber equilibrated at constant temperature with controlled humidity. From such measurements, increases in the film resistivity are utilized to judge the rate at which damage to the cuprate structure occurs. Typically, the films decompose initially at a modest rate with little increase in resistivity over time. However, once the degradation process creates a sufficient number of corrosion defects to produce a high resistive barrier in the film, a marked increase in resistance is noted. Because sampling current, contact method and measurement intervals influence to some extent the measured lifetime, identical parameters were utilized to evaluate the various samples described herein.

It is clear that temperature and humidity are two important parameters that influence the degradation rate of YBCO. For example, YBCO samples studied at a constant temperature of 23 °C while varying the humidity from 60% to >98% exhibited a lifetime decrease from >10 days for the former to <24 hours for the latter. However, while maintaining the relative humidity at ≥98%, and increasing the temperature from 23°C to 75°C, the YBCO lifetime decreased from >10 days to ~3 hours. In comparison, the TX-YBCO films showed no signs of degradation for >10 days under the severe conditions of 75 °C water vapor and ≥98% humidity. From these studies and numerous other trials not included here, it is clear that major factors which influence the degradation rate are the high- $T_c$  structure (i.e. YBCO vs. TX-YBCO), the humidity content and the temperature.<sup>3</sup>

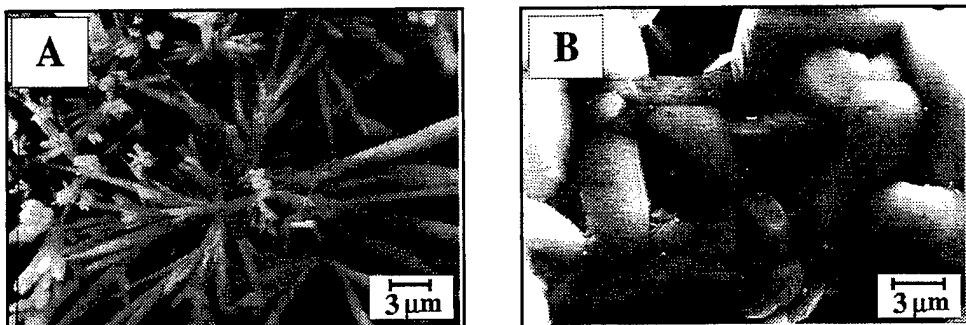


Figure 1: Scanning electron micrographs depicting the surface of a)  $\text{YBa}_2\text{Cu}_3\text{O}_{7-\delta}$  exposed to a room temperature water solution for 2 days and b)  $\text{Y}_{0.6}\text{Ca}_{0.4}\text{Ba}_{1.6}\text{La}_{0.4}\text{Cu}_3\text{O}_{7-\delta}$  exposed to a room temperature water solution for 30 days. The  $\text{YBa}_2\text{Cu}_3\text{O}_{7-\delta}$  surface is decorated with corrosion products while the cation substituted compound shows little sign of degradation.

Considerations of the structure/corrosion reactivity relationships for the YBCO and TX-YBCO materials can provide essential mechanistic information. The parent compound contains Cu(1)-O(1) chains as well as ordered oxygen vacancies ( $\text{V}_\text{O}$ ) at the O(5) sites. Previous reports have suggested that in the early stages of corrosion, water molecules enter the open channels along the O(5) sites and the oxide ions ultimately dock at the O(5) sites.<sup>4</sup> Proton transfer from water to the oxide lattice components leads to the formation of two moles of  $\text{OH}^-$  which occupy both vacancy site and the preexisting occupied oxide site. Internal charge transfer reactions within the modified lattice leads to the evolution of molecular oxygen. Following these initial steps, a series of reactions ensue ultimately leading to the bulk decomposition of the lattice.

Interestingly, the TX-YBCO is expected to be involved in many of the same decomposition steps. However, two important differences exist for the modified compound. First, internal stresses introduced by bond-length mismatch in the intergrowth structures appear to be an important factor that dictates the decomposition kinetics of the YBCO superconductor. Our calculations completed using the bond valence sum theory suggest that the substitution of La for Ba leads to a reduction of the internal strain energy from 1.79% to 0.35%. This reduction in strain may lower the driving force for corrosion. Second, the TX-YBCO material possesses a tetragonal structure in which occupancy at the O(1) and O(5) sites are equivalent. The disordering of these sites may influences the relative electrochemical potentials for the O(1) and O(5) sites, thereby altering the driving force for the charge transfer reaction. Without sufficient internal strain acting as a driving force for charge transfer, the substituted phase may remain resistant to corrosion. Moreover, changes in the structure may alter the rates of water diffusion into and oxygen diffusion out of the high- $T_c$  lattice.

In summary, the preparation of the chemically robust cuprate bulk and film samples has been accomplished. Detailed studies of the corrosion mechanism for these samples suggest that changes in the lattice stress and strain features as well as minor changes in the oxygen ordering properties are responsible for the enhanced stability. Importantly, oxygen mobility within the modified structures is suppressed also making these systems quite attractive from a processing perspective.

**Acknowledgements** This work was supported at the University of Texas by ONR and NSF and at Northrop Grumman by AFOSR.

## References

1. J.-P. Zhou; S.M. Savoy; R.-K. Lo; J. Zhao; M. Arendt; Y.T. Zhu; A. Manthiram; J.T. McDevitt *Appl. Phys. Lett.* **66**, 2900-2902 (1995).
2. J.-P. Zhou; S.M. Savoy; J. Zhao; D.R. Rilet; Y.T. Zhu; A. Manthiram; R.-K. Lo; D. Borich; J.T. McDevitt *J. Am. Chem. Soc.* **116**, 9389-9390 (1994).
3. J.-P. Zhou; R.-K. Lo; S.M. Savoy; M. Arendt; J. Armstrong; D.-Y. Yang; J. Talvacchio; J.T. McDevitt *Physica C* **submitted**, (1996).
4. J.G. Thompson; B.G. Hyde; R.L. Withers; J.S. Anderson; J.D. Fitzgerald; J. Bitmead; M.S. Paterson; A.M. Stewart *Mat. Res. Bull.* **22**, 1715 (1987).

## HTS MULTILAYER PROCESS DEVELOPMENT FOR DIGITAL CIRCUITS

M.G. FORRESTER, B.D. HUNT, J. TALVACCHIO, J.D. MCCAMBRIDGE, R.M. YOUNG, D.L. MILLER, AND J.X. PRZYBYSZ

*Northrop Grumman Corporation, Science & Technology Center  
Pittsburgh, PA, USA*

### Abstract

Digital circuits based on High Temperature Superconductors (HTS) have the potential for offering operation at higher speed, and lower power dissipation than semiconductor circuits, while offering unprecedented performance advantages attributable to the unique quantum mechanical nature of the superconducting state. In order to fully realize this potential, it is necessary to develop a circuit process which integrates reproducible Josephson junctions into epitaxial multilayers. This paper discusses some of the materials and fabrication issues involved in the development of such a process.

### 1. Introduction

Superconducting digital circuits based on Single Flux Quantum (SFQ) logic hold the promise of operating at clock frequencies in the tens of GHz, while dissipating only microwatts per gate. SFQ logic is particularly well suited to moderate size circuits which perform various specialized digital signal processing functions, in applications such as infrared focal plane image processing, encrypted communications, and radar.

The future of HTS digital is shown by the path that LTS digital is following today. One area of intense activity in LTS is high speed analog to digital converters (ADCs), backed by fast digital filters, for sensor applications that require large dynamic range [1-4]. Digital filters, whose

fundamental building block, the multiply-accumulator, was recently demonstrated in LTS [5], are also being applied to enhance the accuracy of GHz-bandwidth ADCs [6].

Josephson digital logic is potentially useful in high-speed data switching for "information highways" [7,8], and for spread spectrum communications, where it offers low-power, high-speed code generators [9,10]. In fact, Josephson digital circuits are so fast that standard semiconductor test equipment can not follow their logic operations, so that on-chip buffers are being used to supply test vectors and capture outputs at GHz rates [11].

As HTS Josephson junctions become more reproducible the high speed of SFQ circuits will become attainable in the more easily utilized 65–77 K temperature range, albeit with somewhat higher power dissipation than in LTS circuits. This allows for the possibility of HTS digital circuits being used in a wide variety of applications where the weight and power requirements of a 4.2 K cryocooler are unacceptable.

## 2. Process Requirements

Realizing the potential of SFQ circuits in HTS will require the development of an integrated circuit process for these complex, multi-element, anisotropic materials. The requirements on this process include:

- Superconducting films with high critical current density ( $> 10^6$  A/cm<sup>2</sup> at 77K), low penetration depth ( $< 0.25$   $\mu$ m at 65 K), low RF losses ( $R_s < 0.5$  m $\Omega$  at 10 GHz and 77 K), smooth morphology (RMS roughness  $< 2$  nm), a high degree of crystalline perfection, and stability with respect to such factors as time, thermal cycling, environmental effects such as moisture, and packaging processes;
- Reproducible Josephson junctions, with high characteristic voltages,  $V_c \equiv I_c R_N$  ( $> 300$   $\mu$ V at 65 K), where  $I_c$  and  $R_N$  are the junction critical current and resistance, respectively;
- Epitaxial insulators which are structurally and chemically compatible with the superconductor layers, with low to moderate dielectric constant ( $\epsilon < 25$ ), low RF losses, low pin-hole density, and smooth morphology;
- Superconductor-to-superconductor contacts, and superconductor-insulator-superconductor crossovers, with high critical current density and low inductance;

- Possibly epitaxial resistor materials compatible with the superconductor and insulator films; and
- Low-resistance, high-adhesion contacts with metals such as gold.

Certainly the key element of the circuit process is the Josephson junction, and the most important property to which the process development must be directed is *reproducibility, and uniformity of critical current*. This is the main factor in determining the yield of working circuits. Given certain design margins for a circuit (that is, ranges of an operating parameter, such as a bias current, within which the circuit will operate correctly), the junction critical currents must not deviate from this range. For well-designed SFQ circuits it is reasonable to expect margins of  $\pm 30\%$ . Assuming a Gaussian distribution of critical currents, with a certain standard

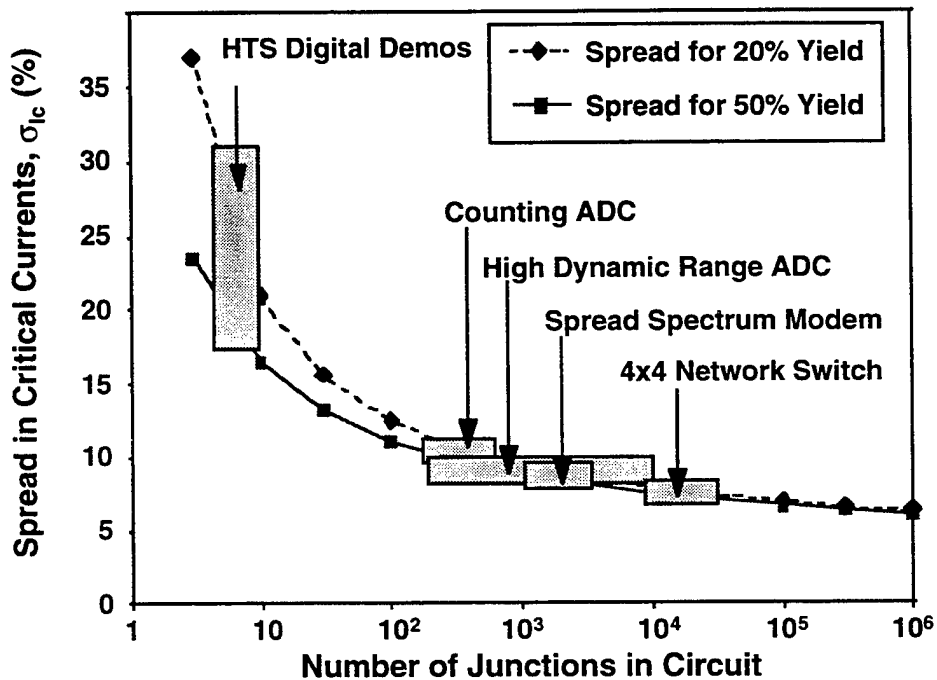


Figure 1. The spread in junction critical currents,  $\sigma_{Ic}$ , required to produce circuits with a given number of junctions. HTS digital circuits demonstrated to date have contained up to about ten junctions, consistent with the typical obtained spreads of 15 to 30%. Useful circuits, requiring 100 to 1000 junctions, will require spreads of about 10% or less.

deviation,  $\sigma$ , one can calculate the expected yield for circuits with a given number of junctions [12]. Figure 1 shows the result of such a calculation, and shows the critical current standard deviation required to obtain yields of 20% and 50%, for circuits of a given junction count. So, for example, to obtain a 50% yield of circuits with 1000 junctions one must have a one-sigma critical current spread of about 9%. Figure 1 illustrates that as spreads are reduced to the 10% range, the achievable circuit complexity increases dramatically for small gains in reproducibility. Of course those small gains may well become increasingly difficult to achieve.

Figure 1 also shows approximate ranges of junction count for various representative circuits for which superconductivity offers potential advantages over competing technologies. A review of these applications is beyond the scope of this article. Demonstrations of HTS digital circuits to date, some of which are described in Section 5.6, have so far been limited to roughly ten junctions or less, which is consistent with the fact that typical  $I_c$  spreads are in the 15 to 30% range.

In addition to having reproducible junctions, it is important that inductances be kept low, which is most practically achieved by integrating the Josephson junctions with a high-quality superconducting groundplane. In SFQ circuits the product of critical current,  $I_c$ , and inductance,  $L$ , is constrained to be of order the flux quantum,  $\Phi_0 = 2.07 \times 10^{-15}$  Wb. This is particularly difficult for HTS since stability against thermal noise dictates that the critical current should be as large as possible, while still meeting this constraint. In addition, the relatively long magnetic penetration depth in HTS ( $\lambda_0 \approx 150$  nm for YBCO, compared to 39 nm for Nb) makes inductances higher for given superconducting layer thicknesses.

Estimates of bit-error-rates for HTS circuits are an area of some controversy, but it is likely that many applications which require extremely low error rates (say  $10^{-20}$  sec<sup>-1</sup>) will never be practical in HTS. However, some applications of interest, such as ADCs, may tolerate much high error rates ( $\sim 10^{-9} - 10^{-6}$ ), and thus should be practical in HTS. Even to maintain these error rates it is likely that junction critical currents will need to be about 0.5 mA, so that a constraint of  $LI_c = \Phi_0$  leads to an inductance of about 4 pH. As we will see later, this is a significant challenge, and will require a complex multilayer process, and a good deal of ingenuity.

In this article we discuss some of the materials and processing issues involved in the development of such a process. The discussion will use as a basis our own experience in demonstrating two prototype processes which meet many, though not all, of the above requirements.

### 3. Epitaxial Film Deposition

#### 3.1. YBCO FILMS

YBCO is currently the material of choice for HTS multilayer circuit development because high-quality films can be grown *in situ* by a wide variety of deposition methods, and can be optimized to have very smooth surface morphology (RMS roughness < 1 nm). The three most important deposition techniques for YBCO, as well as for related epitaxial insulators, are sputtering, pulsed laser deposition (PLD), and co-evaporation.

A detailed review of these deposition techniques is beyond the scope of this article. Recent reviews of this area can be found in the references [13,14,15]. Here we mention only a few aspects of importance to multilayer circuit development.

We routinely use off-axis rf magnetron sputtering from a single, press-and-sintered, nominally stoichiometric target to produce films on two-inch wafers, or on several 1-cm square substrates. By adjusting sputtering conditions, such as argon and oxygen pressures, temperature, and geometry, it is possible to produce YBCO films with excellent superconducting properties –  $T_c > 90$  K,  $J_c > 10^6$  A/cm<sup>2</sup> at above 80 K, and rf surface resistance as low as 0.2 mΩ at 10GHz and 77 K. Such films however often suffer from a high density ( $\sim 10^6$  cm<sup>-2</sup>) of second-phase outgrowths, or "boulders", which are unacceptable for multilayer devices. In practice we adjust the deposition conditions to obtain a surface with as low a density of such outgrowths as possible ( $10^2$  cm<sup>-2</sup> is acceptable), which typically compromises the superconducting properties somewhat. For example,  $T_c$ 's of 85–87 K are typical, with  $J_c$  still exceeding 10<sup>6</sup> A/cm<sup>2</sup> at 77 K. This necessity for compromise is not unique to sputtering, but is also typical in co-evaporated films [16]. Such films may exhibit RMS roughness as low as 1.0 nm, comparable to the smoothest films obtained by any technique.

Negative aspects of off-axis sputtering, in our experience, include slow deposition rate (typically 10 to 40 nm per hour), and relatively poor run-to-run reproducibility. The latter may be associated with changes in the sputtering target as a function of time, such as the erosion of the "racetrack" groove typical in magnetron sputtering, or compositional or density inhomogeneities in the target material. The presence of the spatially extended plasma may also cause preferential resputtering of

material from the deposition chamber hardware, leading to additional copper, for example, being present at the substrate [17].

Pulsed laser deposition offers much higher deposition rate, typically of order 1.0 Å/second, but potentially orders of magnitude higher [15]. The technique is also extremely flexible in that a wide range of materials can be deposited in a given chamber using multi-target carousels now widely available. Since the laser-target interaction is confined to a relatively small volume there is much less potential for the incorporation of contaminants from the chamber hardware than in the case of sputtering. Although PLD is most easily applied to deposition over relatively small areas (~25 mm diameter), various approaches to rastering the beam, target, and substrate can be used to coat diameters as large as 125 mm [18].

The main disadvantage of PLD is the presence on the film of micron-sized particles which have been ejected from the target. This problem can however be greatly reduced by use of off-axis PLD, where the substrate is placed parallel to the axis of the plume of material emerging from the target [19]. Just as for sputtering it is necessary to carefully optimize deposition parameters, such as pressure, temperature, laser energy density and repetition rate, and target surface preparation, in order to avoid the formation of second-phase outgrowths in the YBCO films.

Some of the first HTS films were deposited by coevaporation from elemental sources, either electron beam or thermal [20]. Some of the difficulties encountered in applying this technique to *in situ* growth were associated with the fact that the film requires a zone of high oxygen pressure to oxidize the material, while the evaporation sources need to be in a low pressure in order to ensure ballistic transport of the metal atoms. While the use of a relatively low pressure of atomic oxygen or ozone was successful in producing high-quality films, the coevaporation technique has recently come into its own with the invention of a heater scheme which has the substrates on a rapidly rotating platen which alternately exposes the substrate to an enclosed oven at 2 Pa pressure of oxygen, and an opening through which the evaporants arrive at the substrate from a much lower pressure region (0.01 Pa). This technique has already been used to coat substrates as large as 8 inches in diameter, or twelve 2-inch substrates at a time. This large area capability, combined with deposition rates of 20 nm/min, make the process extremely efficient [21,22].

### 3.2. EPITAXIAL INSULATOR FILMS

The same deposition techniques used for HTS films are routinely used to deposit various epitaxial insulators in the fabrication of multilayer devices. Table 1 lists some of the materials routinely used with YBCO, along with their crystal structure, and bulk values of the lattice constant, dielectric constant, and loss tangent. The most developed material is  $\text{SrTiO}_3$ , but its high values of dielectric constant and loss tangent make it undesirable for high frequency applications. While  $\text{CeO}_2$  and  $\text{ZrO}_2$  are widely used, especially as buffer layers, we favor materials cubic perovskite materials which are lattice matched to YBCO, and which have relatively low dielectric constants, such as  $\text{Sr}_2\text{AlTaO}_6$  or  $\text{Sr}_2\text{AlNbO}_6$ .

A common problem with epitaxial insulator growth over YBCO is that the rate of oxygen diffusion through the insulator is so low that it is practically impossible to oxygenate the underlying YBCO [23]. In practice one can reduce the insulator deposition temperature enough so that the resulting increased defect density allows oxygen diffusion, though not so low

TABLE 1. List of epitaxial insulators compatible with YBCO, and some of their material parameters. Many of these are also used as substrates. In cases where YBCO grows rotated with respect to the insulator the relevant diagonal distance, or simple fraction thereof, is listed for comparison with YBCO.

Material	Structure	Bulk Lattice Constant (Å)	Bulk Dielectric Constant	Bulk Loss Tangent
$\text{LaAlO}_3$	rhombohedral	<3.79>	24	$3 \times 10^{-5}$
$\text{NdGaO}_3$	tetragonal	<3.84>	24	$3 \times 10^{-4}$
$\text{SrTiO}_3$	cubic	3.905	>>100	$> 10^{-2}$
$\text{Sr}_2\text{AlTaO}_6$	cubic	3.895	12	$4 \times 10^{-5}$
$\text{Sr}_2\text{AlNbO}_6$	cubic	3.890	19	$2 \times 10^{-5}$
$\text{MgO}$	cubic	4.212	9.6	$4 \times 10^{-5}$
$\text{CeO}_2$	cubic	3.826	16	--
$\text{ZrO}_2$	cubic	3.634	26	$8 \times 10^{-3}$
(YBCO	orthorhombic	<3.85>	--	--)

that there are electrical shorts. It has also been reported that the presence of an oxygen plasma during the cooldown after the insulator growth is effective in oxidizing the YBCO underneath [24].

Many of the materials listed in Table 1 were first used as substrates for HTS films. Two of the most widely used, for high frequency applications, are lanthanum aluminate,  $\text{LaAlO}_3$ , and neodymium gallate,  $\text{NdGaO}_3$ .  $\text{LaAlO}_3$  is available in up to 3-inch diameter, and  $\text{NdGaO}_3$  up to 2-inch. For multilayer devices  $\text{LaAlO}_3$  is not useful because of twinning. The as-grown crystals are heavily twinned, and after a YBCO film is deposited, typically at 600–800°C, which is above the  $\text{LaAlO}_3$  structural phase transition, these twins reform in new locations. The resulting distortion leads to the wafer surface becoming rough, and can result in movement of previously patterned features over distances of several microns. This makes alignment of the next layer impossible. For this reason we use  $\text{NdGaO}_3$  as the substrate for multilayer devices, since its dielectric properties are acceptable, and it can be grown twin-free. In addition, its structural phase transition is at about 1300°C, so that there is no danger of twins forming during film growth.

A recent review of substrate issues is given in reference [25].

#### 4. HTS Josephson Junctions

While numerous approaches have been used to fabricate HTS SNS junctions or weak links, only a few hold the promise of sufficient reproducibility for use in digital circuits. Figure 2 illustrates some of the most promising approaches (from either a practical or theoretical standpoint), which can be grouped into two categories: grain boundary junctions, and SNS junctions with epitaxial normal layers.

##### 4.1. GRAIN BOUNDARY JUNCTIONS

*Grain boundary (GB) junctions*, rely on the experimental fact that a grain boundary in an HTS film, provided the degree of misorientation is great enough, behaves electrically like an SNS junction or weak link. This was investigated in detail at IBM [26–28], where the dependence of the critical current density,  $J_c$ , on misorientation angle was investigated. The grain boundary may be nucleated in an HTS film at a prescribed location such as a grain boundary in the underlying substrate (*bicrystal junction*) or thin-film template (*biepitaxial junctions* [29,30]), or at a step in the substrate (*step-edge grain boundary, or SEGB, junctions*), as illustrated in Fig. 3(a). The

latter approach actually involves two grain boundaries in series, at the top and bottom of the step, although the critical currents of the two are usually sufficiently different that only the weakest one comes into play in applications [31–37].

The SEGB approach has several merits for use in digital circuits. First, the junctions can be located at arbitrary locations and in any of four crystallographically defined directions with respect to the substrate, since the step locations are typically defined using photolithography and ion milling. This is in contrast to the bicrystal junctions, where the grain boundary location is defined by the fusing of two separate, misoriented pieces of substrate material. Second, the misorientation angle of the grain boundaries fortuitously gives a value of  $J_c$  which is in the right range for digital circuits.

A further advantage of the SEGB approach is that it is straightforwardly generalized to a multilayer configuration, where the step may be formed in a deposited insulator instead of, or in addition to, in the substrate [38]. Such a process, first demonstrated by us, is discussed in section 5.

Ultimately the simplicity of the SEGB approach is a limitation, in that there are few experimental parameters available to adjust the critical current and resistance values. In particular, the degree of critical current reproducibility, while sufficient for applications such as SQUIDs, is probably too limited for demanding applications such as digital circuits.

Obviously the potential for formation of *unwanted* grain boundaries at steps has ramifications for the patterning of multilayer circuits, as will be discussed in Section 5.

#### 4.2. ALL-EXPITAXIAL SNS JUNCTIONS

A more promising approach in these respects is the *all epitaxial SNS* junction, based on the deliberate formation of a nominally SNS structure, using a normal layer which is structurally and chemically matched to the YBCO superconducting electrodes. Demonstrated normal materials which meet these criteria include  $\text{PrBa}_2\text{Cu}_3\text{O}_x$  [39–41],  $\text{PrBa}_2\text{Cu}_{3-x}\text{Ga}_x\text{O}_y$  [42], non-superconducting YBCO [43],  $\text{CaRuO}_3$  [44],  $\text{SrRuO}_3$  [45,46] and various substituted YBCO materials, such as  $\text{Y}_{1-x}\text{Ca}_x\text{Ba}_2\text{Cu}_3\text{O}_x$  [47],  $\text{Y}_{1-x}\text{Pr}_x\text{Ba}_2\text{Cu}_3\text{O}_x$  [48,49], and  $\text{YBa}_2\text{Cu}_{3-x}\text{Co}_x\text{O}_x$  [50,51]. The two most common configurations for such all-epitaxial devices are “edge” (or “ramp” or “ramp-edge”) junctions, and a-axis trilayer junctions, illustrated in Figure 2

(b) and (c), respectively. Of these the edge SNS junction is by far the most well developed, since it is based on c-axis oriented films, which are easier to fabricate than a-axis.

#### 4.2.1. Edge Junctions

The edge junction is formed by depositing a c-axis oriented HTS film (the

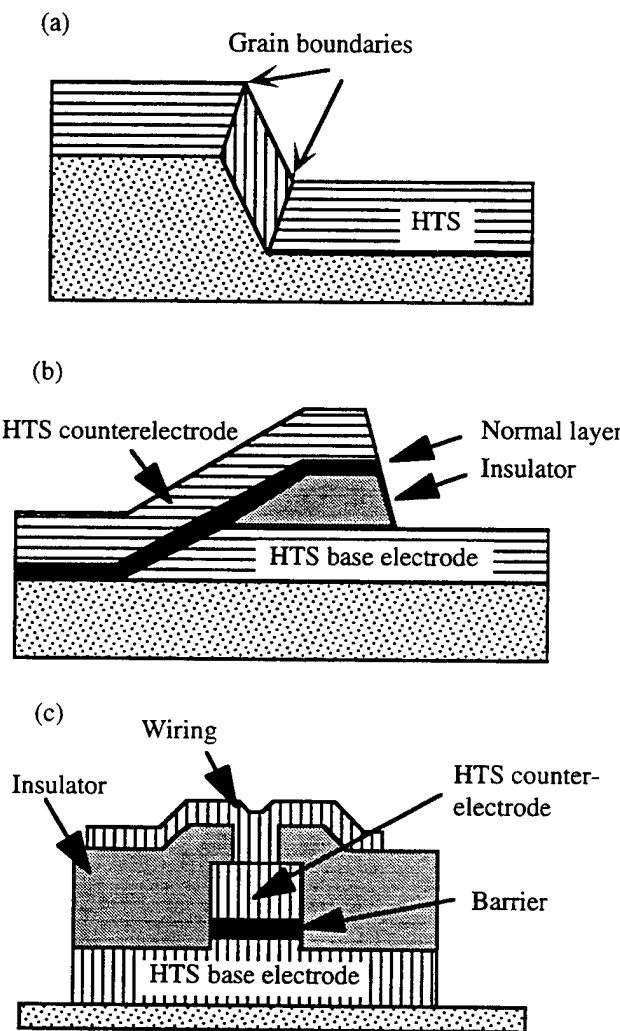


Figure 2. Three types of HTS junctions. (a) Step-edge grain boundary junction (b) Edge, or ramp, SNS junction, and (c) a-axis trilayer junction.

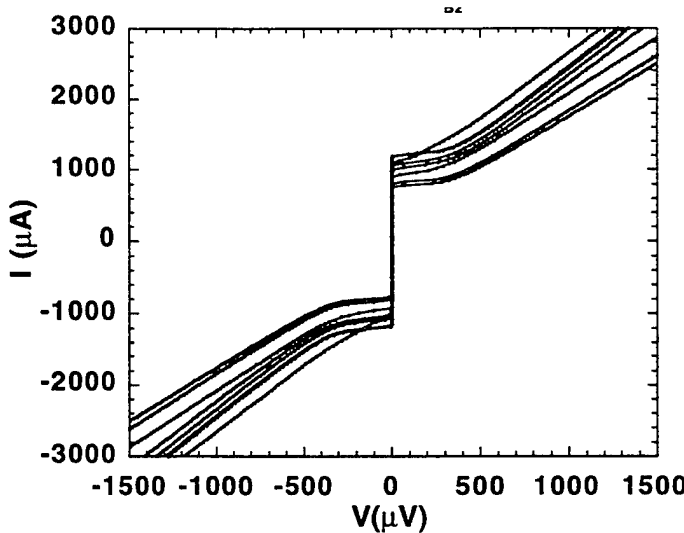


Figure 3. Current voltage characteristics, at 65 K, for eight 4- $\mu\text{m}$  wide SNS edge junctions, with 100  $\text{\AA}$   $\text{YBa}_2\text{Cu}_{2.79}\text{Co}_{0.21}\text{O}_x$  normal metal layer. The uniformity and high  $I_c R_n$  ( $\approx 570 \mu\text{V}$ ) of the junctions is promising for digital circuit applications.

base electrode), followed, usually *in situ*, by an epitaxial insulator. A tapered edge, typically with an angle of 30° or less with respect to the substrate, is formed in this bilayer, commonly by angled ion milling but sometimes by wet-etching [52]. While such a tapered edge is most easily formed by a *unidirectional* milling process, this is generally too restrictive for digital circuits, where it is desirable that junctions be allowed to face in four directions to keep inductances low and allow maximum flexibility in circuit layout. After the edge is formed the sample is cleaned and then the normal layer and top HTS layer, or counterelectrode, are deposited.

Obviously this approach has the disadvantage that one of the key interfaces between superconductor and normal materials is formed *ex-situ*, with the potential for damage associated with ion milling, and formation of a contaminated layer from exposure to air. Ion damage can be quite considerable at typical milling voltages, such as 500 eV, producing a disordered layer of order 4 nm thick [53]. The use of extremely low voltages (down to say, 50 eV) can alleviate, though probably not eliminate, this problem. Techniques have also been demonstrated for formation of the edge junction using shadow techniques in an all *in situ* process [54], although they involve directional depositions and are thus probably not flexible

enough for digital circuit fabrication. As for the effects of atmospheric exposure, they can be reduced by an *in situ* ion clean, immediately before the deposition of the normal layer.

Figure 3 shows current-voltage characteristics for eight 4- $\mu\text{m}$  wide SNS edge junctions, with a 100  $\text{\AA}$   $\text{YBa}_2\text{Cu}_{2.79}\text{Co}_{0.21}\text{O}_x$  normal metal layer. They are consistent with the resistively shunted junction (RSJ) model for a low-capacitance SNS or weak link device. The uniformity and high  $I_cR_n$  ( $\approx 570$   $\mu\text{V}$ ) of the junctions are promising for digital circuit applications. The best such chips have one-sigma spreads in the range of 10–20%, so that, based on Figure 1, circuits with of order 100 junctions should soon be attainable with modest yields.

#### 4.2.2. Trilayer Junctions

An alternative to the c-axis-film-based edge junction is the trilayer junction based on a-axis oriented films, illustrated in Figure 2(c). This junction geometry has the obvious advantage that the key interfaces between superconductor and normal materials can be formed *in situ*, avoiding degradation due to atmospheric exposure or damage associated with ion milling, both of which are unavoidable in the standard edge junction approach. In practice however the relative difficulty of growing high-quality a-axis oriented YBCO films has limited the number of useful demonstrations of this junction geometry. A variant in which (103) oriented YBCO films are used has also been pursued [55].

For circuit use the resistance of such junctions tends to be too low, since the junction size is defined purely lithographically, and thus is typically much larger than that of the edge junction, where one junction dimension is defined by the base electrode film thickness. In addition, the integration of a-axis junctions into a multilayer process will be difficult in that an a-axis oriented YBCO wiring layer connecting the junctions will have very low  $J_c$  ( $\sim 10^4$   $\text{A}/\text{cm}^2$  at 77K, compared to  $\sim 10^6$   $\text{A}/\text{cm}^2$  for c-axis YBCO), which is too low for most circuits. In fact, because of some of these difficulties of junction integration, there has not been to date even a single demonstration of a dc SQUID based on such junctions.

Thus we consider the most promising junction geometry to be the all-epitaxial edge-geometry SNS junction. Much of the discussion in the rest of the paper will focus on issues related to the integration of such junctions into a useful circuit process, with the attributes discussed in the introduction.

## 5. Epitaxial Multilayer Circuit Processing

Although the Josephson junction is the single most important element of a superconducting digital circuit, there are numerous other elements which are required to integrate them into a useful circuit, many of which were enumerated in the introduction. Maintaining the required low gate and interconnect inductance in particular requires a superconducting groundplane to be situated as close as possible to the active layers which contain the junctions, which in turn requires a pinhole-free, low-loss insulator between the superconducting layers.

Figure 4 shows schematic cross sections of two multilayer processes which we have used to demonstrate simple HTS digital circuits. The first is a three-epitaxial-layer process which uses SEGB junctions defined at steps etched part way into the deposited  $\text{SrTiO}_3$  insulator. The second is a six-epitaxial-layer process which incorporates edge SNS junctions, with Co-doped YBCO as the normal layer. In both cases the bottom YBCO layer

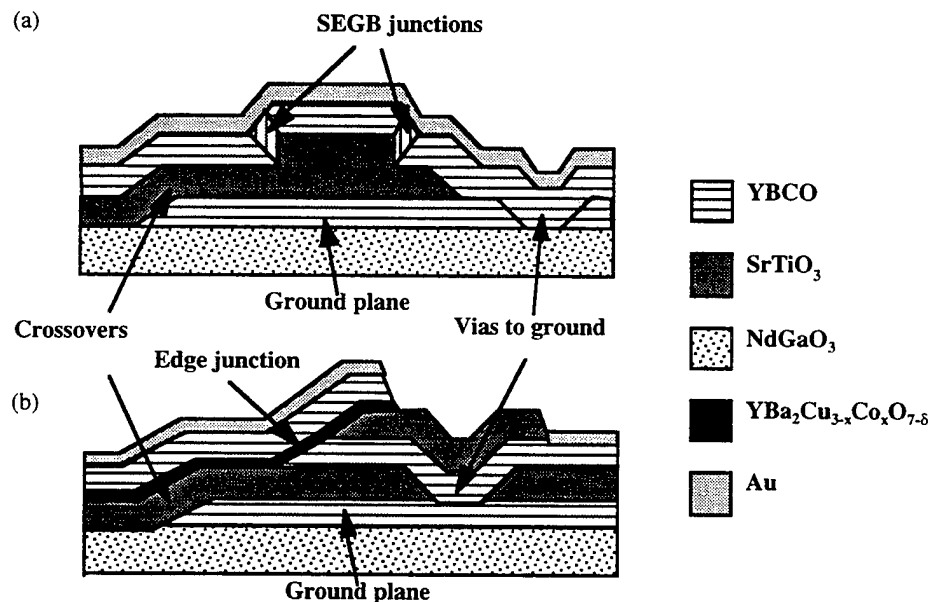


Figure 4. Schematic cross sections of two HTS multilayer processes which we have demonstrated. (a) A three-epitaxial-layer process using SEGB junctions, and (b) a six-epitaxial-layer process using edge SNS junctions.

acts as the ground plane, reducing the inductance of the resulting structures.

In this section we discuss some of the issues involved in building up multiple patterned, epitaxial layers into a useful circuit process. We begin by discussing some generalities about the patterning of such layers.

### 5.1. FILM PATTERNING

The list of processing techniques used in the fabrication of HTS multilayer devices is a fairly short one. The process, at this state of its development, usually consists of a repeating the following set of steps for each of the epitaxial layers (or in some cases for several layers grown *in situ*): 1) Deposit film(s); 2) Define desired pattern by photolithography; 3) Etch film(s); and 4) Remove resist.

Since the integration density is very low at this stage in the development of HTS digital circuits, the demands on photolithography are minimal, and this is usually adequately performed with contact lithography and standard resists. However, due to the requirement that unwanted grain boundaries not form where one epitaxial film grows over the edge of another, measures are taken to ensure that the photoresist *not* have a steep sidewall. This point is intimately related to the usual etch process which is applied to HTS films, which we discuss next.

In the processing of semiconductor circuits, as well as those based on low temperature superconductors, it is common to use a material-selective reactive ion etch (RIE) process, with fluorine and chlorine based gases. Since the fluorides and chlorides of yttrium, barium, and copper are not volatile at temperatures compatible with resist processing, RIE is not useful for HTS. The principal method is thus ion milling with argon, sometimes with oxygen added. This method allows precise pattern definition, and also allows one to obtain the desired tapered edges in the films, typically by milling with the ion beam at a low angle with respect to the substrates, and usually with the substrates rotating about their normal.

Returning to the issue of photolithography, the profile of the tapered edges of the etched films is strongly affected by the profile of the photoresist, and it is usually advantageous to deliberately taper the resist edges. This can be done by “reflowing” the resist at an elevated temperature (typically from 130°C to 180°C). Also, the use of oxygen in the milling gas will tend to erode the photoresist relatively rapidly, making the resist wall recede during the etching, and thus contributing to the taper.

Wet etches can also be used for the patterning of the YBCO layers. For example, in ref. [52] a bromine-in-alcohol etch, first demonstrated by Vasquez [56], was used to prepare edges in bilayers of PBCO (in this case used as an “insulator”) and YBCO for edge junctions. Since the etch rate is highly anisotropic this led to the formation of very shallow tapered edges, about 3° with respect to the substrate. Unfortunately this particular etch is not useful for etching other epitaxial insulators of more interest to HTS digital circuits.

Another technique which has been applied to patterning of HTS films is “lift-off” or “rejection” using a mask of, for example, zirconium oxide on calcium fluoride, which can be dissolved in water after the HTS deposition [57].

Another potentially powerful technique is the use of ion-implantation, to selectively transform regions of an HTS film into an insulator. This has the advantage of leaving a completely planar surface, with no edges at which unwanted grain boundaries might nucleate. Such a process has not yet been used to fabricate a complex multilayer device.

## 5.2. PREPARATION FOR SUBSEQUENT EPITAXIAL GROWTH

There are two factors that necessitate extreme care when preparing a previously deposited and patterned YBCO layer for the growth of an epitaxial overlayer, such as an insulator or another YBCO layer. First YBCO is very reactive, so that a degraded surface layer can form even upon a short exposure to air, and particularly upon processing with photoresist. This layer typically consists of hydroxides, carbonates such as BaCO<sub>3</sub> [56], and hydrocarbons. To ensure high-quality epitaxial overgrowth it is essential to remove this degraded layer. Failure to do so typically leads to subsequent YBCO layers having inferior superconducting properties, and having a large density of defects in the form of Cu-rich second phase particles, or “boulders” which can protrude from the surface by as much as a micron. These can then in turn lead to electrical shorts through insulator films grown over them.

In practice we find that the surface of a patterned YBCO layer is best cleaned of a reacted surface layer by some combination of oxygen plasma, which is very effective in removing hydrocarbons, and ion milling, which etches the surface relatively unselectively. XPS studies of the YBCO surfaces show that carbon peaks caused by exposure to air and to photoresist are completely suppressed when the surface is given a treatment of oxygen

plasma, acetone rinse, second oxygen plasma, and then heating to deposition temperature ( $\approx 700^{\circ}\text{C}$ ) in the sputter gas mixture of argon and oxygen [23].

### 5.3. INSULATOR INTEGRITY

Any of the deposition methods discussed earlier is capable of producing insulators with low pinhole density. In ref. [58] we reported a series of experiments to determine which process parameters had the greatest effect on whether a minimum electrical isolation of  $2 \times 10^4 \Omega\text{-cm}$  was achieved in YBCO/insulator/YBCO trilayer capacitors, using both  $\text{SrTiO}_3$  and  $\text{Sr}_2\text{AlTaO}_6$ . It was found that such factors as the insulator growth temperature in the range of  $660\text{-}750^{\circ}\text{C}$ , whether the layers were deposited without breaking vacuum, interfaces exposed to air, or interfaces exposed to ion-mill processing, were not significant.

Roughness of the first YBCO layer was found to be the key factor in determining electrical isolation. Measurements of the resistance of capacitor structures typically yielded effective resistivities in the  $10^8\text{-}10^9 \Omega\text{-cm}$  range, which is well above the minimum resistivity requirement of  $\sim 10^4 \Omega\text{-cm}$  which we have estimated for high speed digital circuits [23], as long as there was a sufficiently low density ( $\sim 10^2 \text{ cm}^{-2}$  or less) of outgrowths in the bottom YBCO layer.

The disruptive potential of these outgrowths is well illustrated by Figure 5, which shows a cross-sectional TEM image of an SNS edge junction, with a

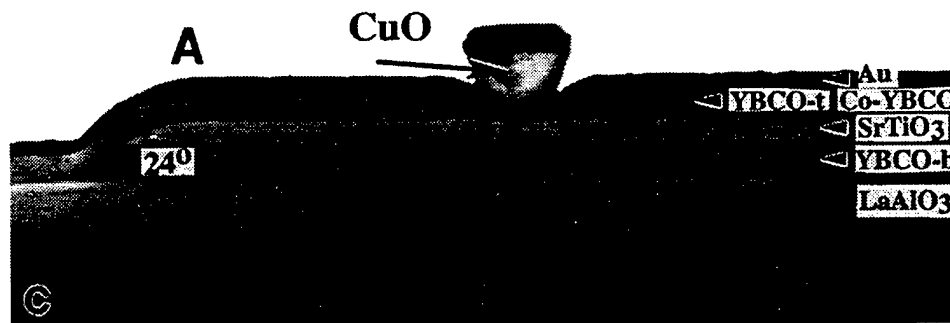


Figure 5. Cross-sectional TEM of an HTS edge junction, showing a CuO "boulder" growing in the top YBCO layer. The presence of such outgrowth in the bottom YBCO layer would typically cause a short through the insulator.

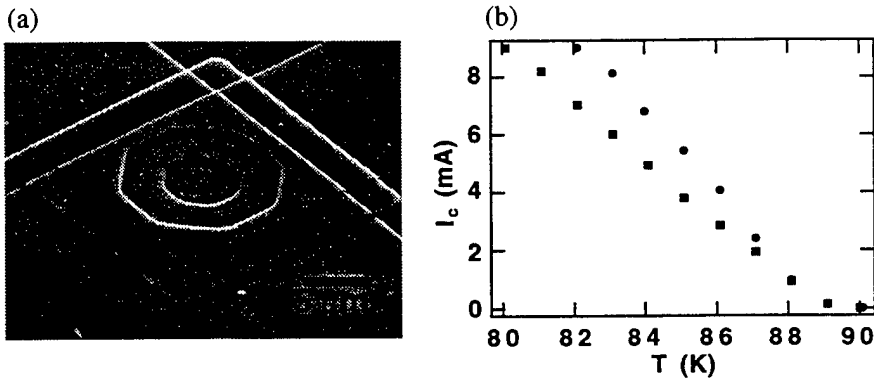


Figure 6. (a) A superconducting via between two YBCO layers. The inner circle is a hole in the bottom YBCO layer to allow a-b-axis contact between the two layers, while the hexagon is the hole through the SrTiO<sub>3</sub> insulator. (b) Critical current vs. temperature for a series array of twelve such vias.

CuO boulder in the top layer. Clearly the presence of such outgrowth in the bottom layer would disrupt the growth of the insulator, and potentially cause a short.

#### 5.4. CROSSOVER AND VIA STRUCTURES

If precautions are taken to ensure that all edges are suitably tapered, as discussed above, then it is generally straightforward to produce crossover structures (where a top HTS films crosses a pattern in the underlying insulator and/or HTS films) and vias (holes in the insulator through which two HTS films contact each other). Crossover  $J_c$ 's in the  $10^5$  A/cm<sup>2</sup> range at 77 K are easily obtained [23], while values above  $10^6$  A/cm<sup>2</sup> have been obtained by use of a novel combination of wet etching and ion milling [59]. The use of planarization techniques potentially allows for essentially no degradation in  $J_c$  compared to a "flat" film [60].

Figure 6 shows a scanning electron micrograph of a typical via structure where two crossed YBCO strips contact each other through a hole in the intervening SrTiO<sub>3</sub>. There is both a-b-axis and c-axis contact between YBCO layers because a hole has been patterned in the bottom YBCO, interior to the hole in the SrTiO<sub>3</sub>. Figure 6(b) shows data for  $I_c$  versus temperature for a series array of twelve such vias. The values obtained are well above junction  $I_c$ 's of interest, and therefore should not be a limitation.

## 5.5. JUNCTIONS & SQUIDS IN MULTILAYERS

We have fabricated and characterized SQUIDs with integrated YBCO ground planes using the multilayer SEGB [38] and SNS [61,62] processes of Figure 4. The properties of the junctions are usually found to be comparable to those fabricated without a ground plane, as long as the ground plane is sufficiently smooth.

Inductance measurements on the SQUIDs yield values of about 1 pH per square at 65 K, which is low enough to be useful for digital circuits, although obtaining a total SQUID inductance as low as 4 pH, as discussed in the introduction, is still a design challenge.

## 5.6. MULTILAYER HTS CIRCUITS

We have also fabricated some simple circuits, with up to ten junctions, using the multilayer processes — to our knowledge the first all-HTS multilayer digital circuits. The most complex, a 1-bit A/D converter is shown in Figure 7, in the SNS version, and was operated successfully at low speed at 65 K [63]. A version based on SEGB JJs was operated up to 60 K.

Other demonstrated circuits include Set-Reset flip-flops and an SFQ-to-dc converter operated at low speed, and a Toggle flip-flop operating correctly, on average, up to 15 GHz.

## 6. Conclusions

There are numerous challenges before us if we are to realize the great potential of HTS digital circuits, the most significant of which is to improve the control, on-chip, chip-to-chip, and run-to-run, of junction critical currents. We believe that the best prospects for this lie with edge-geometry SNS junctions, where spreads approaching 10%, one-sigma, have been observed for as many as twenty junctions.

Further optimization will involve better control of film properties, including surface morphology, which can have a profound effect on junction properties — especially when junctions are fabricated on top of a ground plane. Investigation of new normal-layer materials may also be fruitful, as will more detailed investigation of the formation of the ramp edge, and the

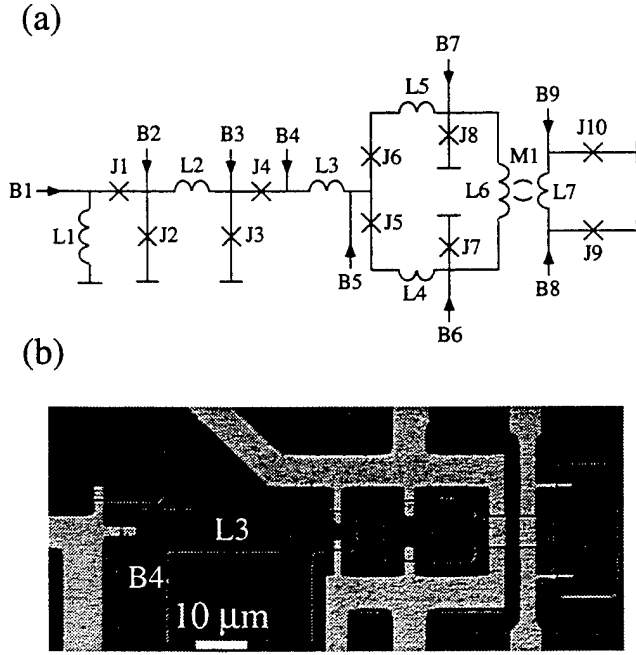


*Figure 7.* Circuit schematic, (a), and optical micrograph, (b), of a multilayer HTS 1-bit analog to digital converter, fabricated using SNS edge junctions. The circuit was operated successfully at 65 K.

growth on that edge. Multilayer configurations with the ground plane on the top of the junctions, which we have recently demonstrated, also require further study, since there are obvious advantages to forming the junctions on the smoothest possible surface — the substrate.

Most of the multilayer work done to date has used  $\text{SrTiO}_3$  or  $\text{PrBa}_2\text{Cu}_3\text{O}_x$  as the deposited insulator, both of which are probably too lossy for high frequency applications. Recently, however, a multilayer junction process incorporating low-loss  $\text{Sr}_2\text{AlNbO}_6$  was demonstrated at Conductus [64]. Further development of low-loss insulators is required.

Much of the development of epitaxial multilayer devices has been driven by the need for SQUIDs for magnetic sensing. However, SQUID applications do not have stringent requirements on junction uniformity, so the impetus for improvements in this area must come from the development of a market for HTS digital products, such as high-resolution and high speed ADCs, network switches, and digital signal processors.

Although the pace of semiconductor development is relentless, we believe that there will be a place for the unique capabilities of a fully developed HTS digital technology.

### Acknowledgements

The authors gratefully acknowledge the assistance of J. C. Brown, G. Faychak, G. Madia, D. Matuza, S. Pieseski, and J. Uphoff. Research performed at Northrop Grumman was supported in part by the Air Force Office of Scientific Research, and by Air Force Wright Laboratory

### References

1. Przybysz, J.X., Miller, D.L., Naviasky, E.H., and Kang, J. H. (1993) Josephson sigma-delta modulator for high dynamic range A/D conversion, *IEEE Transactions on Applied Superconductivity* 3, 2732–2735.
2. Miller, D.L, Przybysz, J.X., Meier, D.L., Kang, J.H., and Worsham, A.H. (1995) Characterization of a superconductive sigma-delta analog to digital converter, *IEEE Transactions on Applied Superconductivity* 5, 2453–2456.
3. Lin, J.C., Polonsky, S. V., Schneider, D.F., Semenov, V.K., Shevchenko, P.N., and Likharev, K.K. (1993) Development of sensitive SFQ-counting A/D converter, *Extended abstracts of the 1993 International Superconductive Electronics Conference, Boulder CO*, pp. 90–91.
4. Przybysz, J.X., Miller, D.L., Kang, J.H., Worsham, A.H., and Meier, D.L., Digital signal processing requirements for single flux quantum cells, *Extended abstracts of the 1993 International Superconductive Electronics Conference, Boulder CO*, pp. 108–109.
5. Herr, Q.P., Vukovic, N., Mancini, C.A., Gaj, K., Ke, Q., Adler, V., Friedman, E.G., Krasniewski, A., Bocko, M.F., and Feldman, M.J. (1996) Design and low speed testing of a four-bit RSFQ multiplier-accumulator, to be published in *IEEE Transactions on Applied Superconductivity*, June 1997.
6. Kaplan, S.B., Rylov, S.V., and Bradley, P.D. (1996) Real-time digital error correction for flash analog-to-digital converter, to be published in *IEEE Transactions on Applied Superconductivity*, June 1997.

7. Worsham, A.H., Przybysz, J.X., Kang, J.H., and Miller, D.L. (1995) A single flux quantum cross-bar switch and demultiplexer, *IEEE Transactions on Applied Superconductivity* **5**, 2996–2999.
8. Worsham, A.H., Miklich, A.H., Miller, D.L., Kang, J.H., and Przybysz, J.X. (1996) Single flux quantum circuits for 2.5Gbps data switching, to be published in *IEEE Transactions on Applied Superconductivity*, June 1997.
9. Kang, J.H., Worsham, A.H., and Przybysz, J.X. (1995) 4.6 GHz SFQ shift register and SFQ pseudorandom bit sequence generator, *IEEE Transactions on Applied Superconductivity* **5**, 2827–2830.
10. Kang, J.H., Przybysz, J.X., Martinet, S.S., Worsham, A.H., Miller, D.L., and McCambridge, J.D. (1996) 3.69 GHz single flux quantum pseudorandom bit sequence generator fabricated with Nb/AlO<sub>x</sub>/Nb, to be published in *IEEE Transactions on Applied Superconductivity*, June 1996.
11. Kirichenko, A.F., and Mukhanov, O.A. (1996) Advanced on-chip test technology for RSFQ circuits, to be published in *IEEE Transactions on Applied Superconductivity*, June 1997.
12. Miller, D.L., Przybysz, J.Z., and Kang, J.-H. (1993) Margins and Yields of SFQ Circuits in HTS Materials, *IEEE Transactions on Applied Superconductivity* **3**, 2728–2731
13. Phillips, J. (1993) Materials issues affecting the new superconducting electronics, in H. Weinstock and R.W. Ralston (eds.), *The New Superconducting Electronics*, Kluwer Academic Publishers, Dordrecht, pp. 59–88.
14. Somekh, R.E., and Barber, Z.H. (1992) The deposition of ceramic superconductors, in R. Kossowsky, B. Raveau, D. Wohlleben, and S.K. Patapics (eds.), *Physics and Materials Science of High Temperature Superconductors, II*, Kluwer Academic Publishers, Dordrecht, pp. 443–469.
15. Chrissey, D.B., and Hubler, G.K., editors (1994) *Pulsed Laser Deposition of Thin films*, John Wiley and Sons, New York.
16. Private communication, Werner Prusheit.
17. Gavaler, J.R., Talvacchio, J., Braggins, T.T., Forrester, M.G., and Gregg, J. (1991) Critical parameters in the single-target sputtering of YBa<sub>2</sub>Cu<sub>3</sub>O<sub>7</sub>, *J. Appl. Phys.* **70**, 4383–4391.
18. Greer, J.A., (1994) Commercial scale-up of pulsed laser deposition, in Chrissey, D.B., and Hubler, G.K., editors (1994) *Pulsed Laser Deposition of Thin films*, John Wiley and Sons, New York.

19. Holzapfel, G., Roas, B., Schultz, L., Bauer, P., and Saemann-Ischenko, G. (1992) *Appl. Phys. Lett.* **59**, 3178.
20. Laibowitz, R.B., Koch, R.H., Chaudhari, P., and Gambino, R.J. (1987) Thin superconducting oxide films, *Phys. Rev. B* **35**, 8821–8823.
21. Berberich, P., Utz, B., Prusseit, W., and Kinder, H. (1994) Homogeneous high quality  $\text{YBa}_2\text{Cu}_3\text{O}_7$  films on 3" and 4" substrates, *Physica C* **219**, 497–504.
22. Prusseit, W., Utz, B., Berberich, P., and Kinder, H. (1994), *Journ. of Supercond.* **7**, 231.
23. Talvacchio, J., Forrester, M.G., and Gavaler, J.R., (1995) Properties of Passive Structures for Multilayer HTS Digital Circuits, *IEEE Transactions on Applied Superconductivity* **5**, 3139–3142.
24. Ockenfuss, G., Wördenweber, R., Scherer, T.A., Unger, R., and Jutzi, W. (1995) In situ low pressure oxygen annealing of  $\text{YBa}_2\text{Cu}_3\text{O}_{7-\delta}$  single and multilayer systems, *Physica C* **243**, 24–28.
25. Phillips, J.M. (1996) Substrate selection for high-temperature superconducting thin films, *J. Appl. Phys.* **79**, 1829–1848.
26. Dimos, D., Chaudhari, P., Mannhart, J., and Legoues, F.K. (1988) Orientation dependence of grain-boundary critical currents in YBCO bicrystals, *Phys. Rev. Lett.* **61**, 219–2222.
27. Dimos, D., Chaudhari, P., and Mannhart, J. (1990) Superconducting transport properties of grain boundaries in YBCO bicrystals, *Phys. Rev. B* **41**, 4038–4049.
28. Gross, R., Chaudhari, P., Kawasaki, M., and Gupta, A. (1991) Superconducting transport characteristics of YBCO grain boundary junctions, *IEEE Trans. Mag.* **27**, 3227–3230.
29. Char, K., Colclough, M.S., Garrison, S.M., Newman, N., and Zaharchuk, G. (1991) Biepitaxial grain-boundary junctions in YBCO, *Appl. Phys. Lett.* **59**, 733–735.
30. Wu, X.D., Luo, L., Muenchausen, R.E., Springer, K.N., and Foltyn, S. (1992) Creation of 45° grain-boundary junctions by lattice engineering, *Appl. Phys. Lett.* **60**, 1381–1383.
31. Simon, R.W., Burch, J.F., Daly, K.P., Dozier, W.D., Hu, R., Lee, A.E., Luine, J.A., Manasevit, H.M., Platt, C.E., Schwarzbeck, S.M., St. John, D., Wire, M.S., and Zani, M.J. (1990) Progress towards a YBCO circuit process, in R.D. McConnell and R. Noufi (eds.), *Science and Technology of Thin Film Superconductors 2*, Plenum Press, New York, pp. 549–558.
32. Jia, C.L., Kabius, B., Urban, K., Herrmann, K., Cui, G.J., Schubert, J., Zander, W., Braginski, A.I., and Heiden, C. (1991) Microstructure of

epitaxial YBCO films on step-edge  $\text{SrTiO}_3$  substrates, *Physica C* **175**, 545–554.

- 33. Jia, C.L., Kabius, B., Urban, K., Herrmann, K., Schubert, J., Zander, W., and Braginski, A.I., (1992) The microstructure of epitaxial YBCO films on steep steps in  $\text{LaAlO}_3$  substrates, *Physica C* **196**, 211–226.
- 34. Herrmann, K., Zhang, Y., Mück, H.M., Schubert, J., Zander, W., and Braginski, A.I. (1991) Characterization of  $\text{YBa}_2\text{Cu}_3\text{O}_7$  Step-Edge Junctions, *Supercond. Sci. & Techn.* **4**, 583–586.
- 35. Herrmann, K., Kunkel, G., Siegel, M., Schubert, J., Zander, W., Braginski, A.I., Jia, C.L., Kabius, B., and Urban, K. (1995) Correlation of YBCO step-edge junction characteristics with microstructure, *J. Appl. Phys.* **78**, 1131–1139.
- 36. Luine, J., Bulman, J., Burch, J., Daly, K., Pettiette-Hall, C., and Schwarzbek, S. (1992) Characteristics of high performance YBCO step-edge junctions, *Appl. Phys. Lett.* **61**, 1128–1130.
- 37. Sun, J.Z., Gallagher, W.J., Callegari, A.C., Foglietti, V., and Koch, R.H. (1993) Improved process for high- $T_c$  superconducting step-edge junctions, *Appl. Phys. Lett.* **63**, 1561–1563.
- 38. Forrester, M.G., Davidson, A., Talvacchio, J., Gavaler, J.R., and Przybysz, J.Z., (1994) Inductance measurements in multilevel high  $T_c$  step-edge grain boundary SQUIDs, *Appl. Phys. Lett.* **65**, 1835–1837.
- 39. Gao, J., Aarnink, W.A.M., Gerritsma, G.J., and Rogalla, H. (1990) Controlled preparation of all high- $T_c$  SNS-type edge junctions and dc SQUIDs, *Physica C* **171**, 126–130.
- 40. Gao, J., Boguslavskii, Y., Klopman, B.B., Terpstra, D., Wijbrans, R., Gerritsma, G.J., and Rogalla, H. (1992) YBCO/PRBCO/YBCO Josephson ramp junctions, *J. Appl. Phys.* **72**, 575–583.
- 41. Barner, J.B., Hunt, B.D., Foote, M.C., Pike, W.T., and Vasquez, R.P. (1993)  $\text{YBa}_2\text{Cu}_3\text{O}_{7-\delta}$ -based, edge-geometry SNS Josephson junctions with low-resistivity  $\text{PrBa}_2\text{Cu}_3\text{O}_{7-\delta}$  barriers, *Physica C* **207**, 381–390.
- 42. Verhoeven, M.A.J., Gerritsma, G.J. and Rogalla, H., Ramp type HTS junctions with  $\text{PrBaCuBaO}$  barriers, *IEEE Transactions on Applied Superconductivity* **5**, 2095–2098.
- 43. Hunt, G.D., Foote, M.C., and Bajuk, L.J. (1991) All-high- $T_c$  edge-geometry weak links utilizing YBCO barrier layers, *Appl. Phys. Lett.* **59**, 982–984.
- 44. Char, K., Colclough, M.S., Geballe, T.H., and Myers, K.E. (1993) High  $T_c$  superconductor-normal-superconductor Josephson junctions using  $\text{CaRuO}_3$  as the metallic barrier, *Appl. Phys. Lett.* **62**, 196–198.

45. Antognazza, L., Char, K., Geballe, T.H., King, L.L.H., and Sleight, A.W. (1993) Josephson coupling of YBCO through a ferromagnetic barrier  $\text{SrRuO}_3$ , *Appl. Phys. Lett.* **63**, 1005–1007.
46. Dömel, R., Horstmann, C., Siegel, M., and Braginski, A.I. (1995) Resonant tunneling transport across YBCO- $\text{SrRuO}_3$  interfaces, *Appl. Phys. Lett.* **67**, 1775–1777.
47. Antognazza, L., Moeckly, B.H., Geballe, T.H., and Char, K. (1995) Properties of high  $T_c$  Josephson junctions with  $\text{Y}_{0.7}\text{Ca}_{0.3}\text{Ba}_2\text{Cu}_3\text{O}_{7-\delta}$  barrier layers, *Phys. Rev. B* **52**, 4559–4567.
48. Polturak, E., Koren, G., Cohen, D., Aharoni, E., and Deutscher, G. (1991) The proximity effect in YBCO/ $\text{Y}_{0.6}\text{Pr}_{0.4}\text{Ba}_2\text{Cu}_3\text{O}_7$ /YBCO SNS junctions, *Phys. Rev. Lett.* **67**, 3038–3041.
49. Stölzel, C., Siegel, M., Adrian, G., Krimmer, C., Söllner, J., Wilkens, W., Schulz, G., and Adrian, H. (1993) Transport properties of YBCO/ $\text{Y}_{0.3}\text{Pr}_{0.7}\text{Ba}_2\text{Cu}_3\text{O}_{7-\delta}$ /YBCO Josephson junctions, *Appl. Phys. Lett.* **63**, 2970–2972.
50. Char, K., Antognazza, L. and Geballe, T.H. (1994) Properties of YBCO/  $\text{YBa}_2\text{Cu}_{2.79}\text{Co}_{0.21}\text{O}_{7-x}$ /YBCO edge junctions, *Appl. Phys. Lett.* **65**, 904–906.
51. Hunt, B.D., Foote, M.C., Pike, W.T., Barner, J.B., and Vasquez, R.P. (1994) High- $T_c$  edge-geometry SNS weak links on silicon-on-sapphire substrates, *Physica C* **230**, 141–152.
52. Faley, M.I., Poppe, U., Jia, C.L., and Urban, K. (1995) Proximity-effect in edge-type junctions with PBCO barriers prepared by Br-ethanol etching, *IEEE Transactions on Applied Superconductivity* **5**, 2091–2094.
53. Jia, C.L., Faley, M.I., Poppe, U., and Urban, K. (1995) The effect of chemical and ion-beam etching on the atomic structure of interfaces in YBCO/PBCO Josephson junctions, *Appl. Phys. Lett.* **67**, 3635–3637.
54. Strikovsky, M.D., and Engelhardt, A. (1996) Ramp-type  $\text{YBa}_2\text{Cu}_3\text{O}_{7-\delta}$  Josephson junctions with high characteristic voltage, fabricated by a new, completely *in situ* growth technique, *Appl. Phys. Lett.* **69**, 2918–2920..
55. Sato, H., Akoh, H., and Takada, S. (1994) Anisotropic Josephson effect in all (103)-oriented  $\text{YBa}_2\text{Cu}_3\text{O}_{7-\delta}$ / $\text{PrBa}_2\text{Cu}_3\text{O}_{7-\delta}$ /YBCO junctions.
56. Vasquez, R.P., Hunt, B.D., and Foote, M.C. (1988) Nonaqueous chemical etch for  $\text{YBa}_2\text{Cu}_3\text{O}_{7-x}$ , *Appl. Phys. Lett.* **53**, 2692–2694.

57. Strikovsky, M.D., Kahlmann, F., Schubert, J., Zander, W., Glyantsev, V., Ockenfuss, G., and Jia, C.L. (1995) Fabrication of YBCO thin-film flux transformers using a novel microshadow mask technique for *in situ* patterning, *Appl. Phys. Lett.* **66**, 3521–3523.
58. Talvacchio, J., Forrester, M.G., Hunt, B.D., McCambridge, J.D., and Young, R.M. (1996) Materials basis for a six-level epitaxial HTS digital circuit process, to be published in *IEEE Transactions on Applied Superconductivity*, June 1997.
59. Li, H.Q., Ono, R.H., Vale, L.R., Rudman, D.A., and Liou, S.H. (1996) A novel multilayer circuit process using  $\text{YBa}_2\text{Cu}_3\text{O}_x/\text{SrTiO}_3$  thin films patterned by wet etching and ion milling, *Appl. Phys. Lett.* **69**, 2752–27554.
60. Marathe, A.P., Ludwig, F., and Van Duzer, T. (1995) Process issues and components for HTS digital integrated circuit fabrication, *IEEE Transactions on Applied Superconductivity* **5**, 3135–3138.
61. Hunt, B.D., Forrester, M.G., Talvacchio, J., McCambridge, J.D., and Young, R.M. (1996) High- $T_c$  superconductor/normal-metal/superconductor edge junctions and SQUIDs with integrated groundplanes, *Appl. Phys. Lett.* **68**, 3805–3807.
62. Forrester, M.G., Hunt, B.D., Talvacchio, J., Young, R.M., and McCambridge, J.D. (1996) Multilayer edge SNS SQUIDs for digital circuits, to be published in *IEEE Transactions on Applied Superconductivity*, June 1997.
63. McCambridge, J.D., Forrester, M.G., Miller, D.L., Hunt, B.D., Przybysz, J.X., Talvacchio, J., and Young, R.M. (1996) Multilayer HTS SFQ analog-to-digital converters, to be published in *IEEE Transactions on Applied Superconductivity*, June 1997.
64. Mallison, W.H., Berkowitz, S.J., Hirahara, A.S., Neal, M.J., and Char, K. (1996) A multilayer  $\text{YBa}_2\text{Cu}_3\text{O}_x$  Josephson junction process for digital circuit applications, *Appl. Phys. Lett.* **68**, 1835–1837.

# Temperature dependence of the magnetic-flux penetration into disk-shaped $\text{YBa}_2\text{Cu}_3\text{O}_{7-\delta}$ thin films

## APPENDIX 20

H. Darhmaoui and J. Jung

Department of Physics, University of Alberta, Edmonton, Alberta, Canada T6G 2J1

J. Talvacchio

Westinghouse Science and Technology Center, Pittsburgh, Pennsylvania 15235

M. A-K. Mohamed\*

Department of Physics, University of Lethbridge, Lethbridge, Alberta, Canada T1K 3M4

L. Friedrich

Department of Electrical Engineering, University of Alberta, Edmonton, Alberta, Canada T6G 2G7

(Received 5 July 1995; revised manuscript received 21 December 1995)

Temperature dependence of the penetration of magnetic flux into  $\text{YBa}_2\text{Cu}_3\text{O}_{7-\delta}$  disk-shaped thin films was investigated at low magnetic fields. We studied the conditions characteristic of complete and incomplete flux-penetration states. The experimental procedure involved the measurements of the profiles of trapped magnetic flux as a function of temperature and the decays of trapped flux at various points across the disk. We determined temperatures and magnetic fields at which the crossover between incomplete and complete flux penetration occurs. This crossover is governed by the temperature dependence of the critical current density. The distributions of the critical currents across the disk in the complete flux-penetration state were found to be temperature independent. No evidence for the Bean-Livingston surface barriers has been found. [S0163-1829(96)03518-7]

## I. INTRODUCTION

Studies of magnetic-flux penetration into superconducting thin films have been recognized as those which provide important information on critical currents, on distribution of shielding currents and weak links, on demagnetization effects, and on complete and partial flux penetration states. Results obtained on thin films of circular geometry (which ensures homogeneous penetration of flux) seem to be particularly useful due to the need for verification of the conventional critical state model. Penetration of magnetic flux into disk-shaped thin films of  $\text{YBa}_2\text{Cu}_3\text{O}_{7-\delta}$  (YBCO) has been studied with the magneto-optical Faraday rotation method.<sup>1,2</sup> Calculation of the distribution of both the axial and radial components of the magnetic field across a thin circular film has been performed by Theuss, Forkl, and Kronmüller<sup>3</sup> for film thicknesses smaller than the London penetration depth. Good agreement was obtained between the calculated distribution of the axial component of the field and the experimental data (Ref. 2). However, the authors admitted that the magneto-optical measurements do not provide an evidence of a complete flux penetration (which is, on the other hand, given by the saturation of dc magnetization in increasing applied magnetic field) due to insensitivity of a central fringe area, of width about 20% of the disk's radius, to the penetrating magnetic field. The available experimental data are insufficient to explain deviation of the magnetic-flux distribution from that predicted by the conventional critical state model. This applies both to the distribution of the radial component of the magnetic induction  $B_r$ , for which there are recorded no experimental data, and to the distribution of the

axial component  $B_z$ , with missing temperature and magnetic-field dependence of the complete flux-penetration states. This information is crucial for the analysis of the critical state model (and its applicability to thin-film superconductors) which has been proposed by Theuss, Forkl, and Kronmüller,<sup>3</sup> Däumling and Larbalestier,<sup>4</sup> Conner and Malozemoff,<sup>5</sup> and Brandt.<sup>6</sup> The leading conclusion of this analysis is that in the case of thin-film circular samples, the critical state model requires modification by taking into account dominating influence of the gradient of the field component  $\partial B_r / \partial z$  on the critical current density  $J_c = (1/\mu_0)(\partial B_r / \partial z - \partial B_z / \partial r)$ , where  $\partial B_r / \partial z$  is much larger than  $\partial B_z / \partial r$ . Therefore, the critical state in the disk occurs rather through the thickness  $d$ , and not the radius  $r$ . Theuss, Forkl, and Kronmüller<sup>3</sup> showed that in the absence of the experimental data for the radial component  $B_r(r)$ , one could calculate it using experimental results for  $B_z(r)$ . Their computation consists of the following steps:

- Fitting of the current distribution  $I(r)$  to the Biot-Savart law, so it could reproduce the experimental distribution of  $B_z(r)$ ;
- Calculation of the radial component  $B_r(r)$  from the Biot-Savart law using the current distribution  $I(r)$ ;
- Estimation of  $\partial B_r / \partial z$  by taking  $\partial B_r / \partial z \approx 2B_r(d/2)$  [where  $B_r(d/2)$  is the field on the surface] under the assumption that  $B_r(z)$  vary smoothly through the film thickness  $d$ .

This procedure was used to compare the  $\partial B_z / \partial r \approx B_z(a)$  term (where  $a$  is the radius of the thin-film disk) with that for

$\beta_r/\partial z \approx 2B_r(d/2)/d$  in the formula for the current density. Comparison of the experimental  $B_z(r)$  with the calculated  $\beta_z(r)$  shows that at low magnetic inductions  $B_z(d/2)$  on the disk's surface and  $B_z(a)$  on the disk's surface and at the disk's edge are of the same order of magnitude. This implies that  $\partial B_z/\partial z$  is greater than  $\partial B_z/\partial r$  approximately by a factor of  $a/d$ .

Briefly, the analysis of Theuss, Forkl, and Kronmüller<sup>3</sup> suggests that the knowledge of an experimental distribution  $\beta_z(r)$  across a disk-shaped thin film is essential for an estimation of the distribution of the current  $I(r)$  and its dependence on an external magnetic field, which can be used further to calculate magnetic stray field effects. It is therefore worthwhile to expand the investigations of  $B_z(r)$  by performing the following experiments:

- (a) Measurements of the temperature and magnetic-field dependence of an incomplete-complete flux-penetration states;
- (b) Measurements of the time dependence of the  $B_z(r)$  profiles for an incomplete and complete flux-penetration states, and
- (c) Measurements of the magnitude of the applied magnetic field required for a full flux penetration.

We have attempted to make the above measurements using a Hall-probe scanning system. A Hall-probe scanning system has been used by us since 1988 for studies of magnetic-flux distributions and persistent currents in YBCO ceramic disks and rings (Ref. 7). This system provides better accuracy regarding the measurement of a magnitude of the magnetic field than the corresponding magneto-optical Faraday effect method. It is also free of the unwanted change in sensitivity, shown by a magneto-optical method,<sup>3</sup> during the measurement of the field distribution between the edge and the center of the disk-shaped sample. A Hall-probe scanning system also allows to measure, with high accuracy, the time-dependent changes in  $B_z(r)$  at any point along the disk's diameter.

The measurements of the flux penetration condition were made using the distribution of the trapped field rather than the shielding field. The advantage of that is much more precise determination of the transition between the partial and complete penetration of magnetic flux. The results were compared with the predictions of the existing critical state models<sup>3-6</sup> and with the measurements of the flux and current distributions in a square-shaped thin film of YBCO by Xing *et al.*<sup>8</sup> and Grant *et al.*<sup>9</sup>

## II. EXPERIMENTAL PROCEDURE

### A. Sample's preparation and characterization

Two thin-film YBCO disks, having diameter of 15 mm and thickness of 5000 Å (disk No. 1) and 2000 Å (disk No. 2), were sputter-deposited on (100)-oriented  $\text{LaAlO}_3$  substrates using off-axis dc magnetron sputtering from a stoichiometric YBCO target.<sup>10</sup> The films were *c*-axis oriented, with the *c* axis perpendicular to the disk's plane. The resistance measurement of superconducting transition gave  $T_c$  ( $\lambda=0$ ) of 90.3 K for disk No. 1, and of 89.2 K for disk No. 2. The measurement of the real part of ac susceptibility  $\chi(T)$  with  $f=3.22$  kHz and  $H_{\text{rms}}=1.8$  G, revealed  $T_c=87$  K, for

disk No. 1 and 86 K for disk No. 2, and the width of the superconducting transition  $\Delta T \approx 1.5$  K in both cases. The imaginary part of ac susceptibility  $\chi'(T)$  shows a sharp peak at 86 K for disk No. 1 and at 85 K for disk No. 2.

### B. Magnetic-flux-penetration measurement procedure

Magnetic-flux penetration was inferred from the measurements of the trapped magnetic-flux density across the disk as a function of temperature and applied magnetic field. The measurements were done with a scanning Hall-probe system. A Hall probe of the sensitive area of  $0.4 \text{ mm}^2$  and sensitivity of 20–30 mG was used to record distributions of magnetic field at a distance of 1.6 mm above the disk. Time dependence of the magnetic-flux density was measured with a Hall probe at various points along the disk's diameter for a time range of up to  $10^4$  sec. The details of the experimental setup, that was used in these studies, are reported in Ref. 11. The measurement of magnetic-flux penetration was based on the following procedure. After zero-field cooling (ZFC) the disk down to various temperatures below  $T_c$ , the external magnetic field was applied in a direction perpendicular to the disk's plane and parallel to the film's *c* axis (the external magnetic field over a range 0–750 G was generated by non-superconducting solenoid). This was followed by the measurement of the profile of the axial component of the shielding field (which is the difference between the applied field and the field measured by the probe) and that produced by the trapped field when the external magnetic field was reduced to zero. The information on an incomplete and complete flux penetration was obtained by

- (a) plotting the magnitude of the trapped field in the disk's center versus temperature for a constant applied magnetic field, and by
- (b) plotting the decay rates of the trapped field (recorded at various points along the disk's diameter) versus distance from the disk's center for fixed temperatures and applied magnetic field.

### C. Critical current measurement procedure

The temperature dependence of the critical current was inferred from the temperature dependence of the magnetic field generated at the center of a ring by the persistent circulating current at the critical level. The ring of the outer diameter of 8.5 mm and the inner diameter of 5 mm was etched from disk No. 1 using the photolithography technique. The persistent current was induced in the zero-field-cooled ring by applying and subsequently switching off the external magnetic field. The profile of the magnetic field produced by the current was measured with a scanning Hall probe. The profile due to the current has a single maximum at the ring's center, which can be distinguished from that due to the magnetic vortices trapped in the ring's bulk which exhibits two maxima above the ring's bulk and a minimum in the ring's center. The magnitude of the critical current is proportional to the saturation value of the magnetic induction in the ring's center according to the Biot-Savart law (this can be achieved by increasing the external magnetic field). The magnetic-field dependence of the critical current was measured in the field-cooled ring. After field cooling down to a

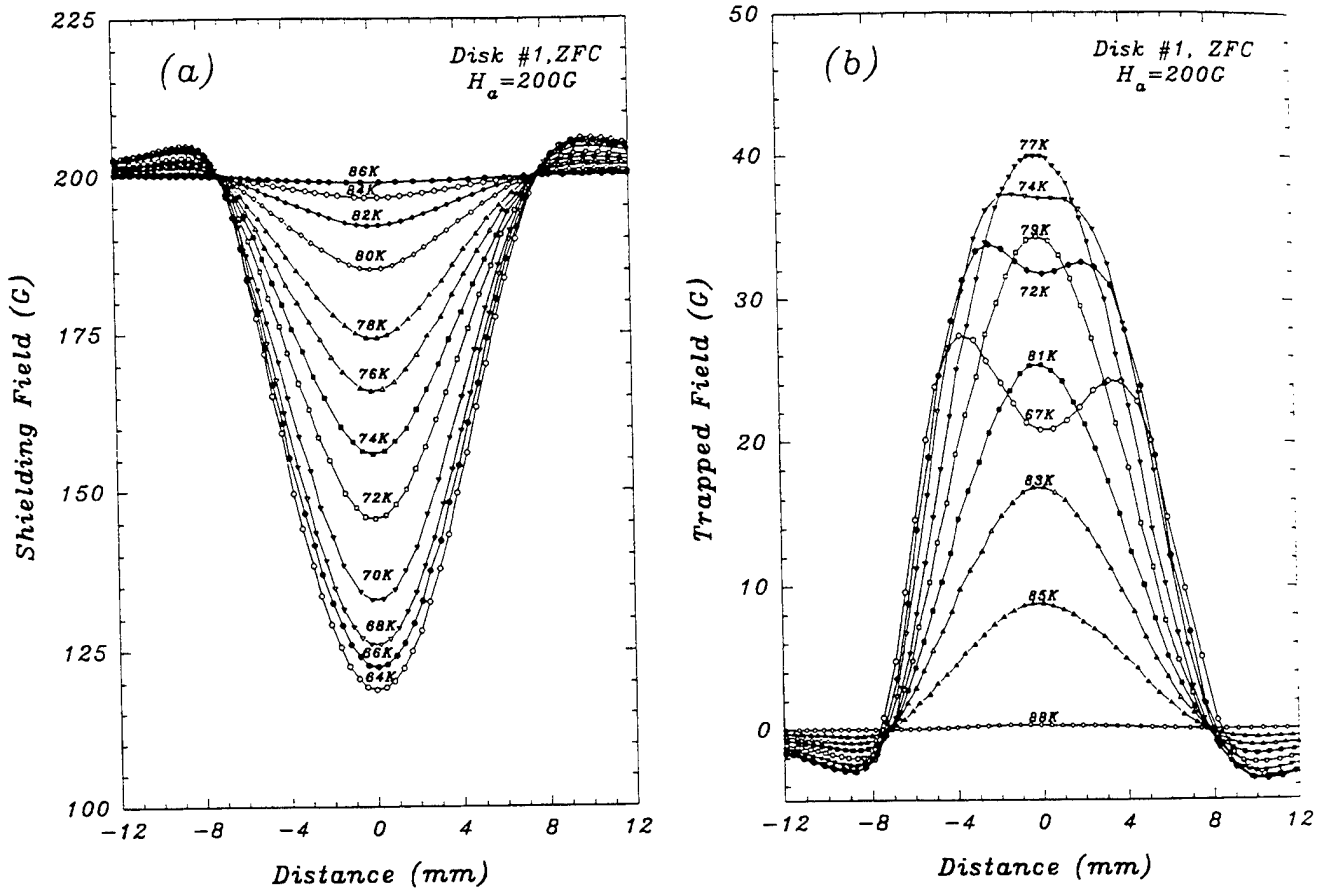


FIG. 1. (a) The profiles of the magnetic field shielded by the zero-field-cooled disk No. 1 at various temperatures between 60 and 90 K, in the presence of an external field of 200 G. The profiles are measured by a scanning Hall probe at a distance of 1.6 mm from the sample. Distances  $\pm 7.5$  mm and  $-7.5$  mm mark the disk edges. (b) The profiles of the magnetic field trapped in the zero-field cooled disk No. 1 at various temperatures between 60 and 90 K after the external field of 200 G was switched off. Note that above 77 K the complete flux-penetration state was reached.

certain temperature, the additional external magnetic field was applied. This was followed by the measurements of the axial component of the persistent current's self-field, when the additional external field was reduced to zero. In this case, the self-field of the current was superposed on the Meissner field. Similarly to the ZFC case, the value of the critical current was determined from the saturation value of the axial component of the current's self-field in the ring's center (see Ref. 11 for details of this procedure).

### III. EXPERIMENTAL RESULTS

The profiles of the magnetic field shielded by disk No. 1 when an external magnetic field of 200 G was applied to the zero-field-cooled (ZFC) sample are plotted in Fig. 1(a) for various temperatures between 60 and 86 K. These distributions do not indicate which temperature corresponds to a complete penetration of the magnetic flux into the disk. This information is provided by the profiles of the magnetic field trapped in the disk at various temperatures when the external field of 200 G was reduced to zero [Fig. 1(b)]. The crossover between partial and complete flux penetration can be seen even clearer in Fig. 2 where the magnetic field trapped in the disk's center is plotted versus temperature for constant applied magnetic fields of 40, 80, 123, and 200 G. The maxi-

mum in the trapped field (and the inflection point on the shielding field versus temperature curve) indicate the cross over temperature. The magnitude of the trapped field at the maximum decreases linearly with increasing crossover temperature [Fig. 3(a)]. This could also be seen in Fig. 2(d). The maximum trapped field is also proportional to the minimum magnitude of the applied field required for a complete flux penetration [Fig. 3(b)]. The temperature dependence of the maximum field trapped in the disk and that of the magnetic field generated by the critical persistent current circulating in the ring coincide (Fig. 4). Figures 5(a) and 5(b) show the distributions of the trapped magnetic flux measured across disk No. 1 at 79 K (corresponding to the complete flux penetration state after a field of 200 G was applied to the zero-field-cooled sample) and at 67 K (corresponding to the incomplete flux penetration). They are plotted together with the distribution of the normalized decay rates  $S = (1/B_0)dB/d\ln t$  for the motion of the trapped flux ( $S$  was measured over a time range  $1-10^4$  sec). The complete flux penetration condition is characterized by the normalized decay rates which do not vary much ( $0.012 < S < 0.015$ ) across the disk. For the incomplete flux penetration  $S$  has a minimum (at  $S=0.0045$ ) at the disk's center and a maximum (at  $S=0.012$ ) at the disk's edge. The magnetic field trapped in the disk's center when a field of 200 G was applied to the

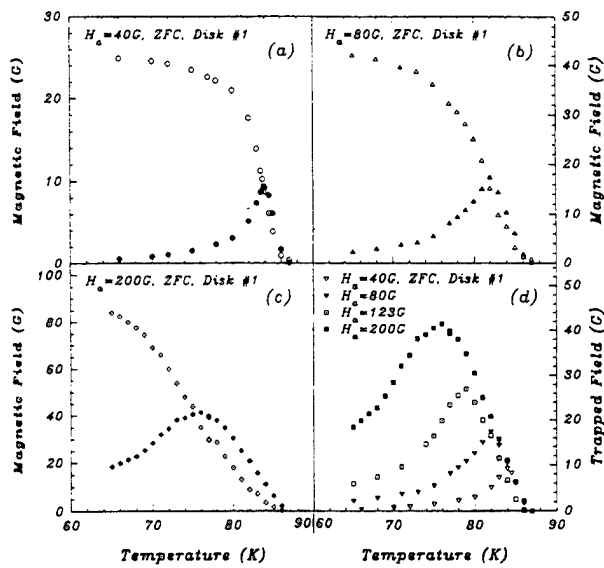


FIG. 2. Open symbols mark temperature dependence of the magnetic field shielded in the center of the zero-field-cooled disk No. 1 in the presence of external fields of 40 G (a), 80 G (b), and 200 G (c). Solid symbols mark temperature dependence of the magnetic field trapped in the center of the disk after the applied field was reduced to zero. The maximum trapped field indicates the crossover between the partial and complete flux-penetration states. Note that this maximum coincides with the inflection point on the shielding field versus temperature curve. (d) Temperature dependence of the field trapped in disk No. 1, plotted for various applied fields between 40 and 200 G. The complete flux-penetration state is common for all trapped fields at temperatures higher than that corresponding to the maximum trapped field. Discrepancies observed for various applied fields are caused by the time decay of the trapped field.

zero-field-cooled sample is plotted with the corresponding normalized decay rates versus temperature (over a range of 55–85 K) in Fig. 5(c). The decay rates are independent of temperature at temperatures corresponding to the complete (with average  $S=0.015$ ) and incomplete (with average  $S=0.0055$ ) flux penetration states. The decay rates in the complete flux-penetration regime are approximately two times the value observed for the incomplete flux penetration at the same temperature range [Figs. 5(c) and 5(d)]. The normalized decay rates  $S$  were measured at the disk's center for a complete flux-penetration state (after applying a saturating magnetic field of 750 G to the zero-field-cooled sample) over a range of temperatures between 60 and 85 K. The decay rates are logarithmic in time up to a maximum waiting time of  $10^4$  sec. The decay rates  $S$  are plotted, together with the corresponding flux-pinning energy  $E_0=kT/S$  and the trapped field, versus temperature in Fig. 5(d). The transition between complete and incomplete flux penetration can be seen also in disk No. 2, however, the applied magnetic field required to reach the full flux-penetration state at fixed temperature, is about a factor of 4 smaller than the corresponding applied field for disk No. 1. Figure 6(a) shows different stages of flux penetration into disk No. 2 at 30 K, after an increasing external magnetic field (up to 750 G) was applied to the zero-field-cooled sample. The distributions of the trapped magnetic field, in a complete flux-penetration state are presented in Fig. 6(b) for temperatures between 30

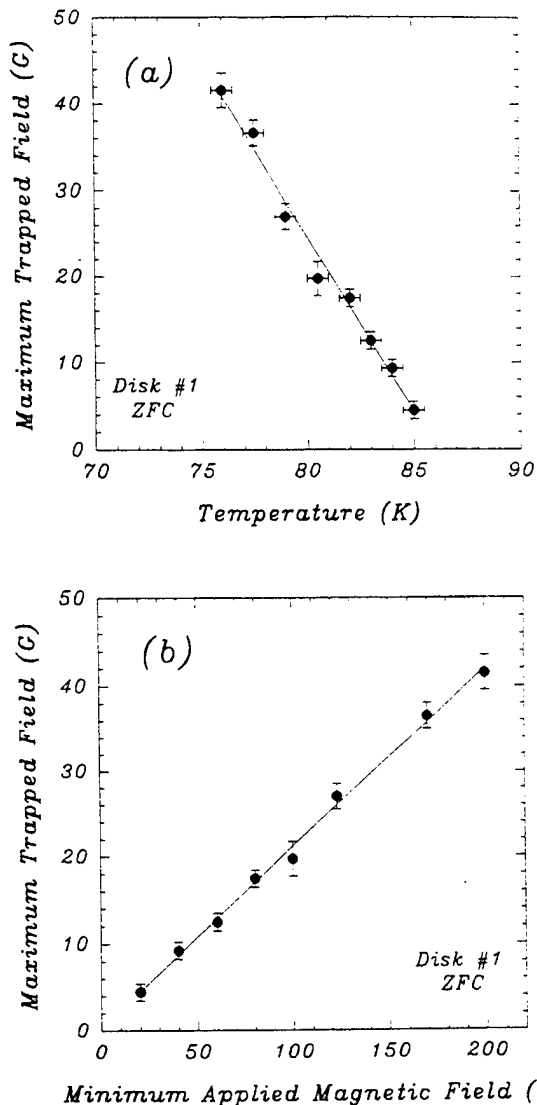


FIG. 3. (a) Temperature dependence of the maximum magnetic field which can be trapped in the center of the zero-field-cooled disk No. 1. (b) Dependence of the maximum trapped field on the minimum magnitude of the external magnetic field required for a complete flux penetration.

and 85 K. The field trapped in the disk's center decreases linearly with increasing temperature [Fig. 6(c)]. For ring No. 1, the magnetic field trapped in the center of the zero-field-cooled ring, when a field of 200 G was applied to it, is plotted together with the corresponding normalized decay rates versus temperature (over a range of 50–85 K) in Fig. 7(a). The decay rates are independent of temperature at temperatures above 64 K, corresponding to the full critical state (with average  $S=0.0145$ ), and at temperatures below 63 K, corresponding to the partial critical state (with average  $S=0.0025$ ). The distributions of the trapped magnetic field, in a full and partial critical state, are presented in Fig. 7(b), for temperatures between 50 and 90 K.

#### IV. DISCUSSION

The profiles of the magnetic induction measured across the thin-film disk, when an external field is shielded by it

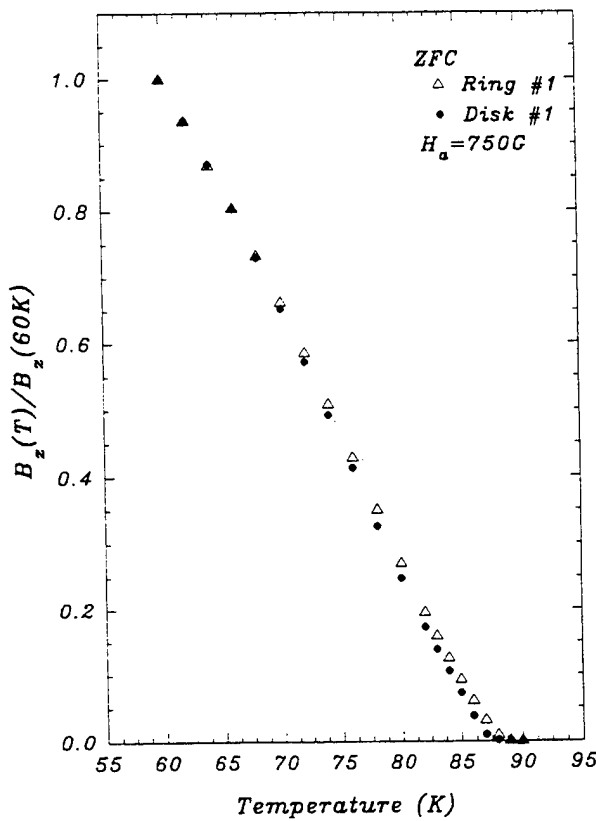


FIG. 4. Temperature dependence of the maximum field trapped in the zero-field-cooled disk No. 1 (solid symbols) and that of the magnetic field generated by the critical persistent current circulating in the zero-field-cooled ring No. 1 (open symbols) which was etched out from the disk No. 1. A magnetic field of 750 G was used to saturate the trapped magnetic field and the persistent current.

[Fig. 1(a)], show a very smooth pyramidlike shape. No surface steps which could suggest the influence of the Bean-Livingston surface barriers have been observed over the applied temperature range. The existence of the surface steps in the magnetic induction at the edges of a zero-field-cooled YBCO single crystal in the magneto-optically measured induction profiles (for the applied magnetic fields of 290–330 G and temperatures 55–60 K) have been interpreted by Dorosinskii, Nikitenko, and Polyanskii<sup>12</sup> as due to the Bean-Livingston surface barriers. The pyramidlike shape of the induction profiles generated by the thin-film disks [Fig. 1(a)] is observed at all applied temperatures (over a range of 64–84 K). These profiles do not provide any indication of a crossover between the partial and complete flux penetration into the disk. The partial-complete flux-penetration crossover can be seen in the temperature dependence of the profiles of the magnetic field trapped in the zero-field-cooled disk [Fig. 1(b)] when a constant external field is applied to the sample. It is interesting that the nonuniform flux trapping observed at temperatures corresponding to a partial flux-penetration regime transforms itself into the uniform one at higher temperatures when the whole sample is in the critical state (in the complete flux-penetration regime). By simply plotting the magnitude of the magnetic field trapped in the disk's center (which is measured after applying and subsequently removing a constant external field) versus temperature (Fig. 2), one can determine the crossover temperatures from the

partial to complete flux penetration. This temperature is given by the inflection point on the shielding magnetic temperature curve [Figs. 2(a)–2(c)]. The crossover temperature decreases with the increasing magnitude of the applied magnetic field [Fig. 2(d)]. All crossover temperatures indicate the maximum amount of the field ( $B_z$ )<sub>max</sub> that can be trapped in the disk's center. This means that at temperatures above the crossover temperatures the full critical state is reached across the disk. In this regime,  $B_z(T)_{\text{max}}$  is proportional to temperature:  $B_z(T) \propto (T - T_c)$ .  $B_z(T)_{\text{max}}$  is also proportional to the minimum applied magnetic field  $B^*$  required for the complete flux penetration at a given temperature. This is not surprising since  $B^*$  equals  $B_z \propto I_c$ , the field shielded at the surface and in the center of the disk, when it just reaches the full critical state. The proportionality of  $B_z(T)_{\text{max}} \propto I_c(T)$  means that both must have the same temperature dependence. This was verified using a ring-shaped sample, which was etched from disk No. 1. In the persistent current mode, the magnetic induction generated in the ring's center is due entirely to the current and it is directly proportional to the magnitude of the current. The measurements of the saturation value of the magnetic induction at various temperatures gave  $I_c(T) \propto (T - T_c)$ , the same temperature dependence as that for  $B_z(T)_{\text{max}}$  trapped in the disk's center (Fig. 4).  $B_z(T)_{\text{max}} \propto I_c(T)$  for the disk is also consistent with the calculation of the magnetic induction from the Biot-Savart law.<sup>2,4,13,14</sup>

The partial and complete flux-penetration regimes for the disk are characterized by different flux-relaxation phenomena. In the complete flux-penetration state, the normalized decay rate  $S = (1/B_0)(dB/d \ln t)$  measured at various points across the disk fluctuates between 0.012 and 0.015 (with an average value of 0.0135). In the partial flux-penetration state,  $S$  changes from a minimum value of 0.0045 at the disk center up to a maximum equilibrium value of 0.012 at the disk's edge (Fig. 5). We have not observed a distinct influence of the Bean-Livingston surface effects on the magnetic relaxation across the sample. In the trapped field mode ( $H_{\text{appl}} = 0$ ), the Bean-Livingston model<sup>15</sup> assumes that the flux lines near the surface experience an attractive image force by the surface, causing the energy per unit length to increase with a distance from the surface and in consequence faster magnetic relaxation at the surface in comparison to that in the bulk.

The magnitude of  $S$  measured in the complete flux-penetration state and that measured in the disk's center in the partial flux-penetration state is weakly temperature dependent [Figs. 5(c) and 5(d)] and independent of the magnitude of the trapped magnetic flux.  $S$  jumps to higher values above a temperature of 74 K which corresponds to a transition between incomplete and complete flux penetration after applying a magnetic field of 200 G. The weak temperature dependence of  $S$  in the disk's center for an incomplete penetration is surprising but it could mean that we record  $S$  in the complete flux penetration reduced by a constant amount of the flux-creep rate towards the center of the disk. The weak temperature dependence of  $S$  is also seen for the partial critical state in ring No. 1 [Fig. 7(a)]. The trapped flux in the ring [Fig. 7(b)] is a superposition of the self-field due to a persistent circulating current and the field of vortices trapped in the bulk of the ring. A persistent current can be induced in the

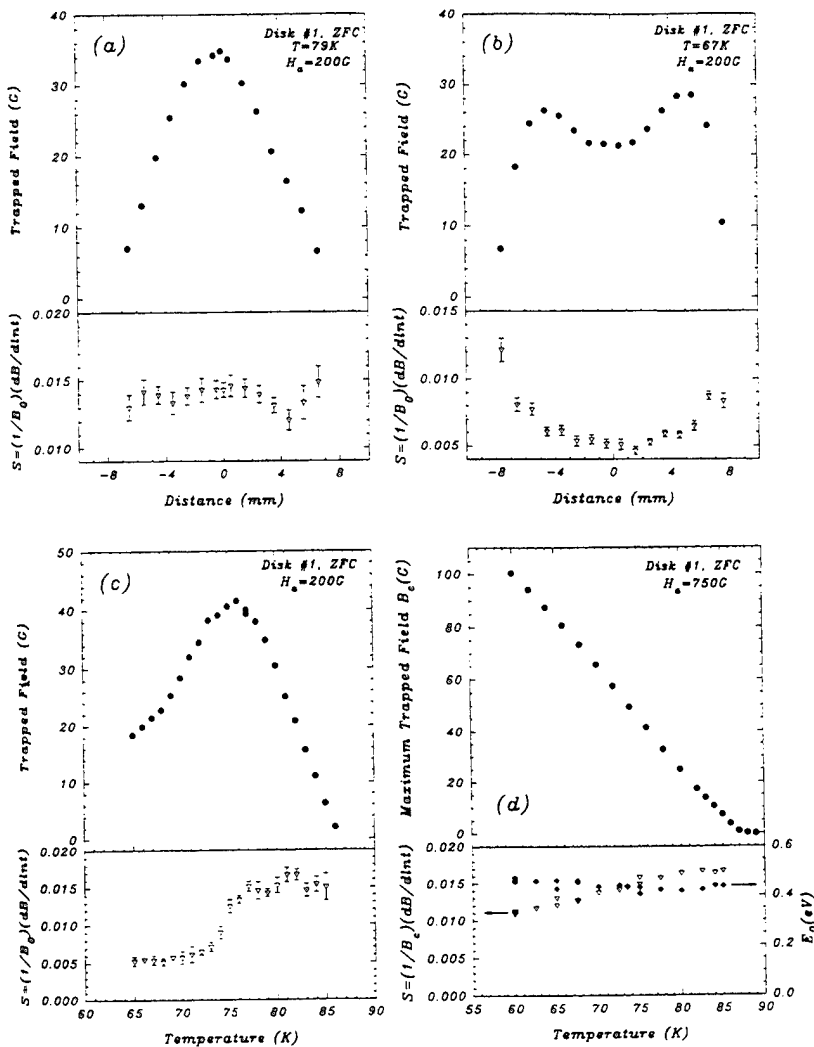


FIG. 5. (a) The upper part: The distributions of the trapped magnetic field measured across disk No. 1 at 79 K, which represent the case of the complete flux penetration after a field of 200 G was applied to the zero-field-cooled sample. The lower part: The corresponding distributions of the normalized decay rate  $S = (1/B_0)dB/d\ln t$  for the motion of the trapped flux. (b) The distributions of the trapped field and the normalized decay rate  $S$  measured across disk No. 1 at 67 K, which represent the case of the incomplete flux penetration after a field of 200 G was applied to the zero-field-cooled sample. (c) Temperature dependence of the trapped field and the normalized decay rate  $S$  measured in the center of disk No. 1 when a field of 200 G was applied to the zero-field-cooled sample. (d) Temperature dependence of the maximum trapped field, the normalized decay rate  $S$  and the corresponding flux-pinning energy  $E_0$  measured in the center of disk No. 1 when a saturating magnetic field of 750 G was applied to the zero-field-cooled sample.

ng when a magnetic flux is introduced into the ring's hole by applying and subsequently switching off the external magnetic field. During this process, the ring's bulk is fully penetrated by the magnetic flux, however, the ring is in the partial critical state as long as the magnitude of the circulating persistent current is below its critical value. For the ring, the superposition of both the vortex field and the persistent current's self-field produces smooth pyramid-shaped distributions of  $B_z(r)$ , the same for both the partial and complete critical states [see Fig. 7(b)], however,  $S$  exhibits a sharp jump to higher values at a temperature of 63.5 K which corresponds to a transition between the partial and the complete critical states after applying a magnetic field of 200 G. In the partial critical state,  $S$  has a value approximately two times less than the corresponding one for the disk. In the full critical state  $S$  matches the values obtained for the disk over the same temperature range, confirming independence of  $S$  on the sample geometry in the complete critical state regime. In the partial critical state regime, the behavior of  $S(T)$  is similar for both the disk and the ring, however, the ring's geometry allows one to reach a full critical state at a lower temperature than the corresponding one for the disk. It appears that  $S$  in the partial critical state is governed by the effective gradient of  $\partial B_z/\partial r$ , however, we believe that the distributions of the critical currents or  $B_r(r)$  in the disk and the ring could provide more definite explanation. The weak

temperature dependence of  $S$  in the full critical state close to  $T_c$  for the disk and the ring [Fig. 5(d) and 7(a)] is consistent with data of Keller *et al.*<sup>16</sup> and Isaac *et al.*<sup>17</sup> on the *c*-axis melt-textured YBCO at remanence after application of saturating fields along the *c* axis, and with Malozemoff's and Fisher's model<sup>18</sup> of universality in the current decay and flux creep of YBCO. Close to  $T_c$  (over an applied temperature range of 60–85 K), the normalized decay rate from the maximum value of the trapped field  $S = (1/B_c)(dB/d\ln t) = kT/E_0$  gives the energy barrier in the absence of flux creep  $E_0$  independent of temperature, with an average value of 0.45 eV. This number is very close to that reported for the *c*-axis-oriented melt-textured YBCO.<sup>16,17</sup>

The measurement of the trapped field profiles at constant temperature for various stages of flux penetration into disk No. 2 confirmed that even in the early stages of flux penetration, the full critical state is reached at the disk's edge and it spreads steadily into the disk's center [Fig. 6(a)]. The full critical state is marked by the bell-shaped external envelope of fixed gradient  $\partial B_z/\partial r$ . This gradient decreases down to zero, when temperature of the disk is increased up to  $T_c$  [Fig. 6(b)]. The maximum trapped field  $B_c(T)_{\max}$  is proportional to  $I_c(T)$ , however, the gradient  $(\partial B_z/\partial r)(T)$  does not represent  $J_c(T)$ . According to calculations performed by Däumling and Larbalestier,<sup>4</sup> the magnitude of the trapped magnetic field in the disk's center plane ( $z=0$ ) and in the disk's center

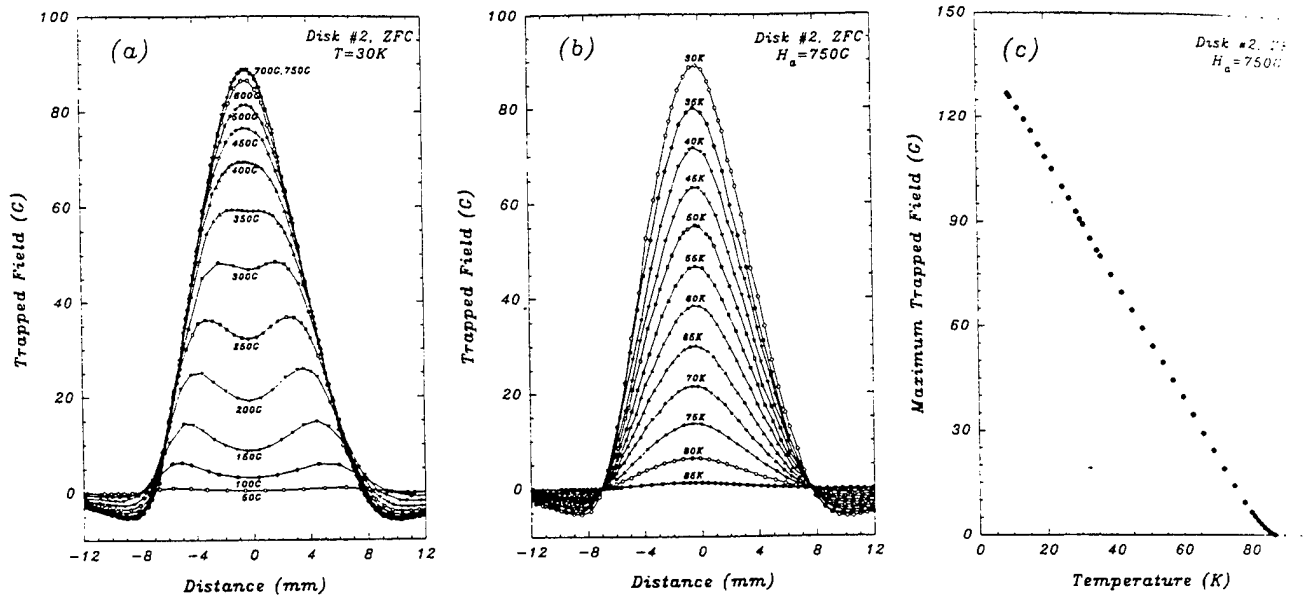


FIG. 6. (a) The distributions of the trapped field in disk No. 2 at 30 K, showing different stages of flux penetration after an increasing applied field (up to 750 G) was applied to the zero-field-cooled sample. Distances +7.5 and -7.5 mm mark the edges of the disk. (b) The distributions of the maximum trapped field in the zero-field-cooled disk No. 2 at various temperatures between 30 and 85 K. An applied field of 750 G was used to reach saturation at each temperature. (c) Temperature dependence of the maximum magnitude of the field trapped in the center of the zero-field-cooled disk No. 2 after applying an external field of 750 G.

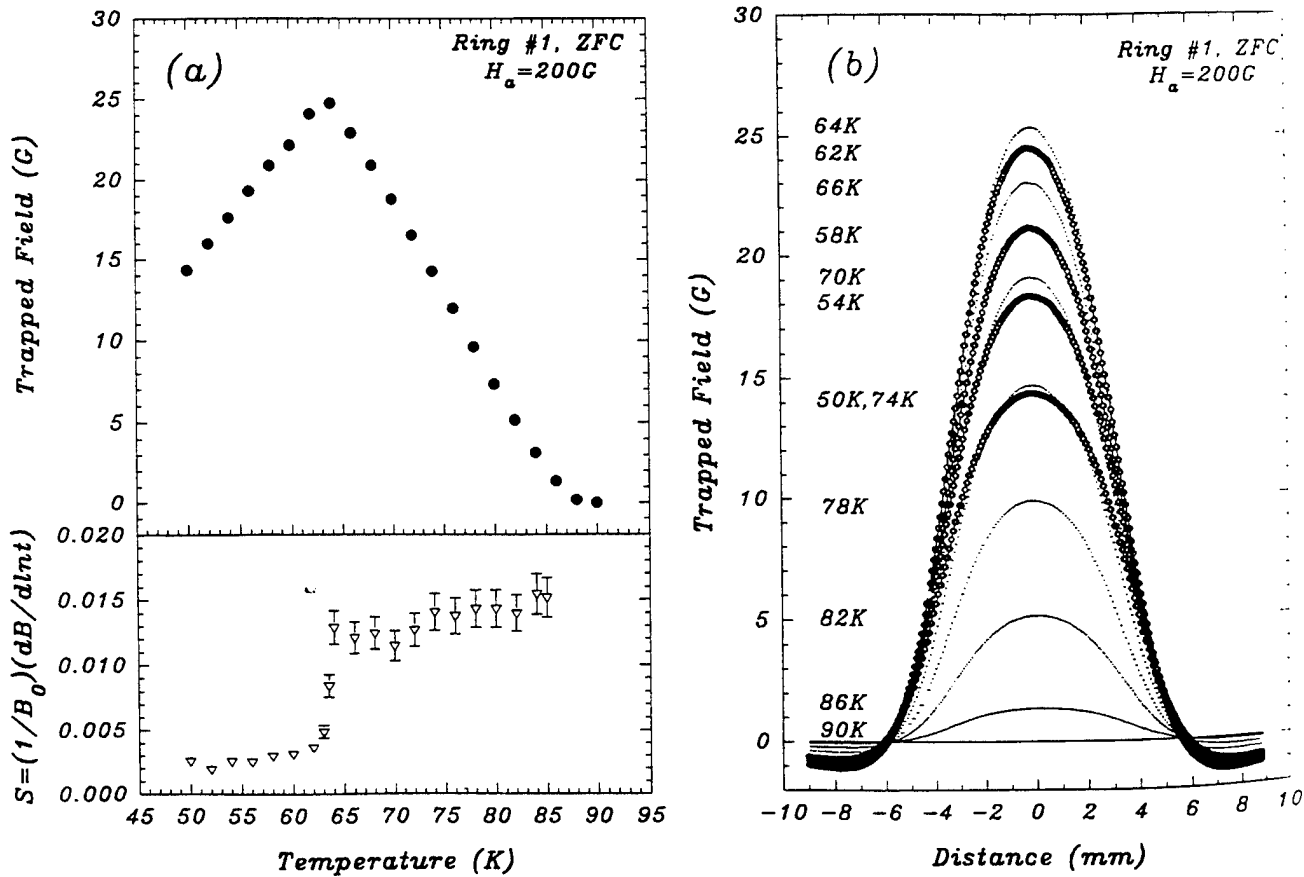


FIG. 7. (a) Temperature dependence of the trapped field and the normalized decay rate  $S$  measured in the center of ring No. 1 when a field of 200 G was applied to the zero-field-cooled sample. (b) The distributions of the trapped field in ring No. 1 at various temperatures between 50 and 86 K, after an external field of 200 G was applied to the zero-field-cooled sample. Distances +4.25, -4.25 mm and -2.50, -2.50 mm mark the outer and inner ring's edges, respectively.

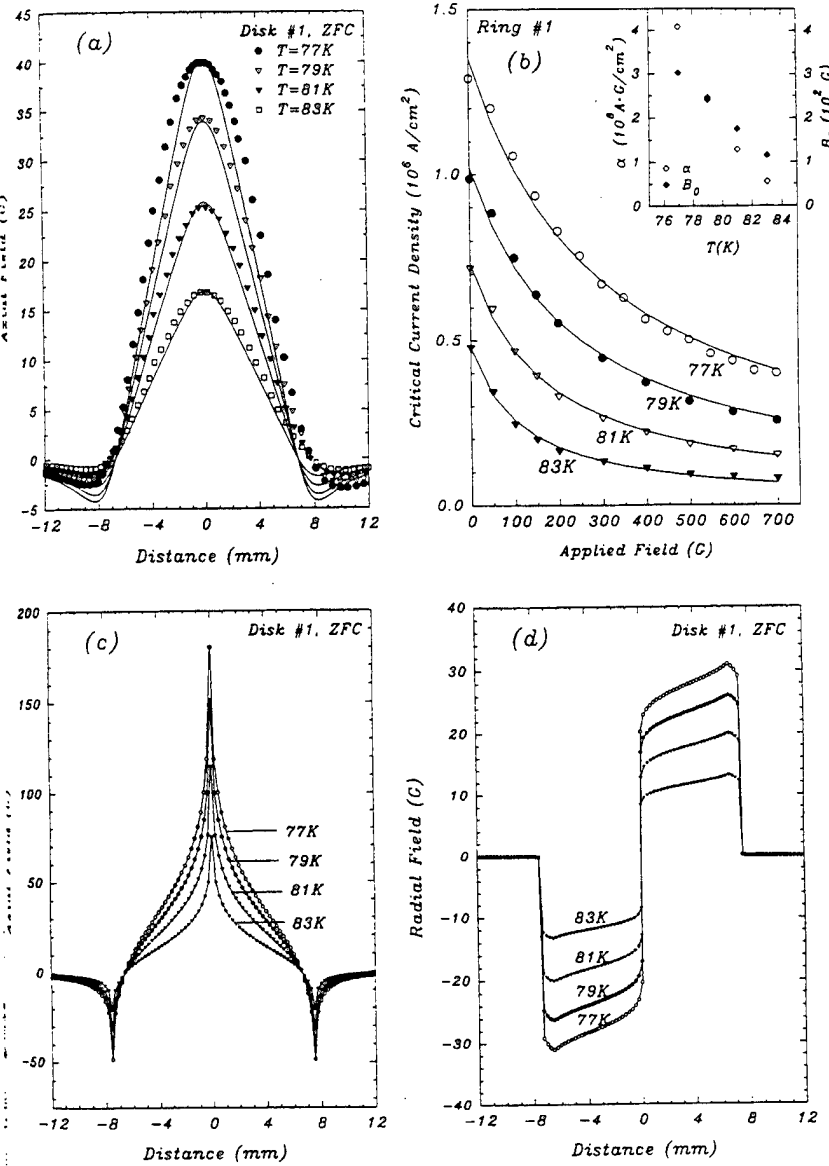


FIG. 8. (a) Symbols represent the profiles of the axial magnetic field trapped in the zero-field-cooled disk No. 1 (the measurement was done with a scanning Hall probe at a distance of 1.6 mm from the disk's surface) at temperatures of 77, 79, 81, and 83 K. A field of 200 G was used to saturate the trapped magnetic field. Solid lines represent the computer computations of the trapped field using the Biot-Savart equations and the Kim's relationships at temperatures of 77, 79, 81, and 83 K [see Fig. 8(b)]. Distances of +7.5 and -7.5 mm mark the disk's edges. (b) Symbols represent the magnetic-field dependence of the critical current density in the zero-field-cooled ring No. 1 at 77, 79, 81, and 83 K. Solid lines represent the Kim's relationships for  $J_c(B) = \alpha/(B + B_0)$  with constants  $\alpha(T)$  and  $B_0(T)$  given in the inset. (c) Computer simulations of the profiles of the axial component of the field trapped in the zero-field-cooled disk No. 1 at 77, 79, 81, and 83 K.  $B_z(r)$  was calculated on the disk's surface using the Biot-Savart equations and the Kim's relationships shown in (b). Distances +7.5 and -7.5 mm mark the disk's edges. (d) Computer simulations of the profiles of the radial component of the field trapped in the zero-field-cooled disk No. 1 at 77, 79, 81, and 83 K.  $B_r(r)$  was calculated on the disk's surface using the Biot-Savart equations and the Kim's relationships shown in (b). Distances +7.5 and -7.5 mm mark the disk's edges. Note the change in the radial field  $B_r(r)$  over a distance  $0 < r < a$ . A decrease in the radial field from a maximum value is about 3.5% per millimeter for all temperatures of the measurement.

$=0$ ) is of order  $J_c d$ . For disk No. 1 the magnitude of  $J_c$  at 77 K is  $1.30 \times 10^6 \text{ A/cm}^2$  (obtained from the measurement of the saturation value of the magnetic induction in the center of ring No. 1, which is directly proportional to the critical current). The maximum trapped magnetic field at  $z=0$  and  $r=0$  should therefore be equal to about 800 G at 77 K. The experiment gives the maximum trapped field of about 40 G at  $z=1.6 \text{ mm}$  and  $r=0$  [Fig. 1(b)], which was obtained by applying a minimum external magnetic field of 200 G. It means that Däumling and Larbalestier formula overestimates the magnitude of the trapped field since it cannot be higher than that of the applied field. The reason for this is that the formula is valid for magnetic-field independent  $J_c$ . The  $J_c$  could be much smaller because of the presence of the local self-fields generated by concentric loops of current flowing in the disk.<sup>5</sup> The self-fields may well exceed 200 G. The question is what is the relationship between the profile of the trapped axial magnetic field as seen by a scanning Hall probe at a distance of 1.6 mm above the thin-film disk that observed in YBCO disk-shaped thin films by means of magneto-optical methods at a distance of  $0.2 \mu\text{m}$  above the surface of the film (Ref. 3).

We performed computer simulations of  $B_z(r, z)$  and  $B_r(r, z)$  in the zero-field-cooled disk No. 1 at temperatures of 77, 79, 81, and 83 K, using the computation methods described in Refs. 4, 5, and 13. The disk was divided into 150 000 ring segments. The axial field  $B_z(r, z)$  and the radial field  $B_r(r, z)$  generated by the current in each ring segment was calculated from the Biot-Savart equation.<sup>19</sup> The total axial field above the sample was calculated by summing up the contributions from the individual current loops. The influence of the self-fields was incorporated into the calculations using the iteration procedure and taking a field dependent  $J_c = \alpha/(B + B_0)$  according to Kim's relationship,<sup>20</sup> with the constants  $\alpha$  and  $B_0$  determined at 77, 79, 81, and 83 K from the measurement of the magnetic-field dependence of the critical current density in ring No. 1 [Fig. 8(b)]. The results for  $B_z(r, z = 1.6 \text{ mm})$  are shown in Fig. 8(a) together with the experimental data for disk No. 1 at 77, 79, 81, and 83 K measured by a scanning Hall probe. The results for  $B_z(r, z = 0.25 \mu\text{m})$  on the disk's surface are given in Fig. 8(c). The shape of the profile at  $z = 0.25 \mu\text{m}$  resembles those observed on the surface of thin-film disks with a magneto-optical method.<sup>23</sup> The gradient  $\partial B_z / \partial r$  at  $r = a/2$  and on the

disk's surface is about a factor of 2 larger than the corresponding one measured by a Hall probe at a distance of 1.6 mm from the disk's surface. At 77 K, the axial field gradient on the disk's surface at  $r=a/2$  is equivalent to the current density  $(1/\mu_0)\partial B_z/\partial r=0.88 \times 10^2 \text{ A/cm}^2$ . The ratio of  $J_c$  (obtained for the ring No. 1 at 77 K) to the current density produced by the axial field gradient on the disk's surface is  $J_c/[(1/\mu_0)\partial B_z/\partial r]=(1.30 \times 10^6 \text{ A/cm}^2)/(0.88 \times 10^2 \text{ A/cm}^2)=1.5 \times 10^4$ . This is equal to the aspect ratio  $a/d=\text{radius}/\text{thickness}=1.5 \times 10^4$ , in agreement with the estimation of the ratio  $(\partial B_z/\partial z)/(\partial B_z/\partial r)=a/d$  in Ref. 3.

The results for  $B_z(r, z=0.25 \mu\text{m})$  on the disk's surface at temperatures of 77, 79, 81, and 83 K are shown in Fig. 8(d).  $J_c(r)=2(1/\mu_0)B_z/d$  represents the distribution of the critical currents. The maximum critical current density occurs at the disk's edge at  $r=a$ .  $J_c(r)$  decreases with  $r$  at a rate of about 3.5% per millimeter. This rate is independent of temperature. Regarding the behavior of  $J_c(r)$ , it is interesting to compare the results of the measurements of the flux and current distributions in a disk-shaped YBCO thin film with those obtained for a square-shaped YBCO thin film (Refs. 8, 9). In the work done by Xing *et al.* and Grant *et al.* (Refs. 8, 9), a scanning Hall probe was applied in order to determine an  $x$ - $y$  distribution of the axial magnetic field  $B_z$  at a temperature of 77 K, and at a distance of 0.25 mm from the sample surface. They constructed a surface map of the saturation magnetization of the YBCO film, which was calculated from the measured  $B_z(x, y)$  using the inverse matrix method. The scans of the critical current densities  $J_c(x)$  and  $J_c(y)$  across the sample were obtained by computing the spatial derivatives of the magnetization. The magnitude of  $J_c(x)$  and  $J_c(y)$  has a maximum near the sample edges.  $J_c(x)$  and  $J_c(y)$  decrease from a value of  $\sim 3 \times 10^6 \text{ A/cm}^2$  at the edge with decreasing  $x$  and  $y$  at a rate of approximately 14% per millimeter, a factor of 4 larger than the corresponding rate for disk-shaped YBCO thin film. The temperature dependence of  $B_z(r)$  in Fig. 8(d) shows that the gradient in  $J_c(r)$  is independent of the magnitude of  $J_c$ . The increase in the gradient of  $J_c(r)$  must, therefore, be caused by the sample square geometry. Recent work on the current and field pattern in rectangular and inhomogeneous superconductors by Schuster *et al.*<sup>21</sup> implies that in square-shaped

samples a strong concentration of electric field can occur along the lines where  $J_c$  changes abruptly. This means a high flux-flow rate and dissipation of energy.

## V. SUMMARY

We investigated the temperature dependence of the penetration process of the magnetic flux into disk-shaped YBCO thin films, especially the transition between the partial and complete flux-penetration states. The complete flux-penetration state is characterized by the normalized logarithmic decay rates constant across the disk ( $0.012 \leq S \leq 0.015$ ).  $S$  in the partial flux penetration state has a minimum in the disk's center ( $S=0.005$ ) and a maximum ( $S=0.012$ ) at the disk's edges. The temperature dependence of the magnetic induction at the transition is governed by the temperature dependence of the critical current. The maximum field trapped in the disk's center and the self-field of the critical current flowing in the ring (which was etched out from the disk) have the same temperature dependence. This confirms that the trapped- or shielding-field profiles above the thin-film disk can be simulated by summing up the self-fields of a large number of concentric current loops. The experiment also confirms that the critical current density  $J_c=(1/\mu_0)\partial B_z/\partial r$  exceeds the current density produced by the axial field  $(1/\mu_0)\partial B_z/\partial r$  by the factor of radius/thickness. We did not observe any flux-penetration effects at the disk's edges, which would suggest the presence of the Bean-Livingston surface barriers in contradiction to recently reported experiments on YBCO single crystals<sup>12</sup> for the similar range of applied magnetic field. We believe that the sample's nonuniformities at the sample's edges may produce Bean-Livingston-like effects.

## ACKNOWLEDGMENTS

We are pleased to acknowledge useful discussions with J. R. Clem. This work was supported by a grant from the Natural Sciences and Engineering Research Council of Canada (NSERC).

\*Current address: The University of Northern British Columbia, Prince George, BC, Canada, V2N 4Z9.

<sup>1</sup>Y. Yokoyama, Y. Hasumi, H. Obara, Y. Suzuki, T. Katayama, S. Gotoh, and N. Koshizuka, *Jpn. J. Appl. Phys.* **30**, L714 (1991).

<sup>2</sup>A. Forkl, *Phys. Scr. T* **49**, 148 (1993).

<sup>3</sup>H. Theuss, A. Forkl, and H. Kronmüller, *Physica C* **190**, 345 (1992).

<sup>4</sup>M. Däumling and D. C. Larbalestier, *Phys. Rev. B* **40**, 9350 (1989).

<sup>5</sup>L. W. Conner and A. P. Malozemoff, *Phys. Rev. B* **43**, 402 (1991).

<sup>6</sup>E. H. Brandt, *Physica C* **235-240**, 2939 (1994).

<sup>7</sup>M. A-K. Mohamed, J. Jung, and J. P. Franck, *Phys. Rev. B* **39**, 9614 (1989).

<sup>8</sup>W. Xing, B. Heinrich, H. Zhou, A. A. Fife, and A. R. Cragg, *J. Appl. Phys.* **76**, 4244 (1994).

<sup>9</sup>P. D. Grant, M. W. Denhoff, W. Xing, P. Brown, S. Govorkov, J.

C. Irwin, B. Heinrich, H. Zhou, A. A. Fife, and A. R. Cragg, *Physica C* **229**, 289 (1994).

<sup>10</sup>J. Talvacchio, M. G. Forrester, J. R. Gavalier, and T. T. Braggs, in *Science and Technology of Thin Film Superconductors II*, edited by R. McConnell and S. A. Wolf (Plenum, New York, 1990), pp. 57-66.

<sup>11</sup>J. Jung, I. Isaac, and M. A-K. Mohamed, *Phys. Rev. B* **48**, 7220 (1993).

<sup>12</sup>L. A. Dorosinskii, V. I. Nikitenko, and A. A. Polyanski, *Phys. Rev. B* **50**, 501 (1994).

<sup>13</sup>D. J. Frankel, *J. Appl. Phys.* **50**, 5402 (1979).

<sup>14</sup>J. D. Jackson, *Classical Electrodynamics* (Wiley, New York, 1962).

<sup>15</sup>C. P. Bean and J. D. Livingston, *Phys. Rev. Lett.* **12**, 14 (1964).

<sup>16</sup>C. Keller, H. Küpfer, R. Meier-Hirmer, U. Welch, V. Selvamanickam, and K. Salama, *Cryogenics* **30**, 410 (1990).

<sup>17</sup>I. Isaac, J. Jung, M. Murakami, S. Tanaka, M. A-K. Mohamed,

and L. Friedrich, Phys. Rev. B **51**, 11 806 (1995).  
A. P. Malozemoff and M. P. A. Fisher, Phys. Rev. B **42**, 6784 (1990).  
W. R. Smythe, *Static and Dynamic Electricity* (McGraw-Hill, New York, 1939), p. 266.

<sup>20</sup>Y. B. Kim, C. F. Hempstead, and A. R. Strnad, Rev. Mod. Phys. **36**, 43 (1964).  
<sup>21</sup>T. Schuster, H. Kuhn, E. H. Brandt, M. V. Indenbom, M. Kläser, G. Müller-Vogt, H. Kronmüller, and A. Forkl, Phys. Rev. B **52**, 10 375 (1995).

**MOLECULAR AND CRYSTAL ENGINEERING OF HIGH-T<sub>C</sub> SUPERCONDUCTOR THIN FILM STRUCTURES AND DEVICES**

**J. T. McDEVITT, J.P. ZHOU, C. E. JONES, R. -K. LO, J. E. RITCHIE, AND J. ZHAO**  
 Department of Chemistry and Biochemistry, University of Texas at Austin, Austin, TX  
 78712

**C. A. MIRKIN, F. XU, AND K. CHEN**  
 Department of Chemistry, Northwestern University, Evanston, IL 60208

**J. TALVACCHIO**  
 Northrop Grumman STC, Pittsburgh, PA 15235

**ABSTRACT**

The poor materials properties have slowed progress towards the practical utilization and commercialization of high-T<sub>C</sub> superconductor systems. Recently, we have identified a number of cation substituted  $\text{YBa}_2\text{Cu}_3\text{O}_7$  derivatives such as  $\text{Y}_{0.6}\text{Ca}_{0.4}\text{Ba}_{1.6}\text{La}_{0.4}\text{Cu}_3\text{O}_7$  ( $T_c = 82\text{K}$ ) which exhibit both good superconducting properties and vastly improved chemical stability relative to the parent compound. Moreover, a new powerful method for controlling the interfacial properties of high-T<sub>C</sub> systems based on a self-assembly of monolayer reagents onto cuprate surfaces has been discovered. In this manuscript, both crystal and molecular engineering approaches for tailoring the surface properties of high-T<sub>C</sub> systems will be discussed.

**CATION SUBSTITUTED  $\text{YBa}_2\text{Cu}_3\text{O}_7$  PHASES**

Recently, researchers worldwide have made considerable progress in the fabrication of high-T<sub>C</sub> superconductor products such as tapes, wires and thin film devices. Unfortunately, only in a few cases have efforts been successful to date to commercialize high-T<sub>C</sub> products. Much of the slow progress in this area can be traced to the poor materials properties, high chemical reactivity and poor oxygen stability exhibited by these systems. [1] To improve the chemical stability, we have doubly doped  $\text{YBa}_2\text{Cu}_3\text{O}_{7-\delta}$ , forming  $\text{Y}_{1-x}\text{Ca}_x\text{Ba}_{2-y}\text{La}_y\text{Cu}_3\text{O}_{7-\delta}$ . These substitutions disrupt the integrity of the  $\text{CuO}_{1-\delta}$  chains while keeping the total oxidation state of the  $\text{Cu}(2)-\text{O}(2)/\text{O}(3)$  arrays nearly constant. In the first part of this paper, the degradation behavior of  $\text{YBa}_2\text{Cu}_3\text{O}_{7-\delta}$  (YBCO) and substituted compound,  $\text{Y}_{0.6}\text{Ca}_{0.4}\text{Ba}_{1.6}\text{La}_{0.4}\text{Cu}_3\text{O}_{7-\delta}$  (TX-YBCO), in water vapor environments are established for bulk and thin film structures.

A dramatic demonstration of the increased stability afforded with the cation substitution is shown in Figure 1. Here bulk samples of YBCO and TX-YBCO following their exposure to aerated water at room temperature is provided. For YBCO, two days water exposure causes the formation of a significant amount of  $\text{BaCO}_3$  crystals which decorate the entire surface of the ceramic sample. This behavior is reminiscent of a sample that has decomposed to a large extent. On the other hand, the TX-YBCO sample treated for 30 days in a similar manner shows no visible signs of corrosion. A greater than 100 fold increase in stability is thus noted for the modified superconductor compound.

Thin films of YBCO and TX-YBCO have been evaluated to explore their processability and durability. Lifetime measurements of the various samples were performed using our previous described resistivity measurement. [2,3] Accordingly, film samples were placed in a water vapor chamber equilibrated at constant temperature with controlled humidity. From such measurements, increases in the film resistivity are utilized to judge the rate at which damage

to the cuprate structure occurs. Typically, the films decompose initially at a modest rate with little increase in resistivity over time. However, once the degradation process creates a sufficient number of corrosion defects to produce a high resistive barrier in the film, a marked increase in resistance is noted. Because sampling current, contact method and measurement intervals influence to some extent the measured lifetime, identical parameters were utilized to evaluate the various samples described herein. Lifetime for the films is defined as the amount of time necessary to reach the failure point of the film specimens.

It is clear that temperature and humidity are two important parameters that influence the degradation rate of YBCO. For example, YBCO samples studied at a constant temperature of 23 °C while varying the humidity from 60% to >98% exhibited a lifetime decrease from >10 days for the former to <24 hours for the latter. However, while maintaining the relative humidity at ≥98% and increasing the temperature from 23°C to 75°C, the YBCO lifetime decreased from >10 days to ~3 hours. In comparison, the TX-YBCO film samples showed no signs of degradation for >10 days under the severe conditions of 75°C water vapor and ≥98% humidity. From these studies and numerous other trials not included here, it is clear that major factors which influence the degradation rate are the high- $T_c$  structure (i.e. YBCO vs. TX-YBCO), the humidity content and the temperature. [4]

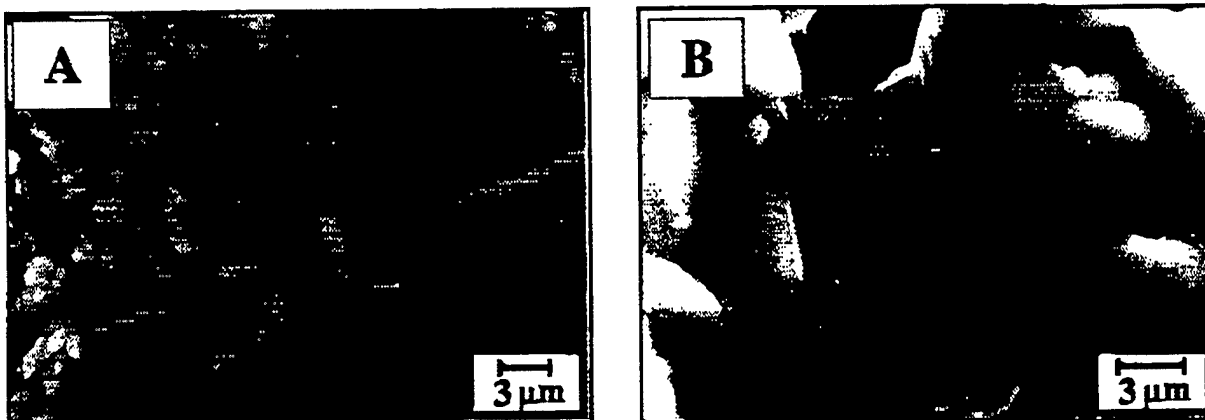


Figure 1: Scanning electron micrographs depicting the surface of a)  $\text{YBa}_2\text{Cu}_3\text{O}_{7-\delta}$  exposed to a room temperature water solution for 2 days and b)  $\text{Y}_{0.6}\text{Ca}_{0.4}\text{Ba}_{1.6}\text{La}_{0.4}\text{Cu}_3\text{O}_{7-\delta}$  exposed to a room temperature water solution for 30 days. The  $\text{YBa}_2\text{Cu}_3\text{O}_{7-\delta}$  surface is decorated with corrosion products while the cation substituted compound shows little sign of degradation.

Considerations of the structure/corrosion reactivity relationships for the YBCO and TX-YBCO materials can provide essential mechanistic information. The parent compound contains  $\text{Cu}(1)\text{-O}(1)$  chains as well as ordered oxygen vacancies ( $\text{V}_\text{O}$ ) at the  $\text{O}(5)$  sites. Previous reports have suggested that in the early stages of corrosion, water molecules enter the open channels along the  $\text{O}(5)$  sites and the oxide ions ultimately dock at the  $\text{O}(5)$  sites. [5] Proton transfer from water to the oxide lattice components leads to the formation of two moles of  $\text{OH}^-$  which occupy both vacancy site and the preexisting occupied oxide site. Internal charge transfer reactions within the modified lattice leads to the evolution of molecular oxygen. Following these initial steps, a series of reactions ensue ultimately leading to the bulk decomposition of the lattice.

Interestingly, the TX-YBCO is expected to be involved in many of the same decomposition steps. However, two important differences exist for the modified compound. First, internal stresses introduced by bond-length mismatch in the high- $T_c$  layered structures appear to be an important factor that dictates the decomposition kinetics of the YBCO superconductor. Our estimates completed using the bond valence sum theory suggest that the substitution of La for

Ba leads to a reduction of the internal strain energy from 1.79% to 0.35%. This reduction in strain may lower the driving force for corrosion. Second, the TX-YBCO material possesses a tetragonal structure in which occupancy at the O(1) and O(5) sites are equivalent. The disordering of these sites may influence the relative electrochemical potentials for the O(1) and O(5) sites, thereby altering the driving force for the charge transfer reaction. Without sufficient internal strain acting as a driving force for charge transfer, the substituted phase may remain resistant to corrosion. Moreover, changes in the structure may alter the rates of water diffusion into and oxygen diffusion out of the high- $T_c$  lattice.

## SELF-ASSEMBLY OF MOLECULAR REAGENTS ONTO $\text{YBa}_2\text{Cu}_3\text{O}_7$ SURFACES

The organization of molecular reagents into monolayer films on the surfaces of solid-state materials provides a convenient and rational approach towards controlling the surface and interfacial properties of these materials. The best characterized and most extensively studied systems have involved linear alkanethiol reagents adsorbed onto gold and other noble metal substrates. The use of long chain hydrocarbons and crystalline substrates yields monolayers which are densely packed, oriented, and highly ordered. A recent survey of the surface coordination chemistry of  $\text{YBa}_2\text{Cu}_3\text{O}_7$  has led to the identification of reliable methods for preparing persistent monolayers on the surface of a cuprate superconductor. [6,7]

Accordingly, carefully chosen adsorbate molecules, such as linear alkylamines and fluorinated alkylamines, are used to tailor the corrosion resistance and surface adhesion properties of  $\text{YBa}_2\text{Cu}_3\text{O}_7$ , Figure 2a. The most striking demonstration of the utility of the monolayer methodology for modification of the cuprate superconductor interfacial properties is shown in Figure 2b and 2c. The illustration provides a dramatic comparison of the ability of a single monolayer formed from  $\text{CF}_3(\text{CF}_2)_7(\text{CH}_2)_2\text{NH}_2$  to exclude water from the surface of a high- $T_c$  ceramic pellet. Here, the uncoated  $\text{YBa}_2\text{Cu}_3\text{O}_7$  pellet degrades rapidly over a period of one day upon soaking in an aerated water solution, as evidenced by the formation of  $\text{BaCO}_3$ . This impurity phase collects on the surface of the superconductor, and its presence

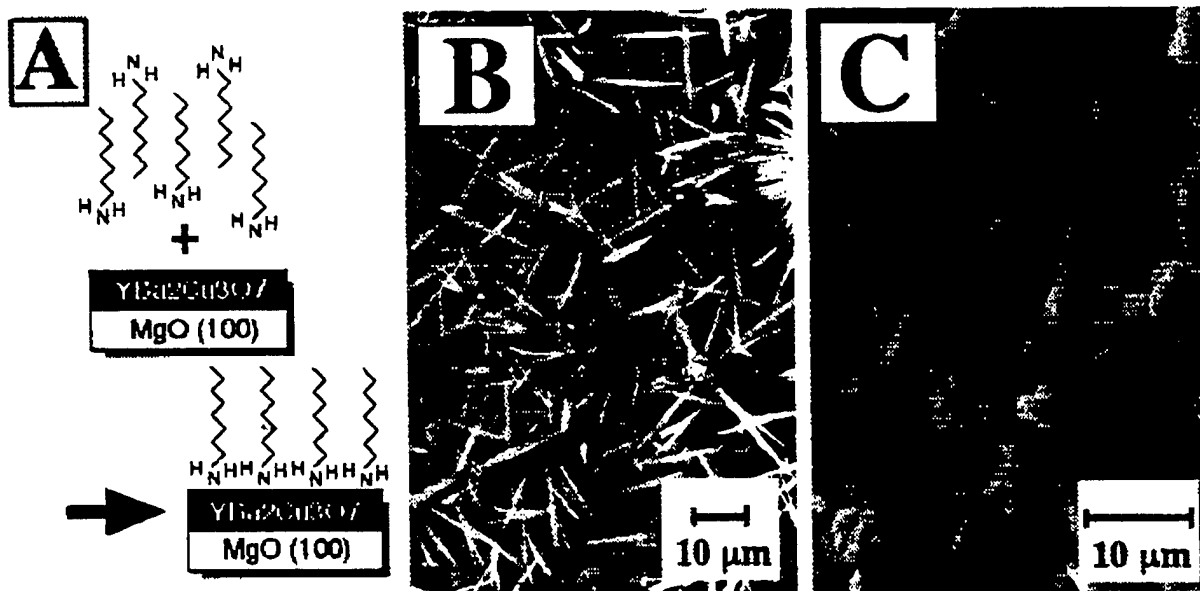


Figure 2 (A) Schematic of the spontaneous adsorption of alkylamines on  $\text{YBa}_2\text{Cu}_3\text{O}_7$ . Here a solution of vapor phase exposure of a  $\text{YBa}_2\text{Cu}_3\text{O}_7$  surface leads to the spontaneous adsorption of a monolayer onto the surface of the superconductor. (B) Bulk polycrystalline sample of  $\text{YBa}_2\text{Cu}_3\text{O}_7$  after 1 day water exposure. (C) Bulk polycrystalline sample of  $\text{YBa}_2\text{Cu}_3\text{O}_7$ , coated with fluorinated alkyl amine reagent after one day water exposure.

is visualized readily by scanning electron microscopy (i.e. the white needle-like crystals in Figure 2b). On the other hand,  $\text{YBa}_2\text{Cu}_3\text{O}_7$  modified with a monolayer of  $\text{CF}_3(\text{CF}_2)_7(\text{CH}_2)_2\text{NH}_2$  shows little signs of corrosion under identical conditions, Figure 2c. This result supports the notion that densely packed adsorbate layers capable of excluding even small molecules such as water can be formed with the described self-assembly method.

Moreover, in recent studies we have also shown that fluorocarbon amine layers can be exploited to alter the surface adhesion properties of  $\text{YBa}_2\text{Cu}_3\text{O}_7$  thin film structures. In the absence of treatment of  $\text{YBa}_2\text{Cu}_3\text{O}_7$  with the fluoroamine reagent, Teflon AF, a fluorocarbon polymer, adheres poorly to the high- $T_c$  surface. However, with a monolayer of  $\text{CF}_3(\text{CF}_2)_7(\text{CH}_2)_2\text{NH}_2$ , the polymer is found to adhere more strongly. The combination of monolayer adhesive and polymer layers serves to create an excellent packaging method for the long term protection of vulnerable  $\text{YBa}_2\text{Cu}_3\text{O}_7$  thin film structures. These results demonstrate that corrosion resistance, adhesion and wetting properties of the high- $T_c$  material can be tailored through judicious choice of adsorbate molecule. Thus, through appropriate choice of adsorbate molecule, superconductor surfaces can now be altered in a controlled manner so as to suit a variety of applications.

## CONCLUSIONS

In summary, the preparation of the chemically robust cuprate bulk and film samples has been accomplished. Two successful strategies for the preparation of chemically stabilized high- $T_c$  superconductors have been described. These include cation substitution and self-assembly methods. Related to the crystal engineering approach, studies of the corrosion mechanism for these samples suggest that changes in the lattice stress and strain features as well as minor changes in the oxygen ordering properties are responsible for the enhanced stability. According to the molecular engineering approach, superconductor surfaces can now be altered in a controlled manner through the appropriate choice of adsorbate molecule to suit a variety of applications. This new method provides a strategy through which the interfacial properties of superconductors can be controlled at the molecular level with an easily exploited method. These new developments will likely influence in a positive manner the processing of high- $T_c$  film structures.

## ACKNOWLEDGEMENTS

This work was supported at the University of Texas at Austin and Northwestern by AFOSR, ONR and NSF and at Northrop Grumman STC by AFOSR.

## REFERENCES

1. A. Barkatt; H. Hojaji; V.R.W. Amaraloon; J.G. Fagan *MRS Bulletin* **18**, 45-52 (1993).
2. J.-P. Zhou; S.M. Savoy; R.-K. Lo; J. Zhao; M. Arendt; Y.T. Zhu; A. Manthiram; J.T. McDevitt *Appl. Phys. Lett.* **66**, 2900-2902 (1995).
3. J.-P. Zhou; S.M. Savoy; J. Zhao; D.R. Rilet; Y.T. Zhu; A. Manthiram; R.-K. Lo; D. Borich; J.T. McDevitt *J. Am. Chem. Soc.* **116**, 9389-9390 (1994).
4. J.-P. Zhou; R.-K. Lo; S.M. Savoy; M. Arendt; J. Armstrong; D.-Y. Yang; J. Talvacchio; J.T. McDevitt *Physica C* submitted, (1996).
5. J.G. Thompson; B.G. Hyde; R.L. Withers; J.S. Anderson; J.D. Fitzgerald; J. Bitmead; M.S. Paterson; A.M. Stewart *Mat. Res. Bull.* **22**, 1715 (1987).
6. K. Chen; C.A. Mirkin; R.-K. Lo; J. Zhao; J.T. McDevitt *J. Am. Chem. Soc.* **117**, 6374-6375 (1995).
7. J.T. McDevitt; C.A. Mirkin; R.-K. Lo; K. Chen; J.-P. Zhou; F. Xu; S.G. Haupt; J. Zhao; D.C. Jurbergs *Chem. Mater.* **18**, 811-813 (1996).

## HIGH-T<sub>C</sub> SNS EDGE JUNCTIONS FOR DIGITAL CIRCUIT APPLICATIONS

BRIAN D. HUNT, MARTIN G. FORRESTER, JOHN TALVACCHIO, JAMES D. McCAMBRIDGE, and ROBERT M. YOUNG

Northrop Grumman Science and Technology Center, 1350 Beulah Rd., Pittsburgh, PA, USA 15235

### ABSTRACT

We have fabricated high-T<sub>c</sub> superconductor/normal-metal/superconductor (SNS) weak links in an edge geometry with integrated YBa<sub>2</sub>Cu<sub>3</sub>O<sub>x</sub> (YBCO) groundplanes using a process which incorporates six epitaxial layers, including a Co-doped-YBCO normal-metal interlayer. The SNS edge junctions were produced using films deposited by both off-axis sputtering and pulsed laser deposition. These devices exhibit narrow J<sub>c</sub> spreads and high I<sub>c</sub>R<sub>n</sub> products in a current density regime suitable for Single-Flux-Quantum (SFQ) circuits. This device technology has been used to fabricate high performance SQUIDs and small-scale SFQ digital circuits.

KEY WORDS: SNS, Josephson junction, edge junction, groundplane, YBa<sub>2</sub>Cu<sub>3</sub>O<sub>x</sub>

### INTRODUCTION

SFQ logic offers the potential of 10 Ghz operation combined with very low power dissipation. Demonstration of SFQ circuits requires the fabrication of high quality Josephson junctions in a multilevel epitaxial process. In particular, junctions with high critical-current - normal-state-resistance (I<sub>c</sub>R<sub>n</sub>) products (>200  $\mu$ V), narrow critical current spreads (<15%), and low junction and interconnect inductances are needed. The inductance constraints are most readily satisfied by incorporation of a superconducting groundplane. We have recently reported on the fabrication of high performance SNS edge junctions and SQUIDs integrated with YBCO groundplanes [1,2] and good progress in this area has also been made by other groups [3,4]. In this paper we present an overview of our work with new details on processing, as well as recent junction, SQUID, and circuit results.

### PROCESS DETAILS

The YBCO, SrTiO<sub>3</sub> (STO), and Co-doped YBCO (usually YBa<sub>2</sub>Cu<sub>2.79</sub>Co<sub>0.21</sub>O<sub>x</sub> - 7% Co), films used in this work were deposited by off-axis rf-magnetron sputtering or by pulsed laser deposition (PLD). To date, sputtering has been used for deposition of every layer for some chips, and is usually utilized for growth of the groundplane and groundplane-insulator. Details of the sputter deposition were given in an earlier paper [1]. Our PLD film process is less mature than our sputtering process, and has primarily been used for YBCO base electrode deposition and for growth of the normal metal and counterelectrode layers. A description of the PLD film process is given in Ref. [2]. The RMS roughnesses of PLD YBCO films in 10x10  $\mu$ m AFM scans were  $\approx$  30 - 50  $\text{\AA}$  compared to  $\approx$  10 - 30  $\text{\AA}$  for the best sputtered films. While the PLD YBCO films were not as smooth as the best off-axis-sputtered films, we have found that our PLD film process appears to be more stable overall, and further optimization of the PLD process is expected to lead to smoother films.

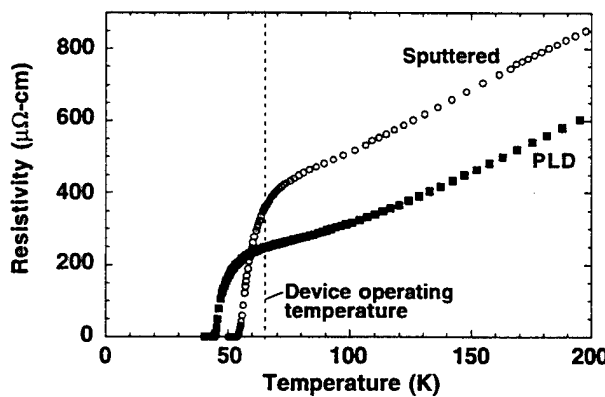


Fig. 1. Resistivity versus temperature for typical 7% Co-doped YBCO thin films produced by off-axis sputtering and laser ablation.

The Co-doped YBCO normal-metal films were grown by both sputtering and PLD under slightly different conditions from YBCO [1, 2]. These deposition parameters produced films with the best electrical properties, although the Co-YBCO films generally contained more outgrowths than optimized YBCO films. We found that the PLD-optimized  $\text{YBa}_2\text{Cu}_{2.8}\text{Co}_{0.2}\text{O}_x$  thin films usually had electrical properties closer to bulk values than the sputtered films as shown in Fig. 1, with transition temperatures more suitable for the desired circuit operating temperature of 65 K. The broader, higher-temperature transition seen with the sputtered Co-YBCO films is believed to be due to inhomogeneous Co incorporation. Nonetheless, both the sputtered and PLD grown Co-YBCO films have been used for fabrication of high quality SNS junctions. We have also fabricated SNS edge junctions using  $\text{Y}_{0.7}\text{Ca}_{0.3}\text{Ba}_2\text{Cu}_3\text{O}_x$  or  $\text{Y}_{0.75}\text{Pr}_{0.25}\text{Ba}_2\text{Cu}_3\text{O}_x$  as normal metals [5], but the Co-doped YBCO devices had  $I_cR_n$  products slightly larger than the Pr-YBCO junctions and about four times higher than the Ca-YBCO devices, so most of our efforts have concentrated on Co-doped-YBCO SNS junctions.

The majority of our work to date has focused on fabricating SNS edge junctions above buried groundplanes using the two configurations shown in Fig. 2. The “double-via” approach shown in Fig. 2a) uses two separate via patterning steps to make contact to the groundplane and base electrode resulting in separate patterning and epitaxial growth of the groundplane, the groundplane insulator, and the base electrode bilayer. Because epitaxial growth over a patterned film is quite sensitive to surface cleanliness of the underlayer, the yield of such a sequence of patterning and growth steps can be reduced, even with the cleaning procedure described in [1]. Fig. 2b) illustrates an alternate “single-via” approach in which an *in-situ*

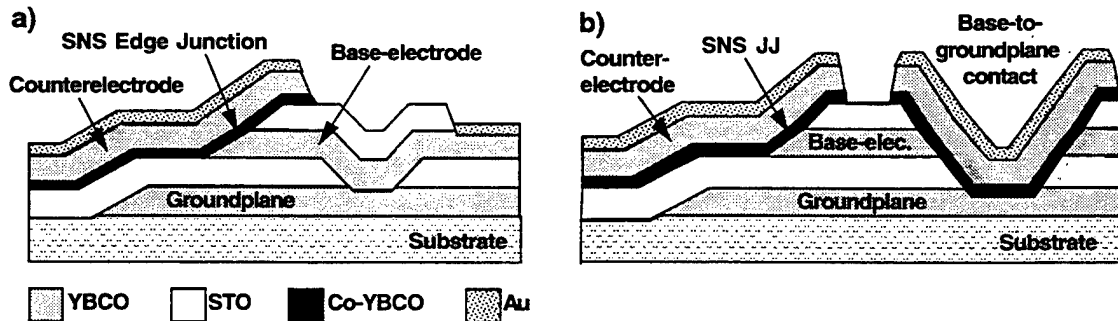


Fig. 2. Schematic cross sections of YBCO/Co-YBCO/YBCO SNS edge junctions integrated with buried YBCO groundplanes a) “Double-via” process, b) “Single-via” process.

STO/YBCO-base-electrode/STO trilayer is grown over the patterned groundplane. In this case contact between the base electrode and groundplane is made through large-area SNS junctions defined by a single via through the trilayer combined with counterelectrode "plugs" patterned at the same time as the junctions. The advantages of this process are a reduced number of mask layers and *in-situ* growth of the base electrode trilayer, an inherently higher yield approach than the double-via process. Potential disadvantages are reduced circuit layout flexibility and lower- $J_c$  via contacts. At the present we are using both processes to produce high quality junctions with groundplanes.

Both the single and double-via processes are based on a buried groundplane configuration to minimize process exposure of completed SNS devices. However, it should be noted that there is no inherent reason to prohibit the use of groundplanes on top. Putting the groundplane above the junctions simplifies the processing, because groundplane morphology is no longer critical. In addition, fabricating the junctions directly on the substrate may ultimately lead to tighter device parameter spreads, and the groundplane and groundplane insulator serve as passivation layers for the buried junctions. We have begun experiments with groundplanes over SNS devices, with promising initial results. In this case we continued processing SNS junctions patterned without Au contacts or buried groundplanes by growing an STO layer and patterning via contacts to the buried electrodes. Finally the YBCO groundplane was deposited and patterned, and Au contacts were defined. Results are discussed in the next section.

## ELECTRICAL RESULTS AND DISCUSSION

SFQ circuits require inductance ( $L$ ) -  $I_c$  products on the order of a single flux quantum,  $\phi_0 = 2000 \text{ pH-}\mu\text{A}$ . Because typical microstrip inductances are about  $1 \text{ pH/}\square$  [1,2], conventional SQUID layouts point to critical currents of a few hundred  $\mu\text{A}$ , with the lower limit set by thermal noise considerations. Fabricating devices with lower  $I_c$  values is accomplished by using thicker N-layers, which leads to an associated reduction in the  $I_c R_n$  products.

Fig. 3 shows data for all eight 4- $\mu\text{m}$ -wide SNS edge junctions on a standard test chip. These devices have no groundplanes and all layers were deposited by off-axis sputtering including the 100  $\text{\AA}$  Co-doped-YBCO normal metal layers. At 65 K the devices exhibit high quality I-V

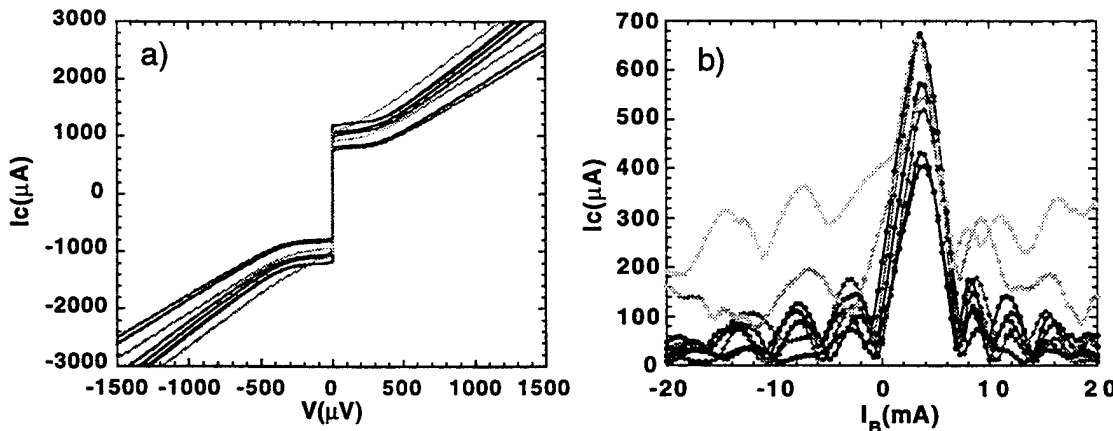


Fig. 3. Data for the eight 4- $\mu\text{m}$ -wide SNS edge junctions without groundplanes with 100  $\text{\AA}$  Co-doped-YBCO normal metal layers on a standard test chip. a) I-V characteristics at 65 K. On average  $J_c = 2.4 \times 10^5 \text{ A/cm}^2$  with a  $1-\sigma$  spread of 15% and  $I_c R_n = 570 \mu\text{V}$ . b)  $I_c$  vs. magnet current at 70 K for a field applied normal to the substrate.

characteristics qualitatively consistent with the resistively-shunted junction (RSJ) model as shown in Fig. 3a). At this temperature the average device parameters and spreads for these junctions were:  $J_c = 2.4 \times 10^5 \text{ A/cm}^2$ ,  $1-\sigma = 15\%$ ;  $I_c R_n = 570 \mu\text{V}$ ,  $1-\sigma = 7\%$ ; and  $R_n A = 2.4 \times 10^{-9} \Omega\text{-cm}^2$ ,  $1-\sigma = 11\%$ . The critical-current magnet field modulation data for these devices at 70 K are presented in Fig. 3b). Six out the eight devices show close-to-ideal Fraunhofer patterns, and even the other two devices have clean central peaks, which indicates conduction through the normal metals layers is fairly uniform. For this particular chip, the average current density and critical currents are larger than required for SFQ circuit applications. We have also demonstrated tight critical current spreads in devices with SFQ-compatible critical currents. Data from one such chip was presented in [2]. In that case the average  $I_c$  was approximately 210  $\mu\text{A}$  with a  $1-\sigma$  spread of 16% and an average  $I_c R_n$  product of 181  $\mu\text{V}$ . This combination of narrow  $I_c$  spreads with device parameters suitable for small-scale SFQ circuits is an important demonstration for the feasibility of SFQ digital applications.

As discussed earlier, another key requirement for SFQ circuits is the incorporation of superconducting groundplanes. We have fabricated high quality Josephson junctions integrated with groundplanes in several configurations. Fig. 4.a) shows I-V data at 65 K for the four 4- $\mu\text{m}$ -wide SNS edge junctions fabricated over YBCO groundplanes on a standard test chip using the “double via” process (Fig. 2.a)). The 150  $\text{\AA}$  Co-doped-YBCO normal metal layers were deposited by off-axis sputtering. The average device parameters for these junctions are:  $J_c = 1.27 \times 10^5 \text{ A/cm}^2$  with a  $1-\sigma$  spread of 20%;  $I_c R_n = 587 \mu\text{V}$  with a  $1-\sigma$  spread of 15%; and  $R_n A = 4.8 \times 10^{-9} \Omega\text{-cm}^2$  with a  $1-\sigma$  spread of 24%. The effectiveness of the groundplanes was qualitatively verified by magnetic-field  $I_c$  modulation studies. Fig. 4b) is a plot of  $I_c$  vs magnet current for a field perpendicular to the substrate at 77 K for junctions with and without a groundplane patch. Both curves approximate the expected  $\sin(x)/x$   $I_c$  modulation, but the junction over the groundplane exhibits a modulation period about four times that of the other junction, demonstrating the magnetic shielding effect of the superconducting film.

The junction parameters of the devices shown in Fig. 4a) are essentially identical to those for junctions without groundplanes: fabricating the edge junctions above the patterned groundplane and groundplane insulator did not degrade the device quality. However, it should also be noted that for some device chips fabricated over rougher YBCO groundplane films (RMS roughness  $\approx 30\text{-}50\text{\AA}$ ) the average  $J_c$  has been higher and the average  $R_n A$  product lower

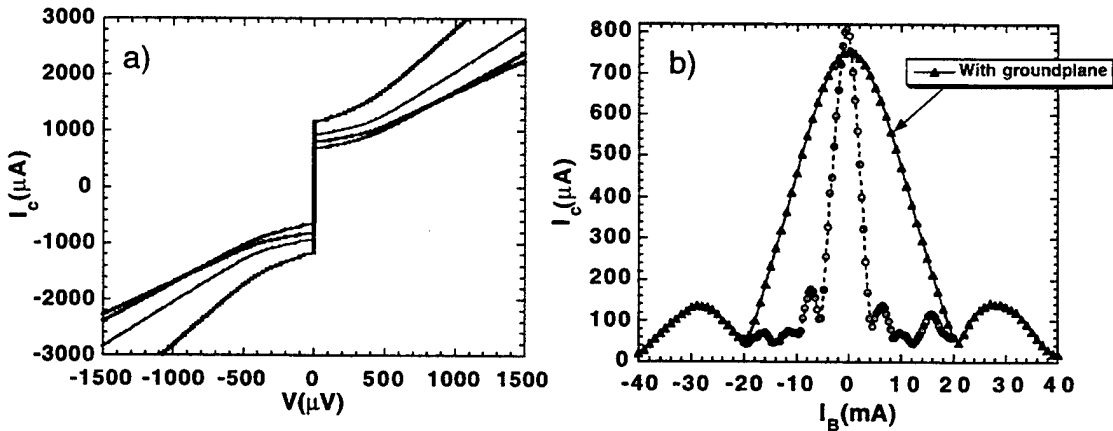


Fig. 4. Data for junctions on groundplanes. a) I-V characteristics at 65 K for the four 4- $\mu\text{m}$ -wide SNS edge junctions with groundplanes with 150  $\text{\AA}$  Co-doped-YBCO normal metal layers on a standard test chip. b)  $I_c$  vs magnet current at 77 K for two devices with 100  $\text{\AA}$  Co-YBCO layers, with and without groundplane patches.

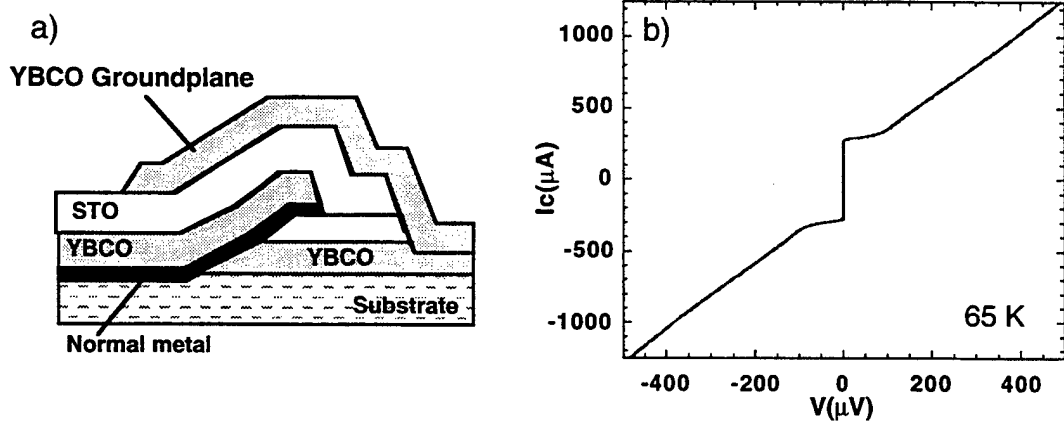


Fig. 5. a) Schematic cross-section of SNS edge junction with an epitaxial insulator and YBCO groundplane added above the device. b) I-V characteristics at 65 K for an SNS edge junction with a 50 Å PLD Co-YBCO N-layer integrated with a groundplane over the junction.

relative to junctions without groundplanes [2]. This may indicate that rougher growth in the upper layers of our multilevel structures is leading to normal metal edge coverage problems. These results emphasize the importance of using the smoothest possible groundplane and insulator films in multilayer structures with buried groundplanes.

We have also fabricated SNS edge junctions in a buried *junction* geometry as sketched in Fig. 5a). While some chips processed with this approach have shown depressed operating temperatures [2], recent devices fabricated with groundplanes above the junctions exhibit RSJ I-V characteristics at 65 K, as shown in Fig. 5b). In this case chips processed with groundplanes on top had I-Vs equivalent to companion chips which had no groundplane added, demonstrating that the junctions can survive high temperature processing. We are in the process of studying groundplane effectiveness in this configuration.

The double-via buried groundplane approach has been used to fabricate direct-injection SQUIDs [1,6]. The voltage modulation at 65 K of one such device is shown in Fig. 6a) as a function of the control current flowing through a microstrip inductor forming part of the SQUID loop. The maximum voltage modulation at this temperature is  $\approx 135 \mu\text{V}$ . The microstrip inductance can be determined from the period of the voltage modulation curves, and Fig. 6b) is a plot of the microstrip inductance per square as a function of temperature for a set

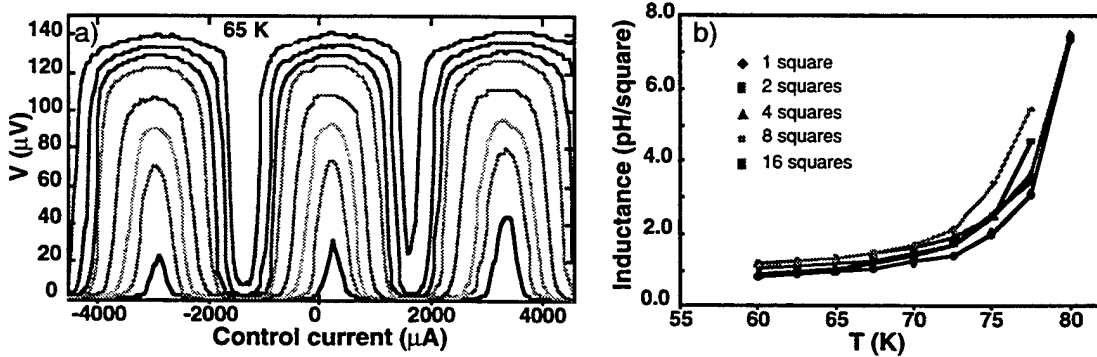


Fig. 6. a) Voltage modulation vs. control current for a direct injection SNS edge junction SQUID with integrated groundplane at 65 K at various bias levels. b) Temperature dependence of the microstrip inductance per square extracted from the  $V$ - $\phi$  curves for five SQUIDs.

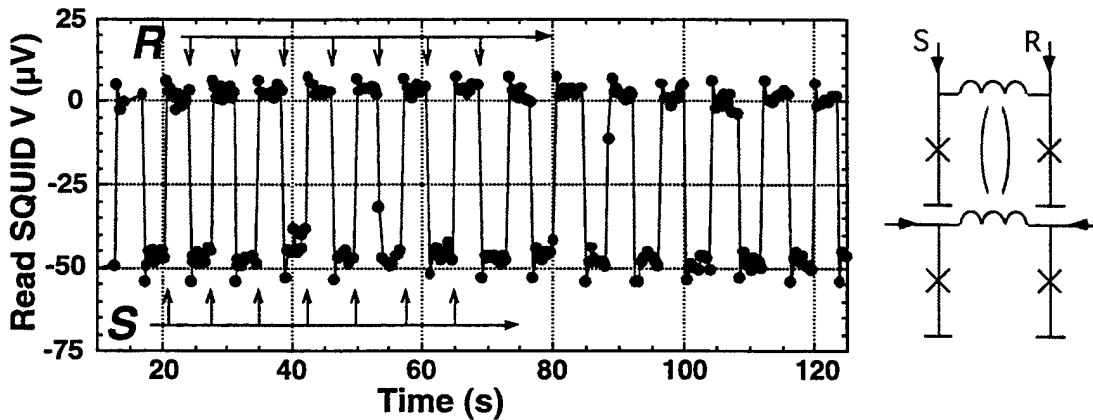


Fig. 7. Low speed test data and schematic diagram for an SNS edge junction R/S flip-flop at 65 K. The Read SQUID modulates by approximately 50  $\mu$ V in response to flux quanta stored in the Data SQUID by set and reset pulses.

of SQUIDs with different microstrip lengths. The inductance is about 1 pH per square at 65 K, which is suitable for fabrication of SFQ circuits.

We have begun using this multilayer device technology to produce small-scale SFQ circuits, including R/S flip-flops with 4 junctions and a 1-bit A/D converter with 10 junctions [7]. Low speed test data for an SNS R/S flip-flop are shown in Fig. 7. The data show Read SQUID voltage modulation of  $\approx 50 \mu$ V in response to flux quanta stored in the Data SQUID by set and reset pulses. This voltage level is about a factor of ten larger than previous test results with Step-Edge Grain Boundary (SEGGB) circuits due to the larger  $I_c R_n$  products of the SNS devices [8]. Mask and test setup modifications are being made to allow GHz testing of the flip-flops.

#### ACKNOWLEDGEMENT

We would like to acknowledge the assistance of J. C. Brown, G. Faychak, G. Madia, D. Matuza, R. Nye, S. Pieseski, and J. Uphoff. This work was supported in part by AFOSR Contract F49620-94-C-0021 and WL/ML Contract F33615-93-C-5355.

#### REFERENCES

1. B. D. Hunt, M. G. Forrester, J. Talvacchio, J. D. McCambridge, and R. M. Young (1996), *Appl. Phys. Lett.* **68**, p 3805.
2. B. D. Hunt, M. G. Forrester, J. Talvacchio, R. M. Young, and J.D. McCambridge (1997), *IEEE Trans. on Appl. Supercond.*, to be published.
3. W. H. Mallison, S. J. Berkowitz, A. S. Hirahara, M. J. Neal, and K. Char (1996), *Appl. Phys. Lett.* **68**, p 3808.
4. M. Hidaka, S. Miura, T. Satoh, W. Hattori, J. S. Tsai, and S. Tahara (1996), 1996 Int. Workshop on Superconduct.-Extended Abstracts, ISTEC, p 101.
5. J. Talvacchio, M.G. Forrester, B.D. Hunt, J.D. McCambridge, and R.M. Young (1997), *IEEE Trans. on Appl. Supercond.*, to be published.
6. M. G. Forrester, B. D. Hunt, J. D. McCambridge, D. L. Miller, J. X. Pryzbysz, J. Talvacchio, and R. M. Young (1997), *IEEE Trans. on Appl. Supercond.*, to be published.
7. J. D. McCambridge, M. G. Forrester, D. L. Miller, B. D. Hunt, J. X. Pryzbysz, J. Talvacchio, and R. M. Young (1997), *IEEE Trans. on Appl. Supercond.*, to be published.
8. M. G. Forrester, J. X. Pryzbysz, J. Talvacchio, J. Kang, A. Davidson, and J. Gavalier (1995), *IEEE Trans. on Appl. Supercond.* **5**, p 3401.

## Structural characterization of $\text{YBa}_2\text{Cu}_3\text{O}_{7-\delta}/\text{Y}_2\text{O}_3$ composite films

P.R. Broussard

*Naval Research Lab, Washington, DC 20375*

M.A. Wall

*Lawrence Livermore National Laboratory, Livermore, CA 94550*

J. Talvacchio

*Northrop Grumman Science and Technology Center, Pittsburgh, PA 15235*

### Abstract

Using 4-circle x-ray diffraction and transmission electron microscopy we have studied the microstructure and in-plane orientation of the phases present in thin film composite mixtures of  $\text{YBa}_2\text{Cu}_3\text{O}_{7-\delta}$  and  $\text{Y}_2\text{O}_3$ . We see a high degree of in-plane orientation and have verified a previous prediction for the in-plane order of  $\text{Y}_2\text{BaCuO}_5$  on (110)  $\text{MgO}$ . Transmission electron microscopy shows the composite films to be a mixture of two phases, with YBCO grain sizes of  $\approx 1 \mu\text{m}$ . We have also compared our observations of the in-plane order to the predictions of a modified near coincidence site lattice model.

61.16.Bg, 61.10.-i, 74.76.Bz, 68.55.-a

Typeset using REVTeX

## I. INTRODUCTION

In thin film growth of  $\text{YBa}_2\text{Cu}_3\text{O}_{7-\delta}$  (YBCO), it is useful to understand the nature of the epitaxial relationships present between impurity phases in the films. This knowledge provides a guide for finding these phases by x-ray diffraction, as seen in the recent study of CuO in YBCO films by Watson et al. [1] Also, in a previous report on thin film composites of YBCO and yttria, [2] we predicted the in-plane orientation of the phase  $\text{Y}_2\text{BaCuO}_5$  (Y-211) which was found in composites grown on (110)  $\text{MgO}$ . In this work, we have studied the microstructure and in-plane orientation of the phases present in thin film composites of YBCO and yttria grown on (100) and (110)  $\text{MgO}$ . In particular, we have studied how the YBCO, yttria, and Y-211 phases grow in relation to the underlying substrate, to understand how these phases appear as impurities in YBCO and to verify our previous prediction.

## II. SAMPLE PREPARATION

The samples were grown by off-axis sputtering onto commercially polished (100) and (110)  $\text{MgO}$  substrates. [2,3] YBCO and yttria were cosputtered in a 100 mTorr gas mixture of 80% argon and 20% oxygen at a total rate of  $\approx 440 \text{ \AA/hour}$ . Under the growth conditions used they would ideally be composed of 91% YBCO by volume. The substrates were at a temperature of  $\approx 700 \text{ }^{\circ}\text{C}$ , and after the growth were furnace cooled in 100 Torr of oxygen. Film thicknesses were  $\approx 1900 \text{ \AA}$ . The samples were studied by 4-circle x-ray diffraction (XRD) and transmission electron microscopy (TEM). The XRD was carried out on a Phillips 4-circle diffractometer. The orientation of the films was determined by standard  $\theta - 2\theta$  scans with diffraction along the sample normal. The crystal quality was studied using rocking curves for diffraction along and at various angles to the sample normal. In-plane order was measured by taking  $\phi$  scans where the diffraction vector for a particular value of  $2\theta$  is at an angle  $\chi$  to the sample normal and  $\phi$  is the angle of rotation about the sample normal. The TEM analysis was performed on a JEOL 200CX microscope using conventional bright field

(BF) and selected area diffraction (SAD) conditions on plan view specimens.

To interpret the in-plane order observed and compare lattice matching of the phases to the substrate and to each other, previous work has used a near coincidence site lattice theory. [4] In this model (for the case when the lattice direction along the growth direction is already determined) the mismatch between the film surface mesh and the substrate surface mesh is given as the percentage difference of the respective position vectors with respect to their average lengths. Since this approach only compares discrete orientations between the two meshes, we have used a computer model to study the matching of an  $N \times N$  mesh of an overlayer onto the substrate mesh for arbitrary angles between the two meshes. We have a rectangular overlayer with lattice constants  $a$  and  $b$  in the directions  $\hat{x}$  and  $\hat{y}$ , and a rectangular substrate mesh with corresponding lattice constants  $c$  and  $d$  in the directions  $\hat{x}'$  and  $\hat{y}'$ , where the primed system is rotated by an angle  $\theta$  with respect to the unprimed system. Then for each overlayer lattice point,  $\vec{r}_{i,j}^o = ia\hat{x} + jb\hat{y}$ , the program finds the corresponding closest lattice point in the substrate layer,  $\vec{r}_{i,j}^s = k_i c\hat{x}' + l_j d\hat{y}'$ , computes the strain for that point, and averages over all overlayer points (excluding the origin):

$$Strain = \frac{1}{N^2 - 1} \sum_{\substack{i,j=0 \\ (i,j) \neq (0,0)}}^N \frac{2 \left| \vec{r}_{i,j}^o - \vec{r}_{i,j}^s \right|}{\left| \vec{r}_{i,j}^o \right| + \left| \vec{r}_{i,j}^s \right|}. \quad (1)$$

We then look for minima in the strain as a function of angle between the lattices that will indicate a preferred orientation of the overlayer on the substrate.

### III. RESULTS

We first consider the composite on (100) MgO, which from  $\theta - 2\theta$  XRD shows the presence of YBCO and yttria in the film. The YBCO phase is c-axis oriented with a lattice constant of  $11.714 \pm 0.004$  Å. The rocking curve width for the YBCO 005 peak is  $0.64^\circ$ , with a comparable width for the YBCO 309 peak. The yttria in the film is oriented (001) with a lattice constant of  $10.594 \pm 0.004$  Å, with a rocking curve width for the yttria 004 peak of

0.98°. The width for the yttria 226 peak is comparable to that of the 004 peak.

In Fig. 1 we present plots of x-ray intensity versus  $\phi$  for the MgO 402, YBCO 309 peak, and the yttria 226 peak. We find in contrast to the case of pure YBCO on (100) MgO [5] that the YBCO in the composite film is primarily oriented at the 45° orientation, or [110] YBCO  $\parallel$  [010] MgO. A smaller amount of YBCO is in the usual cube-on-cube orientation. We find from the  $\phi$  scans that the bulk of the yttria is oriented as cube-on-cube, or [100] yttria  $\parallel$  [100] MgO, with a small amount oriented at 45°, or [110] yttria  $\parallel$  [100] MgO. We also see that the mosaic spread in the  $\phi$  scan is substantially broader for the yttria peaks, with the FWHM being  $\approx 7^\circ$ , but only  $\approx 2.5^\circ$  for the YBCO peaks. This larger peak width is consistent with the larger rocking curve width seen for the yttria. Comparing the YBCO  $\phi$  scan to that for the yttria, we see that the YBCO is oriented with respect to the yttria as [110] YBCO  $\parallel$  [100] yttria, which was seen in studies of yttria on YBCO layers. [6,7] We also see that the intensities of the two phases track as a function of the angle  $\phi$ . This tracking implies that the matching for the YBCO present in this sample is predominantly with the yttria, not the MgO.

Figure 2 shows a TEM BF image of the composite sample on (100) MgO. There are two phases clearly present: equiaxed, highly-faceted islands approximately 1  $\mu\text{m}$  in diameter partially surrounded by a thin phase. We see a high degree of connectivity between the islands in this sample. Analysis of SAD images (not shown) reveals that the islands are c-axis oriented YBCO and the phase between the YBCO grains is (001) oriented yttria. The variation in contrast among the YBCO islands is due to their varying thickness. SAD analysis shows an in-plane orientation relationship of the (202) direction of yttria parallel to the (100) or (010) axis of YBCO, which agrees with what was seen in the XRD analysis. The variation in contrast among the YBCO islands is due to their varying thickness.

Using our lattice model for the case of the composite film on (100) MgO, we compared the matching of yttria (001) to MgO (100), and because the YBCO in this sample seemed to be oriented with the yttria, we also compared the matching of yttria (001) to YBCO (001). For yttria we used  $a=b=10.6$  Å. For yttria (001) on (100) MgO, we find that there is a strong

minima at  $0^\circ$  and another at  $23^\circ$ , but not at  $45^\circ$ . Experimentally, we do not see any yttria misaligned by  $23^\circ$ , but we do observe it at  $45^\circ$ . For YBCO on yttria, we find a clear minima for the  $45^\circ$  alignment, as seen in the films, as well as weaker minima at  $0^\circ$  (cube-on-cube),  $14^\circ$ , and  $21^\circ$ , which we do not observe. From the data and the results of the model, we believe the  $\phi$  scan in Fig. 1 can be explained by two types of microstructure in this sample. The first is where yttria is the initial phase growing on the MgO, and orients as cube-on-cube, and the YBCO that grows subsequently is misoriented by  $45^\circ$ . This type of microstructure is the predominant one in the sample. The second is where YBCO nucleates first on the MgO, growing as cube-on-cube, and the yttria that grows subsequently is misoriented by  $45^\circ$ . Careful study of the SAD images did show evidence of extra diffraction spots, which are most likely due to double diffraction. This would be consistent with the yttria and YBCO phases being on top or underneath each other.

Next, we turn to the composite sample on (110) MgO. As was discussed in Ref. [2], this sample was deposited in the same run as the composite sample on (100) MgO. However, XRD shows no yttria in the film, but instead indicates a-axis oriented Y-211 material. The sample was insulating, even though from XRD the YBCO present in the film is similar to that for pure YBCO on (110) MgO. We find c-axis oriented YBCO with a c-axis constant of  $11.728 \pm 0.004$  Å. The rocking curve width for the YBCO 005 peak is  $0.6^\circ$  (with a comparable width for the YBCO 309 peak). The Y-211 material in the film is oriented (100) with a lattice parameter of  $7.145 \pm 0.004$  Å and has a rocking curve width for the Y-211 200 reflection of  $0.39^\circ$  and  $0.46^\circ$  for the 505 off-axis peak. This indicates that the Y-211 material is more ordered than the YBCO in the film.

If we look at the  $\phi$  scans for peaks from MgO (240), YBCO (309) and Y-211 (320) lines, as in Fig. 3, we see that the YBCO is oriented with  $[100] \text{ YBCO} \parallel [001] \text{ MgO}$ . The Y-211 material is predominantly oriented as  $[010] \text{ Y-211} \parallel [001] \text{ MgO}$ , with about 10% (by volume) of the Y-211 material oriented as  $[010] \text{ Y-211} \parallel [\bar{1}10] \text{ MgO}$ , or a  $90^\circ$  misorientation. In Ref. [2], we predicted that the in-plane order of the (100) Y-211 material on the (110) MgO substrate would be  $[010] \text{ Y-211} \parallel [001] \text{ MgO}$  and  $[001] \text{ Y-211} \parallel [\bar{1}\bar{1}0] \text{ MgO}$ . This is what is

seen for the bulk of the Y-211.

Figure 4 is a TEM BF image of the composite sample on (110) MgO, which clearly shows a two phase structure consisting of irregular-shaped, slightly faceted islands of average width  $0.5 \mu\text{m}$  surrounded by a sea/matrix. Analysis of the SAD images shows the island phase to be c-axis oriented YBCO. Rotational spot splitting is also observed, which results from twinning within the islands of YBCO. The matrix phase is single phase a-axis oriented Y-211. SAD patterns from different parts of the sample had the same orientation, indicating the Y-211 grains are single crystal-like over the region examined ( $\approx 2 \mu\text{m}$ ). Figure 4 shows a small amount of connectivity between the YBCO islands, but for the most part they are isolated. This result is consistent with the sample being insulating.

For the composite sample on (110) MgO, we used Eq. 1 to model the matching of Y-211 (100) to MgO (110) using for Y-211 lattice parameters  $b = 12.16 \pm 0.04 \text{ \AA}$  and  $c = 5.656 \pm 0.002 \text{ \AA}$  (measured for this sample). We find the strongest minima for the predominant orientation of  $[010] \text{ Y-211} \parallel [001] \text{ MgO}$ , but the  $90^\circ$  orientation  $[010] \text{ Y-211} \parallel [\bar{1}10] \text{ MgO}$  also has a strong minima. There is also a weak minima for  $45^\circ$  oriented material. For the case of Y-211 (100) to YBCO (001), we find the best match at a  $45^\circ$  misorientation, and weaker minima for either Y-211 [010] or [001]  $\parallel$  YBCO [100]. Since we did not observe the  $45^\circ$  misorientation in the x-ray scans, we conclude that the Y-211 and YBCO phases grow on the (110) MgO substrate, unlike the case for a composite sample on (001) MgO with YBCO and yttria, where the evidence is that the bulk of the YBCO grains grow on yttria, not on the (100) MgO.

#### IV. DISCUSSION

One of the major motivations for this work was to understand why different phases form on (100) MgO than (110) MgO substrates for composite samples. The in-plane ordering we observe suggests that phase formation is driven by lattice matching to the substrate. However, if we use Eq. 1 to predict how yttria or Y-211 will grow on the two orientations of

MgO, the results do not agree with our XRD studies. For (001) yttria, the model predicts a lower strain for growth on (100) MgO compared to (110) MgO. For a-axis oriented Y-211, the model also predicts a lower strain for growth on (100) MgO, not (110) MgO, with an in-plane orientation at 45°. These results suggest that if substrate lattice matching is driving the formation of Y-211 on (110) MgO, then Y-211 should also form on (100) MgO. Our studies show otherwise.

Another approach to understanding the growth of Y-211 on (110) MgO is to assume it is controlled by the bulk phase diagram for the Y-Ba-Cu-O system. We would estimate from the location of the composite sample on (110) MgO in the Y-Ba-Cu-O phase diagram (in Ref. [2]) that there should be 49% YBCO, 39% Y-211 and 12% CuO by volume. However, from Fig. 4 we find that the volume fraction of YBCO is only 35%, and neither XRD or TEM shows the presence of CuO in the films. Clearly the growth mechanism on (110) MgO is not fully understood.

## V. CONCLUSIONS

We have seen by both XRD and TEM that composite films of YBCO and yttria exhibit a great deal of in-plane orientation. We have successfully verified the prediction in Ref. [2] that composites grown on (110) MgO have a-axis oriented Y-211 present with a predominant in-plane orientation of [010] Y-211  $\parallel$  [001] MgO, but some fraction of the Y-211 phase is oriented at 90° to this. The composites on (001) MgO show in-plane orientations that indicate two types of microstructure, either yttria on YBCO or YBCO on yttria. The sizes of the YBCO grains are  $\approx 1 \mu\text{m}$  for the composites on (100) MgO, while on (110) MgO YBCO forms oblong islands of up to several microns in length. Our attempts at studying the lattice matching using a modified near coincidence site lattice model did show that we could understand the observed in-plane orientations, but could not explain the occurrence of different phases growing on (100) and (110) MgO.

## REFERENCES

- [1] I.M. Watson, M.P. Atwood, and J.J. Cumberbatch, *Thin Solid Films* **251**, 51 (1994).
- [2] P.R. Broussard, V.C. Cestone, and L.H. Allen, *J. Appl. Phys.* **77**, 252 (1995).
- [3] G.L. Waytena, H.A. Hoff, C.L. Vold, P.R. Broussard, J.H. Claassen, V.C. Cestone, and J.A. Sprague, *J. Appl. Phys.* **76**, 2380 (1994).
- [4] T.S. Ravi, D.M. Hwang, R. Ramesh, Siu-Wai Chan, L. Nazer, C.Y. Chen, A. Inam, and T. Venkatesan, *Phys. Rev. B* **42**, 10141 (1990); D.M. Hwang, T.S. Ravi, R. Ramesh, Siu-Wai Chan, C.Y. Chen, L. Nazer, X.D. Wu, A. Inam, and T. Venkatesan, *Appl. Phys. Lett.* **57**, 1690 (1990).
- [5] E.J. Williams and W.M. Stobbs, *Physica C* **208**, 96 (1993).
- [6] K. Hirata, K. Yamamoto, K. Iijima, J. Takada, T. Terashima, Y. Bando, and H. Mazaki, *Appl. Phys. Lett.* **56**, 683 (1990).
- [7] Q.Y. Ying, C. Hilbert, N. Kumar, D. Eichman, M. Thompson, H. Kroger, and D.M. Hwang, *Appl. Phys. Lett.* **59**, 3037 (1991).

## FIGURES

FIG. 1. X-ray intensity (log scale) versus  $\phi$  for diffraction along the yttria 226,  $\text{YBa}_2\text{Cu}_3\text{O}_{7-\delta}$  309 and the  $\text{MgO}$  402 peaks for the composite sample grown on (100)  $\text{MgO}$ . The curves are offset for clarity.

FIG. 2. Bright field plan view TEM images for the composite sample grown on (100)  $\text{MgO}$  showing YBCO grain structure with yttria at the grain boundaries. The darker faceted islands are the YBCO phase, with the yttria phase showing up as white in the grain boundaries.

FIG. 3. X-ray intensity (log scale) versus  $\phi$  for diffraction along the  $\text{Y}_2\text{BaCuO}_5$  320,  $\text{YBa}_2\text{Cu}_3\text{O}_{7-\delta}$  309 and the  $\text{MgO}$  240 peaks for the composite sample grown on (110)  $\text{MgO}$ . The curves are offset for clarity.

FIG. 4. Bright field plan view TEM image for the composite sample grown on (110)  $\text{MgO}$  showing the morphology of the sample at low magnification. The lighter region is the Y-211 phase, with the YBCO phase in oblong islands.

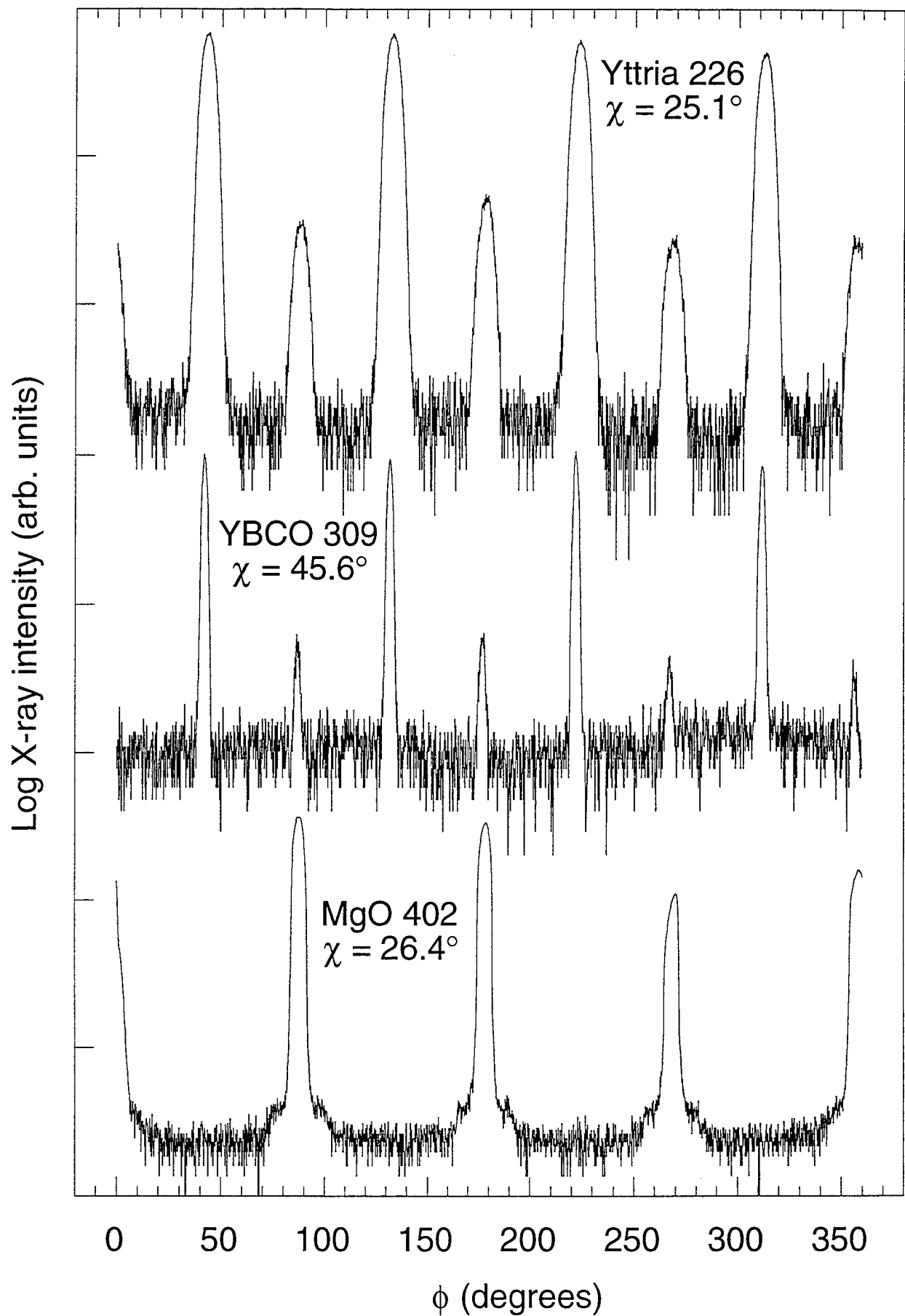
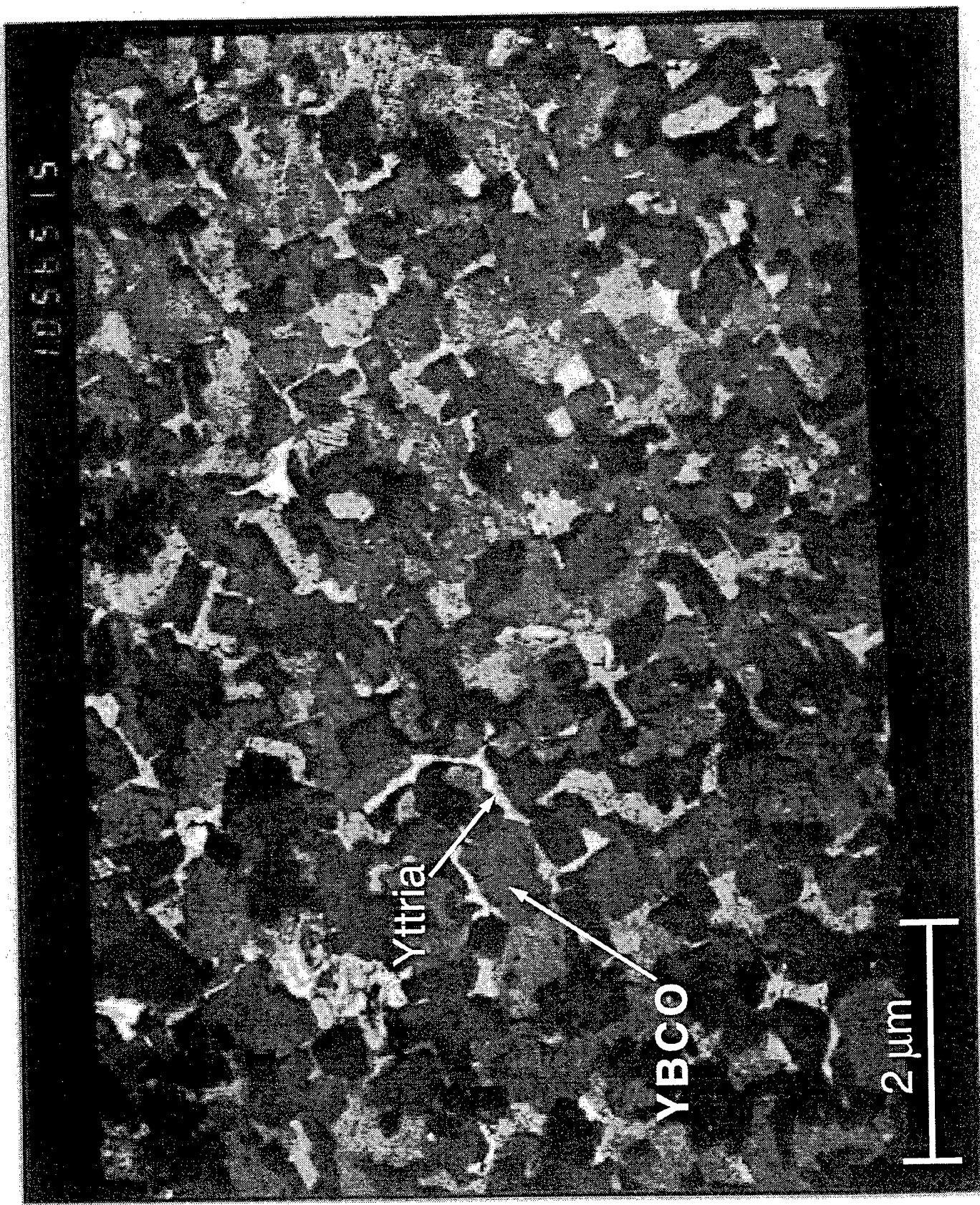


Figure 1: P.R. Broussard et al.

Figure 2  
Broussard



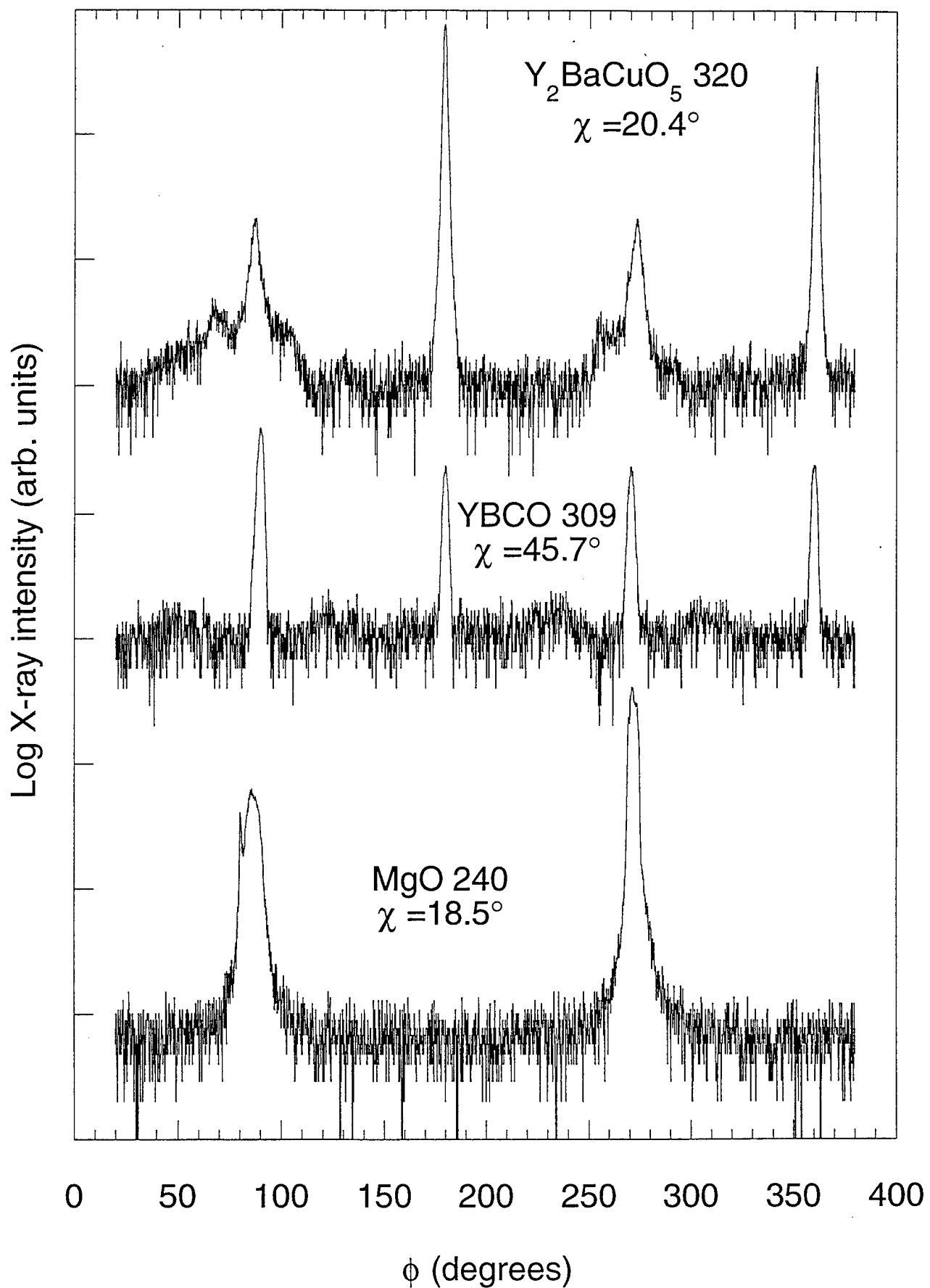
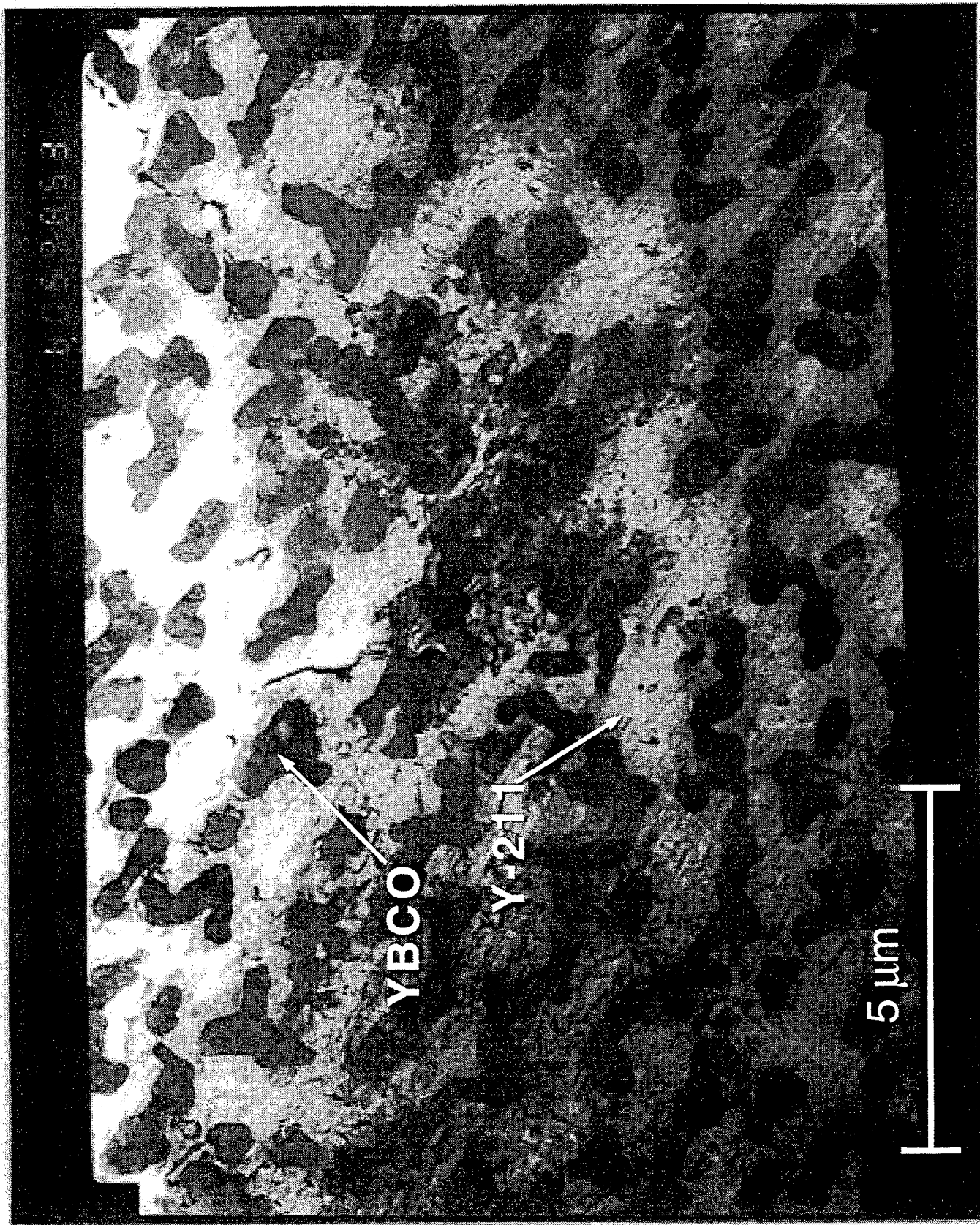


Figure 3: P.R. Broussard et al.

Figure 4  
Broussard



# Environmental degradation properties of $\text{YBa}_2\text{Cu}_3\text{O}_{7-\delta}$ and $\text{Y}_{0.6}\text{Ca}_{0.4}\text{Ba}_{1.6}\text{La}_{0.4}\text{Cu}_3\text{O}_{7-\delta}$ thin film structures

Ji-Ping Zhou <sup>a</sup>, Rung-Kuang Lo <sup>a</sup>, Steven M. Savoy <sup>a</sup>, Mark Arendt <sup>a</sup>,  
Jeff Armstrong <sup>a</sup>, Du-Yu Yang <sup>a</sup>, John Talvacchio <sup>b</sup>, John T. McDevitt <sup>a,\*</sup>

<sup>a</sup> Department of Chemistry and Biochemistry, The University of Texas, Austin, TX, 78712-1167, USA

<sup>b</sup> Northrop Grumman STC, Pittsburgh, PA 15235, USA

Received 4 March 1996; revised manuscript received 28 August 1996

---

## Abstract

Utilization of the high temperature superconductor,  $\text{YBa}_2\text{Cu}_3\text{O}_{7-\delta}$ , in commercial applications is becoming increasingly feasible. Before full advantage of this material can be taken, however, the lifetime, oxygen stability and processability of this ambient reactive superconductor must be improved. Corrosion resistance of  $\text{YBa}_2\text{Cu}_3\text{O}_{7-\delta}$  and a cation substituted compound,  $\text{Y}_{0.6}\text{Ca}_{0.4}\text{Ba}_{1.6}\text{La}_{0.4}\text{Cu}_3\text{O}_{7-\delta}$ , were studied and their lifetimes in aqueous environments were determined. Results indicate a dramatic enhancement in the stability against environmental degradation for the cation substituted phase. Important mechanistic factors responsible for the enhanced corrosion resistance of the substituted phase over the parent compound are discussed.

**Keywords:** High- $T_c$  thin film; Superconductor lifetime measurement; Corrosion; Surface characterization; Environmental degradation

---

## 1. Introduction

Recently, researchers worldwide have made a tremendous amount of progress in the fabrication of high- $T_c$  superconductor products such as tapes, wires and thin film devices [1–3]. Unfortunately, only in a very few cases have efforts to commercialize high- $T_c$  products been successful. Many of the problems associated with the commercialization of the superconductors can be traced to poor physical, chemical and materials properties exhibited by the cuprate

compounds. In particular, the most commonly utilized cuprate superconductor,  $\text{YBa}_2\text{Cu}_3\text{O}_{7-\delta}$ , tends to degrade rapidly when exposed to the atmosphere due to reactions with  $\text{CO}$ ,  $\text{CO}_2$  and  $\text{H}_2\text{O}$  [4]. Moreover, problems have been noted with the loss of surface oxygen and electromigration mediated rearrangement of the oxygen ion locations within the lattice [5]. Successful fabrication of high- $T_c$   $\text{YBa}_2\text{Cu}_3\text{O}_{7-\delta}$  junctions will require the formation of an epitaxial SNS structure having a smooth and atomically abrupt interface free of degradation and oxygen loss [6]. To meet such stringent requirements, further improvements in the chemical durability, oxygen stability and processability of high- $T_c$  phases are necessary.

---

\* Corresponding author. Fax: +1 512 471 8696.

There are two major ways utilized for preventing the environmental degradation of high- $T_c$  materials. The first involves the formation of protective barriers which serve to slow the diffusion of the corrosive reagents ( $H_2O$ ,  $CO_2$ ,  $CO$ , acids, etc.) to the surface of the superconductor. Metals such as Al, Ag and Au [7,8] as well as insulating oxides such as  $MgO$ ,  $LaAlO_3$  and  $SrTiO_3$  [9,10] have been studied in this context. Unfortunately, the deposition of metals onto  $YBa_2Cu_3O_{7-\delta}$  can lead to the formation of a galvanically coupled electrochemical cell which effectively increases the rate of decomposition of the high- $T_c$  material by a factor of  $10^2$  to  $10^3$  [11,12]. Our systematic studies of the galvanic corrosion will be published soon elsewhere. Many insulators, on the other hand, while not subject to galvanic effects, possess incompatible thermal expansion and high dielectric properties that makes their inclusion in some high- $T_c$  devices questionable [13]. Recently, protective barriers formed from amorphous carbon layers of 20–200 nm thickness have been studied in the context of providing short term stabilization suitable, perhaps, for the processing of cuprate films [14].

Through recent work, we have begun to tailor chemically the high- $T_c$  materials properties so that the serious material limitations currently associated with the processing of small scale and large scale high- $T_c$  structures and devices can be avoided [11,12]. Accordingly, the second area involves the design and preparation of cation modified  $YBa_2Cu_3O_{7-\delta}$  samples which are intrinsically more stable and more processable than the parent compound. This lattice

engineering approach has led to the discovery of tailored superconductor materials such as  $Y_{1-x}Ca_x-Ba_{2-y}La_yCu_3O_{7-\delta}$  [11,12]. These substitutions disrupt the integrity of the  $CuO_{1-\delta}$  chains while keeping the total oxidation state of the  $[Cu(2)-O(2)/O(3)]$  arrays nearly constant. Stability measurements indicate that the chemical resistance to degradation is significantly enhanced by these chemical substitutions [11,12].

In this study, the degradation behavior of  $YBa_2Cu_3O_{7-\delta}$  (YBCO) and a cation substituted compound,  $Y_{0.6}Ca_{0.4}Ba_{1.6}La_{0.4}Cu_3O_{7-\delta}$  (TX-YBCO), in water vapor environments are established for thin film structures. Results indicate an enhanced stability against aqueous-environmental degradation for the cation substituted phase. In addition, important mechanistic factors responsible for the enhanced corrosion resistance of the substituted phase over the parent compound are discussed.

## 2. Experimental

The thin films of YBCO and TX-YBCO with 1500 Å thickness were prepared using off-axis magnetron sputtering [15], molecular organic chemical vapor deposition (MOCVD) [16] and pulsed laser deposition (PLD) [17]. The sputtered films exhibited much smoother surface morphologies as measured by atomic force microscopy (AFM) than those obtained by MOCVD. Values of surface mean roughness of 7.4 nm were obtained for the PLD films, 0.6 nm for the sputtered films and 59.2 nm MOCVD

Table 1  
 $YBa_2Cu_3O_{7-\delta}$  (YBCO) and  $Y_{0.6}Ca_{0.4}Ba_{1.6}La_{0.4}Cu_3O_{7-\delta}$  (TX-YBCO) film lifetimes as a function of water vapor exposure.

Sample	Deposition procedure	Substrate	Film orientation	$T_c$ (K)	Vapor Temperature (°C)	Condition humidity (%)	Lifetime (hrs)
YBCO	PLD	$MgO$	$c$	90	75	≥ 98	3.3
YBCO	PLD	$MgO$	$c$	90	75	≥ 98	3.0
YBCO	PLD	$MgO$	$c$	90	75	≥ 98	2.5
YBCO	Sputtering	$LaAlO_3$	$c^a$	91	23	60	≥ 30.0
YBCO	Sputtering	$LaAlO_3$	$c^a$	91	23	≥ 98	34.0
YBCO	Sputtering	$LaAlO_3$	$c$	91	75	≥ 98	2.2
YBCO	MOCVD	$LaAlO_3$	$c^a$	91	75	≥ 98	3.5
TX-YBCO	PLD	$MgO$	$c$	79	75	≥ 98	> 30.0

<sup>a</sup> These specimens possessed a small portion of  $a$ -axis orientation as determined by X-ray powder diffraction and AFM measurement.

<sup>b</sup> Standard deviation of first three samples is 1.021(4).

prepared films. To further characterize the quality of the films, 4-point probe resistivity and X-ray powder diffraction measurements were completed. Moreover, the surface resistance values of selected thin films were also investigated [15,16]. Transition temperatures and axis orientation of the various studied samples are summarized in Table 1. Values of critical current and surface resistance for the samples prepared by sputtering and MOCVD methods are consistent with state-of-the-art samples as described previously [15,16]. In order to study further the corrosion behavior of these film samples, optical microscopy, scanning electron microscopy, transmission electron microscopy, environmental scanning electron microscopy and x-ray photoelectron spectroscopy measurements were completed.

### 3. Results and discussion

Methods for the measurement of the lifetimes of ceramic samples have been described previously [18]. From many prior studies, detailed comparisons between different studies are not made readily due to differences in sample purity, sample geometry, particle size, environment, etc. One the most reliable procedures for quantifying the degradation rates for bulk samples involves the preparation of powders with controlled particle sizes using single phase ceramic pellets as starting materials [18]. With such

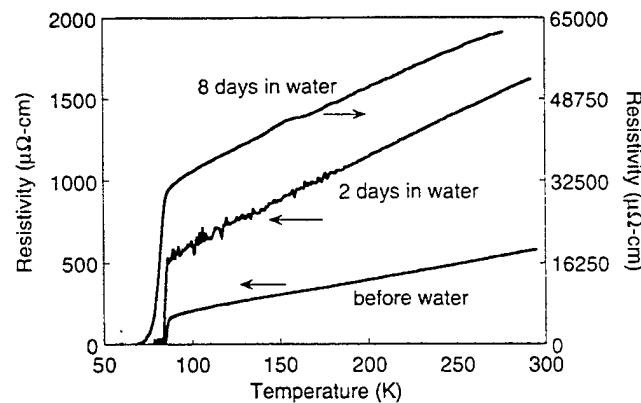


Fig. 2. Resistivity versus temperature curves recorded for a single  $\text{YBa}_2\text{Cu}_3\text{O}_{7-\delta}$  film specimen that was soaked in aerated water at room temperature for the noted time periods.

samples, the geometric and purity factors are controlled carefully. The intrinsic lifetimes of the powders are measured by X-ray powder diffraction (XRD) by noting the time necessary for the original superconductor phase to decompose to 50% of the original phase content [18]. Crystalline impurities are readily identified in these studies. Using such a methodology, a  $\geq 100$  fold increase in the stability of TX-YBCO relative to YBCO has been noted [11,12].

In our initial attempts to utilize XRD to explore the degradation rate of high- $T_c$  films, samples of *c*-axis oriented films of YBCO were deposited *c*-to  $\text{MgO}(100)$  substrates using the method of PLD [17]. These films were there soaked in aerated water solution and XRD data was acquired as a function of exposure time. Provided in Fig. 1 is data for a representative film before exposure and after 11 days soaking in room temperature aerated water. Although there are changes in the intensity of the characteristic (001) reflections for *c*-axis oriented YBCO, no crystalline corrosion products are apparent after this lengthy water exposure. Rather, the only suggestion of chemical damage to the film is a decrease in the intensity of the diffraction signals.

Similarly, when the resistivity vs. temperature curves were acquired before and after water exposure, little changes in the  $T_c$  value were noted, as shown in Fig. 2. Greater than 90% of the thickness of the high- $T_c$  film can be degraded and yet such samples display superconducting transition temperatures close to their original values. However, in-

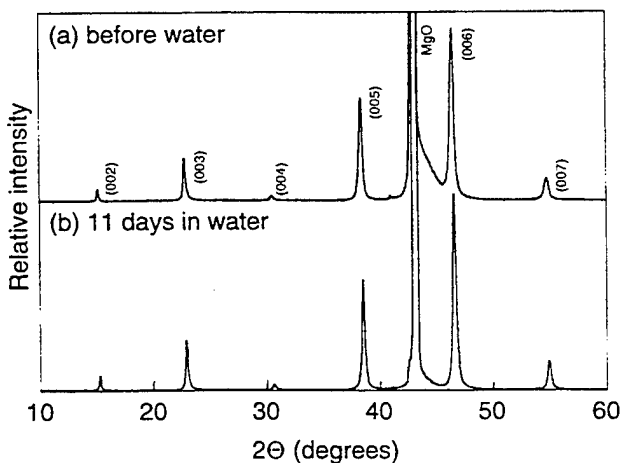


Fig. 1. XRD patterns of  $\text{YBa}_2\text{Cu}_3\text{O}_{7-\delta}$  films that were soaked in aerated water solution at room temperature for various amounts of time: (a)  $\text{YBa}_2\text{Cu}_3\text{O}_{7-\delta}$  film before corrosion, (b)  $\text{YBa}_2\text{Cu}_3\text{O}_{7-\delta}$  film soaked in water for 11 days.

creases in room temperature resistivity and decreases in critical current values can be used as a more sensitive probe to evaluate the volume fraction of superconductivity and its decrease upon water exposure. Furthermore, upon inspection of the surface of these films by scanning electron microscopy and optical microscopy, it is clear that significant amount of damage has occurred to the films.

Although qualitative in nature, the differences in surface morphology noted in the water exposure films suggest that many of the same problems noted in prior literature for bulk YBCO are also present in their film counter parts. The above crystallographic data suggest, however, that either amorphous degradation products collect on the surface of the corroded films or soluble materials are formed and dissolve in the solution.

Moreover, careful inspection of the resistivity data shows that although no significant changes in  $T_c$  are noted, dramatic increases in the normal state resistivity occur. Such an observation suggests that an amorphous degradation layer collects on top of a chemically pristine layer in the initial stages of corrosion. In support of this view is the transmission electron micrograph image which is shown in Fig. 3 for a YBCO film that was soaked in aerated water at room

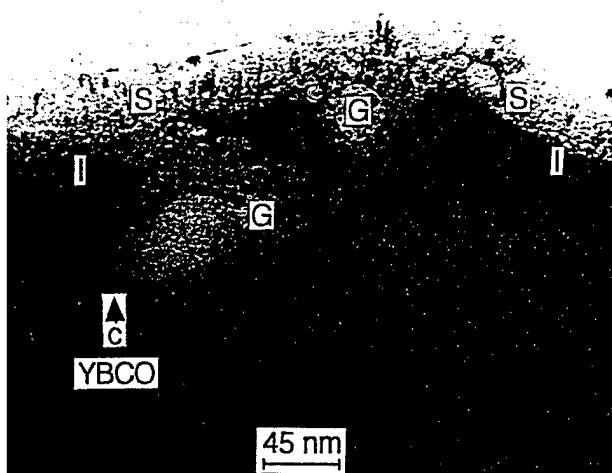


Fig. 3. Transmission electron micrograph recorded for a c-axis oriented  $\text{YBa}_2\text{Cu}_3\text{O}_{7-\delta}$  film (1500 Å initial thickness) that is supported on an  $\text{MgO}$  (100) substrate. Prior to the measurement, the sample was soaked in water solution for a period 3 days at room temperature. Here labels "S" refer to an amorphous surface layer, "I" represent interior regions where little corrosive damage is noted and "G" depicts interior regions of gray appearance where significant amounts of localized decomposition are noted.

temperature for 3 days. Here, an amorphous degradation layer (labeled S) is found at the exterior surface of the film. In selected locations, additional regions which appear as gray structures (labeled G) become localized within the interior portion of the film. Studies of the TEM images show that samples which did not receive the water treatment lacked the gray areas. Interestingly, selected area diffraction studies of the gray regions did not yield the expected lattice fringes, but regions immediately surrounding these areas produced high resolution images reminiscent of the pristine material. Thus, the gray regions appear to be water damaged locations which exist within the interior of the film. Although not shown, there are also additional regions spaced at intervals of  $\sim 5000$  Å where severe damage has occurred spanning locations near the surface of the film down to the substrate. Rapid adsorption of water along the grain boundaries is likely to be responsible for this localized corrosion behavior.

The above mentioned resistivity measurements and prior studies [19] have provided qualitative information related to the degradation rate of high- $T_c$  YBCO films. In particular, the dramatic changes of resistivity obtained for corroded film samples indicate that the resistivity measurement is a relatively ideal method to estimate the film lifetime. Accordingly, it is desirable to employ such a technique to compare the reactivity rates of high- $T_c$  film samples prepared by different deposition methods as well as to evaluate the corrosion resistance of the above stated cation substituted forms of YBCO.

Recently, we have developed a reliable technique that can be used to quantify the lifetime of high- $T_c$  films in accelerated corrosion experiments [11,12]. Accordingly, film samples are placed in a water vapor chamber equilibrated at constant temperature with controlled humidity and quasi-dc four probe resistivity measurements are acquired as a function of time (Fig. 4). From such measurements, increases in the film resistivity are utilized to judge the rate of damage to the cuprate structure. Typically, the films degrade initially at a modest rate with little increase in resistivity over time. However, once the degradation process creates a sufficient number of corrosion defects to produce a highly resistive barrier in the film, a marked increase in resistance is noted (Fig. 5). Interestingly, the films usually show a catas-

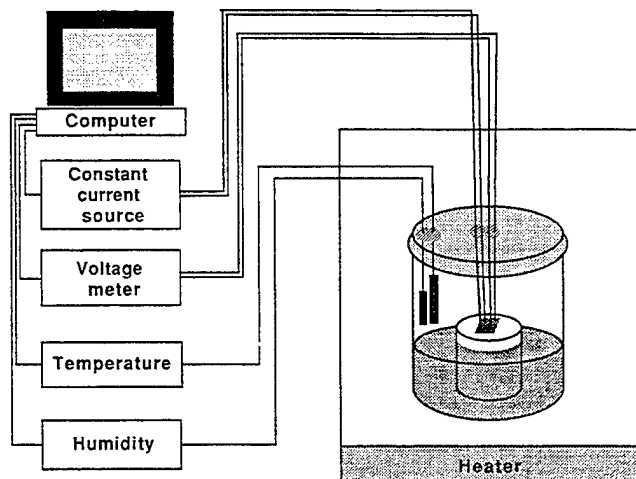


Fig. 4. Schematic illustration depicting an apparatus capable of estimating the lifetime of high- $T_c$  films and devices in accelerated corrosion measurements. Here, resistivity measurements are completed on high- $T_c$  films which are located within a chamber where humidity and temperature can be regulated. Lifetimes are estimated as the length of time required for catastrophic contact failure to occur.

trophic decomposition near one or both of the current passing electrodes (Fig. 6). Because sampling current, contact method and measurement intervals also influence to some extent the measured lifetime, identical parameters are utilized to evaluate the various samples [20]. Lifetime for the films is defined as the amount of time necessary to reach the failure point of the film specimens. The results for the lifetimes of several films are summarized in Table 1. Before considering the influence of conditions, film deposition method and superconductor composition it is important to quantify the reproducibility of the resistivity lifetime measurement. Consequently, included at the top of Table 1 are three identical  $\text{YBa}_2\text{Cu}_3\text{O}_7$  samples prepared by PLD that each received an exposure to water vapor at 75°C with relative humidity of  $\geq 98\%$ . Under such conditions, lifetime values were measured and found to cluster around  $2.9 \pm 0.5$  hours. Lifetime deviation well outside of this range can be attributed to changes in conditions, deposition method, or superconductor formulation.

Important to note is the fact that the areas near the metal contacts are found to degrade  $\geq 10^2$  more rapidly than remotely spaced regions. Thus, the described lifetime method (by design) serves to interrogate the reactivity of high- $T_c$  films near metal con-

tact areas. Since this area represent the most vulnerable region of many high- $T_c$  thin film devices, the described method can be used as an important tool for the study of the durability of high- $T_c$  thin film devices, a topic which has to date received little attention.

From these studies, three very important parameters which influence the water vapor degradation rates of the film samples are noted. These are crystal

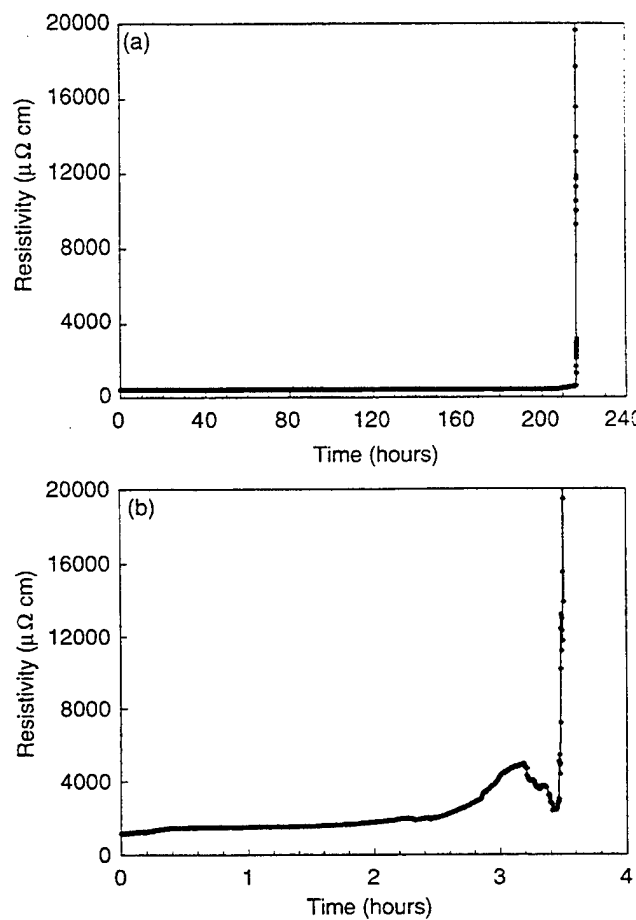


Fig. 5. Resistivity vs. time measurements recorded for a series of *c*-axis oriented  $\text{YBa}_2\text{Cu}_3\text{O}_{7-\delta}$  films (1500 Å thick) supported on  $\text{LaAlO}_3$  (100) substrates. (a) Initially a film prepared by off-axis magnetron sputtering was evaluated with 60% relative humidity at a temperature of 23°C. A constant resistivity value was obtained for the initial 200 hours of the measurement at which time the relative humidity was increased to  $\geq 98\%$  with no change in ambient temperature. Following this change in conditions, contact failure was noted after  $\sim 24$  hours. (b) Similarly, a second  $\text{YBa}_2\text{Cu}_3\text{O}_{7-\delta}$  film specimen prepared by the MOCVD method was exposed to water vapor equilibrated at 75°C and  $\geq 98\%$  relative humidity. This sample was found to degrade at the contact areas following a 3.5 hour exposure time.

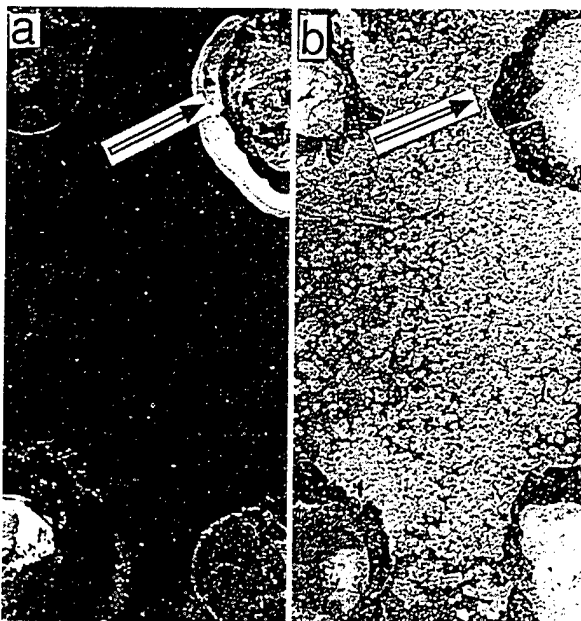


Fig. 6. Optical photographs showing (a) an off-axis magnetron sputtered  $\text{YBa}_2\text{Cu}_3\text{O}_{7-\delta}$  film after its exposure to 60% humidity for 10 days and then at  $\geq 98\%$  humidity for  $\sim 24$  hours at room temperature and (b) a MOCVD deposited  $\text{YBa}_2\text{Cu}_3\text{O}_{7-\delta}$  film after its exposure to  $75^\circ\text{C}$  water vapor for 3.5 hours. The catastrophic decompositions noted near the contacts are designated by arrows. (film sizes: 6 mm  $\times$  12 mm).

structure, temperature and humidity. Representative conditions which illustrate the influence of these three parameters on the degradation rate are included in Table 1. While keeping the temperature of the YBCO film samples constant at  $23^\circ\text{C}$  and varying the humidity from 60% to  $> 98\%$ , the film lifetime is found to decrease from  $> 10$  days to  $< 24$  hours (Fig. 5a). Increasing the temperature from  $23^\circ\text{C}$  to  $75^\circ\text{C}$  while maintaining a constant humidity leads to dramatic changes in the noted lifetime. For the lower temperature, a lifetime of  $\sim 24$  hours is noted while the higher temperature results in film failure at  $\sim 3$  hours. In comparison, the TX-YBCO films showed no signs of degradation for  $> 10$  days under the severe conditions of  $75^\circ\text{C}$  water vapor and  $\geq 98\%$  humidity [12]. Interestingly, for this type of measurement film deposition method and surface roughness values appear to be less important factors.

In considering the corrosion behavior in water vapor environments, the morphologies of corroded YBCO films were observed by optical microscopy (OM), and environmental scanning electron microscopy (ESEM). In Fig. 6, the corrosion results

obtained for the film samples made by sputtering and MOCVD methods are shown. The areas near the electrodes where the catastrophic decomposition occurs are clearly evident here. A view of the morphology at the corroded contact region obtained by ESEM is illustrated in Fig. 7. Interestingly, these high magnification images reveal periodic features which are likely caused by the passage of current through this region of the film. As shown in Fig. 6a, localized and periodic regions where large amounts of corrosion occur appear as concentric rings which surround the current contact electrode. It is quite plausible (vide infra) that the passage of current serves to

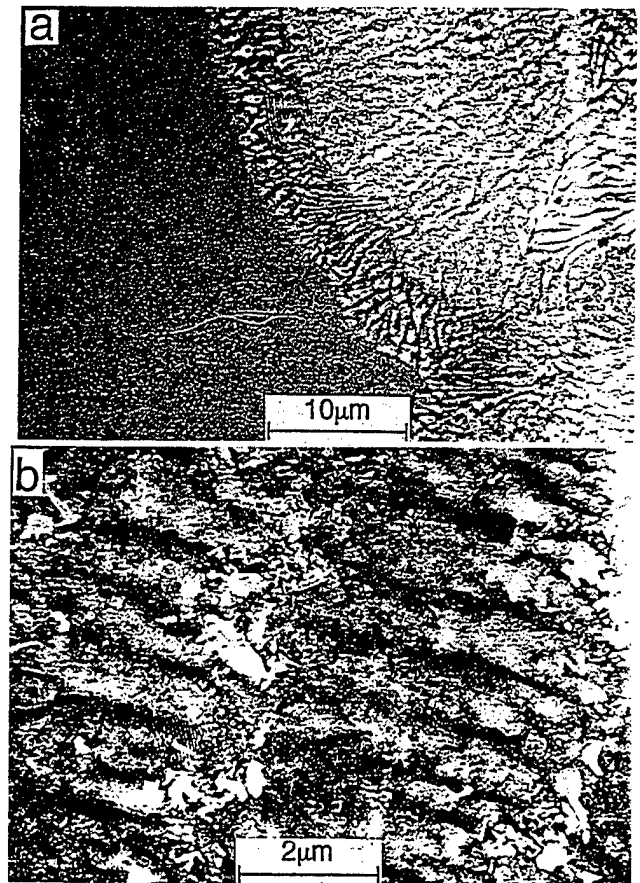


Fig. 7. Images of  $\text{YBa}_2\text{Cu}_3\text{O}_{7-\delta}$  films prepared by the off-axis magnetron sputtering method on  $\text{LaAlO}_3$  (100) substrate following their exposure to water vapor at  $75^\circ\text{C}$  and  $\geq 98\%$  relative humidity. (a) A low magnification view shows the area next to the contacting electrode where corrosion waves appear to grow in concentric fronts which are localized around the contact areas. (b) Higher magnification of the degraded area shows a rippling effect wherein the passage of electrical current near the contact appears to accelerate in a significant manner the decomposition of the high- $T_c$  material.

drive redox reactions in an electrochemical sense that accelerate the decomposition of the high- $T_c$  lattice. More details of corrosion reaction and decomposition processing related to these redox processes will be published in the near future.

A large amount of prior work has documented the utility of the method of X-ray photoelectron spectroscopy (XPS) [21] for the evaluation of the surface reactivity properties of YBCO [22,23]. Analogous to previous studies of the bulk reactivity of the ceramic superconductors where  $\text{BaCO}_3$  degradation products have been identified, XPS studies have noted the formation of carbon rich surface layers on the high- $T_c$  samples following their exposure to water [24]. In a similar manner, we have examined the surface characteristics of YBCO and TX-YBCO thin film specimens. Using an Ar-depth sputtering rate of 0.1 nm per minute, depth profile results obtained for the corroded YBCO sample exposed to 75°C water vapor for 3.5 hours are shown in Fig. 8a. Here the carbon content remains relatively constant during the profile duration. In addition, the relative signals from the other lattice constituents are found to be  $\sim 10$  times lower than that obtained for pristine YBCO samples [25]. On the contrary, XPS depth profile results for TX-YBCO samples exposed to same conditions show very little carbon contamination as shown in Fig. 8b. Interestingly, the surface elemental composition of the water treated TX-YBCO samples rapidly return to the normal concentration ratios after only  $\sim 3$  minutes of sputtering. Moreover, little (if any) change of the composition for the corroded YBCO films is noted after 10 minutes of sputtering.

Further evidence for the formation of a surface  $\text{BaCO}_3$  layer on YBCO is found from an evaluation of the C1s XPS spectra for water soaked samples. Data for the water treated YBCO sample is provided in Fig. 9a where two prominent signals at 284.6 eV and 289.3 eV are noted. Literature precedent [24,26] suggests the former peak can be attributed to the presence of an adventitious carbon layer and the latter is due to the formation of a  $\text{BaCO}_3$  layer. Following 10 minutes of Ar-ion sputtering, significant signals for both sources of carbon contamination remain present, suggesting a degradation layer thickness  $\geq 10$  Å. On the contrary, the similarly treated TX-YBCO films show little signs of carbonate contamination as indicated in Fig. 9b. Clearly,

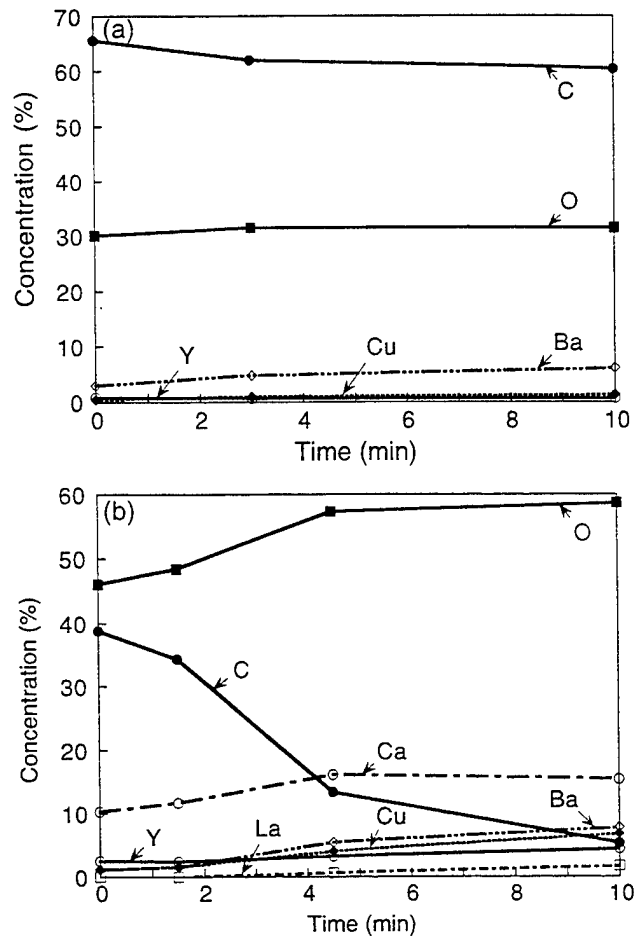


Fig. 8. XPS depth profiles showing (a) a  $\text{YBa}_2\text{Cu}_3\text{O}_{7-\delta}$  film and (b) a  $\text{Y}_{0.6}\text{Ca}_{0.4}\text{Ba}_{1.6}\text{Ca}_{0.4}\text{Cu}_3\text{O}_{7-\delta}$  film, both deposited on  $\text{MgO}$  (100) substrates after their exposure to water vapor equilibrated at 75°C and  $\geq 98\%$  relative humidity for 3.5 hours. (Ar-sputtering rate: 1 Å per minute).

the surface of the YBCO film is much less stable than that of TX-YBCO, in agreement with that observed for the bulk YBCO materials in aqueous environments where a 100-fold increase in the lifetime has been noted for TX-YBCO relative to the parent compound [27,28].

Considerations of the structure/corrosion reactivity relationships for the YBCO and TX-YBCO materials can provide essential mechanistic information related to this important class of materials. The parent compound, YBCO contains  $\text{Cu}(1)\text{-O}(4)$  chains as well as ordered oxygen vacancies ( $\text{V}_o$ ) at the  $\text{O}(5)$  sites [29]. Previous reports have suggested that in the early stages of corrosion, water enters the open channels along the  $\text{O}(5)$  sites and ultimately docks at a  $\text{O}(5)$  site. Proton transfer from water to the oxide

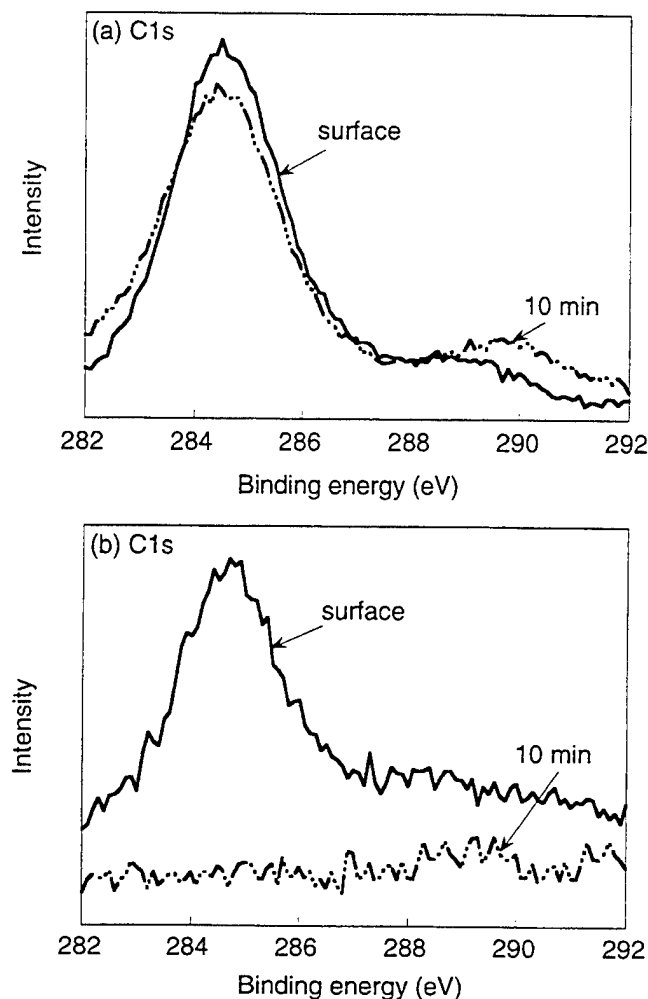


Fig. 9. XPS spectra showing the C1s regions for two *c*-axis oriented high- $T_c$  films (1500 Å thick) on MgO (100) prepared by pulsed laser ablation. Both film specimens were exposed to water vapor for 3.5 hours that was equilibrated at 75°C and  $\geq 98\%$  relative humidity. (a) Data for  $\text{YBa}_2\text{Cu}_3\text{O}_{7-\delta}$  and (b)  $\text{Y}_{0.6}\text{Ca}_{0.4}\text{Ba}_{1.6}\text{Ca}_{0.4}\text{Cu}_3\text{O}_{7-\delta}$  are provided.

components leads to the formation of two moles of  $\text{OH}^-$  which occupy both a vacancy site and a preexisting occupied oxide site [30]. Internal charge transfer within the  $[\text{CuO}]^+$  structures leads to the reduction of the copper sites and the oxidation of the

oxide components. The latter results in the evolution of molecular oxygen as described in Table 2, where the proposed degradation reaction sequence is summarized [31]. As stated above, the current supplied during resistivity measurement appears to accelerate the redox reactions in a significant manner. Clearly, the rapid and localized corrosive decomposition in regions adjacent to the electrodes supports this notion. At more remote locations, the decomposition occurs at a rate of  $10^2$  to  $10^3$  times more slowly as estimated by SEM. Following these initial steps, a series of reactions ensue ultimately leading to the bulk decomposition of the lattice [4,32].

Interestingly, the TX-YBCO might be expected to be involved in many of the same decomposition steps. However, two important differences exist for the TX-YBCO compound. First, our calculations completed using the bond valence sum theory [32] suggest that the substitution of La for Ba leads to a reduction of the internal strain energy from 1.79% to 0.35%. This reduction in strain may lower somewhat the driving force for corrosion. Second, and perhaps more important, the TX-YBCO material possesses a tetragonal structure in which occupancy at the O(4) and O(5) sites are equivalent [34] (called O(1) and O(5) in Ref. [34]). The disordering of these sites likely influences the rate of water diffusion into the lattice and oxygen evolution from the lattice interior. Both of these steps are involved in the initial stages of decomposition of the high- $T_c$  lattice. Thus, changes in the internal solid-state diffusion of water into and molecular oxygen out of the lattice may play a major role in dictating the decomposition rate of the lattice.

These studies truly emphasize the importance of gathering an atomic level understanding of the corrosion behavior of the high- $T_c$  superconductor systems. With such an understanding, crystal engineering of

Table 2  
Summary of corrosion reactions of  $\text{YBa}_2\text{Cu}_3\text{O}_{7-\delta}$  in water environments.

1) $\text{V}_0 + \text{O}_0^- + \text{H}_2\text{O} \rightarrow 2\text{OH}^-$	Water adsorbs into the vacancy sites, followed by proton transfer
2) $2[\text{CuO}]^+ \rightarrow 2\text{Cu}^{++} + 1/2\text{O}_2$	Charge transfer occurs along with breaking of the Cu(1)–O(4) bond which results in the release of molecular oxygen.
3) $\text{Ba}^{++} + 2\text{OH}^- \rightarrow \text{Ba}(\text{OH})_2$	Hydroxide reacts with Ba–O(1) layer to yield $\text{Ba}(\text{OH})_2$ .
4) $\text{Ba}(\text{OH})_2 + \text{CO}_2 \rightarrow \text{BaCO}_3 + \text{H}_2\text{O}$	Atmospheric $\text{CO}_2$ reacts with $\text{Ba}(\text{OH})_2$ to produce $\text{BaCO}_3$ and $\text{H}_2\text{O}$ , the latter of which propagates the first reaction.

the high- $T_c$  lattice can be completed as demonstrated herein in a systematic manner so as to generate superconductor materials with tailored materials properties. Further studies related to the oxygen diffusion and relaxation behavior for TX-YBCO as well as YBCO/TX-YBCO double layers and superlattice structures are now in progress in our laboratories.

#### 4. Conclusion

In summary, resistivity vs. temperature, resistivity versus water exposure time, TEM, ESEM and XPS measurements have been completed to evaluate the degradation behavior of YBCO and TX-YBCO thin film structures. All experiments point to the decomposition of YBCO films in a manner consistent with the now well documented behavior for the bulk ceramic compounds. However, it is clear from the studies described herein that the film decomposition rate is significantly slower than that recorded for the bulk compounds. This effect is likely related to a surface area effect as well as a lack of exposure of open channels along the  $b$ -axis for the studied  $c$ -axis oriented films. Interestingly, noble metal contact layers such as gold as well as the passage of current through the film samples are found to increase the decomposition rate of the films in a dramatic fashion. The contact pads in high- $T_c$  devices represent the “Achilles’ heel” for the cuprate thin film structures. Development of reliable and durable superconductor devices will require that attention be paid to the prevention of corrosion at this location. Fortunately, we find that the cation substituted cuprate films can be prepared which exhibit both good superconducting properties as well as excellent corrosion resistance and enhanced processability. The degradation rate for TX-YBCO films is found to be at least 100 times slower than the YBCO films under the same conditions. Studies of XPS depth profiling has revealed that reactions which propagate into the bulk of YBCO film do not occur to any great extent for films of TX-YBCO. The adverse reactivity problems and lack of stable oxygen ion compositions can be traced to be undesirable water diffusion into the high- $T_c$  lattice and oxygen diffusion out of the superconductor. These results indicate that the substitutions of lanthanum and calcium for barium and

yttrium are the key factor leading to generation of the chemically resistant YBCO phase. Reorganization of the bonding in the [Cu(1)-O(4)/O(5)] framework results in a significantly reduced internal strain and changes in the solid-state diffusion characteristics that appear to prevent rapid corrosion. These stabilized high- $T_c$  cuprate systems will allow for more controlled studies that demand a degradation free material and will increase in a substantial manner the longevity and reproducibility of devices fabricated from high- $T_c$  superconductors.

#### Acknowledgments

The research completed at The University of Texas at Austin was supported by the Office Naval Research and the National Science Foundation. Allen J. Bard, John B. Goodenough, A. Manthiram, John M. White, Lew Rabenberg and Hugo Steinfink are thanked for use of their instruments. The Northrop-Grumman work was supported by AFOSR. MOCVD films were grown at EMCORE under ONR/ARPA support.

#### References

- [1] A.P. Malozemoff, IEEE Spec. 30 (December 1993) 26.
- [2] X.D. Wu, S.R. Foltyn, P. Arendt, J. Townsend, C. Adams, I.H. Campbell, P. Tiwari, Y. Coulter and D.E. Peterson, *Appl. Phys. Lett.* 65 (1994) 1961.
- [3] See, for example, R. Gross, P. Chaudhari, M. Kawasaki, M.B. Ketchen and A. Gupta, *Appl. Phys. Lett.* 57 (1990) 727; F.C. Wellstood, J.J. Kingston and J. Clarke, *Appl. Phys. Lett.* 56 (1990) 2336.
- [4] M.F. Yan, R.L. Barnes, H.M. O’Bryan Jr., P.K. Gallagher, R.C. Sherwood and S. Jin, *Appl. Phys. Lett.* 51 (1987) 532.
- [5] H.W. Zandbergen, R. Gronskey and G. Thomas, *Phys. Status Solidi* 105 (1988) 207.
- [6] B. Oh, R.H. Koch, W.J. Gallagher, R.P. Robertazzi and W. Eidelloth, *Appl. Phys. Lett.* 59 (1991) 123.
- [7] D.M. Hill, H.M. Meyer, J.H. Weaver and D.L. Nelson, *Appl. Phys. Lett.* 53 (1988) 1657.
- [8] Q.Y. Ma, M.T. Schmidt, L.S. Weinman, E.S. Yang, S.M. Sampere and S.W. Chan, *J. Vac. Sci. Technol. A* 9 (1991) 390.
- [9] D.S. Mallory, A.M. Kadin and P.H. Ballantine, *Superconductivity Applications for Infrared and Microwave Devices II* (SPIE, Bellingham, WA, 1991), pp. 66–67.

[10] B.R. David, D. Grundler, R. Eckart, K. Fanghänel, J.P. Krumme, V. Doormann and O Dössel, *Supercond. Sci. Technol.* 7 (1994) 287.

[11] J.P. Zhou, D.R. Riley, Y.T. Zhu, A. Manthiram and J.T. McDevitt, *J. Am. Chem. Soc.* 116 (1994) 9389.

[12] J.P. Zhou, S.M. Savoy, R.-K. Lo, J. Zhao, M. Arendt, Y.T. Zhu, A. Manthiram and J.T. McDevitt, *Appl. Phys. Lett.* 66 (1995) 2900.

[13] K. Char, L. Antognazza and T.H. Geballe, *Appl. Phys. Lett.* 63 (1993) 2420.

[14] J.D. Tatum, J.W.H. Tsai, M. Chopra, J.M. Philips and S.Y. Hou, *J. Appl. Phys.* 77 (1995) 6370.

[15] J.R. Gavaler, J. Talvacchio, and R.W. Weinert, *IEEE Trans. Appl. Supercond.* 5 (1995) 1173.

[16] C.S. Chern, S. Liang, Z.Q. Shi, S. Yoon, A. Safari, P. Lu, B.H. Kear, B.H. Goodreau, T.J. Marks, and S.Y. Hou, *Appl. Phys. Lett.* 64 (1994) 3181.

[17] D. Dijkkamp, T. Venkatesam, X.D. Wu, S.A. Shaheen, N. Jisrawi, Y.H. min-Lee, W.L. McLean and M. Croft, *Appl. Phys. Lett.* 51 (1987) 619.

[18] J.P. Zhou, D. Riley, A. Manthiram, M. Arendt, M. Schmerling and J.T. McDevitt, *Appl. Phys. Lett.* 63 (1993) 548.

[19] D.R. Riley, D. Jurbergs, J.P. Zhou, J. Zhao, J.T. Markert and J.T. McDevitt, *Solid State Commun.* 88 (1993) 431.

[20] For the measurements described in this paper, copper pressure clips (0.35 mm × 4.5 mm) were mounted at the four corners of the high- $T_c$  films. Silver paint was thereon applied to insure good electrical contact to the sample. Following the evaporation of solvent from the conductive paint, the copper electrode and silver regions were coated with a layer of Apiezon wax. Such a coating procedure excludes the direct exposure of the copper and silver conductors to the water environment. For the actual resistance measurements, a quasi-dc reverse bias current of  $\pm 5 \times 10^{-5}$  to  $5 \times 10^{-6}$  A was utilized. Influence of contact potentials can be excluded from the measurement with this protocol. A one second delay following the application of the current was used to allow the voltage to stabilize prior to its measurement. Data values were recorded at one minute time intervals with no current being applied to the sample during the dwell times. Current density values at the contact areas are estimated to be  $3.3 \times 10^{-2}$  to  $3.3 \times 10^{-3}$  A/cm<sup>2</sup>.

[21] Instrumental resolution of 1 eV has been determined from the full width at half maximum of Ag3d<sub>5/2</sub>, Au4f<sub>7/2</sub> and Cu2p<sub>3/2</sub>.

[22] P. Salvador, J.L.G. Fierro, J. Amador, C. Cascales and I. Rasines, *J. Solid State Chem.* 81 (1989) 240.

[23] R.P. Vasques, M.C. Foote and B.D. Hunt, *J. Appl. Phys.* 66 (1989) 4866.

[24] H. Behner, K. Rührnschopf, G. Wedler and W. Rauch, *Physica C* 208 (1993) 419.

[25] P.C. Healy, S. Myhra and A.M. Stewart, *Philos. Mag. B* 58 (1988) 257.

[26] A.Z. Moshfegh, Y.Q. Wang, Y.Y. Sun, A. Mesarwi, P.H. Hor and A. Ignatiev, *Physica C* 218 (1993) 396.

[27] J.P. Zhou, D.R. Riley and J.T. McDevitt, *Chem. Mater.* 5 (1993) 361.

[28] J.P. Zhou and J.T. McDevitt, *Solid State Commun.* 86 (1993) 11.

[29] J.J. Capponi, C. Chailout, A.W. Hewat, P. Lijay, M. Marrezio, N. Nguyen, B. Ravear, J.L. Sopubeyroux, J.L. Tholence and R. Tournier, *Europhys. Lett.* 3 (1987) 1301.

[30] J.G. Thompson, B.G. Hyde, R.L. Withers, J.S. Anderson, J.D. Fitz Gerald, J. Bitmead, M.S. Paterson and A.M. Stewart, *Mat. Res. Bull.* 22 (1987) 1715.

[31] R. Zhao and S. Myhra, *Physica C*, 230 (1994) 75.

[32] H. Kitaguchi, J. Takada, A. Osaka, Y. Miura, N. Yamamoto, Y. Oka, M. Kiyama, T. Unesaki and Y. Tomii, *Funtai Oyobi Funmatsu Yakin* 34 (1987) 651.

[33] I.D. Brown, *J. Solid State Chem.* 90 (1991) 1952.

[34] C.R. Slater and C. Greaves, *Supercond. Sci. Technol.* 5 (1992) 205.

## Multilayer HTS SFQ Analog-to-Digital Converters

James D. McCambridge<sup>a</sup>, Martin G. Forrester, Donald L. Miller, Brian D. Hunt, John X. Pryzbysz, John Talvacchio, and Robert M. Young  
Northrop Grumman Science & Technology Center, Pittsburgh, PA 15235-5098

**Abstract**—We have fabricated and measured high  $T_c$  superconductor single flux quantum 1-bit flux-counting analog-to-digital converters (ADCs). The ADCs were made with a multilayer all-epitaxial process which incorporates 10 edge SNS (superconductor-normal-superconductor) or step-edge grain boundary (SEGB) Josephson junctions with a  $\text{YBa}_2\text{Cu}_3\text{O}_{7-8}$  groundplane. The ADC consists of a quantizer connected to a Toggle flip-flop through a buffer-like stage. Direct readout of the flux state of the T flip-flop was made with a Read SQUID inductively coupled through a hole in the groundplane. The circuits were operated at 65 K and low speeds. The SNS circuits outperformed the SEGB circuits because of their higher readout voltages and tighter critical current spreads.

### I. INTRODUCTION

There have been a number of recent demonstrations of high  $T_c$  superconductor (HTS) digital circuits, both single flux quantum (SFQ) architecture [1]–[5] and others [6], [7]. Typically, they have been constrained to the use of a single HTS layer [1]–[5], low operating temperatures [1], [3], [4], or low ultimate operating speed (compared to SFQ logic) [6], [7]. A single-layer circuit process imposes severe topological constraints on circuit layout and low operating temperatures obviate the advantages of HTS materials. In order for an HTS circuit process to reach even the modest integration densities necessary for simple applications, it must include an HTS groundplane with at least two additional HTS layers (with the attendant dielectrics) to keep inductances low and for flexibility in interconnection and fan-out/fan-in. One also needs a robust junction technology which allows  $I_c$  targeting and the capability of orienting the junction in any direction, if HTS circuits are to become anything more than a laboratory curiosity.

We have fabricated and tested simple HTS flux-counting analog-to-digital converters (ADCs) with an integrated HTS groundplane, using both edge superconductor-normal metal-superconductor (SNS) and step-edge grain boundary (SEGB) Josephson junctions. We chose to build a flux-counting ADC because it contains key elements common to general SFQ circuits. More sophisticated multi-bit flux-counting ADCs have been demonstrated using low  $T_c$  superconductors [8]–[12]. Ours is the first demonstration of a multilayer process

that is suitable for manufacturing large, high-speed circuits which operate near the temperature of liquid nitrogen.

### II. DESIGN AND FABRICATION

Our circuit diagram is shown at the top of Fig. 1. It is the first stage (1-bit) of a unidirectional flux-counting SFQ ADC [13], [14], incorporating an asynchronous DC-to-SFQ converter [15] as the quantizer (L1, J1, J2) and a Toggle flip-flop [15] as the bit scaler (J5, J6, J7, J8, L6). Direct readout of the flux state of the T flip-flop is through an inductively-coupled Read SQUID (M1, J9, J10, L7) biased in the voltage

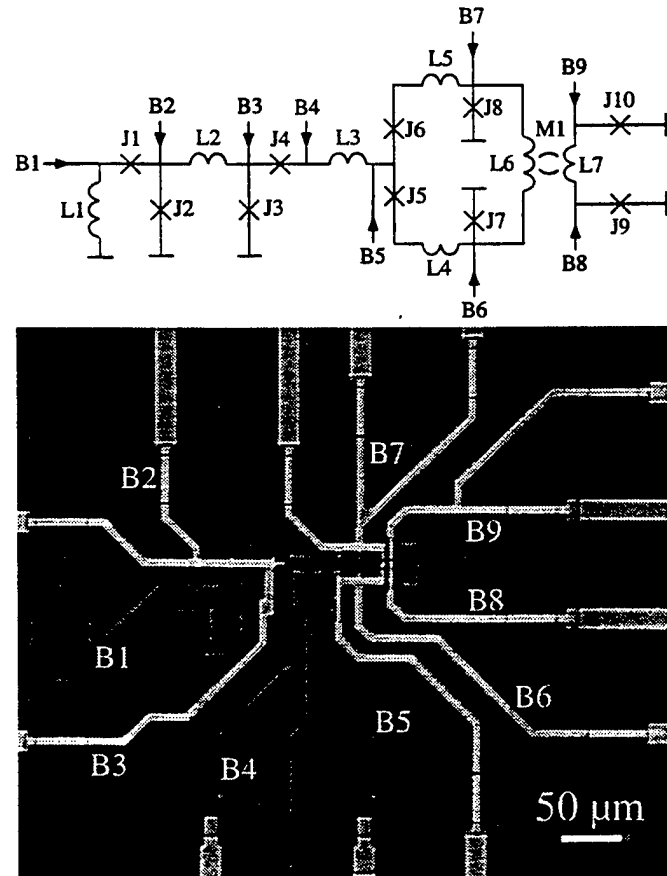


Fig. 1. The one-bit edge SNS ADC. Top: schematic diagram, omitting parasitic inductances and voltage taps:  $J_1 = J_2 = J_5 = J_6 = 2.2 \mu\text{m}$  wide (nominally  $250 \mu\text{A}$ ).  $J_3 = J_4 = J_7 = J_8 = 3 \mu\text{m}$  ( $330 \mu\text{A}$ ).  $J_9 = J_{10} = 1.5 \mu\text{m}$  ( $175 \mu\text{A}$ ).  $L_1 = 14.5 \square$ ,  $L_2 = 4 \square$ ,  $L_3 = 6 \square$ ,  $L_4 = L_5 = 2 \square$ ,  $L_6 = 8 \square + 6.5 \mu\text{H}$ ,  $L_7 = 3.6 \square + 6.5 \mu\text{H}$ , and  $M_1 = 3.5 \mu\text{H}$ .  $B_2 = 175 \mu\text{A}$ ,  $B_4 = 120 \mu\text{A}$ ,  $B_5 = 500 \mu\text{A}$ ,  $B_6 = 270 \mu\text{A}$ , and  $B_7 = -55 \mu\text{A}$ . Bottom: large scale optical micrograph of the circuit in the edge SNS process. The holes in the groundplane are RF chokes. The base electrode is dark, the counter electrode (with *in situ* Au cap layer) is light. The ground contact vias are not visible on the base electrode islands.

Manuscript received August 27, 1996.

Supported in part by AFOSR contract F49620-94-0021.

<sup>a</sup>electronic mail: mccambjd@cis.pgh.wec.com

state. It should be noted that J4 is necessitated by the layout constraints imposed by edge-type junctions: there must be an even number of junctions in any superconducting loop.

We made this 10 junction circuit using two HTS multi-layer processes (with minor modifications of the design) which are described in detail elsewhere [16]-[19]. We recently developed a 6 layer edge SNS junction process with an integrated groundplane which had both higher  $I_c R_n$  and better  $J_c$  reproducibility than the SEGB circuit process [17]. The SNS process began by depositing a 225 nm  $\text{YBa}_2\text{Cu}_3\text{O}_{7-\delta}$  (YBCO) groundplane onto a  $\text{NdGaO}_3$  (NGO) substrate. The groundplane was then patterned by photolithography and ion milling. The chips were rotated during all sputter deposition and ion milling steps. All edge angles were kept shallow ( $\sim 25^\circ$ ) to avoid grain boundary formation. A 240 nm thick layer of  $\text{SrTiO}_3$  (STO) was then deposited and vias were milled. The base electrode (225 nm) and its STO insulator (150 nm) were deposited and patterned together. Finally, the 7% Co-doped YBCO N layer (typically 10-30 nm), the 200 nm counter electrode, and an *in situ* 100 nm Au cap were deposited and patterned. A schematic cross-section of the completed process

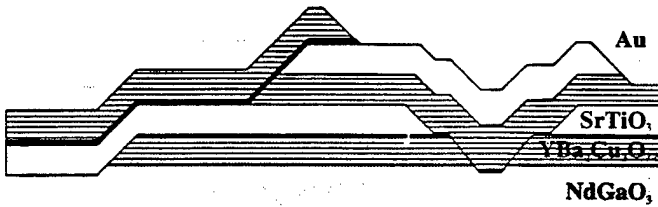


Fig. 2. Schematic of the edge SNS "double via" process. Contact to ground is made through the base electrode. All films were sputter deposited and patterned by ion milling [17]-[19].

is shown in Fig. 2.

SNS junction widths were nominally 1.5, 2.2, or 3.0  $\mu\text{m}$ . The circuit was laid out assuming the critical current density  $J_c \approx 500 \mu\text{A}/\mu\text{m}^2$  ( $I_c = 175, 250$ , or  $330 \mu\text{A}$ ) and the microstrip inductance per square  $L_{\square} \approx 1 \text{ pH}$  at  $T = 65 \text{ K}$ . The Read SQUID was magnetically coupled to the T flip-flop using a hole in the groundplane over which L6 and L7 crossed. This is shown in Fig. 3. The hole was 10  $\mu\text{m}$  long and 19  $\mu\text{m}$  wide and the inductors were 5  $\mu\text{m}$  wide. We approximated this structure as a coplanar waveguide directional coupler to calculate its contribution to the mutual and self-inductances [20]. We calculated the mutual and self inductances for this configuration to be 3.5 pH and 6.5 pH respectively. These estimates are lower bounds on the inductance contribution of the groundplane hole—they neglect the kinetic inductance, but include Chang's empirical end correction [20]. Nominal SNS circuit parameters are given in Fig. 1.

The first ADCs that we successfully fabricated used a 3 layer process which incorporated SEGB Josephson junctions over a groundplane [16]. The general processing parameters and circuit design bore many similarities to the later SNS

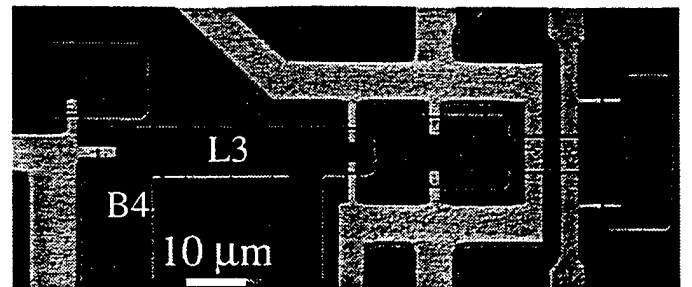


Fig. 3. Optical closeup of the SNS ADC showing the coupled T flip-flop and Read SQUID on the right. Ground contact vias are barely visible as light patches on the base electrode islands. Note the relatively high parasitic inductance (number of squares) necessary to form the junctions.

process discussed above. The SEGB design assumed  $I_c$  of the junctions and  $L_{\square}$  to be the same as the SNS process. The groundplane hole coupling was also identical to the earlier scheme. Fig. 4 is an optical micrograph of the area around the T flip-flop and Read SQUID for the SEGB ADC.

JSPICE simulations using the design values for the SNS and SEGB ADCs gave similar values for optimal biases and bias margins [21], [22]. The most sensitive biases were those to the T flip-flop: B5 had the narrowest margins at  $2I_{c5} \pm 15\%$ ; the biases and margins for the total bias  $I_T = B6 + B7$  and the flux bias  $I_F = B6 - B7$  were  $0.4I_{c7} \pm 30\%$  and  $0.6I_{c7} \pm 40\%$  respectively (see Fig. 1).

### III. TESTING AND RESULTS

We tested the ADC circuits in a magnetically-shielded, temperature-controlled cryostat which operated above the helium bath. The operating temperature was adjusted using a LakeShore DRC-91C controller so that  $J_c$  and  $L_{\square}$  were close to the design values. Biases were supplied by 15-bit digital-to-analog converters (HP 34524/HP 3235). We switched between voltage taps using a relay multiplexer (HP 44470A/HP 3488A). The voltages were measured by a Stanford Research 560 preamplifier and a National Instruments 16-bit ADC board. The lines to the sample were heavily-filtered twisted pairs, with low-pass cutoff frequencies  $(RC)^{-1} \approx 10 \text{ Hz}$ .

The edge SNS ADC outperformed the SEGB ADC: it had fewer errors and higher output voltages. This is a reflection of the better  $J_c$  reproducibility and higher  $I_c R_n$  of the SNS proc-

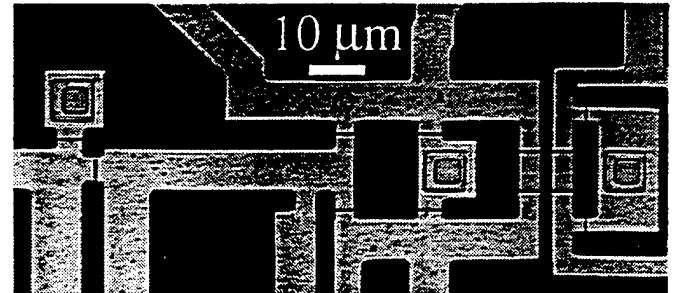


Fig. 4. Optical closeup of a SEGB ADC. Ground contact vias are clearly visible as nested squares. Design parameters were essentially the same as the SNS ADC.

ess. SQUID voltages scale with  $I_c R_n$  [23]. We have seen voltage modulations as large as 130  $\mu$ V in an SNS SQUID ( $I_c R_n \sim 500 \mu$ V) at 65 K [17], which is almost a factor of 10 better than its SEGB counterpart ( $I_c R_n \sim 50 \mu$ V) [16]. Circuit margins are degraded from their ideal values by wide process spreads. The SNS process has produced chips with  $1-\sigma J_c$  spreads as small as 12% [17], which is much better than we have ever achieved with SEGB junctions. We will therefore concentrate on the characterization of the SNS ADC.

#### A. Edge SNS ADC

We checked the YBCO film quality by measuring individual SQUIDs on the same chip as the ADC. Microstrip inductances  $L_{\square} \approx 1 \text{ pH}$  were measured at 65 K, in agreement with earlier results and design values [16], [17]. We also measured critical currents at a number of points in the circuit. The inferred local  $J_c = 675-1000 \mu\text{A}/\mu\text{m}^2$  at 65 K was considerably higher than the  $500 \mu\text{A}/\mu\text{m}^2$  design value. We could not simply operate the ADC at a higher temperature because of the consequent increase of  $L_{\square}$ . The fabricated circuit suffered from parasitic inductances associated with the narrowness of the junctions and the layout of the ground contacts, which amounted to 1-2  $\square$  per junction (see Fig. 3). Additionally, we find that our estimate for the self inductance contribution of a groundplane hole (which neglected the kinetic inductance) was too low.

In Fig. 5 we plot the modulation of the Read SQUID  $I_c$  vs. the control current  $I_{con} = (B8 - B9)/2$ . The depth of modulation of  $I_c$  yields the total inductance of the SQUID, assuming no asymmetry between junctions [17]. However, the effective total inductance inferred from the modulation depth (45 pH) is much larger than the sum of the geometric and groundplane hole inductance ( $\sim 20 \text{ pH}$ ). This implies a significant asymmetry between J9 and J10 [23]. Additionally, the critical currents of the 1.5  $\mu\text{m}$  (nominally 175  $\mu\text{A}$ ) junctions (J9 and J10) were often low—we suspect the culprit was ion milling edge damage. The periodicity of  $I_c$  gives us the microstrip inductance between current contacts [16], [17]. (See Fig. 3 for the Read SQUID geometry.) At 65 K,  $L_7 = 13.1 \text{ pH}$ , of which  $\sim 4 \text{ pH}$  are due to microstrip. The inductance due to the groundplane hole is therefore  $\sim 9 \text{ pH}$ , almost 40% higher than our design estimate of 6.5 pH. However, the measured mutual inductance between L6 and L7 was 3.3 pH, quite close to our estimate of 3.5 pH. As a consequence of the high  $J_c$  and additional sources of inductance, the  $LI_c$  products were as much as a factor of 2 higher than the design values in Fig. 1.

Testing of the ADC was relatively straightforward. Ramping up the current B1 causes J2 to pulse every  $\approx \Phi_0/L_1$ , with the position of the first threshold set by the bias B2. If the rest of the circuit is properly biased, these pulses propagate to the bistable T flip-flop and trigger it to switch states. The flux state of the T flip-flop (i.e., the current in L6) can be directly sensed by the Read SQUID, which is biased into

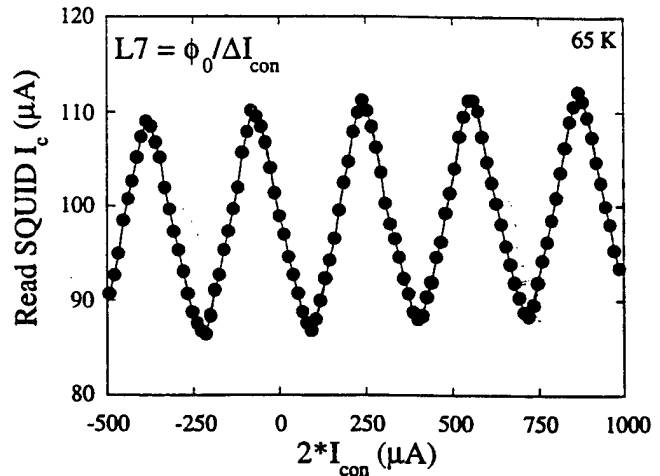


Fig. 5.  $I_c$  vs.  $2I_{con} = B8 - B9$  for the Read SQUID. The period of  $\sim 315 \mu\text{A}$  gives a value for  $L_7 = 13.1 \text{ pH}$ ,  $\sim 9 \text{ pH}$  of which is due to the hole in the groundplane. The depth of modulation implies a total SQUID inductance of  $\sim 45 \text{ pH}$ , which is much greater than the geometric inductance. Asymmetry between junctions J9 and J10 is the source of this discrepancy.

the voltage state. As the flux in L6 toggles between 0 and  $\Phi_0$ , the Read SQUID voltage should change between two corresponding levels.

Our usual procedure was to set the DC biases to their nominal levels (scaled by the “local”  $J_c$ ) and then fix an appropriate bias point for the Read SQUID. We then ramped B1 at  $\sim 15 \mu\text{A}/\text{s}$  to 0.5-2 mA while watching the voltage across the Read. Biases B5-7 were then adjusted to achieve proper operation. Alternatively, we determined bias points for the T flip-flop by measuring its lobe boundaries. The lobe boundary measurements were difficult to interpret because the inductances were often large enough to store multiple flux quanta.

In Fig. 6 we plot two successive traces of the Read SQUID voltage V against B1, the input current to the quantizer, at 65 K. We averaged the voltage for  $\sim 100 \text{ ms}$  at each

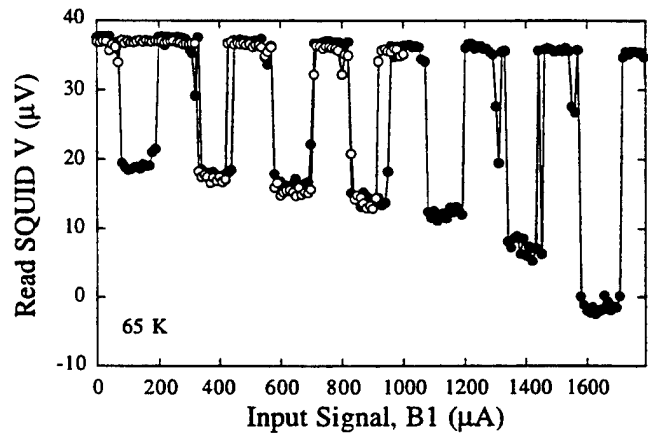


Fig. 6. The SNS ADC in operation at 65 K. The Read SQUID voltage switches between two levels, corresponding to the flux state of the toggle flip-flop. The open and closed symbols are two successive ramps of B1 taken two minutes apart which show some instability in the switching thresholds. However, the 125  $\mu\text{A}$  average period agrees well with the design value,  $\Phi_0/L_1 \approx 130 \mu\text{A}$ .

bias point. Occasionally, a switch occurred during averaging. This shows up in Fig. 6 as an intermediate voltage between the two "stable" values. The Read voltage has a  $\approx 125 \mu\text{A}$  period. The microstrip inductance inferred from this period  $L_{\square} = (\Phi_0/\Delta I)/14.5 \square = 1.1 \text{ pH}$  agrees well with our recent independent measurements [16]-[19]. The drift in the Read voltage is an artifact of the measurements. This particular sample had ground contact problems: due to a resistive ground contact, large input signals modified the Read SQUID bias, changing its output.

Both traces show evidence for threshold instability. Our ADC is not immune to thermal and electronic noise: first, variations in  $J_c$  decrease the operating margins of the circuit; the closer circuit operation is to the margins, the higher the error rate. Second, it is not clear that the design values of  $I_c$  ( $J7 = J8 = 330 \mu\text{A}$ ) themselves are large enough at 65 K to ensure a low thermal-activation error rate [4]. Our measurements of  $J_c$  on this circuit showed a wider spread (675-1000  $\mu\text{A}/\mu\text{m}^2$ ) than the best we have obtained for the edge SNS process [17]. Both vulnerabilities are reflected in our measurements of the margins of  $B5$ ,  $I_F$ , and  $I_T$ , which were all smaller than 5%. Admittedly, the margins are ill-defined, since even in the best case, errors were present.

#### IV. CONCLUSIONS

We have designed, fabricated, and demonstrated HTS SFQ 1-bit counting ADCs which operated at low speeds at 65 K. We used a 6 epilayer process which included an integrated groundplane and edge SNS junctions as well as a 3 epilayer SEGB process. This is the first demonstration of a circuit process extendible to making SFQ circuits of technological interest (10s-100s of Josephson junctions) which operate at high temperatures.

#### ACKNOWLEDGMENT

We thank J. C. Brown, G. J. Faychak, G. A. Madia, D. M. Matuza, S. J. Pieleski, and J. H. Uphoff for technical assistance. We also thank A. H. Miklich and M. L. Farich for useful discussions.

#### REFERENCES

- [1] Z. G. Ivanov *et al.*, "An experimental implementation of high- $T_c$ -based RSFQ set-reset trigger at 4.2 K," *Supercond. Sci. Tech.*, vol. 7, pp. 239-41, 1994.
- [2] M. G. Forrester *et al.*, "A single flux quantum shift register operating at 65 K," *IEEE Trans. Appl. Supercond.*, vol. 5, pp. 3401-4, 1995.
- [3] V. K. Kaplunenko *et al.*, "Voltage divider based on submicron slits in a high  $T_c$  superconducting film and two bicrystal grain boundaries," *Appl. Phys. Lett.*, vol. 67, pp. 282-4, 1995.
- [4] S. Shokhor *et al.*, "All-high- $T_c$  superconductor rapid-single-flux-quantum circuit operating at  $\sim 30$  K," *Appl. Phys. Lett.*, vol. 67, pp. 2869-71, 1995.
- [5] B. Oelze *et al.*, "Rapid single-flux-quantum balanced comparator based on high- $T_c$  bicrystal Josephson junctions," *Appl. Phys. Lett.*, vol. 68, pp. 2732-4, 1996.
- [6] S. M. Schwartzbeck *et al.*, "SAIL high temperature superconductor digital logic: improvements and analysis," *IEEE Trans. Appl. Supercond.*, vol. 3, pp. 2710-3, 1993.
- [7] S. J. Berkowitz *et al.*, "High-temperature superconducting Josephson fluxon-antifluxon transistors," *Conductus, Inc.*, unpublished, 1996.
- [8] L. V. Filippenko *et al.*, "Experimental implementation of analog-to-digital converter based on the reversible ripple counter," *IEEE Trans. Appl. Magn.*, vol. 27, pp. 2464-7, 1991.
- [9] S. Rylov, "Measurements of dynamic range and linearity of flux-quantizing A/D converters," *IEEE Trans. Appl. Supercond.*, vol. 3, pp. 2558-61, 1993.
- [10] V. K. Kaplunenko *et al.*, "Experimental implementation of SFQ NDRO cells and 8-bit ADC," *IEEE Trans. Appl. Supercond.*, vol. 3, pp. 2662-5, 1993.
- [11] D. L. Miller *et al.*, "Josephson counting analog-to-digital converter," *IEEE Trans. Appl. Magn.*, vol. 27, pp. 2761-4, 1991.
- [12] F. Kuo, "Superconducting A/D converters based on Josephson binary counters," *IEEE Trans. Appl. Magn.*, vol. 27, pp. 2883-6, 1991.
- [13] J. P. Hurrell, D. C. Pridmore-Brown, and A. H. Silver, "Analog-to-digital conversion with unlatched SQUID's," *IEEE Trans. Elect. Dev.*, vol. ED-27, pp. 1887-96, 1980.
- [14] G. S. Lee and D. A. Petersen, "Superconductive A/D Converters," *IEEE Proc.*, vol. 77, pp. 1264-73, 1989.
- [15] K. K. Likharev and V. K. Semenov, "RSFQ logic/memory family: a new Josephson-junction technology for sub-terahertz-clock-frequency digital systems," *IEEE Trans. Appl. Supercond.*, vol. 1, pp. 3-28, 1991.
- [16] M. G. Forrester *et al.*, "Inductance measurements in multilevel high  $T_c$  step-edge grain boundary SQUIDS," *Appl. Phys. Lett.*, vol. 65, pp. 1835-7, 1994.
- [17] B. D. Hunt *et al.*, "High- $T_c$  superconductor/normal-metal/superconductor edge junctions and SQUIDS with integrated groundplanes," *Appl. Phys. Lett.*, vol. 68, pp. 3805-7, 1996.
- [18] B. D. Hunt *et al.*, "High- $T_c$  Edge SNS Josephson junction with integrated groundplanes," *IEEE Trans. Appl. Supercond.*, submitted this conference.
- [19] M. G. Forrester *et al.*, "Multilayer edge SNS SQUIDS for digital circuits," *IEEE Trans. Appl. Supercond.*, submitted this conference.
- [20] W. H. Chang, "Measurement and calculation of Josephson junction device inductances," *J. Appl. Phys.*, vol. 52, pp. 1417-25, 1981.
- [21] S. R. Whiteley, "Josephson junctions in spice3," *IEEE Trans. Magn.*, vol. 27, pp. 2902-5, 1991.
- [22] Q. P. Herr and M. J. Feldman, "Multiparameter optimization of RSFQ circuits using the method of inscribed hyperspheres," *IEEE Trans. Appl. Supercond.*, vol. 5, pp. 3337-40, 1995.
- [23] T. Van Duzer and C. W. Turner, *Principles of Superconductive Devices*, New York, NY: Elsevier, 1981, pp. 165-227.

## Materials Basis for a Six-Level Epitaxial HTS Digital Circuit Process

J. Talvacchio, M. G. Forrester, B. D. Hunt, J. D. McCambridge, and R. M. Young  
Northrop Grumman Science and Technology Center, Pittsburgh, PA 15235-5098

X. F. Zhang and D. J. Miller  
Argonne National Laboratory, Argonne, IL 60439

**Abstract** — We have developed a process for fabrication of HTS single-flux-quantum logic circuits based on edge SNS junctions which requires six epitaxial film layers and six mask levels. The process was successfully applied to fabrication of small-scale circuits ( $\leq 10$  junctions). This paper examines the materials properties affecting the reproducibility of YBCO-based SNS junctions, the low inductance provided by an integrated YBCO ground plane, and electrical isolation by  $\text{SrTiO}_3$  or  $\text{Sr}_2\text{AlTaO}_6$  ground-plane and junction insulator layers. Some of the critical processing parameters identified by electrical measurements, TEM, SEM, and AFM were control of second-phase precipitates in YBCO, oxygen diffusion, Ar ion-milling parameters, and preparation of surfaces for subsequent high-temperature depositions.

### I. INTRODUCTION

Practical application of Single Flux Quantum (SFQ) logic circuits fabricated in High- $T_c$  Superconductors (HTS) is limited at present by a low level of integration of Josephson junctions with sufficiently uniform characteristics. SFQ gates must have a low inductance,  $L$ , consistent with a quantum of flux,  $LI_c \sim \Phi_0 = 2 \text{ mA-pH}$ , and a Josephson critical current,  $I_c$ , on the order of 0.5 mA for thermal noise stability. Two approaches for achieving such low inductances are to use an integrated thin-film HTS groundplane or to use submicron lithography. We chose to follow the former approach in the process described here.

The requirements for junction reproducibility are shown in Fig. 1 following the discussion in [1]. Reproducibility is expressed as the standard deviation of Josephson critical currents,  $I_c$ . The calculation of junction count for a particular level of junction reproducibility assumes a Gaussian distribution of critical currents, and circuit component margins of 30%, which have been shown to be realistic in both simulations and LTS circuit measurements for SFQ circuits. Since there is always some chance with a Gaussian distribution that a junction's  $I_c$  will fall outside of circuit margins, circuit yield is expected to be  $< 100\%$  even for small-scale circuits with low junction counts.

Manuscript received August 27, 1996.

This work was supported in part by AFOSR Contract F49620-94-C-0021, USAF WL/ML Contract No. F33615-93-C-5355, and ONR Contract N00014-96-C-0007. Work at Argonne was supported by the U.S. DOE Office of Basic Energy Sciences (#W-31-109-ENG-38) and the National Science Foundation Office of Science and Technology Centers (DMR 91-20000).

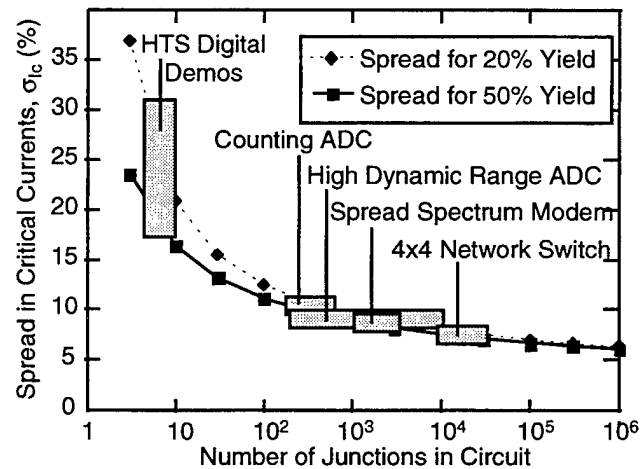


Fig. 1. The spread in junction critical currents,  $\sigma_{I_c}$ , required to produce circuits with a given junction count. Small-scale circuit demonstrations made to date are consistent with relatively large spreads in  $I_c$  of 20-30%. To fabricate SFQ circuits of practical interest with hundreds to thousands of junctions and reasonable yields,  $I_c$  spreads must be reduced to  $\leq 10\%$ .

Fig. 1 shows that one should expect no more than the small-scale SFQ circuit demonstrations made to date as long as  $\sigma_{I_c} = 20-30\%$ . To fabricate circuits of practical interest with hundreds to thousands of junctions and reasonable yields,  $I_c$  spreads must be reduced to  $\leq 10\%$  while still satisfying the requirement for  $LI_c \sim \Phi_0$ .

Details are published elsewhere of junction electrical properties and some process issues [2-3], inductance measurements [4], and one of the circuits fabricated with this process [5]. The emphasis of this paper is in showing how the materials properties needed for groundplane integration and improved junction reproducibility are affected by the details of our integrated circuit fabrication process. Although the number of essential film layers is exactly the same, it is important to distinguish the multilayer film process for HTS digital circuits described here from that needed for integrating magnetometer pick-up coils with SQUIDS as in [6]. In the case of magnetometers, there is a minimal overlap of YBCO film layers which occurs only at crossovers. Junctions are fabricated directly on the substrate.

### II. INTEGRATED CIRCUIT FABRICATION PROCESS

Major process steps we followed to integrate edge SNS junctions on an HTS groundplane are shown in Fig. 2. A minimum of six mask levels and six epitaxial oxide film

layers are needed for this process. Two additional epitaxial film layers were sometimes used, a 300 Å  $\text{SrTiO}_3$  (STO) buffer layer between the substrate and groundplane, and a 300 Å STO cap layer deposited on top of the groundplane to protect the YBCO surface during processing. Since neither the presence or absence of these layers affected the sequence of process steps, we omitted them from the schematic cross sections of multilayers. Next we will describe in detail each of the six steps shown in Fig. 2.

### A. Groundplane Deposition and Patterning

YBCO groundplane films 2250 Å thick were deposited by 90° off-axis rf magnetron sputtering with a process described in [7]. In all cases,  $\text{NdGaO}_3$ (110) substrates were used. In some cases, 2-inch diameter wafers were used which were diced into  $1\text{ cm} \times 1\text{ cm}$  chips at some point before circuit fabrication was completed so deposition parameters for the junction films could be varied while keeping groundplane fabrication parameters constant.

Fig. 3 shows the mask layout for (3a) a wafer, (3b) a chip, and (3c) a standard junction test subchip. The dark band on the subchip is the base electrode with two wire bond pads. The rest of the bonding pads are connected in pairs to the top electrodes of 20 devices. The edge SNS devices face in all four in-plane directions since this is a constraint imposed by the need for low-inductance connections in SFQ circuits. Junctions are spread out across each subchip to give a more complete measurement of junction uniformity.

Film patterning was done with photoresist masks reflowed for 5 min at 130°C. Wafers were tilted 50° from normal and rotated during 150 eV Ar ion milling to produce edges that angled 20-30° from the substrate plane. The same process was used to pattern single or multiple layers. SIMS endpoint detection prevented over-milling.

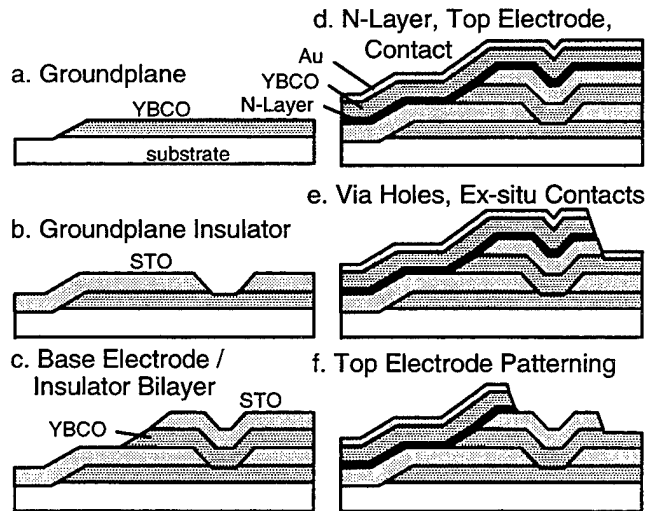


Fig. 2. The major process steps for fabrication of SFQ circuits with SNS junctions integrated on groundplanes for low inductance. The effect of each step on materials properties critical for groundplane integration and junction reproducibility are described in the text.

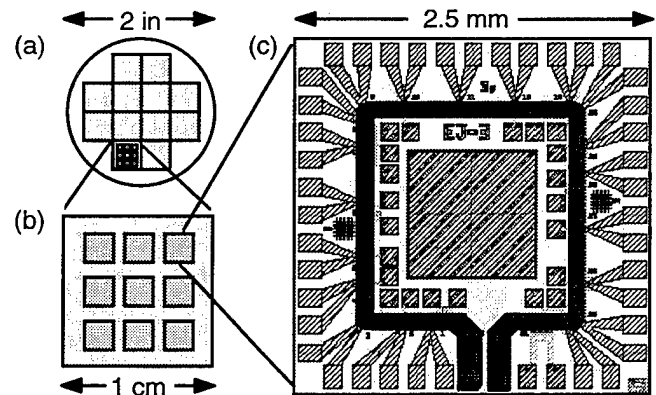


Fig. 3. YBCO groundplanes were deposited and patterned on 2-inch wafers (a) which were diced into  $1\text{ cm} \times 1\text{ cm}$  chips (b) for deposition of subsequent layers. Each chip had nine subchips where (c) was one of our standard patterns for measurement of twenty 3-μm-wide devices.

### B. Groundplane Insulator Deposition and Patterning

Before we brought any patterned wafer up to ~700°C for deposition of a subsequent epitaxial layer, we cleaned the surface with an *ex-situ* oxygen plasma and a 150 eV Ar/O<sub>2</sub> ion mill to remove ~100 Å from the surface. XPS studies were used to ensure that hydrocarbon and fluorine residues were completely removed by the time the sample was brought to the desired deposition temperature [8].

Both  $\text{SrTiO}_3$  and  $\text{Sr}_2\text{AlTaO}_6$  (SAT) grown by off-axis sputtering were developed for epitaxial insulator films. Groundplane insulators were nominally 2400 Å thick but films used for insulator development varied in thickness between 1000 Å and 3000 Å without apparent thickness dependence. The important properties for the groundplane insulator were good electrical isolation and vias to ground capable of carrying currents greater than the junction critical currents (Fig. 2b).

A series of experiments were performed to determine which process parameters had the greatest effect on whether a minimum electrical isolation of  $2 \times 10^4 \Omega\text{-cm}$  was achieved in YBCO/insulator/YBCO trilayer capacitors. We found that the insulator growth temperature in the range of 660-750°C, whether the layers were deposited without breaking vacuum, interfaces exposed to air, or interfaces exposed to ion-mill processing, were not significant factors. We also found that room temperature measurements were good predictors of isolation at 77K.

However, roughness of the first YBCO layer was found to be the key factor in determining electrical isolation. Fig. 4 shows the defect density in insulators inferred from the fraction of 35 capacitors per chip ranging in area from  $1\text{ mm} \times 1\text{ mm}$  to  $250\text{ }\mu\text{m} \times 250\text{ }\mu\text{m}$ . In [9], the defect density, D, is calculated from the “yield,” the fraction of capacitors exceeding the minimum resistivity criterion, based on,

$$\text{yield} = (\# \text{ working}) / (\# \text{ tested}) = \exp(-D / \text{Area}) \quad (1)$$

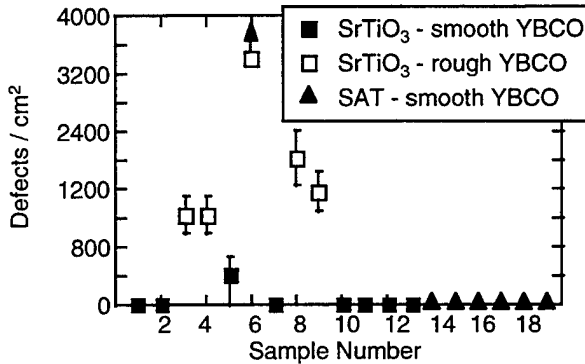


Fig. 4. Defect density for a series of 19 samples with 35 YBCO / SAT or STO / YBCO trilayer capacitors on each. Samples labeled as "smooth" had  $\leq 10^3$  copper oxide precipitates per  $\text{cm}^2$  in the lower YBCO film and, for all but one sample, no measured electrical defects.

Since we used two capacitors in series to measure yield,  $D$  was determined from,

$$\text{yield} = 1 - (1 - \exp(-D / \text{Area}))^2 \quad (2)$$

The data in Fig. 4 are for a numbered series of samples with STO deposited on either rough or smooth YBCO base layers and SAT deposited on smooth YBCO. Error bars were based on potential changes in the yield by  $\pm 1$  capacitor. For smooth films, only one leaky capacitor was found in 14 samples with a total of 490 capacitors. Nearly all of the capacitors exceeded the resistivity criterion by 4 or 5 orders of magnitude.

The definition of "rough" and "smooth" films in this case was based on the density of copper oxide precipitates which can be clearly seen, identified, and counted in an SEM. Smooth films had a density of  $\leq 10^3/\text{cm}^2$  such "boulders," whereas rough films typically had  $10^5\text{-}10^6/\text{cm}^2$ .

A cross-sectional TEM image of a YBCO edge SNS junction without a ground plane is shown in Fig. 5 to show the contrast between relatively smooth film layers, with rms roughness as low as 10-15 Å, and copper oxide boulders which disrupt insulator growth if they nucleate in one of the lower YBCO film layers.

Results of measurements of SAT and STO dielectric constants are shown in Figs. 6(a) and (b), respectively. Both data sets were independent of frequency in the measurement

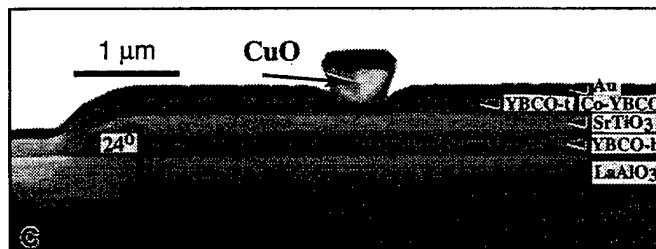


Fig. 5. Cross-sectional TEM image of an edge SNS junction without a ground plane showing the contrast between relatively smooth film layers and the potential for copper oxide "boulders" to disrupt multilayer structures. In this case, the boulder nucleated in the YBCO counterelectrode so it only disrupted the Au contact layer.

range up to 10 kHz. For SAT,  $\epsilon(77\text{K}) \approx 26$  is in good agreement with SAT films grown by pulsed laser deposition [10], but is significantly higher than for bulk samples where  $\epsilon(90\text{K}) = 11.8$  [11]. For STO,  $\epsilon(300\text{K})$  is in reasonable agreement with bulk samples but our STO films showed much less dependence on temperature than expected from bulk. Although we have made no direct measurements of dielectric loss, the anomalous behavior of STO films compared with bulk appears to be favorable since average voltage measurements of toggle flip-flops fabricated with STO groundplane and junction insulators indicated that they operated up to 15 GHz [12].

### C. Base Electrode / Junction Insulator Formation

A YBCO base electrode 2250 Å thick and a junction insulator 1500 Å thick were sputter-deposited and patterned to form the structure shown in Fig. 2(c). The edge patterned at this step deserves special consideration since it formed one interface of SNS junctions. In addition to the *ex-situ* ion-mill cleaning described earlier, this edge was subjected to an *in-situ* 100 eV Ar ion mill to remove a few monolayers just before deposition of the normal-conducting, "N-layer."

### D. N-Layer and Counterelectrode Processing

Results in [13] and [14] showed that the N-layer in SNS junctions which had the closest structural match to YBCO

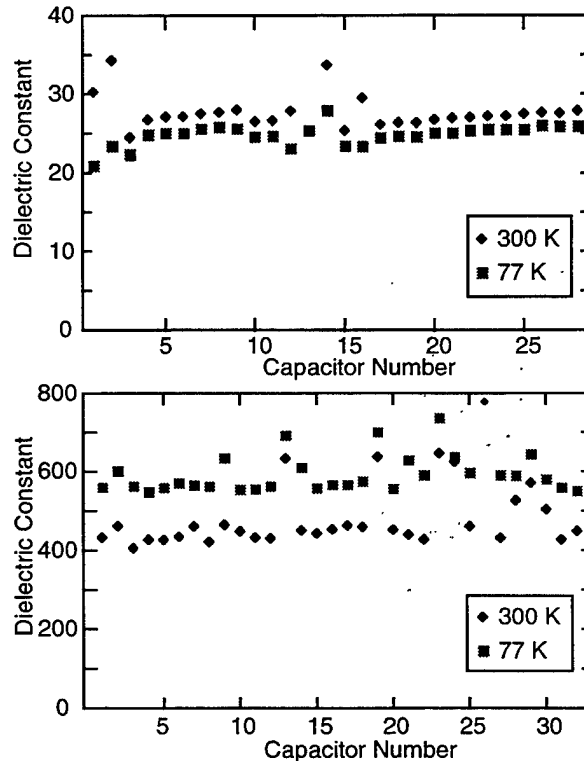


Fig. 6. Dielectric constants for (a) SAT and (b) STO epitaxial thin films deposited on YBCO. In comparison with bulk dielectrics, the most significant difference is the weak temperature dependence of STO.

led to junction characteristics which could best be explained by the standard model of proximity effects at S-N interfaces. Fig. 7 summarizes the dependence of junction critical current density,  $J_c$ , on N-layer thickness for three different N-layers based on doping YBCO with sufficient cobalt, calcium, and praseodymium, respectively, to reduce  $T_c$  to  $\sim 50$ K. For these N-layer evaluation experiments, we did not use a ground plane or rotate the samples during ion milling so all junction edges face the same direction.

Each data point in Fig. 7 represents the average  $J_c$  for all junctions on a chip and the error bars indicate the  $J_c$  spread. The normal-state coherence lengths,  $\xi_n(77K)$ , calculated

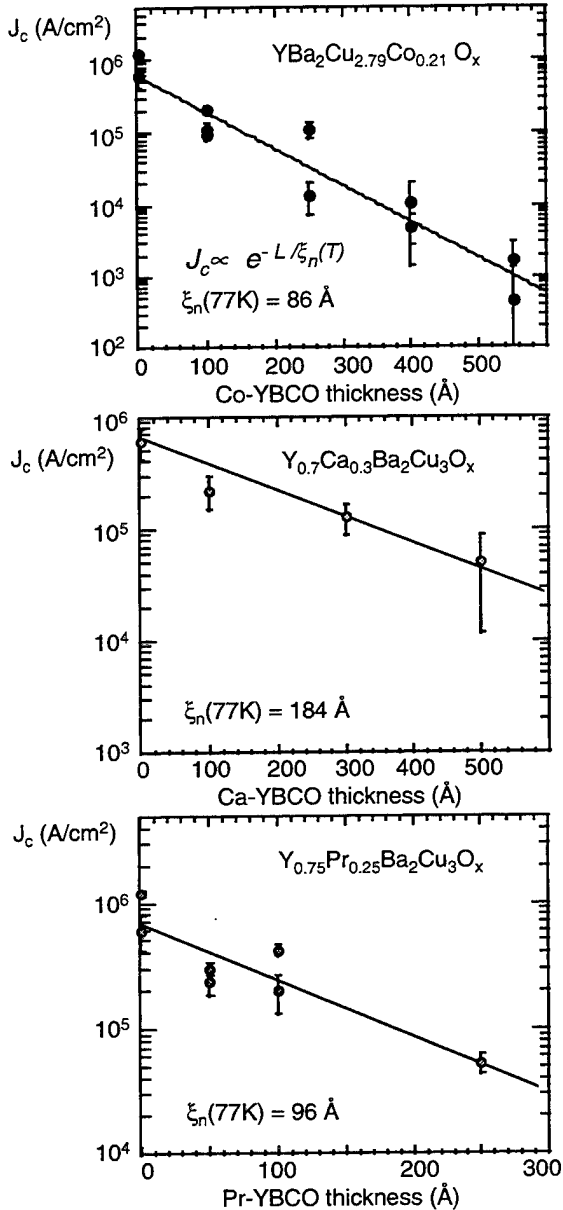


Fig. 7. Junction critical current density,  $J_c$ , plotted as a function of N-layer thickness for Co, Ca, and Pr-doped YBCO N-layers. Each data point represents the average  $J_c$  for all junctions on a chip and the error bars indicate the  $J_c$  spread. The exponential dependence of  $J_c$  on N-layer thickness shows the extent of our control over S-N interfaces and N-layer thickness.

from the slope of the lines drawn in Fig. 7 are larger than expected from resistivities,  $\rho(77K)$ , that varied from low values of 60-100  $\mu\Omega\text{-cm}$  for Ca-YBCO to high values of 300-600  $\mu\Omega\text{-cm}$  for Co-YBCO. However, the fact that  $J_c$  was an exponential function of N-layer thickness indicated that both edge formation and N-layer film growth on tapered edges were controlled processes.

High  $I_c R_n$  products for Co-YBCO junctions, 160-180  $\mu\text{V}$  at 77K and  $\sim 500$   $\mu\text{V}$  at 65K, led us to focus on Co-YBCO. The Pr-YBCO junctions had  $I_c R_n$  products that were just marginally lower but  $I_c R_n$  for the Ca-YBCO junctions was a factor of 4 lower.

As shown schematically in Fig. 2(d), the selected N-layers, typically 75-200  $\text{\AA}$  thick, YBCO top electrodes 2000  $\text{\AA}$  thick, and 1000  $\text{\AA}$  Au contact layers were deposited sequentially without breaking vacuum. Although this process was originally developed using rf sputtering, indications of inhomogeneity in sputtered Co-YBCO encouraged us to fabricate junctions with N-layers, and necessarily, top YBCO electrodes, grown by pulsed laser deposition (PLD). Fig. 8 shows the differences in typical  $\rho(T)$  curves for sputtered and PLD Co(7%)-YBCO where the higher  $T_c$ , broader transition, and higher  $\rho(T)$  for the sputtered film were interpreted as signs of inhomogeneity. So far, the properties of our PLD junctions were not grossly different from sputtered junctions but the single chip with the tightest spread in  $I_c$  was fabricated with PLD.

#### E. Via Holes and Base Electrode Contacts

Fig. 2(e) shows the circuit structure after a via hole was ion milled to the YBCO base electrode and an *ex-situ* Au contact to the base electrode was patterned by lift-off. Via holes, crossovers, and step coverage were the subjects of a separate study of such passive structures for HTS digital circuits [8]. SEM micrographs of a test via and crossover are shown in Figs. 9(a) and (b), respectively. The most important characterization of these structures were

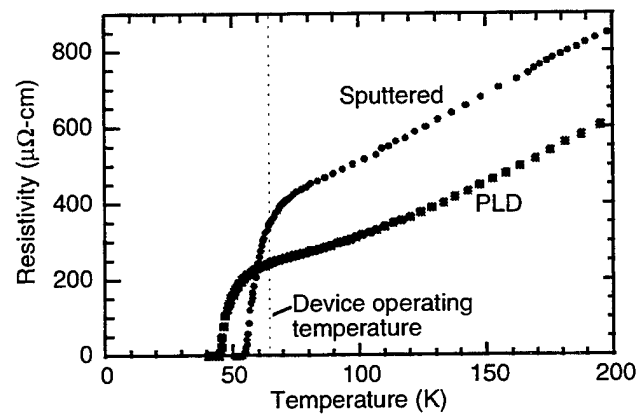


Fig. 8. Resistivity vs. temperature for typical Co-(7%)-YBCO films deposited by sputtering and PLD. Although sputtered films have resulted in junctions with desirable properties, their higher  $T_c$ , broader transition, and higher  $\rho(T)$  were interpreted as signs of inhomogeneity.

measurements of electrical isolation (Fig. 4) and measurements of critical currents through vias and for films over steps. We designed vias in our circuits to have a large perimeter for contact compared to junction widths so they were never found to limit  $J_c$ . Fig. 10 shows that  $J_c(T)$  for YBCO films covering 20 steps in either an STO underlayer or STO isolating YBCO cross-unders, was degraded by approximately one order of magnitude but could be kept larger than typical  $J_c$ s for either SEGB or SNS junctions.

#### F. Top Electrode Patterning

The last mask level was used to pattern the trilayer consisting of the N-layer, top YBCO electrode, and *in-situ* Au contact layer. Typical variations in the morphology of sputtered trilayers are shown in Fig. 11. Junctions for all three pictures had smooth base electrode films. In Fig. 11(a), both the Co-YBCO layer and YBCO top electrode were deposited at a low total sputter pressure of 125 mtorr. Under these conditions, it is relatively easy to avoid formation of copper oxide boulders and a-axis oriented YBCO outgrowths, and to obtain smooth surfaces on planar film regions. However, step coverage was poor as can be seen both in the junction area and in the rough pattern transferred by ion milling along the entire base electrode edge.

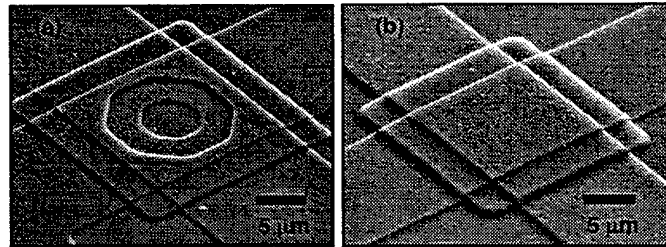


Fig. 9. Scanning electron micrographs of (a) a via hole and (b) a crossover test structure. These passive structures were characterized by measurements of electrical isolation as in Fig. 4, and  $J_c$  measurements as in Fig. 10.

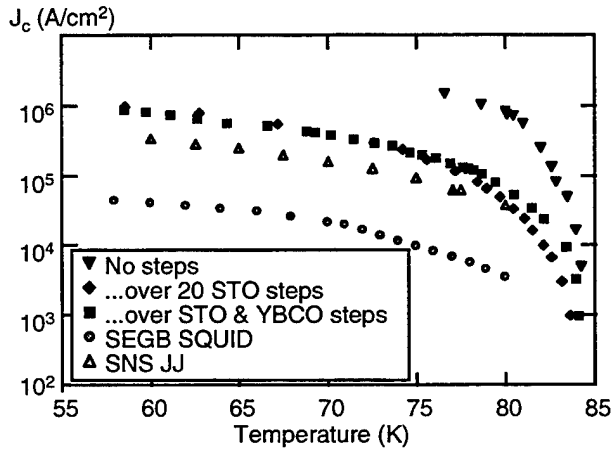


Fig. 10. Critical current density,  $J_c(T)$ , comparisons for YBCO films showing that coverage over multiple 20-30° steps degrades  $J_c$  by approximately an order of magnitude but not enough to cause a problem for SEGB or SNS-based circuits.

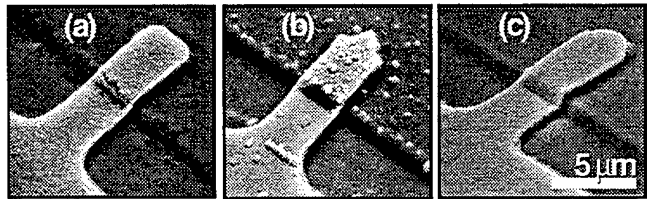


Fig. 11. Junctions 3  $\mu\text{m}$  wide fabricated on smooth YBCO base electrodes. N-layers and YBCO top electrodes grown at low pressure (a) tended to exhibit poor step coverage whereas films grown at high pressure (b and c) were susceptible to boulder formation as in (b).

Figs. 11(b) and (c) show Co-YBCO and YBCO films deposited with the same Ar:O<sub>2</sub> ratio of 2:1 as in Fig. 11(a), but with a total pressure of 185 mtorr. In these cases, good step coverage was achieved but both the N-layer and top electrodes were susceptible to boulder formation. We believe that the difficulty in obtaining the film morphology shown in Fig. 11(c) was the greatest contributing factor to spread in junction critical currents.

A cross-sectional TEM micrograph of a junction without a ground plane is shown in Fig. 12. This sample had a 100 Å thick sputtered Co-YBCO N-layer (not distinguishable in the image) and a smooth edge as in Fig. 11(c). Simulations of phase contrast showed that the cobalt-doped layer could only be seen for a few select specimen thicknesses and defocus conditions. Nevertheless, it was observed that the bottom film was nearly free of defects up to the interface while the top electrode had stacking faults in the junction region.

#### III. POSSIBLE ORIGINS OF JUNCTION VARIABILITY

Having established a baseline process for SNS junction and HTS digital circuit fabrication, we examined whether variations in the critical currents of junctions produced in this way were due to fluctuations in the parameters we controlled or due to intrinsic materials properties. In this section, we will present the results of experiments designed

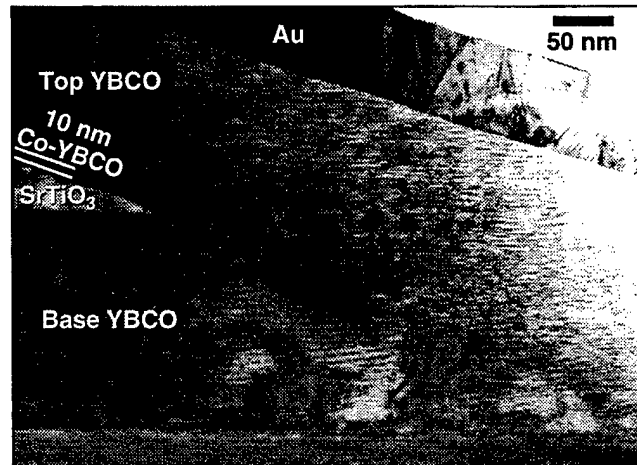


Fig. 12. Cross-sectional TEM micrograph of a junction with Co-YBCO N-layer and a smooth edge as in Fig. 11(c). Since the Co-doped layer could not be distinguished, the only visible defects are stacking faults in the top YBCO film in the vicinity of the junction.

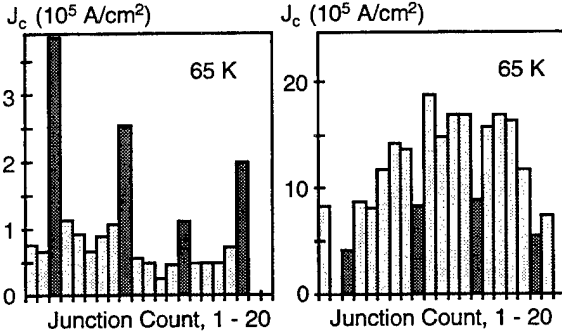


Fig. 13. Junction critical current density vs. junction number for two chips with Co-YBCO N-layers. YBCO <110> junctions (highlighted) tended to have different  $J_c$ s than <100> but not consistently larger or more uniform.

to test whether some intrinsic materials properties of YBCO were limiting junction reproducibility.

We always aligned photomasks so junction edges faced in YBCO <100> in-plane directions. However, some of our 20-device subchips (Fig. 3c) had 4 junctions with edges facing in <110> directions to test whether crystal anisotropy or twinning affected  $J_c$  uniformity. Fig. 13 shows  $J_c$  data for two such chips with the <110> data highlighted. Typically, YBCO <110> junctions tended to have different  $J_c$ s than <100> but not consistently larger or more uniform.

To test these ideas further, we fabricated junctions with  $Y_{1-x}Ca_xBa_{2-x}La_xCu_3O_y$  (YCBLCO,  $x = 0.4$ ) tetragonal electrodes. YCBLCO was shown to be highly resistant to corrosion [15], and we measured lower oxygen diffusion rates with in-furnace resistivity measurements at 400-500°C than in undoped YBCO films. I-V characteristics for 10 junctions on one chip fabricated with YCBLCO electrodes are shown in Fig. 14. Junction resistance tended to be high so  $I_c R_n$  at 65K was 500  $\mu$ V even though the electrode  $T_c$  was just 78K. Junction  $I_c$  uniformity was poor over large areas because these initial sets of YCBLCO films had a  $10^5/cm^2$  density of CuO boulders.

#### IV. CONCLUSIONS

The YCBLCO experiment confirms the conclusion stated previously that the most important attribute for integration of junctions with groundplanes and for improved  $I_c$  uniformity is to produce smooth multilayer film surfaces. Small-scale circuits could be fabricated and demonstrated with our process because we have some control over this factor. However, experiments designed to determine intrinsic limits to  $I_c$  uniformity will not be definitive until this extrinsic factor is completely controlled.

#### ACKNOWLEDGMENT

We acknowledge the assistance of J. H. Uphoff, J. C. Brown, J. G. Faychak, G. A. Madia, D. M. Matuza, R. Nye, and S. J. Pieseski, discussions with C. L. Pettiette-Hall, J. M. Murduck, J. Luine, H. Mallison, K. Char, and S. Berkowitz, and long-standing contributions from J. R. Gavaler.

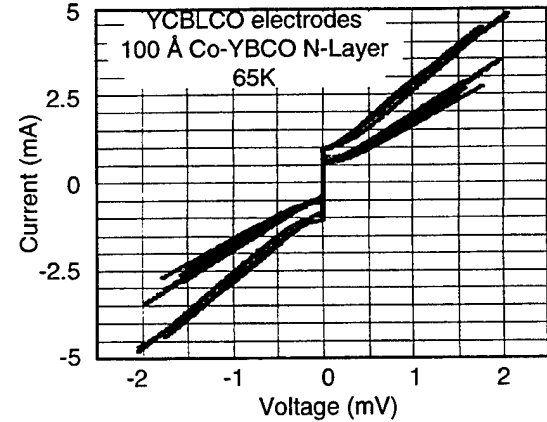


Fig. 14. I-V characteristics for 10 junctions fabricated with YCBLCO electrodes and Co-YBCO N-layers to test the effects of tetragonal structure and lower oxygen mobility.

#### REFERENCES

- [1] D. L. Miller, J. X. Przybysz, and J.-H. Kang, "Margins and Yields of SFQ Circuits in HTS Materials," *IEEE Trans. on Applied Superconductivity* 3(1), 2728 (1993).
- [2] B. D. Hunt, M. G. Forrester, J. Talvacchio, J. D. McCambridge, and R. M. Young, "High- $T_c$  SNS Edge Junctions and SQUIDs with Integrated Groundplanes," *Appl. Phys. Lett.* 68(26), 3805 (1996).
- [3] B. D. Hunt, M. G. Forrester, J. Talvacchio, J. D. McCambridge, and R. M. Young, "High- $T_c$  SNS Edge Junctions with Integrated YBCO Groundplanes," this volume.
- [4] M. G. Forrester, B. D. Hunt, J. D. McCambridge, D. L. Miller, J. X. Przybysz, J. Talvacchio, and R. M. Young, "Multilayer Edge-SNS SQUIDs for Digital Circuits," this volume.
- [5] J. D. McCambridge, M. G. Forrester, D. L. Miller, J. X. Przybysz, B. D. Hunt, J. Talvacchio, and R. M. Young, "Multilayer HTS Counting A/D Converter," this volume.
- [6] L. P. Lee, K. Char, M. S. Colclough, and G. Zaharchuk, "Monolithic &&K SQUID Magnetometer," *Appl. Phys. Lett.* 59, 3051 (1991).
- [7] J. R. Gavaler, J. Talvacchio, T. T. Braggins, and M. G. Forrester, "Critical Parameters in the Single-Target Sputtering of YBCO," *J. Appl. Phys.* 70, 4383 (1991).
- [8] J. Talvacchio, M. G. Forrester, and J. R. Gavaler, "Properties of Passive Structures for Multilayer HTS Digital Circuits," *IEEE Trans. on Applied Superconductivity* 5(2), 3139 (1995).
- [9] K. P. Daly, J. M. Murduck, C. L. Pettiette-Hall, and M. Sergant, "Integration of Step-Edge Grain-Boundary Josephson Junctions with YBCO Multilayers for Electronic Applications," *IEEE Trans. Appl. Superconductivity* 5(20), 3131 (1995).
- [10] A. T. Findikoglu, C. Doughty, S. Bhattacharya, Q. Li, X. X. Xi, T. Venkatesan, R. E. Fahey, A. J. Strauss, and J. M. Phillips, "Sr<sub>2</sub>AlTaO<sub>6</sub> Films for Multilayer High-Temperature Superconducting Device Applications," *Appl. Phys. Lett.* 61(14), 1718 (1992).
- [11] R. Guo, J. Sheen, A. S. Bhalla, F. W. Ainger, S. Erdel, E. C. Subbarao, and L. E. Cross, *Mater. Res.* 10(1), 18 (1995).
- [12] J. D. McCambridge, M. G. Forrester, D. L. Miller, J. X. Przybysz, B. D. Hunt, J. Talvacchio, and R. M. Young (unpublished).
- [13] K. Char, L. Antognazza, and T. H. Geballe, *Appl. Phys. Lett.* 65, 904, (1994).
- [14] B. D. Hunt, M. C. Foote, W. T. Pike, J. B. Barner, and R. P. Vasquez, *Physica C* 230, 141 (1994).
- [15] J. P. Zhou, J.-S. Zhou, J. B. Goodenough, and J. T. McDevitt, "Physical and Chemical Properties of Y-C-Ba-La-Cu-O," *J. Superconductivity* 8, 651 (1995).

## High- $T_c$ SNS Edge Junctions with Integrated $\text{YBa}_2\text{Cu}_3\text{O}_x$ Groundplanes

Brian D. Hunt, Martin G. Forrester, John Talvacchio, Robert M. Young, and James D. McCambridge  
Northrop Grumman Science and Technology Center, Pittsburgh, PA 15235

**Abstract**—We have fabricated high- $T_c$  SNS weak links in an edge geometry with integrated  $\text{YBa}_2\text{Cu}_3\text{O}_x$  (YBCO) groundplanes and  $\text{SrTiO}_3$  insulators, using a process which incorporates six epitaxial layers, including a Co-doped-YBCO normal-metal interlayer. The SNS edge junctions were produced using films deposited by both off-axis sputtering and pulsed laser deposition. These devices exhibit tight  $J_c$  spreads and high  $I_c R_n$  products in a current density regime well-suited for SFQ circuit fabrication. We also describe results on SNS junctions fabricated in a novel “slot” geometry, designed to reduce junction and interconnect inductances.

### I. INTRODUCTION

Single Flux Quantum (SFQ) logic offers the promise of 10 GHz operation coupled with microwatt power dissipation at the logic gate level. Realization of this potential requires the fabrication of high quality Josephson junctions in a multilevel epitaxial process. In particular, junctions with high critical-current - normal-state-resistance ( $I_c R_n$ ) products ( $>200 \mu\text{V}$ ), tight critical current spreads ( $<15\%$ ), and low junction and interconnect inductances are needed. The inductance constraints are most readily satisfied by incorporation of a superconducting groundplane.

We have recently reported on the fabrication of high performance SNS edge junctions and SQUIDs integrated with YBCO groundplanes[1], and good progress in this area has also been made by other groups[2], [3]. In this paper we discuss fresh aspects of the fabrication, including details of a new pulsed laser deposition process, alternate multilayer processing schemes, and recent results on the effect of edge angle variations on device properties. We also present new electrical data for SNS junctions with and without groundplanes with emphasis on devices with critical currents suitable for SFQ circuits. Finally we show results on a novel “slot junction” geometry, which enables the fabrication of lower inductance junctions and interconnects.

### II. PROCESS DETAILS

#### A. Film Growth

The YBCO,  $\text{SrTiO}_3$  (STO), and Co-doped YBCO (usually  $\text{YBa}_2\text{Cu}_{2.8}\text{Co}_{0.2}\text{O}_x$ ), films used in this work

Manuscript received August 27, 1996.

This work was supported in part by AFOSR Contract F49620-94-C-0021 and WL/ML Contract F33615-93-C-5355.

were deposited by off-axis rf magnetron sputtering or by pulsed laser deposition (PLD). To date, sputtering has been used for deposition of every layer for some chips, and is always utilized for growth of the groundplane and groundplane-insulator, because the best sputtered films tend to be smoother than typical PLD films, which helps guarantee good electrical isolation between YBCO layers. Details of the sputter deposition were given in an earlier paper [1].

Our PLD film process has been primarily used for YBCO base electrode deposition and for completing junctions with growth of the normal metal and cointerelectrode layers. Base electrode films were grown on STO buffer layers on  $\text{NdGaO}_3$  (NGO) substrates. Typical YBCO deposition parameters were a nominal substrate block temperature of 805°C with a target-to-substrate distance of 5 cm, and an oxygen pressure of 400 mT. We were able to eliminate a-axis grain formation in the YBCO films by using targets with a small amount of La doping ( $\text{YBa}_{1.95}\text{La}_{.05}\text{Cu}_3\text{O}_x$ ), a composition motivated by the possibility of obtaining higher  $T_c$  films [4]. La-doped YBCO films had  $T_c \approx 87\text{-}91 \text{ K}$ , and RMS roughnesses for 2000 Å films in a 10x10  $\mu\text{m}$  AFM scan were  $\approx 30\text{-}50 \text{ \AA}$  (this compares to  $\approx 10\text{-}30 \text{ \AA}$  for the best sputtered films). Local smoothness of the PLD films was generally good ( $\approx 15 \text{ \AA}$  on a 2x2  $\mu\text{m}$  scan), but scattered submicron outgrowths made the RMS roughness over larger areas somewhat worse.

The Co-doped YBCO films were grown under similar conditions except that the oxygen pressure was 600 mT. These deposition parameters produced films with the best electrical properties, but the 600 mT Co-YBCO films contained more outgrowths than for lower pressure growth. We found that the PLD-optimized  $\text{YBa}_2\text{Cu}_{2.8}\text{Co}_{0.2}\text{O}_x$  thin films had electrical properties closer to bulk values than our best sputtered films: typical  $T_{cn}$  values were  $\approx 45 \text{ K}$  with 65 K resistivities of  $250 \mu\Omega\text{-cm}$ , compared to  $\approx 55 \text{ K}$  and  $350 \mu\Omega\text{-cm}$  for the sputtered films.

#### B. Multilayer Processes

1) *Buried groundplane processes*: Requirements for the fabrication of high performance multilayer circuits include the need for acceptable electrical isolation, high current density ( $J_c$ ) vias and crossovers, high quality epitaxy of all layers, and complete oxidation of buried YBCO films. Details of the processing steps used to produce SNS edge junctions over buried groundplanes

which meet these constraints were presented in [1]. In that work our multilayer process used two separate via patterning steps to make contact to the groundplane and to the base electrode. The result of this “double-via” approach is separate patterning and epitaxial overgrowth of the groundplane, the groundplane insulator, and the base electrode bilayer. Because epitaxial growth over a patterned film is quite sensitive to surface cleanliness of the underlayer, the yield of such a sequence of patterning and growth steps can be reduced, even with the cleaning procedure described in [1].

More recently we have also successfully produced edge junctions with groundplanes using a variation on this process in which a STO/YBCO-base-electrode/STO trilayer is grown over the patterned groundplane as illustrated in Fig. 1. In this case contact between the base electrode and groundplane is made through large-area SNS junctions defined by a single via through the trilayer combined with counterelectrode “plugs” patterned at the same time as the junctions. The advantages of this “single-via” process are a reduced number of mask layers and *in-situ* growth of the base electrode trilayer, an inherently higher yield approach than the double-via process. Potential disadvantages are reduced circuit layout flexibility and lower- $J_c$  via contacts. This approach is similar to a process first reported by Conductus [2]. At the present we are using both processes to produce junctions with groundplanes.

2) *Groundplanes on top*: Both the single and double-via processes are based on a buried groundplane configuration to minimize process exposure of completed SNS devices. However, it should be noted that there is no inherent reason to prohibit the use of groundplanes on top. Putting the groundplane above the junctions simplifies the processing, because groundplane morphology is no longer critical. In addition, fabricating the junctions directly on the substrate may ultimately lead to tighter device parameter spreads, and the groundplane and groundplane insulator serve as passivation layers for the buried junctions.

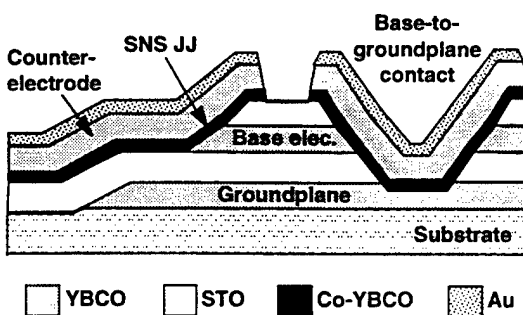


Fig. 1. Schematic cross section of a YBCO/Co-YBCO/YBCO SNS edge junction integrated with a YBCO groundplane in the “single-via” process. Contact between the groundplane and base electrode is provided by a counterelectrode plug.

We have begun experiments with groundplanes over SNS devices, with promising initial results. In this case we processed previously tested junctions without groundplanes by ion milling off the Au contacts, growing an STO layer, and patterning via contacts to the buried electrodes. Finally the YBCO groundplane was deposited and patterned, and Au contacts were defined. Results are discussed in Section III.

### C. Tapered Edge Effects

Tapered base electrode edges with edge angles less than 45° are important for avoiding grain boundary formation in the counterelectrode[4]. Circuit layout considerations also make it desirable that the edge junction properties be independent of edge orientation. These constraints motivated the development of the reflowed-resist tapered edge process described in [1], which produced edge tapers of ≈30°. More recently, other results [5],[6] suggested that even shallower edges might be desirable. These reports led us to develop a modified tapered edge process utilizing an argon-oxygen gas mixture combined with the reflowed resist process reported earlier [1]. We found that milling at 300 eV in a 10% O<sub>2</sub> in Ar mixture at 45° produced 14° edges for lines of 20 μm or larger (all angles measured from the horizontal). Milling at 60° under these conditions produced tapered edges of 11.5°.

Our preliminary results with these shallower edge angles have revealed unexpected problems with *void formation* on edges below 15° in junctions completed by PLD at our normal counterelectrode deposition pressure of 400 mT. Higher pressure growth (up to 600 mT) improved the edge coverage, but resulted in increased CuO boulder formation. In the worst cases the voids were detectable in an optical microscope as an irregular edge, but AFM or SEM studies were needed to actually resolve the voids. Away from the device edges, film growth was uniform without holes. Sputtered SNS weak links showed better edge coverage over the shallow edges (at high deposition pressures), but both the PLD and sputtered devices exhibited nonideal electrical behavior, as discussed below.

## III. ELECTRICAL RESULTS AND DISCUSSION

### A. SNS Junctions Without Groundplanes

1) *Devices with shallow edge angles*: PLD-completed devices fabricated on the 11.5 and 14° edges at growth pressures of 400-600 mT often exhibited “flux-flow” IV characteristics and nonideal magnetic field modulation of the critical currents, and tended to have degraded  $I_c$  spreads. In contrast, PLD devices on ≈30° edges showed excellent electrical behavior (next

section). These initial results also show that junction  $R_n A$  products correlate with the edge angles:  $R_n A$  products for three chips with 100 Å Co-YBCO interlayers and edge angles of 11.5°, 14°, and 30° were 51.5, 17.2, and 1.4  $\Omega \cdot \mu\text{m}^2$ , respectively. While it is not surprising that junctions with voids at the edge exhibit higher resistances, these results *suggest* that the high  $R_n A$  products we observe even for the 30° edge devices [1] may be caused by nonuniform conduction associated with small voids along the edges.

Although the sputtered SNS devices had fewer obvious problems with edge coverage, they also tended to exhibit degraded junction quality and  $J_c$  spreads. The difficulties we observe with growth over shallow YBCO edges may be eliminated by further optimization of the growth conditions. However, our current efforts, described in the remainder of the paper, are focused on edge junctions with edge angles close to 30°, with which we can routinely produce high quality devices.

2) *Devices with 30° edges*: SFQ circuits require inductance ( $L$ ) -  $I_c$  products on the order of a single flux quantum,  $\phi_0 \approx 2000 \text{ pH} \cdot \mu\text{A}$ . Because typical microstrip inductances are about 1  $\text{pH}/\square$  [1],[2], conventional SQUID layouts point to critical currents of a few hundred  $\mu\text{A}$ , with the lower limit set by thermal noise considerations. Fabricating devices with lower  $I_c$  values is accomplished by using thicker N-layers, which leads to an associated reduction in the  $I_c R_n$  products.

Fig. 2 shows the I-V characteristics at 65 K for nineteen 3-μm-wide SNS edge junctions without groundplanes with a 75 Å Co-doped-YBCO normal metal layer, which meet the SFQ critical current constraints (one junction of the twenty total on the test subchip was not measured due to a probe wiring problem). For this chip the base electrode YBCO-STO bilayer was sputter deposited and the normal metal and counterelectrode were grown by PLD. The average device parameters and spreads for these junctions were:

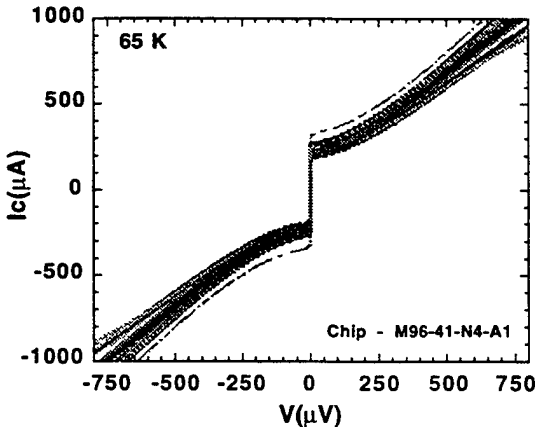


Fig. 2. I-V data at 65 K for nineteen 3-μm-wide junctions on a test chip without groundplanes with a 75 Å Co-doped YBCO interlayer. The 1- $\sigma$   $J_c$  spread is 16% and the average  $I_c R_n$  product is 181  $\mu\text{V}$ .

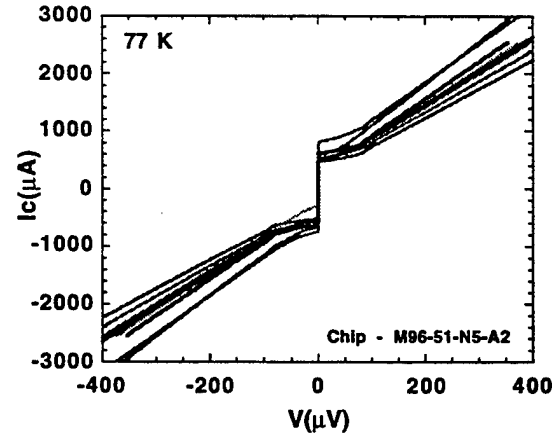


Fig. 3. I-V characteristics at 77 K for nine 4-μm-wide junctions with integrated groundplanes and 75 Å Co-YBCO interlayers. The 1- $\sigma$   $J_c$  spread is 16% and the average  $I_c R_n$  product is 100  $\mu\text{V}$ .

$J_c = 5.0 \times 10^4 \text{ A/cm}^2$ , 1- $\sigma = 16\%$ ;  $I_c R_n = 181 \mu\text{V}$ , 1- $\sigma = 13\%$ ; and  $R_n A = 3.7 \times 10^{-9} \Omega \cdot \text{cm}^2$ , 1- $\sigma = 12\%$ . The average values of critical current and resistance were 213  $\mu\text{A}$  and 0.82  $\Omega$ . The current densities of these devices were lower than the  $J_c$  values of devices with sputtered Co-YBCO interlayers of similar thickness due to the different electrical properties of the sputtered and PLD Co-YBCO films. All but one of the devices exhibited nearly complete magnetic field modulation of the critical currents, with close to the expected  $I(\sin x)/x$  behavior. The combination of tight  $J_c$  spreads, large  $I_c R_n$  products, and small, SFQ-compatible critical currents seen on this chip is an important demonstration for the viability of HTS SFQ digital circuits.

### B. SNS Junctions With Groundplanes

1) *Buried groundplanes*: The I-V characteristics for a recent set of nine 4-μm-wide SNS edge junctions over groundplanes are shown in Fig. 3. These junctions were fabricated using the double-via process with a sputtered groundplane and groundplane insulator, and a PLD base electrode, 75 Å Co-YBCO layer, and counterelectrode. In this case the test chip contained fewer individual junctions, but included other test structures such as SQUIDs and  $J_c$  bridges. At 77 K the average device parameters and spreads for these junctions were:  $J_c = 7.5 \times 10^4 \text{ A/cm}^2$ , 1- $\sigma = 16\%$ ;  $I_c R_n = 100 \mu\text{V}$ , 1- $\sigma = 13\%$ ; and  $R_n A = 1.3 \times 10^{-9} \Omega \cdot \text{cm}^2$ , 1- $\sigma = 10\%$ . At 65 K the average  $J_c$  increased to  $2.9 \times 10^5 \text{ A/cm}^2$  with a 1- $\sigma$  spread of only 7%, demonstrating that very tight  $J_c$  spreads can be achieved over a groundplane, albeit with  $I_c$  values too large for SFQ applications in this case. These results also illustrate a trend seen for our recent groundplane chips: for a given N-layer thickness the average  $J_c$  has been higher and the average  $R_n A$  product lower relative to junctions without

groundplanes. This behavior was not seen in our earlier work [1], where junctions were very similar whether on or off of groundplanes. The more recent groundplane data may indicate that rougher growth in the upper layers of our multilevel structures is leading to device edge coverage problems, and, indeed, recent groundplane films have been somewhat rougher than in the previous work. These devices have proved suitable for fabrication of high quality SQUIDs and small-scale SFQ circuits [7],[8], and we expect that further improvements in the film process will lead to improved devices with reproducible characteristics both on and off of groundplanes.

1) *Groundplanes on top*: Two chips have been processed to add groundplanes over previously tested junctions as described in Section II. These devices exhibited RSJ I-V characteristics with very similar parameters to those before the groundplanes were added, *except* that the operating temperature of the junctions was reduced by about 20 degrees. At 50 K the average device values were:  $J_c = 1.8 \times 10^5 \text{ A/cm}^2$ ;  $I_c R_n = 476 \mu\text{V}$ ; and  $R_n A = 3.1 \times 10^{-9} \Omega\text{-cm}^2$ . This suggests that the high temperature insulator and YBCO growths done after junction fabrication led to oxygen depletion in the junction region, and we are investigating annealing procedures to re-oxygenate the devices.

### C. Slot-Defined SNS Edge Junctions

Obtaining SFQ-compatible  $I_{c,0}$  products can be aided by patterning a slotted insulator layer over the SNS device edge as shown in Fig. 4a). This modification of the SNS edge junction geometry enables the use of wide, low-inductance counterelectrodes, while maintaining the small junction area needed for small- $I_c$ , high  $R_n$  devices. The additional insulator layer also allows increased flexibility in circuit layout by enabling wiring to cross base electrode edges without shorting. In our initial experiments with the slot geometry, we patterned 3- $\mu\text{m}$  wide slots in a 500  $\text{\AA}$  STO layer, combined with 10  $\mu\text{m}$ -wide counterelectrodes. Fig. 4b) shows typical I-V and  $I_c(B)$  modulation data for a slot-junction device with no groundplane with a sputtered 200  $\text{\AA}$  Co-YBCO normal metal layer at 77 K. We have also fabricated slot-defined junctions and SQUIDs integrated with groundplanes, and SQUID measurements show the expected inductance reduction[7].

### ACKNOWLEDGEMENT

We would like to acknowledge the assistance of J. C. Brown, G. Faychak, G. Madia, D. Matuza, R. Nye, S. Pieseski, and J. Uphoff. We also acknowledge useful discussions with A. Kleinsasser, K. Char, H. Mallison, and S. Berkowitz.

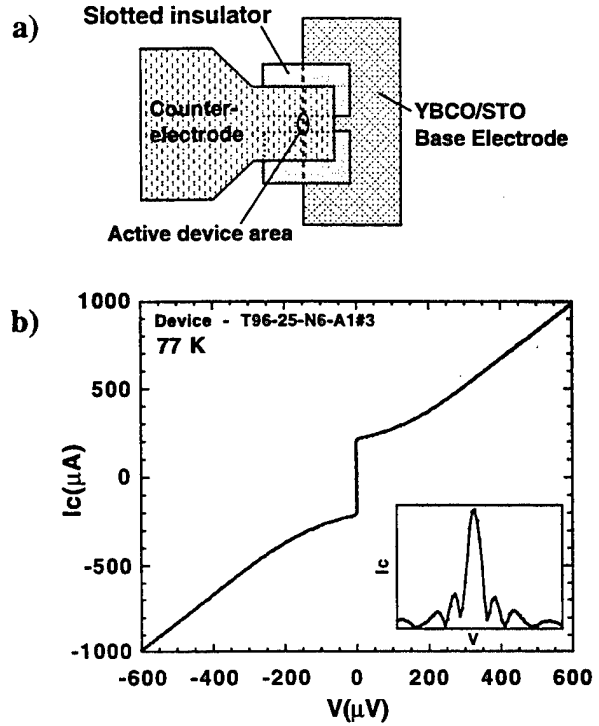


Fig. 4. a) Schematic diagram of slot-defined SNS edge junction. b) I-V and  $I_c(B)$  (inset) data for a sputtered slot junction with a 200  $\text{\AA}$ -YBCO normal metal layer at 77 K.

### REFERENCES

- [1] B. D. Hunt, M. G. Forrester, J. Talvacchio, J. D. McCambridge, and R. M. Young, "High- $T_c$  SNS edge junctions and SQUIDs with integrated groundplanes" *Appl. Phys. Lett.* vol. 68, pp. 3805-3807, 1996.
- [2] W. H. Mallison, S. J. Berkowitz, A. S. Hirahara, M. J. Neal, and K. Char, "A multilayer YBCO Josephson junction process for digital circuit applications" *Appl. Phys. Lett.* vol. 68, pp. 3808-3810, 1996.
- [3] M. Hidaka, S. Miura, T. Satoh, W. Hattori, J. S. Tsai, and S. Tahara, "A high- $T_c$  sampler circuit", *1996 Int. Workshop on Superconduct. Extended Abstracts*, ISTE, pp.101-104, 1996.
- [4] B. D. Hunt, M. C. Foote, W. T. Pike, J. B. Barner, and R. P. Vasquez, "High- $T_c$  edge-geometry SNS weak links on silicon-on-sapphire substrates", *Physica C*, vol. 230, pp.141-152, 1994.
- [5] W. H. Mallison, Conductus, Inc., Sunnyvale, CA, personal communication, 1996.
- [6] M. I. Faley, U. Poppe, C. L. Jia, and K. Urban, "Proximity effect in edge type junctions with PBCO barriers prepared by Br-ethanol etching", *IEEE Trans. on Appl. Supercond.*, pp. 2091-2094.
- [7] M. G. Forrester, B. D. Hunt, J. D. McCambridge, D. L. Miller, J. X. Pryzbysz, J. Talvacchio, and R. M. Young, "Multilayer Edge SNS SQUIDs for Digital Circuits", *IEEE Trans. on Appl. Supercond.*, this vol.
- [8] J. D. McCambridge, M. G. Forrester, D. L. Miller, B. D. Hunt, J. X. Pryzbysz, J. Talvacchio, and R. M. Young, "Multilayer HTS Flux-Counting A/D Converters", *IEEE Trans. on Appl. Supercond.*, this vol.

## Multilayer Edge SNS SQUIDs for Digital Circuits

Martin G. Forrester, Brian D. Hunt, John Talvacchio, Robert M. Young, and James D. McCambridge  
Northrop Grumman Science and Technology Center, Pittsburgh, PA 15235

**Abstract** — We have fabricated and characterized direct-injection High Temperature Superconducting (HTS) SQUIDs using a six-epitaxial-layer process which integrates edge geometry superconductor-normal-superconductor (SNS) junctions with an HTS ground plane. The period of the SQUID threshold curves was used to infer microstrip inductances of approximately 1 pH/□ at 65 K. Total SQUID inductances as low as  $\approx 5$  pH were inferred from the measured critical current modulation depth. A novel junction geometry was used in some devices to reduce the parasitic inductances of the junction leads by approximately 1 pH. Maintaining such low inductances is particularly important for Single Flux Quantum digital circuits.

### I. INTRODUCTION

Digital circuits based on HTS Josephson junctions have the potential for GHz operation with power dissipation of microwatts per gate, operating at temperatures attainable with compact cryocoolers (e.g. 65 K). To realize this potential it is necessary to develop a fabrication process based on reproducible, manufacturable, high  $I_c R_n$  junctions. In addition, for maximum circuit layout flexibility, it is desirable to use an integrated groundplane to minimize inductance,  $L$ , in order that the product  $L I_c$  be approximately equal to the flux quantum,  $\Phi_0$ . For SFQ circuits in particular, thermal noise constraints dictate that  $I_c$  should be as large as possible, while meeting the constraint that  $L I_c \approx \Phi_0$ .

For certain applications, such as A/D converters, we believe that a reasonable compromise is to have  $I_c \approx 0.5$  mA, so that a typical inductance would be 4 pH. Such low inductances can be achieved in a single HTS layer by using narrow slit inductors, patterned with, for example, e-beam lithography [1]. However this approach suffers from parasitic mutual inductance between slits, and does not allow superconducting crossover interconnections, which are required for circuits of even modest levels of integration. The use of the base electrode of an edge (or “ramp”) junction as a local ground to produce low inductances has also been demonstrated [2], but this also is not sufficiently flexible for more complex circuits.

We have recently reported on the fabrication of SNS edge junctions and SQUIDs with an integrated YBCO ground plane, using a flexible process with six epitaxial layers[3]. We have found the critical current uniformity of such edge

junctions to be superior to other approaches such as grain boundary junctions.

Here we present more detail on SQUID inductance measurements, and in particular the inference of total SQUID inductance from the depth of critical current modulation. In addition we present results for a modified process which reduces parasitic inductances associated with the narrow junction leads.

### II. DEVICE FABRICATION

The two baseline fabrication processes used are illustrated in Fig. 1, and are described in detail elsewhere [3],[4]. Epitaxial YBCO, Co-doped YBCO, and SrTiO<sub>3</sub> (STO) films were deposited by off-axis rf magnetron sputtering from stoichiometric targets onto NdGaO<sub>3</sub> substrates. Patterning was performed by ion milling, with the substrates mounted on a tilted, rotating, water cooled sample stage, using a reflowed photoresist mask to obtain edge tapers of  $\approx 25-30^\circ$ .

For the “double via” process of Fig. 1(a) there are four separate high-temperature growth steps, each followed by an ion mill patterning step and an ion cleaning. A YBCO ground plane (typically  $\approx 200$  nm thick) is deposited and patterned first, followed by the  $\approx 250$  nm STO groundplane insulator. The third deposition is of the 100–200 nm base electrode, followed in-situ by a STO cap layer. The tapered edges required for junction formation are then milled in this bilayer. Finally the N-layer, typically 10-30 nm of YBa<sub>2</sub>Cu<sub>2.79</sub>Co<sub>0.21</sub>O<sub>x</sub>, and a 200 nm thick YBCO counterelectrode, with an in-situ Au contact layer, are

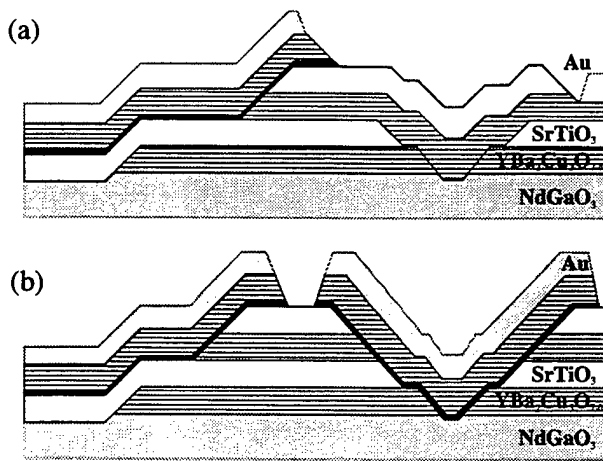


Fig. 1. Schematic cross sections of the two processes used to fabricate edge SNS junctions and SQUIDs over groundplanes. The “double via” process, (a), reduces the number of separate epitaxial growth steps compared to the “single via” process, (b), but necessitates that ground contacts be large area junctions.

Manuscript received August 27, 1996.

This work was supported in part by the Air Force Office of Scientific Research, Contract F49620-94-C-0021 and by Air Force Wright Labs Contract F33615-93-C-5355.

deposited and patterned. In this process contacts to ground are made directly from the base electrode through vias in the STO groundplane insulator. If desired, vias are also milled through the base electrode cap layer, and filled by an ex-situ Au deposition, to provide direct electrical contact to the base electrode.

The “single via” process is similar to one developed at Conductus [5], and involves only three high temperature depositions because the groundplane insulator is deposited at the same time as the base electrode and its insulator. This trilayer is then patterned twice — once to cut a via hole through the entire trilayer, and once to cut the base electrode edge. Contacts to ground are then completed by a plug of counterelectrode and N-layer, with the disadvantage that such contacts are necessarily junctions, albeit of width significantly larger than the “deliberate” junctions. The advantage is that reducing the number of epitaxial growths steps tends to increase the process reliability.

A photograph of a completed direct-injection SQUID, fabricated with the double-via process, is shown in Fig. 2(a).

### III. MEASUREMENTS

The fabricated 1-cm chips were mounted in commercial 44-pin ceramic chip carriers for measurement. The carrier was inserted into a magnetically-shielded, temperature-

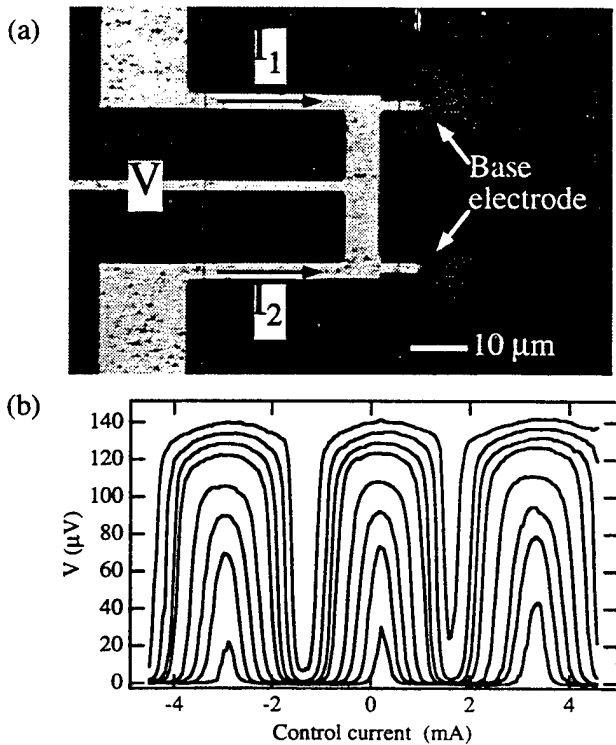


Fig. 2. (a) Photograph of typical direct injection SQUID fabricated with the “double via” process, with definitions of bias currents. Some devices did not have the center tap, in which case the voltage was measured on one of the current leads. (b) Voltage versus control current, at various bias levels, for a typical SQUID at 65 K.

controlled cryostat with twisted-pair leads filtered with a cutoff frequency of about 10 Hz. Measurements were performed under computer control.

Flux was applied to the SQUIDs by direct current injection into opposite ends of a microstrip inductor formed by the counterelectrode, the groundplane insulator, and the ground plane. With current  $I_1$  injected in one end and  $I_2$  in the other the control current is given by  $I_{\text{cont}} = (I_1 - I_2)/2$ , and the flux applied to the SQUID is given by  $L_{\mu} I_{\text{cont}}$  where  $L_{\mu}$  is the microstrip inductance. Typically we measured the SQUID voltage,  $V$ , versus  $I_{\text{cont}}$  at various levels of total bias,  $I_1 + I_2$ , as a function of temperature. We also measured the critical current, using a voltage criterion of 2  $\mu$ V, as a function of  $I_{\text{cont}}$  at a few selected temperatures. Since the leads of the ceramic chip carrier were slightly magnetic we usually observed some shifting of the SQUID threshold curves.

## IV. ELECTRICAL RESULTS

### A. Voltage modulation and microstrip inductance

Voltage modulation of a typical SQUID with a short (~1 square) microstrip inductor is shown in Fig. 2(b) at various total bias levels, at 65 K, where this particular device had the following parameters:  $I_c \approx 1.75$  mA,  $R_n \approx 0.25$   $\Omega$ , total inductance  $L_{\text{tot}} \approx 10$  pH (inferred from  $I_c$  modulation depth as discussed in the next section). The maximum voltage modulation is about 135  $\mu$ V peak-to-peak, with  $(dV/d\Phi)_{\text{max}} \approx 1.8$  mV/ $\Phi_0$ . Corresponding values at 77 K were 40  $\mu$ V and 230  $\mu$ V/ $\Phi_0$ , respectively. For the listed SQUID parameters the expected peak-to-peak voltage modulation, using equation 7 of [6], is about 30  $\mu$ V. The measured value is larger than expected because of strong resonances which we observe in the current voltage characteristics of these SQUIDs (although not in single junctions), which lead to high values of  $dV/dI$  in certain bias regions, and thus to higher values of  $dV/d\Phi \approx (dV/dI)(dI/d\Phi)$ .

From the period,  $\Delta I_{\text{cont}}$ , of voltage modulation data of the type shown in Fig. 2(b), we calculate the inductance of the microstrip using  $L_{\mu} = \Phi_0/\Delta I_{\text{cont}}$ . This is shown in Fig. 3 for SQUIDs with various lengths of inductor, normalized to the number of squares between the inside edges of the current leads. Typical values are in the range 1–1.5 pH/ $\square$  at 65 K, similar to values we have previously reported for SQUIDs fabricated using a simpler process incorporating step edge grain boundary junctions [7]. As can be seen in Fig. 3 there is an appreciable spread in inductance from one device to another at high temperatures. This is thought to be due to local variations in the  $T_c$  of the ground plane and/or base electrode, and thus in the penetration depth, possibly due to incomplete oxidation [8]. The  $T_c$  of the these layers was often found to be suppressed to below 85 K, compared to 87 K for the counterelectrode. Diffusion of oxygen through the

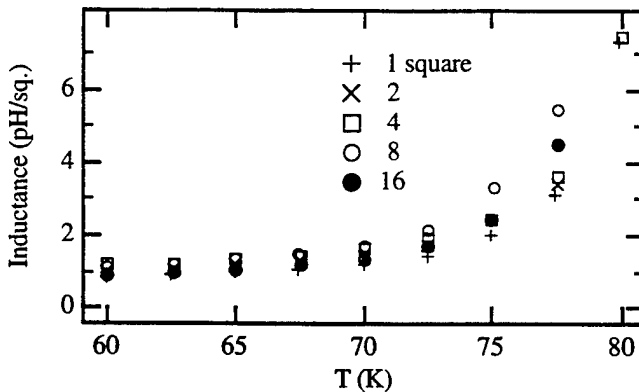


Fig. 3. Microstrip inductance per square inferred from the period of  $V-I_{cont}$  curves, for various lengths of microstrip inductor.

insulating layers of such a complex structure is an issue which will require further attention.

#### B. $I_c$ Modulation and Total Inductance

Although one can in principle infer the total SQUID inductance from the depth of the voltage modulation, the resonances in the I-V characteristics, referred to in the previous section, complicate such an analysis. It is simpler to use instead the depth of critical current modulation.

Typical data are shown in Fig. 4 at three different temperatures. To infer the SQUID inductance from such data we use the following expression [6]:

$$\frac{\Delta I_c}{I_c} \approx \frac{1}{1 + \beta_L} \left( 1 - 3.57 \frac{\sqrt{k_B T L}}{\Phi_0} \right), \quad (1)$$

where,  $\Delta I_c$  is the measured SQUID critical current modulation depth, and  $\beta_L = L I_c / \Phi_0$ . The second term in parentheses takes account of the effect of thermal noise currents in the SQUID inductance. Solving (1) for  $L$  gives an upper bound on the inductance, since any critical current

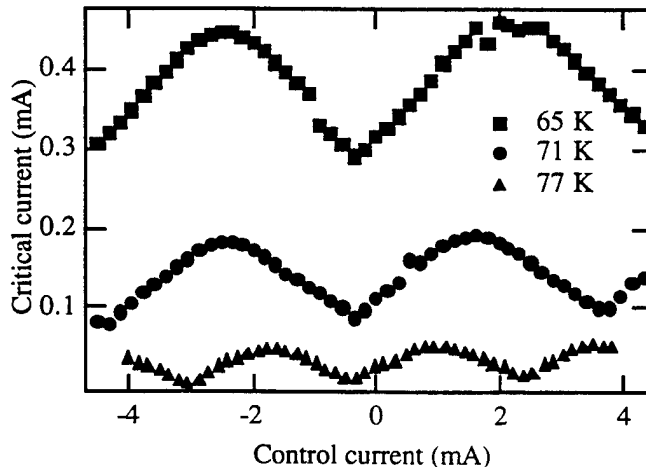


Fig. 4. Critical current versus control current for a typical SQUID. Note that the curves are shifted due to trapped flux.

asymmetry between the two junctions will reduce the modulation depth. The SQUID lobe patterns typically did not show significant skewing so we ignore this correction.

The total inductance inferred from (1) is plotted in Fig. 5(a) for ten different SQUID layouts of the general type shown in Fig. 2(a). They differ in the length of the microstrip inductor, the lengths of the junction leads, and details of the ground contact arrangement. The lowest inductance device is about 5 pH, at 65 K – quite close to the nominal 4 pH goal.

In what follows it is useful to calculate a normalized measure of SQUID inductance which we call the “effective

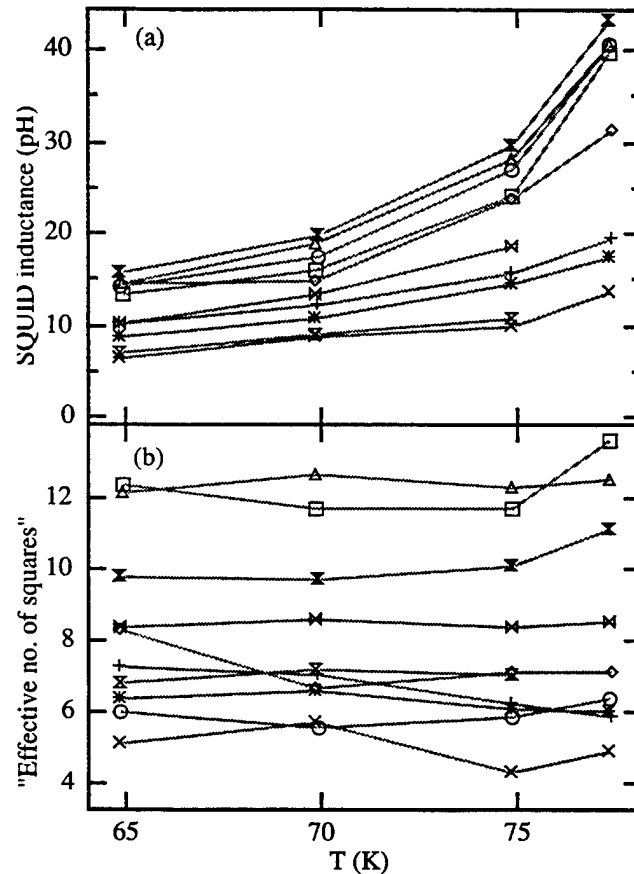


Fig. 5. (a) Total SQUID inductance, inferred from  $I_c$  modulation depth, for ten different SQUID layouts. (b) “Effective number of squares”, obtained by dividing the total SQUID inductance by the inductance per square. It is essentially independent of temperature, as it should be.

number of squares”,  $N_{eff} \equiv L_{tot}/L_{\square}$ , where  $L_{\square}$  is the inductance per square measured from the modulation period. This is useful because it normalizes out variations in the YBCO penetration depth, and therefore allows us to compare inductances of different SQUID layouts from different chips. It is plotted in Fig. 5(b) for the devices of Fig. 5(a), and is found to be roughly independent of temperature, as it should be. In general it agrees well with simple counting of squares in the SQUID layout, although there are some unresolved discrepancies in the smaller SQUIDs which we hope to investigate further.

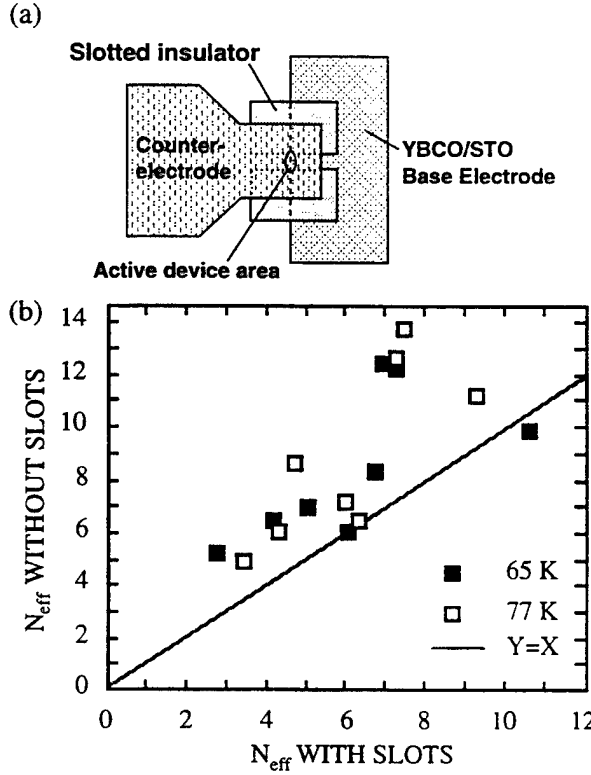


Fig. 6. (a) Schematic diagram of a slot-defined edge junction. (b) Normalized total SQUID inductances, expressed as effective number of squares, for devices fabricated without vs. with slot-defined junctions. The slot junctions reduce the junction lead inductance and thus the SQUID inductance.

## V. SQUIDS WITH SLOT-DEFINED JUNCTIONS

A significant fraction of the total SQUID inductance is in the junction leads, which are typically  $1.5 - 4 \mu\text{m}$  wide (in order to obtain critical currents of order  $0.5 \text{ mA}$ ) and  $4 - 5 \mu\text{m}$  long, and therefore contributing  $\approx 1 - 3$  squares per junction. One approach to reducing this parasitic inductance is to simply make the junction leads shorter by allowing the distance between the base electrode edge and the wide section of the counterelectrode to be reduced. The lower limit on this distance will be set by alignment accuracy and the finite extent of the shallow base electrode edge, and it is probably impractical to reduce it much below  $1 - 1.5 \mu\text{m}$ .

Here we present an alternative or supplementary approach, illustrated in Fig. 6, which we term "slot junctions" [4]. Here the junction width is determined not by the lead width, but by a slot opening in an epitaxial insulator layer deposited and patterned after the base electrode edge is patterned. This allows the junction lead to be much wider than the junction itself, reducing the inductance.

We have tested the concept by fabricating eight different SQUID designs both with and without the use of the slot process. We measured the total inductance and inductance per square for the devices, and calculated  $N_{eff}$ . In Fig. 6(b) we plot  $N_{eff}$  for the "slotless" devices on the vertical axis, and for the "slotted" devices on the horizontal axis for these eight devices, at 65 and 77 K. Although there is scatter in the data it is clear that overall the slot devices have lower inductance,

with an average inductance reduction of approximately two squares, or one square per junction. For example the device which had  $N_{eff} = 5$  was reduced to  $\approx 3$  in the slot process. Because these particular devices had a longer penetration depth than usual (about  $0.3 \mu\text{m}$ , compared to the more typical  $0.25 \mu\text{m}$ ) the total inductance was still  $4.5 \text{ pH}$ , but implementation of such a device with higher quality films with  $1 \text{ pH}/\square$  should result in a  $3 \text{ pH}$  SQUID.

In addition to reducing the junction parasitic inductance the addition of the slot insulator allows much greater circuit layout flexibility since it allows one to run counterelectrode wiring over the base electrode without forming a junction.

## VI. CONCLUSIONS

We have demonstrated that the integration of an HTS ground plane with HTS edge junctions can produce microstrip inductances of  $1 \text{ pH}/\square$ , and SQUIDs with total inductances as low as  $\sim 5 \text{ pH}$ , at 65 K. The demonstrated slot-defined junction process can reduce the latter to about  $3 \text{ pH}$  for films with  $0.25 \mu\text{m}$  penetration depth. The use of more aggressive photolithographic design rules can reduce this further, which will improve the margins of HTS SFQ circuits. The use of the additional slot insulator also makes the process more flexible in that it allows the counterelectrode to be used more fully for wiring over the base electrode.

## ACKNOWLEDGMENT

We would like to acknowledge the assistance of J. C. Brown, G. Faychak, G. Madia, D. Matuza, R. Nye, S. Pieseski, and J. Uphoff. We also acknowledge useful discussions with J. Przybysz, A. Miklich, J. Luine, J. Murduck, K. Char, H. Mallison, and S. Berkowitz.

## REFERENCES

- [1] V.K. Kaplunenko et al., "Novel design of rapid single flux quantum logic based on a single layer of a high- $T_c$  superconductor," *Appl. Phys. Lett.* vol. 67, pp. 138-140, 1995.
- [2] R.J. Wegerink, G.J. Gerritsma, E.M.C.M. Reuvekamp, M.A.J. Verhoeven, and H. Rogalla, "An HTS quasi-one junction SQUID-based periodic threshold comparator for a 4-bit superconductive flash A/D converter," *IEEE Trans. Appl. Supercond.* vol. 5, pp. 3452-3458, 1995.
- [3] B.D. Hunt, M.G. Forrester, J. Talvacchio, J.D. McCambridge, and R.M. Young, "High- $T_c$  SNS edge junctions and SQUIDs with integrated groundplanes" *Appl. Phys. Lett.* vol. 68, pp. 3805-3807, 1996.
- [4] B.D. Hunt, M.G. Forrester, J. Talvacchio, R.M. Young, and J.D. McCambridge, "High- $T_c$  SNS edge junctions with integrated  $\text{YBa}_2\text{Cu}_3\text{O}_x$  groundplanes," this volume.
- [5] W.H. Mallison, S.J. Berkowitz, A.S. Hirahara, M.J. Neal, and K. Char, "A multilayer YBCO Josephson junction process for digital circuit applications," *Appl. Phys. Lett.* vol. 68, pp. 3808-3810, 1996.
- [6] K. Enpuku, Y. Shimomura, and T. Kisu, "Effect of thermal noise on the characteristics of a high  $T_c$  superconducting quantum interference device," *J. Appl. Phys.* vol. 73, pp. 7929-7934, 1993.
- [7] M.G. Forrester, A. Davidson, J. Talvacchio, J.R. Gavaler, and J.X. Przybysz, "Inductance measurements in multilevel high  $T_c$  step-edge grain boundary SQUIDS," *Appl. Phys. Lett.* 65, pp. 1835-1837, 1994.
- [8] J. Talvacchio, M.G. Forrester, and J.R. Gavaler, "Properties of passive structures for multilayer HTS digital circuits," *IEEE Trans. Appl. Supercond.* vol. 5, pp. 3139-3142, 1995.

## A New Three Terminal Vortex Flow Device

A. Davidson and N.F. Pedersen\*

Northrop Grumman Science and Technology Center, Pittsburgh, PA 15235, USA

**Abstract**— Part of the reason for the failure of magnetically controlled Abrikosov vortex flow devices has been low magnetic coupling coefficients, combined with pinning: control currents tend to drive the control electrode normal before sufficient flux is coupled to the flux flow channel to overcome pinning. We have observed that interesting devices may use direct injection of flux, without an isolated control electrode. Experimental studies using opposite polarity currents show dramatic effects in device characteristics; simulations show that these effects are manifestations of vortex interactions.

### I. INTRODUCTION

Three terminal devices based on vortex flow are interesting for applications [1]-[4]. Some devices are based on Josephson vortices [1], [2], while another possibility is to use Abrikosov vortices [3], [4]. Typically in such devices vortices are generated at one edge of wide junction [1], [2] or a thinned section of a film by a magnetic field from a nearby control current. While the modeling for Josephson vortex flow devices seems to be much better understood - based on accumulated experience with long Josephson junctions, Abrikosov vortex flow devices seem to behave in a qualitatively similar manner, although only little information is available on important parameters such as voltage output level, high frequency cutoff, noise properties etc.

We report here measurements on a new type of Abrikosov vortex flow devices. The device is fabricated by creating a thinned section of a YBCO film, where creation and flow of Abrikosov vortices may take place. The control current is applied as a direct current (vortex) injection into the thinned section instead of using the magnetic field from a nearby control line, as is usually the case.

In our modeling we take the injection principle and the details of the geometry into account, however we use the dynamics of the much better understood Josephson vortices. Nevertheless most features of the experimental curves can be understood from our model based on the actual sample geometry and the long Josephson junction model with current injection. In section II we discuss the sample fabrication and the experimental results. In section III the model and numerical results are presented. In section IV a comparison between the model calculations and the experiments is made. A conclusion and summary is given in section V.

### II. SAMPLE AND EXPERIMENTAL RESULTS

A typically device geometry is shown in Fig. 1a and b, while Fig. 1c is a photograph of a sample. The thinned section where the Abrikosov vortex move is inside the area shown by the dashed curve linking all three electrodes A, B, and C. We call samples of this geometry type I. In some cases we fabricated samples where the thinned section only extends between electrodes B and C and A and C, but not between A and B. Such samples we define as type II samples. All samples are fabricated on a 300 nm thick YBCO film on a LaAl<sub>2</sub>O<sub>3</sub> substrate. The thinned section is obtained by ion milling using Argon ions with an energy of 300 V, at an angle 30° off of the beam axis, and with sample rotation, and is thought to be between 150 and 200 nm thick. All measurements were conducted by

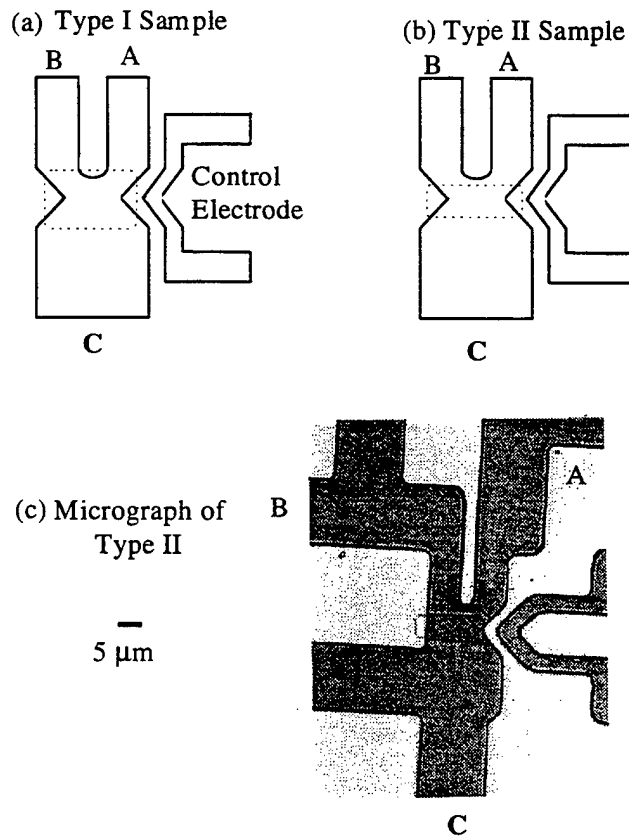


Fig. 1. Geometrical form of Type I and Type II Samples. The rectangular region in the center, more or less  $5 \times 10$  microns, has been thinned by ion milling. Hence the Type II sample, (b), has a higher critical current link between the A and B electrodes than the Type I sample (a). A micrograph of a fabricated device is shown in (c).

Manuscript received August 27, 1996

This work was supported in part by the U.S. Air Force, under Grant AFOSR F49620-94-C-0021

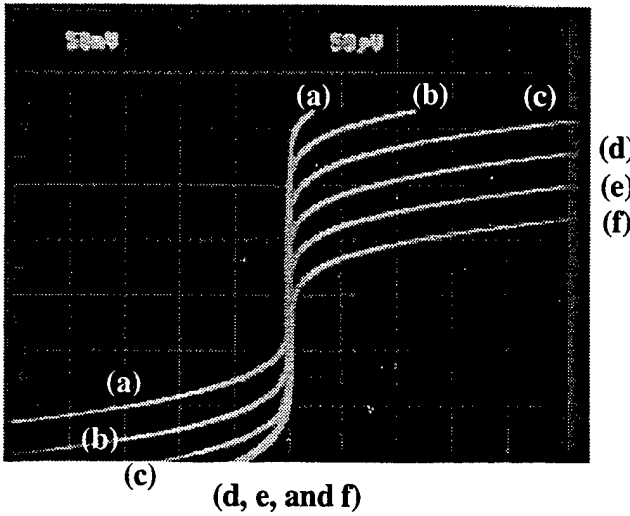


Fig. 2. Current-Voltage Characteristic of Type I Device, measured from electrodes A to C in Fig. 1. Control current was injected from B to C, at 0, 3, 6, 9, 12 and 15 mA for curves (a) through (f). Curves (a), (b), and (c) shift symmetrically as the injection current is increased. Curves (d) through (f) shift the curves in the upper right quadrant, but not in the lower left. The vertical axis is current, 5 mA per division, and the horizontal axis is voltage, 50  $\mu$ V per division.

immersion of samples in liquid nitrogen at 77 K. The isolated control electrode had no measurable effect, and was not used in any measurements reported here.

Fig. 2 shows a series of experimental IV-curves for a sample of type I. IV-curves are measured between electrodes B and C, while the control (injection) current  $i_c$  (which is the parameter for the different curves in Fig. 2) is applied between electrodes A and C. We note that the IV-curves are asymmetric with current reversal (or equivalently injection current reversal). This feature is not observed for vortex flow devices with a traditional control line. We note that the level of injection current is comparable to that of

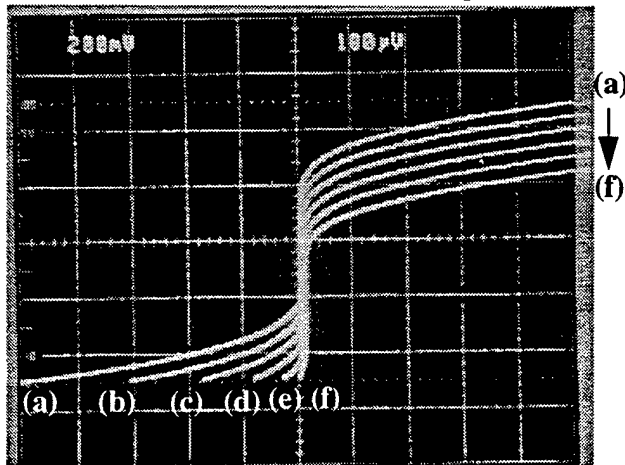


Fig. 3. Current-Voltage Characteristic of Type II Device, measured from electrodes A to C in Fig. 1. Control current was injected from B to C, at 0, 0.5, 1, 1.5, 2, and 2.55 mA for curves (a) through (f). All curves shift symmetrically as the injection current is increased. The vertical axis is current, 2 mA per division, and the horizontal axis is voltage, 100  $\mu$ V per division.

the IV-curves for a visible voltage modulation. This is typical of most Josephson vortex flow devices [1], [2].

Comparable curves from a sample of type II, shown in Fig. 3, do not show the asymmetry described above. As can be understood from the geometry of samples of type II (Figure 1), current injection at electrode B will be strongly coupled to electrode A, so that the currents simply add. Under these conditions, the injection current is expected to shift the measured IV curves up and down the current axis, with no other effect. The voltage modulation of the IV-curves are typically less than 100  $\mu$ V for both types of samples, but we ascribe this low voltage level to the fact that we have not yet optimized the thickness and geometry of the vortex flow section of the samples.

Now we can understand the shift in curves (a), (b), and (c) in Fig. 2. Evidently, the injection current from these curves is below a threshold, or critical current, and the injection current in electrode B adds directly to the measurement current in electrode A. But for injection current higher than 6 mA (c) the threshold is exceeded, and the currents and voltages redistribute to give the asymmetric effect. In an effort to understand the asymmetry, we constructed a Josephson vortex flow model.

### III. MODEL AND NUMERICAL SIMULATIONS

The model is shown in Fig. 4 for type I samples where current is injected into the weakened region. The letters A, B, C correspond to the letters used in Fig. 1. Between electrodes A, B current goes predominantly near sample edges, thus creating a vortex flow from injector junction A, C into junction B, C through an inductance and a Josephson junction. A current distribution with spikes at the edges is represented by the numbers along the top of the junctions in Fig. 4. Such a current distribution was mostly used in the simulations; removing the singularities only produced quantitative changes, not qualitative.

To simplify the calculations we assumed fluxons to be Josephson, not Abrikosov vortices, thus allowing us to use the highly damped sine-Gordon model [5]. We expect that

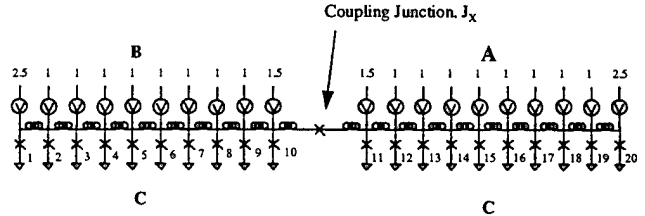


Fig. 4. Josephson Transmission Line Model of Vortex Flow. The flux flow devices are modeled as two regions of Josephson lines connected by a junction in the middle. A, B, and C correspond to the electrodes in Fig. 1. 10 junctions are shown, but 20 were typically used. The numbers along the top represent the assumed current distribution, peaking along the edges. Simulations used two junctions per Josephson penetration depth.

most features are similar for Abrikosov and Josephson vortices.

In the simulations the junctions A-C and B-C each consists of 20 Josephson elements modeling a Josephson transmission line 10 penetration depths long. Each junction element was assumed to be highly overdamped, so that shunt capacitance could be ignored, and the voltage could be normalized to the  $I_c R_n$  product of the junctions. Time was thus normalized to  $\phi_0 / I_c R_n$ , where  $\phi_0$  is the flux quantum, 2.07 mVpsec. The coupling junction between A and B was assumed to have the same value as all the individual junctions in AC and BC. All specific values of junction parameters are in reference to a single Josephson element (e.g. the critical current of one junction element, rather than the critical current of the entire A, C electrode).

Fig. 5 shows current-voltage characteristics generated by a numerical integration of the equations of motion of this model. The injection current was  $I_{AC} = 0, 1, 1.5, 2, 3$  and 4 in normalized units. The current distribution has spikes along the edges as shown in Fig. 4.

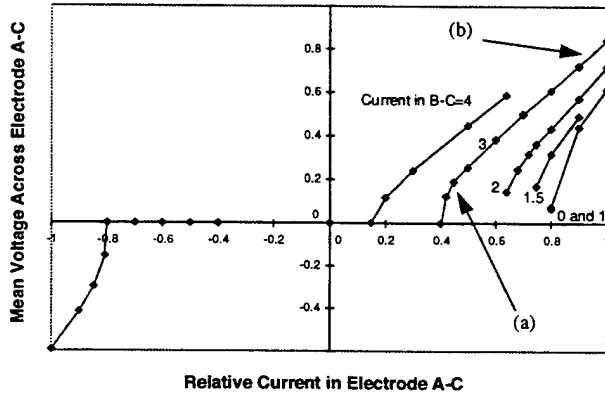


Fig. 5. Current Voltage Characteristic generated by the Josephson Vortex flow model. Negative bias currents were unaffected by current injection through B-C. Points labeled as (a) and (b) are illustrated in subsequent figures to show the fluxon dynamics for the parameters indicated.

In Fig. 5 we note the strong asymmetry of the IV-curves, similar to curves d, e, and f in the experimental curves in Fig. 2. We note that there is a threshold such that the modulation of the IV-curve is small when the injection current is small. This is like the change in behavior from curves a, b, and c in the measurement. The numerical model allows us to look into the dynamic features connected with different parts of the IV-curve. Thus Fig. 6 plots the voltage of each of the 40 junctions in the two Josephson transmission lines of the model, as a function of time, and displays the dynamics that corresponds to the point labeled (a) in Fig. 5. Along the Junction Number axis, junctions 1-20 form port B-C, and junctions 21-40 form port A-C. We note that no fluxons are created at the right edge of junction AC, but that fluxons are injected into junction AC from

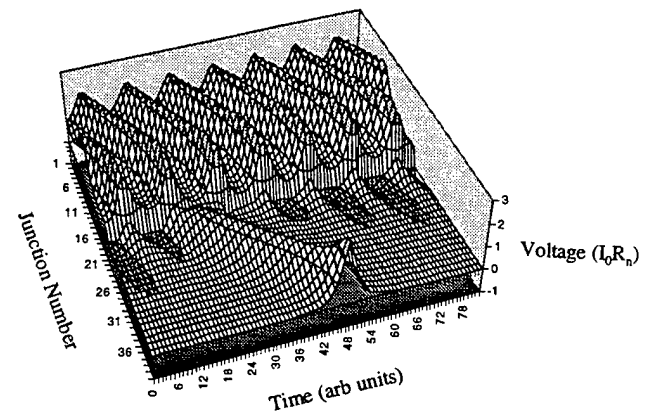


Fig. 6. 3D view of Josephson Vortices for point (a) in Fig. 5. Fluxons enter the structure at junction 1, move through that Josephson transmission line, and mainly leave through the coupling junction. (The voltage across the coupling junction is not shown here.) Occasionally, a vortex is injected into port AC, and leaves the structure at junction 40.

injector junction BC. The injected fluxons give rise to a voltage in junction AC.

This figure also explains why if the measurement current is reversed, the current injection at port B-C has no effect on port A-C.: In that case, the current bias in port A-C forces vortices to move back toward the injector junction. Hence no fluxons can move through the device, and the voltage remains zero until the applied bias current exceeds the threshold for fluxon injection at the edge of A-C.

Fig. 7 is another example of fluxon dynamics corresponding to point b in Fig. 5. Here port A-C is being injected with fluxons from junction B-C, as in Fig. 6, but also from antifluxons being injected from its own open edge. The figure shows the fluxons annihilating with the anti-fluxons in the middle of junction A-C.

We have also done simulations where the coupling junction was replaced with a large critical current junction, or with a fixed inductance. Under these conditions, we obtained simple IV curve shifts, as shown in Fig. 3.

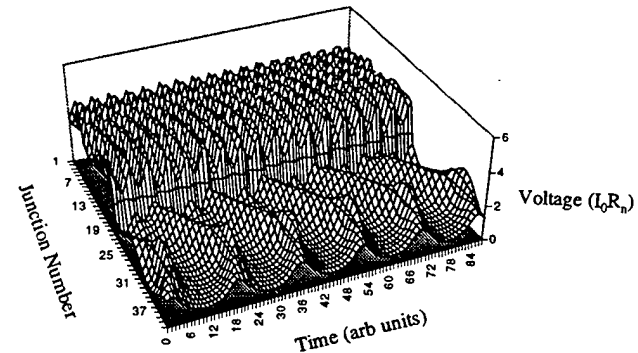


Fig. 7. 3-D view of vortex dynamics corresponding to point (b) in Fig. 5. Here more vortices are injected from port B-C into port A-C, and anti-vortices are also nucleated at the free edge of port A-C. Vortices and anti-vortices annihilate in the middle of port A-C.

#### IV. DISCUSSION

The transfer response of a three terminal thin film flux flow structure shows interesting asymmetries, and a responsiveness not observed in magnetically coupled devices. This leads to two views of the operation of such a device. One is that we could be simulating an applied magnetic field by having one overbiased port full of fluxons, in close proximity to the port under observation. Those fluxons are like the flux from an external electrode, but they have already overcome any pinning forces, and are ready to move when a bias current of the appropriate direction is applied.

The other view is that the asymmetries that we observed are of the type expected for rectifying junctions. Appropriate current biases might then set up the right kind of vortex-antivortex interaction to allow for amplification by a process analogous to that in semiconductor bipolar transistors. We speculate that anti-vortices introduced in the right way, would control vortices moving through a channel, with gain.

#### V CONCLUSION

Our experiments, like many others, have shown that epitaxially grown YBCO thin films are not conducive to magnetically controlled thin film Abrikosov flux flow devices. Evidently, flux pinning, and possibly an edge barrier to flux entry, make predictable device difficult to produce. Our experiments were all performed on devices immersed in liquid nitrogen to eliminate heating as a confounding cause of flux motion. We never observed any voltage modulation as the result of current in an isolated control electrode, although we looked for it.

However, we designed our experimental devices with

multiple ports, so that control could be achieved by direct injection. Under these conditions, we observed asymmetries in device characteristics that could not be explained as simple addition of currents. Under conditions when the two ports were most independent, we observed fairly strong asymmetry on current reversal in one of the ports.

By modeling the device as two Josephson transmission lines, coupled by a small Josephson junction, were able to generate IV curves similar to those observed experimentally. In these simulations we were able to identify fluxoid motion and interaction as the source of the asymmetry, and so it is likely that this is also the case in our experimental devices. A bipolar type of flux injection device may therefore be possible to develop.

\*Permanent address: Physics Department, Technical University of Denmark, DK-2800 Lyngby, Denmark

#### References.

- [1] R. Gross, R. Geredemann, L. Alff, T. Bauch, A. Beck, O.M. Froelich, D. Koelle, A. Marx. "Physics and performance of high temperature superconducting vortex flow transistors," *Applied Superconductivity*, vol2, no 7/8 ( 1995 ).
- [2] Y.M. Zhang, D. Winkler, P.Å. Nilsson and T. Claeson,"Flux flow transistors based on long YBCO bicrystal grain boundary junctions," *Appl. Physics lett.* 64, 1153 ( 1994 ).
- [3] J. S. Martens , V.M. Hietala, T.A. Plut, D.S. Ginley, G.A. Vawter, C.P. Tigges, M.P. Siegal, Julia M. Phillips, S.Y. Hou, "Flux flow microelectronics," *IEEE Trans Appl. Superconductivity* 3, 2295 (1993).
- [4] K. Miyahara, K. Tsuru, S. kubo, M. Suzuki, "Characteristics of High Tc superconducting flux flow transistors with submicron channels," *IEEE Trans Appl. Superconductivity* 5, 3381 (1995).  
M. Kusunoki, H. Akaike, A. Fujimaki, H. Hayakawa, "Superconducting flux flow transistors with submicrometer structures," *IEEE Trans Appl. Superconductivity* 5, 3389 (1995).
- [5] D.W. McLaughlin and A.C. Scott, "Perturbation analysis of fluxon dynamics," *Phys. Rev. A* 18, 1652 ( 1978 ).

## Identification of grain boundary effects in current–voltage curves of polycrystalline high- $T_c$ superconductors

J.D. Hettinger <sup>a</sup>, K.E. Gray <sup>a,\*</sup>, D.J. Miller <sup>a</sup>, D.H. Kim <sup>a</sup>, D.G. Steel <sup>a</sup>,  
B.R. Washburn <sup>a</sup>, J. Sharping <sup>a</sup>, C. Moreau <sup>a</sup>, M. Eddy <sup>b</sup>, J.E. Tkaczyk <sup>c</sup>,  
J. DeLuca <sup>c</sup>, J.H. Kang <sup>d</sup>, J. Talvacchio <sup>d</sup>

<sup>a</sup> Materials Sciences Division, Argonne National Laboratory, Argonne, IL, 60439, USA

<sup>b</sup> Superconductor Technologies, Inc., Santa Barbara, CA, 93111, USA

<sup>c</sup> General Electric Corporate Research and Development, Schenectady, NY 12301, USA

<sup>d</sup> Westinghouse Science and Technology Center, Pittsburgh, Pennsylvania 15235, USA

Received 16 September 1996; revised manuscript received 25 October 1996

---

### Abstract

Dissipation and critical current densities in high- $T_c$  superconductors can depend on both intragranular flux creep and intergranular weak links. Separating these effects in polycrystals can be a formidable task. We present current–voltage data which can in some cases identify weak-link behavior, and verify it by using ion irradiation to greatly diminish the contribution from flux creep. We conclude that the occurrence of significant weak links in series with so-called strongly-coupled current paths may be more common than previously deduced.

PACS: 74.40 + k; 74.60.Ge; 74.50.+r

---

### 1. Introduction

The coupling of superconductivity across grain boundaries in high- $T_c$  superconductors (HTS) is far more difficult and problematic than it is for conventional metallic superconductors (e.g., NbTi or Nb<sub>3</sub>Sn). As a result, dissipation and critical current density limitations in HTS cannot be readily interpreted in terms of flux creep alone: weak links at

grain boundaries can play an important role. In addition, the high-temperature operation made possible with HTS, together with its short coherence length, leads to significantly greater thermally-activated flux creep. As a result it is particularly difficult to separate these effects in HTS polycrystals. This liability hampers efforts to enhance the critical current density,  $J_c$ , since the ways of improving grain boundary weak links differ from those for flux creep, and attempts to improve one can often affect the other, sometimes in unexpected and/or adverse ways.

One significant interpretational roadblock, is that the two- or three-dimensional arrays of polycrys-

\* Corresponding author. Fax: +1 630 252 9595.

<sup>1</sup> Present address: Department of Chemistry and Physics, Rowan College, Glassboro, NJ, USA.

talline grains make us suspect of simple models in which grains are only considered in series or in parallel. It is likely that the actual current paths can vary as one alters the magnetic field,  $B$ , temperature,  $T$ , or the current density,  $J$ . One popular approach is to interpret the sharp drop in  $J_c$  in very small magnetic fields as a necking down of the effective area carrying the supercurrent. The ensuing plateau in  $J_c$ , often found in polycrystals out to higher fields, is then considered as evidence for strongly-coupled paths in the remaining area. While data has been interpreted to support this model [1], it is unlikely to be so simple in all cases. This paper address the open question: is  $J_c$  limited *only* by the fractional area of strongly-coupled paths or do residual weak links in series with these paths dominate?

The full current-voltage curve,  $I(V)$ , offers the possibility of a more insightful view into the detailed current transport than  $J_c$  alone. In addition, measurements [2,3] and predictions [4–6] of the  $I(V)$  for both purely grain-boundary transport [2,4] and purely flux-creep dissipation [3,5,6] are available: unfortunately, the  $I(V)$  shapes are virtually indistinguishable [6] and only the parameters modeling the curves are different. In spite of this, we will show that  $I(V)$  data can in some cases identify weak-link behavior, and will verify this conclusion by using ion irradiation to greatly diminish the contribution from flux-creep dissipation.

## 2. Sample fabrication and characterization

This work studies  $I(V)$  in both polycrystalline and epitaxial samples of two Tl-cuprates: the highly anisotropic  $Tl_2Ba_2CaCu_2O_x$  (Tl-2212) and  $TlBa_2-Ca_2Cu_3O_x$  (Tl-1223) with an intermediate anisotropy. Although the four types of samples are not made identically, their transport properties are similar in important aspects and we will present evidence that there are no relevant differences other than the grain connectivity. Epitaxial films of phase pure Tl-2212 were made at Superconductor Technologies, Inc., using laser ablation with a post-deposition anneal in a controlled  $O_2$  and Tl environment: they showed rocking curves with a full-width at half maximum of  $< 0.4^\circ$ . Such films display very reproducible superconducting properties, particularly in high magnetic

fields where their irreversibility behavior is very nearly identical from sample to sample (for the samples used here,  $T_c$  ranged from 102.6 to 104 K). Polycrystalline films of phase pure Tl-2212 were made from sputtered precursors containing an excess of Tl on MgO substrates, which were processing in a sealed Au foil in a flowing oxygen ambient at a temperature of 850°C with a bulk Tl-2212 pellet to stabilize the vapor pressures (for the sample reported here,  $T_c = 101.3$  K). For epitaxial films of Tl-1223, Tl-free precursors were sputtered onto single-crystalline  $LaAlO_3$  substrates and sent to GE for reaction in an oxygen ambient using their two-step thallination process [7] with a sample temperature of 860°C and a Tl-oxide boat temperature of 745°C (for the sample reported here,  $T_c = 111.4$  K). The Tl-oxide weight gain was consistent with the amount of precursor converting to the 1223 phase and the rocking curve FWHM was  $1^\circ$ . Polycrystalline films of Tl-1223 were made in a similar manner except for the use of spray pyrolysis by GE to deposit the Tl-free precursor onto polycrystalline, Y-stabilized zirconia substrates (for the samples used here,  $T_c$  ranged from 110.8 to 114 K). These samples developed a highly-organized, in-plane texture (i.e., a colony microstructure) during processing [8]. We used x-ray diffraction to confirm phase purity and orientation.

## 3. Transport measurements

A comparison between the temperature-dependent resistance of polycrystalline and epitaxial films is shown in Fig. 1. This data implies that the weak links are relatively less detrimental at low temperatures, but a possibly more insightful comparison is the field-dependent  $J_c$ , shown in Fig. 2. Importantly, these data demonstrate the essentially identical irreversibility behavior for all four Tl-2212 samples and also for all four Tl-1223 samples (albeit at higher fields because of the reduced anisotropy [9]). This indicates a virtually identical flux-creep behavior, with the only sample-to-sample differences being their grain connectivity (weak-link behavior). It should be realized that epitaxy does not guarantee the absence of weak links: dislocation and impurity-phase segregations can and do occur, but one of the weakest links, high-angle grain boundaries [10], are

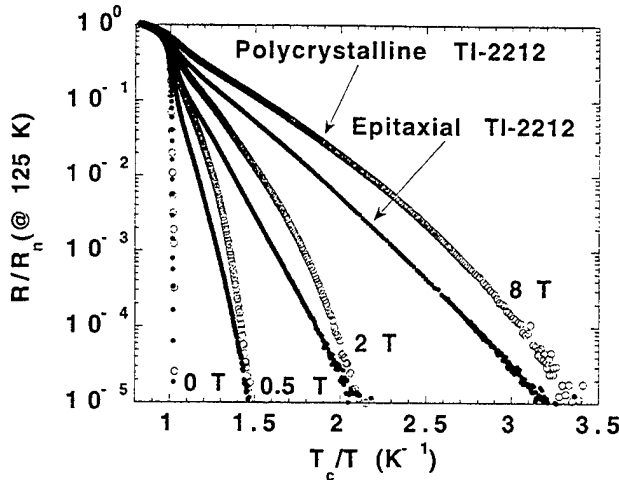


Fig. 1. Comparison of thermally-activated resistance near  $T_c$  for polycrystalline and epitaxial films of Tl-2212 for various (indicated) magnetic fields.

virtually nonexistent. Thus the similarity of  $J_c$  in the plateau region for all the polycrystals is coincidental, and, e.g., polycrystalline Tl-1223 films have been made [11] with significantly larger and smaller  $J_c$  in the plateau region. Also epitaxial samples with higher  $J_c$  at low fields have been made [12].

A second, somewhat weaker conclusion, relates to the conjecture [1] that the wide plateau in  $J_c$  is evidence for a narrow well-connected path through polycrystalline materials. The difficulty is that the epitaxial material shows a much stronger field dependence at fields just below the point where the

curves separate ( $\sim 1.5$  T for Tl-1223 and  $\sim 0.2$  T for Tl-2212). It seems hard to imagine a model of a strongly connected path with a weaker field dependence than that for epitaxial films. This observation could indicate that the necked-down region which carries the current still contains weak links in series with the current flow, but that these are less field sensitive, i.e., like the familiar low- $J_c$  plateau region of polycrystalline samples.

#### 4. Single weak-link and pure flux-creep $I(V)$

Weak-link and flux-creep current-voltage curves,  $I(V)$ , have been separately measured in epitaxial films with [2,10] and without [3,12] artificial, high-angle grain boundaries (HAGB). Most HAGB data are on  $\text{YBa}_2\text{Cu}_3\text{O}_7$ , and typical sample fabrication is described in Ref. [2]. That zero-field data [2] was fit over a range of currents and temperatures to the Ambegaokar-Halperin [4] (AH) theory of thermally-activated, phase-slip dissipation in Josephson junctions. Two examples [2] are shown in Fig. 3 for a  $24^\circ$ -[001]-tilt, bicrystal, grain boundary. The low-current, linear region for 85.5 K indicates thermal activation and the nonlinear increase to the junction's normal state resistance (at around  $10^{-4}$  A) represents current-induced phase slips occurring as the unfluctuated critical current is surpassed. Below 81 K, the thermally-activated regime is reduced below the noise level.

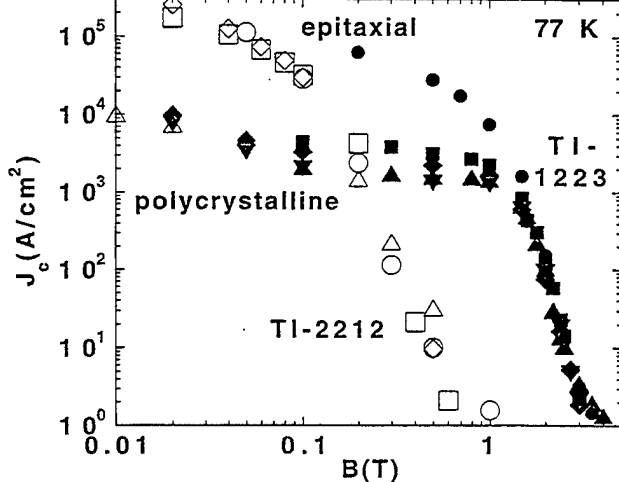


Fig. 2. Field dependence of  $J_c$  at 77 K for: epitaxial Tl-1223 (filled circles); polycrystalline Tl-1223 (other filled symbols); polycrystalline Tl-2212 (open triangles); and epitaxial Tl-2212 (other open symbols).

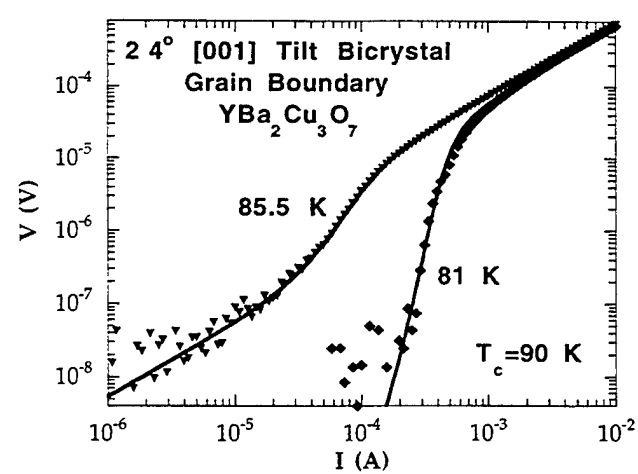


Fig. 3. Experimental current-voltage curves from Ref. [2] for an artificial grain boundary in  $\text{YBa}_2\text{Cu}_3\text{O}_7$  at two selected temperatures, together with fits to the AH theory [4].

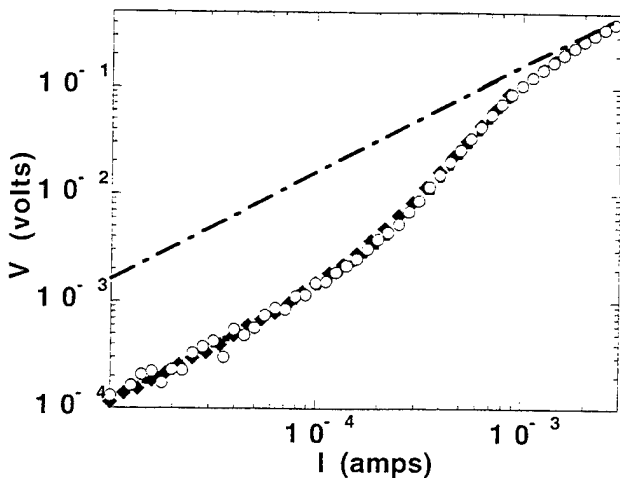


Fig. 4. Comparison of the experimental  $I(V)$  for a 36.8°-[001]-tilt, bicrystal, grain boundary (open circles) at 30 K and a field of 2 mT (20 G) and for flux-creep dissipation in an epitaxial film, without a grain boundary, at 86.5 K and a field of 1 T, shows virtually identical shape. Also shown is a fit of the grain-boundary data to the AH theory [4] and its normal-state resistance.

The flux-creep dissipation in a similarly-made epitaxial film, without an artificial grain boundary, is shown in Fig. 4 at a temperature of 86.5 K and a field of 1 T. It shows the same low-current, linear region representing thermally-activated flux creep followed by nonlinear response when the Lorentz force [13] is sufficiently large to depin vortices without thermal activation. It can be fit to reasonable extensions of the basic flux-creep model of Ref. [5]. To underscore the potential similarity of this  $I(V)$  with that of a weak-link Josephson junction, the data for a 36.8°-[001]-tilt, bicrystal, grain boundary are also shown in Fig. 4 for 30 K and a field of 2 mT (20 gauss), together with a fit to the AH theory [4] and the normal-state junction resistance. These sets of data are virtually indistinguishable [6], implying that the *shape* of  $I(V)$  curves alone cannot determine the origin of dissipation.

## 5. Polycrystalline $I(V)$ measurements

The  $I(V)$  for polycrystalline and epitaxial Tl-2212 films are compared in Fig. 5 at 40 K and 4 T. Note that the  $I(V)$  are expressed as  $E(J)$  using the intrinsic electric field,  $E$ , and current density,  $J$ , and since  $40 \text{ K} \ll T_c$ , the small differences in  $T_c$  are unimportant. The enhancement of dissipation in the polycrys-

tal is only apparent for  $J \geq 10^4 \text{ A/cm}^2$ . Because the  $E(J)$  are similar at the lowest  $J$ , we choose to interpret the polycrystal  $E(J)$  as the series sum of contributions from flux creep in the grains and weak links between the grains. Thus in the absence of flux creep we anticipate that the polycrystal data would follow the dashed line at low current. In other words, while both effects are correctly described by curves like Figs. 3 and 4, the flux creep (epitaxial) data are below the critical current (and thus dominated by thermal activation, like the flux-creep data of Fig. 4 or the 85.5 K curve of Fig. 3) while the weak links are near or above their critical current (and thus dominated by current-induced phase slips, like the 81 K curve of Fig. 3). Note however, that this interpretation assumes uniform current flow throughout the polycrystalline film for  $J < 10^4 \text{ A/cm}^2$ . If the current necks down, then the local  $E$  and  $J$  values would differ from that calculated using the sample dimensions:  $E$  and  $J$  would be spatially varying and therefore not comparable to the epitaxial sample. Fortunately there is an internal consistency: as the effective  $E$  across the weak-link grain boundaries drops significantly below that for flux creep, the driving force for a non-uniform current distribution disappears. Thus above  $10^4 \text{ A/cm}^2$  the currents may be nonuniformly distributed, but below that value, they should be uniform.

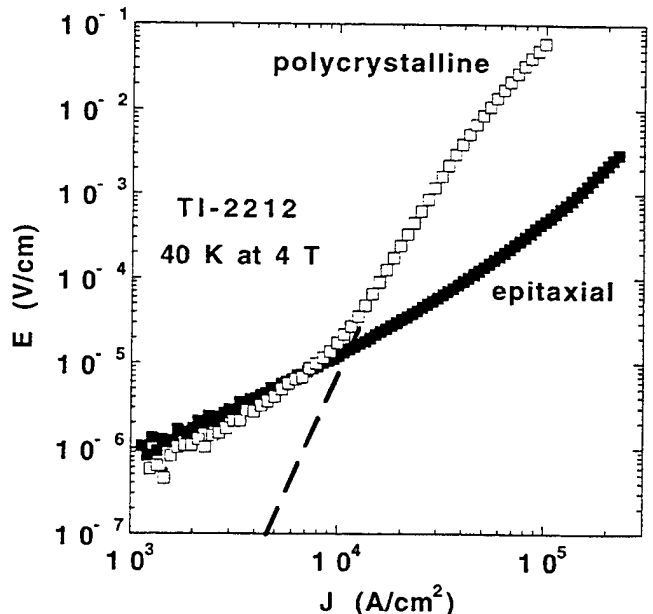


Fig. 5. Comparison of the  $E(J)$  for polycrystalline (solid triangle) and epitaxial (open square) films of Tl-2212 at 40 K and 4 T.

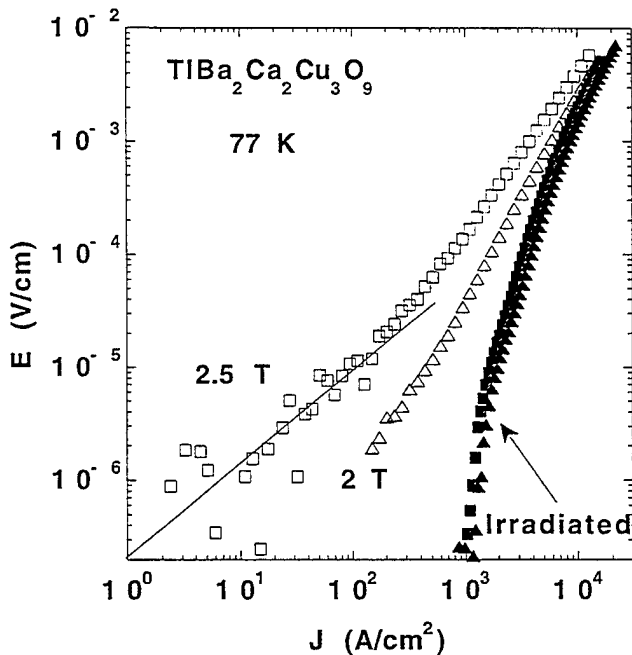


Fig. 6. The  $E(J)$  data for a polycrystalline film of Tl-1223 at 77 K before and after heavy-ion irradiation which substantially increases the flux pinning.

In order to confirm this experimentally, additional pinning is introduced by heavy-ion irradiation. Since this greatly decreases the flux creep dissipation, the model predicts that  $E(J)$  should change to reveal the dashed line of Fig. 5. In order to test this separation of flux-creep and weak-link dissipation, we have irradiated a polycrystalline film of Tl-1223 and measured  $E(J)$  before and after irradiation. Details of the irradiation are given in Ref. [14]. The data thus obtained are shown in Fig. 6 and confirm the model presented above: the highly non-linear, high- $J$  portion of  $E(J)$  is largely unchanged and the linear, low- $J$  portion has disappeared into the noise. This result represents a new experimental procedure to check on the sources of dissipation in polycrystalline samples, which should be both general and useful.

## 6. Summary

Separating the effects of intragranular flux creep and intergranular weak links in polycrystals of high- $T_c$  superconductors can be a formidable task. They affect both dissipation and critical currents. We have

shown current-voltage data for each case separately and demonstrated that in some cases  $I(V)$  data on polycrystals can reveal weak-link contributions to dissipation. To verify this general and potentially useful procedure, we have ion irradiated samples to greatly diminish the flux-creep contribution, and find behavior entirely consistent with the model.

As a result of these observations, we reexamine previously proposed models [1] suggesting that weak-link-free current paths exist in a relatively small fraction of a sample's cross-sectional area. For example, the slight *decrease* of  $J_c$  after ion-irradiation in the intermediate-field, plateau region of the  $J_c(B)$  data of Ref. [15] seems to suggest that flux creep is irrelevant, while such behavior is expected [1] if weak links limit  $J_c$ . The increased pinning due to ion irradiation does shift the irreversibility to higher fields [7,14,15], and thus  $J_c$  over *that* field range does increase, but only up to the weak-link-limited value (extrapolated from lower fields).

Thus, although the conclusion that the actual area of the current path shrinks as field increases seems reasonable and consistent with available data, the further conclusion that the remaining current path is strongly-coupled and without relevant weak links is in conflict with some experimental data, presented here and in Ref. [15]. This implies that comparing  $J_c$  to that of an epitaxial film *can only give a lower limit* on the area of the actual current-carrying path. Importantly, attaining increases in  $J_c$  can then result from *either* increasing the current-carrying area or improving the residual weak-link grain boundaries.

## Acknowledgements

The authors acknowledge useful discussions with Alex Gurevich and Dave Christen. This research is supported by the U.S. Department of Energy, Basic Energy Sciences-Materials Sciences, and Energy Efficiency and Renewable Energy, as part of a program to develop electric power technology, under contract #W-31-109-ENG-38, and the National Science Foundation-Office of Science and Technology Centers under contract DMR 91-20000. BRW, JS and CM were supported by the Division of Educational Programs.

## References

- [1] D.K. Christen et al., in: Proc. 7th Japan-US Workshop on High- $T_c$  Superconductors.
- [2] D.G. Steel, J.D. Hettinger, D.J. Miller, F. Yuan, K.E. Gray, J.H. Kang and J. Talvacchio, *Appl. Phys. Lett.* 68 (1996) 120.
- [3] R.H. Koch, V. Foglietti, W.J. Gallagher, G. Koren, A. Gupta and M.P.A. Fisher, *Phys. Rev. Lett.* 63 (1989) 1511; M.N. Kunchur, D.K. Christen and J.M. Phillips, *Phys. Rev. Lett.* 70 (1993) 998.
- [4] V. Ambegaokar and B.I. Halperin, *Phys. Rev. Lett.* 22 (1969) 1364.
- [5] Y.B. Kim, C.F. Hempstead and A.R. Strnad, *Rev. Mod. Phys.* 36 (1964) 43.
- [6] Alex Gurevich has pointed out (private communication) that thermal activation over a sinusoidal pinning potential for flux creep [see P. Martinoli, *Phys. Rev. B* 17 (1978) 1175], simulates thermal activation over the washboard potential appropriate to Ref. [4] for Josephson junctions.
- [7] J.A. DeLuca, P.L. Karas, J.E. Tkaczyk, P.J. Bednarczyk, M.F. Garbauskas, C.L. Briant and D.B. Sorensen, *Physica C* 205 (1993) 21.
- [8] D.M. Kroeger, A. Goyal, E.D. Specht, Z.L. Wang, J.E. Tkaczyk, J.A. Sutliff and J.A. DeLuca, *Appl. Phys. Lett.* 64 (1994) 106;
- E.D. Specht, A. Goyal, D.M. Kroeger, J.A. DeLuca, J.E. Tkaczyk, C.L. Briant and J.A. Sutliff, *Physica C* 226 (1994) 76.
- [9] D.H. Kim, K.E. Gray, R.T. Kampwirth, J.C. Smith, D.S. Richeson, T.J. Marks, J.H. Kang, J. Talvacchio and M. Eddy, *Physica C* 177 (1991) 431.
- [10] D. Dimos, P. Chaudhari, J. Mannhart and F.K. LeGoues, *Phys. Rev. Lett.* 61 (1988) 219.
- [11] J.E. Tkaczyk, J.A. Sutliff, J.A. DeLuca, P.J. Bednarczyk, C.L. Briant, Z.L. Wang, A. Goyal, D.M. Kroeger, D.H. Lowndes and E.D. Specht, *J. Mater. Res.* 10 (1995) 2203.
- [12] T.J. Doi, T. Yuasa, T. Ozawa and K. Higashiyama, *Jpn. J. Appl. Phys.* 33 (1994) 5692; C.A. Wang, Z.F. Ren, J.H. Wang and D.J. Miller, *Physica C* 245 (1995) 171.
- [13] The force is perhaps more correctly thought of as the magnetic pressure due to the flux gradient caused by the transport current density; see P.W. Anderson and Y.B. Kim, *Rev. Mod. Phys.* 36 (1964) 39.
- [14] K.E. Gray, J.D. Hettinger, D.J. Miller, B.R. Washburn, C. Moreau and C. Lee, *Phys. Rev. B* 54 (August 1, 1996).
- [15] J.E. Tkaczyk, J.A. DeLuca, P.L. Karas, P.J. Bednarczyk, D.K. Christen, C.E. Klabunde and H.R. Kerchner, *Appl. Phys. Lett.* 62 (1993) 3031; J.D. Hettinger et al., private communication.

(Submitted to Journal of Materials Research 6/27/97)

**Development of a reliable materials base  
for superconducting electronics**

JiPing Zhou, Rung-Kuang Lo<sup>a</sup> and John T. McDevitt\*

Department of Chemistry and Biochemistry, University of Texas at Austin, Austin, Texas 78712

John Talvacchio, Martin G. Forrester and Brian D. Hunt

Northrop Grumman Science and Technology Center, Pittsburgh, Pennsylvania 15235

Q.X. Jia and D. Reagor

Superconductivity Technology Center, Los Alamos National Laboratory, Los Alamos,  
New Mexico 87545

**Abstract**

Careful studies of the corrosion, redox, galvanic and oxygen evolution/uptake reactions associated with  $\text{YBa}_2\text{Cu}_3\text{O}_7-\delta$  and related compounds have been completed. These studies have led to an understanding of the many factors that contribute to the poor material characteristics exhibited by these popular high- $T_c$  phases. With knowledge of the structure-reactivity relationships, a powerful crystal engineering approach has been developed that is capable of producing cation substituted versions of  $\text{YBa}_2\text{Cu}_3\text{O}_7-\delta$ ; the resulting compounds therefrom produced exhibit markedly improved processability, oxygen stability and durability characteristics. These materials have been combined in thin film structures so as to make prototype SNS junctions and SQUID sensors which exhibit promising device performance characteristics.

**Key words:** high- $T_c$  superconductor materials, crystal engineering, corrosion, oxygen evolution/uptake, capped  $\text{YBa}_2\text{Cu}_3\text{O}_7$  thin films, SNS junction, SQUID sensor.

---

<sup>a</sup> Current address: 3M Austin Center, 3801 River Place Blvd., Austin, TX 78726

## I. INTRODUCTION

The compound  $\text{YBa}_2\text{Cu}_3\text{O}_7-\delta$  was identified in 1987<sup>1</sup> as a promising high- $T_c$  material soon after the initial discovery of cuprate superconductivity. To date, this formulation remains the most popular and highly studied of the high- $T_c$  materials. Much effort worldwide has been devoted to the development and refinement of processing methods for the preparation of wire, tapes and thin film devices which are fabricated using this compound.<sup>2-4</sup> Although a few high- $T_c$  products have reached the marketplace or will soon do so (i.e. superconducting quantum interference devices, NMR pickup coils, microwave filters, etc.), further improvements in device performance characteristics are needed before many thin film electronic devices can be utilized. Many of the materials problems associated with the high temperature superconductors can be traced to poor physical, chemical and mechanical properties exhibited by the cuprate compounds.<sup>5,6</sup>

It is now well documented in the scientific literature that the  $\text{YBa}_2\text{Cu}_3\text{O}_7$  compound decomposes rapidly upon exposure to water or water vapor. No less than 300 scientific publications document the reactivity characteristics of high- $T_c$  ceramic and thin film samples. However, the notion that many of the types of adverse chemical degradation reactions which are known to contribute to the decomposition of bulk compounds may also be responsible for microscopic damage occurring in the processing of high- $T_c$  junctions and devices is less appreciated now. Indeed, recent experiments completed by the McDevitt group have revealed initial evidence which suggests that chemically stabilized cuprate materials can be used to create functional high- $T_c$  products which display advanced performance characteristics. The evaluation and control of the crystal environment in the regions close to the active junctions represents an essentially important area of research where little information currently exists in the literature. Accordingly, the small feature sizes and the inaccessibility of most high- $T_c$  junctions make their direct chemical evaluation difficult.<sup>7,8</sup> Indirect evidence for junction damage as measured by device performance characteristics is inadequate for solving the many formidable problems that exist in the high- $T_c$  device fabrication area.

A number of important studies have been completed which suggest chemical reactions occur within the confines of the junction areas of high- $T_c$  devices. Oxide ion motion in grain boundaries and artificial junction structures is thought to be a major problem associated with such devices. Moreover, it has been recognized that material differences and lattice mismatching give rise to thermal stress/strain along the junction areas, leading to oxygen electromigration and interfacial resistance problems.<sup>8,9</sup> In order to control the interfacial resistance, researchers have recently focused on barrier materials (i.e. N-layer compounds) derived from the parent compound,  $\text{YBa}_2\text{Cu}_3\text{O}_7$ , in which cation substitutions destroy (or weaken) superconductivity therein. The most promising N-layer compounds studied to date possess structural features similar to those exhibited by the superconducting electrode materials such as  $\text{Y}_{0.7}\text{Ca}_{0.3}\text{Ba}_2\text{Cu}_3\text{O}_{7-\delta}$ ,<sup>10</sup>  $\text{YBa}_2\text{Cu}_{2.79}\text{Co}_{0.21}\text{O}_{7-\delta}$ ,<sup>7</sup>  $\text{Y}_{0.6}\text{Pr}_{0.4}\text{Ba}_2\text{Cu}_3\text{O}_{7-\delta}$ ,<sup>11</sup> and  $\text{PrBa}_2\text{Cu}_3\text{O}_{7-\delta}$ .<sup>12</sup> However, even with such compositions, which presently represent the most promising N-layer compounds studied to date, the reproducibility of junction parameters (i.e. critical current ( $I_c$ ) and normal state resistance ( $R_n$ )), is still problematic. The variation of critical current  $I_c$  from 12% to over 40% on eleven 1-cm<sup>2</sup> chips (16 subchips) was observed with Co-substituted  $\text{YBa}_2\text{Cu}_3\text{O}_7$  as the N-layer. Before a number of promising high- $T_c$  digital devices are realized,<sup>8</sup> further increase in junction reproducibility is needed.

Over the last several years, we have begun to assemble an extensive database on the reactivity characteristics of high- $T_c$  compounds.<sup>6,13,14</sup> From these studies, important mechanistic details which may be responsible for the rapid decomposition of the cuprate compounds have been identified. Recent experiments have identified a strong correlation between corrosion rate and lattice stress/strain as well as oxygen ordering characteristics for  $\text{YBa}_2\text{Cu}_3\text{O}_7$  derivatives. Such behavior suggests that with appropriate knowledge of the structure/property characteristics of such compounds, lattice engineering approaches capable of producing new superconductor formulations with enhanced processability/performance characteristics may be possible.

With such information, a rational strategy has been developed for the systematic modification of the high- $T_c$  lattice structure so that improved materials characteristics can be

obtained. Development of procedures for the localization of the oxygen within the lattice represents an important step in the direction of identifying a reliable materials base that can be exploited for the preparation of superconducting devices which exhibit enhanced reliability, durability and performance characteristics. New formations optimized simultaneously both for superconducting properties and processability/durability/oxygen stability have been identified using such a crystal engineering approach. In this paper, this approach is described in detail as are the properties of new high- $T_c$  compositions suitable for the preparation of high- $T_c$  electronic devices.

## II. EXPERIMENTAL

Bulk ceramic samples of  $Y_{1-y}Ca_yBa_{2-y}La_yCu_3O_{7-\delta}$  were prepared by solid-state reactions using cation substitution levels that promote chemical stability in the lattice.<sup>15</sup> A sintering temperature of 940°C and exposure to 1.0 atm of oxygen were used to prepare the compounds, conditions which are similar to those used to synthesize the parent compound,  $YBa_2Cu_3O_{7-\delta}$ . The sintered samples were annealed at 430°C for 24 hours in flowing oxygen. A maximum doping concentration for  $Y_{1-y}Ca_yBa_{2-y}La_yCu_3O_{7-\delta}$  of  $y=0.4$  was used to form pure phase compounds without noticeable presence of impurities. Chemical homogeneity of such samples have been confirmed by neutron diffraction studies completed by Slate et al.<sup>16</sup> and Rajagopal et al.<sup>17</sup>

High- $T_c$  thin films of the various cuprate phases were prepared with slightly different deposition conditions at the three participating institutions. Survey experiments were completed at The University of Texas of Austin. As new formulations with promising materials characteristics were identified from studies of the bulk compounds, the same formulations were prepared and characterized as thin film specimens. Here the method of pulsed laser ablation (PLD) was exploited. A single target was mounted in a deposition chamber which was evacuated to a base pressure of  $1 \times 10^{-7}$  torr. A KrF excimer laser beam (248 nm, pulse width 20 ns) was focused

onto the target at an angle of 45 degree to produce an energy density at the target surface of  $2 \text{ Jcm}^{-2}$ . The substrates were mounted at a distance of 5 cm from the target surface. Optimal results were obtained for films deposited at  $820^\circ\text{C}$  with deposition rate of  $1 \text{ \AA}$  per pulse and oxygen partial pressure of 100 mtorr. After deposition the samples were cooled to  $450^\circ\text{C}$  where they were maintained for approximately 20 minutes in the presence of 1 torr oxygen, and then cooled to room temperature in the same oxygen atmosphere. All other compounds mentioned in the paper, such as  $\text{Y}_{1-x}\text{Ca}_x\text{Ba}_{2-y}\text{La}_y\text{Cu}_3\text{O}_{7-\delta}$  ( $0.275 \leq x \leq 0.4$  and  $0.325 \leq y \leq 0.4$ ) and  $\text{R}_{1-x}\text{Ca}_x\text{Ba}_{2-y}\text{La}_y\text{Cu}_{3-z}\text{M}_z\text{O}_{7-\delta}$  ( $\text{R} = \text{Y, Gd, and Pr}$ ;  $\text{M} = \text{Co, Ni and Zn}$ ;  $0 \leq x \leq 0.4$ ;  $0 \leq y \leq 0.4$ ;  $0 \leq z \leq 0.4$ ) were prepared in a similar manner.

Fundamental studies of the materials dependence of high- $T_c$  SNS junctions were explored at the Northrop Grumman Science and Technology Center. Here  $90^\circ$  off-axis RF magnetron sputtering was used to create edge-type SNS junctions via a process described previously.<sup>18</sup>

Functional SQUID devices were prepared and tested at Los Alamos National Laboratory. To fabricate SQUIDs with a ramp edge-geometry SNS configuration, (100) oriented  $\text{LaAlO}_3$  was used as a substrate. A pulsed laser deposition technique was used to deposit both top and bottom  $\text{YBa}_2\text{Cu}_3\text{O}_{7-\delta}$  electrodes, N-layer  $\text{Pr}_{0.4}\text{Gd}_{0.2}\text{Ca}_{0.4}\text{Ba}_{1.6}\text{La}_{0.4}\text{Cu}_3\text{O}_7$ , and insulating layer  $\text{CeO}_2$  to isolate the top and bottom electrodes. The PLD used a 308 nm  $\text{XeCl}$  excimer laser that operates at a repetition rate of 20 Hz and produces 20 ns pulses with an energy density of  $2 \text{ Jcm}^{-2}$ . All depositions except for  $\text{CeO}_2$  were done at a temperature of  $775^\circ\text{C}$  and an oxygen pressure of 200 mtorr for  $\text{YBa}_2\text{Cu}_3\text{O}_{7-\delta}$ ;  $\text{CeO}_2$  was deposited at  $650^\circ\text{C}$ . Conventional photolithography was used to define the location of the device, and ion milling with 250 eV  $\text{Ar}$  ions was used to etch the film and to form the ramp edge. The substrate temperature and oxygen pressure during both the N-layer and top  $\text{YBa}_2\text{Cu}_3\text{O}_{7-\delta}$  electrode deposition and the bottom  $\text{YBa}_2\text{Cu}_3\text{O}_{7-\delta}$  electrode deposition were the same. Detailed device fabrication procedures and processing considerations can be found elsewhere.<sup>10</sup>

Phase composition, lattice constants and film orientations for the cuprate compounds were characterized by x-ray diffraction (XRD). These studies indicate that, although complicated

stoichiometries such as  $R_{1-x}Ca_xBa_{2-y}La_yCu_{3-z}M_zO_{7-\delta}$  are exploited to prepare the ceramic pellets, thin films and devices, the materials are readily prepared as single phase compounds. Further characterization of the ceramics and films was completed using 4-probe conductivity and SQUID magnetometry measurements.

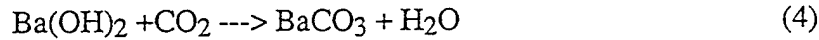
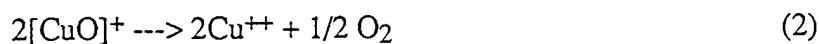
In order to explore galvanic coupling between cuprate samples and various metal contact layers, a variety of electrochemical measurements were performed. Open circuit potentials of various metals and superconductors were measured in two different solutions with constant stirring, i.e. an aqueous 0.6 M NaCl solution and 0.6 M NaCl buffered solution containing acetic acid/sodium acetate mixture to maintain the pH at 4.6. The potentials were measured with respect to a sodium saturated calomel electrode (SSCE) reference. Corrosion potentials measured at open circuit ( $E_{CO}$ 's) were recorded for different materials after soaking in the buffer solution for an hour to establish a stable condition. A Princeton Applied Research PAR 273 potentiostat was used to measure the galvanic currents between the working electrode ( $YBa_2Cu_3O_7$ ) and a variety of counter metal electrodes. The distance between two electrodes was held at  $\sim 1.5$  cm. Furthermore, to explore the influence of the metal layers on the corrosion rate of  $YBa_2Cu_3O_7$ , scanning electron microscopy (SEM) images of these same structures were evaluated following their exposure to water solution. The metals selected for such studies were Au, Ag, Cu and Pt. Each metal layer was  $\sim 1000$  Å in thickness and was deposited directly onto the surface of c-axis oriented films of  $YBa_2Cu_3O_7$ .

To explore the influence of oxygen level and cation substitution concentration on the mobile charge carriers, thermoelectric power (TEP) or Seebeck measurements were carried out on  $YBa_2Cu_3O_{7-\delta}$  and  $Y_{1-y}Ca_yBa_{2-y}La_yCu_{3}O_{7-\delta}$  samples having different oxygen contents and doping concentration. These measurements were made on sintered bar samples using a small reversible temperature difference of 0.3-1 K. In all cases, the data were corrected for the contribution of the gold connecting leads, which was measured separately using a Pb standard.

### III. RESULTS AND DISCUSSION

#### A. Chemical reasoning

The compound,  $\text{YBa}_2\text{Cu}_3\text{O}_7-\delta$  tends to degrade rapidly when exposed to the atmosphere due to reactions with  $\text{CO}$ ,  $\text{CO}_2$  and  $\text{H}_2\text{O}$ .<sup>5</sup> The reactions among the  $\text{YBa}_2\text{Cu}_3\text{O}_7-\delta$  compound, water and  $\text{CO}_2$  can be described according to the following equations:<sup>19</sup>



Likewise,  $\text{YBa}_2\text{Cu}_3\text{O}_7$  contains Cu(1)-O chains as well as ordered vacancies ( $\text{V}_\text{O}$ ) at the oxygen sites. In the early stages of corrosion, water molecules enter the open channels which run parallel with the b-axis and ultimately dock at the vacancy sites. Proton transfer from water to the oxide compounds leads to the formation of two moles of  $\text{OH}^-$  which occupy both a vacancy site and a preexisting occupied oxide site. Internal charge transfer within the  $[\text{CuO}]^+$  structures leads to the reduction of copper sites and the oxidation of oxide components. The latter results in the evolution of molecular oxygen as described in Equation (2). Following these steps, barium ions leach away preferentially from the surface of the compound due to the large hydration energy of  $\text{Ba}^{2+}$  as well as the high solubility of  $\text{Ba}(\text{OH})_2$  in water. Reacting gradually with the atmospheric  $\text{CO}_2$ ,  $\text{Ba}(\text{OH})_2$  is transformed into the sparingly soluble  $\text{BaCO}_3$  compound as described in Equation (4). Although certain aspects related to the corrosion mechanism remain unclear to date, lattice strain,<sup>20-22</sup> oxygen vacancies,<sup>23</sup>  $\text{Cu}^{3+}/\text{Cu}^{2+}$  species<sup>5</sup> and impurity phases<sup>6</sup> are known to be important contributing factors to the  $\text{YBa}_2\text{Cu}_3\text{O}_7$  corrosion process.

Essential to an understanding of the reactivity characteristics of  $\text{YBa}_2\text{Cu}_3\text{O}_{7-\delta}$  is a detailed understanding of structural features of the parent lattice. The  $\text{YBa}_2\text{Cu}_3\text{O}_{7-\delta}$  compound possesses an oxygen-deficient perovskite structure. The unit cell of  $\text{YBa}_2\text{Cu}_3\text{O}_{7-\delta}$  can be broken down into four layers, i.e. Cu(2)-O layer, Cu(1)-O layer, Ba-O layer and an oxygen deficient Y layer.<sup>24</sup> The lattice structure and four cation-oxygen layers are shown in Figure 1a. Interestingly, all of these layers have been shown to be receptive to various cation and anion substitutions. In many cases, phase pure compositions having lattice structures similar to the parent compound can be generated. Indeed, the phase composition-structure-property relationships for these superconductors substituted at the Y site,<sup>25</sup> Ba site<sup>26-28</sup> and/or Cu sites<sup>29</sup> have been examined extensively.

Through recent studies, experimental evidence suggests that lattice strain/stress is a major factor responsible for the enhanced reactivity displayed by the  $\text{YBa}_2\text{Cu}_3\text{O}_{7-\delta}$  family of compounds.<sup>13,20</sup> Based on this knowledge, the McDevitt group has developed a program to tailor from the crystal-level, new materials derived from the  $\text{YBa}_2\text{Cu}_3\text{O}_{7-\delta}$  compounds that exhibit enhanced durability and processability. Essential to this crystal engineering approach is the identification of cation substituted materials in which both the superconductivity and processability/durability properties can be optimized. Here cation compositions are chosen so that the high- $T_c$  lattice can be assembled with minimal stress and strain. To accomplish this objective, the strategically important Ba-O and Cu-O<sub>2</sub> layers must be prepared with good bond-length matching. Important to note here is the fact that this criterion is not met well for the parent compound. In the case of  $\text{YBa}_2\text{Cu}_3\text{O}_7$ , the Ba-O distance is too large to match well with the Cu-O framework.<sup>20</sup> Although there are several candidates which possess close ionic radius to  $\text{XBa}^{2+}$  (1.52 Å, where the Roman numeral X indicates the ion coordination number), such as  $\text{XSr}^{2+}$  (1.36 Å),  $\text{XCa}^{2+}$  (1.23 Å),  $\text{XK}^+$  (1.59 Å) and  $\text{XLa}^{3+}$  (1.27 Å),<sup>30</sup> only  $\text{La}^{3+}$  is capable of both forming a single phase compound as well as reducing the lattice stress/strain problem.

To demonstrate the suitability of  $\text{La}^{3+}$  substitution into the parent lattice for reducing stress/strain problems, estimates of the bond-length matching are made with the bond length sum method.<sup>21,22</sup> Here the average Ba(La)-O bond length determined for  $\text{YBa}_{2-y}\text{La}_y\text{Cu}_3\text{O}_{7-\delta}$  (0.1 <

$y < 0.4$ ) from powder diffraction data is compared with that expected for Ba(La)-O obtained from "stress free" model compounds.<sup>20</sup> The results are listed in Table 1 along with the equations that are used for calculation of the expected unstrained bond lengths as well as for the calculated strain values. It can be seen from these values that the substitution of La<sup>3+</sup> for Ba<sup>2+</sup> leads to a reduction of the internal strain energy from 1.79% for YBa<sub>2</sub>Cu<sub>3</sub>O<sub>7</sub> to 0.35% for YBa<sub>1.6</sub>La<sub>0.4</sub>Cu<sub>3</sub>O<sub>7- $\delta$</sub> . Unfortunately, the incorporation of La<sup>3+</sup> into YBa<sub>1-y</sub>La<sub>y</sub>Cu<sub>3</sub>O<sub>7- $\delta$</sub>  has been shown to cause a rapid decrease in  $T_c$  with increasing La<sup>3+</sup> content because the copper holes are trapped in the Cu(1)O<sub>x</sub> plane at a-axis oxygen/vacancy sites.<sup>28</sup>

However, a cosubstitution of Ca<sup>2+</sup> for Y<sup>3+</sup> and La<sup>3+</sup> for Ba<sup>2+</sup> in the Y<sub>1-y</sub>Ca<sub>y</sub>Ba<sub>2-y</sub>La<sub>y</sub>Cu<sub>3</sub>O<sub>7- $\delta$</sub>  system has been found to compensate the Cu valence and maintain the  $T_c$  above 80 K. For this system, an orthorhombic to tetragonal transition is found to occur at  $y \sim 0.4$ .<sup>15,31</sup> Here the oxygen occupancy frequencies at the O(4) and O(5) sites are found to be identical. A similar situation with respect to oxygen ordering characteristics has been noted previously for tetragonal samples of YBa<sub>2</sub>Cu<sub>3</sub>O<sub>6.70</sub>.<sup>15</sup> Notably, our previous work indicates that changes in oxygen content in YBa<sub>2</sub>Cu<sub>3</sub>O<sub>7- $\delta$</sub>  ( $0 < \delta < 1$ ) serve to influence the degree of stability for this compound and that YBa<sub>2</sub>Cu<sub>3</sub>O<sub>7- $\delta$</sub>  samples having intermediate oxygen contents corroded more slowly than do samples with either higher or lower oxygen contents.<sup>13,14</sup>

Importantly, the described cation substitutions are found to disrupt the integrity of the Cu(1)O<sub>x</sub> chains while keeping the total oxidation state of the [Cu(2)-O(2)/O(3)] arrays nearly constant in the Y<sub>1-y</sub>Ca<sub>y</sub>Ba<sub>2-y</sub>La<sub>y</sub>Cu<sub>3</sub>O<sub>7- $\delta$</sub>  system. The orthorhombic to tetragonal phase transition observed with increasing cation substitution supports this supposition. Higher electrostatic attraction between the incorporated +3 cation with adjacent oxide ions in the Cu(1)O chain layer may be responsible for a local disordering of oxide ions in this layer. Within the cosubstituted compounds, our results have shown that the compositional formula of Y<sub>0.6</sub>Ca<sub>0.4</sub>Ba<sub>1.6</sub>La<sub>0.4</sub>Cu<sub>3</sub>O<sub>6.96</sub> possesses the most desirable size matching characteristics for the various layers. This compound also possesses high corrosion resistance in water environments as well as enhanced processability (*vide infra*).<sup>32,33</sup>

## B. Oxygen mobility and variable temperature oxygen content measurements

Mechanistic information related to the corrosion and oxygen evolution characteristics of the  $\text{YBa}_2\text{Cu}_3\text{O}_7$  and cation modified compounds can be inferred from structure/reactivity studies. Experimental data reveal marked decreases in the corrosion and oxygen evolution rates in the cosubstituted compounds. The phase structure transforms from orthorhombic to tetragonal, resulting in different oxygen distribution in the  $\text{Cu}(1)\text{O}_x$  plane for the two different compositions, as shown in Figure 1a and 1b. Elimination of the open channels along the b-axis caused by the cation substitution may be responsible for this effect. Alternatively, the substitution of  $\text{La}^{3+}$  into the  $\text{Ba}^{2+}$  site may serve to effectively lock the chain oxygen atoms in place through increased electrostatic and/or higher coordination number preference.<sup>16,17</sup> Because the corrosion reactions occur through a series of complex steps which involve redox transformations with commensurate  $\text{O}_2$  evolution, localization of the lattice oxygen through this process may prevent corrosion. More important than the mechanistic implications is the fact that the corrosion and oxygen evolution/mobility reactions appear to be closely tied to one another (*vide infra*).

A comparison of the water reactivity of  $\text{YBa}_2\text{Cu}_3\text{O}_7$  and  $\text{Y}_{0.6}\text{Ca}_{0.4}\text{Ba}_{1.6}\text{La}_{0.4}\text{Cu}_3\text{O}_7$  samples is provided in Figure 2a and 2c. Here, the unsubstituted pellet sample is found to evolve  $\text{O}_2$  soon after its immersion in the water. The sample becomes completely coated with  $\text{BaCO}_3$  crystallites after 2 days in aerated water, as shown in Figure 2a, indicating the sample has decomposed to a significant extent. Remarkably, similar bulk samples of  $\text{Y}_{0.6}\text{Ca}_{0.4}\text{Ba}_{1.6}\text{La}_{0.4}\text{Cu}_3\text{O}_7$  show no oxygen evolution characteristics and appear to be extremely stable with respect to water reactivity. A sample of the modified compound soaked in aerated water solution for 1 month is displayed in Figure 2c. Accordingly, the scanning electron micrograph for the cation modified sample reveals an exterior region which appears to be free of corrosion precipitates. High corrosion resistance in water is also found for a modified N-layer compound  $\text{Gd}_{0.6}\text{Ca}_{0.4}\text{Ba}_{1.6}\text{La}_{0.4}\text{Cu}_{2.79}\text{Co}_{0.21}\text{O}_7$  as shown in Figure 2d. This compound is well suited for use as a barrier for SNS junctions (*vide infra*). In contrast, the traditional barrier

compound,  $\text{GdBa}_2\text{Cu}_{2.79}\text{Co}_{0.21}\text{O}_7$  is found to exhibit low water and oxygen stability characteristics as illustrated in Figure 2b.

The characteristics of water reactivity for the compounds of  $\text{YBa}_2\text{Cu}_3\text{O}_7$  and  $\text{GdBa}_2\text{Cu}_{2.79}\text{Co}_{0.21}\text{O}_7$  suggest that the corrosion and oxygen evolution/mobility reactions are connected to one another. *Evaluation of the reaction sequence described in Equations 1-4 above, would suggest that the chemical coupling of such processes is reasonable. Thus, steps taken to eliminate water corrosion reactivity are expected to result in beneficial effects related to oxygen stability. We suggest here that our previously identified cation substitution routes found to be effective for enhancing high- $T_c$  water stability can also be applied to stabilize the oxide ions within the cuprate lattice.*

Studies of the equilibrium oxygen content as probed by elevated temperature quenching studies reveal an important thermodynamic tie between oxygen content level and cation substitution pattern. In order to compare the oxygen stability characteristics of different lattice structures, the oxygen contents of  $\text{YBa}_2\text{Cu}_3\text{O}_{7-\delta}$  and  $\text{Y}_{0.6}\text{Ca}_{0.4}\text{Ba}_{1.6}\text{La}_{0.4}\text{Cu}_3\text{O}_{7-\delta}$  samples at different temperature have been measured. The pellet samples were equilibrated at different temperatures in 1 atm of  $\text{O}_2$  and then quenched thermally with liquid nitrogen to rapidly halt the oxygen diffusion. Studies of this type were completed over the temperature range from 30° to 800°C. The oxygen contents for the  $\text{YBa}_2\text{Cu}_3\text{O}_{7-\delta}$  and  $\text{Y}_{0.6}\text{Ca}_{0.4}\text{Ba}_{1.6}\text{La}_{0.4}\text{Cu}_3\text{O}_{7-\delta}$  were then determined using an iodometric titration method with a reproducibility of  $\pm 0.03$  oxygen per formula unit.<sup>34</sup> Figure 3 shows the results of oxygen contents vs. quenching temperature. Here it can be seen that for temperatures above 450°C, a significant difference exists between the two compositions in their capacity to hold onto the lattice oxygen. The  $\text{Y}_{0.6}\text{Ca}_{0.4}\text{Ba}_{1.6}\text{La}_{0.4}\text{Cu}_3\text{O}_{7-\delta}$  compound shows a stable oxygenation state at elevated temperatures of  $7-\delta$  of 6.65, whereas the  $\text{YBa}_2\text{Cu}_3\text{O}_{7-\delta}$  compound exhibits a continual decrease in oxygen content at similar temperatures.

In addition to experiments probing the thermodynamic dependence on oxygen content, additional experiments probing the kinetic issues related to oxygen uptake/evolution were completed. Here the rate of change of oxygen content for the various compounds were evaluated

for c-axis oriented films using *in situ* resistivity vs. time measurements following changes in oxygen environments. Shown in Figure 4 are such data sets where  $\text{YBa}_2\text{Cu}_3\text{O}_{7-\delta}$  and  $\text{Y}_{0.6}\text{Ca}_{0.4}\text{Ba}_{1.6}\text{La}_{0.4}\text{Cu}_3\text{O}_{7-\delta}$  films are held initially in an oxygen rich environment at 450°C and then cycled between 1.0 torr and 1.0 atm of  $\text{O}_2$ . Increases/decreases in film resistance can be used to quantify the loss/gain of oxygen in the film. Remarkably, the  $\text{Y}_{0.6}\text{Ca}_{0.4}\text{Ba}_{1.6}\text{La}_{0.4}\text{Cu}_3\text{O}_7$  formulation shows a factor of four decrease in oxygen uptake/loss as compared to  $\text{YBa}_2\text{Cu}_3\text{O}_7$ . Importantly, these results demonstrate that oxygen stability and diffusion rates within the high- $T_c$  lattice can be controlled through appropriate lattice substitution.<sup>35</sup> Interestingly, prior work of Tallon and Mellander has shown that substitution at the rare earth substitution by  $\text{Gd}^{3+}$ ,  $\text{Nd}^{3+}$ ,  $\text{La}^{3+}$  at the  $\text{Y}^{3+}$  site leads to 20, 50, 100, respectively, enhancement (relative to the Y system) in the oxygen mobility within the lattice. Here the expansion of the lattice cage with the use of larger rare earth ions is thought to the enhanced oxygen diffusion rate. On the other hand, our examinations of the rare earth ion dependence on the water corrosion rate shows that substitution at the rare earth site is ineffective in slowing the adverse water corrosion reactions. Again, the strategic importance of substitution at the  $\text{Ba}^{2+}$  site is emphasized.

Evaluation of the cation composition and structural characteristics of the various systems yields important clues to possible reasons for enhanced oxygen stability for the doubly substituted systems. Increasing the substitution level,  $x$ , within the family of compounds of  $\text{R}_{1-x}\text{Ca}_x\text{Ba}_{2-x}\text{La}_x\text{Cu}_3\text{O}_{7-\delta}$  to a value of  $\sim 0.4$  leads to a structural transformation from orthorhombic, observed at low substitution levels, to tetragonal seen at higher levels. In addition to changes in lattice symmetry, differences in the internal bond distances within the solid-state structure yield evidence that the strength of oxide ion bonding increases for the cation substituted lattice relative to the parent compound.<sup>17</sup> Most relevant here are the  $\text{Cu}(1)\text{-O}(4)$  bond distances which reflect the stability of the oxide ion which can be displaced from the lattice. For the  $\text{YBa}_2\text{Cu}_3\text{O}_7$  compound, a value of 1.942 Å is observed for the bond length.<sup>24</sup> On the other hand, the  $\text{Y}_{0.6}\text{Ca}_{0.4}\text{Ba}_{1.6}\text{La}_{0.4}\text{Cu}_3\text{O}_{7-\delta}$  formulation exhibits a bond length of 1.924 Å.<sup>17</sup>

Since the O(4) ion is located within the O(2)-Ba/La-O(4) plane, the increased charge in the layer caused by La<sup>3+</sup> for Ba<sup>2+</sup> substitution is largely responsible for the observed increase in bond strength at this oxide ion site.

Similar tetragonal structural changes in YBa<sub>2</sub>Cu<sub>3</sub>O<sub>7-δ</sub>-based materials can be fostered through alteration in the oxygen content as well as selective substitution at the copper site. For the former case, YBa<sub>2</sub>Cu<sub>3</sub>O<sub>6</sub> is obtained by removing oxygen from the fully oxygenated compound. For the YBa<sub>2</sub>Cu<sub>3</sub>O<sub>7-δ</sub> system, small changes of the Cu(1)-O(4) bonding length with decreasing oxygen content are observed and a bond length of 1.944 Å is measured for δ~0.5.<sup>36</sup> We have found YBa<sub>2</sub>Cu<sub>3</sub>O<sub>6.05</sub> to be more water reactive than YBa<sub>2</sub>Cu<sub>3</sub>O<sub>6.96</sub>.<sup>14</sup> For YBa<sub>2</sub>Cu<sub>3-x</sub>Cu<sub>x</sub>O<sub>7±δ</sub>, an increase in Cu(1)-O(4) bond length to 1.936 Å for x=0.3 and 1.940 Å for x = 0.5 is found.<sup>37</sup> We note this material also exhibits rapid decomposition in water.

### C. Electrochemical measurements

As mentioned above, the decomposition of YBa<sub>2</sub>Cu<sub>3</sub>O<sub>7</sub> and related compounds occurs according to a sequence of complex steps in which redox reactions are known to occur. While the starting material YBa<sub>2</sub>Cu<sub>3</sub>O<sub>7</sub> possesses a copper formal valence of +2.33, all copper containing corrosion products have exclusively Cu<sup>2+</sup> constituents. Thus, it is expected that coupling redox reactions to the chemistry of the cuprate system may serve to alter the decomposition rate for the material. As we have pointed out previously, high-T<sub>C</sub> devices at the metal contact layers are particularly vulnerable to parasitic redox reactions.<sup>19</sup>

To explore the suitability of various metal contact layers in high-T<sub>C</sub> film structures, ~1000 Å thick Au, Ag, Cu and Pt overlayers were deposited onto c-axis oriented films of YBa<sub>2</sub>Cu<sub>3</sub>O<sub>7-δ</sub>. Although all metals formed smooth textures prior to water exposure, severe decomposition in locations adjacent and underneath the metal overlayer is noted as shown in Figure 5. Areas in the film samples remotely spaced from the contact metal section were found to degrade much more slowly than in the metal coated region as reported previously.<sup>19</sup> Thus, a clear acceleration is noted

for the degradation rate which is attributable to a galvanic coupling of the two different conductors. Results obtained by SEM show corrosion rates vary widely depending on the ease of oxidation of the metal layer. An effective coupling and drastically accelerated corrosion occurs for the Cu/YBa<sub>2</sub>Cu<sub>3</sub>O<sub>7-δ</sub> (Figure 5a) and Ag/YBa<sub>2</sub>Cu<sub>3</sub>O<sub>7-δ</sub> (Figure 5b), less severe decomposition in the Au/YBa<sub>2</sub>Cu<sub>3</sub>O<sub>7-δ</sub> (Figure 5c) and more stable coupling in the Pt/YBa<sub>2</sub>Cu<sub>3</sub>O<sub>7-δ</sub> (Figure 5d). The Cu pad is the most severely degraded and shows no clear boundary with uncorroded area, however, others show a clear boundary as indicated in Figure 5.

Although the electron microscopy measurements yield useful qualitative information regarding the decomposition rates at metal/superconductor contacts, it is desirable to acquire a more quantitative measure of corrosion rates. Current and potential measurements are common methods to precisely quantify the corrosion rates which occur when two electrically connected metals couple to one another in a galvanic manner. Included in Table II is a list of metal open circuit potentials for a variety of contacting metals as well as the open circuit corrosion potentials for YBa<sub>2</sub>Cu<sub>3</sub>O<sub>7-δ</sub> and Y<sub>0.6</sub>Ca<sub>0.4</sub>Ba<sub>1.6</sub>La<sub>0.4</sub>Cu<sub>3</sub>O<sub>7-δ</sub>. The galvanic current density of In/YBa<sub>2</sub>Cu<sub>3</sub>O<sub>7-δ</sub> is found to be ~100 times larger than that of either Ag or Cu. Similarly, the Mg electrode coupled to YBa<sub>2</sub>Cu<sub>3</sub>O<sub>7-δ</sub> displays rapid decomposition characteristics. On the other hand, currents from Pt/ and Au/superconductor couples are below instrument limits, indicating that the interaction between these metals and the superconductor is much less than with other metals. The sign of current flow indicates that the cuprate superconductors are reduced and metals are oxidized during the galvanic corrosion process. With the more active In and Mg metals, the final appearance for the superconductor assemblage is yellowish. This behavior suggests that Cu<sup>+</sup> species is formed during redox decomposition of YBa<sub>2</sub>Cu<sub>3</sub>O<sub>7-δ</sub> in the presence of such active metals. The presence of Cu<sub>2</sub>O corrosion product has been confirmed by XRD.<sup>14</sup> Because Cu ions represent the only lattice component of YBa<sub>2</sub>Cu<sub>3</sub>O<sub>7-δ</sub> that might be expected to exhibit redox active characteristics under normal conditions, it is concluded that the fate of the Cu containing degradation products will depend highly on the metal layer's oxidation/reduction potential.

In addition to the pragmatic aspects related to the appropriate choice of metal contact layers, applied potential dependence of cuprate superconductor corrosion rates can yield essential information related to the mechanism of lattice decomposition. Thus, a series of similarly prepared  $\text{YBa}_2\text{Cu}_3\text{O}_{7-\delta}$  pellets were soaked in a water solution while being biased at potentials of -0.8 V, 0 V and +0.8 V vs a Sodium Saturated Calomel Electrode reference (SSCE). The SEM micrographs recorded for such samples are shown in Figure 6. The data reveal a marked dependence of corrosion rate on applied potential bias. The sample exposed to the most negative potential decomposed most rapidly as illustrated in Figure 6a. Intermediate in reactivity rate was the sample held at 0 V as shown in Figure 6b, which is covered by crystalline  $\text{BaCO}_3$ . Both of these samples showed significant amounts of surface-localized corrosion products. On the other hand, corrosion is largely suppressed for the sample which received the 0.8 V applied bias. These results indicate that potentials more negative than the  $E_{\text{co}}$  (open circuit corrosion potential vs. SSEC) of  $\text{YBa}_2\text{Cu}_3\text{O}_{7-\delta}$  accelerate the corrosion and potentials more positive than  $E_{\text{co}}$  suppress the corrosion. The important implication of this result is that if reduction of the superconductor is prevented, the high- $T_{\text{c}}$  lattice can be stabilized indefinitely. Since molecular oxygen evolution occurs commensurate with Cu ion reduction in order to preserve charge balance within the lattice, further evidence is obtained for the strong coupling of the water and oxygen reactivity properties.

Similarity of  $E_{\text{co}}$  values for both  $\text{YBa}_2\text{Cu}_3\text{O}_{7-\delta}$  and  $\text{Y}_{0.6}\text{Ca}_{0.4}\text{Ba}_{1.6}\text{La}_{0.4}\text{Cu}_3\text{O}_{7-\delta}$  is noted as summarized in Table II. The observed small differences indicate that the subtle structural differences in two systems do not influence to a great extent the thermodynamic driving forces for redox reactions. Thus, it is reasonable to conjecture that the marked increase in stability of  $\text{Y}_{0.6}\text{Ca}_{0.4}\text{Ba}_{1.6}\text{La}_{0.4}\text{Cu}_3\text{O}_{6.96}$  relative to  $\text{YBa}_2\text{Cu}_3\text{O}_{6.96}$  noted here is caused by changes in the water absorption rate into the lattice and/or oxygen diffusion out of the lattice caused by previously stated structural changes.<sup>16,17</sup> Apparently, the galvanic corrosion reactions studied here are not very sensitive to this factor.

#### D. Optimization of the transition temperature

We have now evaluated over 50 composition using the method for stabilization of  $\text{YBa}_2\text{Cu}_3\text{O}_{7-\delta}$  by cation substitution into the parent lattice. Summarized in Table III are selected compounds studied in this context. While  $\text{R}_{0.6}\text{Ca}_{0.4}\text{Ba}_{1.6}\text{La}_{0.4}\text{Cu}_3\text{O}_{6.96}$  ( $\text{R} = \text{Y}$  and  $\text{Gd}$ ) exhibits a  $\geq 100$  fold stability relative to  $\text{YBa}_2\text{Cu}_3\text{O}_{6.96}$ , the cosubstituted compound exhibits superconductivity at temperatures  $\sim 12\text{K}$  lower than the parent system. This value of  $T_c$  is uncomfortably close to 77 K, making the use of liquid nitrogen as a cryogen unlikely for any application that requires high critical current values. Thus, it is desirable to identify similar compositions which exhibit the enhanced materials characteristics while at the same time possessing transition temperatures above 80 K.

It is now well accepted by the scientific community that copper valence value is one of the dominant factors that controls the superconducting properties of the cuprate compounds. In an effort to try to increase the transition temperatures for the cation substituted compounds, careful studies of the composition dependence of the transition temperatures of the lattice engineered cuprate phases were completed. Since the  $\text{YBa}_2\text{Cu}_3\text{O}_7$  structure possesses two distinctly different copper sites with their own respective coordination geometries, it is essential that the contribution from both sites be ascertained independently of one another. The sheet copper valence is thought to be tied more closely to the superconducting properties than the chain copper sites. In other words, the  $\text{Cu}(2)\text{-O}_2$  sheets are thought to play a dominant role in the superconductivity, whereas the  $\text{Cu}(1)\text{O}_x$  chains serve the role of a charge reservoir.<sup>38</sup> To probe this issue carefully, a series of thermoelectric power (TEP) measurements on  $\text{YBa}_2\text{Cu}_3\text{O}_{7-\delta}$  ( $0.46 < \delta < 0.09$ ) and  $\text{Y}_{1-y}\text{Ca}_y\text{Ba}_{2-y}\text{La}_y\text{Cu}_3\text{O}_{7-\delta}$  ( $0.1 \leq y \leq 0.4$ ) samples were completed. These studies show that the measured value of TEP depends primarily on the oxygen content for the  $\text{YBa}_2\text{Cu}_3\text{O}_{7-\delta}$  system and on the substitution concentration of Ca and La for the  $\text{Y}_{1-y}\text{Ca}_y\text{Ba}_{2-y}\text{La}_y\text{Cu}_3\text{O}_{7-\delta}$  system. Unlike the parent compound, the TEP value for  $\text{Y}_{0.6}\text{Ca}_{0.4}\text{Ba}_{1.6}\text{La}_{0.4}\text{Cu}_3\text{O}_7$  samples appears to be dominated by the contribution from the  $\text{Cu}(2)\text{-O}_2$  sheets due to suppression of the signal from

chain layer.<sup>39</sup> Apparently, the Ca and La substitutions lead to structural changes and electrostatic charge redistributions within the lattice that are responsible for localization of the charge carriers within the chain structures. These results demonstrate that the TEP, the hole concentration (i.e. Cu valence) and the  $T_c$  can be adjusted by the oxygen content and/or the doping concentration of Ca and La in the two systems.

Accordingly, we have recently prepared new compounds in the family of  $Gd_{1-x}Ca_xBa_{2-y}La_yCu_3O_{7-\delta}$  ( $0 \leq x \leq 0.4$  and  $0 \leq y \leq 0.4$ ) for the purpose of increasing  $T_c$  further for the chemically stabilized high- $T_c$  compounds, exhibited the  $T_c$  values between 83 K and 77 K, as shown in Figure 7 and summarized in Table IV. In the data here, the oxygen contents were measured using iodometric titrations.<sup>34</sup> Important for the control of the transition temperature values is the sheet copper valence values. For the compound  $Gd_{0.65}Ca_{0.35}Ba_{1.625}La_{0.375}Cu_3O_7$ , an average Cu valence of 2.325 has been measured; and an average value of 2.380 has been obtained for the compound  $Gd_{0.625}Ca_{0.375}Ba_{1.675}La_{0.325}Cu_3O_7$ .<sup>40</sup> It should be noted that the  $T_c$  values are higher for all under-doped compounds ( $x < y$ ), and lower for all over-doped compounds ( $x > y$ ) than that of the balanced formulations ( $x = y$ ). From these data, it is apparent that  $Y_{0.6}Ca_{0.4}Ba_{1.6}La_{0.4}Cu_3O_7$  formulation ( $x = y = 0.4$ ) is an over-doped compound, which is consistent with the results obtained by neutron diffraction of the  $Y_{1-x}Ca_xBa_{2-y}La_yCu_3O_{7-\delta}$  system ( $0.1 \leq y \leq 0.4$ ).<sup>16,17</sup>

It should be pointed out that in order to achieve high corrosion resistance properties it was necessary to adjust the Ca and La doping levels so that a tetragonal structure is obtained. It is expected that if Ca doping level is further decreased to make the structure more underdoped,  $T_c$  will be further lowered below 81 K.

To explore the environmental reactivity characteristics of these compounds, samples were exposed to aerated water at 25°C for 7 to 30 days. Similar results to those shown in Figure 2 were obtained for the  $Gd_{1-x}Ca_xBa_{2-y}La_yCu_3O_{7-\delta}$  compounds.<sup>40</sup> The measurements demonstrate in a convincing fashion that  $Gd_{1-x}Ca_xBa_{2-y}La_yCu_3O_{7-\delta}$  samples ( $0.275 \leq x \leq 0.4$  and  $0.325 \leq y \leq$

0.4), including  $\text{Gd}_{0.6}\text{Ca}_{0.4}\text{Ba}_{1.6}\text{La}_{0.4}\text{Cu}_3\text{O}_7$ , with a tetragonal structure display remarkably high corrosion resistance as compared to the samples of  $0.1 \leq x = y \leq 0.3$  from the same family. The reactive samples having lower substitution levels possess orthorhombic crystal structures.

Having completed a large number of cation substitutions into the  $\text{YBa}_2\text{Cu}_3\text{O}_7-\delta$  lattice, we note that some increase in transition temperature up to 83K for the stable compounds can be achieved with judicious choice of rare earth ion and careful selection of doping level. Similarly, samples exhibiting moderate stability with  $T_c$  values 85-87K can be achieved with the  $\text{YBa}_{2-x}\text{Sr}_x\text{Cu}_3\text{O}_7-\delta$  system. For  $\text{YBa}_{2-x}\text{Sr}_x\text{Cu}_3\text{O}_7-\delta$  the stability is ~5 greater than  $\text{YBa}_2\text{Cu}_3\text{O}_7-\delta$ , but far more reactive than the doubly substituted systems described above.

In order to achieve both high superconducting transition temperature values and good environmental protection capabilities, we prepared a series of  $\text{YBa}_2\text{Cu}_3\text{O}_7-\delta/\text{Y}_{0.6}\text{Ca}_{0.4}\text{Ba}_{1.6}\text{La}_{0.4}\text{Cu}_3\text{O}_7-\delta$  (and related) bilayer structures. Pulsed laser ablation using stoichiometric targets of the respective compounds were used to prepare such systems. Shown in Figure 8 are resistivity values for a 3000Å  $\text{YBa}_2\text{Cu}_3\text{O}_7-\delta$  coated with 500Å of  $\text{Pr}_{0.4}\text{Gd}_{0.2}\text{Ca}_{0.4}\text{Ba}_{1.6}\text{La}_{0.4}\text{Cu}_3\text{O}_7-\delta$ . Interestingly, the bilayer structure exhibits a  $T_c$  value of ~90 K, close to the of uncapped  $\text{YBa}_2\text{Cu}_3\text{O}_7-\delta$ . Moreover, the capped structure displays excellent corrosion resistance as probed by AFM (*vide infra*), optical microscopy and accelerated corrosion measurements based on resistivity studies.

### E. Lattice engineering of N-layer compounds

Arguably, the development of a more reliable materials base represents one of the most critical factors for the further development of high- $T_c$  superconductor devices. Although difficult to prove through direct experimental measurements, it has been conjectured that motion of oxide ions at the junction areas represents a significant problem with the currently prepared high- $T_c$  devices.<sup>7</sup> Assuming this limitation is dominant for both electrode and barrier materials, we have begun to develop a new materials database in which oxygen stability characteristics are optimized

through the crystal engineering approach. Here, new N-layer compounds from the family of  $R_{1-x}Ca_xBa_{2-y}La_yCu_{3-z}M_zO_{7-\delta}$  ( $R = Y, Gd$  and  $Pr$ ;  $M = Co, Ni$  and  $Zn$ ;  $0 < x < 0.4$ ;  $0 < y < 0.4$ ;  $0 < z < 0.4$ ) have been synthesized and their stability, electrical, magnetic and crystallographic characteristics are evaluated in a systematic manner.

Critically important to the selection of materials within the  $R_{1-x}Ca_xBa_{2-y}La_yCu_{3-z}M_zO_{7-\delta}$  family is the above described prior work within the  $R_{1-x}Ca_xBa_{2-y}La_yCu_3O_{7-\delta}$  system for  $x = y = 0.4$ .<sup>33,40</sup> The inclusion of  $Ca^{2+}$  and  $La^{3+}$  substitutions combined with prior promising N-layer compositions are exploited here for the development of new N-layer compounds.

To demonstrate the utility of the described approach, the following four compositions were evaluated in some detail:

$Gd_{0.6}Ca_{0.4}Ba_{1.6}La_{0.4}Cu_{2.79}Co_{0.21}O_{7-\delta}$  ( $Co(0.21)$ ),  
 $Gd_{0.6}Ca_{0.4}Ba_{1.6}La_{0.4}Cu_{2.79}Ni_{0.21}O_{7-\delta}$  ( $Ni(0.21)$ ),  
 $Gd_{0.6}Ca_{0.4}Ba_{1.6}La_{0.4}Cu_{2.87}Zn_{0.13}O_{7-\delta}$  ( $Zn(0.13)$ ), and  
 $Pr_{0.4}Gd_{0.2}Ca_{0.4}Ba_{1.6}La_{0.4}Cu_3O_{7-\delta}$  ( $Pr(0.4)$ ). Although these compositions possess complicated formulas, in each case, single phase ceramic samples are readily prepared using conventional solid-state approaches. Similarly, standard methods of laser ablation and off-axis magnetron sputtering can be exploited to generate high quality, oriented films of such materials (*vide infra*). Characteristics of resistivity are shown in Figure 9a and Table V, obtained by 4-probe resistivity vs. temperature measurements. All of the compounds display a superconducting transition by transport measurements in the temperature range of 40 K to 50 K.

For SNS junctions, it is desirable to identify N-layer compounds that yield reproducible normal state resistance values ( $R_n$ ) at working temperature  $\leq 77$  K. Table V lists results of relative resistivity change ( $\Delta\rho/\rho$  %) near onset temperature of 60 K to 75 K. Here, a positive value indicates a semiconductor character and a negative value signifies a metallic character.

In order to further explore the properties of the new compounds, dc SQUID measurements were acquired as shown in Figure 9b. In contrast to characteristics of resistivity, the susceptibility

measurements indicate that both Ni(0.21) and Zn(0.13) substituted compounds are bulk insulators. Moreover, a very small volume of the superconducting phase is contained in Co(0.21) and an intermediate amount for the Pr(0.4) substituted samples. It is important to note that cation substitution for the Cu site leads to significant weakening of the superconducting properties. This finding is confirmed as the Pr substitution concentration is increased from 0.4 to 0.6, as shown in Figure 9c. Consequently, the critical substitution concentration of the phase transition can be identified from the data in Figure 9b and 9c. Compositions of Co(~0.21), Ni(0.21) Zn(0.13) and Pr(0.5) are found to possess substitution levels where the superconductor phase content is minimized while at the same time avoiding signatures for magnetic components that may degrade device performance characteristics. A continual increase of substitution concentration, such as Pr(>0.5), leads to the elimination of the filamentary superconductivity phenomenon. This type of behavior is consistent with the prior report for Co(>0.3) substituted  $\text{YBa}_2\text{Cu}_3\text{O}_{7-\delta}$ .<sup>41</sup> We find that the influence of Co, Ni, Zn and Pr substitutions on the superconducting properties in  $\text{R}_{1-x}\text{Ca}_x\text{Ba}_{2-y}\text{La}_y\text{Cu}_{3-z}\text{M}_z\text{O}_{7-\delta}$  system is similar to that observed for the  $\text{YBa}_2\text{Cu}_3\text{O}_{7-\delta}$  system.

The phase contents for these systems were further characterized by x-ray diffraction. The XRD studies reveal that no major phase transformations occur as the substitution levels are altered over the above described range. Rather, subtle changes in lattice constants are noted for higher substitution levels. Lattice constant mismatching ( $\Delta\ell/\ell$  %) among  $\text{YBa}_2\text{Cu}_3\text{O}_{7-\delta}$ ,  $\text{GdBa}_2\text{Cu}_3\text{O}_{7-\delta}$ ,  $\text{PrBa}_2\text{Cu}_3\text{O}_{7-\delta}$ ,  $\text{YBa}_2\text{Cu}_{2.79}\text{Co}_{0.21}\text{O}_{7-\delta}$ ,  $\text{Y}_{0.6}\text{Ca}_{0.4}\text{Ba}_{1.6}\text{La}_{0.4}\text{Cu}_3\text{O}_{7-\delta}$ ,  $\text{Gd}_{0.6}\text{Ca}_{0.4}\text{Ba}_{1.6}\text{La}_{0.4}\text{Cu}_3\text{O}_{7-\delta}$  and Pr(0.4, 0.5 and 0.6)-compounds are listed in Table VI. The mismatch is  $\leq 1.88\%$  in a-axis and  $\leq 1.43\%$  in c-axis for Pr(0.4, 0.5 and 0.6)-compounds. The results are similar to those obtained for  $\text{PrBa}_2\text{Cu}_3\text{O}_{7-\delta}$  which has been used previously as a promising N-layer material.<sup>12</sup> These studies indicate that the Pr(0.4, 0.5 and 0.6)-compounds and common high- $T_c$  electrode material are compatible with one another.

As described above for the superconductor formulations, the reactivity properties of the N-layer compounds were completed. The corrosion experiments exploited bulk samples and films which were exposed to water for specific periods of time. The measurements demonstrated that

$Gd_{0.6-x}Pr_xCa_{0.4}Ba_{1.6}La_{0.4}Cu_{3-z}M_zO_{7-\delta}$  ( $M = Co, Ni$  and  $Zn$ ;  $0 \leq x \leq 0.6$ ;  $0 \leq z \leq 0.4$ ) displayed remarkably high corrosion resistance as compared to the conventional N-layer compounds such as  $Y_{0.7}Ca_{0.3}Ba_2Cu_3O_{7-\delta}$ ,  $YBa_2Cu_2.79Co_{0.21}O_{7-\delta}$ ,  $Y_{0.6}Pr_{0.4}Ba_2Cu_3O_{7-\delta}$  and  $PrBa_2Cu_3O_{7-\delta}$ . Results for the water and oxygen stability properties for both conventional and the new lattice engineered N-layer systems are summarized in Table VI.

In addition to reactivity studies of ceramic samples, thin film specimens of the various compositions were soaked in water and their surface morphologies were probed before and after such treatments using the atomic force microscope (AFM). The film samples of  $YBa_2Cu_3O_{7-\delta}$  ( $T_c = 90$  K, 3000 Å),  $Pr_{0.4}Gd_{0.2}Ca_{0.4}Ba_{1.6}La_{0.4}Cu_3O_{7-\delta}$  ( $T_c = 24$  K, 3000 Å) and capped  $YBa_2Cu_3O_{7-\delta}$  ( $T_c = 90$  K, 3000 Å) with  $Pr_{0.4}Gd_{0.2}Ca_{0.4}Ba_{1.6}La_{0.4}Cu_3O_{7-\delta}$  (500 Å) were soaked in water at room temperature for 11 days. The AFM images for such specimens are shown in Figure 10. While the  $YBa_2Cu_3O_{7-\delta}$  films are corroded from such treatments, resulting in formation of pits for less than 5 days water exposure, no pits were detected for the capped  $YBa_2Cu_3O_{7-\delta}$  film even after 11 days water treatment. Similarly, the  $Pr_{0.4}Gd_{0.2}Ca_{0.4}Ba_{1.6}La_{0.4}Cu_3O_{7-\delta}$  N-layer film displays high corrosion resistance.

#### F. Utilization of new materials for preparation of functional devices

Having acquired a database for the reactivity characteristics for the cation substituted compounds and the parent compound  $YBa_2Cu_3O_{7-\delta}$ , further studies demonstrating the suitability of new compounds for the creation of high- $T_c$  SNS junctions have been completed and important parameters of critical currents  $I_c$  and bulk resistance  $R_n$  have been measured. It should be emphasized that device fabrication using the new compositions is only at the initial stages of development. Further optimization of deposition and processing steps is required before the suitability of the new compositions can be assessed.

The junctions were prepared by laser ablation with a high tilt angle ( $q < 20^\circ$ ). Values obtained for  $I_cR_n$  vs. reduced temperature are shown in Figure 11. Here the two electrodes,

$\text{YBa}_2\text{Cu}_3\text{O}_7-\delta$  and  $\text{Y}_{0.6}\text{Ca}_{0.4}\text{Ba}_{1.6}\text{La}_{0.4}\text{Cu}_3\text{O}_7-\delta$  (2000 Å each), are compared using in both cases a traditional compound  $\text{YBa}_2\text{Cu}_{2.79}\text{Co}_{0.21}\text{O}_7-\delta$  (75-200 Å) as the N-layer material with Au (1000 Å) for the contact layers. The I-V characteristics for 10 junctions on one chip fabricated with  $\text{Y}_{0.6}\text{Ca}_{0.4}\text{Ba}_{1.6}\text{La}_{0.4}\text{Cu}_3\text{O}_7-\delta$  as electrodes indicate that  $I_{\text{c}}R_{\text{n}}$  values of 310-560 μV at reduced temperature of 0.83 (65K/78K) and 600-850 μV at reduced temperature of 0.73 (57K/78K). These values are superior to those of 120-220 μV (74K/89K) and 390-580 μV (65K/89K) obtained for  $\text{YBa}_2\text{Cu}_3\text{O}_7-\delta$ . These  $I_{\text{c}}R_{\text{n}}$  products represent typical values obtained for the two systems. Further experiments are required before meaningful statements can be made regarding junction reproducibility characteristics; however, our initial studies demonstrate an important materials dependence of the device performance characteristics. The oxygen stabilized high- $T_{\text{c}}$  phases, when exploited as the electrode material, appear to yield devices which are superior to those achieved with the conventional materials. These  $I_{\text{c}}R_{\text{n}}$  values are (to our knowledge) the highest yet reported for operation temperatures below 65 K.

Our preliminary efforts to fabricate edge-geometry SNS junctions and dc SQUIDs using  $\text{Pr}_{0.4}\text{Gd}_{0.2}\text{Ca}_{0.4}\text{Ba}_{1.6}\text{La}_{0.4}\text{Cu}_3\text{O}_7-\delta$  as a barrier also yield quite promising results. Figure 12a shows the I-V curve from a typical dc SQUID. The SQUID had a dimension of 10 μm wide bridge for each junction and a 22 nm  $\text{Pr}_{0.4}\text{Gd}_{0.2}\text{Ca}_{0.4}\text{Ba}_{1.6}\text{La}_{0.4}\text{Cu}_3\text{O}_7-\delta$  N-layer barrier. The I-V characteristic of the junctions can be well described by resistively shunted junction (RSJ) model.<sup>42</sup> The  $I_{\text{c}}R_{\text{n}}$  for each junction were 0.065 mA and 0.35 Ω, respectively, which agreed very well with the values extracted from RSJ fit to the I-V curve. Figure 12b shows the voltage modulation vs. magnetic flux characteristics of the same dc SQUID of Figure 11a. The curve is nicely periodic and shows little, if any, hysteresis. The voltage modulation of the SQUID shows the expected bias current dependence and exhibits maximum value of 7.5 μV. However, further work is required to increase the junction resistance values which are low for  $\text{Pr}_{0.4}\text{Gd}_{0.2}\text{Ca}_{0.4}\text{Ba}_{1.6}\text{La}_{0.4}\text{Cu}_3\text{O}_7$ . Nevertheless, the interface resistance noted here is negligibly small. Moreover, the ratio of peak-to-peak ( $V_{\text{pp}}$ ) voltage modulation to  $I_{\text{c}}R_{\text{n}}$  product is over 30% in the present study. For a comparison, the ratio  $V_{\text{pp}}/I_{\text{c}}R_{\text{n}}$  of 5% has been reported for  $\text{NdBa}_2\text{Cu}_3\text{O}_7$  when used as a

N-layer barrier.<sup>43</sup> The more ideal behavior for the modified N-layer suggests that problems at the junction area attributed in the past to oxygen loss may be minimized for the new system.

#### IV CONCLUSIONS

Careful studies of the structure/reactivity characteristics of cuprate compounds have been completed. Lattice stress and strain and oxygen ordering characteristics have been identified as essential issues which influence the reactivity properties of these copper oxide materials. Studies focusing on the mechanism of decomposition of high- $T_c$  samples have revealed strong coupling between water reactivity, copper redox chemistry and oxide/oxygen evolution/uptake. This new mechanistic knowledge has led us to the development of a new materials base which includes both superconducting formulations and complimentary N-layer compounds. Chemical purity, water/oxygen stability characteristics, lattice parameters and resistivity vs. temperature features for the compounds have been acquired. Initial High- $T_c$  SNS junctions and SQUID sensors incorporating the new materials have been prepared. Promising device performance characteristics have been achieved for these systems. Further careful experiments are needed in the future to optimize both the materials choice and processing methods for the fabrication and study of high- $T_c$  devices in which all components in the junction area (both superconductor and N-layer) exploit stabilized formulations

#### ACKNOWLEDGMENT

The research in The University of Texas at Austin was supported by the Office Naval Research and the Welch Foundation. Professors Allen J. Bard, John B. Goodenough, John T. Markert and Hugo Steinfink are thanked for use of their instruments.

## REFERENCES

1. M.K. Wu, J.R. Ashburn, C.J. Torng, P.H. Hor, R.L. Meng, L. Gao, Z. J. Huang, Y.Q. Wang, and C. W. Chu, *Phys. Rev. Lett.*, **58**, 908 (1987).
2. X.D. Wu, S.R. Foltyn, P. Arendt, J. Townsend, C. Adams, I.H. Campbell, P. Tiwari, Y. Coulter, and D. E. Peterson, *Appl. Phys. Lett.* **65**, 1961 (1994).
3. R. Gross, P. Chaudhari, M. Kawasaki, M.B. Ketchen, and A. Gupta, *Appl. Phys. Lett.* **57**, 727 (1990).
4. F.C. Wellstood, J.J. Kingston, and J. Clarke, *Appl. Phys. Lett.* **56**, 336 (1990).
5. M.F. Yan, R.L. Barnes, H.M. O'Bryan Jr., P.K. Gallagher, R.C. Sherwood, and S. Jin, *Appl. Phys. Lett.* **51**, 532 (1987).
6. J. P. Zhou, D. Riley, A. Manthiram, M. Arendt, M. Schmerling and J.T. McDevitt, *Appl. Phys. Lett.* **63**, 548 (1993).
7. K. Char, L. Antognazza, and T.H. Geball, *Appl. Phys. Lett.* **65**, 904 (1994).
8. B.D. Hunt, M. G. Forrester, J. Talvacchio, J.D. McCambridge, and R.M. Young, *Appl. Phys. Lett.* **68**, 3805 (1996).
9. K. Char, L. Antognazza, and T.H. Geball, *Appl. Phys. Lett.* **63**, 2420 (1994).
10. Q.X. Jia, D. Reagor, S.R. Foltyn, M.Hawley, C. Mombourquette, K.N. Springer, and X.D. Wu, *Physica C* **228**, 160 (1994).
11. Q.X. Jia, X.D. Wu, D.W. Reagor, S.R. Foltyn, R.J. Houlton, P. Tiwari, C. Mombourquette, I.H. Campbell, F. Garzon, and D.E. Peterson, *Appl. Phys. Lett.* **78**, 2871 (1995).
12. M.I. Faley, U. Poppe, H. Soltner, C. L. Jia, M. Siegel, and K. Urban, *Appl. Phys. Lett.* **63**, 2139 (1993).
13. J.P. Zhou, D.R. Riley, J.T. McDevitt, *Chem. Mater.* **5**, 361 (1993).
14. J.P. Zhou, J.T. McDevitt, *Solid State Commun.* **86**, 11 (1993).
15. A. Manthiram, and J.B. Goodenough, *Physica C* **159**, 760 (1989).
16. C. R. Slater and C. Greaves, *Supercond. Sci. Technol.* **5**, 205 (1992).
17. H. Rajagopal, A. Sequeira, R. Ganguly, and J.V. Yakhmi, *J. Superconductivity* **9**, 615 (1997).
18. J.R. Gavaler, J. Talvacchio, T.T. Braggins, and M.G. Forrester, *J. Appl. Phys.* **70**, 4383 (1991).

19. J.P. Zhou, R.-K. Lo, S.M. Savoy, M. Arendt, J. Armstrong, D-Y. Yang, J.Talvacchio and J.T. McDevitt, *Physica C* **273**, 223 (1997).
20. I.D. Brown, *J. Solid State Chem.* **90**, 1952 (1991),
21. I.D. Brown, *Phys.Chem. Mineral.* **15**, 30 (1987).
22. I.D. Brown and D. Altermatt, *Acta Crystallogr. Sect. B* **41**, 244 (1985).
23. J.G. Thompson, B.G. Hyde, R.L. Withers, J.S. Anderson, J.D. Fitz Gerald, J. Bitmead, M.S. Paterson, and A.M. Stewart. *Mat. Res. Bull.* **22**, 1715 (1987); H.W. Zandbergen, R. Gronsky, and G. Thomas, *Phys. Stat. Sol.* **105**, 207 (1988).
24. W.I.F. David, W.T.A. Harrison, J.M.F. Gunn, O. Moze, A.K. Soper, P. Day, J.D. Jorgensen, D.G. Hinks, M.A. Beno, L. Soderholm, D.W. Capone II, I.K. Schuller, C.U. Segre, K. Zhang, and J.D. Grace, *Nature* **327**, 310 (1987).
25. S. Uchida, In *Low Temperature Physics: Progress in High Temperature Superconductivity*, edited by J. Heiras, R.A. Barrio, T. Akathi, and J. Taguena, (*Proc.IX Winter Meeting*, 5, World Scientific, Singapore, 1988), p.63.
26. B.W. Veal, W.K. Kwok, A. Umezawa, G.W. Crabtree, J.D. Jorgensen, J.W. Downey, L.J. Nowicki, A.W. Mitchell, A.P. Paulikaus, and C.H. Sowers, *Appl. Phys. Lett.* **51**, 279 (1987).
27. C.U. Segre, B. Dabrowski, D.G. Hinks, K. Zhang, J.D. Jorgensen, M.A. Beno, and I.K. Schuller, *Nature* **329**, 227 (1987).
28. A. Manthiram, X.X. Tang, and J.B. Goodenough, *Phys. Rev. B* **37**, 3734 (1988).
29. J.M. Tarascon, P. Barboux, P.F. Miceli, L.H. Greene, G.W. Hull, M. Eibschutz, and S.A. Sunshine, *Phys. Rev. B* **37**, 7458 (1988).
30. R. D. Shannon, *Acta Cryst. A* **32**, 751 (1976).
31. Y. Tokura, J.B. Torrance, T.C. Huang, and A.I. Nazzal, *Phys. Rev. B* **28**, 7156 (1988).
32. J.P. Zhou, D.R. Riley, Y.T. Zhu, A. Manthiram, and J. T. McDevitt, *J. Am. Chem. Soc.* **116**, 9389 (1994).
33. J.P. Zhou, S.M. Savoy, R.-K. Lo, J. Zhao, M. Arendt, Y.T. Zhu, and J.T. McDevitt, *Appl. Phys. Lett.* **66**, 2900 (1995).

34. A. Manthiram, J.S. Swinnea, Z.T. Sui, H. Steinfink, J.B. Goodenough, *J. Am. Chem. Soc.* **109**, 667 (1987).
35. L.T. Tallon and B.-E. Mellander, *Science* **258**, 781 (1992).
36. P. Strobel, J.J. Capponi, C. Chaillout, M. Marezio, and J. L. Tholence, *Nature* **327**, 306 (1987).
37. J.M. Tarascon, P. Barboux, P.F. Miceli, L.H. Greene, G.W. Hull, M. Eibschutz, and A. Sunshine, *Phys. Rev. B* **37**, 7458 (1988).
38. R.J. Cava, B. Batlogg, K.M. Rabe, E.A. Rietman, P.K. Gallagher, and L.W. Rupp Jr., *Physica C* **156**, 523 (1988).
39. J.-S. Zhou, J.P. Zhou, J.B. Goodenough, and J.T. McDevitt, *Phys. Rev. B*, **51**, 3250 (1995).
40. J.P. Zhou and J.T. McDevitt, *IEEE Trans. Appl. Supercond.* (in press 1997).
41. B. Moeckly and K. Char, *Physica C* **265**, 283 (1996).
42. W.C. Stewart, *Appl. Phys. Lett.* **12**, 277 (1968); D.E. McCumber, *J. Appl. Phys.* **39**, 3113 (1968).
43. B. Oh, Y.H. Choi, S.H. Moon, H.T. Kim, and B.C. Min, *Appl. Phys. Lett.* **69**, 2288 (1996).
44. K. Kebede, C.S. Jee, J. Schwegler, J.E. Crow, T. Mihalisin, G.H. Myer, R.E. Salomon, P. Schlottmann, M.V. Kuric, S.H. Bloom, and R.P. Guertin, *Phys. Rev. B* **40**, 4453 (1989).
45. M. Cantoni, and H.U. Nissen, *Physica C* **211**, 404 (1993).

TABLE I. Calculation of Ba(La)-O1 bond lengths (R), strains (e) in  $\text{YBa}_{2-y}\text{La}_y\text{Cu}_3\text{O}_7$  ( $0.1 \leq y \leq 0.4$ ).

La concentration (y)	0.0	0.1	0.2	0.3	0.4
Calculated R ( $\text{\AA}$ )	2.798	2.785	2.772	2.759	2.746
Measured R ( $\text{\AA}$ )	2.748	2.748	2.742	2.738	2.736
Difference $\Delta R$ ( $\text{\AA}$ )	-0.050	-0.037	-0.030	-0.021	-0.010
Strain e (%)	-1.79	-1.33	-1.07	-0.75	-0.35

Equation sums for calculation of bond lengths and strains

Bond valence sum (BVS)	$V_i = \sum s_{ij}$	$V_i$ —bond valence sum $s_{ij}$ —bond valence
	$s_{ij} = \exp [(R_O - R_{ij}) / B]$	$R_O$ —tabulated bond length ( $\text{\AA}$ ) B—constant (0.37)
	$R_{ij} = R_O - B \ln s_{ij}$	$R_{ij}$ —bond length ( $\text{\AA}$ )
Difference $\Delta R$	$\Delta R_{ij} = [(a/2) 2^{1/2}] - R_{ij}$	$a$ (or b)—lattice constant ( $\text{\AA}$ )
Strain e (%)	$e = R_{ij} / [(a/2) 2^{1/2}]$	

Here, the bond valence sum of cation (i) is a summation of the bond valence between cation(i) and anion (j). The bond valence ( $s_{ij}$ ) is dependent on the corresponding bond length ( $R_{ij}$ ). The analysis has been simplified somewhat in that the small effect of the  $\text{CuO}_2$  sheet puckering for  $\text{YBa}_2\text{Cu}_3\text{O}_7$  is ignored.<sup>20,21</sup> The  $R_O$  value represents the tabulated ionic radius.<sup>22</sup> Values for the mixture of cations are obtained from the weighted average of the constituent ions, e.g.  $R_{ij} = (1.6(\text{Ba-O}) + 0.4(\text{La-O}))/2$  is used for the  $\text{YBa}_{1.6}\text{La}_{0.4}\text{Cu}_3\text{O}_7$  compound. Values of  $R_{ij}$  measured can be obtained precisely from neutron diffraction. In the absence of such data, approximate values for the average bond length are obtained from the lattice parameters as measured by x-ray powder diffraction, e.g.  $R_{ij} = (a/2) 2^{1/2}$  for the average of the  $(\text{Ba}_{1.6}\text{La}_{0.4})\text{-O}$  bond length.

Table II. Open circuit potentials for a variety of metals,  $\text{YBa}_2\text{Cu}_3\text{O}_7-\delta$  and  $\text{Y}_{0.6}\text{Ca}_{0.4}\text{Ba}_{1.6}\text{La}_{0.4}\text{Cu}_3\text{O}_7-\delta$  samples recorded in a 0.6 N NaCl solution and a pH~4.6 buffer solution (sodium acetate/acetic acid).

Electrode material	Solution	Potential (V vs. SSCE)
Au	0.6 M NaCl	0.24
Ag	0.6 M NaCl	-0.09
Cu	0.6 M NaCl	-0.25
In foil	0.6 M NaCl	-0.68
Mg ribbon	0.6 M NaCl	-1.65
Pt	0.6 M NaCl	0.32
$\text{YBa}_2\text{Cu}_3\text{O}_7$ pellet	0.6 M NaCl	0.43
$\text{YBa}_2\text{Cu}_3\text{O}_7$ pellet	pH~0.46 buffer	0.95
$\text{YBa}_2\text{Cu}_3\text{O}_7$ film	0.6 M NaCl	0.51
$\text{YBa}_2\text{Cu}_3\text{O}_7$ film	pH~0.46 buffer	0.98
$\text{Y}_{0.6}\text{Ca}_{0.4}\text{Ba}_{1.6}\text{La}_{0.4}\text{Cu}_3\text{O}_7$ pellet	0.6 M NaCl	0.45
$\text{Y}_{0.6}\text{Ca}_{0.4}\text{Ba}_{1.6}\text{La}_{0.4}\text{Cu}_3\text{O}_7$ pellet	pH~0.46 buffer	0.96
$\text{Y}_{0.6}\text{Ca}_{0.4}\text{Ba}_{1.6}\text{La}_{0.4}\text{Cu}_3\text{O}_7$ film	0.6 M NaCl	0.75
$\text{Y}_{0.6}\text{Ca}_{0.4}\text{Ba}_{1.6}\text{La}_{0.4}\text{Cu}_3\text{O}_7$ film	pH~0.46 buffer	0.99

TABLE III. Transition temperature and stability for  $\text{YBa}_2\text{Cu}_3\text{O}_{7-\delta}$  family.

Composition	$T_c$ (K)	Structure (O/T) <sup>a</sup>	Water Reactivity R/S <sup>b</sup>	Oxygen Stability R/S <sup>b</sup>
$\text{YBa}_2\text{Cu}_3\text{O}_{6.96}$	90	O	R	R
$\text{YBa}_2\text{Cu}_3\text{O}_{6.59}$	60	O	R	R
$\text{YBa}_2\text{Cu}_3\text{O}_{6.05}$	--	T	R	R
$\text{YBa}_{1.9}\text{Sr}_{0.1}\text{Cu}_3\text{O}_{6.96}$	90	O	R	R
$\text{YBa}_{1.8}\text{Sr}_{0.2}\text{Cu}_3\text{O}_{6.96}$	89	O	R	R
$\text{YBa}_{1.6}\text{Sr}_{0.4}\text{Cu}_3\text{O}_{6.96}$	87	O	R	R
$\text{YBa}_{1.4}\text{Sr}_{0.6}\text{Cu}_3\text{O}_{6.97}$	85	O	M	M
$\text{Y}_{0.9}\text{Ca}_{0.1}\text{Ba}_{1.9}\text{La}_{0.1}\text{Cu}_3\text{O}_{6.97}$	85	O	R	R
$\text{Y}_{0.8}\text{Ca}_{0.2}\text{Ba}_{1.8}\text{La}_{0.2}\text{Cu}_3\text{O}_{6.96}$	83	O	M	M
$\text{Y}_{0.7}\text{Ca}_{0.3}\text{Ba}_{1.7}\text{La}_{0.3}\text{Cu}_3\text{O}_{6.95}$	80	O	M	M
$\text{Y}_{0.6}\text{Ca}_{0.4}\text{Ba}_{1.6}\text{La}_{0.4}\text{Cu}_3\text{O}_{6.96}$	80	T	S	S
$\text{Gd}_{0.9}\text{Ca}_{0.1}\text{Ba}_{1.9}\text{La}_{0.1}\text{Cu}_3\text{O}_{6.96}$	85	O	R	R
$\text{Gd}_{0.8}\text{Ca}_{0.2}\text{Ba}_{1.8}\text{La}_{0.2}\text{Cu}_3\text{O}_{6.96}$	83	O	M	M
$\text{Gd}_{0.7}\text{Ca}_{0.3}\text{Ba}_{1.7}\text{La}_{0.3}\text{Cu}_3\text{O}_{6.97}$	80	O	M	M
$\text{Gd}_{0.6}\text{Ca}_{0.4}\text{Ba}_{1.6}\text{La}_{0.4}\text{Cu}_3\text{O}_{6.96}$	80	T	S	S

<sup>a</sup> "O" refers to "orthorhombic" and "T" refer to "tetragonal"; <sup>b</sup> Water reactivity and oxygen stability are determined from observations of ceramic samples upon exposure to water. In case of water reactivity, the rate of appearance of  $\text{BaCO}_3$  crystals is used to evaluate the decomposition rate. For oxygen stability, the evolution rate of oxygen bubbles from the sample surface is observed. Qualitative descriptions of the water reactivity and oxygen stability are included in the Table. A composition is designated as "R" (i.e. reactive) if it exhibits decomposition characteristics similar to  $\text{YBa}_2\text{Cu}_3\text{O}_{6.96}$ . For system exhibiting a modest increase in stability, a "M" label (moderate) is applied. These systems exhibit 10 to 50 times increase in stability relative to  $\text{YBa}_2\text{Cu}_3\text{O}_{6.96}$ . For systems exhibiting very stable properties, a label of "S" (stable) is exploited. These systems possess  $\geq 100$  fold increase in stability relative to  $\text{YBa}_2\text{Cu}_3\text{O}_{6.96}$ .

TABLE IV. Effects of doping concentration and average Cu valence ( $Cu^{n+}$ ) on transition temperature.

Sample composition	Doping <sup>a</sup> level	$Cu^{n+}$	$T_c$ <sup>b</sup> (K)
Gd <sub>0.725</sub> Ca <sub>0.275</sub> Ba <sub>1.625</sub> La <sub>0.375</sub> Cu <sub>3</sub> O <sub>7</sub>	under	2.30	81
Gd <sub>0.675</sub> Ca <sub>0.325</sub> Ba <sub>1.625</sub> La <sub>0.375</sub> Cu <sub>3</sub> O <sub>7</sub>	under	2.317	82
Gd <sub>0.65</sub> Ca <sub>0.35</sub> Ba <sub>1.625</sub> La <sub>0.375</sub> Cu <sub>3</sub> O <sub>7</sub>	under	2.325	83
Gd <sub>0.6</sub> Ca <sub>0.4</sub> Ba <sub>1.6</sub> La <sub>0.4</sub> Cu <sub>3</sub> O <sub>7</sub>	balanced	2.33	81
Gd <sub>0.625</sub> Ca <sub>0.375</sub> Ba <sub>1.65</sub> La <sub>0.35</sub> Cu <sub>3</sub> O <sub>7</sub>	over	2.34	78
Gd <sub>0.625</sub> Ca <sub>0.375</sub> Ba <sub>1.675</sub> La <sub>0.325</sub> Cu <sub>3</sub> O <sub>7</sub>	over	2.38	77

<sup>a</sup> For this study a copper formal valence value of 2.33 is considered to be balanced. Formal copper oxidation levels less than this value are considered as "under-doped" and those greater are described as being "over-doped"; <sup>b</sup>  $T_c$  is the transition temperature at zero resistance. Note: the oxygen content employed as 7 is based on samples treated at complete same condition and iodometric titration results of 6.96-7.03.

TABLE V. Compositions and resistivity properties for various N-layer compounds.

<u>composition</u>	<u><math>T_c/T_o</math></u> <sup>a</sup> (K)	<u><math>\Delta\rho/\rho</math></u> <sup>b</sup> (% at $T_o$ -295K)	<u><math>\Delta\rho/\rho</math></u> <sup>c</sup> (% at 60-75K)
$Pr_{0.4}Gd_{0.2}Ca_{0.4}Ba_{1.6}La_{0.4}Cu_3O_{7-d}$ ( $Pr(0.4)$ )	40/44	-61.2	-3.24
$Gd_{0.6}Ca_{0.4}Ba_{1.6}La_{0.4}Cu_{2.79}Co_{0.21}O_{7-d}$ ( $Co(0.21)$ )	45/55	-64.3	-9.69
$Gd_{0.6}Ca_{0.4}Ba_{1.6}La_{0.4}Cu_{2.79}Ni_{0.21}O_{7-d}$ ( $Ni(0.21)$ )	48/53	-53.3	+0.74
$Gd_{0.6}Ca_{0.4}Ba_{1.6}La_{0.4}Cu_{2.87}Zn_{0.13}O_{7-d}$ ( $Zn(0.13)$ )	45/50	-54.9	+0.46

<sup>a</sup>  $T_c$  is the zero resistance transition temperature and  $T_o$  is the onset temperature; <sup>b</sup> resistivity change at the onset temperature relative to the value at room temperature; <sup>c</sup> resistivity change at 60 K relative to that at 75 K.

TABLE VI. Lattice parameters and chemical reactivity properties of  $\text{YBa}_2\text{Cu}_3\text{O}_{7-\delta}$ ,  $\text{GdBa}_2\text{Cu}_3\text{O}_{7-\delta}$ , Ca and La substituted superconducting electrodes, and Co and Pr substituted N-layer compounds.<sup>16,37,44,45</sup>

Sample	Function E/N <sup>a</sup>	a-axis (Å)	b-axis (Å)	c-axis (Å)	Mismatching YBCO <sup>b</sup>	$\Delta\ell/\ell$ (%) GBCO <sup>c</sup>	Water Reactivity R/S <sup>d</sup>	Oxygen Stability R/S <sup>e</sup>
$\text{YBa}_2\text{Cu}_3\text{O}_{7-\delta}$	E	3.819	3.886	11.678			R	R
$\text{GdBa}_2\text{Cu}_3\text{O}_{7-\delta}$	E	3.836	3.895	11.699			R	R
$\text{Y}_{0.6}\text{Ca}_{0.4}\text{Ba}_{1.6}\text{La}_{0.4}\text{Cu}_3\text{O}_{7-\delta}$	E	3.851	3.851	11.653	$\Delta\text{a/a}$ —0.83 $\Delta\text{b/b}$ —0.90 $\Delta\text{c/c}$ —0.21	0.39 1.12 0.39	S	S
$\text{Gd}_{0.6}\text{Ca}_{0.4}\text{Ba}_{1.6}\text{La}_{0.4}\text{Cu}_3\text{O}_{7-\delta}$	E	3.866	3.866	11.701	$\Delta\text{a/a}$ —1.23 $\Delta\text{b/b}$ —0.51 $\Delta\text{c/c}$ —0.45	0.78 0.74 0.01	S	S
$\text{PrBa}_2\text{Cu}_3\text{O}_{7-\delta}$	N	3.880	3.922	11.704	$\Delta\text{a/a}$ —1.59 $\Delta\text{b/b}$ —0.92 $\Delta\text{c/c}$ —0.22	1.14 0.69 0.04	R	R
$\text{YBa}_2\text{Cu}_{2.79}\text{Co}_{0.21}\text{O}_{7-\delta}$	N	3.867	3.867	11.684	$\Delta\text{a/a}$ —1.25 $\Delta\text{b/b}$ —0.48 $\Delta\text{c/c}$ —0.05	0.80 0.71 0.12	R	R
$\text{Pr}_{0.4}\text{Gd}_{0.2}\text{Ca}_{0.4}\text{Ba}_{1.6}\text{La}_{0.4}\text{Cu}_3\text{O}_{7-\delta}$	N	3.875	3.875	11.661	$\Delta\text{a/a}$ —1.46 $\Delta\text{b/b}$ —0.28 $\Delta\text{c/c}$ —0.14	1.01 0.51 0.32	S	S
$\text{Pr}_{0.5}\text{Gd}_{0.1}\text{Ca}_{0.4}\text{Ba}_{1.6}\text{La}_{0.4}\text{Cu}_3\text{O}_{7-\delta}$	N	3.885	3.885	11.697	$\Delta\text{a/a}$ —1.72 $\Delta\text{b/b}$ —0.02 $\Delta\text{c/c}$ —0.16	0.01 0.16 0.01	S	S
$\text{Pr}_{0.6}\text{Ca}_{0.4}\text{Ba}_{1.6}\text{La}_{0.4}\text{Cu}_3\text{O}_{7-\delta}$	N	3.891	3.891	11.720	$\Delta\text{a/a}$ —1.88 $\Delta\text{b/b}$ —0.12 $\Delta\text{c/c}$ —0.35	1.43 0.10 0.17	S	S

<sup>a</sup> Function "E" and "N" refer to "electrode" and "N-layer" materials; <sup>b</sup>  $\text{YBa}_2\text{Cu}_3\text{O}_{7-\delta}$  = YBCO; <sup>c</sup>  $\text{GdBa}_2\text{Cu}_3\text{O}_{7-\delta}$  = GBCO; <sup>d</sup> For the water reactivity, R is reactive and S is stable; and <sup>e</sup> For the oxygen stability, R is reactive and S is stable. See footnotes for Table III.

## FIGURE CAPTIONS

FIG. 1. Lattice structures for  $\text{YBa}_2\text{Cu}_3\text{O}_7$  and  $\text{Y}_{0.6}\text{Ca}_{0.4}\text{Ba}_{1.6}\text{La}_{0.4}\text{Cu}_3\text{O}_7$  compounds. Show here are a) the  $\text{YBa}_2\text{Cu}_3\text{O}_7$  perovskite structure which contains the  $\text{CuO}_2$ ,  $\text{CuO}$ ,  $\text{BaO}$ , and  $\text{Y}$  layers stacked along the  $c$ -axis. During the initial stages of corrosion molecules of water enter the high- $T_C$  lattice through the open channels which exist along the  $b$ -axis at  $\text{CuO}$  chain layers. The open lattice structure should facilitate the internal oxygen diffusion. b) On the other hand, the  $\text{Y}_{1-y}\text{Ca}_y\text{Ba}_{2-y}\text{La}_y\text{Cu}_3\text{O}_7$  material for  $x = y = 0.4$  possesses a tetragonal structure in which rearrangement of oxide ions in the  $\text{CuO}$  chain layer results in the loss of the open channels. These structural changes should serve to restrict internal diffusion of  $\text{H}_2\text{O}/\text{O}_2$  and reduce reactivity exhibited by the cation-substituted compound.

FIG. 2. Scanning electron micrographs showing changes in the surface morphologies of ceramic pellets of various cuprate materials that were exposed to room temperature aerated water solution. a)  $\text{YBa}_2\text{Cu}_3\text{O}_7$  pellet is shown prior to its water exposure for 2 days; b)  $\text{YBa}_2\text{Cu}_{2.79}\text{Co}_{0.21}\text{O}_7$  pellet is illustrated following its soaking in water for 2 days; c)  $\text{Y}_{0.6}\text{Ca}_{0.4}\text{Ba}_{1.6}\text{La}_{0.4}\text{Cu}_3\text{O}_7$  prior to water treatment for 30 days; and d)  $\text{Y}_{0.6}\text{Ca}_{0.4}\text{Ba}_{1.6}\text{La}_{0.4}\text{Cu}_{2.79}\text{Co}_{0.21}\text{O}_7$  sample is shown following a 30 days water exposure.

FIG. 3. Oxygen stoichiometry vs. quenching temperature measured for cuprate ceramic pellet samples which were equilibrated at different temperatures in 1 atm of  $\text{O}_2$  and then quenched in liquid nitrogen. Two different samples of compositions  $\text{YBa}_2\text{Cu}_3\text{O}_7$  and  $\text{Y}_{0.6}\text{Ca}_{0.4}\text{Ba}_{1.6}\text{La}_{0.4}\text{Cu}_3\text{O}_7$  were evaluated in this manner. Oxygen content values were determined via iodometric titrations.

FIG. 4. Resistance vs. time data recorded for two 2000 Å thick films of  $\text{YBa}_2\text{Cu}_3\text{O}_7-\delta$  (marked as A) and  $\text{Y}_{0.6}\text{Ca}_{0.4}\text{Ba}_{1.6}\text{La}_{0.4}\text{Cu}_3\text{O}_7-\delta$  (marked as B) maintained at a temperature of  $450^\circ\text{C}$  in a vacuum chamber. Films were fully oxygenated in 1.0 atm of  $\text{O}_2$ . Then at  $t$  (time) = 0, the  $\text{O}_2$  content was decreased to 1.0 torr. Here the  $\text{YBa}_2\text{Cu}_3\text{O}_7-\delta$  sample is found to lose oxygen much more rapidly than  $\text{Y}_{0.6}\text{Ca}_{0.4}\text{Ba}_{1.6}\text{La}_{0.4}\text{Cu}_3\text{O}_7-\delta$  as indicated by a factor 4. The process was then reversed with oxygen content increasing to 1.0 atm at a time as indicated by curve. The effect is shown again to occur more slowly for the  $\text{Y}_{0.6}\text{Ca}_{0.4}\text{Ba}_{1.6}\text{La}_{0.4}\text{Cu}_3\text{O}_7-\delta$  compound.

FIG. 5. Scanning electron micrographs of various metal layers (~1000 Å thick) which were deposited directly on top of a  $\text{YBa}_2\text{Cu}_3\text{O}_{7-\delta}$  thin film and then exposed to water solution for 1 hour the following samples were evaluated in this context: a)  $\text{Cu}/\text{YBa}_2\text{Cu}_3\text{O}_{7-\delta}$ , b)  $\text{Ag}/\text{YBa}_2\text{Cu}_3\text{O}_{7-\delta}$ , c)  $\text{Au}/\text{YBa}_2\text{Cu}_3\text{O}_{7-\delta}$ , and d)  $\text{Pt}/\text{YBa}_2\text{Cu}_3\text{O}_{7-\delta}$ . The Cu pad is the most severely degraded and shows no clear boundary with uncorroded area, however, others show a clear boundary by arrows.

FIG. 6. A series of scanning electron micrographs are provided for three identical  $\text{YBa}_2\text{Cu}_3\text{O}_7$  pellets soaked in aerated water solution for a period of 1 day. The influence of applied potential on the rate surface corrosion was evaluated for sample a) at -0.8 V, b) at 0.0 V and c) at +0.8 V vs. the SSCE reference. While samples held at -0.8 and 0.0 V degraded rapidly, the specimen biased at 0.8 V showed little, if any, evidence for decomposition.

FIG. 7. Resistivity vs. temperature curves in the superconducting transition region are provided for seven compounds in the  $\text{Gd}_{1-x}\text{Ca}_x\text{Ba}_{2-y}\text{La}_y\text{Cu}_3\text{O}_{7-\delta}$  system ( $0 \leq x \leq 4$  and  $0 \leq y \leq 4$ ). Small differences in the x and y substitution levels are used to evaluate the transition temperature dependence of Copper valence.

FIG. 8. Resistivity vs. temperature measurements for thin film samples:  $\text{YBa}_2\text{Cu}_3\text{O}_{7-\delta}$  film (3000 Å) with  $T_c$  of 90 K,  $\text{Pr}_{0.4}\text{Gd}_{0.2}\text{Ca}_{0.4}\text{Ba}_{1.6}\text{La}_{0.4}\text{Cu}_3\text{O}_{7-\delta}$  ( $\text{Pr}(0.4)$ ) (3000 Å) with  $T_c$  of 28 K and capped  $\text{YBa}_2\text{Cu}_3\text{O}_{7-\delta}$  (3000 Å) with  $\text{Pr}(0.4)$  (500 Å) and  $T_c$  of ~90 K.

FIG. 9. a) Resistivity vs. temperature measurements for compounds:

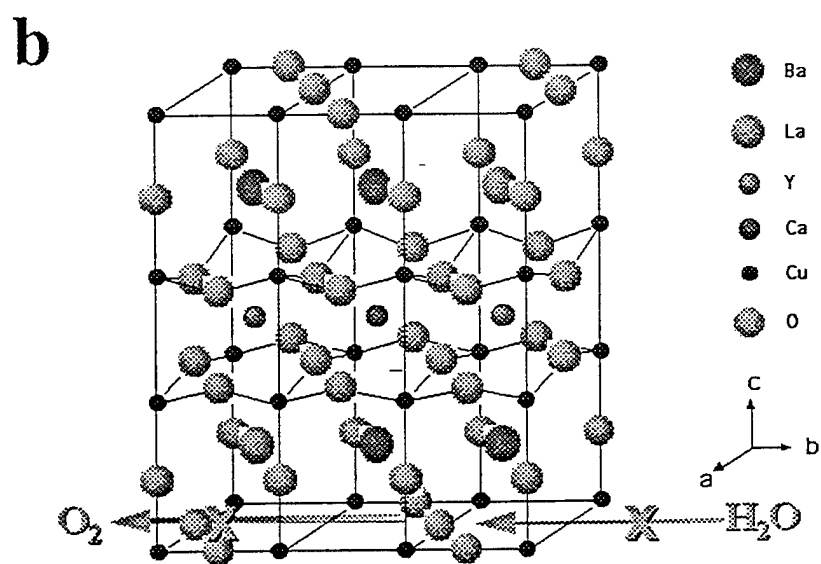
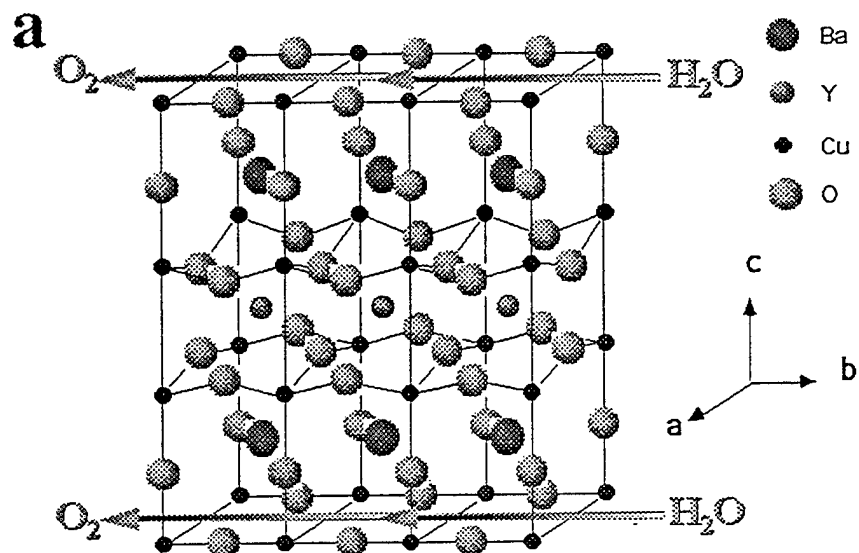
$\text{Gd}_{0.6}\text{Ca}_{0.4}\text{Ba}_{1.6}\text{La}_{0.4}\text{Cu}_{2.79}\text{Co}_{0.21}\text{O}_{7-\delta}$  ( $\text{Co}(0.21)$ ),  $\text{Gd}_{0.6}\text{Ca}_{0.4}\text{Ba}_{1.6}\text{La}_{0.4}\text{Cu}_{2.79}\text{Ni}_{0.21}\text{O}_{7-\delta}$  ( $\text{Ni}(0.21)$ ),  $\text{Gd}_{0.6}\text{Ca}_{0.4}\text{Ba}_{1.6}\text{La}_{0.4}\text{Cu}_{2.87}\text{Zn}_{0.13}\text{O}_{7-\delta}$  ( $\text{Zn}(0.13)$ ), and  $\text{Pr}_{0.4}\text{Gd}_{0.2}\text{Ca}_{0.4}\text{Ba}_{1.6}\text{La}_{0.4}\text{Cu}_3\text{O}_{7-\delta}$  ( $\text{Pr}(0.4)$ ). All such systems exhibit transition  $T_c$  values in the range of 40 to 50 K. b) Magnetization susceptibility vs. temperature of the same four compounds. c) Magnetization susceptibility of  $\text{Gd}_{0.6-x}\text{Pr}_x\text{Ca}_{0.4}\text{Ba}_{1.6}\text{La}_{0.4}\text{Cu}_3\text{O}_{7-\delta}$  ( $x = 0.4, 0.5, 0.6$ ) compounds.

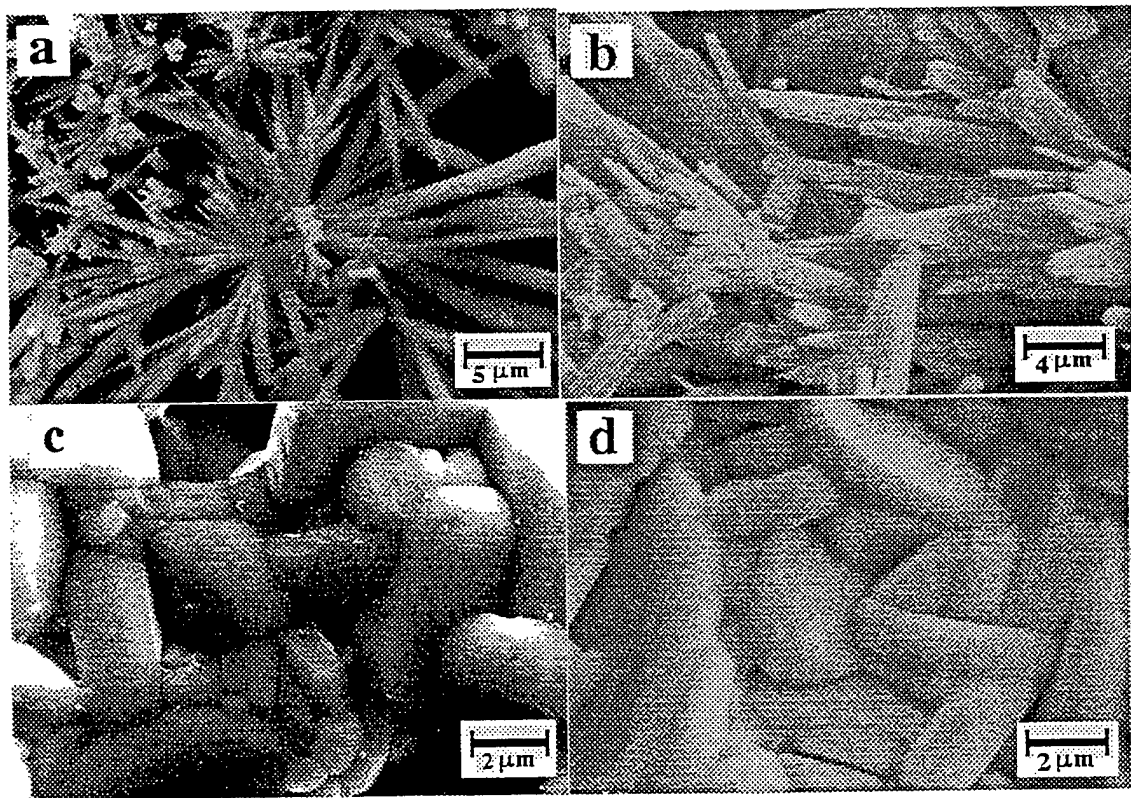
FIG. 10. Surface morphological details obtained for film samples by atomic force microscopy before and after their exposure to water solution for 11 days. The following samples were evaluated in this context: a)  $\text{YBa}_2\text{Cu}_3\text{O}_{7-\delta}$  film (3000 Å) before, b)  $\text{YBa}_2\text{Cu}_3\text{O}_{7-\delta}$  film (3000 Å) after water, c)  $\text{Pr}_{0.4}\text{Gd}_{0.2}\text{Ca}_{0.4}\text{Ba}_{1.6}\text{La}_{0.4}\text{Cu}_3\text{O}_{7-\delta}$  film (3000 Å) before, d)  $\text{Pr}_{0.4}\text{Gd}_{0.2}\text{Ca}_{0.4}\text{Ba}_{1.6}\text{La}_{0.4}\text{Cu}_3\text{O}_{7-\delta}$  film (3000 Å) after water, e)  $\text{YBa}_2\text{Cu}_3\text{O}_{7-\delta}$  (3000 Å) capped with  $\text{Pr}_{0.4}\text{Gd}_{0.2}\text{Ca}_{0.4}\text{Ba}_{1.6}\text{La}_{0.4}\text{Cu}_3\text{O}_{7-\delta}$  (500 Å) after water.

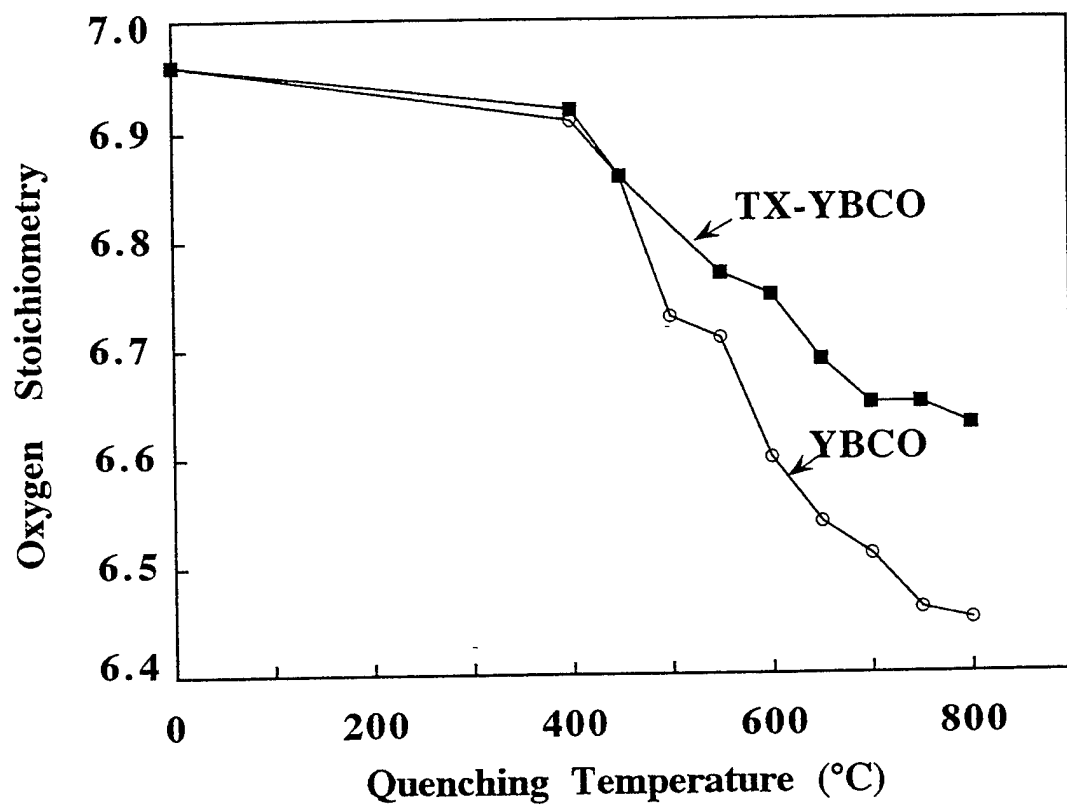
Å) before and f) capped  $\text{YBa}_2\text{Cu}_3\text{O}_{7-\delta}$  film after water treatment. The water treated bare  $\text{YBa}_2\text{Cu}_3\text{O}_{7-\delta}$  film exhibits severe pits, as indicated by "I". The monolithic  $\text{Pr}_{0.4}\text{Gd}_{0.2}\text{Ca}_{0.4}\text{Ba}_{1.6}\text{La}_{0.4}\text{Cu}_3\text{O}_{7-\delta}$  film and the capped  $\text{YBa}_2\text{Cu}_3\text{O}_{7-\delta}$  show no evidence for such surface decomposition.

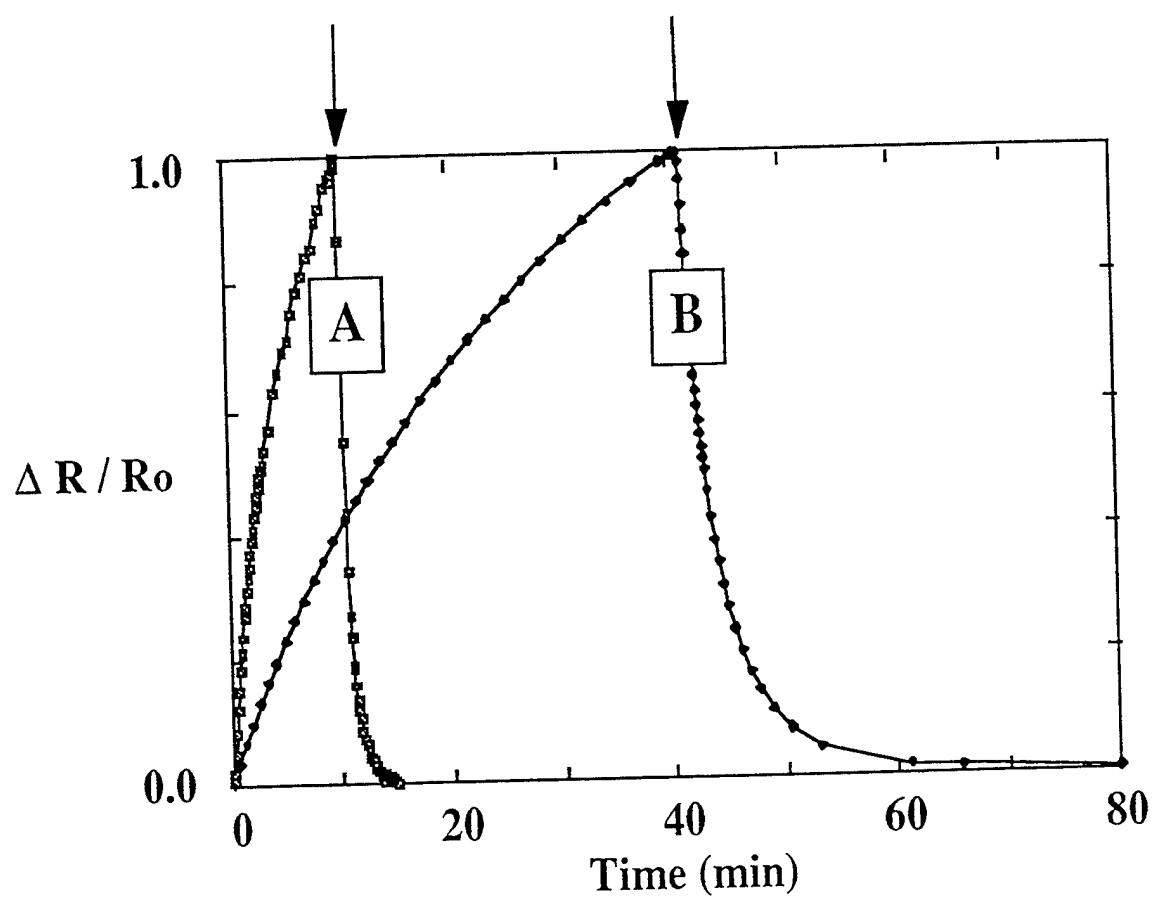
FIG. 11. Values of  $I_c R_n$  are compared for edge-type SNS junctions as a function of reduced temperature (i.e.  $T/T_c$ ). Data is provided for two different superconductor electrode materials: a)  $\text{YBa}_2\text{Cu}_3\text{O}_{7-\delta}$  (marked as A) and  $\text{Y}_{0.6}\text{Ca}_{0.4}\text{Ba}_{1.6}\text{La}_{0.4}\text{Cu}_3\text{O}_{7-\delta}$  (marked as B). In both cases  $\text{YBa}_2\text{Cu}_{2.79}\text{Co}_{0.21}\text{O}_{7-\delta}$  is used as the N-layer material.

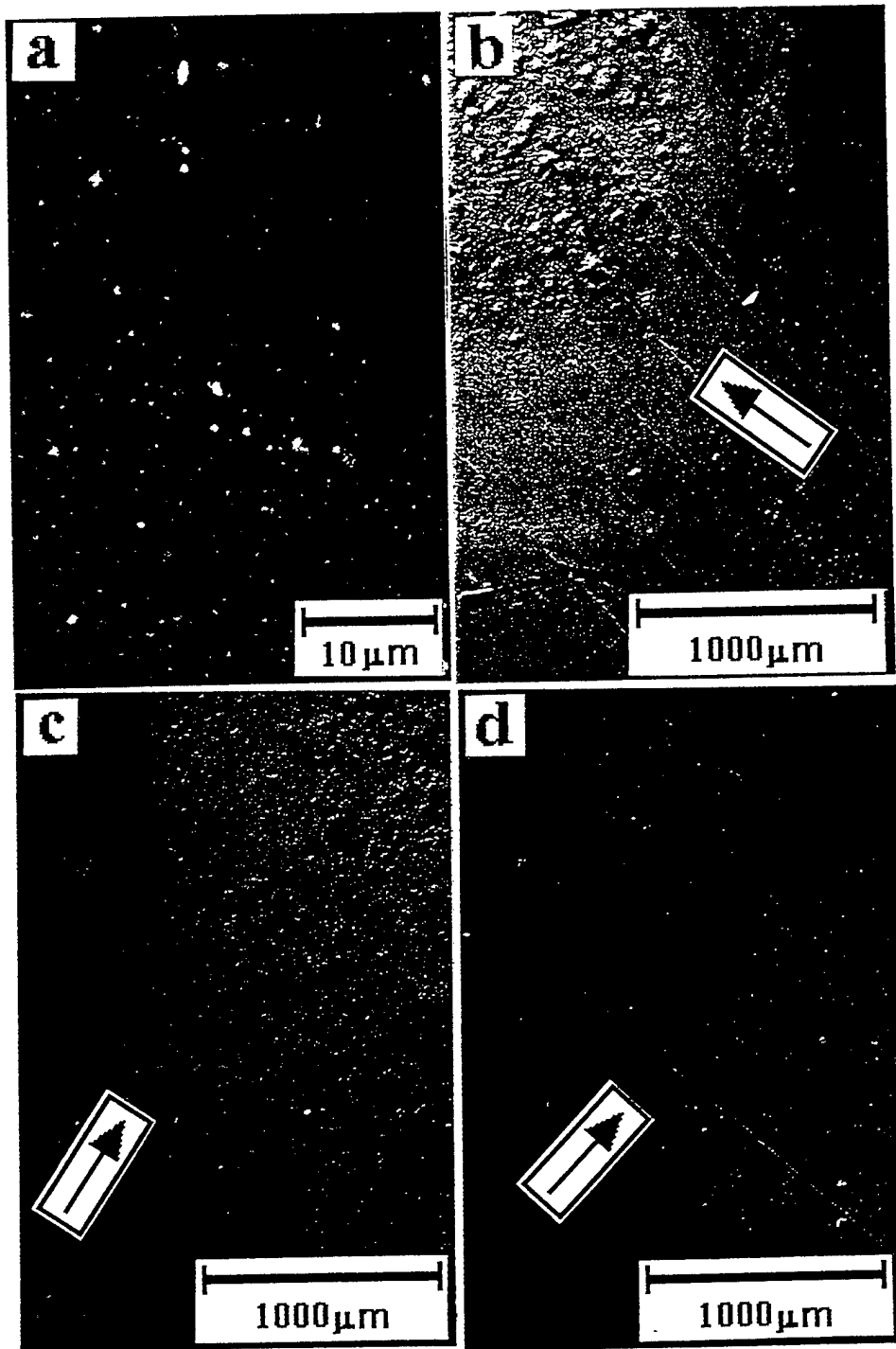
FIG. 12. Performance characteristics for an edge-geometry SNS dc SQUID (10  $\mu\text{m}$  for each junction) prepared using  $\text{YBa}_2\text{Cu}_3\text{O}_{7-\delta}$  as electrodes with 22 nm  $\text{Pr}_{0.4}\text{Gd}_{0.2}\text{Ca}_{0.4}\text{Ba}_{1.6}\text{La}_{0.4}\text{Cu}_3\text{O}_{7-\delta}$  as a N-layer barrier. The devices was operated at 75.5K. Shown are the a) current vs. voltage characteristics and b) voltage modulation vs. magnetic flux characteristics of the SQUID.

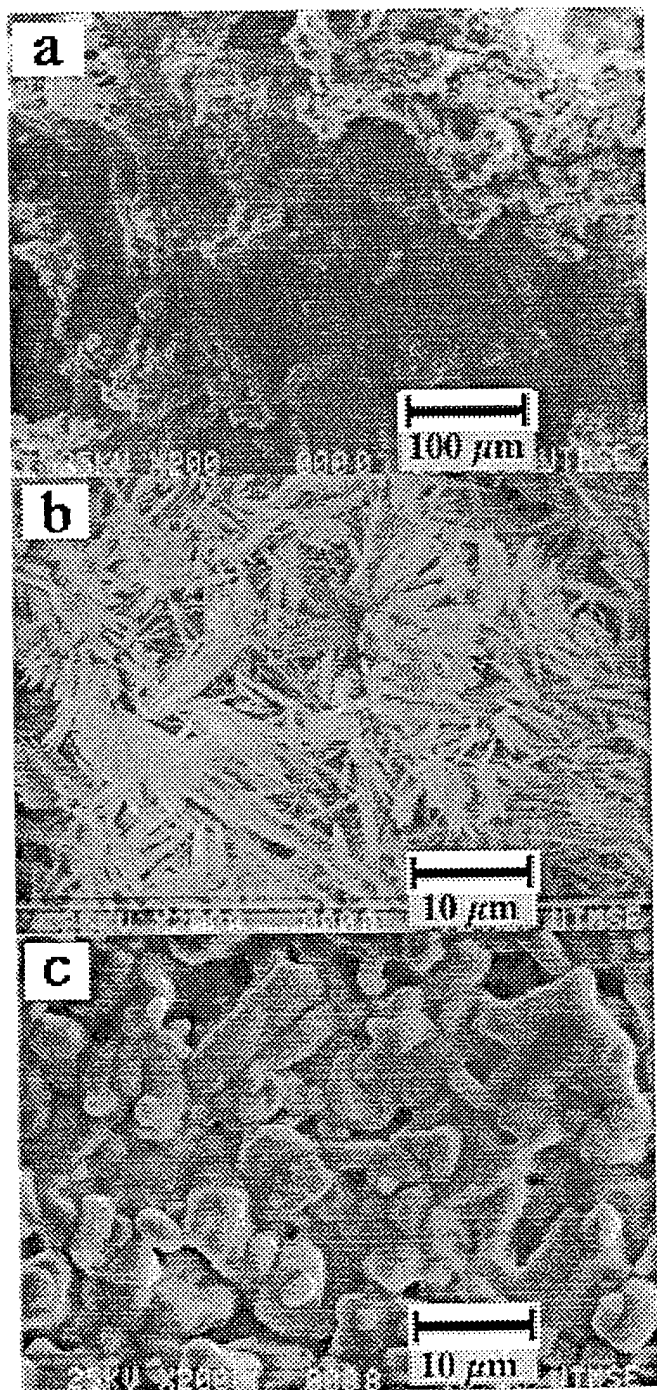


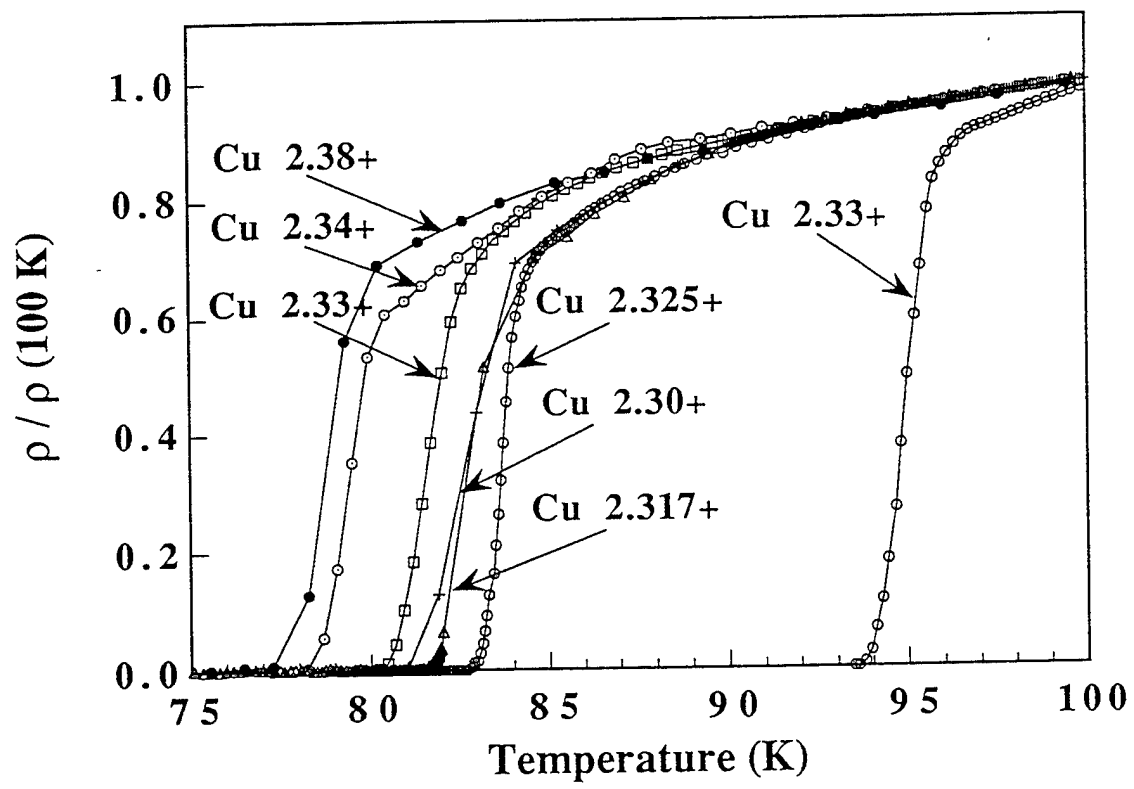


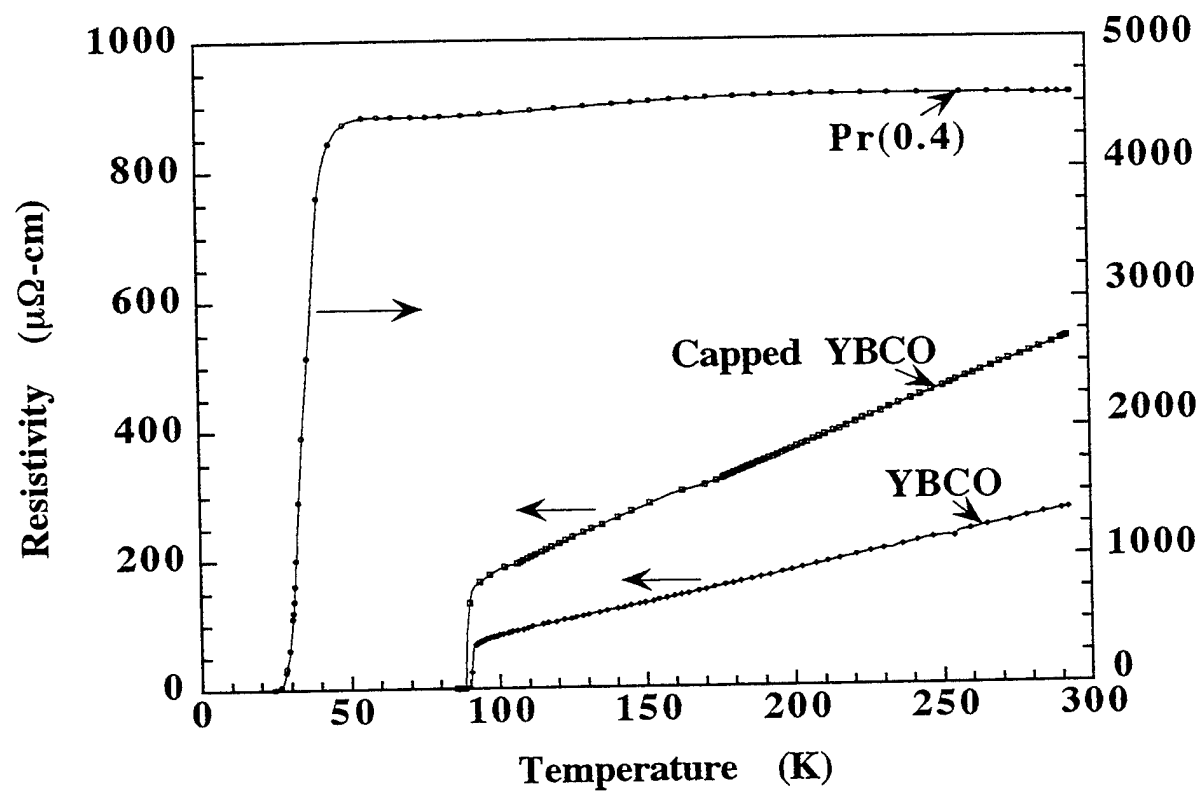


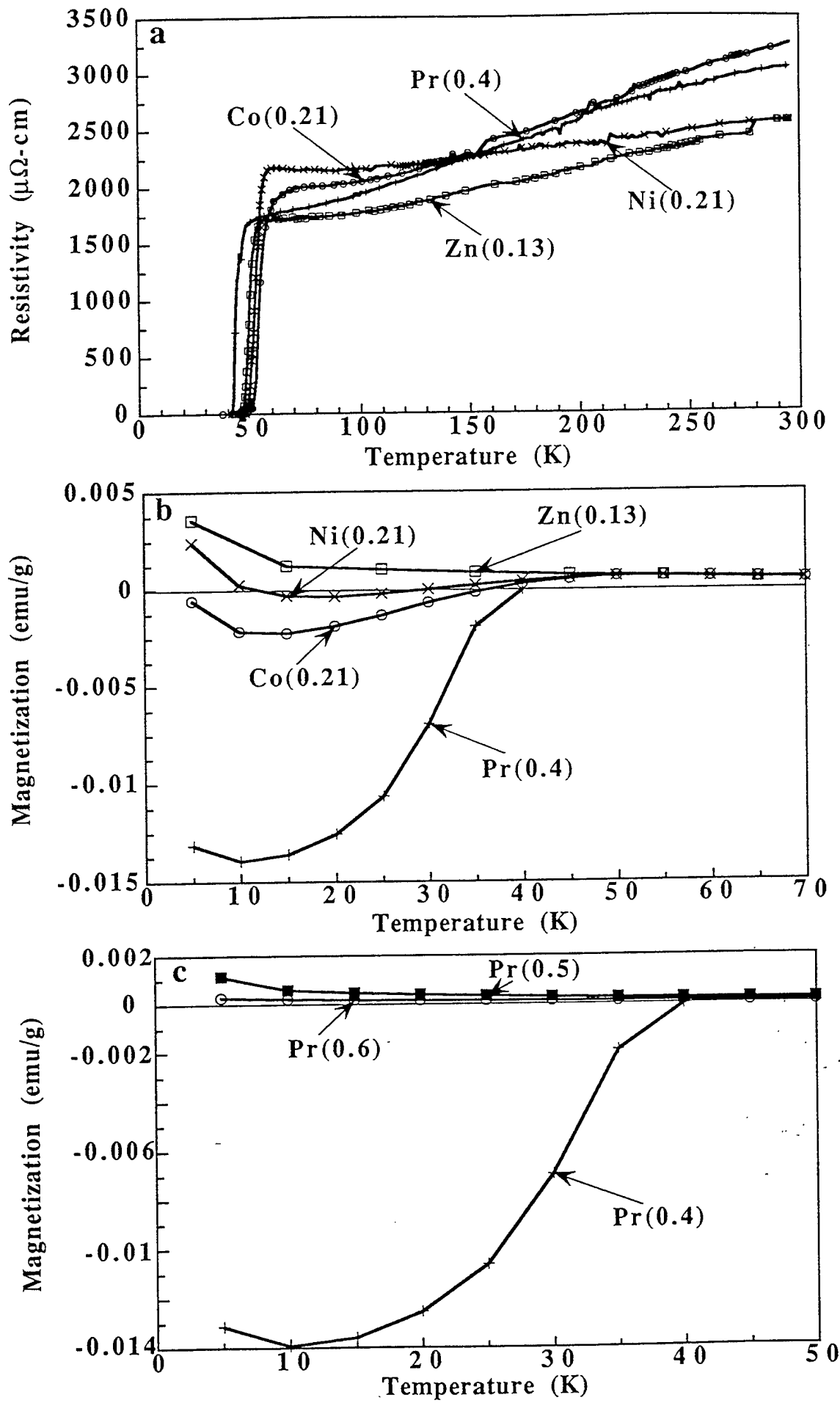


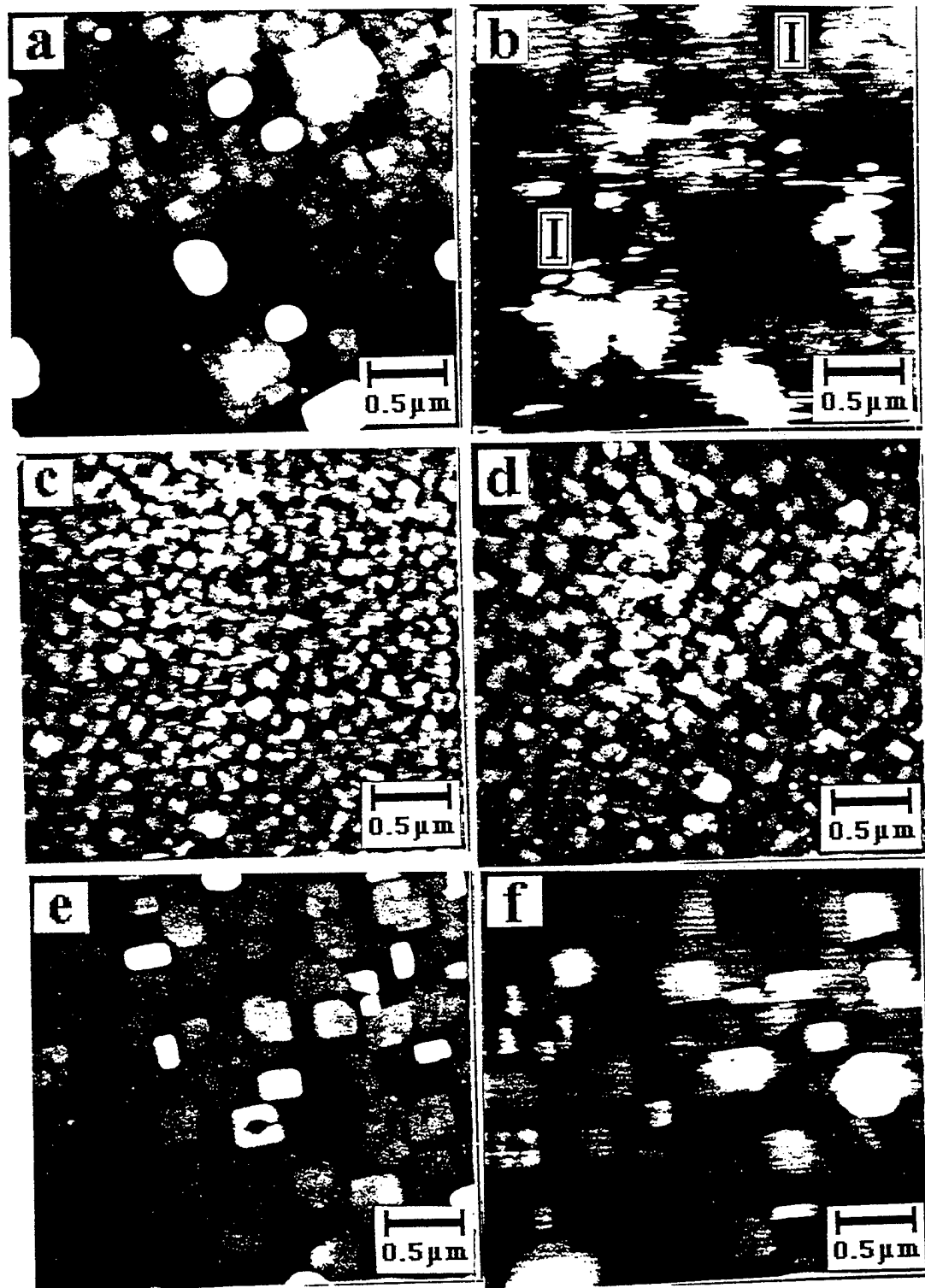


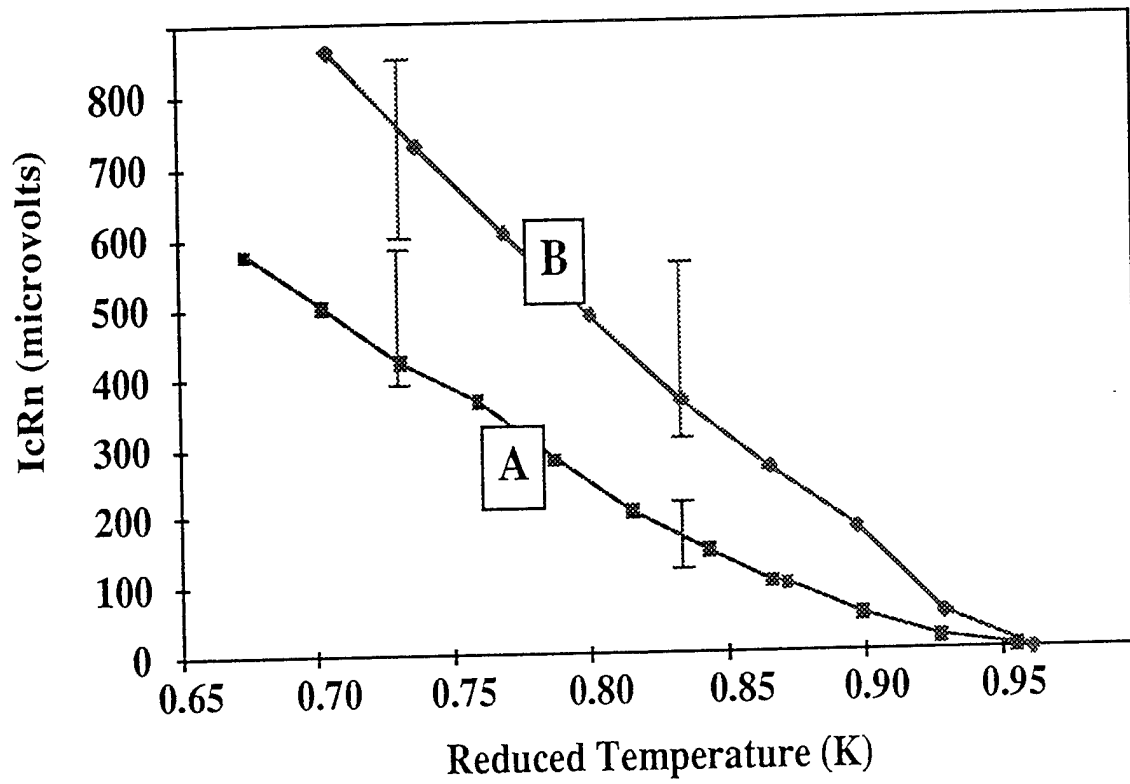


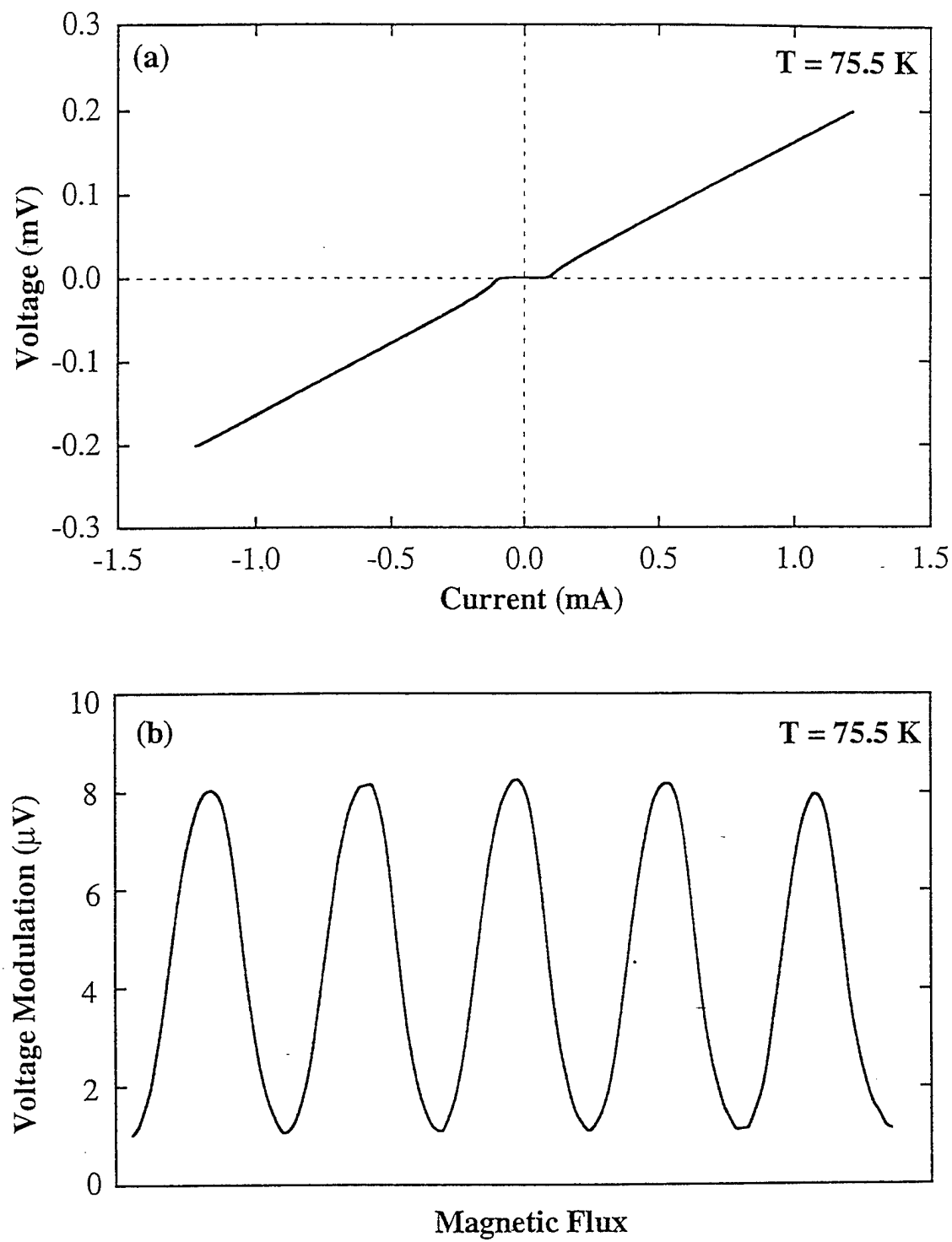












## High-Resistance SNS Edge Junctions

Brian D. Hunt, Martin G. Forrester, John Talvacchio, and Robert M. Young  
Northrop Grumman Science and Technology Center, Pittsburgh, PA 15235

**Abstract**—HTS SFQ digital circuit applications require high resistance HTS Josephson junctions. We have investigated the factors affecting the resistance of SNS edge junctions which use Co-doped Y-Ba-Cu-O as the normal metal layer. Several parameters are found to have a surprisingly large effect on device resistance. Controlling these factors has enabled the fabrication of high-quality, high-resistance ( $\approx 1 \Omega$ ) SNS edge junctions with  $1-\sigma I_c$  spreads down to 10% and critical currents and  $I_c R_n$  products suitable for SFQ digital applications.

### I. INTRODUCTION

High Temperature Superconductor (HTS) digital circuit applications based on Single Flux Quantum (SFQ) logic require the fabrication of high quality Josephson junctions in a multilevel epitaxial process. One HTS junction technology of particular interest has been edge-geometry superconductor/normal-metal/superconductor (SNS) weak links with  $\text{YBa}_2\text{Cu}_{3-x}\text{Co}_x\text{O}_7$  (Co-doped YBCO) as the normal metal interlayer ("N-layer"). Good progress has been made in integrating Co-YBCO edge junctions with superconducting groundplanes[1]-[4], but further improvements are needed to build practical digital circuits. In particular, SFQ circuits require junctions with high critical-current - normal-state-resistance ( $I_c R_n$ ) products ( $> 300 \mu\text{V}$ ), and tight critical current spreads ( $I_c 1-\sigma < 10\%$ ). SFQ design constraints on  $I_c R_n$  products and thermal noise considerations also point towards SNS critical currents of  $\approx 500 \mu\text{A}$  at 65 K. The bounds on  $I_c R_n$  and  $I_c$  indicate that device resistances greater than  $\approx 0.5 \Omega$  are needed for functional SFQ circuits.

The resistance of an SNS junction is determined by the sum of the resistance of the normal metal layer and the interface resistances. In the "ideal" case of zero interface resistances we can estimate the device resistance for typical device cross-sectional areas ( $A \approx 4 \mu\text{m}$  wide by  $0.2 \mu\text{m}$  thick), normal metal resistivities ( $\rho_n \approx 250 \mu\Omega\text{-cm}$  for  $\text{YBa}_2\text{Cu}_{2.8}\text{Co}_{0.2}\text{O}_7$  at 65K), and normal metal thicknesses ( $L = 100 \text{ \AA}$ ):  $R_n = \rho_n L / A \approx 0.03 \Omega$ . It is apparent that SNS devices without significant interface resistance are unsuitable for SFQ applications. Note that inductance constraints make smaller devices undesirable, while higher resistivity N-layers would have shorter normal metal coherence lengths,  $\xi_n$ , and smaller  $I_c R_n$  products.

Increasing SNS device resistances to a practical level requires the addition of interface resistance without significant degradation of the inherent  $I_c R_n$  product, which is possible through the incorporation of inhomogeneous interface resistance to reduce the effective device area [1]. We have found that a number of factors can dramatically affect SNS device resistances, while preserving SFQ-compatible  $I_c R_n$  products in some cases. These factors include the base electrode edge angle, the base electrode material, and the deposition parameters of the normal metal and counterelectrode.

### II. FABRICATION DETAILS

Details of our SNS junction fabrication process have been described previously [1],[3],[4], but a brief summary will be given here. Base electrode YBCO films are deposited by off-axis sputtering or pulsed laser deposition (PLD), typically on a  $\text{CeO}_2$  or  $\text{SrTiO}_3$  (STO) buffer layer and with a  $\text{CeO}_2$  or STO cap. Our PLD-deposited base electrodes are often La-doped, ( $\text{YBa}_{2-x}\text{La}_x\text{Cu}_3\text{O}_7$  with  $x=0.025-0.05$ ) because we have found that a small amount of La can help eliminate  $a$ -axis formation [3]. The base electrode edges are patterned using reflowed photoresist and Ar ion milling with rotation. An Ar/O<sub>2</sub> mixture is sometimes used during milling to adjust the edge angle.

Although some groups have reported roughening of annealed YBCO edges [5],[6], we see no evidence for this effect with our own process. Fig. 1 shows an atomic force microscope (AFM) scan of a  $\text{NdGaO}_3/\text{CeO}_2/\text{La}-\text{YBCO}/\text{STO}$  base electrode edge after Ar ion mill patterning at 300 eV followed by a 100 eV *in-situ* Ar ion cleaning step. The pictured edge was annealed at  $\approx 805^\circ\text{C}$  for 15 minutes in  $\text{O}_2$  to simulate the typical edge treatment just before normal metal and counterelectrode growth. The RMS roughness measured on the edge is approximately 8 Å both before and after annealing. Possible differences between our process and those used by groups reporting rough edges include our use of tapered resist milling masks[6], and lower temperature edge annealing [5].

Recently we have also investigated Br etching for edge cleaning [7]. The etching is typically done in a 0.3% Br in methanol solution for 10-30 sec. Initial results indicate that Br etching is an effective cleaning treatment. Following edge cleaning, the  $\text{Co}_{0.2}\text{-YBCO}$  and counterelectrode are deposited and patterned, and the devices are ready for bonding and testing.

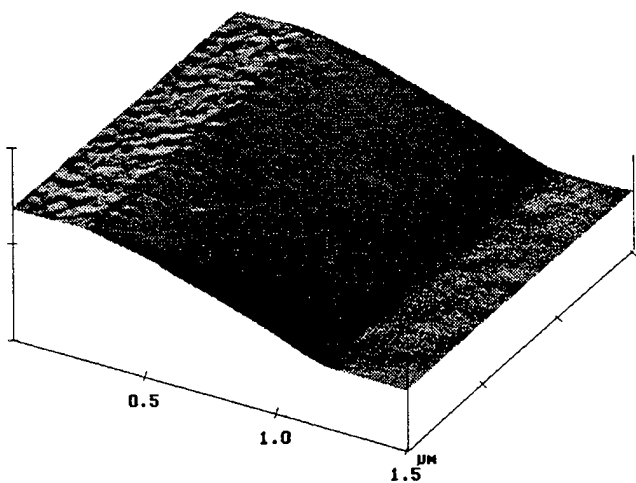


Fig. 1. AFM scan of La-YBCO base electrode edge after annealing at 805°C for 15 min. The RMS roughness on the edge is 8 Å. The z-range is 0.5  $\mu\text{m}$  per div.

### III. RESULTS

#### A. Factors Affecting SNS Device Resistance

Because of the importance of high resistance SNS junctions for SFQ applications, we undertook a study of some of the parameters which could affect device resistance. Here we will concentrate on three factors that have a strong influence on SNS edge junction resistance: the base electrode edge angle, the base electrode material, and the deposition conditions of the normal metal and counterelectrode.

To study the effect of edge angle, we fabricated a series of SNS junctions on base electrodes with edge angle ranging from  $\approx 12^\circ$  to  $36^\circ$  (measured from the horizontal). These junctions showed a wide range of resistances and electrical behavior [3]. We observed that devices with relatively shallow edges ( $<15^\circ$ ) generally exhibited *void formation* in the counterelectrode (and possibly the normal metal layer) at the base electrode edges. The tapered-edge SNS junctions also showed "flux-flow" I-V characteristics and nonideal magnetic field modulation of the critical currents, consistent with nonuniform conduction through the devices. In addition, we found that the device resistances correlated with the base electrode edge angles, with  $R_{nA}$  products ranging from approximately  $50 \Omega\text{-}\mu\text{m}^2$  for  $11.5^\circ$  edges to less than a few  $\Omega\text{-}\mu\text{m}^2$  for edge angles greater than  $25^\circ$ . The SNS junctions produced on steeper edges also exhibited much more ideal electrical behavior, as will be seen below. The void formation, the magnetic field modulation data, and the high  $R_{nA}$  products associated with the shallow-edge devices are all consistent with a reduction in the effective area for these junctions.

We have also found that the base electrode material and deposition technique can have a strong effect on SNS device resistances. We see significant differences in  $R_{nA}$  products for junctions fabricated with PLD YBCO, sputtered YBCO, and PLD La-doped YBCO base electrodes. Table I presents 77 K data for ion-mill-cleaned PLD  $\text{YBa}_{1.95}\text{La}_{0.05}\text{Cu}_3\text{O}_7$  and PLD  $\text{YBa}_2\text{Cu}_3\text{O}_7$  base electrodes with  $30^\circ$  edge angles, 50 Å  $\text{Co}_{0.2}\text{-YBCO}$  normal metal layers, and two different PLD growth conditions for the normal metal and counterelectrode. For either growth condition we see more than an order of magnitude reduction in the  $R_{nA}$  product for the YBCO base electrode relative to the La-YBCO base electrode, with an even larger associated increase in current density. Sputtered base electrodes typically exhibit  $R_{nA}$  products  $\approx 0.3 - 0.7$  times smaller than PLD La-YBCO base electrodes.

Table I also illustrates the dramatic effect that the normal metal and counterelectrode growth can have on SNS device resistances. Previous work had suggested that using oxygen-argon gas mixtures during PLD could reduce the number of particles in YBCO films [8]. We discovered that high pressure  $\text{O}_2/\text{Ar}$  growth of the N-layer and counterelectrode resulted in a large reduction in  $R_{nA}$  and increase in  $J_c$  relative to our standard growth conditions of 600 mT  $\text{O}_2$  for the N-layer and 400 mT  $\text{O}_2$  for the counterelectrode. The lowest  $R_{nA}$  products are obtained for the combination of PLD YBCO base electrodes and 800 mT normal metal and counterelectrode growth. In this case,  $R_{nA} = 0.03 \Omega\text{-}\mu\text{m}^2$ , which is within a factor of  $\approx$  two of the zero-interface-resistance limit. The small resistances seen in this case may be due in part to the better edge coverage we generally see for higher pressure deposition [3].

#### B. SNS Current-Voltage Characteristics

Fig. 2 shows the I-V characteristics at 65 K for nineteen 4- $\mu\text{m}$ -wide SNS edge junctions with 50 Å Co-doped-YBCO normal metal layers. For this chip the

TABLE I  
 $R_{nA}$  AND  $J_c$  DEPENDENCE ON FABRICATION PARAMETERS

Base electrode	$R_{nA} (\Omega\text{-}\mu\text{m}^2)$	$J_c (\text{A}/\text{cm}^2)$	N&C growth
PLD La-YBCO	4.56	$\approx 2 \times 10^2$	Standard <sup>a</sup>
PLD YBCO	0.42	$2.9 \times 10^4$	Standard <sup>a</sup>
PLD La-YBCO	0.76	$4.4 \times 10^3$	800 mT $\text{O}_2:\text{Ar}$ <sup>b</sup>
PLD YBCO	0.03	$6.5 \times 10^5$	800 mT $\text{O}_2:\text{Ar}$ <sup>b</sup>

Average SNS chip data at 77 K showing dependence of  $R_{nA}$  and  $J_c$  on base electrode material and the normal metal (N) and counterelectrode (C) growth conditions. The N-layers are 50 Å of Co-YBCO and all base electrodes have  $\text{CeO}_2$  buffer and cap layers. Ion mill edge cleaning was used for all cases.

<sup>a</sup>Standard PLD N&C growth conditions are: N-layer - 805°C, 600 mT  $\text{O}_2$ ; counterelectrode - 805°C, 400 mT  $\text{O}_2$ .

<sup>b</sup>The  $\text{O}_2:\text{Ar}$  ratio is 1:1.

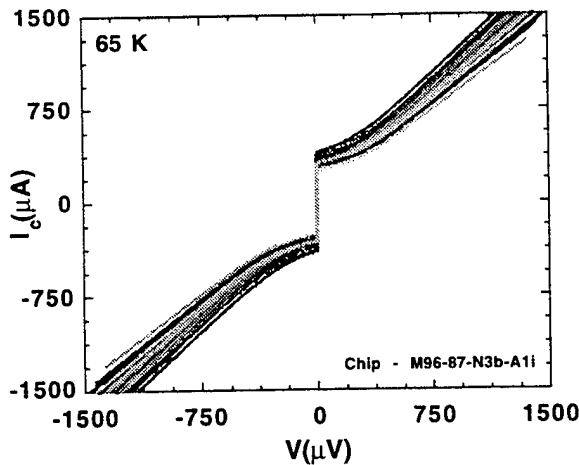


Fig. 2. I-V data at 65 K for a chip with junction parameters suitable for SFQ logic. There are nineteen 4- $\mu\text{m}$ -wide junctions with 50 $\text{\AA}$  Co-doped YBCO interlayers and an average resistance of 0.97  $\Omega$  ( $1-\sigma = 6\%$ ). The average  $I_c$  is 327  $\mu\text{A}$  ( $1-\sigma = 13\%$ ) and the average  $I_c R_n$  product is 315  $\mu\text{V}$  ( $1-\sigma = 9\%$ ).

base electrode YBCO-STO bilayer was sputter deposited, the edges were cleaned by Br etching, and the normal metal and counterelectrode were grown by PLD using the standard growth conditions described above. The average device parameters and spreads for these junctions were:  $J_c = 4.1 \times 10^4 \text{ A/cm}^2$ ,  $1-\sigma = 13\%$ ;  $I_c R_n = 315 \mu\text{V}$ ,  $1-\sigma = 9\%$ ; and  $R_n A = 0.77 \Omega \cdot \mu\text{m}^2$ ,  $1-\sigma = 6\%$ . The average values of critical current and resistance were 327  $\mu\text{A}$  and 0.97  $\Omega$ . The combination of large resistances and  $I_c R_n$  products, tight  $J_c$  spreads, and small, SFQ-compatible critical currents seen on this chip is an important demonstration for the feasibility of HTS SFQ digital circuits.

#### IV. DISCUSSION

We have found that several factors have a significant effect on SNS edge junction resistance, including the base electrode edge angle, the base electrode material, and the deposition parameters of the normal metal and counterelectrode. We believe these factors are primarily affecting the interface resistances of the devices, rather than the "bulk" properties of the normal metal interlayer, because high resistivity N-layers would have shorter coherence lengths and smaller  $I_c R_n$  products (barring resonant tunneling effects). While adding interface resistance to an SNS device cannot increase the inherent  $I_c R_n$  product [9], reducing the active area of the device through an inhomogeneous interface resistance can increase the resistance without reducing  $I_c R_n$  [1]. Because SFQ circuits work at an approximately fixed current level, adding interface resistance in this way can increase the *practical*  $I_c R_n$  product.

A variety of evidence suggests that the resistance variations are, in fact, due primarily to effective area

variations of the active area in the junctions. This evidence includes the observation of voids for shallow edges, as well as some data not presented here [10]: the correlation between  $J_c$  and  $R_n A$  spreads; the scaling behavior of  $J_c$  as a function of  $R_n A$ ; and the scaling of  $R_n A$  as a function of N-layer thickness. The nearly ideal  $I_c(B)$  modulation [1] and the tight  $I_c$  spreads indicate that the area inhomogeneity is on a fine scale relative to the size of the junctions. While the detailed nature of the interface resistance is not understood at this point, we have demonstrated control of SNS device resistances over a wide range. We have also shown that these techniques can be used to fabricate high-quality, high-resistance SNS edge junctions with properties suitable for SFQ circuits.

#### ACKNOWLEDGEMENT

We would like to acknowledge the assistance of J. C. Brown, G. Faychak, G. Madia, D. Matuza, R. Nye, S. Pieseski, and J. Uphoff.

#### REFERENCES

- [1] B. D. Hunt, M. G. Forrester, J. Talvacchio, J. D. McCambridge, and R. M. Young, "High-T<sub>c</sub> SNS edge junctions and SQUIDs with integrated groundplanes" *Appl. Phys. Lett.* vol. 68, pp. 3805-3807, June 1996.
- [2] W. H. Mallison, S. J. Berkowitz, A. S. Hirahara, M. J. Neal, and K. Char, "A multilayer YBCO Josephson junction process for digital circuit applications" *Appl. Phys. Lett.* vol. 68, pp. 3808-3810, June 1996.
- [3] B. D. Hunt, M. G. Forrester, J. Talvacchio, R. M. Young, and J. D. McCambridge, "HTS SNS edge junctions with integrated YBCO groundplanes", *IEEE Trans. on Applied Superconductivity*, June 1997, in press.
- [4] M. G. Forrester, B. D. Hunt, J. Talvacchio, R. M. Young, and J. D. McCambridge, "Multilayer edge SNS SQUIDs for digital circuits", *IEEE Trans. on Applied Superconductivity*, June 1997, in press.
- [5] C. Horstmann, P. Leinenbach, A. Engelhardt, R. Dittmann, U. Memmert, U. Hartmann, A.I. Braginski, "Correlation between ramp morphology and properties of ramp-type junctions", *IEEE Trans. on Applied Superconductivity*, June 1997, in press.
- [6] D.H.A. Blank, G.J.H.M. Rijnders, R.M.H. Bergs, M.A.J. Verhoeven, and H. Rogalla, "Characterization of ramp-type YBCO junctions by AFM", *IEEE Trans. on Applied Superconductivity*, June 1997, in press.
- [7] R.P. Vasquez, B.D. Hunt, and M.C. Foote, "Nonaqueous chemical etch for  $\text{YBa}_2\text{Cu}_3\text{O}_{7-x}$ ", *Appl. Phys. Lett.* vol.53, pp. 2692-2694, December 1988.
- [8] A. Kuhle, J.L. Skov, S. Hjorth, I. Rasmussen, and J.B. Hansen, "Smooth  $\text{YBa}_2\text{Cu}_3\text{O}_{7-x}$  thin films prepared by pulsed laser deposition in  $\text{O}_2/\text{Ar}$  atmosphere", *Appl. Phys. Lett.* vol.64, pp. 3178-3180, June 1994.
- [9] K. A. Delin and A. W. Kleinsasser, "Stationary Properties of High T<sub>c</sub> Proximity Effect Josephson Junctions", *Supercond. Sci. Technol.*, vol. 9, p. 227, 1996.
- [10] B. D. Hunt, M. G. Forrester, J. Talvacchio, and R. M. Young, unpublished.

## HIGH-RESISTANCE HTS EDGE S-N-S JUNCTIONS FOR DIGITAL CIRCUITS

M. G. Forrester, B. D. Hunt, J. Talvacchio, and R. M. Young  
Northrop Grumman Corporation  
Science & Technology Center  
1350 Beulah Road, Pittsburgh, PA 15235

## ABSTRACT

Current HTS circuit process development focuses mainly on SNS junctions, in contrast to the SIS junctions used in the more well-developed low temperature superconducting (LTS) technology. Despite the fact that S-N-S junctions have intrinsically low resistance we have found that it is possible to fabricate HTS S-N-S edge junctions with sufficiently high resistance for digital circuits ( $\sim 1 \Omega$ ), and with critical current spreads as low as 10%, one-sigma. We argue that one significant factor in producing such high resistances is a reduction in the effective *area* of the junctions.

## INTRODUCTION

Due to the difficulties inherent in fabricating S-I-S Josephson junctions based on HTS, a great deal of effort has been directed to developing S-N-S junctions, which have more relaxed materials requirements. In particular, edge (or ramp) geometry junctions, based on c-axis oriented YBCO films, have been the vehicle for exploration of a number of junction interlayers ("N-layers"). Our own efforts to develop HTS Single Flux Quantum (SFQ) digital circuits have emphasized the use of Co-doped YBCO. We, and colleagues at Conductus, have demonstrated the integration of these junctions with an HTS ground plane, producing the low inductance structures required for SFQ circuits [1-3], and we have used such a process to demonstrate simple HTS SFQ circuits incorporating up to ten junctions [4].

The use of Co-doped YBCO, and related materials, was motivated by the desire to minimize inhomogeneity at the S-N interfaces, which may be due to extrinsic effects such as etch damage, or to more intrinsic factors such as lattice-constant or thermal expansion mismatch, and which is thought to lead to lack of reproducibility and uniformity in junction parameters [5]. Since the doped YBCO N-layers are structurally well-matched to the YBCO electrodes the resulting junctions may be more ideal in that their resistance is dominated by the resistance of the N-layer material itself, rather than an interface resistance, and thus the junctions may be expected to be more reproducible.

In practice this approach leads to lower junction resistances ( $\lesssim 0.1 \Omega$ ) than is desirable for digital circuits ( $\sim 1 \Omega$ ), however we have found that a number of fabrication parameters can have a large effect on the junction resistance, so that we can obtain a wide range of resistances while still achieving good reproducibility. While we do not yet understand the detailed mechanisms by which these fabrication parameters affect junction resistance, nor in fact what all the important parameters are, our data suggest that one important factor is changes in the effective area of the junctions.

## JUNCTION FABRICATION

We have previously described the details of our junction fabrication process [1,6]. Briefly, films are deposited by either off-axis RF magnetron sputtering, at typical deposition temperatures of 780°C, or by on-axis pulsed laser deposition (PLD), typically at 805°C. The edge junction base electrode is capped by an epitaxial layer of either SrTiO<sub>3</sub> or CeO<sub>2</sub>, and the

base electrode edges are etched with a 150eV-300eV Ar<sup>+</sup> source. An important aspect of the PLD process is that we sometimes use YBCO doped with a small amount of La (YBa<sub>1.95</sub>La<sub>0.05</sub>Cu<sub>3</sub>O<sub>x</sub>), which was initially chosen because it simplified the elimination of *a*-axis grains.

While several factors influence the junction resistance we focus here on three: base electrode material and deposition technique; normal layer deposition conditions; and base electrode edge angle.

## RESULTS

### Effect of Base Electrode Material

Fig. 1 shows a set of current-voltage characteristics for a set of SFQ-compatible junctions utilizing sputtered YBCO base electrodes, exhibiting relatively narrow critical current spreads. Junction parameters are given in the caption. Of particular note is the average resistance,  $R_N = 0.97 \Omega$ , which is about sixty times higher than the nominal resistance expected from the resistance of the N-layer itself, which, assuming our measured a-b resistivity of 250  $\mu\Omega\text{-cm}$ , is 0.016  $\Omega$ . In the case of PLD La-YBCO base electrodes we typically observe even higher resistances, sometimes as high as 100 $\Omega$ , while PLD YBCO base electrodes typically lead to significantly lower resistance. Results for the dependence of  $R_{NA}$  on N-layer thickness,  $d_N$ , are shown in Fig. 2 for these three base electrode materials, where each data point represents an average over at least 18 junctions. Despite the scatter in the data it is apparent that the high junction resistances, in the case of PLD La-YBCO and sputtered YBCO base electrodes, are associated with a high effective resistivity, or a reduced effective area. According to conventional proximity effect models, such a high resistivity would lead to an extremely short normal metal coherence length, inconsistent with the observed magnitudes of critical current density. We therefore suggest that reduced area is the explanation. Also, for the two high resistance cases, it is fairly clear that the normal resistance is not dominated by a *series* resistance associated with the interface, since there is no significant vertical offset in  $R_{NA}$  versus  $d_N$ .

### Effect of N-layer Deposition Conditions

For a given base electrode material we have found that a change in the deposition conditions of the normal layer can have a large effect on  $R_N$  and  $J_c$ . For example, for a PLD YBCO base electrode, increasing the deposition pressure from 400 mT to 800 mT led to a factor of ten reduction in junction resistance (and a factor of more than 100 increase in  $J_c$ ) so that we obtained junction resistances as low as 0.03  $\Omega$  for a 50  $\text{\AA}$  Co-YBCO N-layer, which is only a factor of two higher than the expected intrinsic resistance. We have not yet studied this case in detail, since the resulting junctions have too low resistance to be useful for digital applica-

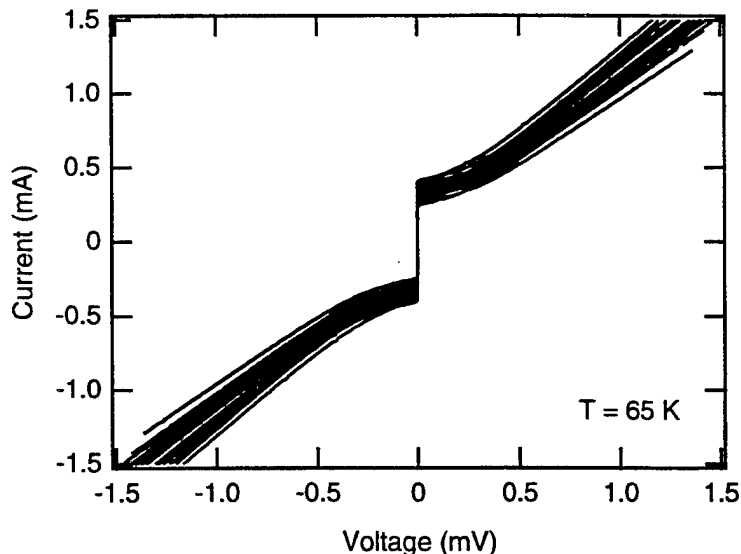


Fig. 1 – Current-Voltage characteristics for a set of 19 edge S-N-S junctions with parameters suitable for digital logic. Average parameters are:  $J_c = 4.1 \times 10^4 \text{ A/cm}^2$ ,  $R_{NA} = 7.7 \times 10^9 \Omega\text{-cm}^2$ ,  $R_N = 0.97 \Omega$ ,  $I_c R_N = 315 \mu\text{V}$ ,  $J_c$  spread (1-sigma) = 13%,  $R_N$  spreads (1-sigma) = 6%. The N-layer was 50 $\text{\AA}$  of PLD-deposited YBa<sub>2</sub>Cu<sub>2.79</sub>Co<sub>0.21</sub>O<sub>x</sub>, and the base electrode 2000  $\text{\AA}$  of sputtered YBCO.

tions, but we suggest that the increased pressure typically leads to better coverage, in the case of the base electrode by the normal layer, and thus effective area more closely approaching the nominal junction area.

For the cases discussed so far we infer that the area inhomogeneity is on a length scale small compared to the nominal junctions dimensions, because the measured dependence of critical current on magnetic field,  $I_c(B)$ , is usually quite close to the behavior expected for a uniform junction. However, the fact that the minima in  $I_c(B)$  are sometimes lifted above zero is consistent with nonuniform supercurrent conduction. The fact that we are able to observe critical current spreads as narrow as 10% (one-sigma) also argues against more gross area fluctuations.

#### Effect of Base Electrode Edge Angle

For both of the above cases the inferred effective area reduction can not be directly observed by any of our readily available analytical techniques. However, when we fabricate base electrode edges with angles much less than our standard 20–30°, measured with respect to the substrate, we directly observe that *voids* form in the normal and/or counterelectrode films grown over this shallow edge. While the reasons for this poor growth are currently unknown the effects are readily measurable in the electrical characteristics of the resulting junctions. For

example,  $I_c(B)$  is no longer ideal, but rather is representative of a small number of parallel weak links. In addition, the junction resistance is considerably higher than for steeper (~30°) edges with better coverage, as illustrated in Fig. 3.

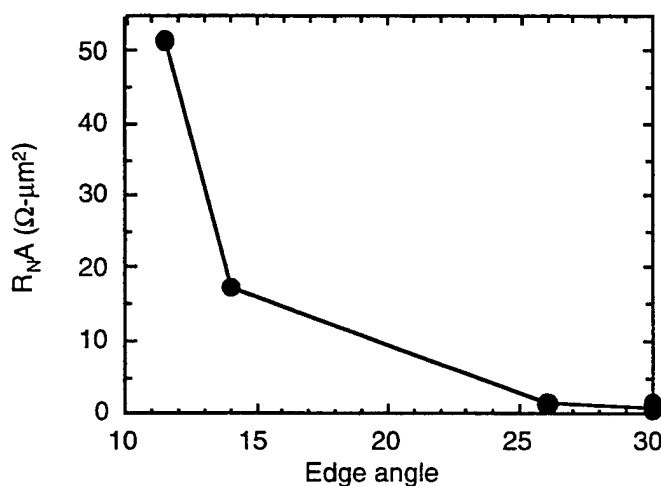


Fig. 3 – Junction resistance versus edge angle for PLD-deposited normal layer and counterelectrode. The increase in resistance is due to gross problems in coverage by the normal layer and/or counterelectrode.

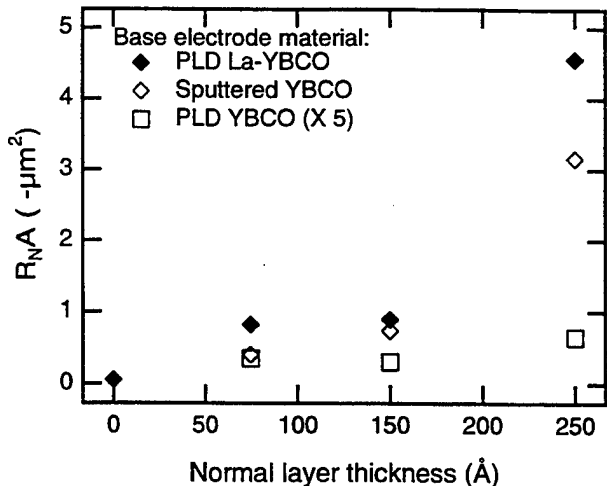


Fig. 2 – Junction resistance (times nominal junction area) versus N-layer thickness for three different base electrode materials, illustrating the broad range of resistances obtained. Data for PLD YBCO are multiplied by a factor of five to improve readability.

#### DISCUSSION

We have argued that, for our HTS edge junctions, reduction in the effective area is at least partly responsible for the observed high junction resistances. This area inhomogeneity appears, in many cases, to be on a sufficiently fine length scale that the junctions behave relatively ideally in a magnetic field, and that relatively good critical current reproducibility is achievable. Further evidence that the

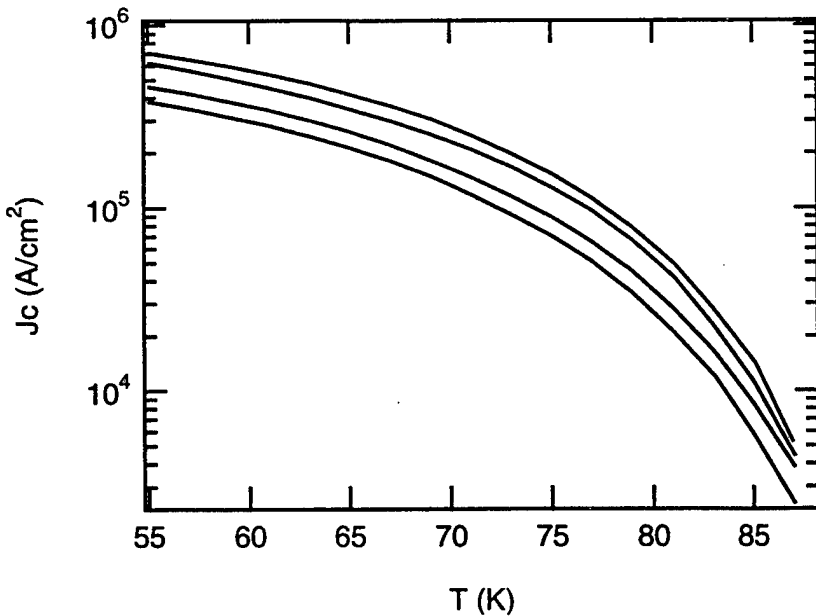


Fig. 4 – Critical current density versus temperature for four junctions on a chip. The curves differ mainly in their vertical displacement on a semi-log plot, consistent with effect area differences between the junctions.

measured  $I_c$  spreads are influenced strongly by area fluctuations is provided by the temperature dependence of  $I_c(T)$  for different junctions on a chip. As shown in Fig. 4, we usually observe that semi-log plots of  $I_c(T)$  show the data for different junctions to differ mainly in their vertical offset, which is consistent with different areas rather than, for example, different N-layer thicknesses or normal-metal coherence lengths.

We do not yet know whether this inhomogeneity, which may be different for quasiparticle- and supercurrents, will prevent us from obtaining the level of  $I_c$  control required for complex digital circuits, although we find the results to date quite encouraging.

## REFERENCES

1. Hunt, B.D., Forrester, M.G., Talvacchio, J., McCambridge, J.D., and Young, R.M. (1996) High- $T_c$  superconductor/normal-metal/superconductor edge junctions and SQUIDs with integrated groundplanes, *Appl. Phys. Lett.* **68**, 3805–3807.
2. Forrester, M.G., Hunt, B.D., Talvacchio, J., Young, R.M., and McCambridge, J.D. (1996) Multilayer edge SNS SQUIDs for digital circuits, to be published in *IEEE Transactions on Applied Superconductivity*, June 1997.
3. Mallison, W.H., Berkowitz, S.J., Hirahara, A.S., Neal, M.J., and Char, K. (1996) A multilayer  $\text{YBa}_2\text{Cu}_3\text{O}_x$  Josephson junction process for digital circuit applications, *Appl. Phys. Lett.* **68**, 1835–1837.
4. McCambridge, J.D., Forrester, M.G., Miller, D.L., Hunt, B.D., Przybysz, J.X., Talvacchio, J., and Young, R.M. (1996) Multilayer HTS SFQ analog-to-digital converters, to be published in *IEEE Transactions on Applied Superconductivity*, June 1997.
5. Char, K., Antognazza, L. and Geballe, T.H. (1994) Properties of YBCO/ $\text{YBa}_2\text{Cu}_{2.79}\text{Co}_{0.21}\text{O}_{7-x}$ /YBCO edge junctions, *Appl. Phys. Lett.* **65**, 904–906.
6. Hunt, B.D., Forrester, M.G., Talvacchio, J., Young, R.M., and McCambridge, J.D. (1996) High- $T_c$  SNS edge junctions with integrated  $\text{YBa}_2\text{Cu}_3\text{O}_x$  groundplanes, to be published in *IEEE Transactions on Applied Superconductivity*, June 1997.